

## Durham E-Theses

---

# *THE ENGINEERING BEHAVIOUR OF A WEAKLY BONDED SOIL INCLUDING THE UNSATURATED STATE*

Ali Rahman, Zulfahmi

### How to cite:

---

Ali Rahman, Zulfahmi (2008) *THE ENGINEERING BEHAVIOUR OF A WEAKLY BONDED SOIL INCLUDING THE UNSATURATED STATE*, Durham theses, Durham University. Available at Durham E-Theses Online: <http://etheses.dur.ac.uk/1352/>

### Use policy

---

The full-text may be used and/or reproduced, and given to third parties in any format or medium, without prior permission or charge, for personal research or study, educational, or not-for-profit purposes provided that:

- a full bibliographic reference is made to the original source
- a [link](#) is made to the metadata record in Durham E-Theses
- the full-text is not changed in any way

The full-text must not be sold in any format or medium without the formal permission of the copyright holders.

Please consult the [full Durham E-Theses policy](#) for further details.

---

Academic Support Office, Durham University, University Office, Old Elvet, Durham DH1 3HP  
e-mail: [e-theses.admin@dur.ac.uk](mailto:e-theses.admin@dur.ac.uk) Tel: +44 0191 334 6107  
<http://etheses.dur.ac.uk>





**THE ENGINEERING BEHAVIOUR OF  
A WEAKLY BONDED SOIL INCLUDING THE  
UNSATURATED STATE**

**ZULFAHMI ALI RAHMAN**

**BSc (HONS.) (UNIVERSITI KEBANGSAAN MALAYSIA), MSc  
(UNIVERSITY OF WALES CARDIFF)**

**USTINOV COLLEGE**

**SCHOOL OF ENGINEERING**

**DURHAM UNIVERSITY**



**A Thesis submitted for the degree of Doctor of Philosophy at  
Durham University**

**July 2008**

**17 DEC 2008**

The copyright of this thesis rests with the author or the university to which it was submitted. No quotation from it, or information derived from it may be published without the prior written consent of the author or university, and any information derived from it should be acknowledged.

## **STATEMENT OF COPYRIGHT**

The copyright of this thesis rests with the author. No quotation from it should be published in any form, including electronic and the internet, without the author's prior written consent. All information derived from this thesis must be acknowledged appropriately.

## **DECLARATION**

The work described in this thesis was carried out in the School of Engineering at the Durham University between January 2003 and June 2006. All the work was carried out by the author unless otherwise stated and has not previously been submitted for a degree at this or any other university.

## **FINANCIAL SUPPORT**

The financial support of the studies is fully supported by Human Resources Development (Science and Technology Division), Ministry of Science, Technology and Innovation Malaysia Fellowship.

# **ABSTRACT**

## **The Engineering Behaviour of a Weakly Bonded Soil including the Unsaturated State**

**Zulfahmi Ali Rahman**

**Durham University, 2008**

Testing of an artificially weakly bonded material has been carried out to help our understanding of the role of bonding in natural soils, such as tropical residual soils that usually bonded in nature and frequently exist in an unsaturated state. The use of artificial specimens allows reproducibility of bond strength, which is difficult to achieve with naturally bonded soils, such as residual soil. The artificial samples were prepared with void ratio of 0.6 by mixing sand and kaolin before firing at 500°C for 5 hours. A new technique for producing looser samples was also developed using coriander seeds. These artificial bonded samples are reproducible and are not age-dependent. The bond formed has many advantages over cement or other bonding agents that require a curing period and show a change in strength with time.

In order to observe the interaction between sand and kaolin, the thin sections of the samples were prepared and investigated under a microscope. Microscopic studies showed that the fired kaolin forms bridges between the sand grains, as well as coating the grains. The loose sample showed a very small amount of ash residue left after firing at high temperature.

The engineering behaviour of these artificially weakly bonded samples was investigated in triaxial tests. Destructured material (where the bonding was broken down) was also tested to provide a reference state for a comparison. Conventional drained and undrained triaxial compression tests were performed on artificially bonded and destructured samples in a saturated state. A series of constant water content tests were also carried out on artificially weakly bonded samples in an unsaturated state at various initial matric suctions.

The saturated behaviour of destructured and bonded samples was studied in order to understand the influence of bond structure and provide a useful reference for the interpretation of the unsaturated tests. The destructured samples showed no significant peak in  $q/p'$  ratio in comparison with the bonded samples. All bonded and destructured samples sheared at lower stresses sustained higher values of stress ratio than those sheared at higher confining pressure. The effect of bonding was clearly seen when comparing the stress ratio values between bonded and destructured materials. The bonded samples achieved a higher stress ratio values if compared with the destructured samples. However, with an increase in stress level, the bond strength decreases progressively at failure, therefore the peak in stress ratio dropped closer to that of the destructured material. A normalisation of the stress paths was performed in order to compare the results from different tests on bonded and destructured materials. The effect of bonding was evident from the normalised stress paths.

A series of constant water content tests were performed on unsaturated samples with suction ranging from zero up to 500kPa. The unsaturated samples were initially consolidated under mean net stresses of 50, 100 and 300kPa before shearing under constant water content conditions. The water retention curve (WRC) was determined for a drying path. It showed a very steep change at suction between 2 – 4kPa before flattened when the degree of saturation,  $S_r$ , dropped below 25%. During consolidation, samples experienced initial compression before levelled off with time. Samples with higher suction showed less compression in comparison to samples with lower suction. The matric suction for all samples, generally showed an initial decrease after applying a mean net stress,  $p-u_a$ , but then levelled off with time.

The stress-strain curve for samples with zero and low suction sheared at lower stress showed a clear peak compared to samples sheared at higher stress which indicated more ductile behaviour. The volume change of the samples during shearing showed the influence of mean net stress and suction. The peak strength surfaces plotted in  $q -$  suction space were parallel and indicated some curvature. The curvature of the ultimate strength in shear strength - suction relationship showed that the contribution of suction to strength represented by friction angle,  $\phi^b$  was not constant.



The initial and final bond yield surfaces were represented by a linear increase with mean net stress over the stress range investigated. As matric suctions increased higher, both bond yield surfaces dropped back close to yield surface for lower matric suctions.

The critical state stress ratios  $M_a$  (mean net stress component) and  $M_b$  (matric suction component) were used to examine the critical state of the bonded material in unsaturated conditions. It was found that  $M_a$  is higher than the saturated critical state stress ratio,  $M_s$  (i.e.  $\phi^a > \phi'$ ), therefore, the assumption that  $\phi^a = \phi'$  is not always valid. The changes in  $M_a$  and  $M_b$  can be related to three different phase of water retention behaviour. This pattern of behaviour is probably explained by the narrow range of pore size in the uniform bonded sand.

A relationship between water content and matric suction was studied based on the WRC at each stage of suction equalisation, consolidation and shearing. The CDLs or Continuously Disturbed Lines (representing the water content – suction relationship at ultimate state) were plotted. It was interesting to see that samples with initial low suction showed an increase in suction to reach the CDL while samples with initial high suction showed a decrease to approach the CDL. The decrease in suction during shearing for samples with high initial suction was accompanied by dilation behaviour in terms of volumetric strain. This behaviour is the opposite of what might be expected. In saturated soils, dilative behaviour would produce a drop in pore water pressure (increase in suction). This opposite behaviour expressed by unsaturated samples under shear emphasises the role of fabric in controlling the engineering behaviour of unsaturated soils.

## **ACKNOWLEDGEMENTS**

This research has been carried out in the Applied Mechanics Division of the School of Engineering and Computer Science. First of all I would like to thank Public Service Department and Government of Malaysia who kindly provided financial support during my study in Durham University. Without their permission and support, I would not probably be here.

I would like to express my highest gratitude to my supervisors Dr. D.G. Toll and Dr. Domenico Gallipoli for their guidance and discussion/comment throughout the work. Through their persistent commitment and support, I finally managed to prepare this thesis. I am really enjoying my life as research student here event there were some difficult times which I took it as a challenge. As usual, every problem has the solution; however it needs patience, courage and commitment to solve it.

I also would like to express my appreciation to all the technical staff of the Soil Mechanics Laboratories, especially to Bernard MacEleavey and Steve Richardson who are always willing to give tremendous assistance. Their willingness, tolerance and support throughout the years are greatly acknowledged. I like to thank Michael who spent some time to get involve with computational work in the laboratory. I also would to thank to Collin and other technical staff from Mechanical workshop of Engineering School for their remarkable help in preparing numerous special supporting equipments during this study. I would like to thank Mr. Sales for making thin sections and Geological Department of Durham University for the use of microscope with digital camera facility.

My thanks are also go to Paul, Garreth, Grace, Peter, Sergio, Juaou, Paul and many others for their kindness and friendship throughout these years.

I also want to thank to Lukman, Amin, Badrul, Asmadi, Talib and Anese and their families for their friendship and help during our stay in a peaceful village of Bowburn. Their continuous and priceless friendship, commitment and support have made life interesting and more enjoyable in Durham.

I would like to convey my highly gratitude to my wife, Arina and sons, Muhammad Amir Syafiq, Muhammad Hakimi and Muhammad Haziq and Nurlina Yamini for their deeply understanding, support and patience throughout the years. My wife Arina, your personal persistent help, encouragement and patience are profoundly appreciated. To my parent in-law, Mr. Alwi and family, I would like to convey my appreciation for being compassionate and encourage throughout the years while we were abroad. Thank for taking care of Muhammad Haziq during this period.

Finally, I am deeply grateful to my lovely parents, Mr. Ali Rahman and Djumiah Hj. Arsjad who are constantly praying for my success in my study. Your love, patience and encouragement are very much appreciated and no word could I say how thankful I am to both of you. Profound thanks also to my sisters and their husbands, Noorhusni and Noorjanis as well as their families for looking after our parent while I was studying here. To all my nieces I pray for your success and happiness. Ameen.

## **CONTENTS**

STATEMENT OF COPYRIGHT	i
DECLARATION	i
FINANCIAL SUPPORT	i
ABSTRACT	ii
ACKNOWLEDGEMENTS	v
CONTENTS	vii
LIST OF FIGURES	xiii
LIST OF TABLES	xxx
LIST OF SYMBOLS	xxxii
ABBREVIATIONS	xxxiii
1 INTRODUCTION	1
1.1 GENERAL	1
1.2 OBJECTIVES OF THIS RESEARCH	3
1.3 LAYOUT OF THE THESIS	4
2 LITERATURE REVIEW	6
2.1 INTRODUCTION	6
2.2 UNSATURATED SOIL BEHAVIOUR.	6
2.2.1 General	6
2.2.2 Matric Suction and Axis Translation Technique	7
2.2.3 Stress State Variables and Soil Strength	10
2.3 PREVIOUS RESEARCH	15



2.3.1 General	15
2.3.2 Studies on Saturated Behaviour of Bonded and Destructured Soils	16
2.3.3 Studies on Unsaturated Behaviour of Soils	38
2.3.4 Critical State of Granular Material	53
2.4 CONCLUSIONS	59
3 SAMPLE PREPARATION	62
3.1 INTRODUCTION	62
3.2 REVIEW OF PREVIOUS METHODS OF SAMPLE PREPARATION	62
3.2.1 General Overview	62
3.2.2 Techniques Adopted by Maccarini (1987) and Bressani (1990)	65
3.2.3 Technique Adopted by Malandraki (1994)	68
3.3 PREPARATION OF ARTIFICIAL BONDED AND DESTRUCTURED SOILS	70
3.3.1 Artificial Bonded Samples	71
3.3.1.1 Void ratio 0.6	71
3.3.1.2 Void ratio 0.9	75
3.3.1.2.a Wet and wax techniques	75
3.3.1.2.b Polystyrene technique	75
3.3.1.2.c Seed technique	77
3.3.2 Artificial Destructured Samples	79
3.3.3 Microscopic Observation of Artificial Soil	83
3.4 CONCLUSIONS	87
4 TESTING EQUIPMENT AND PROCEDURES	88
4.1 INTRODUCTION	88
4.2 BRIEF DESCRIPTION OF CONTROL SYSTEM	88
4.2.1 Hardware	88
4.2.2 Triax Program	89

4.3 TRIAXIAL INSTRUMENTATION	91
4.3.1 The Equipment	91
4.3.1.1 Saturated tests	92
4.3.1.2 Unsaturated tests	95
4.3.2. Calibration of Measurement Devices	97
4.3.3 Calibration of Volume Change	98
4.4 TRIAXIAL TESTS	110
4.4.1 Saturation, Suction Equalisation and Consolidation Processes	110
4.4.1.1 Saturated tests	110
4.4.1.2 Unsaturated tests	111
4.4.2 Shearing Stage	115
4.5 CONCLUSIONS	117
5 SATURATED DESTRUCTURED MATERIAL	118
5.1 INTRODUCTION	118
5.2 DRAINED TRIAXIAL TESTS	118
5.2.1 Description of Testing	119
5.2.2 Stress Strain Behaviour	119
5.2.3 Peak Strength, Stress Paths and Bounding Surfaces	123
5.3 UNDRAINED TRIAXIAL TESTS	126
5.3.1 Description of Testing	129
5.3.2 Stress Strain Behaviour	129
5.3.3 Stress Paths and Bounding Surfaces	133
5.4 COMPARISON BETWEEN DRAINED AND UNDRAINED BEHAVIOUR OF DESTRUCTURED SAMPLES	137
5.4.1 Stress Ratios for Destructured Samples	137
5.4.2 Bounding Surface for Destructured Samples	139
5.5 CRITICAL STATE OF DESTRUCTURED SAMPLES	143

5.5.1 The Critical State	144
5.5.2 Normalisation	152
5.6 FINAL REMARKS	162
 6 SATURATED BONDED MATERIAL	 164
6.1 INTRODUCTION	164
6.2 DRAINED TRIAXIAL TESTS	164
6.2.1 Description of Testing	165
6.2.2 Stress Strain Behaviour	165
6.2.3 Stress Paths and Bounding Surfaces	172
6.2.4 Bond Yields and Yield Surfaces	175
6.3 UNDRAINED TRIAXIAL TESTS	184
6.3.1 Description of Testing	184
6.3.2 Stress Strain Behaviour	184
6.3.3 Stress Paths and Bounding Surfaces	189
6.3.4 Bond Yields and Yield Surfaces	192
6.4 COMPARISON BEHAVIOUR BETWEEN DRAINED AND UNDRAINED BEHAVIOUR ON BONDED SAMPLES	200
6.4.1 Stress Ratios for Bonded Samples	200
6.4.2 Bounding Surface for Bonded Samples	203
6.4.3 First and Bond Yield Surfaces for Bonded Samples	206
6.5 COMPARISON BETWEEN BONDED AND DESTRUCTURED SAMPLES IN DRAINED AND UNDRAINED TESTS	211
6.5.1 Stress Ratios in Drained Tests	211
6.5.2 Stress Ratios in Undrained Tests	213
6.5.3 Bounding Surfaces in Drained and Undrained Tests	220
6.6 THE CRITICAL STATE OF BONDED SAMPLES	226
6.6.1 The Critical State	226
6.6.2 Normalisation	243
6.7 FINAL REMARKS	250

<b>7 BEHAVIOUR OF BONDED MATERIAL IN UNSATURATED STATE</b>	<b>254</b>
7.1 INTRODUCTION	254
7.2 CONSTANT WATER CONTENT TRIAXIAL TESTS	255
7.2.1 Description of Testing	255
7.2.2 Water Retention Curve	256
7.2.3 Volume and Suction Behaviour during Consolidation Stage	260
7.2.3.1 Volume change	260
7.2.3.2 Suction change	265
7.2.4 Stress Strain Behaviour	274
7.2.5 Volume Change and Suction Behaviour	278
7.2.6 Suction Path	288
7.2.7 Stress Ratio	293
7.2.8 Bond Yield and Yield Surface	298
7.3 THE CRITICAL STATE FOR UNSATURATED BONDED SOILS	314
7.3.1 The Critical State	314
7.3.2 Critical State Stress Ratios	329
7.3.2.1 Mean net stress component, $M_a$	331
7.3.2.2 Suction component, $M_b$	332
7.3.3 Water Content at Critical State	339
7.4 FINAL REMARKS	343
<b>8 CONCLUSIONS AND RECOMMENDATIONS</b>	<b>349</b>
8.1 INTRODUCTION	349
8.2 CONCLUSIONS	349
8.2.1 Techniques in Sample Preparation and Testing	349
8.2.2 Behaviour of Destructured Material in Saturated State	350
8.2.3 Behaviour of Bonded Material in Saturated State	351
8.2.4 Behaviour of Unsaturated Soil in Bonded State	352

8.3 RECOMMENDATIONS	354
REFERENCES	357
APPENDIX I	
APPENDIX II	
APPENDIX III	



	<b>LIST OF FIGURES</b>	<b>Page</b>
Figure 2.1:	The relationship between suction and pore diameter (after Toll et al. 1987)	9
Figure 2.2:	The unconfined triaxial test on compacted Talybont clay with and without translation; (a) Deviator stress vs. strain; (b) matric suction vs. strain during test with axis translation (after Bishop and Blight 1963)	10
Figure 2.3:	The state surface for void ratio and degree of saturation (after Matyas and Radhakrishna 1968)	14
Figure 2.4:	The extended Mohr-Coulomb failure envelope for unsaturated soils (after Fredlund and Rahardjo 1993)	14
Figure 2.5:	Results from one-dimensional compression tests on residual soils (after Vargas 1953)	16
Figure 2.6:	The results from the oedometer tests on residual clays at volcanic origin (after Wesley 1974)	17
Figure 2.7:	Stress vs. strain curves for Labrador clay (after Sangrey 1972)	18
Figure 2.8:	Stress vs. strain curves of a weak soil from the Pacific site(after Clough et al.. 1981)	18
Figure 2.9:	The position of first and second yields for artificially bonded samples (after Maccarini 1987)	20
Figure 2.10:	A tentative explanation of first and second yields (after Vaughan et al.. 1988)	22
Figure 2.11:	(a)Yield surfaces developed from four different artificial bonded soils; (b) the strength envelopes of the different mixture; (c) secant stiffness vs. confining effective stress for different series of artificial soil (after Bressani 1990)	23
Figure 2.12:	The results of the drained triaxial test on two different structured soils. (a) schematic stress path; stress vs. strain curves of (b) Saint-Vallier clay (c) soft carbonate rock (after Leroueil and Vaughan 1990)	25

Figure 2.13:	The yield curves defined from three different structured materials.(after Leroueil and Vaughan 1990)	26
Figure 2.14:	(a) ultimate states from standard pressure drained triaxial tests; (b) stress paths from standard undrained tests; (c) normalised stress paths for drained tests; (d) normalised stress paths for undrained tests (after Coop 1990)	27
Figure 2.15:	(a) Deviatoric stress, $q$ vs. axial strain curves of drained tests; (b) volumetric strain vs. axial strain curves; (c) typical small strain response (after Airey 1993)	28
Figure 2.16:	The effect of (a) cement content and (b) density on stress yield (after Huang and Airey 1993)	28
Figure 2.17:	The results from the drained triaxial and direct shear box tests on undisturbed residual soils. (a) drained triaxial test; (b) direct shear box test (after Maccarini 1993)	29
Figure 2.18	The initial tangent stiffness from isotropically confined drained triaxial test (after Maccarini 1993)	30
Figure 2.19:	The secant stiffness of tests carried out on Corinth marl (a) at $\epsilon_a=0.1\%$ ; (b) at $\epsilon_a=0.2\%$ (after Bressani 1993)	30
Figure 2.20:	State paths for cemented soil (a) low confining pressures and (b) high confining pressures (after Coop and Atkinson 1993)	31
Figure 2.21:	State paths for natural calcarenite soil at (a) low confining pressures and (b) high confining pressures; (c) isotropic compression lines of samples treated with and without fines (after Coop and Atkinson 1993)	32
Figure 2.22:	The normalized stress paths of artificially cemented soil with different bond strengths (after Cuccovila and Coop 1993)	33
Figure 2.23:	(a) Bounding surface between bonded and destructured samples; (b) yield points identified from stiffness vs. strain curve ( $p_o'=11\text{kPa}$ ); (c) zones of behaviour for bonded soil (after Malandraki and Toll 1996)	35

Figure 2.24:	(a) The compression and swelling of saturated soils; (b) Critical state for partially saturate and unbonded dry soils (c) normal compression line of unbonded dry soils (after Lee and Coop 1993)	36
Figure 2.25:	Failure envelopes of different types of samples in $q:p'$ space (after Asghari et al.. 2003)	37
Figure 2.26:	The affect of stress level and grading on volumetric strains; (a) small shear strains; (b) larger shear strains; (c) mobilize friction angles (after Coop et al.. 2004)	37
Figure 2.27:	The intersection line between failure envelope and $\tau : (u_a - u_w)$ plane for (a) compacted shale; (b) compacted boulder clay (after Fredlund and Rahardjo 1993; data from Bishop et al.. 1960)	39
Figure 2.28:	The results of consolidated drained tests on unsaturated silt. (a) Deviator stress versus strain curves; (b) water volume change vs. strain; (c) volume change vs. strain (after Blight 1967)	40
Figure 2.29:	Effects of matric suction on shear strength for Madrid clay from (a)direct shear tests; (b) triaxial tests (after Escario 1980)	40
Figure 2.30:	The failure envelopes for residual soil from decomposed granite sample. (a) $\tau$ vs. $(\sigma - u_a)$ ; (b) $\tau$ vs. $(u_a - u_w)$ (after Ho and Fredlund 1982)	41
Figure 2.31:	Direct shear tests on Madrid grey clay under controlled matric suction. (a) Shear stress vs. net confining pressure with various matric suction; (b) shear stress vs. matric suction relationship (after Escario and Saez 1986)	42
Figure 2.32:	Yield surfaces in $p: q: s$ space (after Alonso et al. 1990)	42
Figure 2.33:	The yield surface for unsaturated soil (after Wheeler and Sivakumar 1995)	43
Figure 2.34:	The yield curve and the locations of the critical state lines for different suction, $s = 0, 100$ and $200$ kPa (after Zakaria et al. 1995)	44



Figure 2.35:	The effect of matric suctions on yield points in unsaturated condition for two different consolidation pressures (after Geiser et al. 1998)	45
Figure 2.36:	The deviator stress versus strain curves for (a) CD and (b) CW tests. The failure envelope for (c) CD test and (d) CW test (after Taha et al. 2000)	46
Figure 2.37:	The results of the multi-stage CD triaxial tests on undisturbed residual soils. (a) Bukit Timah formation; (b) Jurong Sedimentary formation (after Toll et al. 2000)	47
Figure 2.38:	The highest values of $\phi^b$ angle obtained from the total cohesion versus matric suction for both type of sample. (a) Bukit Timah formation; (b) Jurong Sedimentary formation (after Toll et al. 2000)	47
Figure 2.39:	The result of shearing-infiltration direct shear test under 275kPa net normal stress and 200kPa matric suction. (a) shear stress vs. horizontal displacement; (b) matric suction and horizontal displacement vs. elapsed time; (c) water volume change and vertical displacement vs. elapsed time (after Wong et al. 2000)	48
Figure 2.40:	The result of shearing-infiltration triaxial test under 50kPa net confining pressure and 50kPa matric suction. (a) deviator stress versus axial strain; (b) axial strain and base or mid-height matric suctions versus elapsed time; (c) volumetric or water volume change strain versus elapsed time (after Wong et al. 2000)	48
Figure 2.41:	The influence of matric suction on the shape and location of the after compaction loading-collapse loci (LC) (after Mancuso et al. 2000)	49
Figure 2.42:	Deviator stress, $q$ and pore water pressure change, $\delta u$ against axial strain in constant water content tests at net confining stress: (a) 50kPa; (b) 150kPa; (c) 250kPa (after Toll and Ong 2003)	51
Figure 2.43:	Stress path in $q: p'$ space for drained and constant water content tests at high degree of saturation (Toll and Ong 2003)	52

Figure 2.44:	Soil water retention curves of prepared samples. The effect of void ratio on matric suction; (a) bonded soils; (b) destructured soils; and effect of bonding (c) on samples with 0.6 void ratio (after Walker et al. 2005)	52
Figure 2.45:	Failure envelopes for (a) young soil; (b) mature residual soils and: (c) intercept of cohesion values for both soils (after Reis and Vilar 2005)	53
Figure 2.46:	Relationship between $q'/p':\varepsilon_a$ and $\varepsilon_v:\varepsilon_a$ for dense sands (after Atkinson and Bransby 1978)	54
Figure 2.47:	Schematic diagram showing definition of critical state for drained and undrained tests (after Yamamuro and Lade 1998)	57
Figure 2.48:	The critical state line defined for Merriespruit tailing dam from undrained triaxial compression test, which showed contractive behaviour. The “confidence zones” represent an error allowance on void ratio of 0.05 either side of the critical state line (after Fourie and Papageorgiou 2001)	58
Figure 2.49:	(a) Critical state line for Leighton Buzzard sand showing curvature; (b) Critical state for undrained tests on contractive samples of Erksak 330/0.7 sand (initial state of all samples was above the critical state line)(after Been et al. 1991)	59
Figure 3.1:	Temperature’s effect on kaolin (a and b) and quartz sand (c) (after Grim 1953)	67
Figure 3.2:	Effect of kaolin content on the strength of bond structure (after Maccarini 1987)	67
Figure 3.3:	Particle distribution curve for Leighton Buzzard sand used in the preparation of artificial sample	72
Figure 3.4:	Equipment used for sample preparation. Sample (a) is taken out of the mould after drying at room condition (still inside a filter paper tube) while (b) is already fired for 5 hours in the furnace	73
Figure 3.5:	Wet mixture of sand and kaolin is placed into the steel mould with filter paper lining inside	73

Figure 3.6:	Artificial weakly bonded samples with void ratio of 0.6	78
Figure 3.7:	Bonded samples with void ratio of 0.9 prepared by adding the polystyrene particles into wet mixture	78
Figure 3.8:	Coriander seeds ( <i>Coriandrum sativum</i> )	80
Figure 3.9:	Poppy or known as black mustard seeds ( <i>Brassica nigra</i> )	81
Figure 3.10:	Samples prepared using the poppy seeds easily collapsed	82
Figure 3.11:	Artificial loose samples that were prepared by adding coriander seeds with sand and kaolin mixture	82
Figure 3.12:	Microscopic photographs of artificially weakly bonded sample with void ratio 0.6 under x2.5 magnification	85
Figure 3.13:	Microscopic photographs of artificially weakly bonded sample with void ratio 0.9 under x2.5 magnification	86
Figure 4.1:	The <i>Stage Detail</i> for defining the control parameters. Example from the setting up for increasing cell and air pressures during suction equalisation in constant water tests	90
Figure 4.2:	The <i>Control</i> window for increasing the cell and air pressures during suction equalisation under small mean net stress of 5kPa	91
Figure 4.3:	The setting of the triaxial controlling system for saturated tests	94
Figure 4.4:	Control window for increasing the cell pressure to predetermined pressure to achieve targeted confining pressure	95
Figure 4.5:	The setting of the triaxial controlling system for unsaturated tests	96
Figure 4.6:	The temperature variation of the cell before and after wrapping with bubble wrap (from Cell 2)	101
Figure 4.7:	The volume change of the cell during suction equalisation under 600kPa of cell pressure (from Cell3)	102



Figure 4.8:	The calibration of volume change of the cell under 695kPa of cell pressure (from Cell 2)	104
Figure 4.9:	The calibration of volume change of the cell under 895kPa of cell pressure (from Cell 2)	105
Figure 4.10.a:	The volume change of the cell during penetration of piston load into the cell at 600kPa of cell pressure (from Cell 2)	107
Figure 4.10.b:	The volume change of the cell during penetration of piston load into the cell at 600kPa of cell pressure (from Cell 3)	108
Figure 4.11:	Suction equalisation stage. (a) increment of cell and air pressures during first hour of suction equalisation under small $p^*$	114
Figure 4.12:	Pore water pressure changes during shearing of sample under the drained test	116
Figure 5.1:	Stress-strain curves for the drained tests on destructured soils	120
Figure 5.2:	Volume strain curves against axial strain for the drained tests on destructured soils	122
Figure 5.3:	The definition of the maximum rate of dilation from the curves (e.g. cdd15 and cdd400)	124
Figure 5.4:	Effective stress paths for the drained tests on destructured soils	125
Figure 5.5:	Bounding surface and phase transformation lines for the drained tests on destructured soils	127
Figure 5.6:	Stress ratio, $q/p'$ against axial strain for the drained tests on destructured soils	128
Figure 5.7:	Stress-strain curves for the undrained tests on destructured soils	131
Figure 5.8:	Excess pore water pressure against axial strain for the undrained tests on destructured soils	132

Figure 5.9:	Stress ratio, $q/p'$ against axial strain for the undrained tests on destructured soils	134
Figure 5.10:	Effective stress paths for all the undrained tests on destructured soils	135
Figure 5.11:	Bounding surface and phase transformation lines for the undrained tests on destructured soils	136
Figure 5.12.a:	The $q/p'$ ratio versus axial strain for the drained and undrained tests on destructured soils at lower confining pressures	138
Figure 5.12.b:	The $q/p'$ ratio versus axial strain for the drained and undrained tests on destructured soils at intermediated confining pressures	140
Figure 5.12.c:	The $q/p'$ ratio versus axial strain for the drained and undrained tests on destructured soils at high confining pressures	141
Figure 5.13:	Bounding surface lines for the drained and undrained tests on destructured samples	142
Figure 5.14	Phase transformation lines for the drained and undrained tests on destructured samples	144
Figure 5.15:	Paths followed by drained tests on destructured samples in $v - p'$ space	145
Figure 5.16.a:	Stress-strain curves for the drained tests on destructured samples	146
Figure 5.16.b:	Volumetric strain curves for the drained tests on destructured samples	147
Figure 5.17:	Specific volume changes with effective stress, $p'$ for the undrained tests on destructured sample	149
Figure 5.18.a:	Stress-strain curves for the undrained tests on destructured samples	150
Figure 5.18.b:	Excess pore water pressure change for the undrained tests on destructured samples	151
Figure 5.19:	Effective stress paths for the undrained tests on destructured samples	153

Figure 5.20:	Critical state line for drained and undrained tests on destructured samples (error bars were included)	154
Figure 5.21:	Critical state for the drained and undrained tests on destructured samples in $q-p'$ space(error bars were included)	155
Figure 5.22.a:	Normalised stress paths in $q/p'_c - p'/p'_c$ space for drained destructured samples	157
Figure 5.22.b:	Normalised stress paths in $q/p'_c - p'/p'_c$ space for undrained destructured samples	158
Figure 5.23.a:	Normalised stress paths for drained tests in $q/p'_c/M - p'/p'_c$ space	159
Figure 5.23.b:	Normalised stress paths for undrained tests in $q/p'_c/M - p'/p'_c$ space	160
Figure 5.24:	Normalised stress paths for drained and undrained tests in $q/p'_c/M - p'/p'_c$ space	161
Figure 6.1:	Stress-strain curves for the drained tests on bonded soils	166
Figure 6.2:	Volume strain curves for the drained tests on bonded soils	168
Figure 6.3:	Phase transformation curve for the drained tests on bonded soils	170
Figure 6.4:	Stress ratio, $q/p'$ against axial strain for the drained tests on bonded soils	171
Figure 6.5:	Effective stress paths for the drained tests on bonded soils	173
Figure 6.6:	Bounding surface represented by maximum $q/p'$ points for the drained tests on bonded soils	174
Figure 6.7:	(a) Stress-strain curve and (b) secant stiffness plot for cdb15 sample	177
Figure 6.8:	(a) Stress-strain curve and (b) secant stiffness plot for cdb400 sample	178

Figure 6.9:	(a) Stress-strain curve and (b) secant stiffness plot for cdb1000 sample	179
Figure 6.10:	Specific volume curves for the drained tests showing the position of yield points	181
Figure 6.11:	(a) Stress-strain curve and (b) volumetric strain curves for drained tests	182
Figure 6.12:	The first and bond yields surfaces for the drained tests on bonded samples	183
Figure 6.13:	Stress-strain curves for the undrained tests on bonded soils	186
Figure 6.14:	Excess pore water pressure against axial strain for the undrained tests on bonded soils	188
Figure 6.15:	Stress ratio, $q/p'$ against axial strain for the undrained tests on bonded soils	190
Figure 6.16:	Effective stress paths for all the undrained tests on bonded soils	191
Figure 6.17:	Bounding surface and phase transformation lines for the undrained tests on bonded soils	193
Figure 6.18:	(a) Stress-strain curve and (b) secant stiffness plot for cub30 sample	195
Figure 6.19:	(a) Stress-strain curve and (b) secant stiffness plot for cub100 sample	196
Figure 6.20:	(a) Stress-strain curve and (b) secant stiffness plot for cub1000 sample	197
Figure 6.21:	(a) Stress-strain curve and (b) volumetric strain curves for undrained tests	198
Figure 6.22:	Effective stress paths for the undrained tests showing the position of yield points	199
Figure 6.23:	The first and bond yields surfaces for the undrained tests on bonded samples	201



Figure 6.24.a:	The $q/p'$ ratio versus axial strain for the drained and undrained tests on bonded soils at low confining pressures	202
Figure 6.24.b:	The $q/p'$ ratio versus axial strain for the drained and undrained tests on bonded soils at intermediate confining pressures	204
Figure 6.24.c:	The $q/p'$ ratio versus axial strain for the drained and undrained tests on bonded soils at high confining pressures	205
Figure 6.25.a:	Bounding surface lines for the drained and undrained tests on bonded samples	207
Figure 6.25.b:	Best fit line to represent the maximum $q/p'$ points from the drained and undrained tests on bonded samples	208
Figure 6.26:	Phase transformation lines for the drained and undrained tests on bonded samples	209
Figure 6.27:	The yield surfaces for the drained and undrained tests	210
Figure 6.28.a:	The $q/p'$ ratio versus axial strain for drained on bonded and destructured soils at lower confining pressures	212
Figure 6.28.b:	The $q/p'$ ratio versus axial strain for drained test on bonded and destructured soils at intermediate confining pressures	214
Figure 6.28.c:	The $q/p'$ ratio versus axial strain for drained tests on bonded and destructured soils at high confining pressures	215
Figure 6.29.a:	The $q/p'$ ratio versus axial strain for undrained tests on bonded and destructured soils at lower confining pressures	217
Figure 6.29.b:	The $q/p'$ ratio versus axial strain for undrained tests on bonded and destructured soils at intermediate confining pressures	218
Figure 6.29.c:	The $q/p'$ ratio versus axial strain for undrained tests on bonded and destructured soils at intermediate confining pressures	219



Figure 6.30:	Bounding surfaces for the drained bonded and destructured samples	221
Figure 6.31:	Bounding surfaces for the undrained bonded and destructured samples	222
Figure 6.32:	Phase transformation lines for drained bonded and destructured samples	224
Figure 6.33:	Phase transformation lines for the undrained bonded and destructured samples	225
Figure 6.34:	Paths followed by drained tests on bonded samples in $v - p'$ space	227
Figure 6.35.a:	Stress-strain curves for the drained tests on bonded samples with critical state points defined using early approach	228
Figure 6.35.b:	Volumetric strain curves for the drained tests on bonded samples defined using early approach	229
Figure 6.36.a:	Stress strain curves for the drained tests on bonded samples	230
Figure 6.36.b:	Volumetric strain curves for the drained tests on bonded samples	231
Figure 6.37.a:	Stress-strain curves for the undrained tests on bonded samples with critical state points defined using early approach	234
Figure 6.37.b:	Excess pore water pressure change curves for the undrained tests on bonded samples with critical state points defined using early approach	235
Figure 6.38.a:	Stress strain curves for the undrained tests on bonded samples	236
Figure 6.38.b:	Excess pore water pressure change curves for the undrained tests on bonded samples	237
Figure 6.39:	Effective stress paths for the undrained tests on bonded samples	238
Figure 6.40:	Specific volume changes with effective stress, $p'$ for the drained and undrained tests on bonded samples	239

Figure 6.41:	Critical state for drained and undrained tests on bonded samples with upper and lower limits (error bars included)	240
Figure 6.42:	Critical state line for the drained and undrained tests on bonded samples in $q - p'$ space	242
Figure 6.43.a:	Normalised stress paths in $q/p' - p'/p'_c$ space for the drained tests on bonded samples	244
Figure 6.43.b:	Normalised stress paths in $q/p' - p'/p'_c$ space for the undrained tests on bonded samples	245
Figure 6.44.a:	Normalised stress paths in $q/p'/M - p'/p'_c$ space for the drained tests on bonded samples	246
Figure 6.44.b:	Normalised stress paths in $q/p'/M - p'/p'_c$ space for the undrained tests on bonded samples	247
Figure 6.45:	Normalised stress paths in $q/p'/M - p'/p'_c$ space for bonded and destructured materials	248
Figure 6.46:	Comparison between normalised stress paths in $q/p'/M - p'/p'_c$ space between bonded and destructured materials	249
Figure 7.1:	The water retention curve in degree of saturation against matric suction	257
Figure 7.2:	The water retention curve in water content against matric suction	258
Figure 7.3.a:	Specific volume against timer for cwb samples consolidated at $p-u_a=50\text{kPa}$ with zero and low suctions	261
Figure 7.3.b:	Specific volume against timer for cwb samples consolidated at $p-u_a=50\text{kPa}$ with low $S_r$	262
Figure 7.3.c:	Volume change and suction during consolidation under $p-u_a=50\text{kPa}$ for cwb50/124(0.22) test	263
Figure 7.4.a:	Specific volume against timer for cwb samples consolidated at $p-u_a=100\text{kPa}$	264
Figure 7.4.b:	Volume change and suction during consolidation under $p-u_a=100\text{kPa}$ for cwb100/1(0.80) test	266

Figure 7.4.c:	Volume change and suction during consolidation under $p-u_a=100\text{kPa}$ for cwb100/560(0.18) test	266
Figure 7.5:	Specific volume against timer for cwb samples consolidated at $p-u_a=300\text{kPa}$	267
Figure 7.6	Matric suction against timer for cwb samples consolidated at $p-u_a=50\text{kPa}$	268
Figure 7.7.a:	Matric suction against timer for cwb samples consolidated at $p-u_a=100\text{kPa}$	270
Figure 7.7.b:	Specific volume and suction changes during consolidation under $p-u_a=100\text{kPa}$ for cwb100/248(0.19)	271
Figure 7.7.c:	A close up of the suction changes during back pressure and flushing procedure s of cwb100/248(0.19) sample	271
Figure 7.8:	Matric suction against timer for cwb samples consolidated at $p-u_a=300\text{kPa}$	273
Figure 7.9.a:	Stress-strain curves for $p-u_a$ of 50kPa for bonded samples	275
Figure 7.9.b:	Stress-strain curves for $p-u_a$ of 100kPa for bonded samples	276
Figure 7.9.c:	Stress-strain curves for $p-u_a$ of 300kPa for bonded samples	277
Figure 7:10.a:	Volume strain against axial strain for $p-u_a$ of 50kPa	280
Figure 7:10.b:	Volume strain against axial strain for $p-u_a$ of 100kPa	281
Figure 7:10.c:	Volume strain against axial strain for $p-u_a$ of 300kPa	282
Figure 7:11.a:	Volume strain against strain for the cwb50/124(0.22) and cwb300/123(0.23) tests	283
Figure 7:11.b:	Volume strain against strain for the cwb50/3504(0.21) and cwb100/391(0.21) tests	283
Figure 7:12.a:	Excess pwp against axial strain for $p-u_a$ of 50kPa	285
Figure 7:12.b:	Excess pwp against axial strain for $p-u_a$ of 100kPa	286

Figure 7.12.c:	Excess pwp against axial strain for $p-u_a$ of 300kPa	287
Figure 7.13.a:	The variation in deviator stress with suction for $p-u_a$ of 50kPa	289
Figure 7.13.b:	The variation in deviator stress with suction for $p-u_a$ of 100kPa	290
Figure 7.13.c:	The variation in deviator stress with suction for $p-u_a$ of 300kPa	291
Figure 7.14:	The peak strength boundary for $p-u_a$ of 50kPa , 100kPa and 300kPa	292
Figure 7.15.a:	Stress ratio, $q/p^*$ against axial strain for $p-u_a$ of 50kPa	294
Figure 7.15.b:	Stress ratio, $q/p^*$ against axial strain for $p-u_a$ of 100kPa	295
Figure 7.15.c:	Stress ratio, $q/p^*$ against axial strain for $p-u_a$ of 300kPa	296
Figure 7.16:	Maximum stress ratio, $q/p^*$ against mean net stress $p-u_a$ for all series of mean net stresses	297
Figure 7.17:	(a) Stress-strain curve and (b) secant stiffness plot for sample cwb50/0(0.75)	299
Figure 7.18:	(a) Stress-strain curve and (b) secant stiffness plot for sample cwb100/1(0.80)	300
Figure 7.19:	(a) Stress-strain curve and (b) secant stiffness plot for sample cwb300/0(0.38)	301
Figure 7.20.a:	Stress path in $v - (p-u_w)$ space for samples with zero and low suctions at mean net stress, $p-u_w = 50\text{kPa}$	303
Figure 7.20.b:	Stress path in $v - (p-u_w)$ space for samples with zero and low suctions at mean net stress, $p-u_w = 100\text{kPa}$	304
Figure 7.20.c:	Stress path in $v - (p-u_w)$ space for samples with zero and low suctions at mean net stress, $p-u_w = 300\text{kPa}$	305
Figure 7.21.a:	Stress path in $v - (p-u_w)$ space for samples with low $S_r$ at mean net stress, $p-u_w = 50\text{kPa}$	306
Figure 7.21.b:	Stress path in $v - (p-u_w)$ space for samples with low $S_r$ at mean net stress, $p-u_w = 100\text{kPa}$	307



Figure 7.21.c:	Stress path in $v - (p-u_w)$ space for samples with low $S_r$ at mean net stress, $p-u_w = 300\text{kPa}$	308
Figure 7.22:	Mean net stress of 50kPa (a) stress-strain curves (b) volume strain-axial strain curves	309
Figure 7.23:	Mean net stress of 100kPa (a) stress-strain curves (b) volume strain-axial strain curves	310
Figure 7.24:	Mean net stress of 300kPa (a) stress-strain curves (b) volume strain-axial strain curves	311
Figure 7.25:	Excess suction, $\Delta(u_a-u_w)$ against axial strain curves for samples at mean net stress, $p-u_a$ (a) 50kPa (b) 100kPa (c) 300kPa	312
Figure 7.26:	Initial bond yield surface for unsaturated samples	315
Figure 7.27:	Final bond yield surface for the unsaturated samples	316
Figure 7.28:	Stress paths for unsaturated samples with zero suction values	318
Figure 7.29.a:	Stress-strain curves for unsaturated samples of cwb50 with zero and low suction values	319
Figure 7.29.b:	Volume strain curves for unsaturated samples of cwb50 with zero and low suction values	320
Figure 7.30.a:	Stress-strain curves for unsaturated samples of cwb100 with zero and low suction values	321
Figure 7.30.b:	Volume strain curves for unsaturated samples of cwb100 with zero and low suction values	322
Figure 7.31.a:	Stress-strain curves for unsaturated samples of cwb300 with zero and low suction values	323
Figure 7.31.b:	Volume strain curves for unsaturated samples of cwb300 with zero and low suction values	324
Figure 7.32:	Paths followed by saturated and unsaturated samples in $v - (p-u_w)$ space	325
Figure 7.33:	The critical state points for saturated and unsaturated samples with zero and low suctions	327

Figure 7.34:	Critical state lines for bonded saturated and unsaturated samples	328
Figure 7.35.a:	Variation in critical state stress ratios with degree of saturation	334
Figure 7.35.b:	Suction against degree of saturation at critical state	335
Figure 7.36.a:	Variation in critical state stress ratios with suction	337
Figure 7.36.b:	Degree of saturation against suction at critical state	338
Figure 7.37.a:	Plot of water content against suction in natural scale (suction values below 200kPa)	340
Figure 7.37.b:	Plot of water content against suction in natural scale (for all range of suction values)	341
Figure 7.38:	The final water retention curve plots for each stage	342

**PAGE**  
**NUMBERING**  
**AS ORIGINAL**

## LIST OF SYMBOLS

$c'$	Cohesion intercept
$e_o$	Initial void ratio
$\varepsilon_a$	Axial strain
$\varepsilon_v$	Volumetric strain
$G_s$	Specific gravity
$\mu$	Coefficient of friction
$p$	Total stress $(\sigma_1' + 2\sigma_3')/3$
$p'$	Mean effective stress, $(\sigma_1' + 2\sigma_3')/3 - u_w$
$p_o'$	Isotropic consolidation pressure
$p'_e$	Mean effective stress corresponding to NCL at a defined void ratio
$p'_c$	Mean effective stress corresponding to CSL at a defined void ratio
$M$	Slope of critical state line in stress space
$M_a$	Critical state stress ratios with respect to mean net stress, $(p - u_a)$
$M_b$	Critical state stress ratios with respect to matric suction, $(u_a - u_w)$
$M_s$	Saturated critical state stress ratio
$p^*$	Mean neat stress, $(p - u_a)$
$\bar{p}$	Bishop's mean net stress
$q$	Deviatoric stress, $(\sigma_1' - \sigma_3')$
$\sigma_1'$	Effective axial stress
$\sigma_3'$	Effective radial stress
$\varphi'$	Mohr-Coulomb friction angle



$s$	Matric suction, ( $u_a - u_w$ )
$\Delta s$	Excess matric suction
$S_r$	Degree of saturation
$w$	Water content
$u_a$	Pore air pressure
$u_w$	Pore water pressure
$\Delta u / \Delta \epsilon_a$	Rate in excess pore water pressure
$v$	Specific volume, ( $v = 1 + e$ )

### ABBREVIATIONS

c.f.k	Crushed fired sand
pwp	Pore water pressure
cw	constant water content test
h.a.e	High air entry
NCL	Normal consolidation line
CSL	Critical state line
CDL	Continuously disturbed line

## **CHAPTER 1**

## **INTRODUCTION**

### **1.1 GENERAL**

Soils are formed from a variety of processes and can be originated from different kinds of parent rocks and geological environments. Soil can be generated by local weathering of parent rock or further transported to different places. Due to various geological and weathering processes, soils might be structured or destructured. Many earth materials such as clays, granular and residual soils as well as weak rocks are recognized as structured soils. Burland (1990) introduced “structure” term for clays which were studied at a microscopic scale. This structure refers to the combination of fabric and bonding. Meanwhile, for granular materials such as sands, this structure mainly refers to the occurrence of cement between the particles; however, little emphasis has been given to fabric. As a result of a prolonged period of weathering processes gradually changes the soil structure physically or/and chemically, hence influence their engineering behaviour. In general bonds can be formed from various resources such as from deposition of carbonates or hydroxides, or solution and deposition of silica at particle contacts in sands.

The effect of bonding or cementation is clearly important in controlling the mechanical behaviour of structured soils. Many engineering works such as embankments, roads, cut slopes and foundations have been located on this type of soil. A tragic disaster might happen if the bonds are broken. Much research on the fundamental behaviour of structured soils has been carried out mainly on the artificially bonded samples. This is the fact that associated with the difficulty of retrieving undisturbed samples from the ground. The occurrence of weak bonds is not adequately strong to conserve the structure. Natural bonded soils are



heterogeneous and pose variability in void ratio and bond strength. Therefore, many experimental studies on the behaviour of weakly bonded soils have been carried out on artificially bonded samples (Clough et al. 1981; Bressani 1990; Coop and Atkinson 1993; Malandraki 1994; Cuccovillo and Coop 1999; Asghari et al. 2003).

Meanwhile, in humid climatic regions where the annual rainfall and temperature are dominantly high, chemical weathering prevails compared to physical weathering. In-situ weathering gradually decomposes parent rocks from fresh to completely weathered materials (Aung et al. 2000). The degree of weathering varies with depth where the final product of complete in-situ weathering is recognized as residual soils. In many parts of the world, especially in arid and sub-arid areas, soils are in a dry or a partially dry state. In this condition, the pore water pressure has a negative pressure with respect to the air pressure, which is generally atmospheric in the field (Fredlund and Rahardjo 1993). Thus, the negative pore water pressure creates matric suction in the soils, which contributes to an increase of the normal forces at interparticle contacts (hence increasing shear strength and causing elastic compression due to elastic particle deformation) (Wheeler and Karube 1996). However, during heavy rainfall, infiltration of water reduces the suction drastically and changes the state of the soils from stable to unstable because of reduction of shear strength. Many steep natural slopes remain stable in this state but collapse suddenly during heavy rainfall.

Much research has been carried out in order to understand the behaviour of soils in an unsaturated state. Besides the factor of bonding, matric suction definitely plays an important role in controlling the engineering behaviour of such soils. Thus, many engineering organizations have begun to realize the need for a technical discipline that addresses more specifically the soil mechanics problems related to unsaturated soils (Fredlund and Rahardjo 1993).

## 1.2 OBJECTIVE OF THIS RESEARCH

Studies of unsaturated soils have attracted many researchers around the world due to insufficient related information and problems associated with these type of soils. In comparison, unsaturated soil studies are younger than those for saturated soils. A previous study carried out by Malandraki (1994) was further extended in this study by taking into consideration the effect of the soil matric suction. In order to control the properties of the studied material, it is more convenient to prepare artificial soil in the laboratory rather than using natural samples. Therefore, in this study the artificial soil samples were prepared according to the method adopted by Malandraki (1994) with same void ratio and bond strength.

The aims of this study were to investigate the effect of matric suction in governing the behaviour of unsaturated weakly bonded soils. A range of matric suction value was examined under unsaturated condition. In order to give clearer understanding, destructured soils with similar properties as the bonded soil were also studied. The artificially bonded and destructured samples were initially studied under saturated conditions using conventional drained and undrained tests. During investigation under saturated conditions samples were consolidated isotropically under different confining pressures up to 1MPa. Data obtained from the saturated tests would provide useful reference in interpreting results from the unsaturated tests. The critical state concept for the studied material was tested and normalisation of stress paths was also defined in different spaces. A series of constant water content tests was carried out on bonded material consolidated at different mean net stress,  $p-u_a$  and suction ( $u_a - u_w$ ).



### **1.3 LAYOUT OF THE THESIS**

This study has been organized into several sections which are summarized as follows:

In Chapter 2, a review of previous research on natural and artificial soils in saturated conditions for the last 50 years is discussed. Emphasis is given more to related studies associated with artificially bonded soils even though natural bonded soils are also discussed. In a later section, a literature review of previous studies on bonded and destructured unsaturated soils is presented.

Chapter 3 discusses the techniques and raw materials used for preparing the artificial bonded and destructured soils. Several different techniques of preparing samples are discussed in detail in order to obtain artificial bonded soils with two different void ratios (0.6 and 0.9). A microscopic study on thin sections from both void ratios is also discussed at the end of this chapter.

Chapter 4 provides a discussion on the testing equipment and testing procedures used in the laboratory. A brief explanation of the computer control system using Triax software is included. The procedures of calibration of the measuring devices are explained and a detail outline of triaxial setting for saturated and unsaturated tests is also described. At the end of this section, routine procedures adopted for triaxial tests during saturation, equalization, consolidation and shearing stages for saturated and unsaturated samples are discussed.

Chapter 5 presents the results from the triaxial tests on saturated destructured material. The discussion involves the results from both conventional drained and undrained tests in term of stress-strain, volumetric strain-strain, pore water pressure, bounding surfaces and effective stress paths. Comparison of the mechanical behaviour between drained and undrained samples is also discussed. A critical state for the destructured material is examined and discussed. Normalised



stress paths for both drained and undrained samples are presented at the end of section of this chapter.

Chapter 6 presents the results from the triaxial tests on saturated bonded material. A discussion involves the results from the drained and undrained tests in term of stress-strain, volumetric strain-strain, pore water pressure, bounding surfaces and effective stress paths. Comparison on the mechanical behaviour between drained and undrained bonded material is discussed. In addition, comparison of mechanical behaviour between bonded and destructured materials is also discussed in the following section. Again, the critical state for the bonded material is examined and discussed. Normalised stress paths for both drained and undrained samples are presented and comparison is carried out between destructured and bonded materials.

Chapter 7 presents the results from the constant water content tests on the unsaturated bonded samples. A water retention curve for the unsaturated artificially bonded material is presented and discussed. The results from the triaxial constant water content tests are discussed in term of the stress-strain, volumetric strain-strain, pore water pressure (suction) and bond yield surfaces. The results of the saturated tests and some unsaturated tests carried out at high degree of saturation (or low suction) are investigated within the framework of saturated soil behaviour. The unsaturated critical state for the studied soil is also examined and presented.

## **CHAPTER 2**

## **LITERATURE REVIEW**

### **2.1 INTRODUCTION**

In this chapter, the basic information and developments related to unsaturated soil mechanics studies are presented. The concepts of matric suction and its contribution to the shear strength are also discussed. In order to gain background information, this chapter also presents the previous research works that have been carried out related to the saturated and unsaturated soils.

### **2.2 UNSATURATED SOILS BEHAVIOUR**

#### **2.2.1 General**

In many parts of the world, mainly in arid and semi arid origins, soils occur in dry or partially saturated conditions. In such states, soils are very different in engineering behaviour. Hence, we cannot understand these soils within the concepts of classical soil mechanics that has been based on soils under saturated condition. In a partially saturated or unsaturated condition, soil structures are characterised by the interaction between solid particles, air and water. In unsaturated soils, the pore water pressure is lower ( $u_w$  is negative) than atmospheric pressure ( $u_a$  equal zero) and generates suction ( $u_a - u_w$ ) in the soil. Therefore, this additional factor should be taken into account in understanding their behaviour. Early studies have already determined the significant contribution of matric suction in controlling the behaviour of unsaturated soils (Croney et al. 1958, Bishop and Donald 1961 and Bishop and Blight 1963). Since then much research has been carried out, however it was relatively slow compared to the study of

saturated soils (Fredlund and Rahardjo 1993). Thus, a better concept is needed which has a capability to explain the behaviour of soils in unsaturated condition. In the last two decades, many studies have been made and a number of constitutive models have been proposed (e.g. Alonso, et al. 1990; Toll, 1990; Wheeler and Sivakumar 1995; Gallipoli et al. 2003).

### **2.2.2 Matric Suction and Axis Translation Technique**

Matric suction is known as one of the main factors that has a significant effect on the engineering behaviour of unsaturated soils. A reduction in matric suction can decrease the strength of soil, as unsaturated soils become saturated, sometimes resulting in disastrous engineering problems such as slope failure.

The Review Panel Statement (1965) states that soil suction comprises two components, namely matric suction and osmotic (solute) suction. Matric suction is the negative pore water pressure due to the surface tension force at the boundaries (menisci) between the water and gas phase present in unsaturated soils. Meanwhile the solute suction is caused by the presence of dissolved salts within the pore water.

In unsaturated soils, the forces are influenced by the arrangement of water and air within the voids and by the interaction between water, air and the soil skeleton (Vassallo and Mancuso 2000). There are two types of water present in the voids in unsaturated soils. The first is the meniscus water which occurs at the contact points between the particles and the second is known as bulk water that fills the voids within assemblages of particles being bounded by air. As water is further drained out from soil, menisci will start to form at the air-water boundary and previous menisci will become of smaller radius and greater surface tension will be required to maintain the meniscus (Toll et al 1987). The radius of meniscus curvature of contractile skin has a direct implication on the capillary effect (Fredlund and Rahardjo 1993). The radius effect of the meniscus of contractile skin (assumed that the contact angle is zero) is shown in the following equation:

$$(u_a - u_w)_d = 2 \frac{T_s}{R_s} \quad \dots (2.1)$$

where,  $(u_a - u_w)_d$  = matric suction or difference between pore-air and pore-water pressure acting on the contractile skin

$T_s$  = surface tension of the contractile skin or the air-water interface  
(e.g.,  $T_s = 72.75$  MN/m at 20°C)

$R_s$  = radius of curvature of the contractile skin or the radius of the maximum pore size

The effect of height of capillary rise and radius of curvature was also studied by Taylor (1948). An increase in radius of the curvature causes a decrease in capillary height. Toll et al. (1987) showed that the maximum suction which can be achieved is dependent on pore size (Figure 2.1). According to this figure, the suction value increases with decreasing pore size. The maximum pressure that can be sustained by a meniscus of a given radius is clearly higher in clay compared to coarser particles. In addition, the rise of capillary height in soils is very dependant on the distribution of pore size. However, non-uniformity of pore size distribution in soils can result in hysteresis in the soil-water characteristic curve (water retention curve) (Fredlund and Rahardjo 1993).

Measurement techniques that can be used to measure matric suction in soils can be either direct or indirect. In direct techniques, the negative pore water pressure is actually measured by measuring instruments such as a tensiometer, osmotic tensiometer, suction probe and the pressure plate. Meanwhile in indirect techniques, intermediate parameter is measured that can be correlated to suction through a particular calibration or theoretical support (e.g. filter paper method, porous block and thermal conductivity sensors, Ridley 1993).



A measurement of pore water pressure in soil with high suction is almost impossible due to the cavitation problem. When pore water pressure becomes too negative (approximately -100kPa), cavitation is inevitable. The presence of air bubbles in the measuring system causes measurement of pore water pressure is no longer accurate. In order to avoid this problem, Hilf (1956) developed an axis translation technique. This approach has been widely used in order to control matric suction in the laboratory. In this technique, the pore water pressure is referenced to positive pore air pressure. Therefore, by increasing the air pressure to a positive maximum, the water pressure in the measuring system can remain positive, thus cavitation can be avoided. Moreover, it appears that the matric suction value is unaffected by the elevating of the air pressure (Hilf 1956). Bishop and Blight (1963) examined the influence of the axis translation technique on the shear strength of compacted Talybont clay. Unconfined triaxial tests were carried out on two samples, one was tested using axis translation and the other was performed under atmospheric air pressure. The results showed that both samples were identical up to the maximum deviator stress (Figure 2.2).

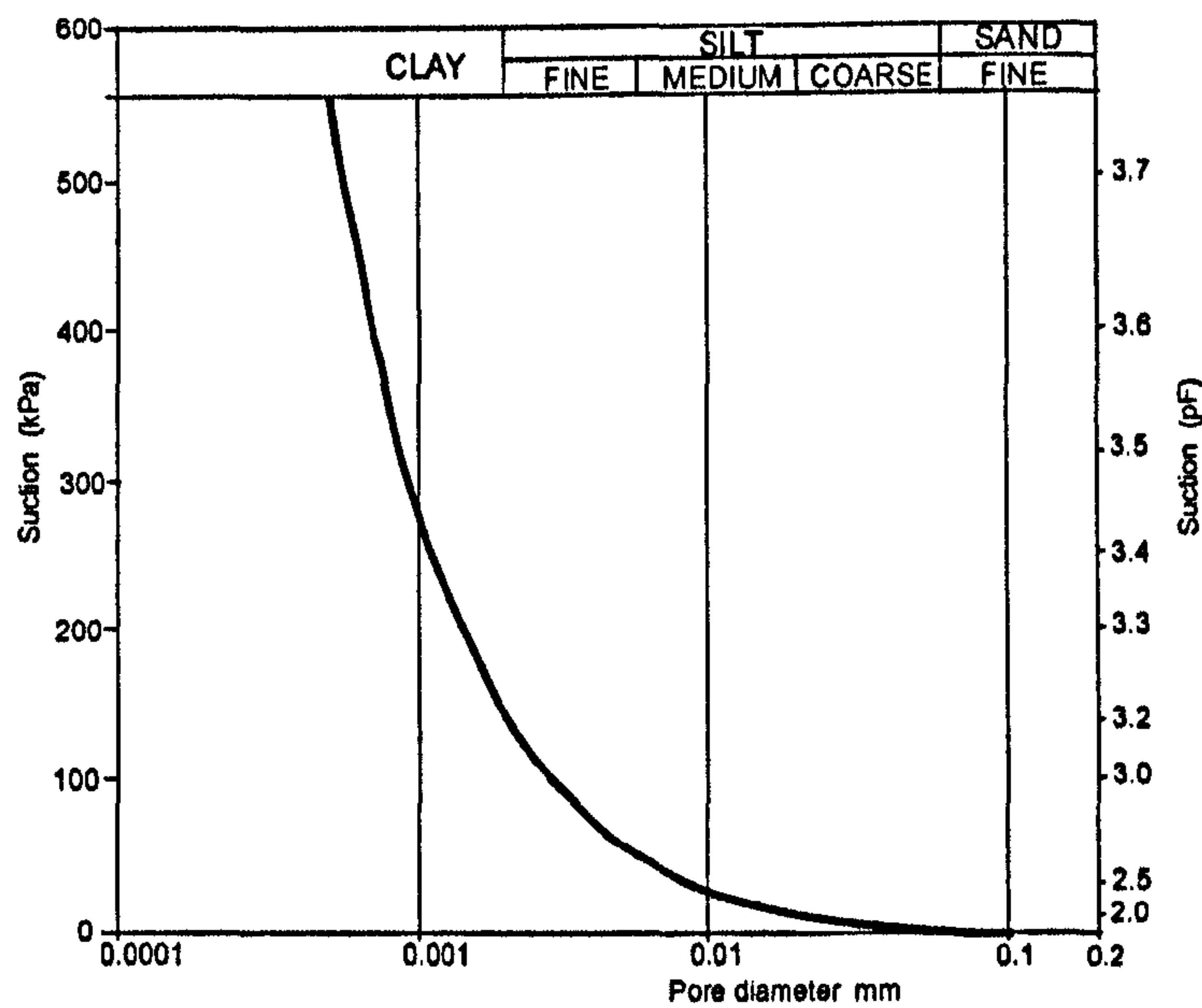


Figure 2.1: The relationship between suction and pore diameter (after Toll et al 1987)



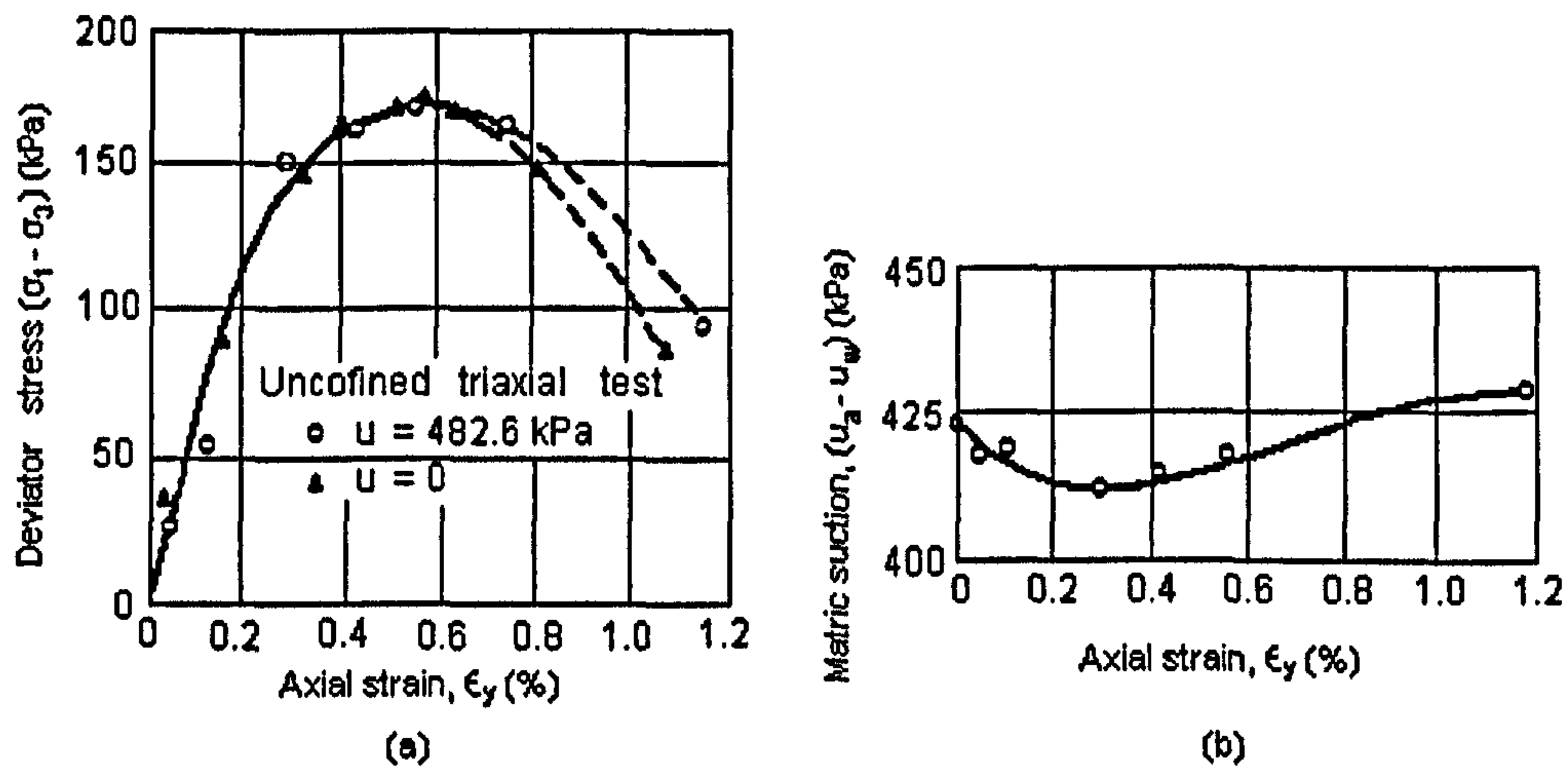


Figure 2.2: The unconfined triaxial test on compacted Talybont clay with and without translation; (a) Deviator stress vs. strain; (b) matric suction vs. strain during test with axis translation (from Bishop and Blight 1963)

### 2.2.3 Stress State Variables and Soil Strength

The shear strength of unsaturated soil has been formulated with regard to the nature of the phase systems, which are different from the saturated condition. In saturated soils, the concept of effective stress has been well recognised since only two phases system exist (solid and water). Meanwhile, in unsaturated soils, three phase systems need to be considered: air, water and solid phases. These three phases interact with each other and give significant impact to the shear strength. Thus it is important to investigate the relationship between stress, strain, strength and water content in studying unsaturated soils' behaviour. Unlike in saturated soils, the changes of water content,  $w$  (or degree of saturation,  $S_r$ ) must be treated independently of volumetric strain, in order to define the volumes of water and air within soil voids (Wheeler and Karube 1996).

Initially, Bishop (1959) tried to explain the behaviour of unsaturated soils by extending the effective stress idea. His equation attempted to combine total stress,

$\sigma$ , pore air pressure,  $u_a$  and pore water pressure,  $u_w$ , within a single effective stress tensor  $\sigma'$ . The constitutive equation (2.2) demonstrates the relationship between the effective normal stress with the net state variable (net stress indicates it is referenced to air pressure,  $\sigma - u_w$ ) and the matric suction ( $u_a - u_w$ ) as shown below.

$$\sigma' = (\sigma - u_a) + \chi(u_a - u_w) \quad \dots (2.2)$$

where,  $\sigma'$  = effective normal stress

$\sigma$  = total stress

$u_a$  = pore air pressure

$u_w$  = pore water pressure

$u_a - u_w$  = matric suction

$\chi$  = factor related to the degree of saturation of the soil

Meanwhile Coleman (1962) proposed the used of “reduced” stress variables represented by  $(\sigma_1 - u_a)$ ,  $(\sigma_3 - u_a)$  and  $(u_a - u_w)$  corresponding to axial, confining and pore water pressures, respectively. Then Bishop and Blight (1963) suggested with a subsequent equation (equation 2.3) after reassessment of the proposed effective stress equation.

$$\tau' = [(\sigma - u_a) + \chi(u_a - u_w)] \tan \varphi \quad \dots (2.3)$$

The validity of Bishop’s effective stress equation was first challenged by Jennings and Burland (1962) regarding the possibility of combining  $\sigma$ ,  $u_a$  and  $u_w$  within a single effective stress component. The argument was based on the fact that the applied external stress on the boundary of a soil element and suction within the pore water act in quantitatively different ways on the soil skeleton. The findings from subsequent studies indicated that the volumetric behaviour is not controlled by similar stress component or by any other single stress variable (Wheeler and Karube 1996). Escario and Suez (1973) revealed that during wetting under decreasing suction ( $u_a - u_w$ ), soil usually increase in volume (swell) when wetting

occurs at a low value of applied net stress ( $\sigma - u_a$ ) and decrease in volume (collapse) if wetting occurs at high value of net stress. When the suction gradually decreases, the soil swells initially and subsequently is followed by collapsing. Thus, the proposed equation proved unable to represent the complex phenomenon of wetting-induced swelling and collapsing within a single effective stress. Therefore, this concept of effective stress could not explain the volume change behaviour in order to explain the shear strength behaviour.

The state surface defining the relationship between void ratio,  $e$  and degree of saturation,  $S_r$  to the net stress,  $\sigma - u_a$  and matric suction,  $u_a - u_w$  was presented by Matyas and Radhakrishna (1968). They proposed the concept of “state parameter” in order to describe the volumetric behaviour of unsaturated soils. The schematic illustration (Figure 2.3) represents the swelling of soil caused by the wetting at low net stress and collapsing of soil during wetting at high value of net stress.

Fredlund and Morgenstern (1977) recommended that the stress state of unsaturated soils could be sufficiently explained based on independent stress state variables by combining any two of the stress states variables ( $\sigma - u_a$ ,  $\sigma - u_w$  and  $u_a - u_w$ ). Later, Fredlund et al. (1978) proposed an equation for shear strength with the two stress state variables of ( $\sigma - u_a$ ) and ( $u_a - u_w$ ). This combination has been found to be the most meaningful combination in engineering practice. The equation using these two stress variables is shown as follows:

$$\tau = c' + (\sigma - u_a) \tan \phi' + (u_a - u_w) \tan \phi^b \quad \dots (2.4)$$

where,  $\tau$  = shear strength

$c'$  = effective cohesion of the soil

$\sigma$  = total stress

$u_a$  = pore air pressure

$u_w$  = pore water pressure

$\varphi'$  = angle of internal friction associated the net normal stress state variable,  
 $(\sigma - u_a)$

$\varphi^b$  = angle of internal friction associated with matric suction  $(u_a - u_w)$

In this combination, the effect of a change in total normal stress can be separated from the effect caused by a change in the pore water pressure (Fredlund and Rahardjo 1993). In addition, in many engineering situations, the field pore air pressure  $u_a$  is zero, so that the net stress and matric suction simplify to total stress  $\sigma$  and negative pore water pressure  $(-u_w)$ , respectively (Wheeler and Karube 1996).

In equation 2.4, an effective angle of internal friction equation,  $\varphi'$  is related to the contribution of the net normal stress state variable while, another internal friction angle,  $\varphi^b$  is related to the contribution of the matric suction variable to the shear strength.

This failure criterion for an unsaturated soil is known as an extended Mohr-Coulomb failure criterion, which shows a smooth transition to the shear strength of saturated soil (Fredlund and Rahardjo 1993). As a soil approaches saturation, the pore water pressure approaches equality with pore air pressure,  $(u_w = u_a)$ . Thus, the unsaturated soil shear strength becomes the shear strength of the saturated soil as matric suction component becomes nil  $(u_a - u_w = 0)$ . The shear strength equation of saturated soil was developed using the effective stress concept (Terzaghi 1936) and Mohr-Coulomb failure criterion as follows:

$$\tau = c' + (\sigma - u_w) \tan \varphi' \quad \dots (2.5)$$

The extended Mohr-Coulomb failure criterion, which incorporates the shear strength of saturated and unsaturated conditions of a soil, can be presented in a three-dimensional plot (Figure 2.4). In saturated soil, the failure envelope is plotted in two-dimensional graph consists of shear strength,  $(\tau)$  and effective normal stress,  $(\sigma - u_w)$ . The third dimension for the extended Mohr-Coulomb failure



criterion is the matric suction component. The intersection line between the extended Mohr-Coulomb failure envelope and the frontal plane is the failure envelope for the saturated condition (Fredlund and Rahardjo 1993).

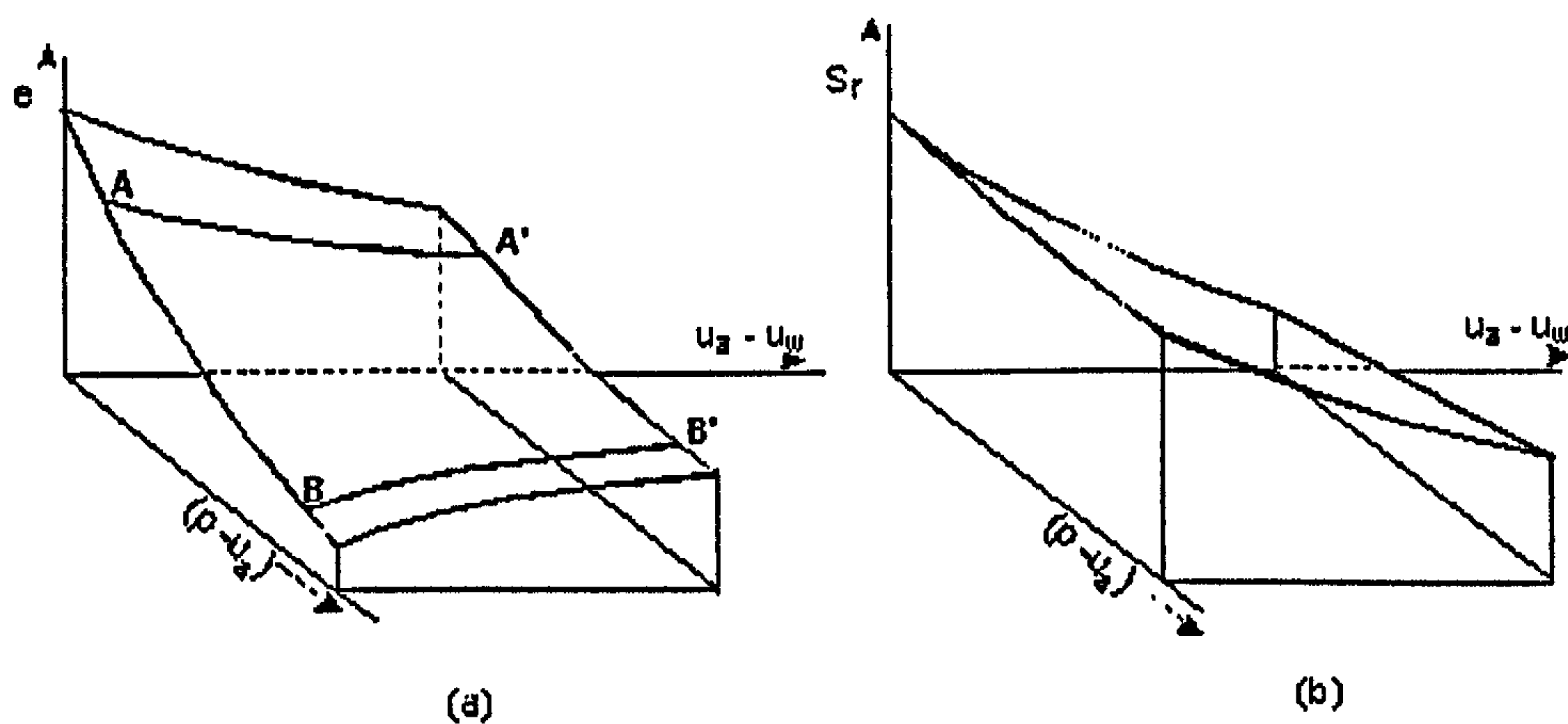


Figure 2.3: The state surface for void ratio and degree of saturation (after Matyas and Radhakrishna 1968)

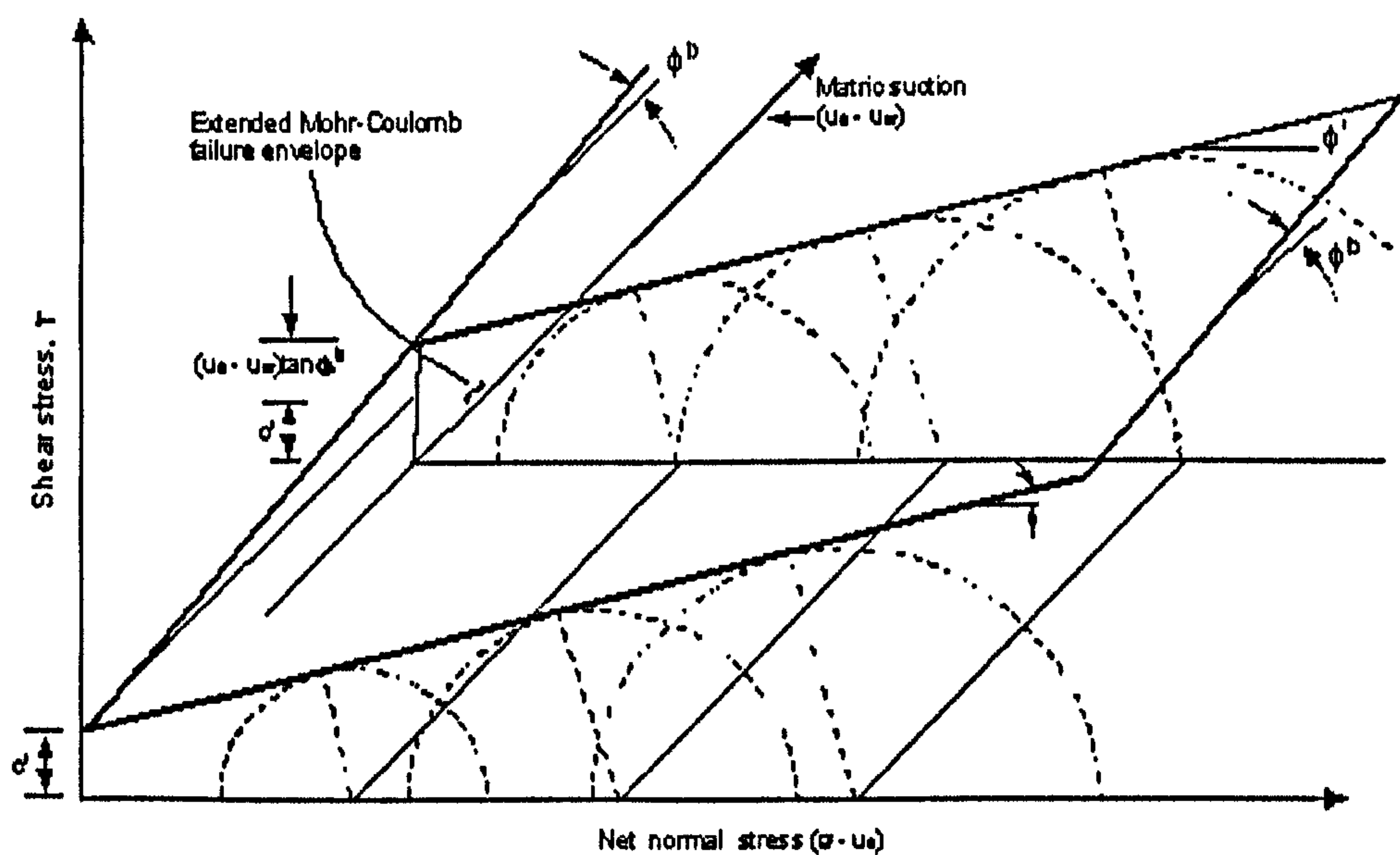


Figure 2.4: The extended Mohr-Coulomb failure envelope for unsaturated soils (after Fredlund and Rahardjo 1993)



## **2.3 PREVIOUS RESEARCH**

### **2.3.1 General**

Soil particles may be held by the presence of bonding between them. Many natural soils are usually weakly bonded and easily destructured due to sampling, transportation and storage. The occurrence of bonding might be inherited from the parent rock or resulting from the crystallization of minerals during weathering. Even though the presence of bonding in residual soils is relatively weak, it provides a component of strength and stiffness, which will have a strong influence on engineering behaviour (Fookes 1997). According to Vaughan et al. (1988) the weak bonds in soils tend to be broken down and destructured by loading and strain and once broken the behaviour is irrecoverable and this changes their engineering behaviour. Early studies on the engineering behaviour of soils were solely confined to saturated conditions. However, in many soil engineering problems, the observed phenomena cannot be successfully described using classical soil mechanics, as many parts of the world, soils are in unsaturated conditions. Hence, the behaviour of soils is influenced by the presence of bonds and suction.

In the last two decades, many attempts have been made to extend the theoretical models of soil behaviour (which have largely been developed from studying the behaviour of remoulded and reconstituted soils) to include the effects of bonded structure on soil behaviour. Several researchers have broadened the critical state framework to include unsaturated soils (Alonso et al. 1990; Toll 1990; Wheeler and Sivakumar 1995).

Vaughan (1985) and Fredlund (1998) urged the need to develop a framework for describing and clarifying the engineering properties of unsaturated soils. It is important to understand the behaviour of residual soils in unsaturated conditions because these deposits most likely occur in unsaturated state.

In the following section, previous researches related to the saturated and unsaturated soils are reviewed.

### 2.3.2 Studies on Saturated Behaviour of Bonded and Destructured Soils

Vargas (1953) studied the characteristics of residual soils from southern Brazil using one-dimensional compression tests on intact samples and remoulded soil samples. Comparison was made between natural soil and remoulded soils prepared at liquid limit and at natural water content. He recognised the effect of structure in residual soils when compared with the remoulded soils (Figure 2.5).

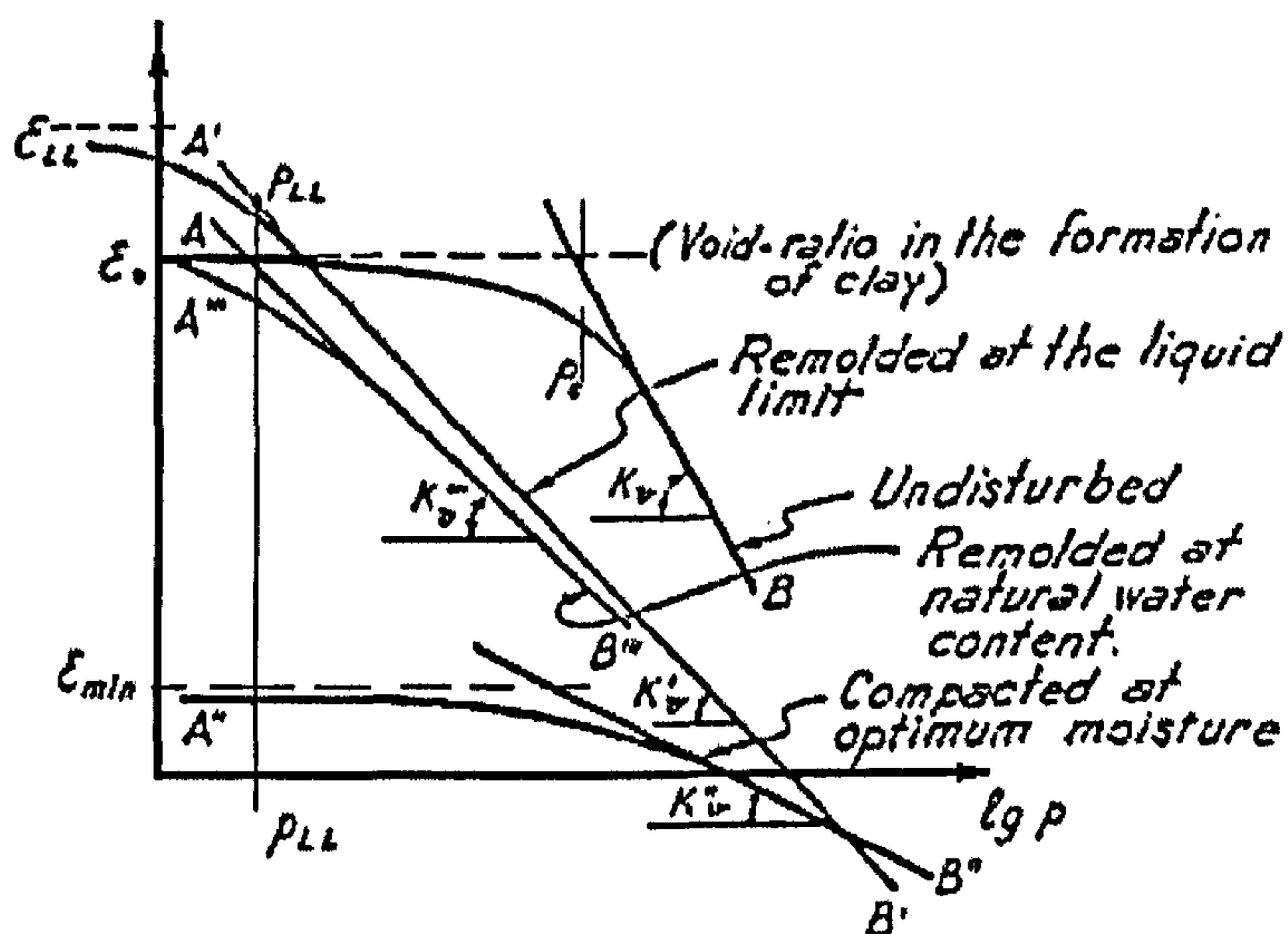


Figure 2.5: Results from one-dimensional compression tests on residual soils (from Vargas 1953)

A study on a residual soil taken from Java was carried out by Wesley (1974) and he found that the undisturbed soil was stiffer compared with the remoulded sample and it could sustain larger pressures compared to a remoulded sample with the same void ratio. It suggested that remoulding the sample caused the breakdown of its structure and permitted a large amount of water to drain out of its structure, thus

the curves for remoulded soils lie at lower void ratios than undisturbed soil (Figure 2.6).

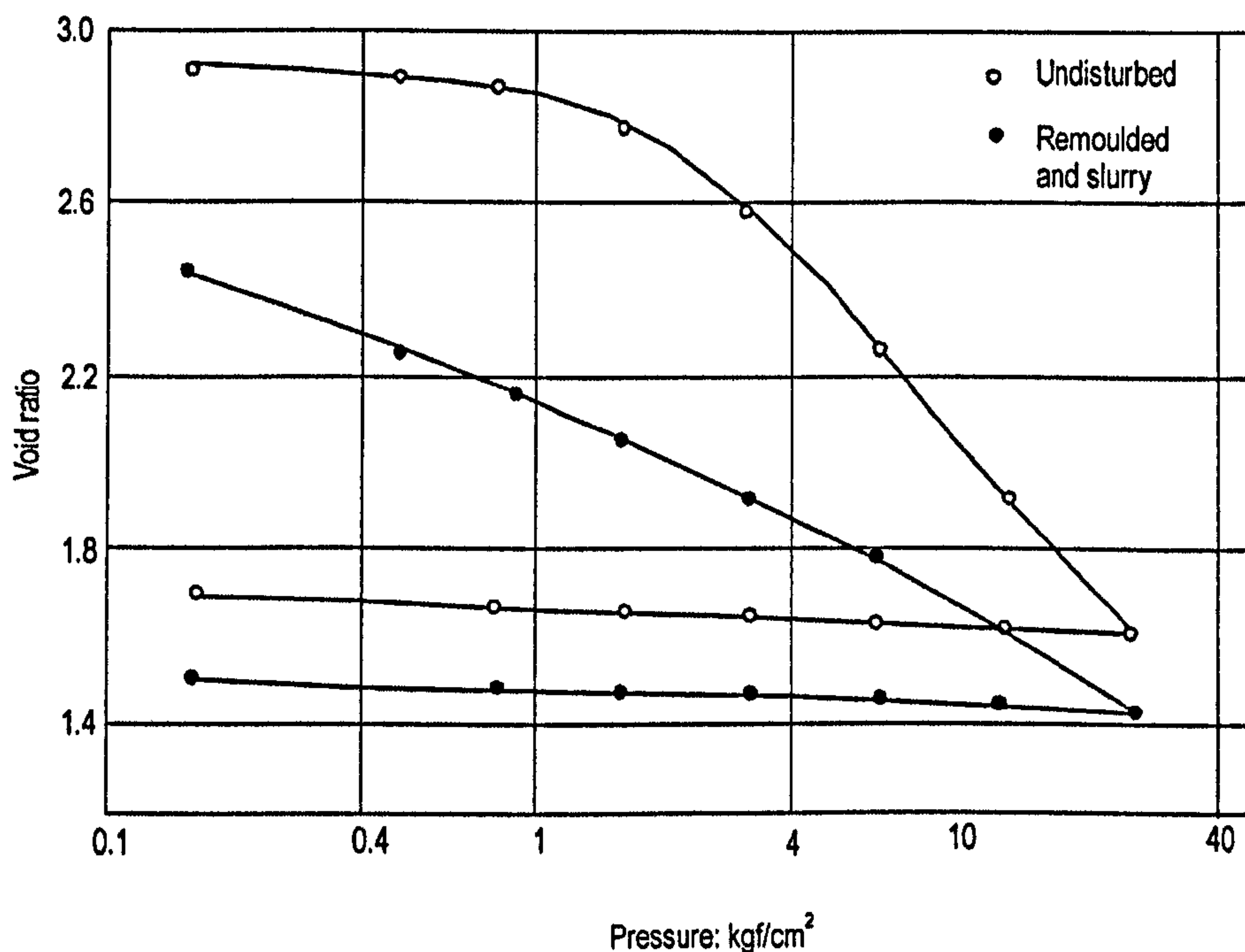


Figure 2.6: The results from the oedometer tests on residual clays of volcanic origin (after Wesley 1974)

A study of natural cemented soils from Canada (Labrador clay) was undertaken by Sangrey (1972). The results from the triaxial tests (Figure 2.7a and 2.7b) showed that the soils were brittle at low confining stress (LA7) where the cementation dominated and small friction resistance was left once bonding was destroyed by shear failure (a). Meanwhile, the behaviour changed to ductile when the stress level increased (LA8) which allowed sufficient frictional resistance to build up after the cementation bonds were broken. Then, LA8 showed a second peak after large strains (d) before deviator stress began to decrease.

Clough et al. (1981) examined the deposits of cemented sands, collected from the Californian coastal area. These deposits, as other cemented soils, were characterized by their stability on natural steep to steeper slopes ( $\geq 60^\circ$ ). These natural slopes failed during seismic vibration as a result of brittle failure. Brazilian tests showed that the tensile strength of weakly cemented soil was 9 to 10 kPa.

Meanwhile from the triaxial drained tests on weakly cemented soils collected from a Pacific site (Figure 2.8) showed similar behaviour; at low confining stress, it was associated with brittle failure and becoming ductile at higher confining pressures.

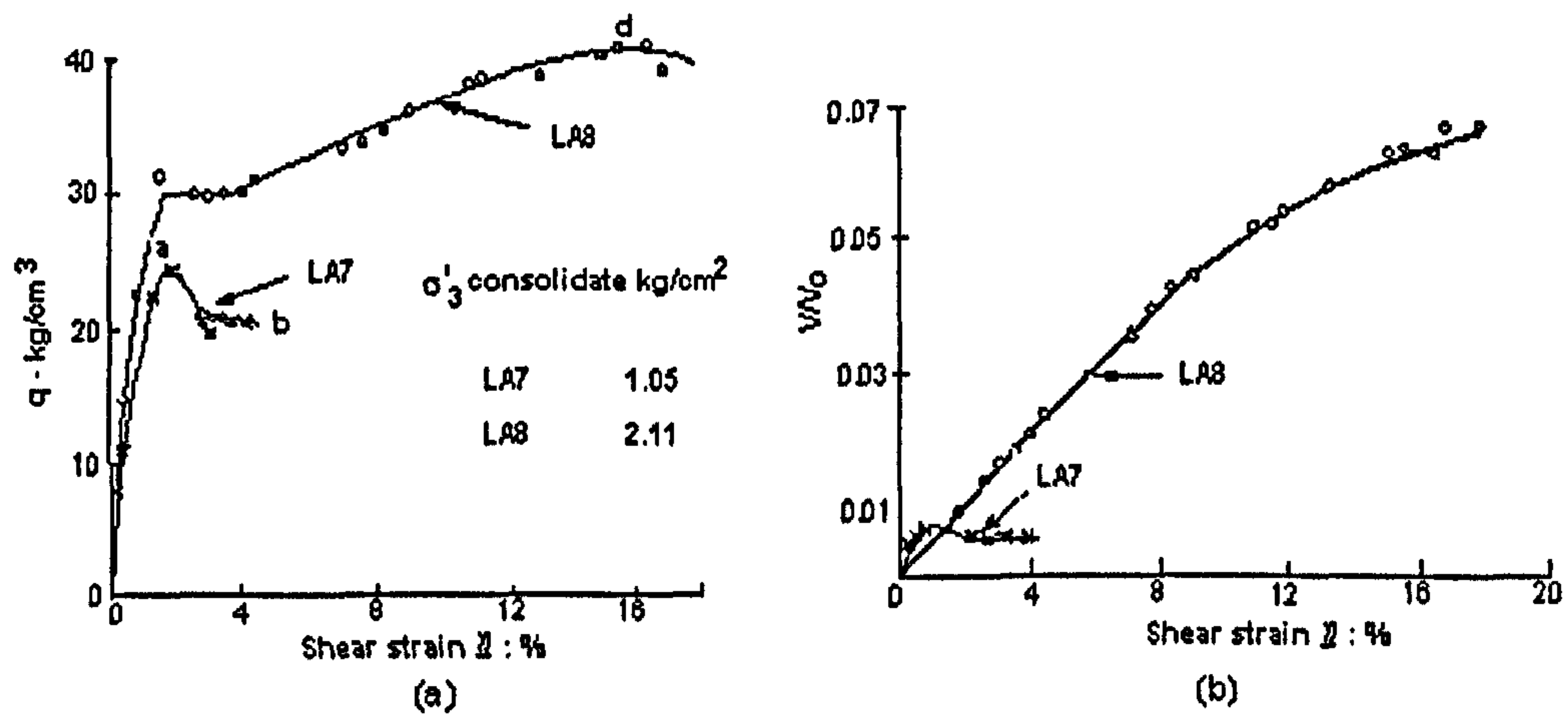


Figure 2.7: Stress vs. strain curves for Labrador clay (after Sangrey 1972)

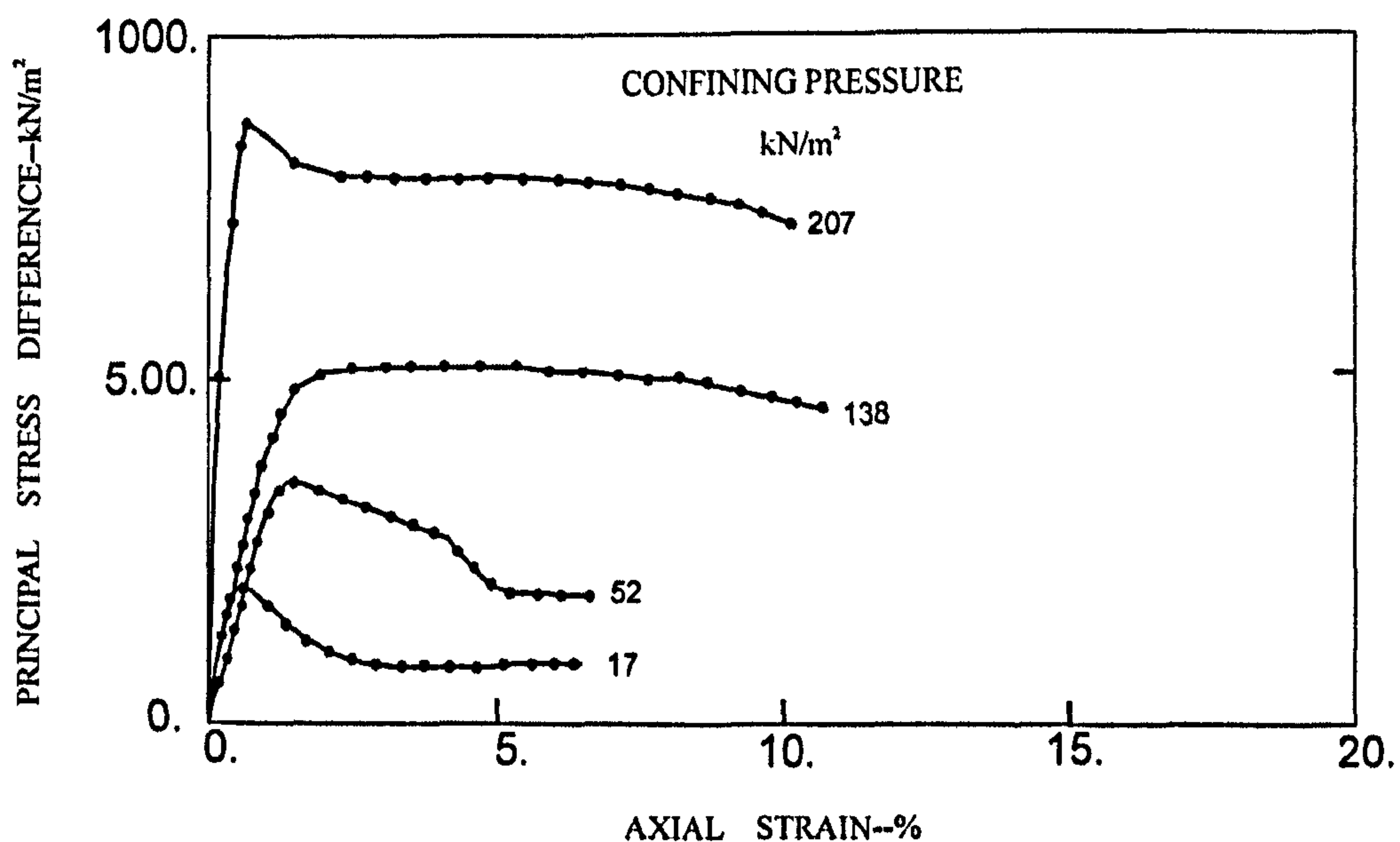


Figure 2.8: Stress vs. strain curves of a weak soils from the Pacific site (after Clough et al 1981)



A study on artificially cemented sands was conducted by Sitar (1981) in order to simulate the property of natural weakly cemented sands. In his conclusion, he highlighted that the behaviour of natural cemented sands was characterized by density, grain size distribution, and grain shape and grain arrangement.

Maccarini (1987) studied the effect of bonds using artificial samples, which were prepared by mixing sand, kaolin 'sand' (crushed fired kaolin or c.f.k.) and kaolin slurry. The idea of adding the c.f.k was to represent weak grains that are usually present in residual soils. The mixture was air-dried and then fired at 500°C for 5 hour in a furnace. Firing the kaolin slurry generated bonds between sand particles. The bond strength of the tested samples was kept uniform by firing at similar temperature and duration of firing.

The first yield was identified at the end of the initial linear portion of the deviatoric stress-axial strain curve meanwhile the second yield was the point of maximum curvature of similar graph plotted at normal stress-strain curve. Figure 2.9a and 2.9b show the first and second yields for two bonded soils at different void ratios. The results from the tests found that the first yield was often muted at lower strain values and better defined for second yield at higher strain. However, by increasing the density of the samples, determination of the second yield became more difficult. He also found that the increment of stress to move from the first yield to second yield, decreased with increasing density, in contrast, increased with decreasing porosity. Meanwhile, the possible states for two samples based on their initial void ratio are shown by Figure 2.9c.



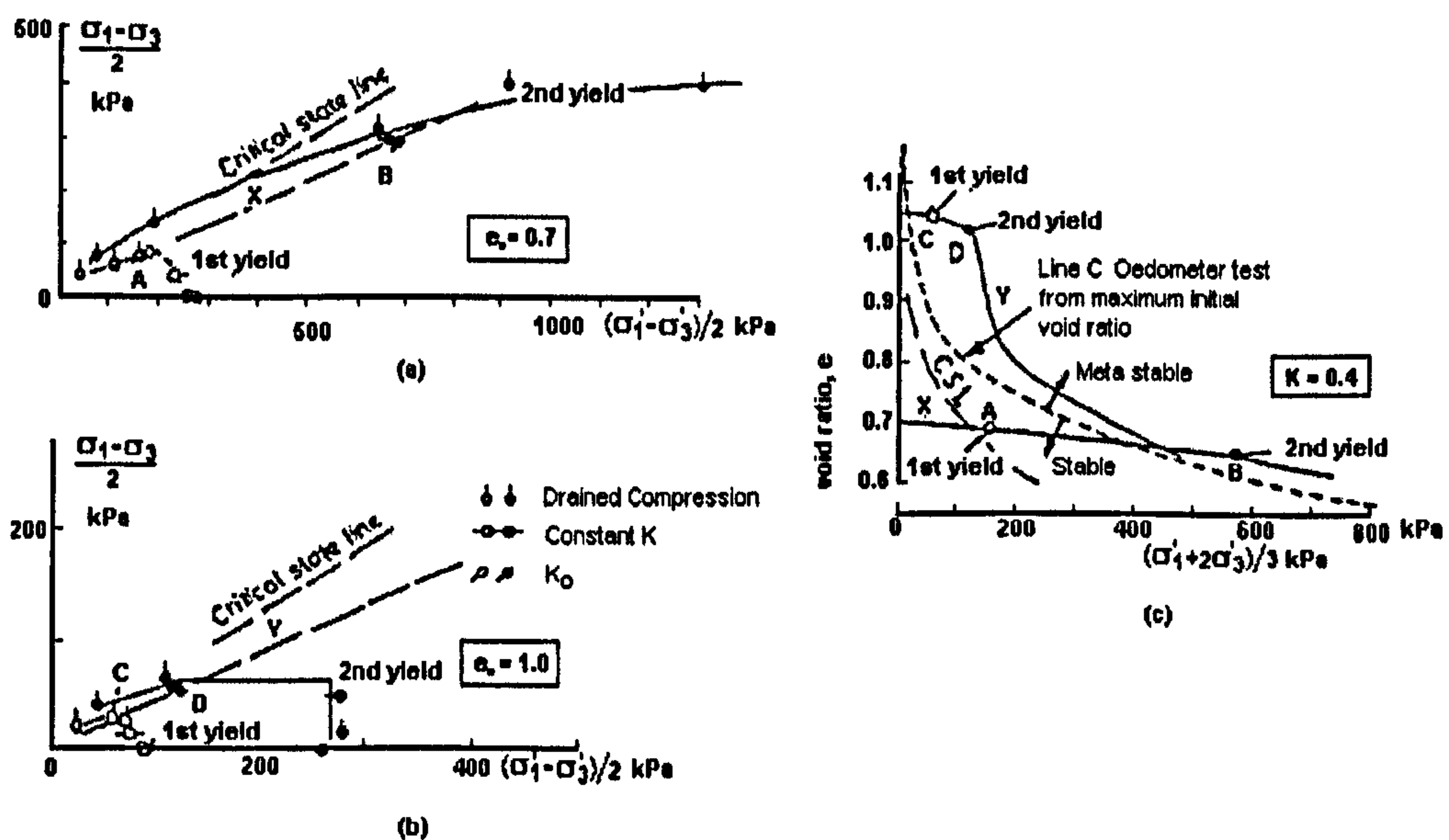


Figure 2.9: The position of first and second yields for artificially bonded samples (after Maccarini 1987)

Vaughan et al. (1988) stated that the stress imposed on a bonded soil is partially carried by the bonds and the partly by interparticle contacts. He added that yield of bonded structure can be mapped in deviatoric stress/mean stress/void ratio space. At initial loading, increasing stress is carried by the bonds and as a result bonded soil becomes stiffer. With increasing bond stress, at some stage some bonds begin to break (yield) and a first yield occurs (Figure 2.10). This is the starting point in which bond strength starts to decrease and with any further increases in bond stress more bond breakdown will happen. At some point, the decrease of bond strength becomes equal to the increase of bond stress, and a second yield occurs (Vaughan 1988). From this point, bonded soil experiences dramatic loss in bond strength and stiffness. The bonded soil will be in destructured state when soil loses its entire bonding.

Bressani (1990) carried out further study based on Maccarini's work using the artificial bonded soils with various densities and different mixtures of sand, c.f.k and kaolin at higher stresses up to 3.5 MPa. Samples were prepared with different compositions and bond strength. Series 100, 200 & 600 had similar composition while series 300 contained c.f.k. Series 100 was prepared to a higher void ratio

compared to 200 & 600. Figure 2.11a presents the results of the tests performed on the four series under the drained triaxial tests. In term of bond strength, series 600 was the strongest among the samples. The yield surface of soil is determined according to the change in behaviour when soil is sheared. The two yields of the bonds were defined from the  $q - \epsilon_a$  curves plotted to natural and log – log scale. Series 600 and 200 showed higher yield surface compared with series 100 and 300. In other hand, series 300 indicated an earlier plunge in the yield surface compared to series 200 ( $\sigma' > 1000$  kPa). It indicated that a change of the mineralogy (presence of c.f.k) had influenced the shape of the yield surface at a particular stress level. The position of yield surface in the stress space was also affected by the void ratio. This can be clearly seen for the samples in series 100 and 200 that had a different void ratio and the same composition.

The peak shear strength envelopes for different series of the artificial samples (Figure 2.11b), clearly show that every envelope superimposes each other at very low stresses. Series 00 represents samples composed of sand and kaolin with half the void ratio compared with series 200. Series 600 had higher value than the other series as shown by test 604; suggesting that bonding influenced the shear strength instead of mineral composition. Unfortunately, the 604 test was not properly defined in this region. At higher stresses, it was clearly seen that series 300 experienced significant drops of its peak strength as a result of there being no quartz present.

Meanwhile it is clearly shown in Figure 2.11b (curves a and b) that both samples had the same yield stresses whether prepared with or without c.f.k. In addition, samples that were prepared without c.f.k showed stiffer states even for samples with the same void ratio and higher bond strength (Figure 2.11c). This conclusion was drawn from a comparison of the secant stiffness (at 0.1% axial strain) during shearing for the different artificial samples. The secant stiffness of each sample was plotted against confining pressure,  $p'$ .

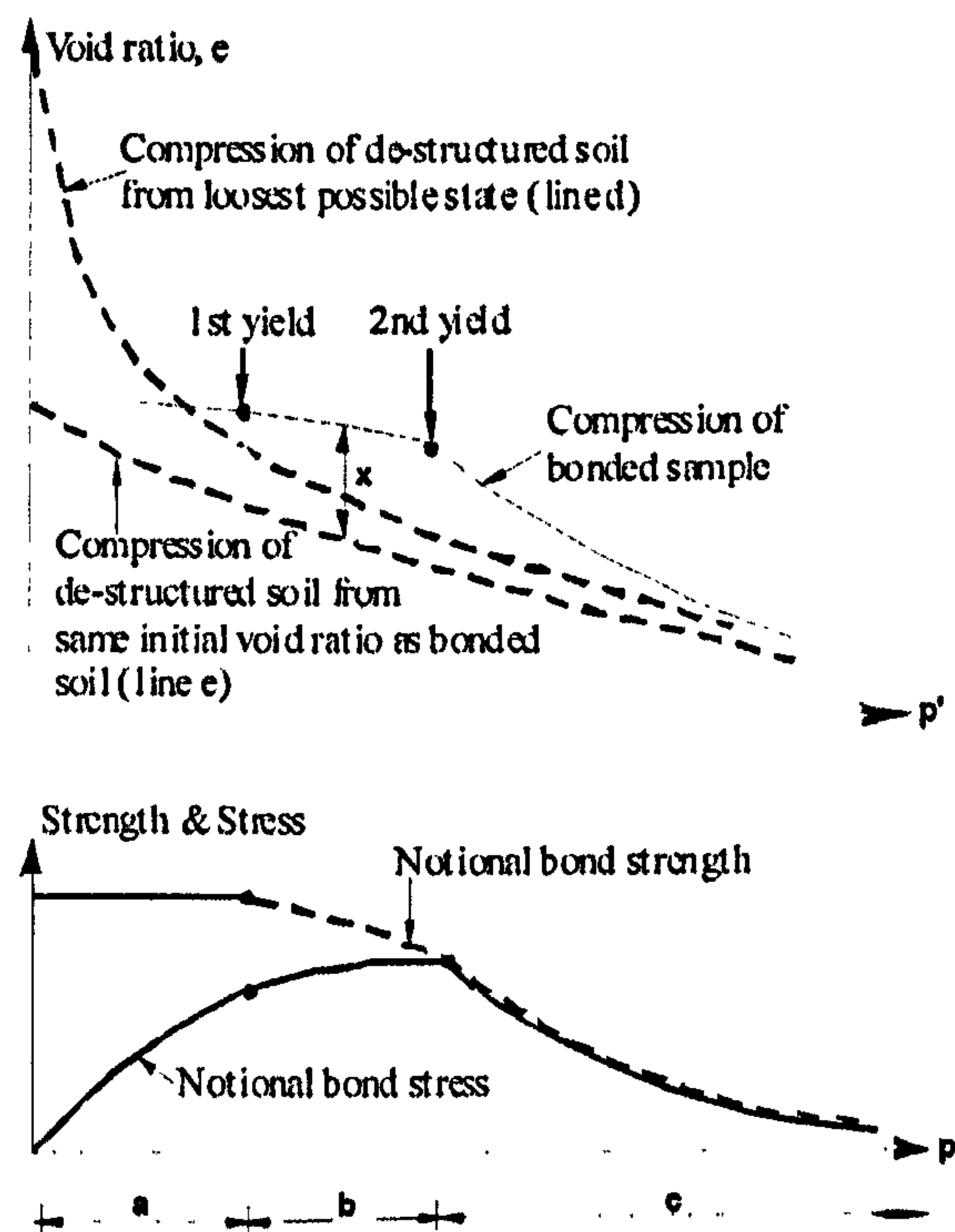


Figure 2.10: A tentative explanation of first and second yield (after Vaughan et al. 1988)

Leroueil and Vaughan (1990) stressed that with the occurrence of structure in soils, whatever its cause (deposition of carbonate, solution and deposition of silica), the effect on the behaviour of soils is very similar. The results from drained triaxial tests for a soft clay (Saint-Vallier clay) and soft carbonate rock (oolitic limestone) revealed a quite similar pattern (Figure 2.12). Some tests from residual soils carried out earlier for a range of materials were mentioned by Bressani (1990) in his study. These included a volcanic agglomerate from Canary Islands (Uriel & Serrano 1973), residual soil from gneiss, Brazil (Sandroni 1981) and residual soil from basalt, Brazil (Maccarini 1987) indicated that the yield curve of each sample was centred on the isotropic line, indicating an isotropic structure pattern (Figure 2.13).

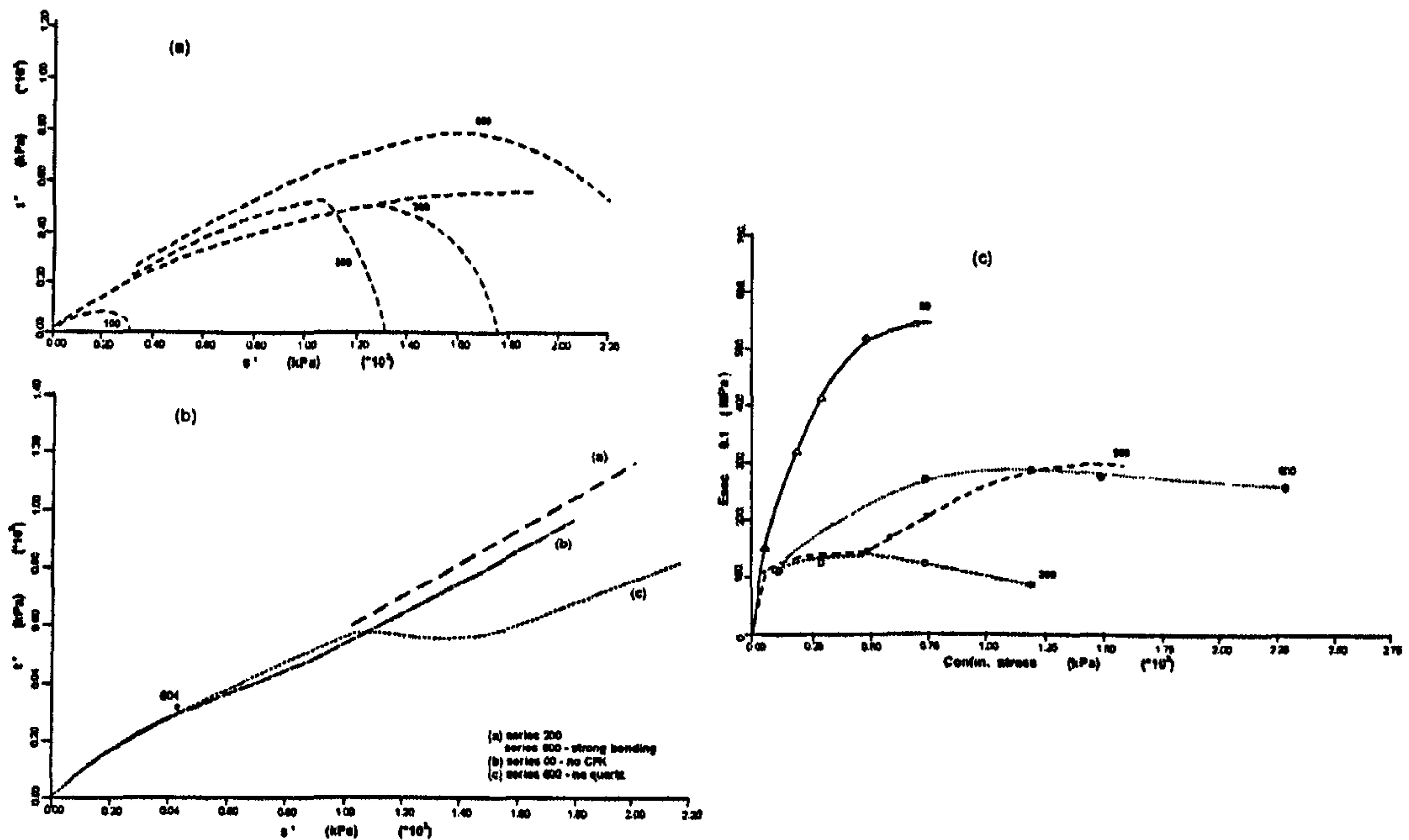


Figure 2.11: (a) Yield surfaces developed from four different artificial bonded soils; (b) the strength envelopes of the different mixture; (c) secant stiffness vs. confining effective stress for different series of artificial soil (after Bressani 1990)

Coop (1990) investigated the mechanical behaviour of uncemented carbonate sands (Dogs Bay sand) collected from the west of the Republic of Ireland. Figure 2.14a shows the ultimate states for all the drained tests carried out at standard pressure (confining stresses up to 700kPa) with  $M=1.65$ . The ultimate state points appear to suggest some curvature to the ultimate failure envelope, however results from the higher pressure (up to 8MPa) tests also gave a same value of  $M=1.65$ , suggesting no influence of stress levels on friction angle,  $\phi'$ . Stress paths for undrained tests at standard pressure are shown in Figure 2.14b. It is clearly seen that the undrained tests achieve higher stress ratios as a result from the dilative behaviour similar to that of overconsolidated clay as the path climbs up a steep Hvorslev surface towards a critical state (Coop 1990). A normalised plot for drained tests is shown in Figure 2.14c indicates a clear state boundary surface. The normalised stress paths for undrained tests were compared to the boundary surface interpreted from the drained tests (Figure 2.14d). It was found that the undrained paths curved quickly towards the Hvorslev surface. For the tests starting wet of



critical, the paths curve away from the Roscoe surface (from drained data), bypassing under the critical state and climb up the Hvorslev surface.

Airey (1993) studied natural carbonate soils using standard drained triaxial tests. The deviator stress increases linearly followed by a gradual rise toward an ultimate state accompanied by significant volumetric strain (Figure 2.15a and 2.15b). The linearity of deviator stress and axial strain responses indicate an elastic response up to yield and further detailed inspection of the volumetric strain responses reveals a departure from linearity well before the yield point as shown in Figure 2.15c. It shows the axial strain increases linearly until yield, however the radial strain only increases linearly until deviator stress reaches about 50% of the yield stress, where the radial strain remains constant until yield. After that both the axial and radial strains rise more rapidly. Airey proposed that the departure from linearity is associated with the breaking of weaker and more highly stressed bonds, until at yield a more rapid progressive breakdown of bonds occurs. He also concluded that the responses of the natural calcarenites were similar to those of other cemented and structured soils.

Huang and Airey (1993) carried out a series of triaxial tests on artificial samples of cemented carbonate sand with a wide range of density (13 to 19kN/m<sup>3</sup>) and cement content (0 to 20%). The effects of cementation and density on the stress yield are shown in Figure 2.16a and 2.16b. It showed that the yield loci increase in size with increase in cement content and density. However the effectiveness of the cementation bonds decreases as the density increases, suggesting that the bonds were relatively weak (i.e. became less effective at higher stresses).

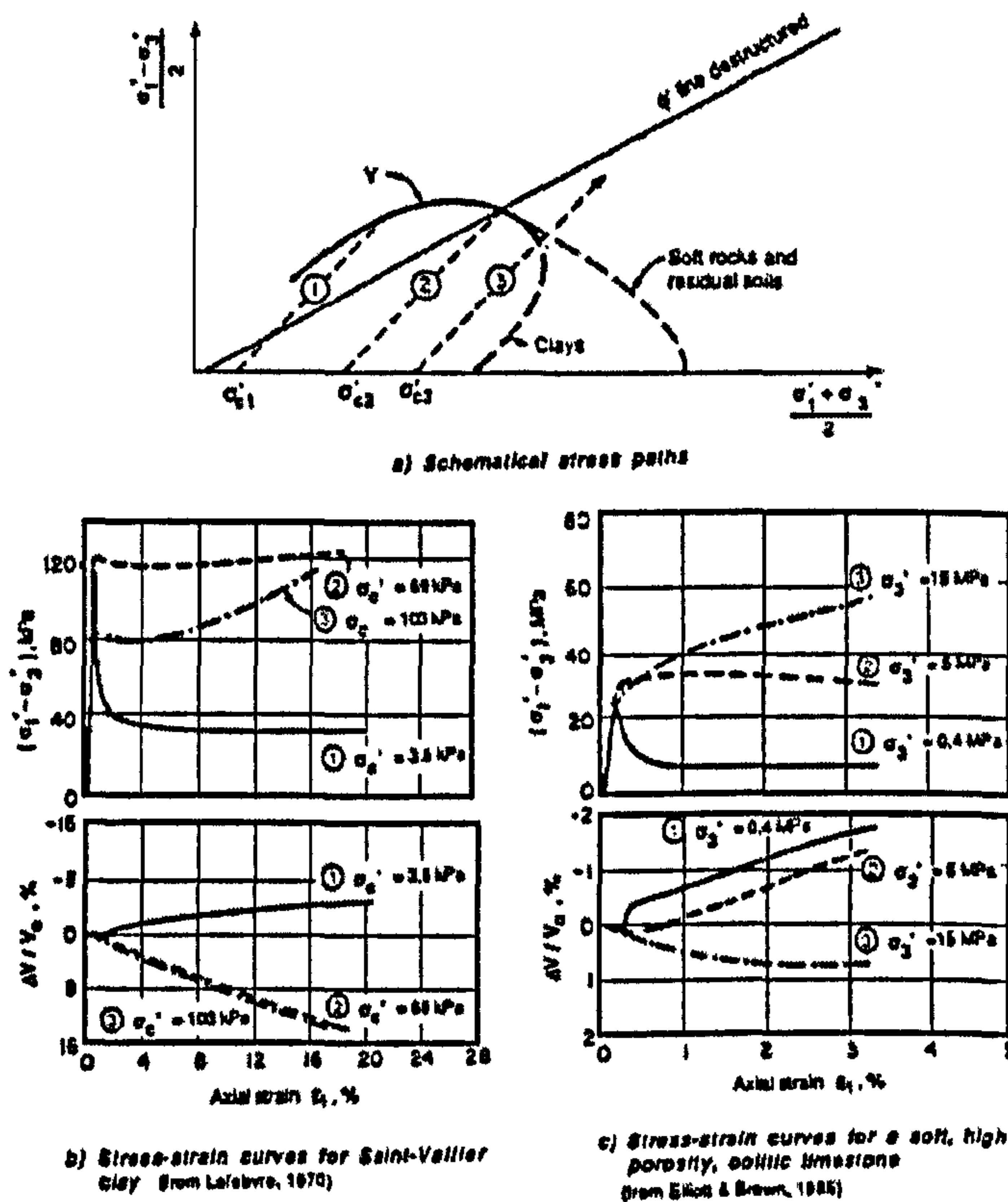


Figure 2.12: The results of the drained triaxial test on two different structured soils. (a) schematic stress path; stress vs. strain curves of (b) Saint-Vallier clay (c) soft carbonate rock (after Leroueil and Vaughan 1990)

Maccarini (1993) presented the results from triaxial drained compression tests and direct shear box tests on undisturbed residual soil samples derived from gneiss rock. Loose and medium dense samples were examined at natural water content. He found that the values of cohesion intercept and friction angle were very similar from both tests. The stress-strain curves from both tests indicated a very similar shape; exhibiting contraction for loose soils (Figure 2.17a and 2.17b) and dilation for medium dense soils. However, in terms of the initial tangential stiffness from the triaxial tests, the loose and medium dense samples showed a change in initial tangent stiffness with confining stress after the occurrence of first bond yield (Figure 2.18). In direct shear box tests, the initial tangential stiffness showed an increase in the initial tangent stiffness, as a function of normal pressure as occurs in sedimentary soils. The difference probably is a result of the different stress path followed in the two types of tests.

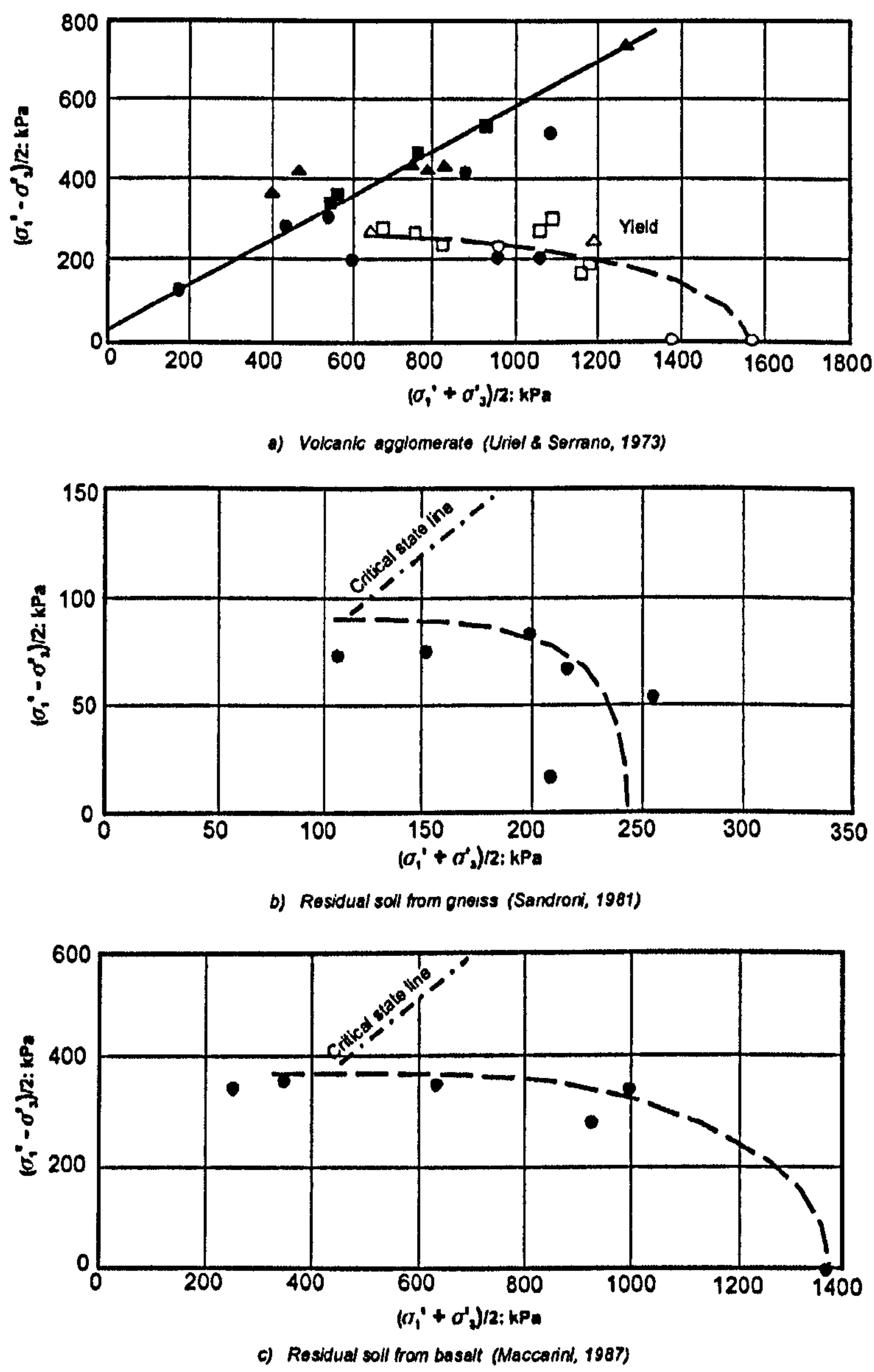


Figure 2.13: The yield curves defined from three different structured materials. (after Leroueil and Vaughan 1990)

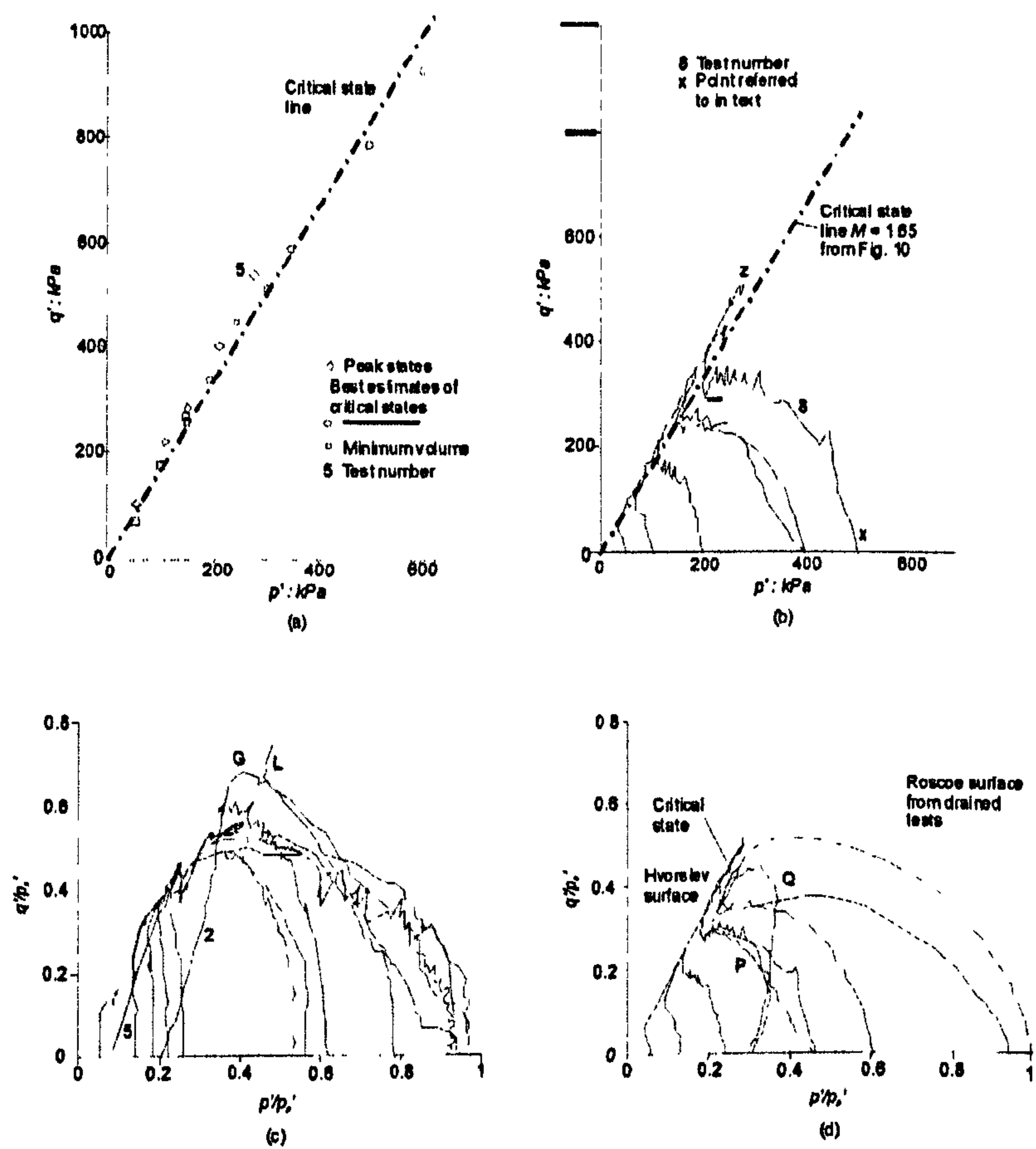


Figure 2.14: (a)Ultimate states from standard pressure drained triaxial tests; (b)Stress paths for standard undrained tests; (c)Normalised stress paths for drained tests; (d)Normalised stress paths for undrained tests (after Coop 1990).



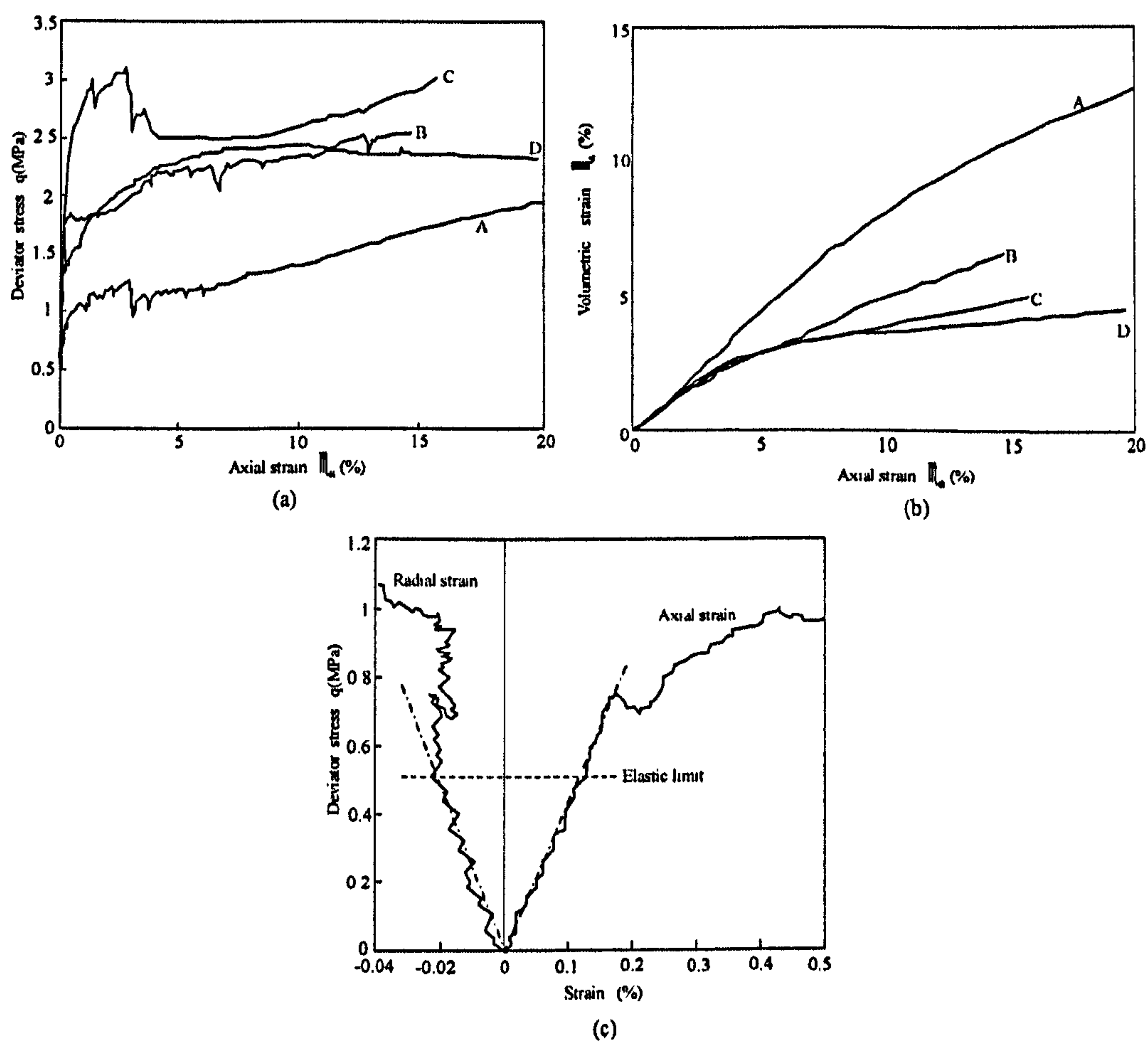


Figure 2.15: (a) Deviatoric stress,  $q$  vs. axial strain curves of drained tests; (b) volumetric strain vs. axial strain curves; (c) typical small strain response (after Airey 1993)

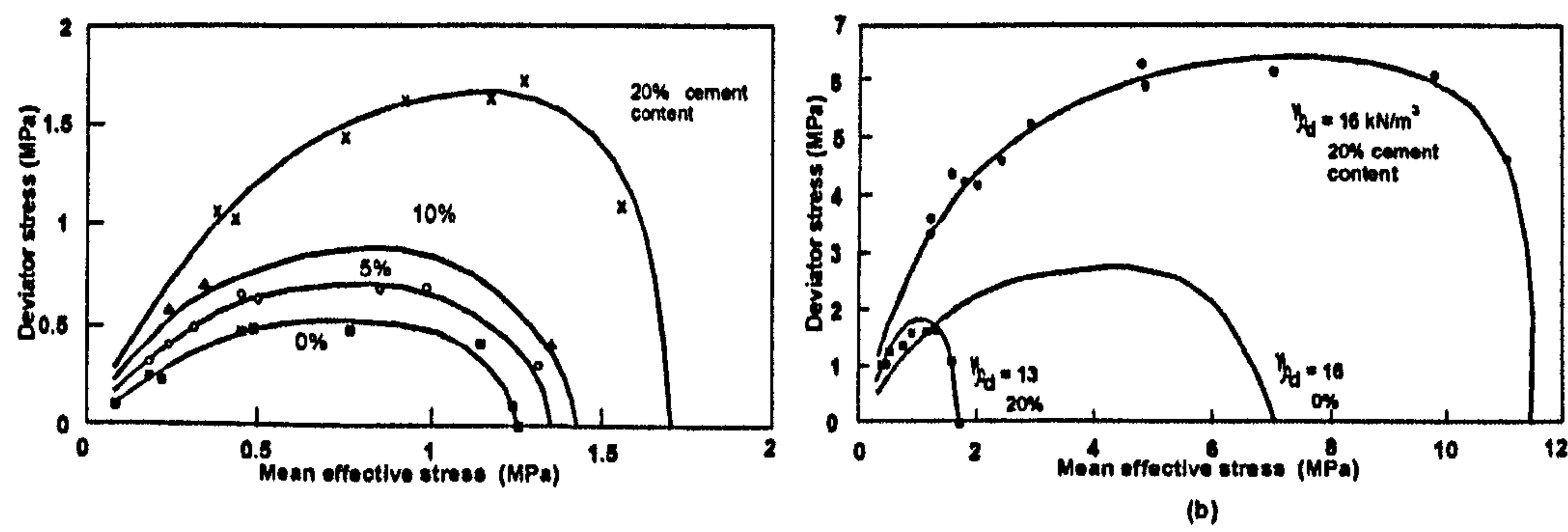


Figure 2.16: The effect of (a) cement content and (b) density on stress yield (after Huang and Airey 1993)

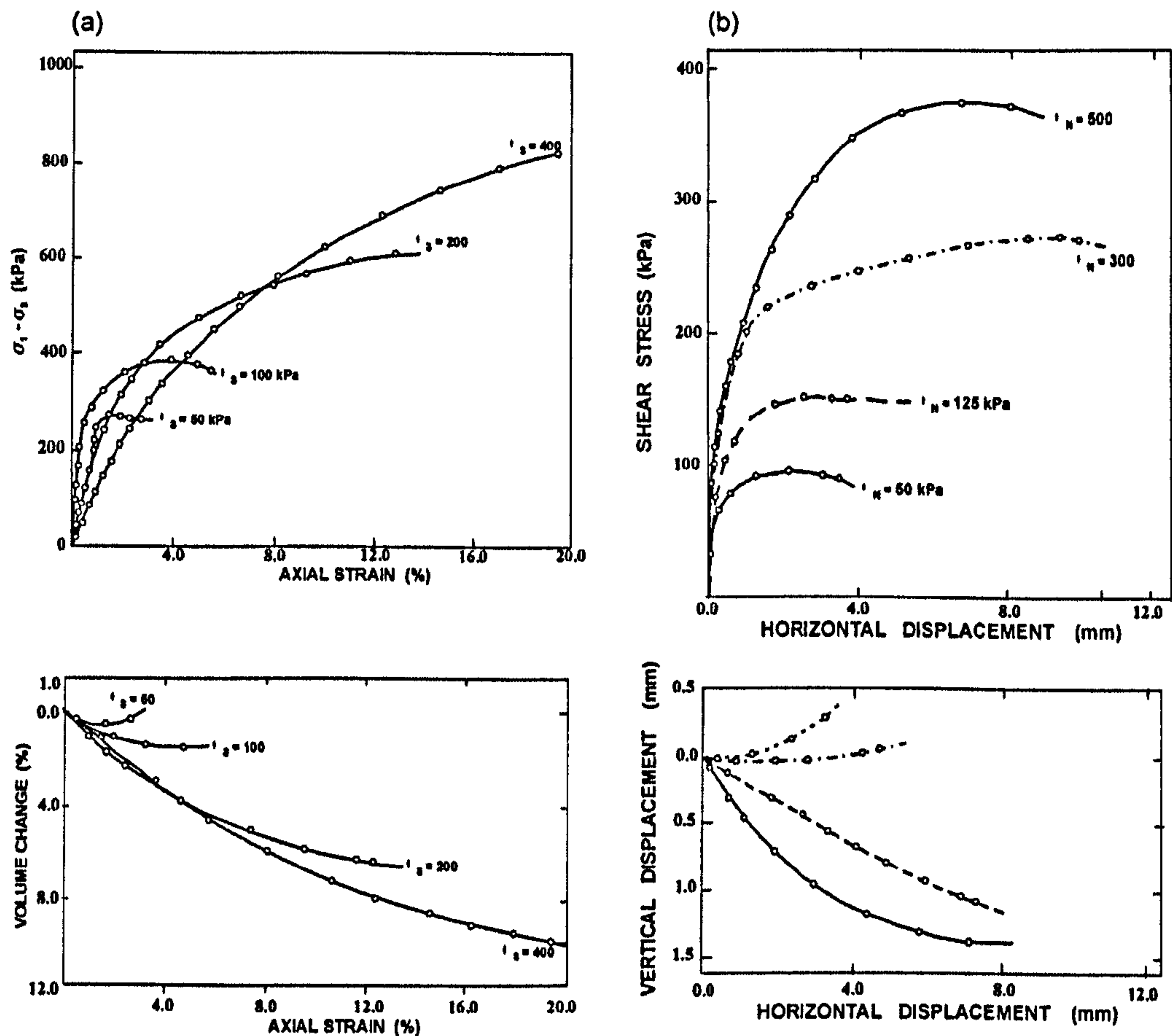


Figure 2.17: The results from the drained triaxial and direct shear box tests on undisturbed residual soils. (a) drained triaxial test; (b) direct shear box test (after Maccarini 1993)

Bressani (1993) studied Corinth marl samples and presented the secant stiffness from drained triaxial tests. He found that the secant stiffness did not have a direct relationship with confining pressure, but was strongly influenced by the yield pressure related to the bonded structure (Figure 2.19).

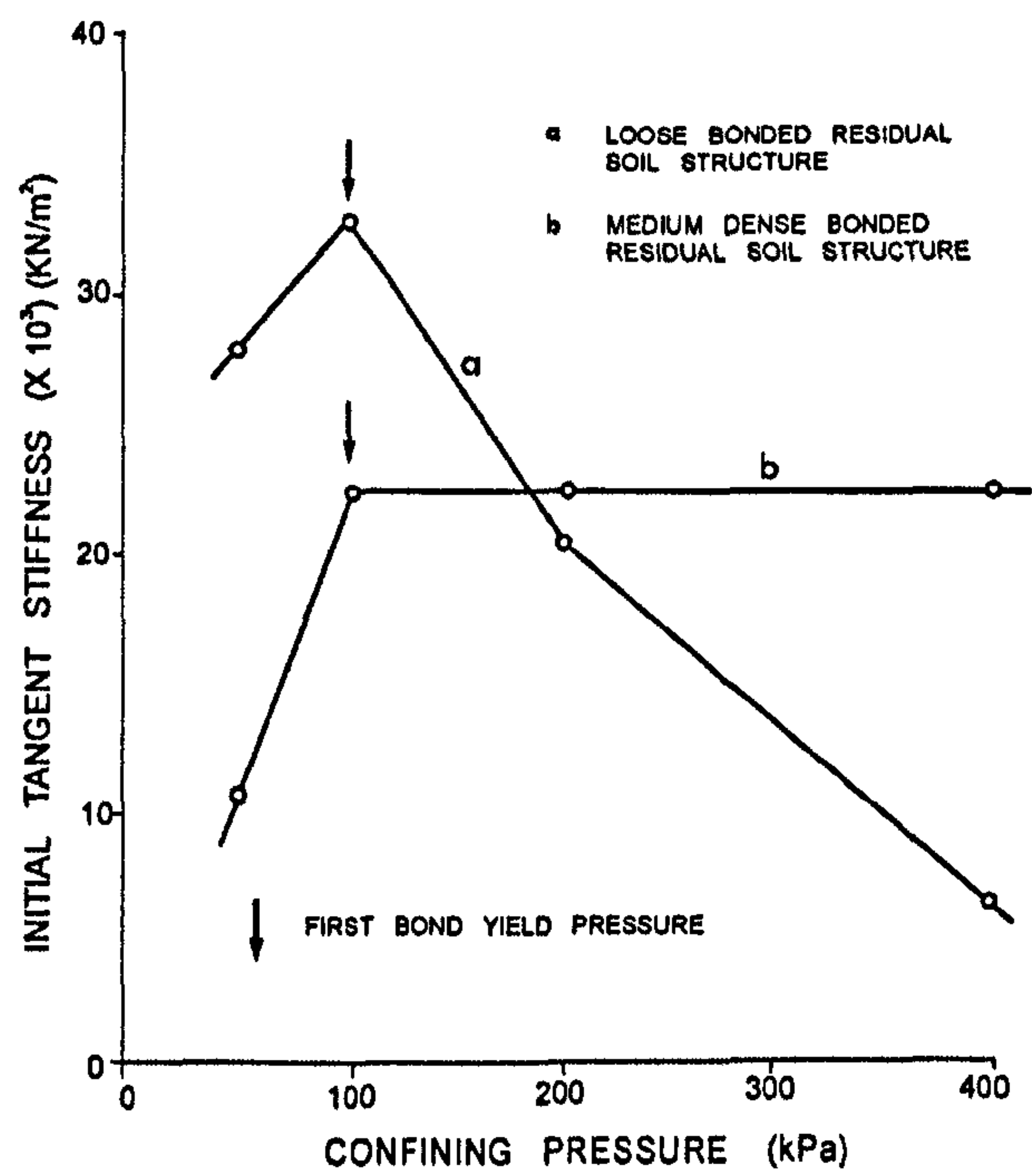


Figure 2.18: The initial tangent stiffness from isotropically confined drained triaxial test (after Maccarini 1993)

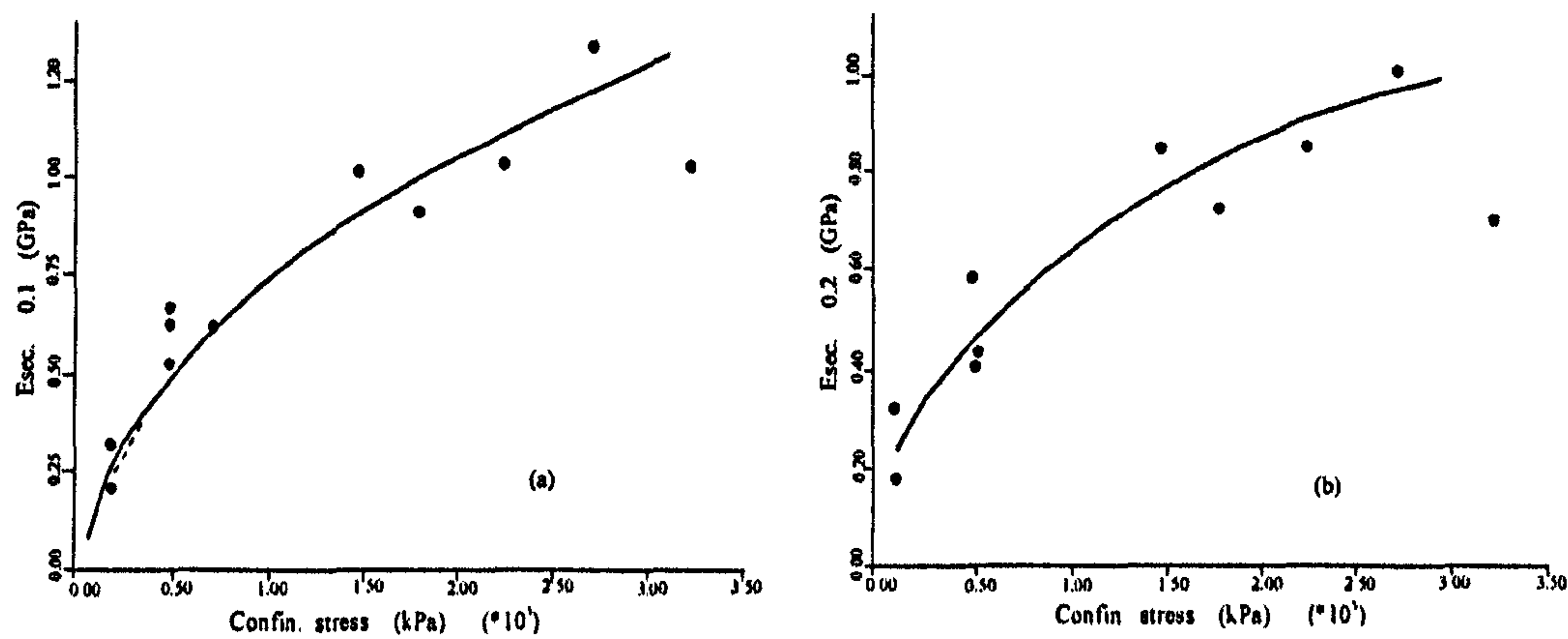


Figure 2.19: The secant stiffness of tests carried out on Corinth marl (a) at  $\epsilon_a = 0.1\%$ ; (b) at  $\epsilon_a = 0.2\%$  (after Bressani 1993)

Coop and Atkinson (1993) examined the behaviour of artificially cemented and uncemented carbonate sand using triaxial testing. Tests were also carried out on natural calcarenite samples taken from North Rankin platform in Australia. A

comparison was made between cemented and uncemented artificial samples prepared with similar grading. They identified yield points from a discontinuity in the stress-strain curves. The initial stress-strain behaviour of the soil was considered to be elastic. The results indicated the yield points for the cemented soils were located outside of the state boundary for uncemented soils (Figure 2.20). The study also found that cemented soil (CEMG) showed a higher peak state in undrained tests than the constant  $p'$  tests (CEMF). The same behaviour was seen in uncemented soils which were stiffer in undrained loading than in drained loading. They concluded that the peak state was influenced by the direction of stress path, drainage conditions and confining pressure. Meanwhile the tests carried out on artificial samples showed good agreement with natural calcarenite samples, as shown in Figure 2.21a and 2.21b. The addition of gypsum plaster contributed to the increasing of finer material to the prepared artificial samples. The study indicated that the addition of gypsum fines resulted in samples with considerably smaller specific volume. Meanwhile, the samples treated with calcium carbonate fines showed very close agreement with samples treated with gypsum indicating that the change in grading influences the behaviour of soils instead of mineral composition (Figure 2.21c).

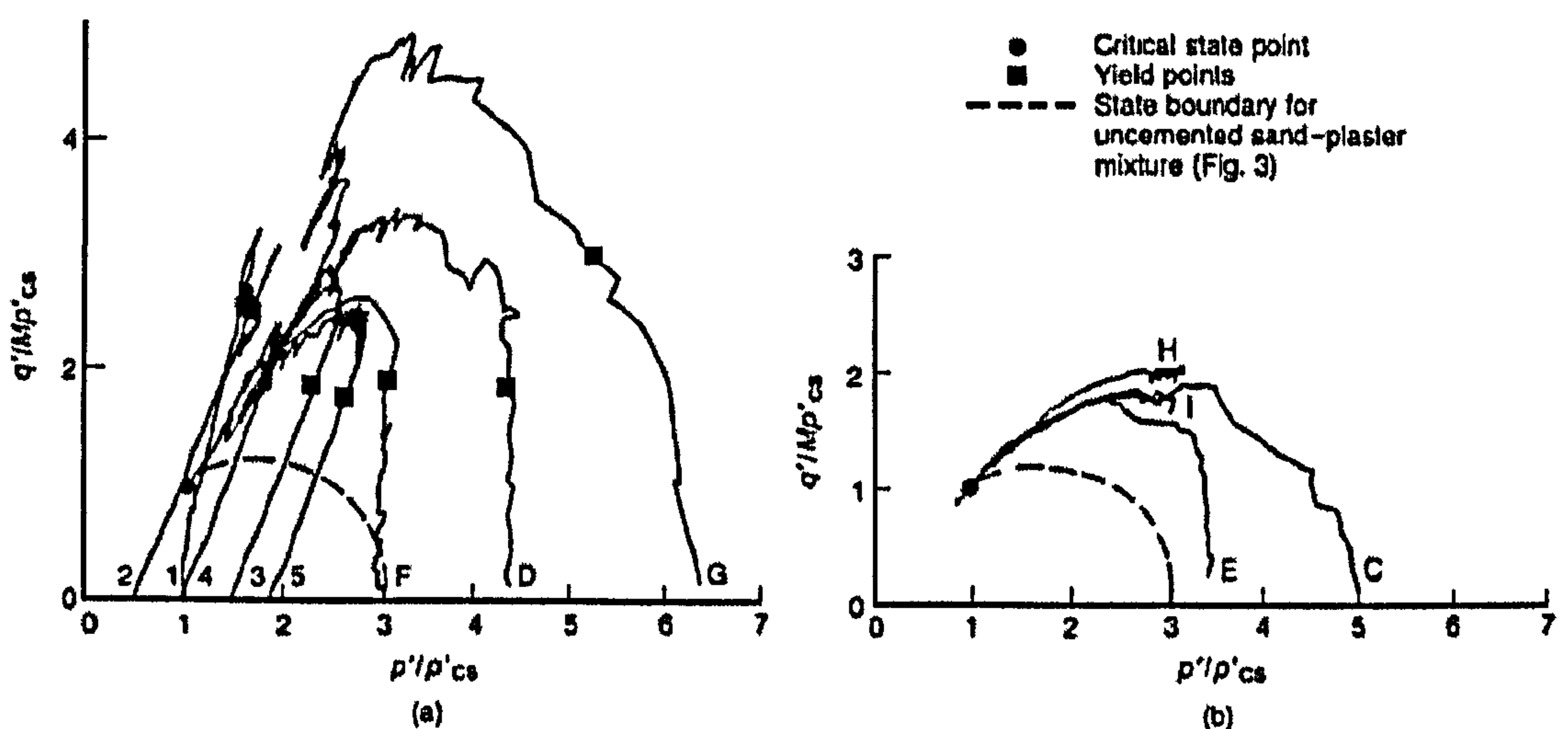


Figure 2.20: State paths for cemented soil (a) low confining pressures and (b) high confining pressures (after Coop and Atkinson 1993)



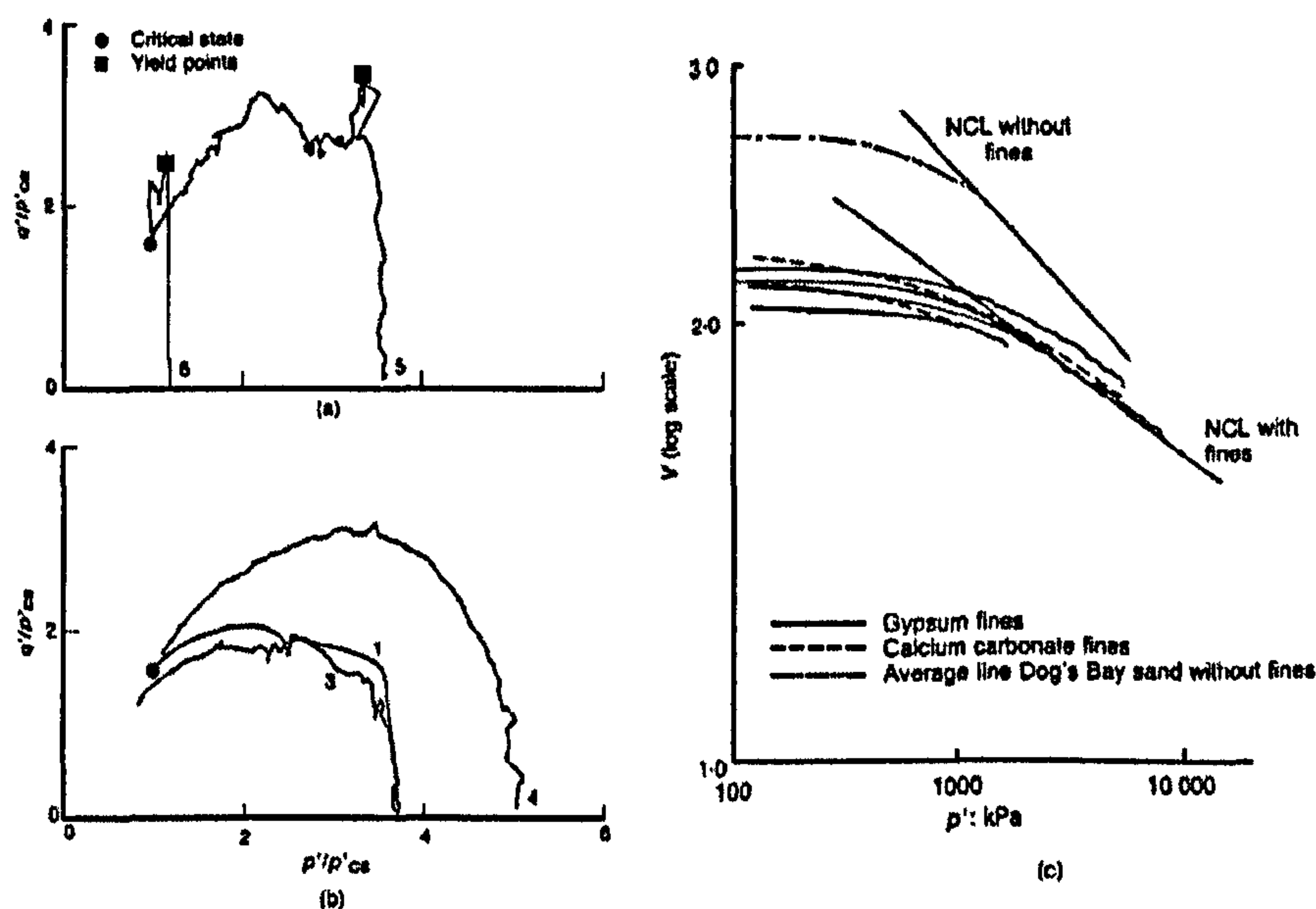


Figure 2.21: State paths for natural calcarenite soil at (a) low confining pressures and (b) high confining pressures; (c) isotropic compression lines of samples treated with and without fines (after Coop and Atkinson 1993)

Cuccovillo and Coop (1993) further examined the behaviour of the same soils with different bond strengths by mixing different ratios of sand and gypsum plaster. Figure 2.22 shows that the soil with high bond strength (same specific volume) reached peak state well outside the intrinsic state boundary surface both during isotropic and shear loading. Meanwhile, lower bond strength could only reach a state outside the intrinsic boundary surface by shearing at low confining stresses.

Malandraki (1994) presented the results from a series of triaxial tests in order to study engineering behaviour of weakly bonded artificial soils. The artificial samples were prepared from the mixture; sand & kaolin with void ratio,  $e = 0.6$ . From drained and undrained tests, the shear strength of bonded soils was seen to be strongly affected by bonded structure. Bonded samples attained higher maximum deviatoric stress than the destructured samples (Figure 2.23a). For loose samples, the yield points were relatively easier to define than the dense samples (Toll and Malandraki 1993). In contrast, the yield points for the denser samples were determined based on the change in stiffness,  $E$ . The two yield points were defined

from the log E versus log strain plot where the stiffness had been calculated as tangent values (Figure 2.23b). The first yield was defined as the first change in stiffness. Meanwhile a clear drop of stiffness afterward represented the second yield.

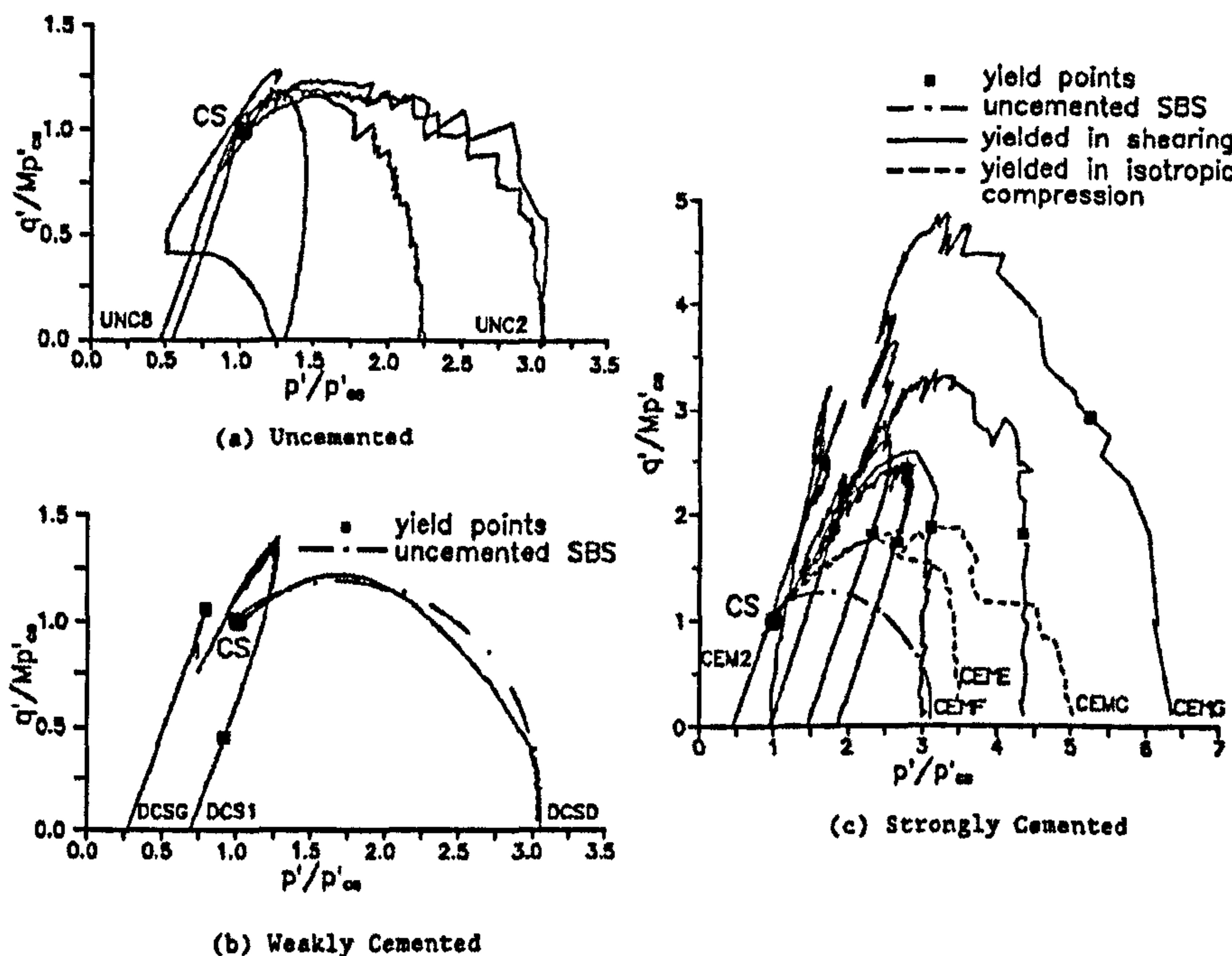


Figure 2.22: The normalized stress paths of artificially cemented soil with different bond strengths (after Cuccovillo and Coop 1993)

The behaviour of bonded soils was divided into three main zones in terms of stress space (Figure 2.23c). At low mean stress (zone 1) the bonds entirely control the behaviour up to failure. In the transitional zone (zone 2), the bonded soil can sustain higher limiting stress ratios than destructured soil due to the post yield influence of the bonds. Meanwhile, in the third zone (zone 3), the effect of the bonds was destroyed before failure was reached at higher stresses. The bounding surface of the bonded soil was found to be affected by different stress path direction and the breakdown of bonds due to shear was not isotropic but related to the direction of the stress path at the yield point (Malandraki 1994). Samples that had yielded earlier when following one stress path direction could still show high stiffness when the stress path direction was changed. The limiting stress ratio that

the soil was able to sustain could be affected due to the changing of the stress path direction during shearing. The breakdown of bonds is anisotropic and not all bonds break when bond yield is initiated (Malandraki and Toll 1996). They also suggested that the bond yield is kinematic, in the sense that it is an expandable/shrinkable surface, but that it is not a moveable surface.

Meanwhile Lee and Coop (1995) performed a series of triaxial tests at standard and high pressures (up to 35 MPa) on decomposed granite soils. The mechanical behaviour of soils was compared in saturated, partially saturated and dry states. They found that each state of sample could be described within a critical state framework with particle breakage as the principal means of plastic volumetric compression. From Figure 2.24a, the compression curves tend to a unique line, which has been named the normal compression line. Each loading line shows an indistinct yield, as a result of the gradual onset of breakage at particle contacts. They also found that the behaviour of saturated samples was very similar to partially saturated samples compacted around optimum water content (Figure 2.24b). On the other hand, samples in a dry state achieved their normal compression line outside that of the saturated soils (Figure 2.24c). Sieve analysis after shearing of the dry samples indicated smaller particle breakage occurred compared to saturated samples.

Asghari et al. (2003) carried out a series of triaxial compression tests on uncemented, artificially cemented and destructured samples. The results showed that the shear strength increases with increasing cement content but the influence of cementation decreases as the confining pressure increases. The failure envelope for the cemented samples also indicated a curved line instead of linear (Figure 2.25).



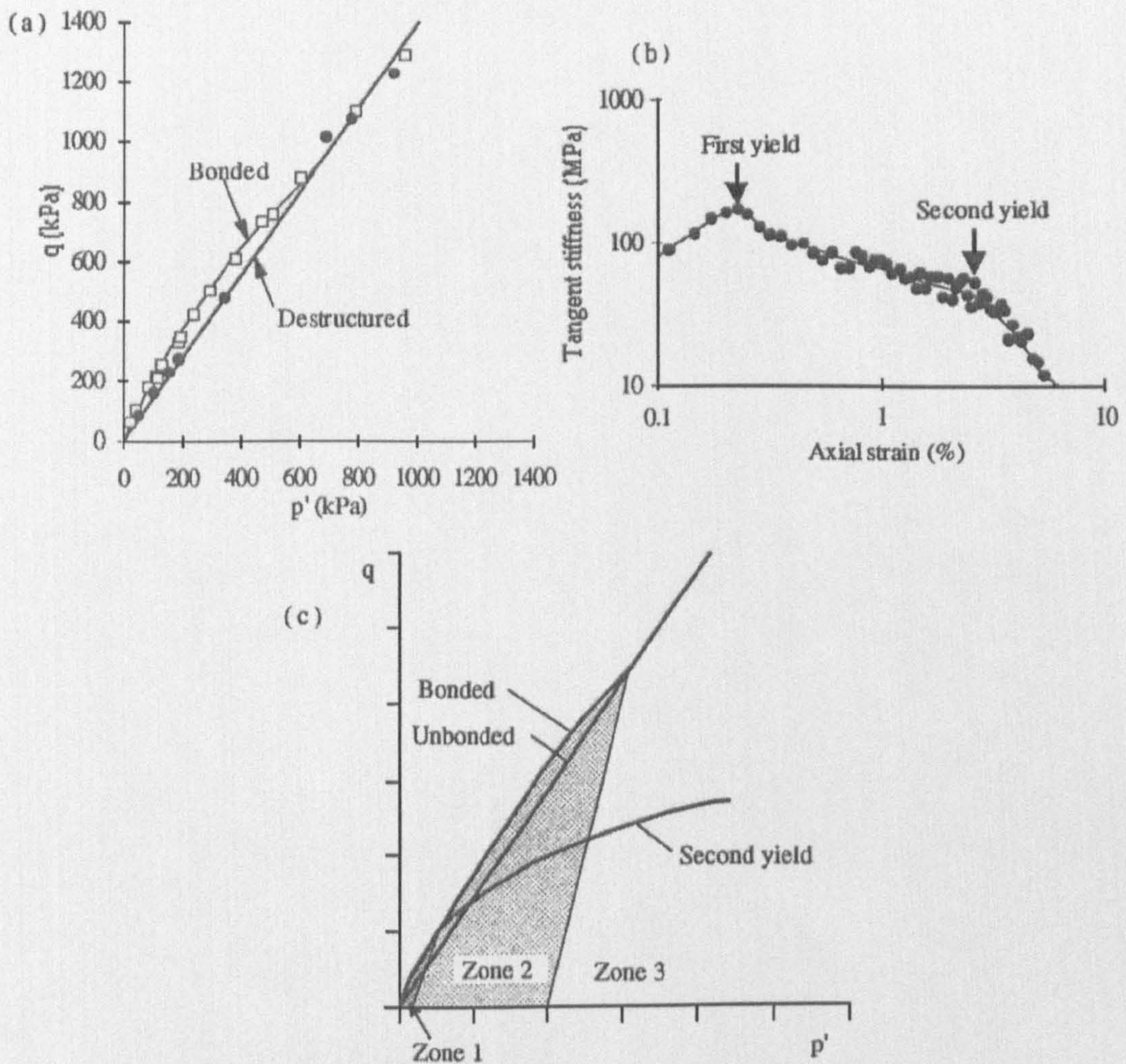


Figure 2.23: (a) Bounding surface between bonded and destructured samples; (b) yield points identified from stiffness vs. strain curve ( $p'_0=11\text{kPa}$ ); (c) zones of behaviour for bonded soil (after Malandraki and Toll 1996)

Coop et al. (2004) presented results from a series of ring shear tests on biogenic carbonated sand. Samples were tested at different particle gradings, densities and stress levels. They concluded that the breakage of particles continues to very large strains far beyond those reached in triaxial tests (Figure 2.26a and 2.26b). The particle breakage is found to be associated with volumetric compression. The figure clearly indicates that most of the tests were under compression except for test RS15 showed dilation initially at smaller strain, however, then became compressive before levelling off at larger strains. The volume change at low shear



strain was found to be highly dependent on the confining stress, however the large volumetric compression due to particle breakage at very large shear strains seemed to be more independent of stress level (refer to RS3, RS5 and RS7 in Figure 2.26b). In addition the mobilized angle of shearing resistance,  $\phi'_{mob}$  was found to be approximately constant at shear strain of about 30% meaning that the value of  $\phi'_{mob}$  is unaffected by the particle breakage (Figure 2.26c).

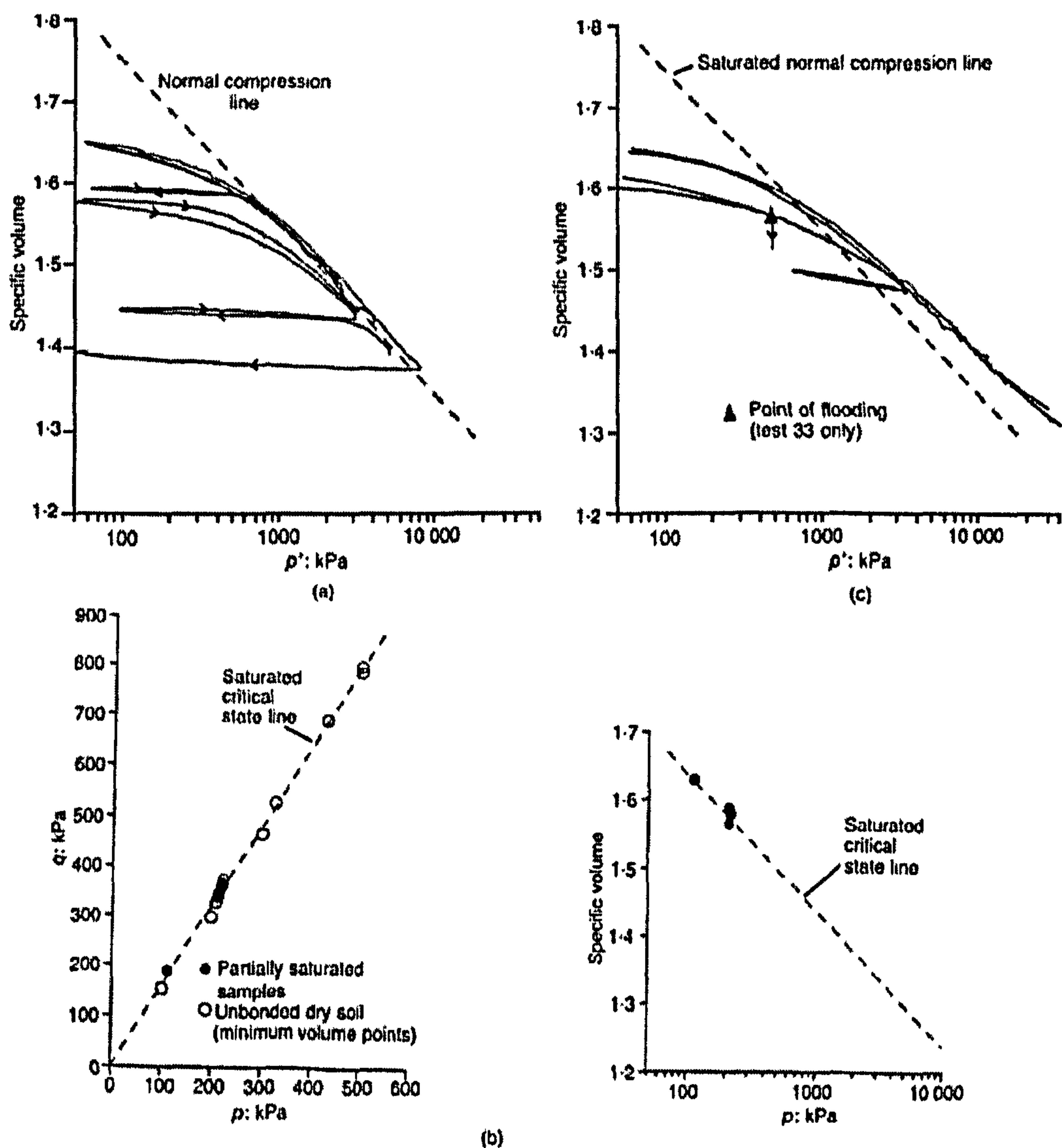


Figure 2.24: (a) The compression and swelling of saturated soils; (b) Critical state for partially saturated and unbonded dry soils (c) normal compression line of unbonded dry soils (after Lee and Coop 1993)

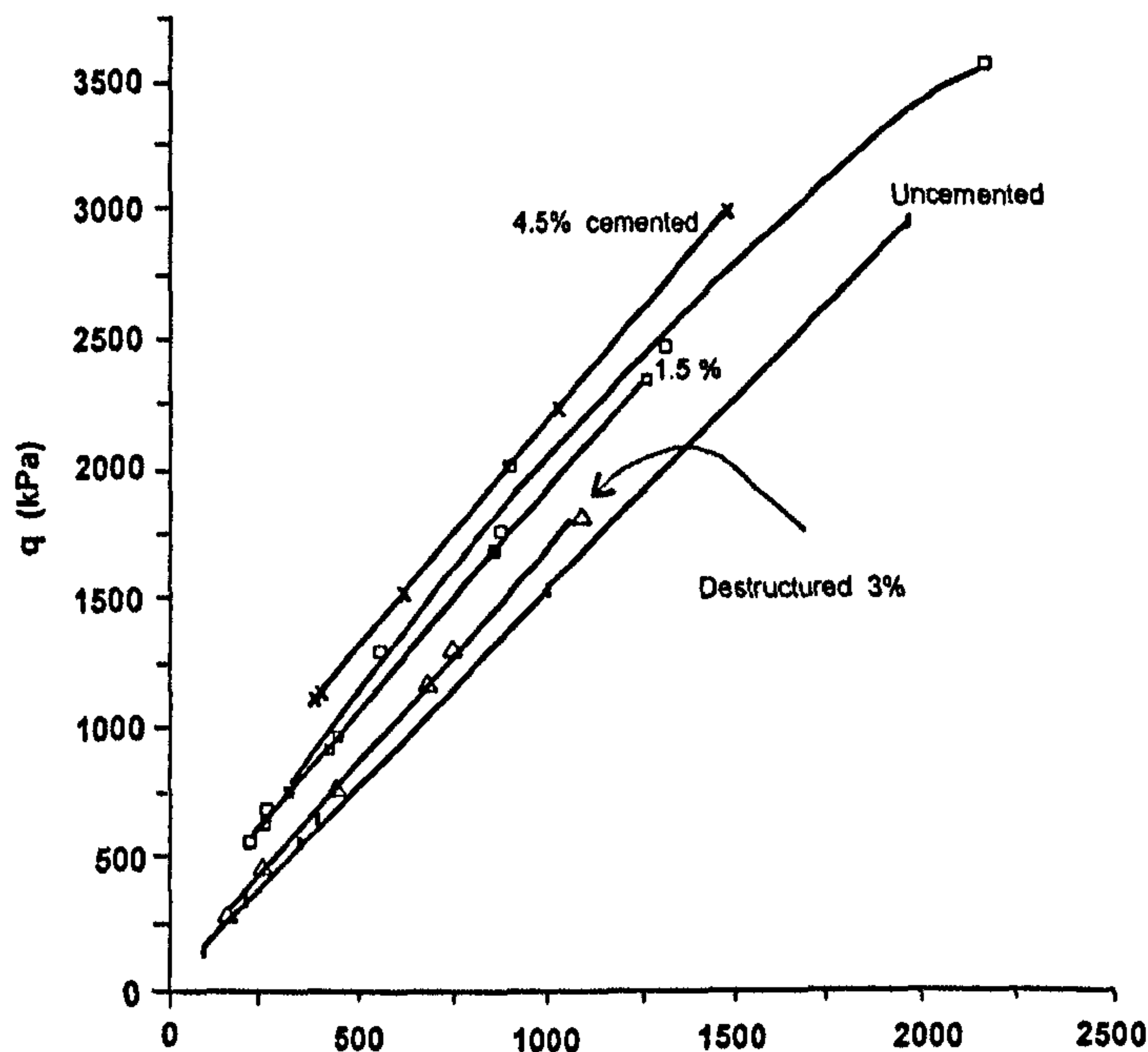


Figure 2.25: Failure envelopes of different types of samples in  $q:p'$  space (after Asghari et al. 2003)

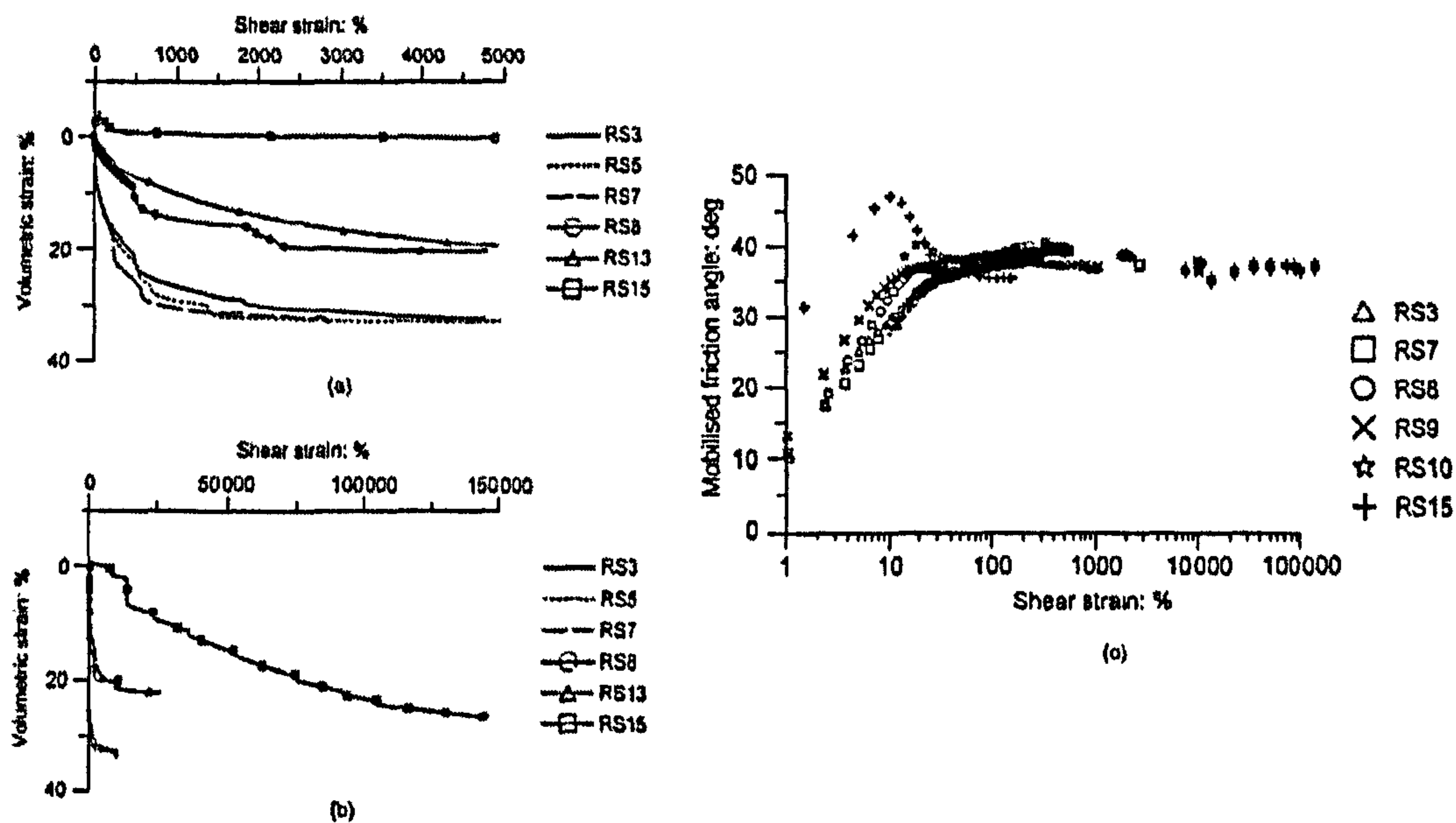


Figure 2.26: The affect of stress level and grading on volumetric strains; (a) small shear strains; (b) larger shear strains; (c) mobilized friction angles (after Coop et al. 2004)

### 2.3.3 Studies on Unsaturated Behaviour of Soils

In an unsaturated condition, matric suction plays as important a role as bonds in the shear strength of residual soils. Matric suction is mainly associated with residual soils, which are commonly found in partially saturated conditions with a continuous air phase in their voids. These soils seem to have high void ratio and some larger macro pores (Fookes 1997). Hence, the pore air pressure,  $u_a$  is approximately equal to atmospheric pressure as a result of high permeability of the soil to air. While the pore water pressure,  $u_w$  is sub-atmospheric due to the presence of small pores within the soils.

Bishop et al. (1960) carried out constant water content triaxial tests on compacted shale and compacted boulder clay. The shale and boulder clay had clay fractions of 22% and 18% respectively. Based on a series of triaxial tests, the saturated compacted shale and boulder clay gave angles of friction,  $\phi'$  of  $24.8^\circ$  and  $27.3^\circ$ , respectively. Fredlund and Rahardjo (1993) presented the data and included the  $\phi^b$  angles for both of the soils as shown in Figure 2.27a and 2.27b. It is clearly seen that the shear strength increased with increasing matric suction.

Blight (1967) studied the effect of matric suction on unsaturated silts through drained triaxial tests. The samples were compacted at a water content of 16.5% (standard AASHTO compactive effort) and brought to three varied matric suction values in a triaxial cell. Constant matric suction was also performed on two samples and tested using two net confining pressures (13.8 and 27.6 kPa). The results showed that the shear strength increased with increasing matric suction as well as an increase in confining pressure (Figure 2.28a). The changes of water volume and changes of soil volume were presented in Figure 2.28b and 2.28c, respectively. These figures suggested that even though the pore water was permitted to dissipate from the soil during shearing, the sample still dilated during shearing.

Escario (1980) performed a series of consolidated drained direct shear tests and triaxial tests on unsaturated Madrid grey clay. The axis-translation technique was used to achieve controlled matric suction conditions for the tests. The result achieved from the direct shear tests exhibited the failure envelope lines were almost parallel upward as a result of increasing in matric suction (Figure 2.29a). Meanwhile, the samples that were examined under different matric suction indicated an increase of shear strength with an increase of the matric suction (Figure 2.29b).

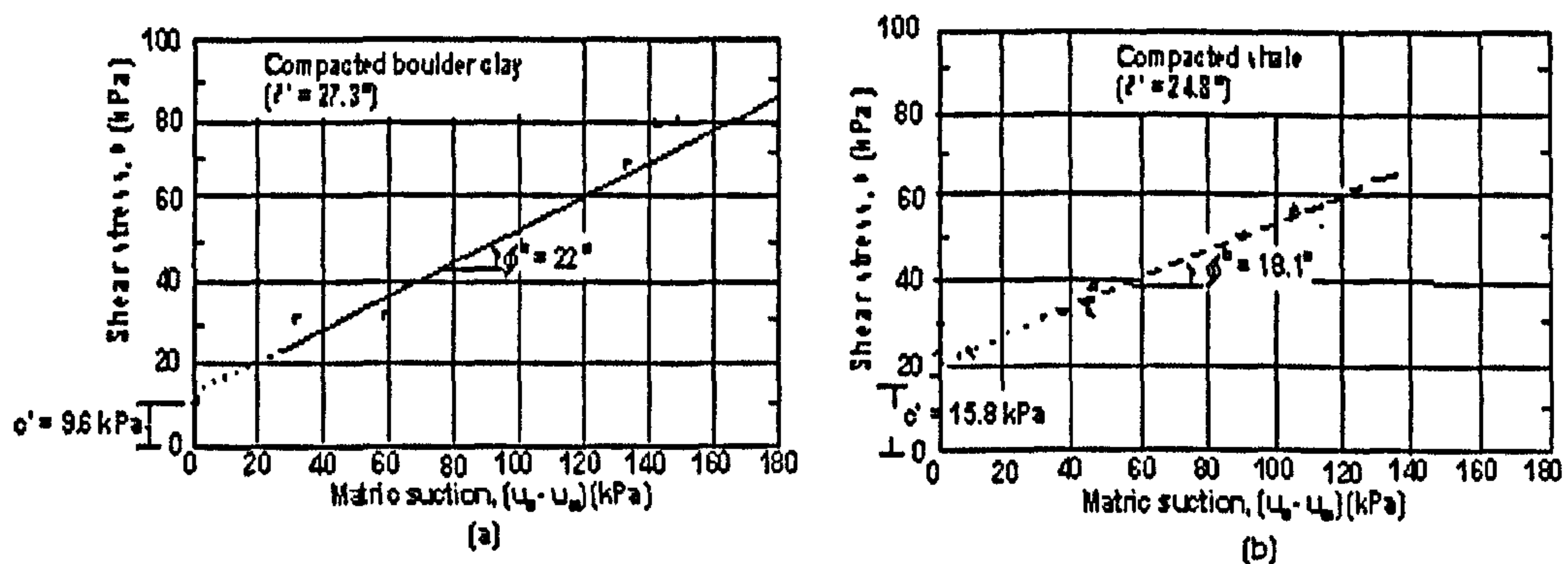


Figure 2.27: The intersection line between failure envelope and  $\tau : (u_a - u_w)$  plane for (a) compacted shale; (b) compacted boulder clay (after Fredlund and Rahardjo 1993; data from Bishop et al. 1960)

Ho and Fredlund (1982) performed a series of multistage triaxial tests on residual soils derived from decomposed rhyolite and decomposed granite collected from Hong Kong. Samples were examined under consolidated drained tests with different applied matric suction using axis-translation. Figure 2.30a shows that the shear strength at failure increases with increasing matric suction at a particular constant confining pressure. By increasing the matric suction and net confining pressure, the failure envelope lines were assumed to be parallel to each other. However the angle  $\phi^b$  was less than the angle of internal friction,  $\phi'$ , as presented in Figure 2.30b.



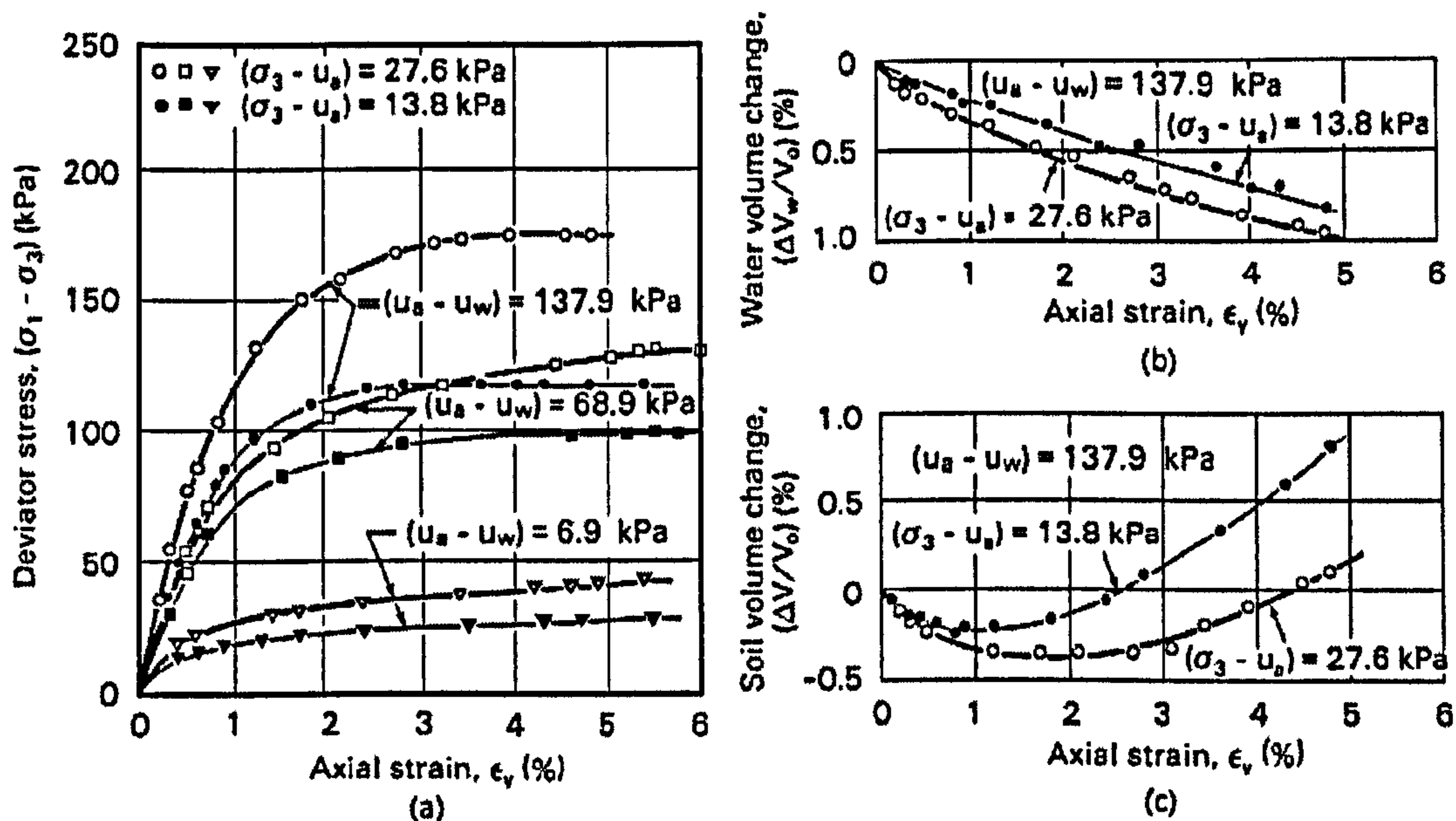


Figure 2.28: The results of consolidated drained tests on unsaturated silt. (a) Deviator stress versus strain curves; (b) water volume change vs. strain; (c) volume change vs. strain (after Blight 1967)

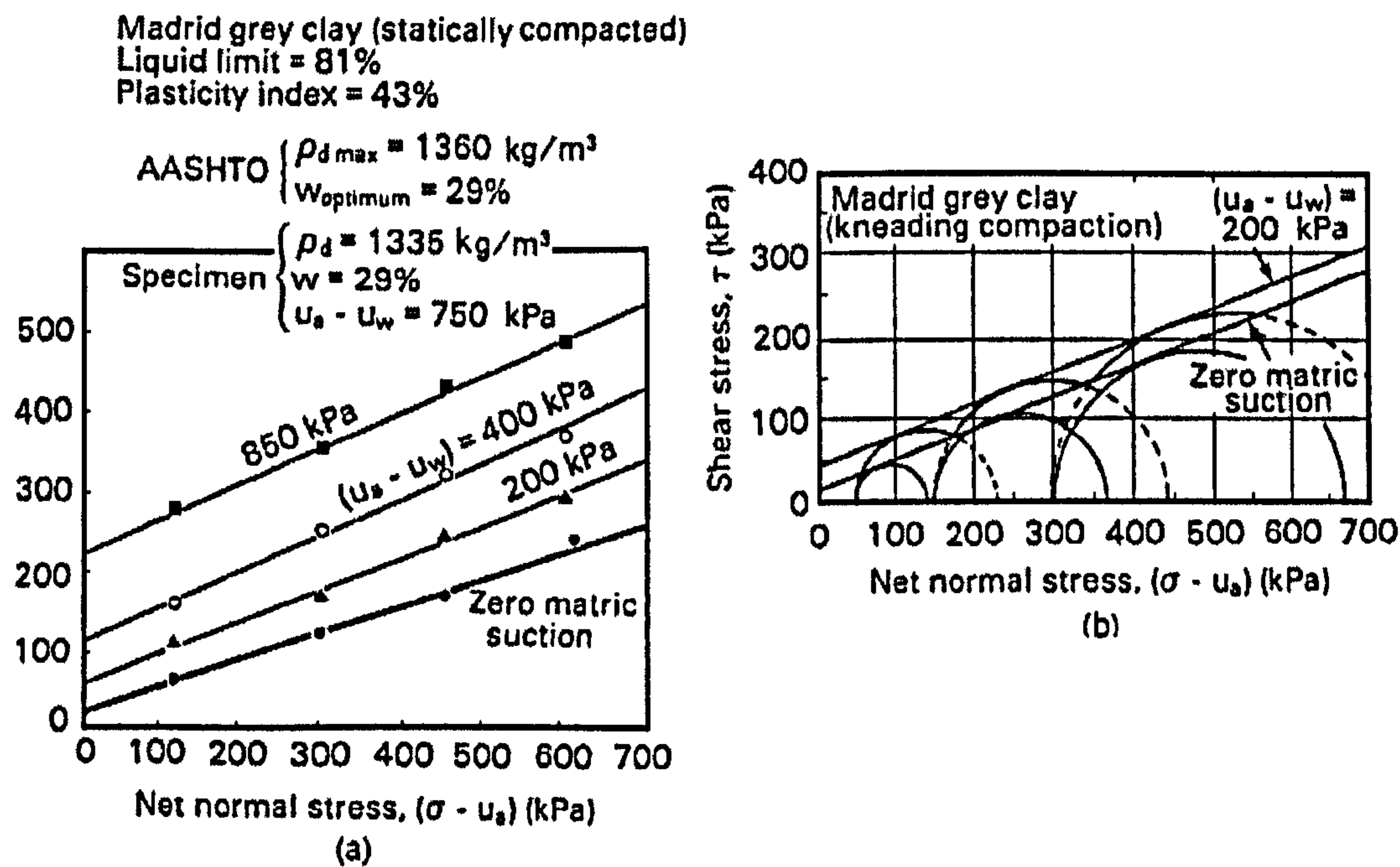


Figure 2.29: Effects of matric suction on shear strength for Madrid clay from (a) direct shear tests; (b) triaxial tests (after Escario 1980)

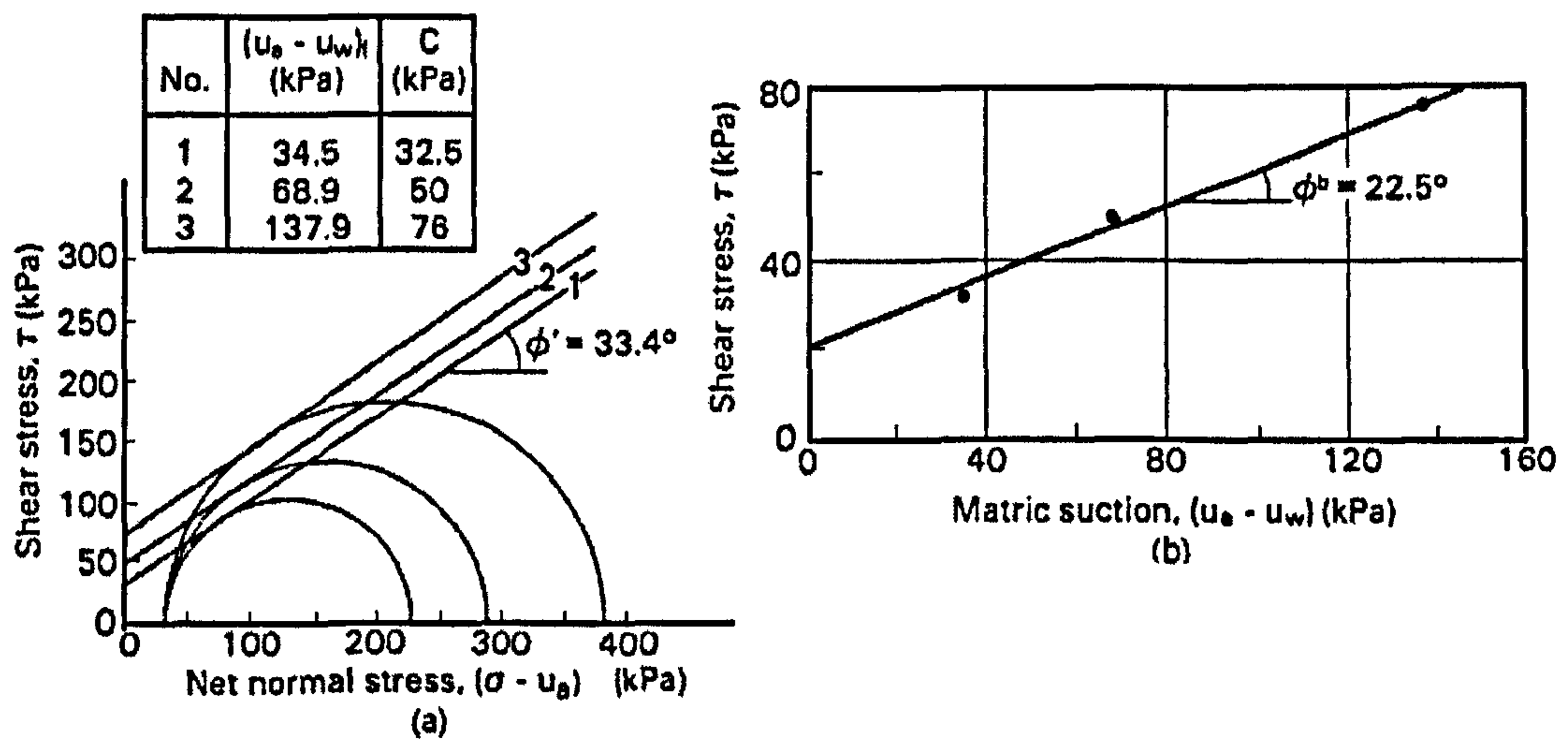


Figure 2.30: The failure envelopes for residual soil from decomposed granite sample.  
(a)  $\tau$  vs.  $(\sigma - u_a)$ ; (b)  $\tau$  vs.  $(u_a - u_w)$  (after Ho and Fredlund 1982)

Escario and Saez (1986) performed a series of direct shear tests on statically compacted remoulded samples from three different soils. The results of the tests are shown in two different ways for each soil (Figure 2.31a and 2.31b). Part (a) of the graphs shows that shear strength,  $\tau$  versus net normal stress,  $(\sigma - u_a)$  is represented by straight lines with tendency to divergence at increasing loads. Meanwhile in part (b) of the graphs show curvature mainly at low suctions when the data were plotted on shear strength,  $\tau$  versus matric suction. The curvature in the later graph suggests that the value of  $\phi^b$  is not constant. The nonlinearity in the shear strength versus matric suction relationship became more noticeable as soils were examined over a wider range of matric suction (Fredlund and Rahardjo 1993). However, based on the trend of the results, it was clearly seen that increasing suction caused an increase in shear strength of the studied soils in an unsaturated state.

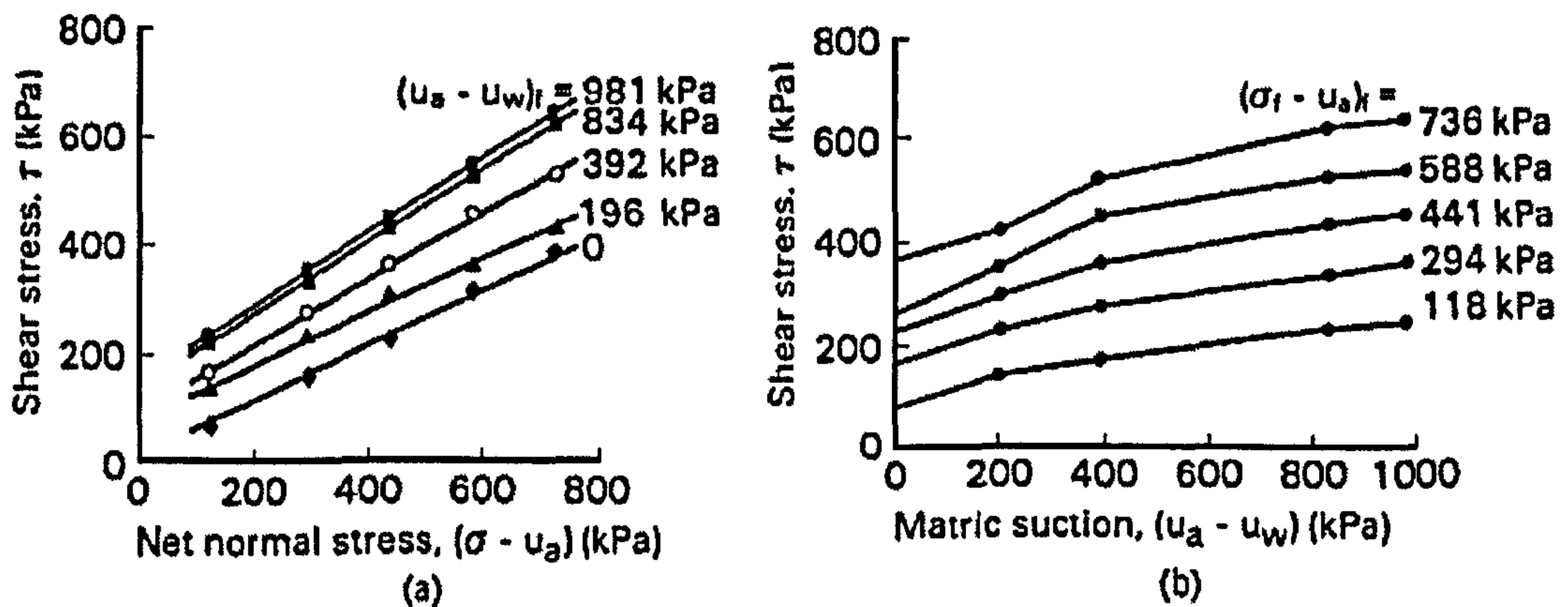


Figure 2.31: Direct shear tests on Madrid grey clay under controlled matric suction.  
 (a) Shear stress vs. net confining pressure with various matric suction;  
 (b) shear stress vs. matric suction relationship (after Escario and Saez 1986)

Alonso et al. (1990) proposed a constitutive model for unsaturated soils by adopting the concept of the modified Cam-Clay model. According to the model, the yield curve at a constant suction,  $s$  is represented by an ellipse (Figure 2.32a). The expansion of the yield curve of the soil is assumed to be linear with suction through a proportional constant of  $k$ . The effect of suction is correlated to an increase in cohesion, maintaining the slope,  $M$  of critical state, critical state line, CSL for saturated conditions. Meanwhile the loading-collapse, LC curve expresses the variation of the yield curve of soil due to an increase in preconsolidation stress,  $p$  with suction (Figure 2.32b).

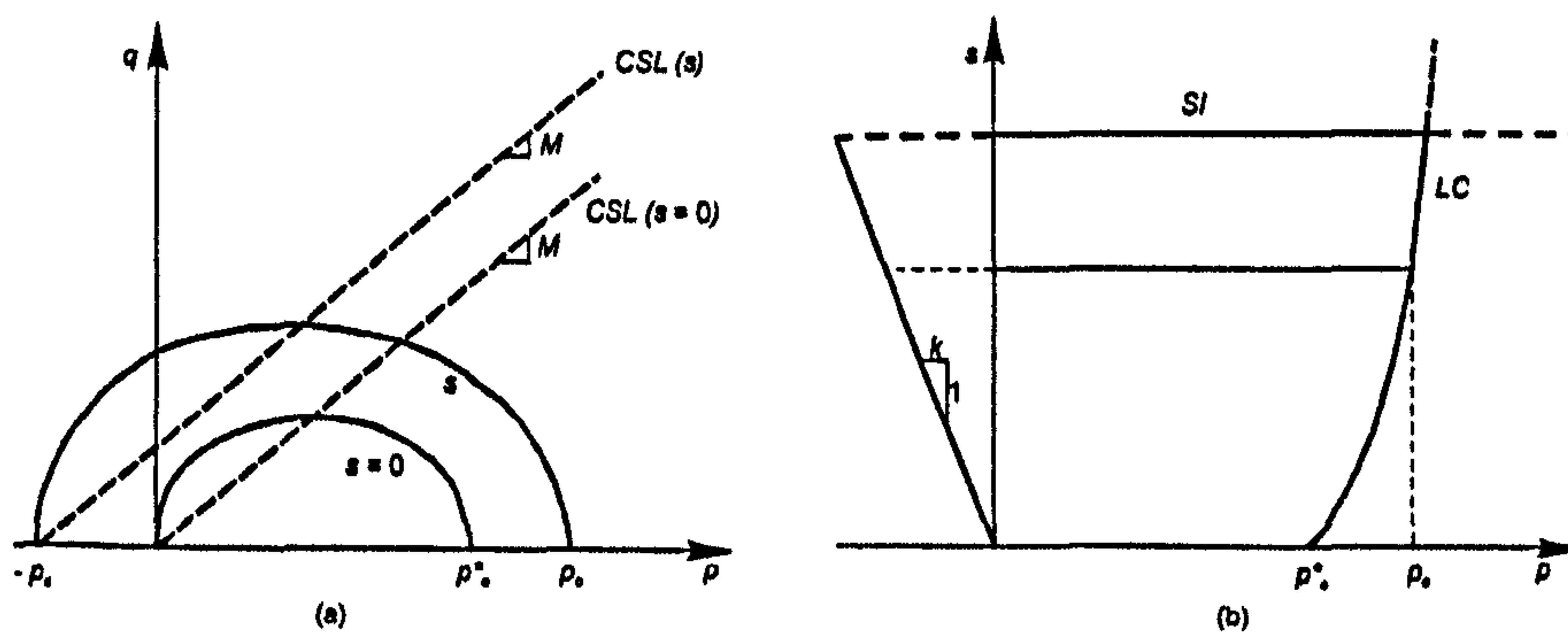


Figure 2.32: Yield surfaces in  $p$ :  $q$ :  $s$  space (after Alonso et al. 1990)

Wheeler and Sivakumar (1995) developed an elasto-plastic model based on experimental work on compacted kaolin under suction-controlled triaxial tests. The proposed model which defines the yield surface in  $q:p:s$  space is able to describe some important features of unsaturated soils behaviour (e.g. influence of suction on strength and collapse on wetting) (Figure 2.33). According to the model, the elastic behaviour if the soil state lies inside the state boundary hyperspace (yield surface) and the plastic volumetric strains starting once the state boundary hyperspace is reached. The plastic volumetric strain corresponds to the expansion of a yield surface.

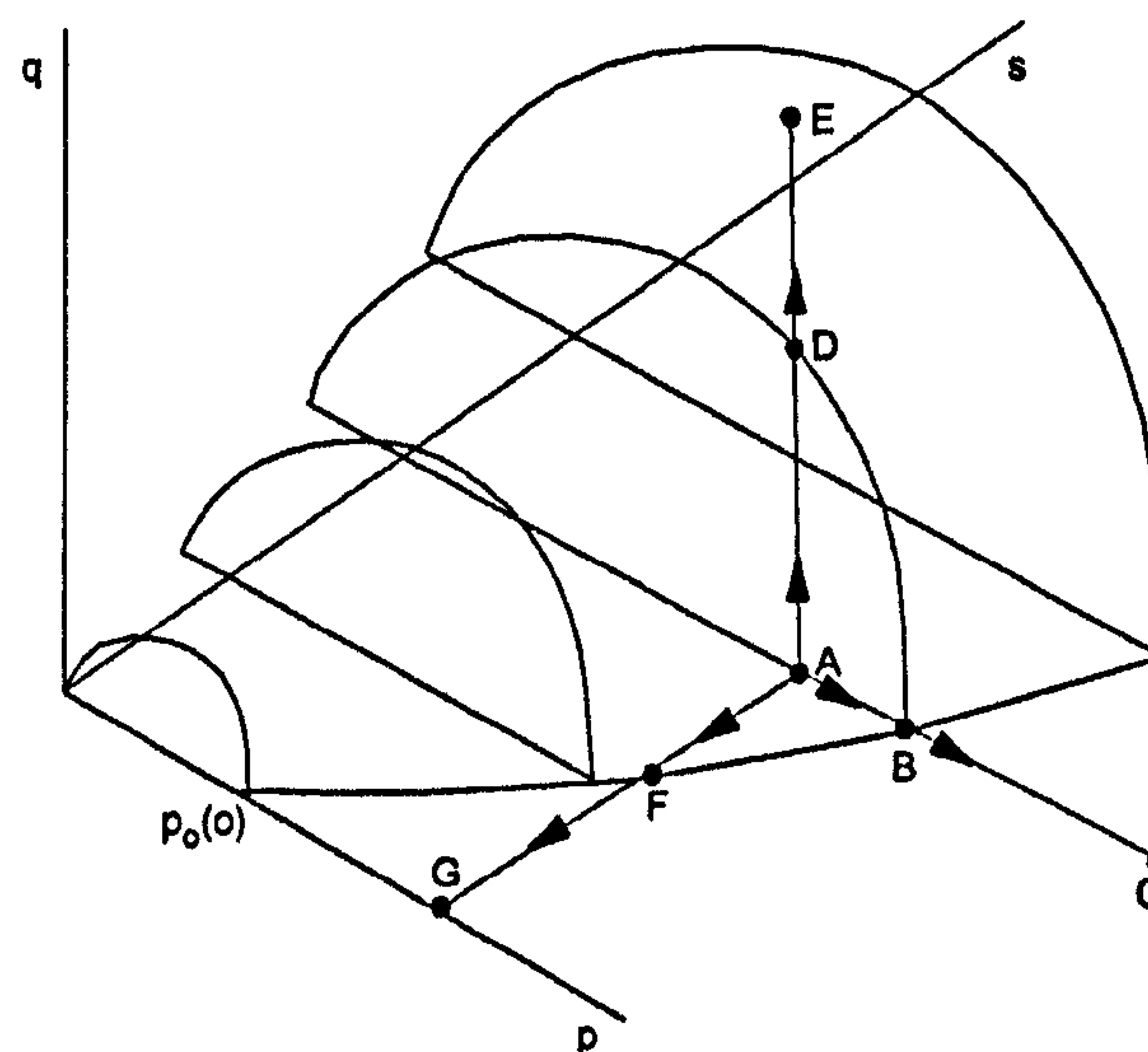


Figure 2.33: The yield surface for unsaturated soil (after Wheeler and Sivakumar 1995)

Zakaria et al. (1995) performed a series of the controlled-suction triaxial tests to investigate the shape of the yield surface on unsaturated compacted speswhite kaolin. The axis translation technique was used to control the matric suction. Figure 2.34 shows the yield values of deviator stress and mean net stress from the tests. It was found that the yield points at suction of 100kPa and 200kPa are reasonably consistent with elliptical constant-suction yield curves, with one axis and apex (highest point) of the ellipse falling on the relevant critical state line. It



also suggested that the size of the constant-suction cross-section of the yield surface increases with increasing of suction.

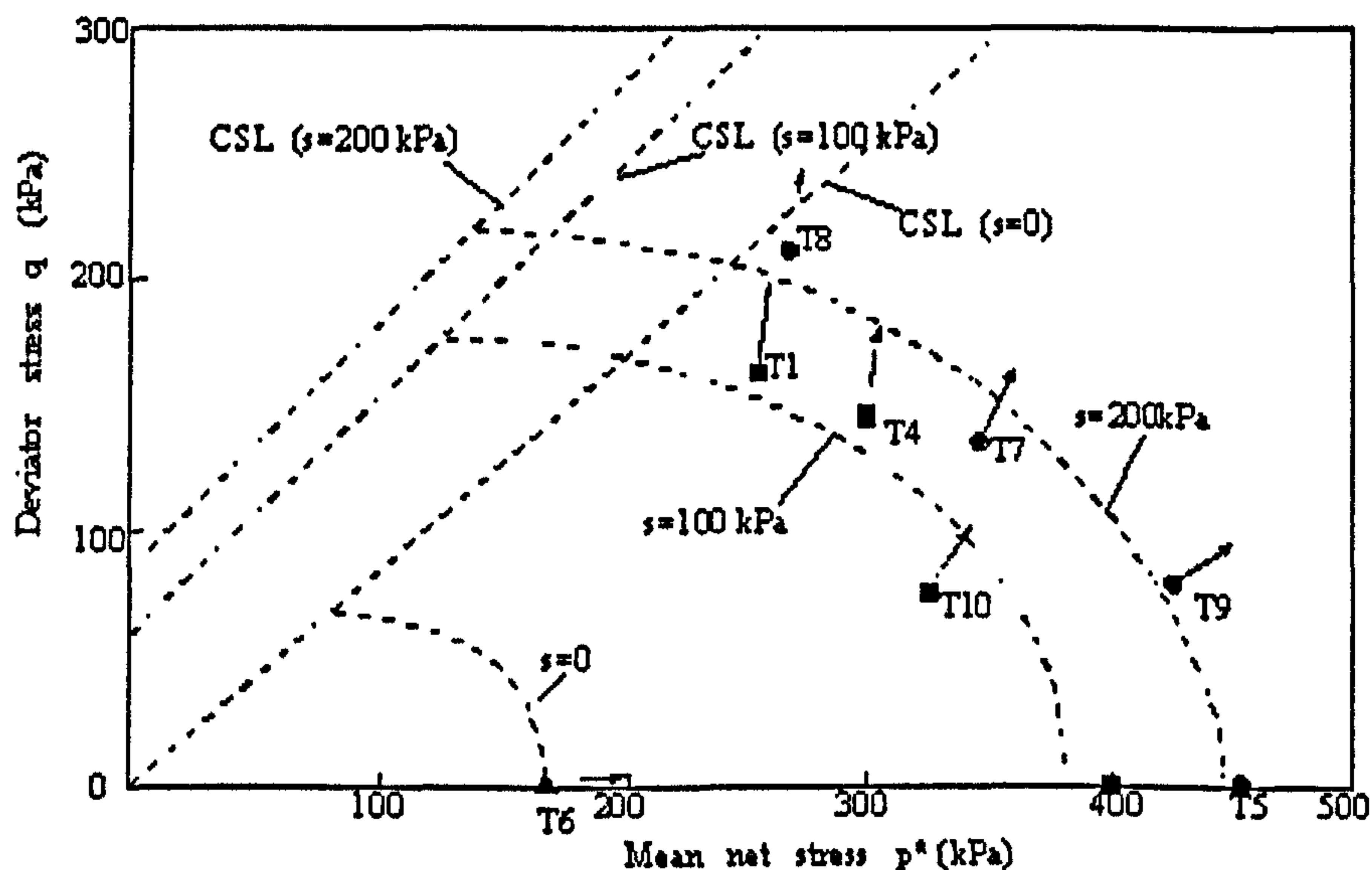


Figure 2.34: The yield curve and the locations of the critical state lines for different suction,  $s = 0, 100$  and  $200$  kPa (after Zakaria et al. 1995)

Geiser et al. (1998) carried out a series of triaxial tests using a modified Bishop and Wesley cell using the axis translation technique. The tests were performed under saturated and unsaturated condition on remoulded sandy silt from Switzerland (region of Sion). They adopted different methods to identify the yield points (pseudo-elastic limit) and shape of the yield surface in the invariant stress space, mean net stress,  $p^*$  against deviator stress,  $q$  and suction,  $s$ . The yield points of eight unsaturated tests were represented in Figure 2.35 apparently indicated a general trend of hardening due to suction (dashed lines). The effect of suction could be seen as a result of a suction-induced preconsolidation ( $p_c$ ).

Taha et al. (2000) studied the mechanical behaviour of natural residual soils derived from granitic rock in Puchong, Malaysia. A series of consolidated drained (CD) and constant water content (CW) triaxial tests were performed. The results showed that the shear strength of the soils increases as the matric suction increases (Figure 2.36a and 2.36b). However, the deviator stress-strain curves from both tests did not exhibit peak points, even at large strains. Based on two-dimensional

projection on shear stress,  $\tau$  versus net normal stress,  $(\sigma - u_a)$ , both tests generated similar value of effective angle of friction,  $\phi'$  ( $26.5^\circ$ ). However, the  $\phi^b$  angle gave two apparently different values (Figure 2.36c and 2.36d).

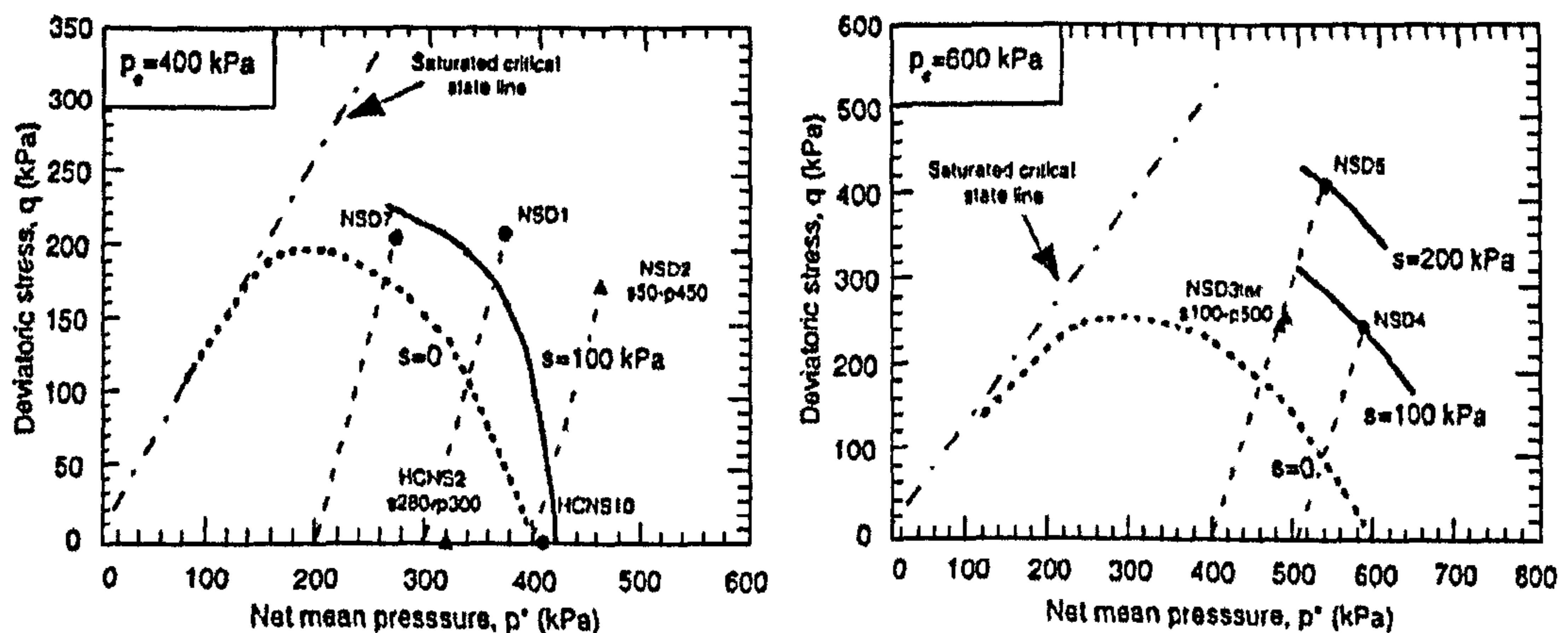


Figure 2.35: The effect of matrix suctions on yield points in unsaturated condition for two different consolidation pressures (after Geiser et al. 1998)

Toll et al. (2000) carried out a series of triaxial tests performed on unsaturated samples of undisturbed residual soils derived from the Bukit Timah and Jurong formations in Singapore. Three different constant net confining pressures were applied and various matrix suctions applied to the samples. The results from multi-stage CD triaxial tests at a constant net confining pressure of 50kPa and increasing matrix suction are presented in Figure 2.37a and 2.37b. The deviator stress-strain curves showed an increase in shear strength as matrix suction increased. It was seen that the strain to failure decreased with each stage as the matrix suction increased. The values of total cohesion,  $c$  (achieved from the intercepts of the extended Mohr-Coulomb failure envelope versus matrix suction) and  $\phi^b$  angle for both residual soils are shown in Figure 2.38. For Bukit Timah soil, the highest value of  $\phi^b$  angle of  $28^\circ$  suggested that the soil desaturated close to matrix suction of 25kPa which was already lower than the  $\phi'$  angle of the soil ( $32^\circ$ ). The  $\phi^b$  angle decreased to almost zero above a matrix suction of 150kPa. Meanwhile the Jurong soil produced an unrealistically high value of friction angle of  $51^\circ$ . It was probably due to the natural heterogeneity of the tested soils, which were not identical, therefore the  $c'$  term contributing to total cohesion could be variable.

Wong et al. (2000) performed a series of tests using modified direct shear and triaxial tests to carry out infiltration shearing tests on granitic soils of Bukit Timah, Singapore. The results from both of the tests indicate that the failure of the specimens during infiltration were due to the decrease of matric suction (Figure 2.39a and 2.39c and Figure 2.40a and 2.40c). It is clearly seen that during infiltration before the failure (Figure 2.39b and 2.40b), the horizontal displacement increased gradually and whilst the axial strain decrease. When failure occurred, both horizontal displacement and axial strain changed drastically with sudden fall of vertical displacement (Figure 2.39c) and greater increase of volumetric strain (Figure 2.40c).

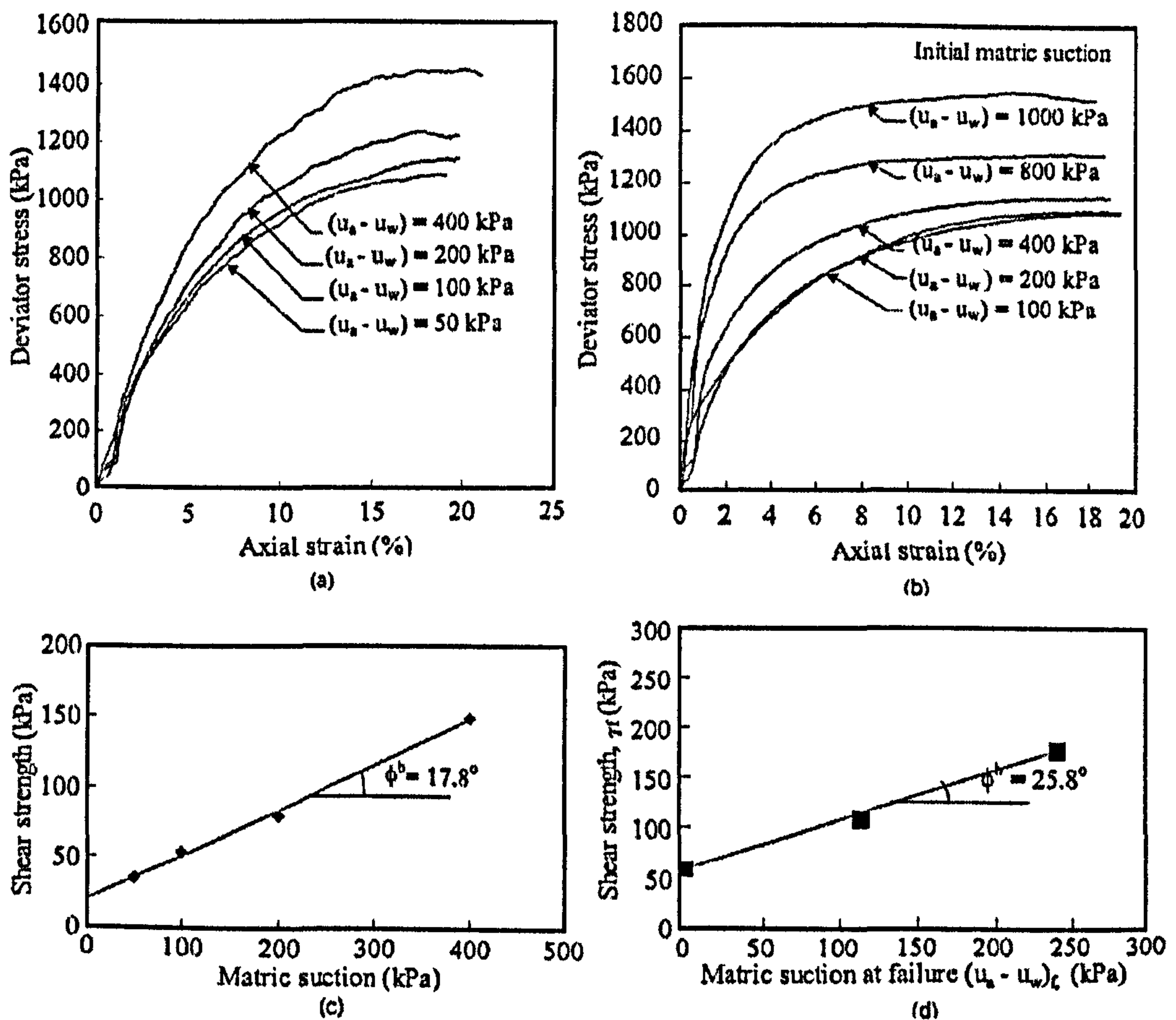


Figure 2.36: The deviator stress versus strain curves for (a) CD and (b) CW tests. The failure envelope for (c) CD test and (d) CW test (after Taha et al. 2000)

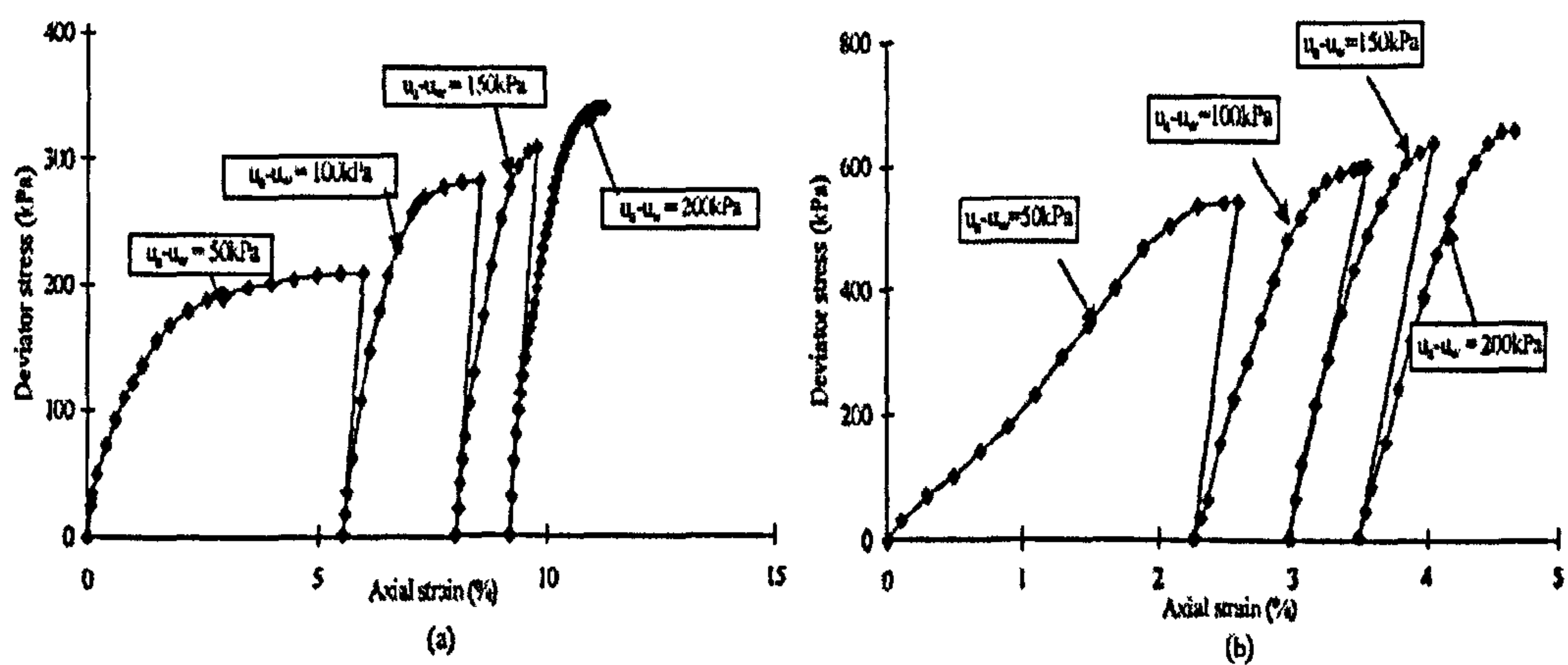


Figure 2.37: The results of the multi-stage CD triaxial tests on undisturbed residual soils. (a) Bukit Timah formation; (b) Jurong Sedimentary formation (after Toll et al. 2000)

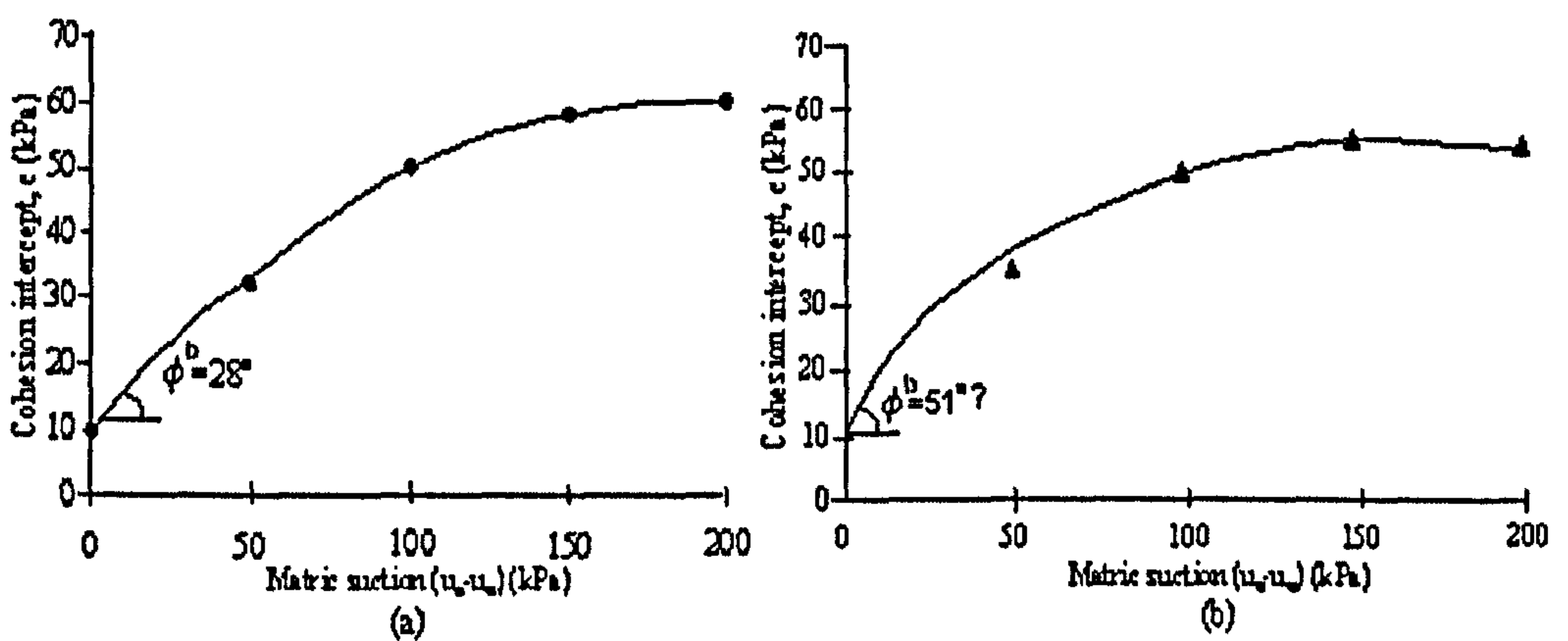


Figure 2.38: The highest values of  $\phi^b$  angle obtained from the total cohesion versus matric suction for both type of sample. (a) Bukit Timah formation; (b) Jurong Sedimentary formation (after Toll et al. 2000)



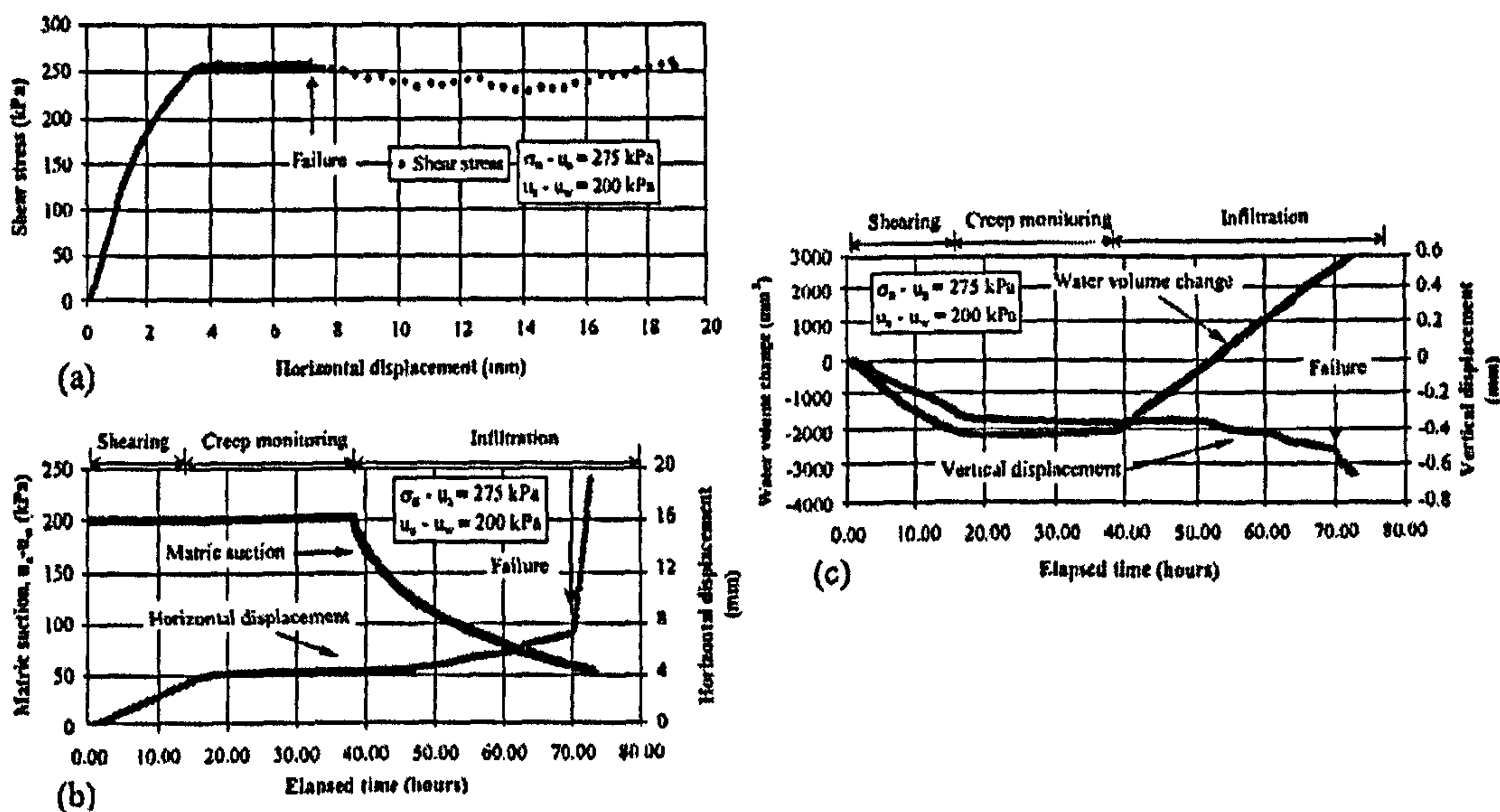


Figure 2.39: The result of shearing-infiltration direct shear test under 275kPa net normal stress and 200kPa matric suction. (a) shear stress vs. horizontal displacement; (b) matric suction and horizontal displacement vs. elapsed time; (c) water volume change and vertical displacement vs. elapsed time (after Wong et al. 2000)

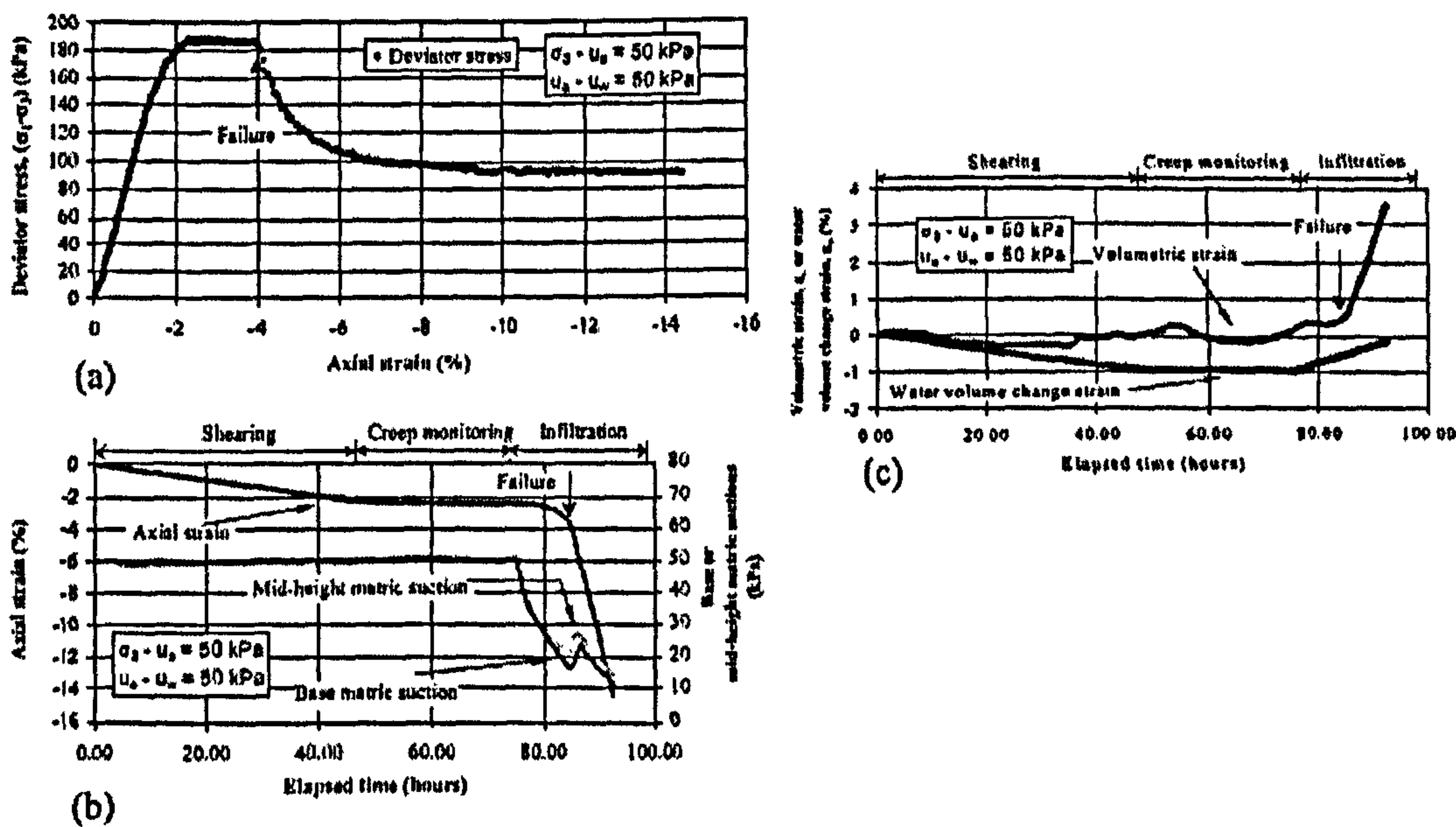


Figure 2.40: The result of shearing-infiltration triaxial test under 50kPa net confining pressure and 50kPa matric suction. (a) deviator stress versus axial strain; (b) axial strain and base or mid-height matric suctions versus elapsed time; (c) volumetric or water volume change strain versus elapsed time (after Wong et al. 2000)

Mancuso et al. (2000) examined the effects of compaction induced fabric and suction on the behaviour of silty sand in unsaturated condition. A series of triaxial tests was carried out on material compacted at the optimum and wet of optimum, under controlled suction conditions. Based on isotropic compression, an increase in moulding water content encourages an increase in compressibility. Figure 2.41 shows that the shape and position of the after compaction loading-collapse loci (LC) were significantly affected by moulding water content. By increasing the suction, the material compacted at optimum moved further to the right side of the graph with yield net stress ranges from 35 to 175kPa. It was suggested that suction significantly affected both stiffness and strength as the ultimate state data points seemed to be well grouped by interpreting them through straight fitting lines having the same  $M$  coefficient in the  $(p-u_a):q$  plane.

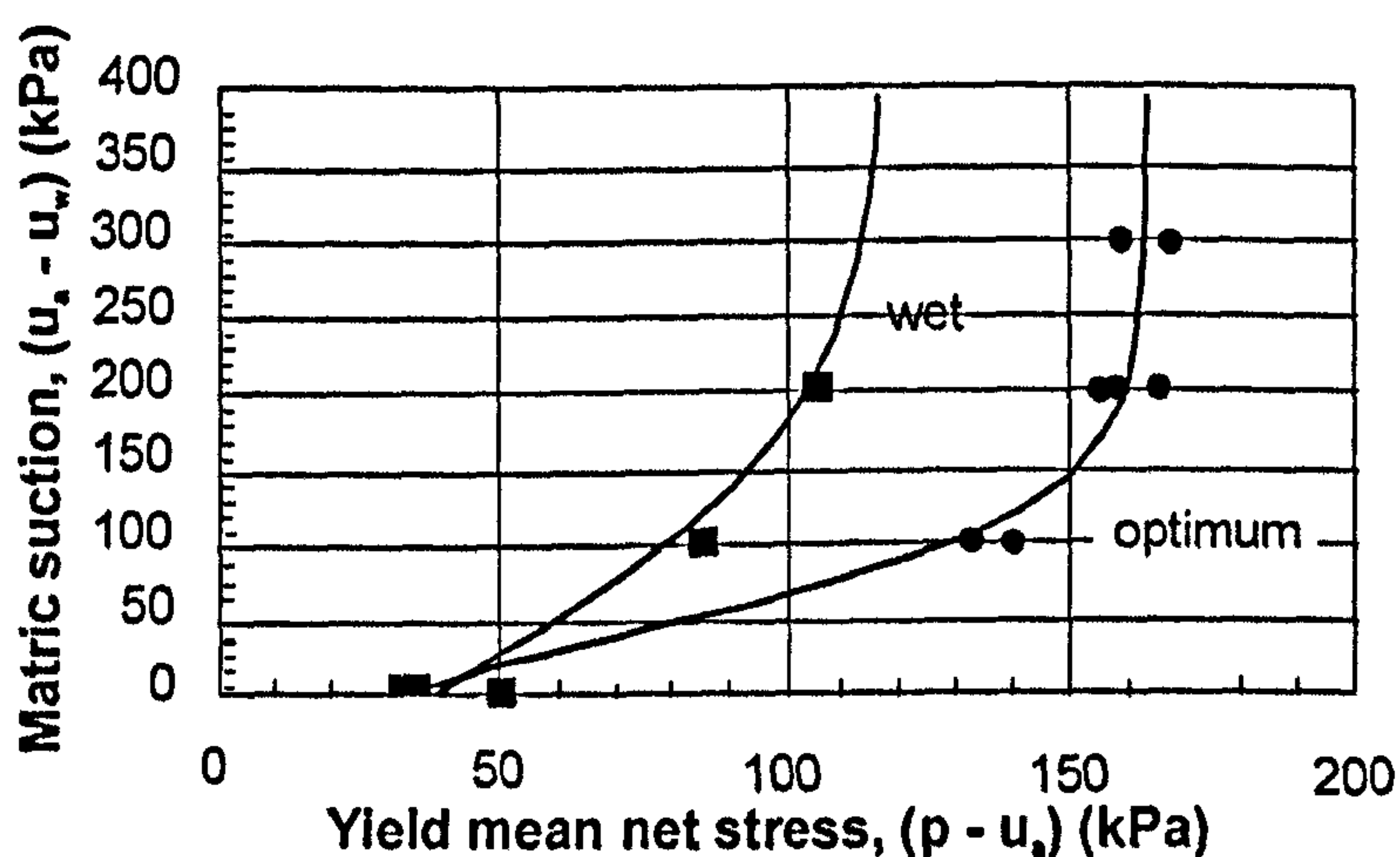


Figure 2.41: The influence of matric suction on the shape and location of the after compaction loading-collapse loci (LC) (after Mancuso et al. 2000)

Toll and Ong (2003) performed a series of triaxial tests on residual sandy clay samples from the Jurong sedimentary deposit, Singapore. Constant water content tests were carried out for unsaturated samples while drained tests were performed on saturated samples. For the drained tests, the true critical state was achieved since the deviator stress and volume strain levelled off at 12% – 15% of axial strain. On the other hand, the deviator stress and pore water pressure from the

constant water content tests (high degree of saturation,  $S_r$ ) continued to change toward the end of the test (Figure 2.42). Figure 2.43 shows the stress path ( $q - p'$  space) for data from drained tests and constant water content tests at high degrees of saturation. Due to difficulties in defining the true critical state condition, the ultimate stress ratio ( $q/p'$ ) was chosen to define the critical state stress ratio ( $M=1.23$ ).

Walker et al. (2005) studied the effect of structure of artificially bonded samples on the water retention curve using different techniques of suction measurement. The studied materials were prepared at void ratios of 0.6 and 0.9 from a mixture of sand and kaolin. Figure 2.44a and 2.44b show that the soil water retention curves are very similar for both bonded and destructured samples at two void ratios. They suggested that it was a result of the presence of relatively coarse pore size of the soil. However, the effect of bonding on the water retention curve is more obvious. At the same matric suction, bonded soils had slightly higher water contents than the destructured soils with the same void ratio. Based on microscopic observation, the presence of clay matrix in destructured soils is discontinuous and offers more surface area than in bonded soils that assists absorption of water during wetting.

Reis and Vilar (2005) studied the stress strain behaviour of gneiss residual soils profile from Vicosa, Brazil. Samples used were classified as from completely weathered material and residual young soils (or saprolite). They found that the failure envelopes for both samples were parallel suggesting that the friction angle ( $\phi$ ) did not vary with suction (Figure 2.45a and 2.45b). However the cohesion intercept values were varied with the suction, indicating a non-linear relationship (Figure 2.45c). The cohesion intercept initially has a tendency to increase faster with suction and then increase with slower rate as suction increases.



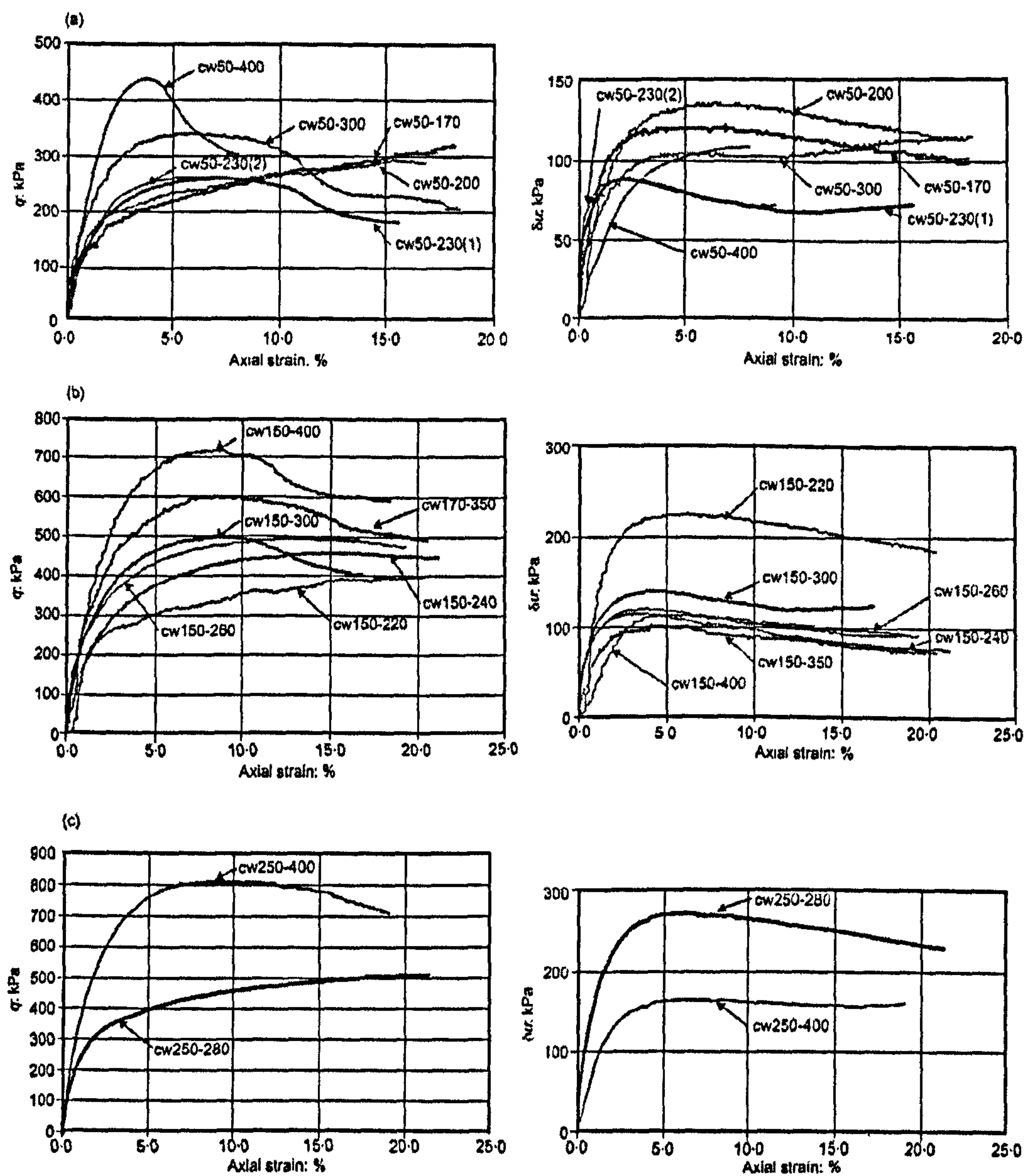


Figure 2.42: Deviator stress,  $q$  and pore water pressure change,  $\delta u$  against axial strain in constant water content tests at net confining stress: (a) 50kPa; (b) 150kPa; (c) 250kPa (after Toll and Ong 2003)



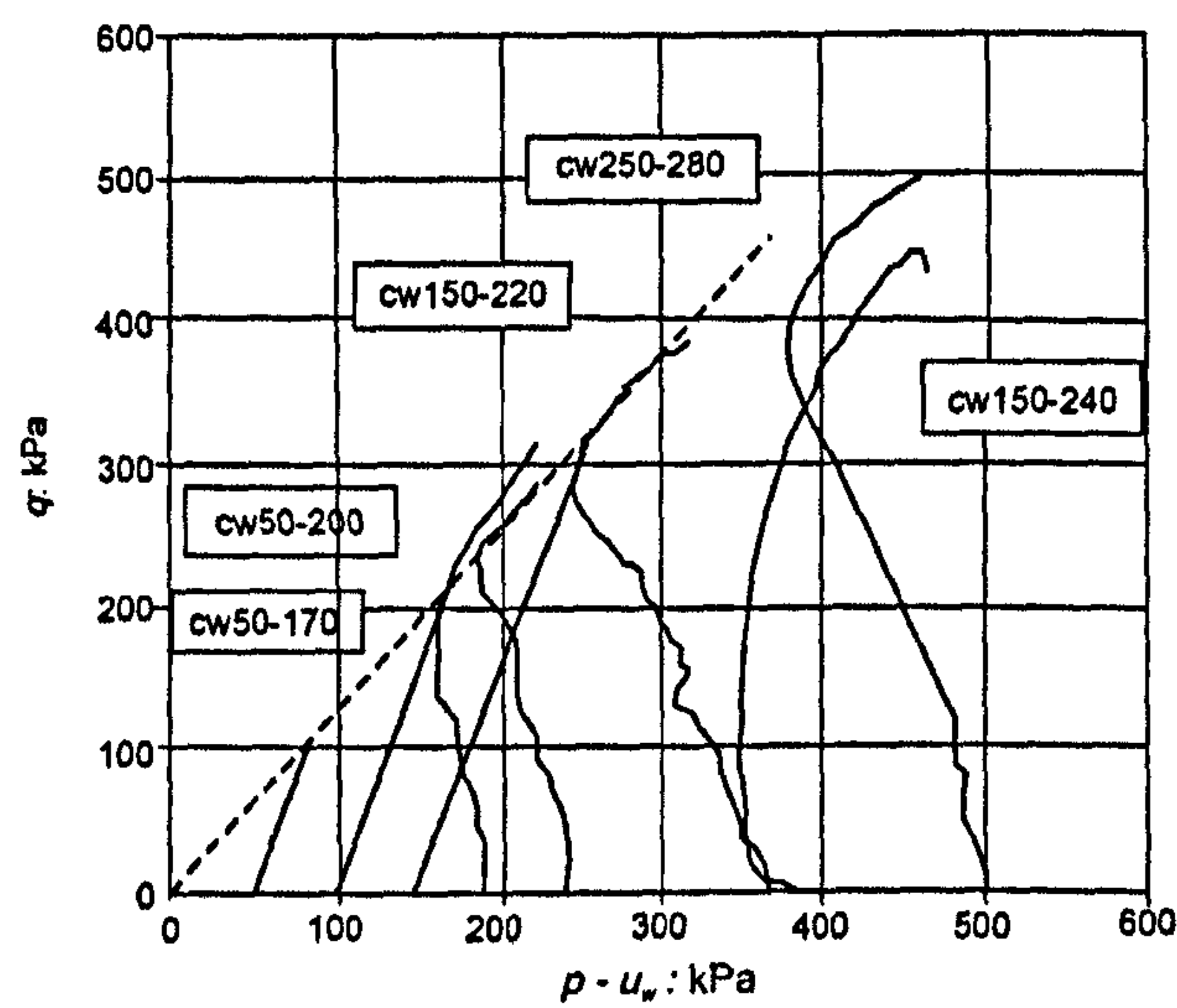


Figure 2.43: Stress path in  $q: p'$  space for drained and constant water content tests at high degree of saturation (Toll and Ong 2003)

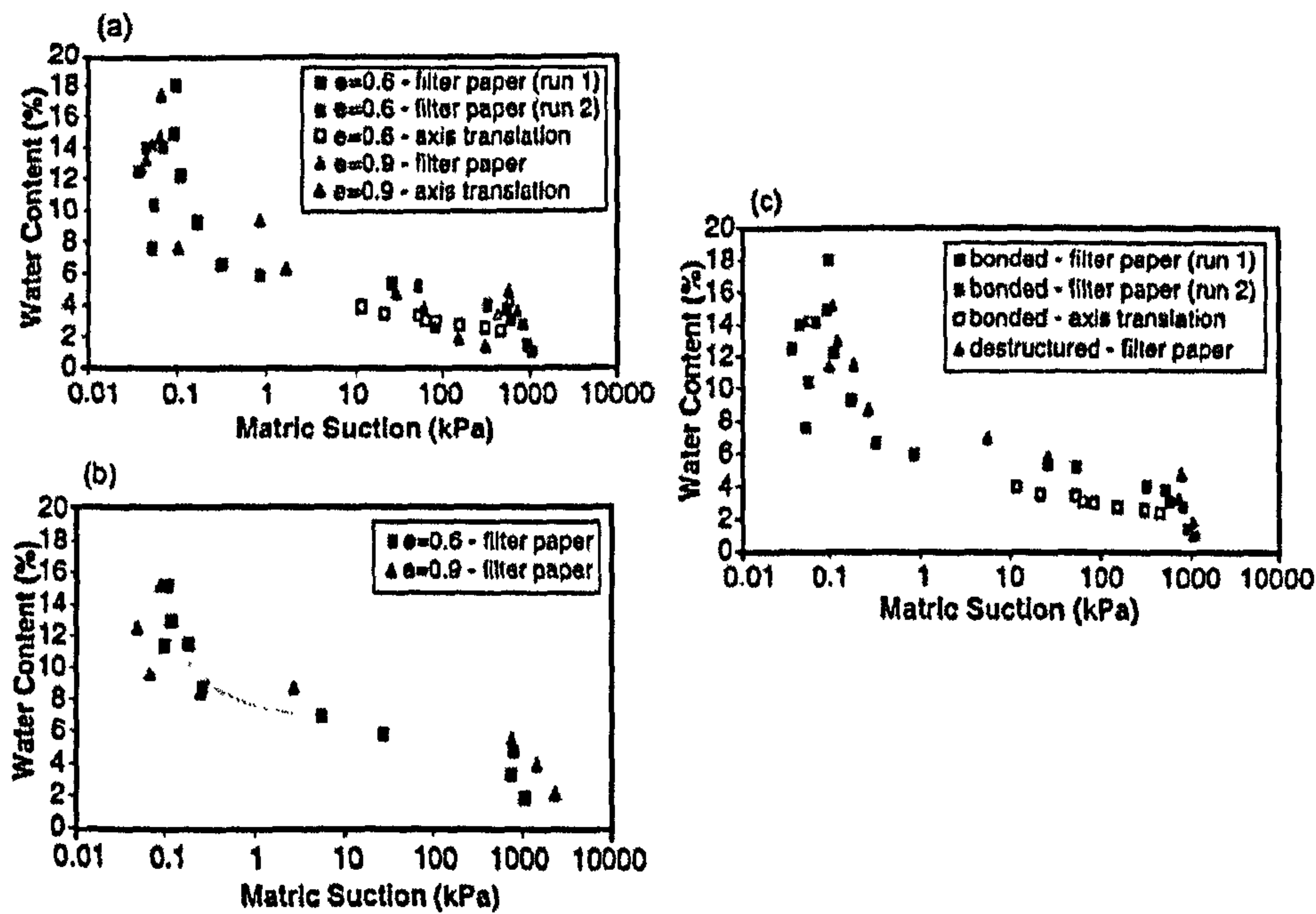


Figure 2.44: Soil water retention curves of prepared samples. The effect of void ratio on matric suction; (a) bonded soils; (b) destructured soils; and effect of bonding (c) on samples with 0.6 void ratio (after Walker et al. 2005)

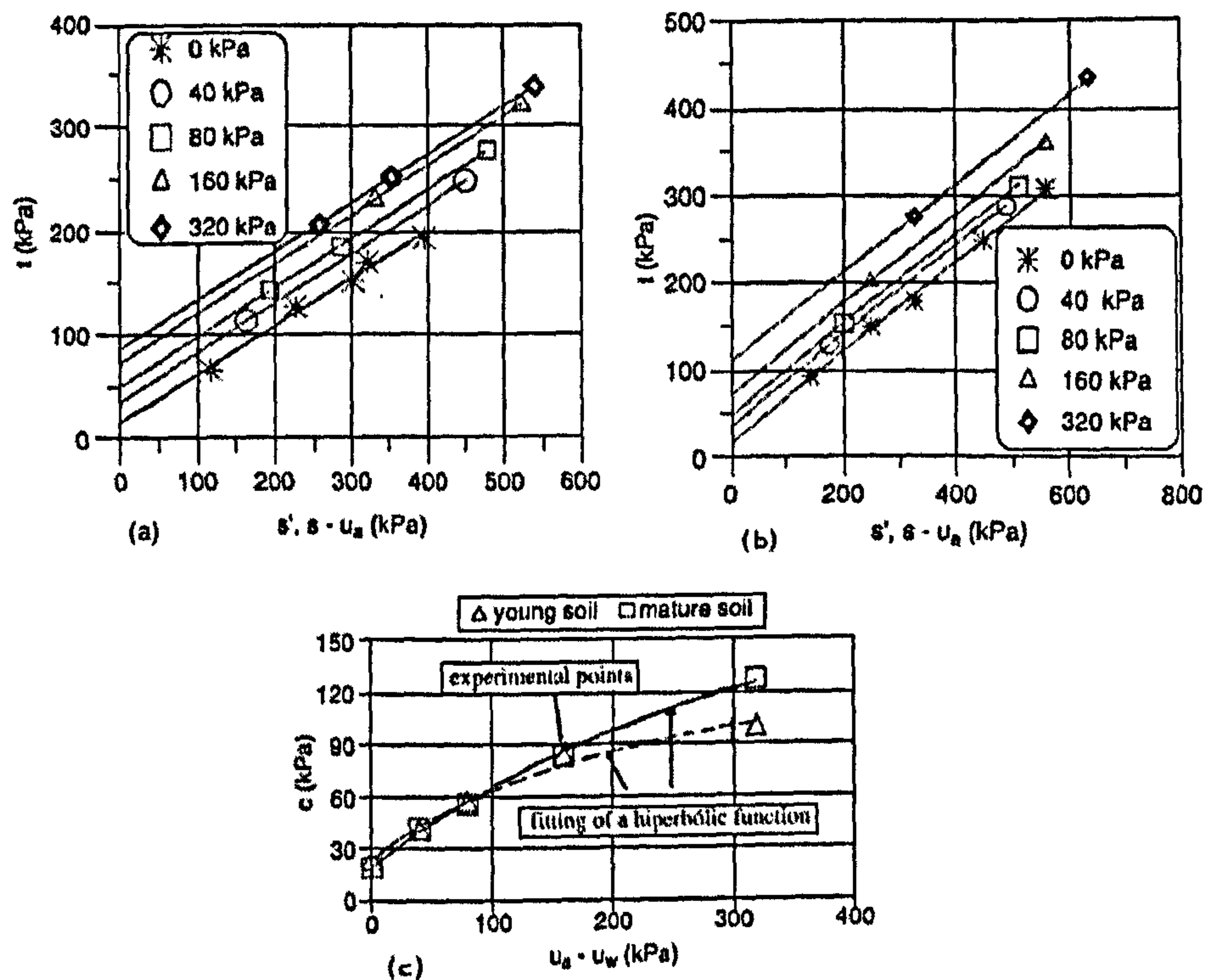


Figure 2.45: Failure envelopes for (a) young soil; (b) mature residual soils and: (c) intercept of cohesion values for both soils (after Reis and Vilar 2005)

### 2.3.4 Critical State of Granular Material

The critical state concept has been used to understand the behaviour of a wide range of earth materials such as clay, clean sand, silty sand and gravelly sand. Taylor (1948) studied the behaviour of clean sands using direct shear tests. He suggested that the peak strength of soils under shearing is partly attributable to the friction among particles and the particle interlocking. The strength of dense sands is predominantly contributed to by the interlocking between particles. He proposed the following equation  $\tau'/\sigma' = \mu + (\delta_v/\delta_u)$ , where  $\tau'$  is the shear stress,  $\sigma'$  is the normal stress,  $\mu$  is the coefficient of friction,  $\delta_v$  is a small increment of vertical movement and  $\delta_u$  is a small increment of horizontal movement. The equation explained that the  $\tau'/\sigma'$  ratio depends on the coefficient of friction,  $\mu$  and the rate of

dilation,  $(\delta_v/\delta_u)$ . Then Schofield and Wroth (1968) extended the theory and proposed a following equation  $q/p' = M - (\delta\varepsilon_v/\delta\varepsilon_s)$ , where  $q/p'$  is the stress ratio,  $M$  is the gradient of critical state line when the rate of volume change is constant,  $\delta\varepsilon_v$  is a small increment in volumetric strain and  $\delta\varepsilon_s$  is a small increment in shear strain ( $-\delta\varepsilon_v$  indicates an expansion). According to this equation, the  $q/p'$  ratio achieves a maximum value at which the sample expands at maximum rate of dilation during shearing (Figure 2.47). At a point where  $q/p' = M$ , the change in shape of sample immediately occurs at a constant volume (where  $\delta\varepsilon_v/\delta\varepsilon_s = 0$ ). Therefore, any strain that having  $q/p'$  ratio less than  $M$ , sample contracts where  $\delta\varepsilon_v/\delta\varepsilon_s$  is positive. Once  $q/p' = M$ , the sample then continues to dilate and achieves the maximum  $q/p'$  ratio at maximum rate of dilation at point C (Figure 2.46).

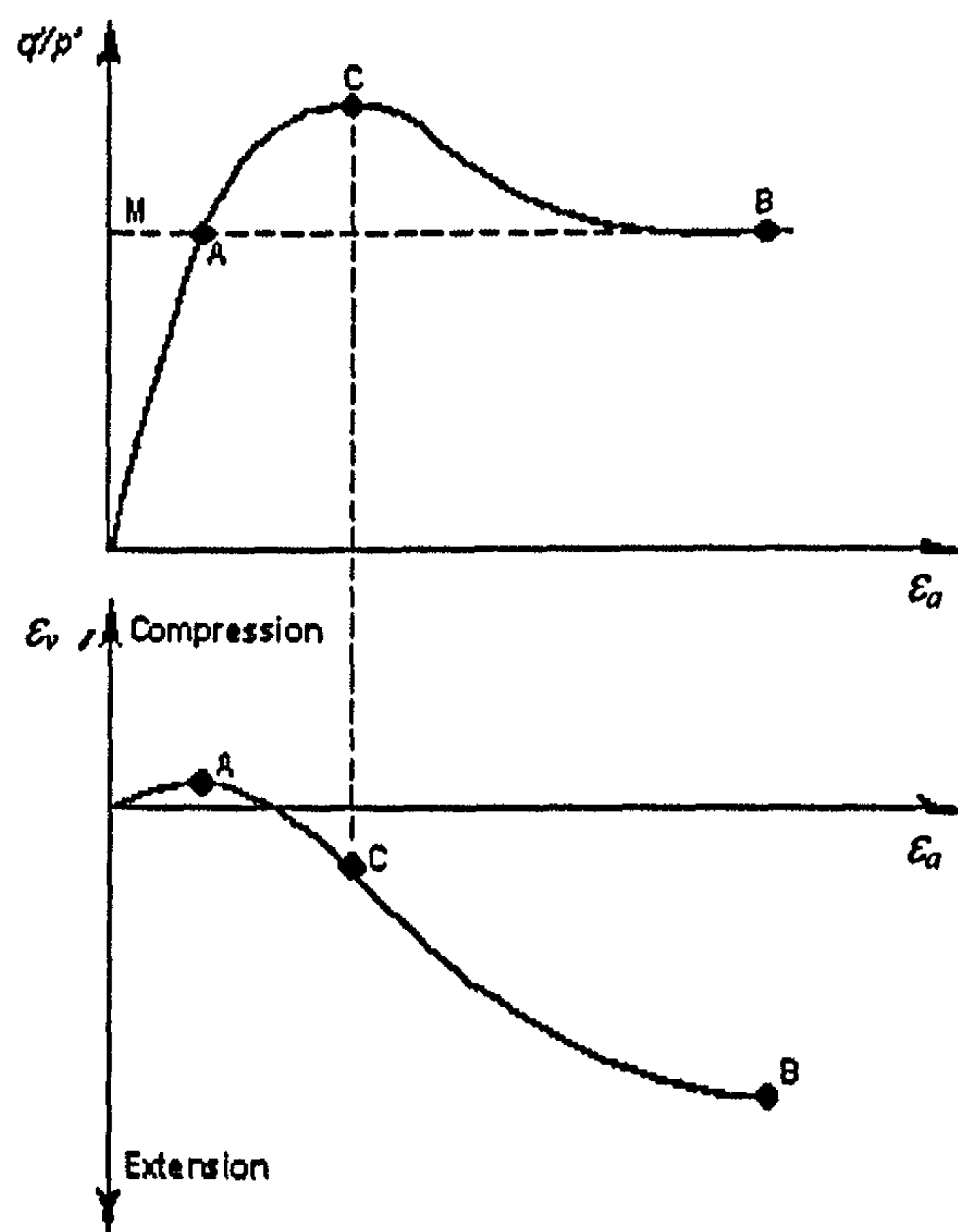


Figure 2.46: Relationship between  $q/p' : \varepsilon_a$  and  $\varepsilon_v : \varepsilon_a$  for dense sands (after Atkinson and Bransby 1978)

Since much work has been concentrated on clean sands, more recently the direction has been changed to focus on sand with proportion present of some fine content. According to Yamamuro and Lade (1998), silty sands are the more

common kind of soil associated with both static and earthquake-induced liquefaction. Lade and Yamamuro (1997) and Zlatovic and Ishihara (1997) found that the presence of significant silt content in sand deposits makes them more prone to liquefaction than clean sands. It is essential to realise that many engineering works are closely related to this kind of material which could have significant influence on stability of foundations due to the occurrence of silt content.

The critical state concept was initially introduced based on the early work of Casagrande (1936). Roscoe et al. (1958) further developed the critical state concept, which is not only applicable to clay but also to sand. Since then many discussions have been issued regarding the different definition to the ultimate state of sand between “critical state” and “steady state”. According to Been et al. (1991), the differences in these two versions lie in the methods of measurement. Casagrande (1936) described the critical state as a state when the void ratio and the normal shear stresses remain constant under continued shearing in drained conditions. Seed and Lee (1967) defined the critical state as the state where the void ratio (after consolidation) and confining pressure are such that zero total volume change is produced at peak failure under drained condition as illustrated schematically in Figure 2.47.a. Meanwhile for steady state researchers (e.g., Castro 1969; Alarcon-Guzman et al. 1988; Konrad 1990; Been et al. 1991; Yamamuro and Lade 1998) the steady state has been defined based on undrained condition for loose (contractive) samples when the void ratio remains constant but the effective mean stress,  $p'$  will change to bring the sample to an ultimate state. Seed and Lee (1967) defined the combination of current void ratio (same as that achieved after consolidation) and effective confining pressure at peak failure considered as the critical state (Figure 2.47b). As mentioned earlier, Been et al. (1991) suggested that the terms critical state and steady state are in fact the same state.

Toll (1988) used the term critical state in studying the behaviour of unsaturated compacted naturally occurring gravel. Toll (1990) analysed the results in terms of



the critical state stress ratios of  $M_a$  (net stress component) and  $M_s$  (suction component). He proposed that the friction angle  $\phi'$  (representing the strength component due to net stress,  $p-u_a$ ) was not constant as suggested by Fredlund et al (1978). The value of  $\phi'$  is influenced by the degree of saturation of the soil which could be explained by the fact that different degree of saturation represent different soil fabrics (Toll (2000). Toll and Ong (2003) also adopted the same approach for results on residual sandy clay samples from the Jurong sedimentary deposit, Singapore. Meanwhile, Lee and Coop (1995) also applied the critical state concept for both drained and undrained tests in their work on decomposed granite soil. On the other hand, Poorooshasb (1989) and Yamamuro and Lade (1998) referred to steady state in their work.

There is much evidence from work carried out on granular material (from sands to gravelly sands) indicating that a unique critical state line is not possible to achieve in  $e-\ln p'$  space (Hosseini et al. 2005). They found that the difference between the upper and lower limit was  $\pm 0.04$ , in terms of void ratio. The possible causes of this probably were related to the heterogeneity in initial soil fabric and structure, which formed during remoulding of the soil even prepared at the same void ratio. Fourie and Papageorgiou (2001) were also concerned about the difficulties in defining the critical state condition accurately due to uncertainties in void ratio determination. They concluded that the void ratio error that resulted from the measurement of the specimen properties might crop up from errors in the measurement of specimen height, diameter, mass and gravity specific gravity. Figure 2.48 shows the critical state line represents the “confidence zone” bounded by upper and lower limits after considering possible combination of errors in void ratio determination of 0.05. Been et al (1991) studied a fine to medium quartzite sand and found that the critical state line was represented by scatter values of void ratio in the range of  $\pm 0.01$  at stress level below 1MPa. Yamamuro and Lade (1998) found that the steady state lines from drained and undrained tests on silty sand samples sheared from the same isotropic compression line coincided at higher pressures, but the two lines became apart at lower pressure. They concluded that for silty sands, a unique

steady state line may not be always guaranteed. Thus, the critical state is clearly represented by a zone of scatter data that confined by lower and upper limits. This is, in fact, consistent with the findings that given by many other researchers (e.g., Konrad 1990; Mooney et al. 1998; Fourie and Papageorgiou 2001).

Been et al. (1991) also found that the critical state line is curved from a series of undrained tests on Leighton Buzzard sand for the stress range 10-500kPa (Figure 2.49a). However, data from the undrained tests on contractive Erksak sand samples indicated that the critical state line curved abruptly at stress level of about 1MPa (Figure 2.49b). They concluded that the change in critical state line was due to a change in mechanism in shearing at high stress levels. At high stress level above 1MPa, some breakage of grains occurs which results in different behaviour.

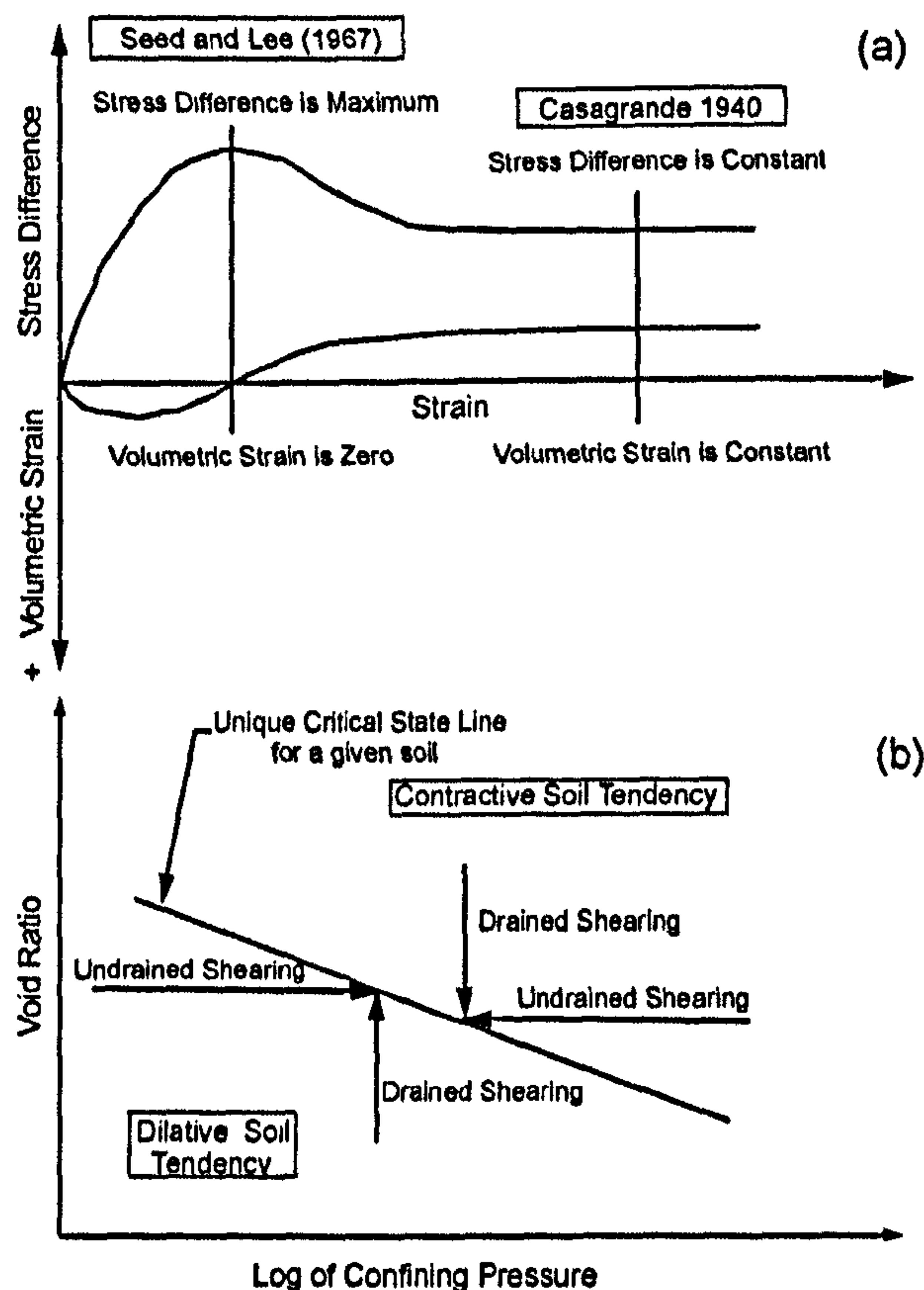


Figure 2.47: Schematic diagram showing definition of critical state for drained and undrained tests (after Yamamuro and Lade 1998)

Luzzani and Coop (1992) carried out ring shear tests in order to investigate the behaviour of two different sands (quartz and carbonate). They found that particle breakage occurred in both sands and continued to a large strain higher than those could be reached in triaxial test. There was some uncertainty on whether the true critical state was achieved in triaxial tests mainly at higher stress levels (particle breakage had completely ended). Further investigation by Coop et al. (2004) used material from biogenic carbonate sand. They demonstrated results from a series of ring shear tests on biogenic carbonate sand indicating a large volumetric compression caused by particle breakage. Other earlier studies also indicated that a presence of small portion of fine sand and silt content show similar behaviour (Lee and Farhoomand 1967; Hardin 1987).

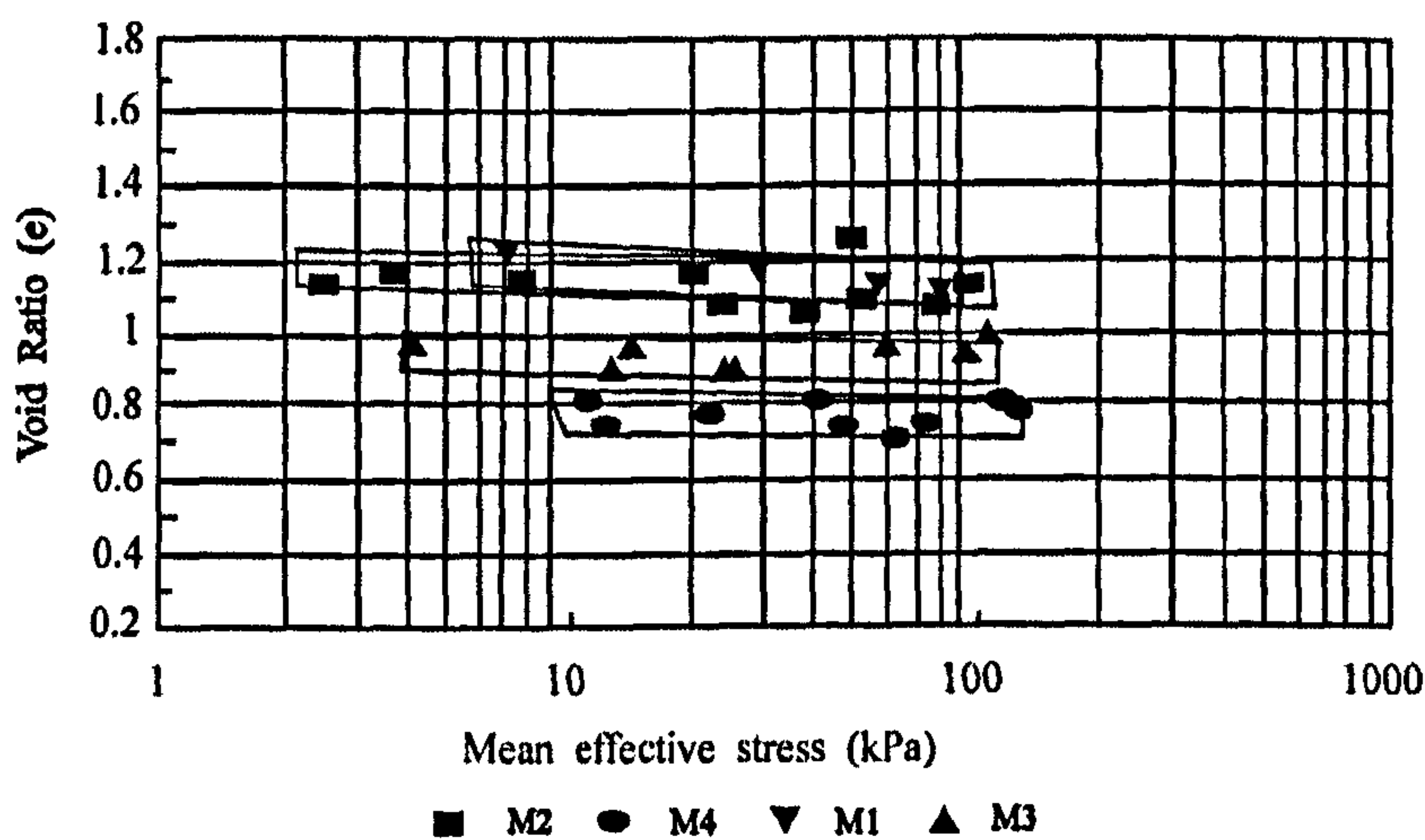


Figure 2.48: The critical state line defined for Merriespruit tailing dam from undrained triaxial compression test, which showed contractive behaviour. The “confidence zones” represent an error allowance on void ratio of 0.05 either side of the critical state line (after Fourie and Papageorgiou 2001)



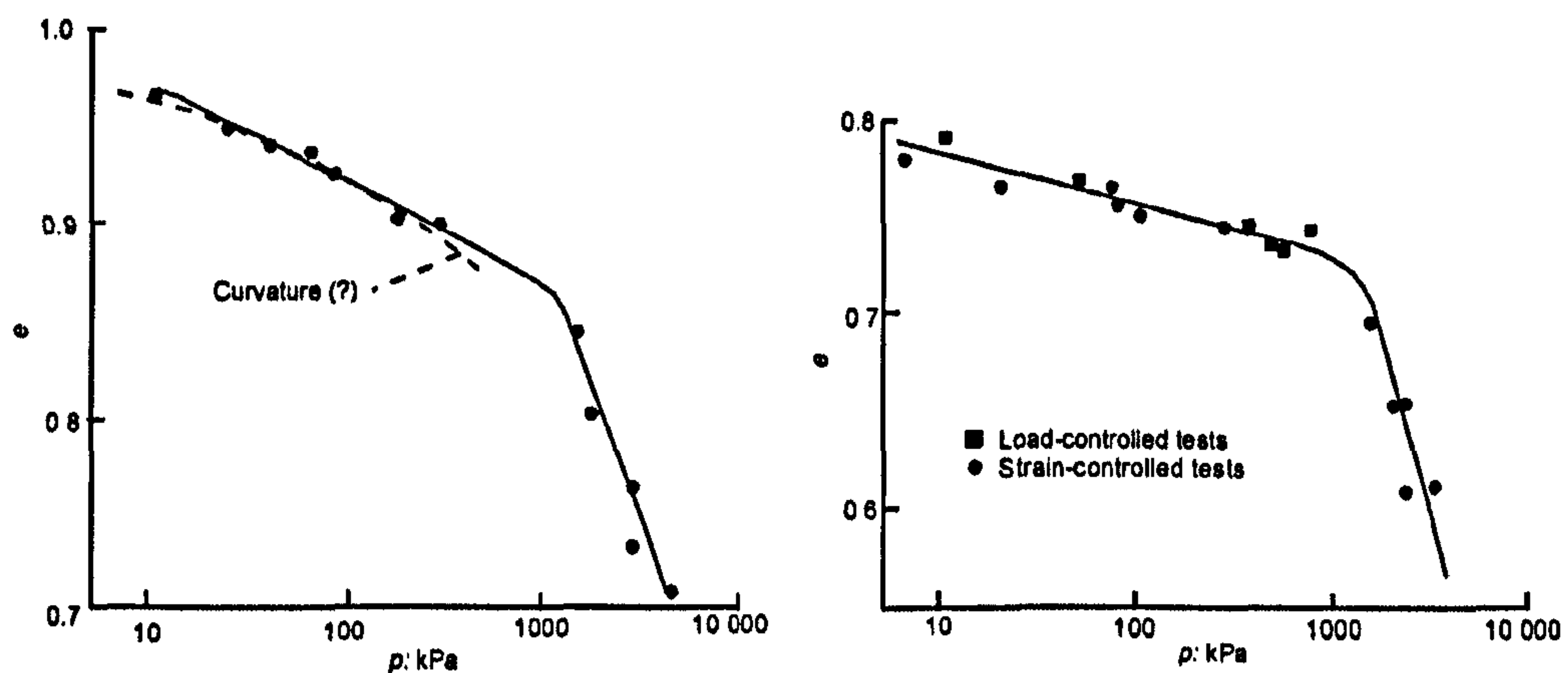


Figure 2.49: (a) Critical state line for Leighton Buzzard sand showing curvature; (b) Critical state for undrained tests on contractive samples of Erksak 330/0.7 sand (initial state of all samples was above the critical state line)(after Been et al 1991)

## 2.4 CONCLUSIONS

Various studies relating to the engineering behaviour of soils have been carried out around the world including saturated and unsaturated conditions. They include a variety of soil types decomposed from different kinds of geological formations and environments. Most of the early studies on soil mechanics were based on saturated soil conditions. On the other hand, research on unsaturated soils studies is quite young and has been carried out, recently in order to establish more reliable and acceptable frameworks for unsaturated soil behaviour. In saturated soil conditions, bond strength and void ratio are two main properties that control the bonded soils. However, due to their partially saturated nature, the mechanical behaviour of soils is also influenced by the presence of air and water occupying the soil's pores.

The previous research on different kinds of natural soil samples clearly indicates that even though the soils' structure has been developed under different processes and sources, their engineering properties are quite similar. This has been acknowledged by the facts that many different soil formations have similar characteristics in terms of the presence of weakly bonded structure. An important



feature is that this aspect of behaviour is not due to the earlier stress history but to the bonded structure. These soils have been well known as structured soils.

Many studies have also been carried out on the behaviour of artificial bonded soils in an attempt to simulate the natural characteristics of soil structure. Instead of using natural soils, the use of artificial samples can minimize the difficulty in sample variability, sampling and storage of natural soils. Natural properties such as bond strength and void ratio can be prepared and reproduced, thus enabling the artificial sample to be examined for various ranges of natural characteristics. Different types of bonding or cementing agents have been used to simulate natural bond such as salt, kaolin and hydrated lime. These artificial samples are sufficiently able to demonstrate the influence of bond structure on soil behaviour and provide good agreement between natural and artificial bonded soils. Studies have also been carried out on destructured soils to obtain more evidence on the effect of bonding on the behaviour of soils.

The studies of the engineering behaviour show that strength and stiffness is clearly affected by the bonded structure. Bonded soils achieve higher max stress ratios compared to destructured samples. As a result of the presence of bonded structure, the value of tangent stiffness is also higher than the destructured material. The failure envelopes for bonded soils tend to show some curvature at higher stresses. This indicates that the effect of bonding is greater at low confining stresses and has less effect with increasing confining stress due to the breaking down of bonds. The breakdown of bonds due to shear may not be isotropic but can be associated with the direction of the stress path at the point of yield.

Since the study of the mechanical behaviour of unsaturated soil is quite new compared to saturated soils, most of the basis of unsaturated soils has been developed from traditional soil mechanics. Up till now, many studies have been carried out in order to understand the influence of unsaturated conditions on the engineering behaviour of such a soil. A wide range of natural and artificial soils have been investigated, aimed at understanding the unsaturated behaviour and

various constitutive models have been developed. Early studies with samples tested under different matric suction clearly indicated the contribution of suction on the shear strength of the soils. However, in later studies showed nonlinearity in the shear strength suggesting that the value of  $\phi^b$  is not constant. As testing technology has advanced, soil samples have been examined under a wider range of suctions, and this phenomenon of a non-linear  $\phi^b$  relationship become more noticeable.

Much research has also been carried out in order to examine the concept of critical state or steady state on the granular soils such as clean sands, gravelly sands and silty sands. The work carried out on granular materials from sands to gravelly sands indicate that a unique critical state line is not possible to achieve in  $e-\ln p'$  space (or  $v-\ln p'$ ). An inevitable change would happen on initial soil fabric and structure during samples preparation. Other possibility was due to the void ratio error resulted from the measurement of the specimen properties. Therefore it is preferable to accept a critical state line with zone of lower and upper limits. Some previous studies also indicated that the critical state line was not a straight line for the low stress range and curved dramatically at high stress level due to some particle breakage, which results in a different behaviour. The presence of small proportions of fine sand and silt content with sand particles showed similar behaviour. It found that the adding of fines also decrease the separation of NCL and CSL, due to the change in grading (specific volume,  $v$  becomes smaller) of the soil.

**CHAPTER 3****SAMPLE PREPARATION****3.1 INTRODUCTION**

In this chapter, the procedures of sample preparation for artificial bonded and destructured soils are explained. Previous techniques developed by other researchers for the preparation of artificial samples are also discussed in this chapter. Finally, the equipment and procedures are described that were used to obtain artificial weakly bonded and destructured samples with similar void ratio and bond strength.

**3.2 REVIEW OF PREVIOUS METHODS OF SAMPLE PREPARATION****3.2.1 General Overview**

Artificial soil samples have been widely used in the study of the engineering behaviour of soil (Maccarini 1987; Bressani 1990; Huang and Airey 1993; Coop and Atkinson 1993; Malandraki 1994; Cuccovillo and Coop 1999; Haeri et al. 2005). The ability to reproduce artificial soils with desired properties (bonding strength, void ratio and particle grading), give some advantages to researchers by providing the capability to investigate the influence of other factors such as stress history (Bressani 1990). The development of the fundamental frameworks of soil mechanics was based on reconstituted samples and artificial samples can provide the data to develop theoretical frameworks for bonded soil.



Bond structures, especially inter-particle bonds, are easily destructured due to disturbance. Due to their sensitivity to disturbance, very careful procedures are required in soil sampling, sample preparation and during shearing of the sample. Vaughan (1988) mentioned that in order to study the effects of bonding on soil behaviour, artificially bonded samples should be used and then be compared with destructured samples produced with similar characteristics. The properties of artificial samples should be reproducible and unchangeable with time, as well as be easy to handle. Thus, all problems associated with difficulties of variability, handling, storage and testing of natural soils can be overcome by using artificial samples (Malandraki 1994).

The use of artificial samples that can simulate the properties of natural soils has been widely used in studying the engineering behaviour of residual soils. Thus, a number of techniques have been developed in order to get reproducible artificial bonded material. Previously, cement was considered to form bonding between grains, however it has disadvantages because of the change of properties with the age of sample (curing). In addition, there are difficulties in preparing reproducible samples with the very small amount of cement needed to produce weak bonding (Maccarini 1987). An attempt to simulate bonded carbonate sands by permitting salts to precipitate within a granular sample seemed to be time consuming and relatively required complicated arrangement of instrumentation (Espinete and Pelaez 1983).

Maccarini (1987) described a method of preparing artificial bonded samples. The same method was also applied by Bressani (1990) in continuing the previous work carried out by Maccarini. Malandraki (1994) adopted this technique, (but without the crushed fired kaolin or c.f.k. sand) in studying the engineering behaviour of the weakly bonded soils (Toll and Malandraki 1993). This technique has been adopted for this study and is described in detail below.

Huang and Airey (1991) used carbonate sand collected from the North West Shelf of Australia as a base soil for preparing artificial samples. To create artificially



cemented soils, gypsum plaster was mixed up with the base soil and compacted into a specially designed mould within 10 minutes. After being loaded for some time, the samples were then permitted to harden. The content of cement used varied between 0 and 20% of the dry weight of base soil while the distilled water added was sufficiently to saturate the mixture after compaction. After the samples had been removed from the mould, they were wrapped with plastic film and kept in plastic bags to cure for more than two weeks under relatively constant humidity.

Coop and Atkinson (1993) prepared artificially cemented and uncemented samples for studying the basic behaviour of carbonate soils. Gypsum plaster was added to carbonate sand from Dog's Bay in Ireland. It was acknowledged by Evans (1987) that gypsum plaster might be the most suitable artificial cementing agent for carbonate soils based on similar unconfined compressive strength for both artificial and natural carbonate soils. For the artificially cemented soil, the sand-plaster had a ratio of 3.33 to 1 by weight. Meanwhile the uncemented soils were established from untreated Dog's Bay sand.

The use of gypsum plaster as a cementing agent was also adopted by Cuccovillo and Coop (1993) to create artificially cemented soils. The sand portion was from Dog's Bay sand which was tested by Coop (1990). They used different amounts of sand and gypsum plaster to produce different strength of bonding. The "strongly cemented soils" had a ratio of 1:3.33 for plaster to sand by weight. Meanwhile "weakly cemented soils" were produced by decreasing the proportion of gypsum plaster to 1:10. A mixture of sand/plaster in an uncemented state was also prepared to examine the influence of bonding. In order to study the effect of the chemistry of the fines material, calcium carbonate instead of gypsum fines were added to the sands.

Malandraki (1994) also attempted to prepared artificial weakly bonded soil by adding different types of available industrial glues (some of which were waterproof) to create bonds between sand particles. The used of phenolic resin produced a strong bond (too strong in comparison with natural residual soils) and

its strength becomes stronger with time. She also tried a phenolic resin manufactured by BP (J2027L) that combined with a catalyst known as Phencat 10 to make it harden. The masses of resin and catalyst were mixed at a ratio of 100:6 and then a small amount was added to quartz sands. The mixture of sand and resin was put into mould and then heated in an oven at 70°C for an hour. However, the resin created a strong bond between the sand particles. The amount of resin was reduced in order to achieve a weaker bond. However, not all the sand particles were coated thus producing heterogeneous samples. Then, she changed the ratio of the resin and catalyst to produce a thinner mixture. The mixture could not provide sufficient bond between the sand particles. She also found that the samples were becoming stronger with time. Even though she modified the amount of the resin and catalyst in order to get homogeneous sample, this always resulted in very strong bonded samples.

Asghari et al. (2003) prepared artificially cemented samples by adding hydrated lime as a cementing agent to base soil of gravelly sand. The wet mixture of soil was transferred into a mould made from P.V.C perforated pipe. The samples are compacted statically in 10 layers to the required height. The samples were then left to dry in a perforated mould for 6 weeks, thus the pozzolanic cementation compounds were produced from reaction between lime and soil silica. The content of added lime varied between 1.5% and 4.5% of the weight of dry soil. The destructured samples were prepared by breaking down the bonded samples which were prepared earlier. Meanwhile uncemented samples were prepared without adding lime to the base soils.

### **3.2.2 Technique Adopted By Maccarini (1987) and Bressani (1990)**

Maccarini (1987) developed a technique for preparing artificial soil in order to simulate the characteristics of residual soil. The mixture he used contained 13% of kaolin, 30% of weak sand-sized particles known as crushed fired kaolin (c.f.k.) and 57% of quartz particles. The c.f.k. particles were used to simulate the presence of weaker particles in natural residual soil. The c.f.k. was prepared by firing kaolin

slurry at higher temperature (higher than used to form bond) and then crushed and sieved to achieve sand size particles. The kaolin use in his study was a spacestone kaolin as used in the pottery industry with  $G_s = 2.61$ . Bressani (1990) also used the same materials adopted by Maccarini (1987). He prepared samples which had different proportions of material and bond strength. The densities of the prepared samples were between 0.6 and 1.5 of initial void ratios. Series 00 and 300 had no c.f.k and quartz grains proportion, respectively.

Firstly, the required proportion of each ingredient was mixed dry. Then distilled water was added to wet the mixture to form slurry. The slurry mixture was stirred thoroughly to remove any trapped air. The slurry was placed into a mould using a spatula. The wet mixture was then permitted to air dry in the laboratory for about 72 hours. The filter paper mould was peeled off, then the samples were put in a furnace and fired at 500°C for 5 hours. After that, the samples were allowed to cool overnight. In order to verify the bond strength, in some case, the samples were fired at 800°C for 3 hours. However, most of Bressani's results were obtained from samples with bonds that were fired at 500°C for 5 hours.

Firing of the kaolin at about 500°C causes an endothermic reaction in which there is a loss in weight of about 12% and a change from expansion to contraction (Figure 3.1.a & b), as described by Grim (1953). Temperatures around 500°C or higher are likely to result in bonding and probably bond strength could be increased at higher temperature (Figure 3.2). Microphotographs from SEM of a loose bonded sample with 13% of kaolin indicated the sand particles were coated by bridges of bonded kaolin (Bressani 1990). The loose sample also exhibited more voids between particles than the dense materials. The firing of quartz sand over the temperature range was minimal and negligible (Figure 3.1.c) where only small endothermic reaction occurs at about 600°C.



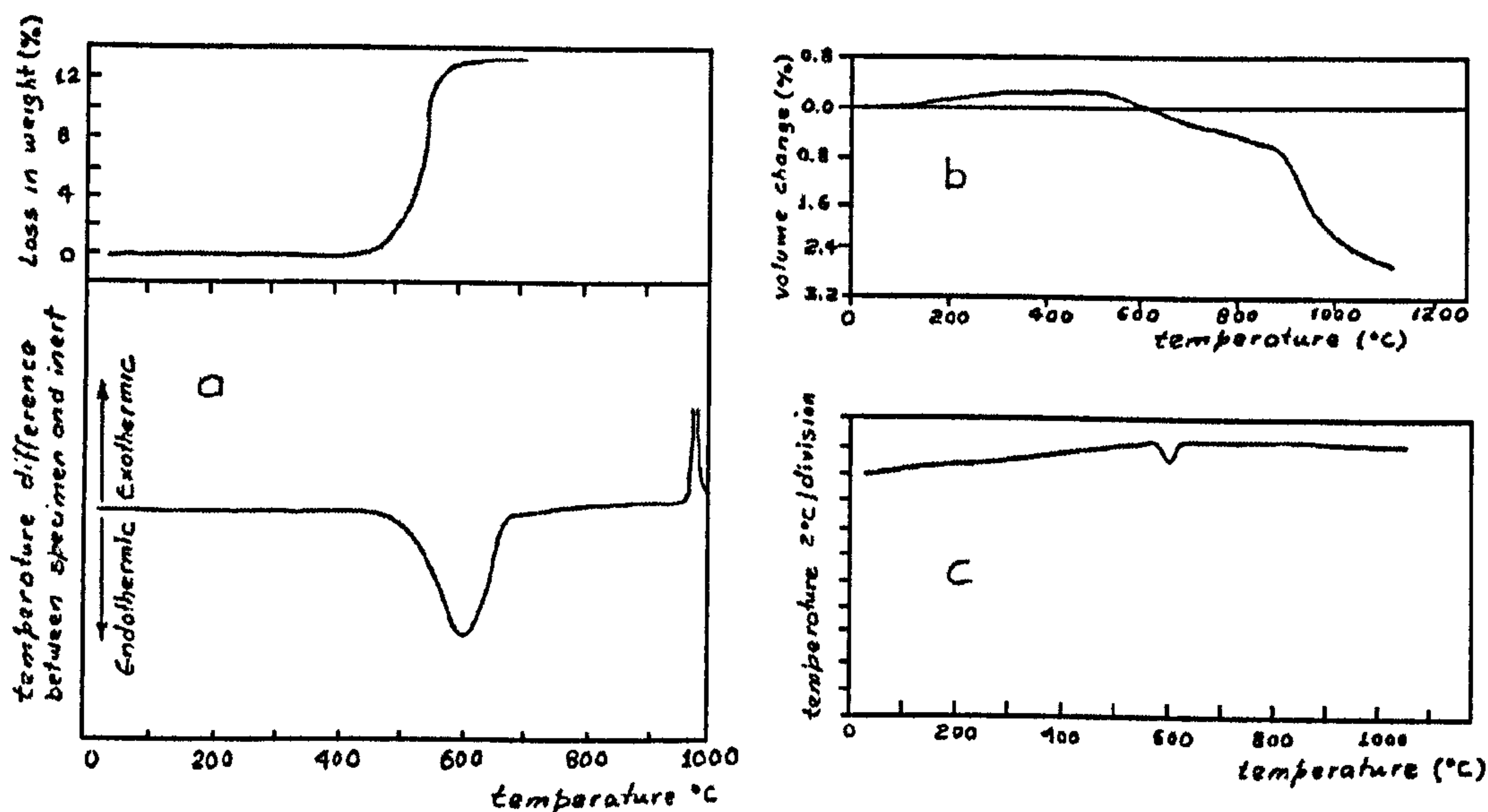


Figure 3.1: Temperature's effect on kaolin (a and b) and quartz sand (c) (after Grim 1953)

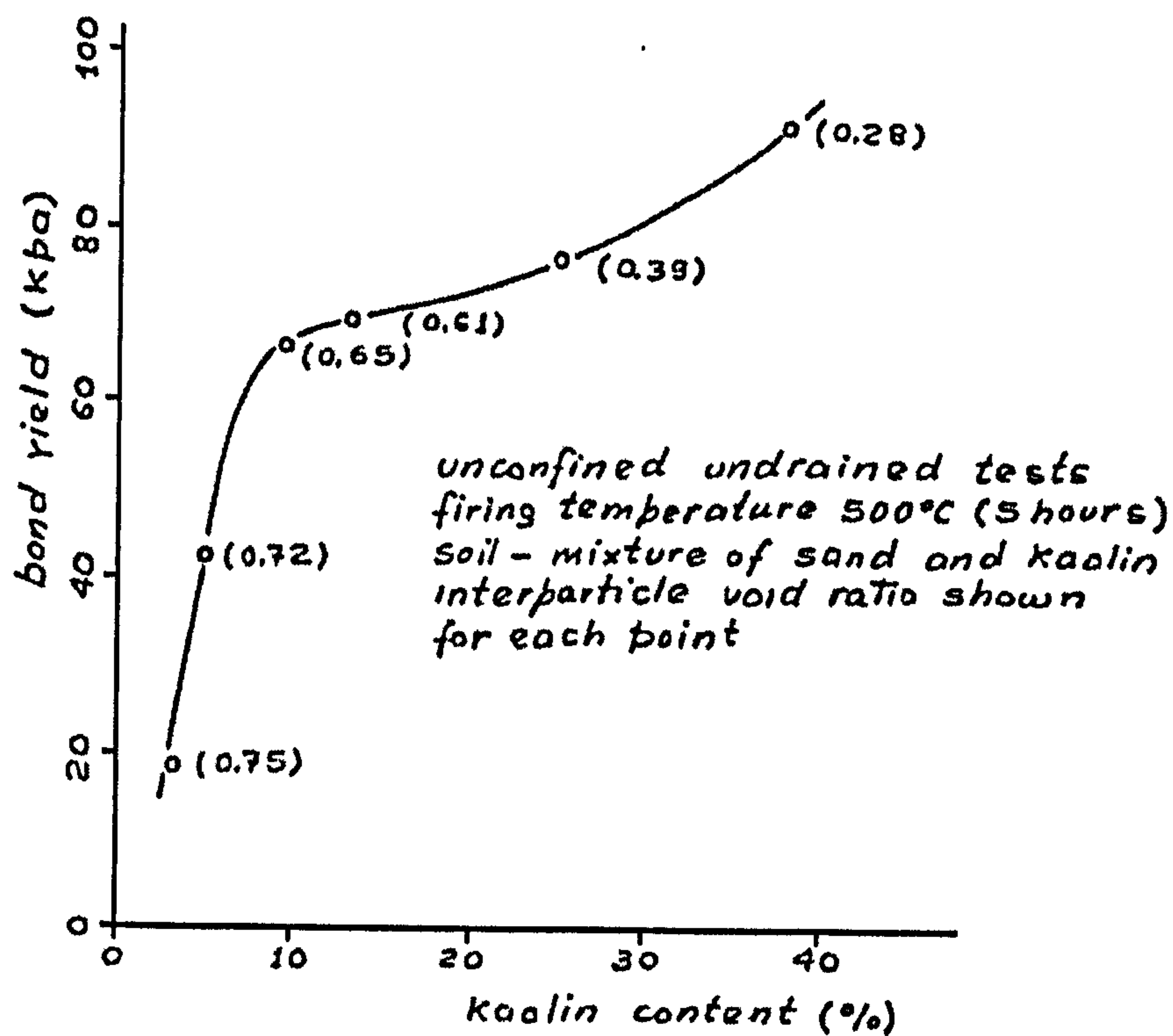


Figure 3.2: Effect of kaolin content on the strength of bond structure (after Maccarini 1987)



Maccarini (1987) also prepared artificial soil samples with different densities. In order to get samples with higher density, the wet mixture was vibrated inside the mould. By vibrating the wet mixture, the sample was more compacted and the void ratio of sample became smaller. Meanwhile the loose samples were prepared using the “lost wax” technique in which wax particles (with similar grading to quartz grains) were added to the wet mixture.

In the lost wax technique, the paraffin wax was chopped by hand and sieved to get similar grading as quartz and c.f.k. grains. The sieved wax was added to the mixture and stirred thoroughly by adding the distilled water. According to Bressani (1990), the amount of added water should not be too much, as the wax tends to float and segregate from the mixture. Then the wet mixture was put into a mould as usual and was allowed to dry at below the melting point of wax. The samples were burnt in an open space as the burning of wax produced a large amount of smoke. The samples were burnt until no smoke was produced. The burning of the samples caused the wax to melt out and vapourise, leaving pores within the samples of the same size as sand grains. As the wax burnt at around 200°C, any influence from this initial firing was likely to be masked by the higher temperature in which the samples then were fired in the furnace (500°C/5 hours)(Bressani 1990).

Deconstructed samples were also prepared by Maccarini and Bressani in order to study the effect of bonding on the behaviour of bonded samples for comparison purposes. The deconstructed samples were obtained by crushing the fresh material after they had been produced in the usual way (Maccarini 1987). A pestle and mortar was used to gently break down the bonded materials.

### **3.2.3 Technique Adopted By Malandraki (1994)**

Malandraki (1994) used a similar technique in preparing artificial bonded and deconstructed samples. However, she only mixed sand and kaolin with 87% and 13 of dried weight, respectively (without c.f.k). After several efforts to create weak bonds using different types of glue were unsuccessful, Malandraki (1994) finally

decided to apply the method developed by Maccarini (1987). She used sand (Leighton Buzzard) with medium grained quartz particles with a uniform grading ranging from 0.6 to 1.2 mm. The particle density of quartz sand was 2.68 while kaolin had  $G_s = 2.61$ . According to Malandraki (1994) the sand used in her study was similar in grain size (medium) but had higher amount of fine material compared with the sand used by Maccarini. The bond strength of samples was achieved by firing the samples in a furnace at 500°C for 5 hours to form samples with void ratio of 0.6 (dense samples).

In Malandraki's technique, the sand and kaolin were initially mixed dry. Then distilled water was added to get the water content required in order to produce sample with the targeted void ratio. The wet mixture was put into a paper mould within a brass-supported mould of 38mm diameter and 76 mm high. She also tilted the mould and let the mixture slide down in order to avoid air being trapped in the mixture. The mixture was allowed to air dry within the mould for about 72 hours. Then, she removed the mould and placed the sample in the furnace and fired at 500°C for 5 hours. The sample then was allowed to cool down overnight after firing in the furnace. Malandraki (1994) found that during the drying, the mixture shrank, with reduction of the void ratio by 0.3. In Malandraki's study, she prepared dense samples with void ratio of 0.6. She mentioned that only one sample was prepared for testing at a time. Malandraki (1994) also managed to achieve the loosest structured state of bonded samples with  $e_o = 0.72$  and the densest had  $e_o = 0.55$ . However, she decided to concentrate using denser sample with  $e_o = 0.6$ . The destructured samples were prepared as carried out by Maccarini. The bonded samples were broke down by hand to destroy the bond. The material was then had distilled water added and was placed in a paper mould. The samples were allowed to air dry to a stage when they were not too wet or too dry, so the samples could be transferred in the triaxial cell.

Malandraki (1994) also prepared samples of sand-kaolin mixtures using a similar technique to that used for bonded samples. The usual procedures were followed except the final stage in which the sample was not fired in the furnace hence, no

bonded fired kaolin was present. The wet mixture of sand-kaolin was left to dry for 72 hours. This sample was prepared with the aim of establishing the effect of the change in nature of fired kaolin on the mechanical behaviour of destructured sample. Based on a comparison between destructured soil and the sand – kaolin mixture, the mechanical behaviour of the destructured one demonstrates higher limiting stress ratio than the sand – kaolin mixture. Meanwhile from the tangential stiffness, the behaviour of destructured samples was relatively stiffer than sand – kaolin mixture and the different is more obvious at 0.1% - 0.5% of strain at higher stresses. Malandraki (1994) explained that kaolin lost 12% of its water content during the firing at 500°C and the nature of the kaolin changes. The breaking down of bonded samples created fired kaolin particles that were very similar to the sand particles in terms of water absorption and shape. Thus, destructured samples formed more random structure, which also caused a higher degree of interlocking between particles than sand – kaolin mixture. This illustrated the need to prepare destructured material by breaking down the bonded soil, rather than simply using the raw ingredients without firing.

### **3.3 PREPARATION OF ARTIFICIALLY BONDED AND DESTRUCTURED SOILS**

The method applied for the preparation of the artificial soil samples in this study was based on the methods applied by Malandraki (1994) and Maccarini (1987). Since it was intended to further the work carried out by Malandraki, the same technique as she used in preparing the artificial bonded and destructured samples was retained. Those samples were prepared in order to achieve samples with void ratios of 0.6. Attempts have also been made to prepare sample with a higher void ratio of 0.9. All the samples were prepared using similar procedures to achieve void ratios as close as possible to the target values (within 0.01).



### **3.3.1 Artificially Bonded Sample**

#### **3.3.1.1 Void ratio 0.6**

The technique used by Malandraki to achieve a sample with void ratio of 0.6 was followed in this work, with minor modification. The maximum and minimum densities defined from this mixture were  $1.69\text{gcm}^{-3}$  and  $1.77\text{gcm}^{-3}$  respectively corresponding to void ratios of 0.50 and 0.71. The proportion of sand and kaolin (87:13) and time and temperature ( $500^{\circ}\text{C}$  for 5 hours) remained the same in order to keep consistency with samples prepared by Malandraki.

The approximate dry weight of sand and kaolin was pre-calculated in order to achieve a void ratio of 0.6. These amounts were based on the volume of a sample with dimensions of 38mm diameter and 76 mm height. The proportion of sand and kaolin mixture (by dry weight) was 87% and 13% respectively (i.e. 127.8g of sand and 19.1g). The sand used is known as Leighton Buzzard sand, which can be classified as uniformly medium sand (Figure 3.3). The dry sand and kaolin were mixed initially, and then distilled water was added to allow the wet kaolin to attach to the sand particles. The sand and kaolin were stirred with a spatula to get a uniform mixture. Initially, a trial and error approach was used in order to know the optimal amount of distilled water to be added to the sand-kaolin mixture in order to achieve a void ratio of 0.6. Based on this approach, it was found that the amount of distilled water used influenced the value of final void ratio (Table 3.1). Thus for uniformity, the amount of distilled water added to the dry mixture of sand and kaolin was 13g (8.8% of the dry weight of the mixture).

The wet mixture then transferred into the steel mould with filter paper lining inside the mould (Figure 3.4 and 3.5). The steel mould used was designed according to BS 1377 (1990): Part 1:4.2.2.7 and was 38 mm diameter and is 76 mm high. It was split into two halves, which were fastened tightly by four bolts. At the earlier stage, it was difficult to gain uniform samples. Wet materials were layered for



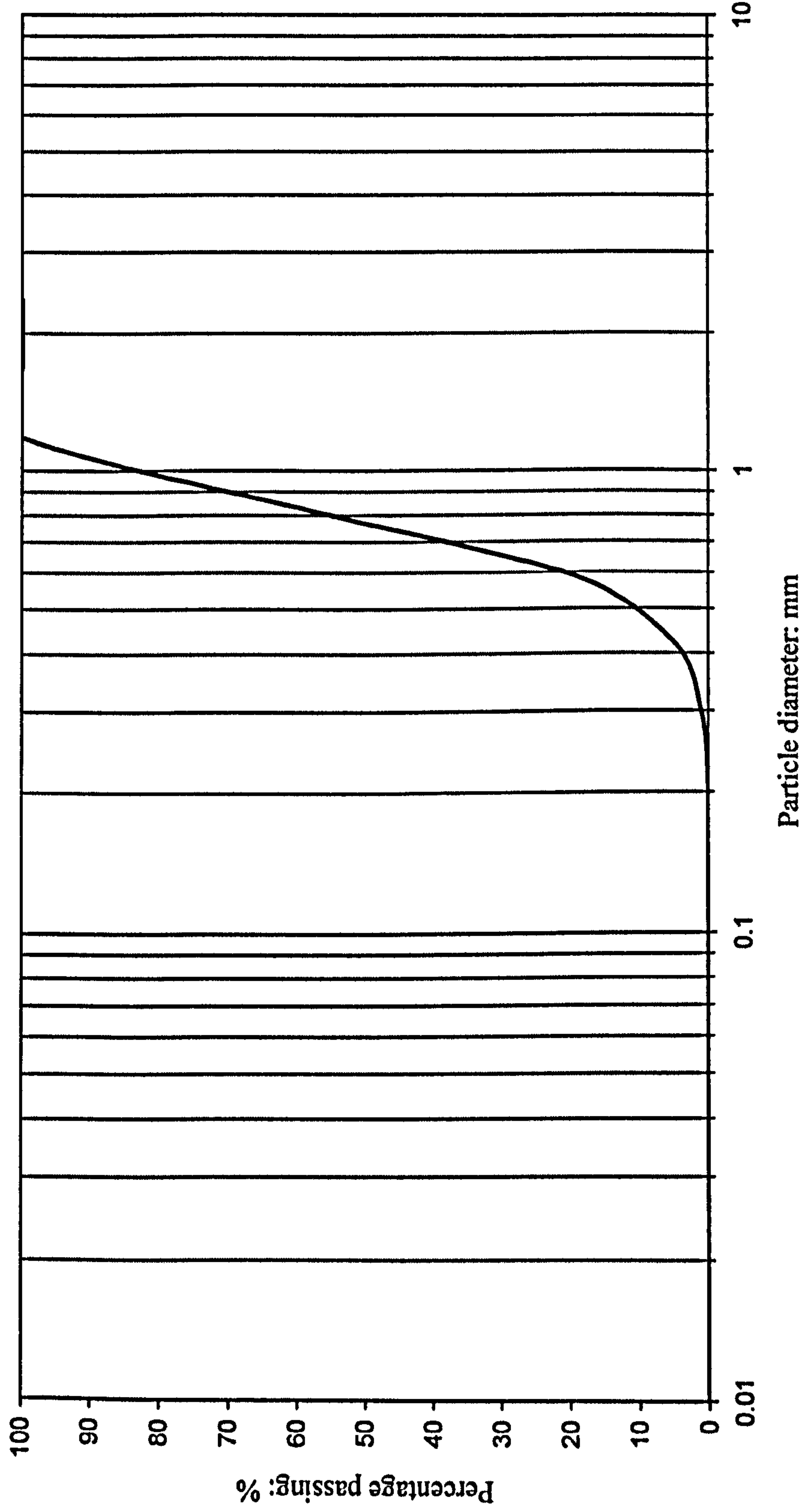


Figure 3.3: Particle distribution curve for Leighton Buzzard sand used in the preparation of artificial sample



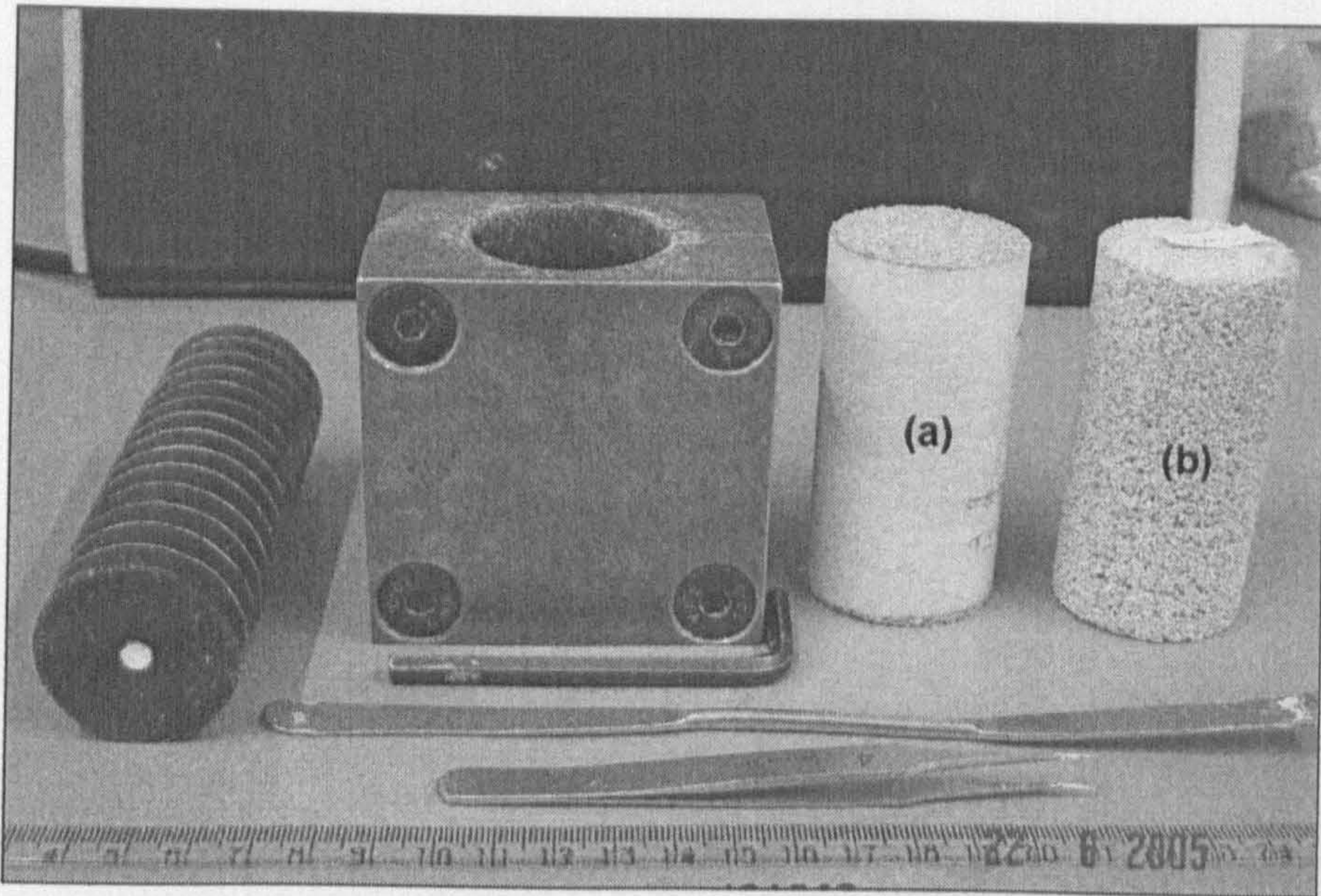


Figure 3.4: Equipment used for sample preparation. Sample (a) is taken out of the mould after drying at room condition (still inside a filter paper tube) while (b) is already fired for 5 hours in the furnace

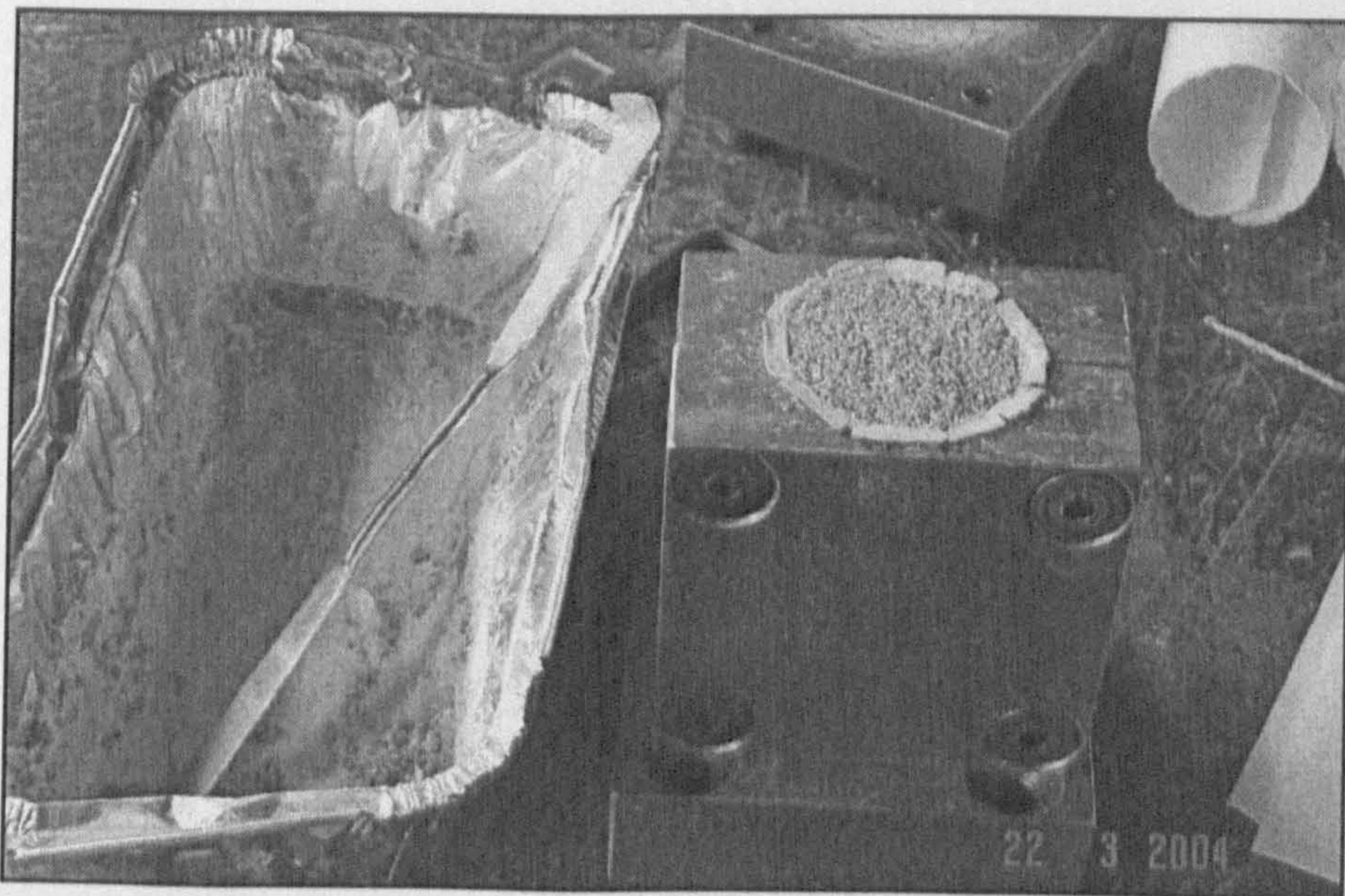


Figure 3.5: Wet mixture of sand and kaolin is placed into the steel mould with filter paper lining inside



about 5 mm thick and gently tamped and levelled using a plastic piston (diameter slightly smaller than steel mould). In order to achieve more uniform distribution of material across the sample, the same amount of wet material was transferred for every layer. Approximately 10g of wet mixture was allocated to each layer. Then each layer was tamped gently and levelled, using plastic piston up to 15 layers all together.

Finally, the top of the wet mixture was pressed down in order to level the surface and push the mixture into the dimension of the steel mould using triaxial loading frame. The wet mixture was allowed to dry inside the mould at room temperature for about 72 hours. Then the mould was opened, the filter paper was peeled off from the sample and the sample was transferred into the furnace and fired at 500°C for 5 hours. Figure 3.6 shows the bonded samples prepared using this technique.

Table 3.1: The variation of water content added to the mixture in order to achieve sample with accurate dimension of the steel mould.

Mass of Water added (g)	Water content (%)	Initial $h_o$ (mm)	Final $h_f$ (mm)	Volume, $V$ (cm <sup>3</sup> )	Final void ratio, $e_f$
10	6.81	80.03	80.59	90.45	0.660
11	7.49	78.60	80.60	89.78	0.656
12	8.17	77.51	78.46	87.30	0.606
13	8.85	76.36	76.85	86.24	0.592
14	9.50	76.32	77.67	87.53	0.613
15	10.21	75.94	76.28	85.78	0.580

Notes:  $h_o$  refers to the height of the sample before fired at 500°C  
 $h_f$  refer s to the height after fired at 500°C

### **3.3.1.2 Void ratio of 0.9**

#### **3.3.1.2.a Wet and wax techniques**

An attempt had been made to apply wet and wax techniques in order to get loose samples. The wet technique was a similar technique to that used by Malandraki (1994). The amount of water added to the sand-kaolin mixture was reduced as at lower water content, suction can support a looser structure. The amount of distilled water added to the sand and kaolin mixture was decreased to about 8 – 10g (5.4% - 6.8% of dry weight of mixture). However, these loose samples were too brittle and crumbled easily, therefore the samples were difficult to handle.

Preparation of samples using wax also raised similar problems (Maccarini 1987). In addition, this technique also produced a lot of smoke during firing in the furnace. Since there was no isolated air ventilated room available in the laboratory, the furnace needed to be placed outside the building when burning off the wax mixture. Therefore an alternative approach was considered in order to achieve loose samples, which required minimum care of handling.

#### **3.3.1.2.b Polystyrene technique**

An attempt was made to prepare loose samples using a technique modified from Medero (2001). Particles of expanded polystyrene were added into the mixture of the wet sand and kaolin in order to achieve higher values of void ratio. The required volume of polystyrene was initially estimated prior to sample preparation. The target final void ratio to be achieved was 0.9. According to Medero (2001), the polystyrene shrinks approximately forty times compared with its initial volume when heated in 110°C for 24 hours. In this study, however the dried mixtures were finally fired in the furnace at 500°C in order to create bonding from the fired kaolin. It would be expected that the polystyrene particles would melt and vaporise leaving larger pores within the sample. Based on the firing of the polystyrene in the furnace at 500°C, only a small amount of hard residue was left (Table 3.2). This



could be an advantage since most of polystyrene evaporates (>95% of initial mass) and left very little residue. However, the presence of this hard residue within the sample could probably create bonding between sand particles and could contribute to the shear strength of the sample.

Table 3.2: The changes in mass of polystyrene due to firing at 500°C

Initial volume ( $V_0$ ), cm <sup>3</sup>	Initial mass ( $m_0$ ), g	Final mass ( $m_f$ ), g	Percentage of residue, %	Loss of mass, g	Percentage of loss, %
2.0504	0.0593	0.0017	2.87	0.0576	97.1
1.7340	0.0398	0.0011	2.76	0.0387	97.2
2.3643	0.0557	0.0016	2.87	0.0541	97.1
2.5116	0.0609	0.0017	2.79	0.0592	97.2
2.3092	0.0517	0.0013	2.51	0.0504	97.5
Mean percentage			2.76		97.2

The polystyrene particles were initially prepared by cutting the polystyrene into small pieces using splinter tweezers. An estimated required volume of polystyrene was calculated in order to create a sample with target void ratio. It would be expected that the pores formed within the sample were generated from interaction between sand to sand grains or sand to fired kaolin or fired kaolin to fired kaolin and from voids which would be left as a result of firing the polystyrene particles.

Firstly, the sand, kaolin and polystyrene particles were dry mixed thoroughly in a mixing bowl. Then distilled water was added to that mixture and stirred thoroughly with a spatula. The amount of added distilled water was 12.5g (10.2% of the dry weight of the mixture). Meanwhile, the amount of polystyrene particles added to the sand-kaolin mixture was also varied between 50% and 90% of the estimated required volume (Table 3.3). Then the wet sand-kaolin-polystyrene mixture was spooned into mould with filter paper lining inside the mould. The mixture was stirred again to ensure that the polystyrene particles were uniformly distributed across the sample. A final layer of the mixture was pressed down using a loading frame in order to push the mixture into the dimension of the mould. After that the

samples were allowed to dry at room temperature for at least 72 hours. The dry mixture then was fired for 5 hours at 500°C in the furnace.

Figure 3.7 shows some of the samples prepared from the mixture of polystyrene, sand and kaolin. The amount of polystyrene used to get the closest void ratio of 0.9 was about 70% of the estimated required volume (Table 3.3).

Table 3.3: The relationship between the amount of polystyrene and the final void ratio

Percentage of the estimated volume of polystyrene, %	Mean void ratio, e
50	0.769
60	0.855
65	0.852
70	0.889
75	0.884
80	0.861
90	0.880

### 3.3.1.2.c Seed technique

The use of seeds in the sample preparation was also carried out in attempt to achieve similar void ratios. This method was designed as an alternative approach for preparing loose samples since earlier techniques were associated with some difficulties. In this technique, seeds were used to replace the role played by the polystyrene particle. Seed is an organic matter and can burn out leaving a small amount of ash, which will probably not create bonding within the sample. Two types of seeds were considered, coriander (*Coriandrum sativum*) and poppy seeds (*Brassica nigra*) (Figure 3.7 and 3.8). These seeds seem to have uniform size and shape (rounded) and are readily available in the market. Based on particle size distribution analyses, coriander seeds could be classified as fine gravel ( $C_u=1.192$ ) meanwhile poppy seeds were classified under coarse sand ( $C_u=1.385$ ). The loss of ignition (L.O.I.) technique described in BS 1377: Part 3:4 (1990) was used in order



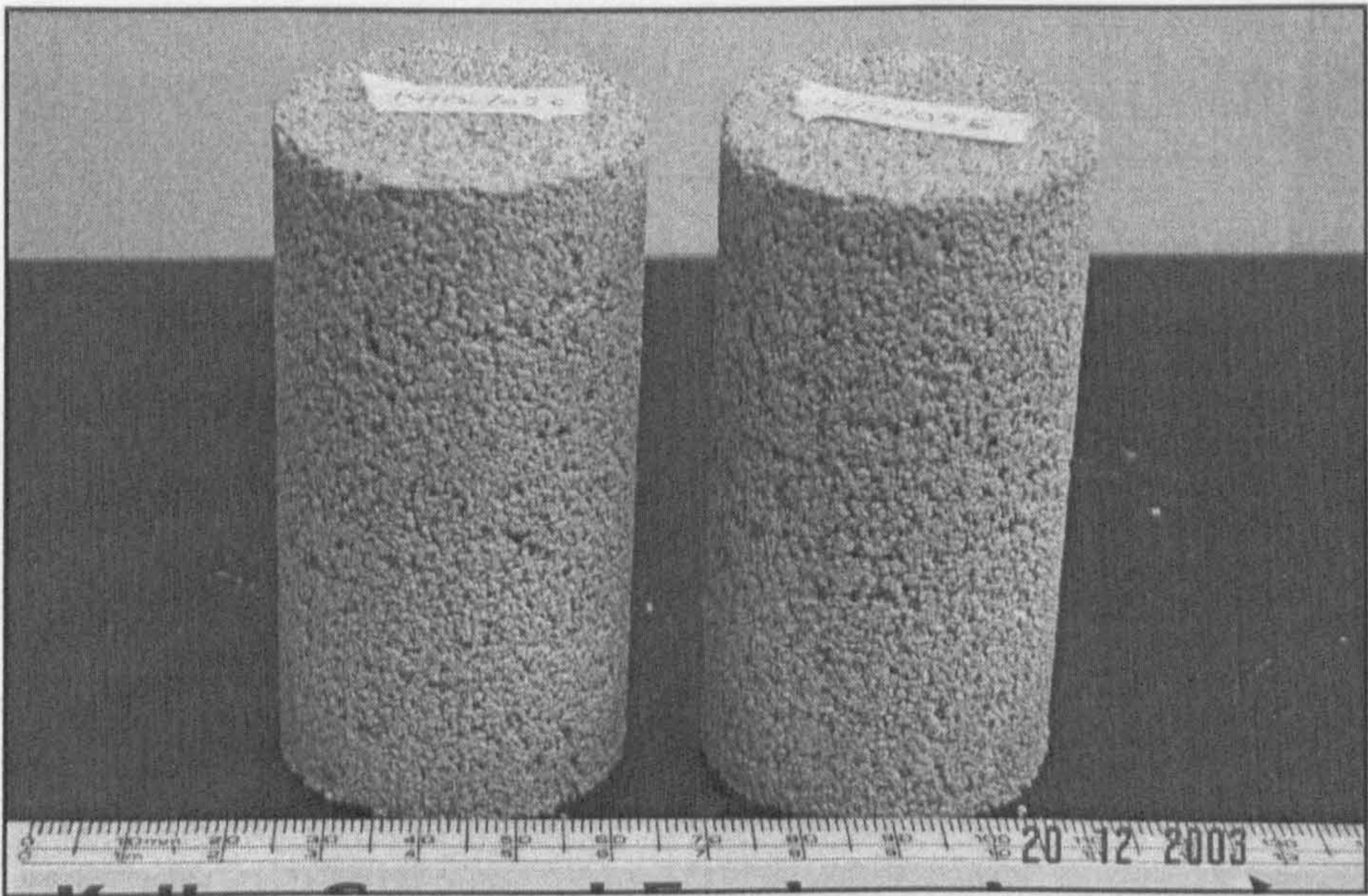


Figure 3.6: Artificial weakly bonded samples with void ratio of 0.6

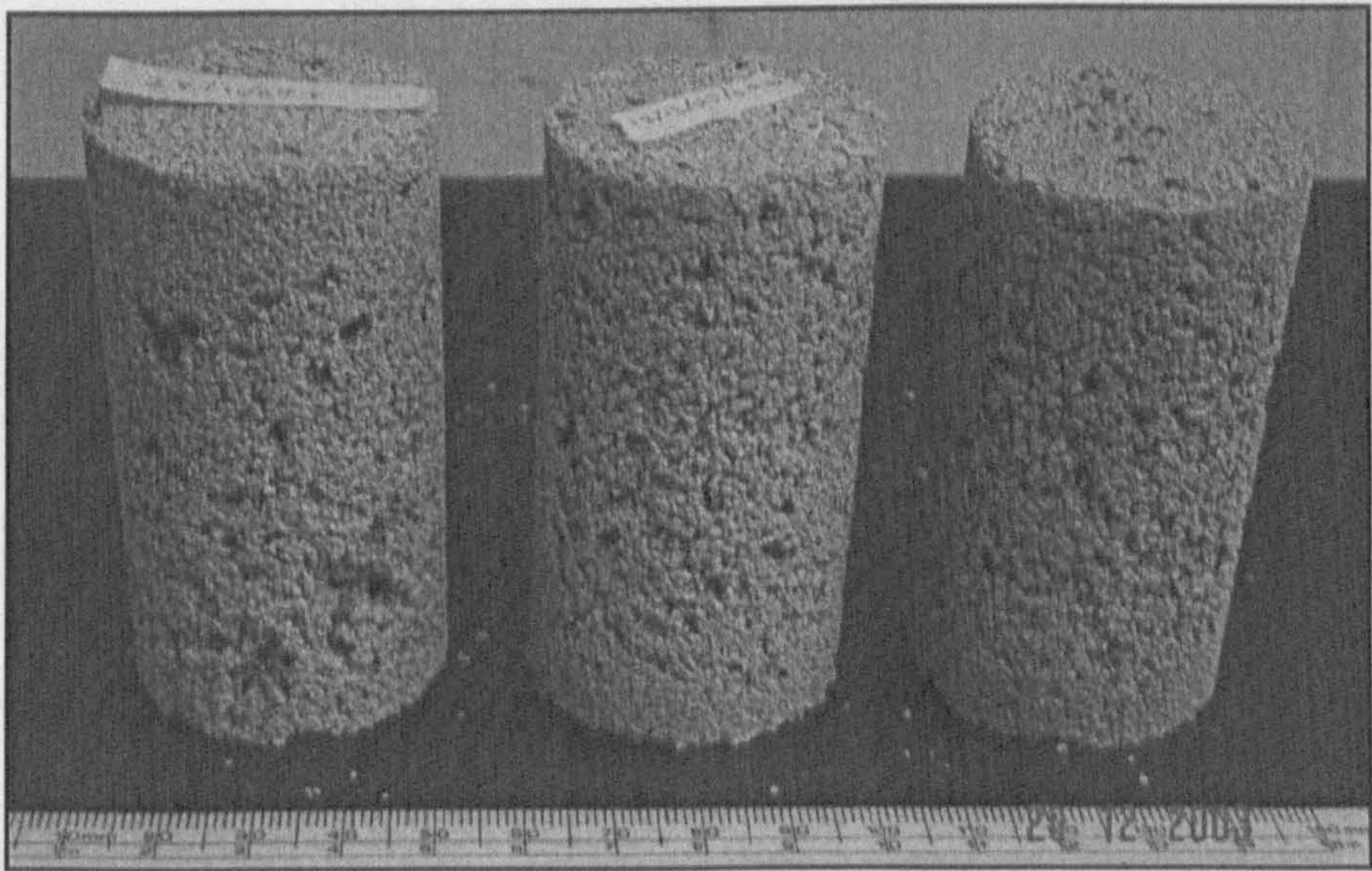


Figure 3.7: Bonded samples with void ratio of 0.9 prepared by adding the polystyrene particles into wet mixture



to burn the coriander and poppy seeds at temperature of 450°C in a furnace for 5 hours. The purpose of carrying this technique was to determine the amount of ash residue left after firing. It was found that the coriander and poppy seeds produced about 3.5% and 4.0% of ash residue, respectively (Table 3.4).

The procedures for sample preparation were similar to the technique mentioned previously. The sand, kaolin and seeds were mixed dry thoroughly with a spatula in a mixing bowl. The amount of added distilled water was 13 g which adequately wetted the kaolin. The wet mixture of sand-kaolin-seeds was spooned into the mould with filter paper lining inside. The sample then was allowed to dry at room temperature for 72 hours before fired at 500°C for 5 hours in a furnace.

Trials were carried out with different amount of added seeds in order to achieve target void ratio (Table 3.5). However, it was difficult to get samples from a mixture of sand-kaolin-poppy seeds because the samples already became broken at the time of firing. This indicated that the samples were so friable and difficult to handle (Figure 3.10). In addition, poppy seeds also produced a lot of smoke when burning (poppy seed contains about 30% of fatty oil). Thus, the samples produced using poppy seeds required careful handling and the technique was not suitable. However, samples prepared with coriander seeds were able to achieve a void ratio of about 0.9. It was found that the amount of the required coriander seeds in order to achieve the closest target void ratio were 3g and 5g. The final samples became slightly darker due to burning of the coriander seeds in the mixture (Figure 3.11).

### **3.3.2 Artificial Destructured Sample**

The destructured samples were prepared from bonded samples, which had been prepared earlier. The bonded sample was put in a sealable plastic bag and then broken down by hand to destroy the bonds between sand particles. The idea of using the previously prepared bonded sample is to achieve properties that are as close as possible between the destructured and bonded samples in terms of



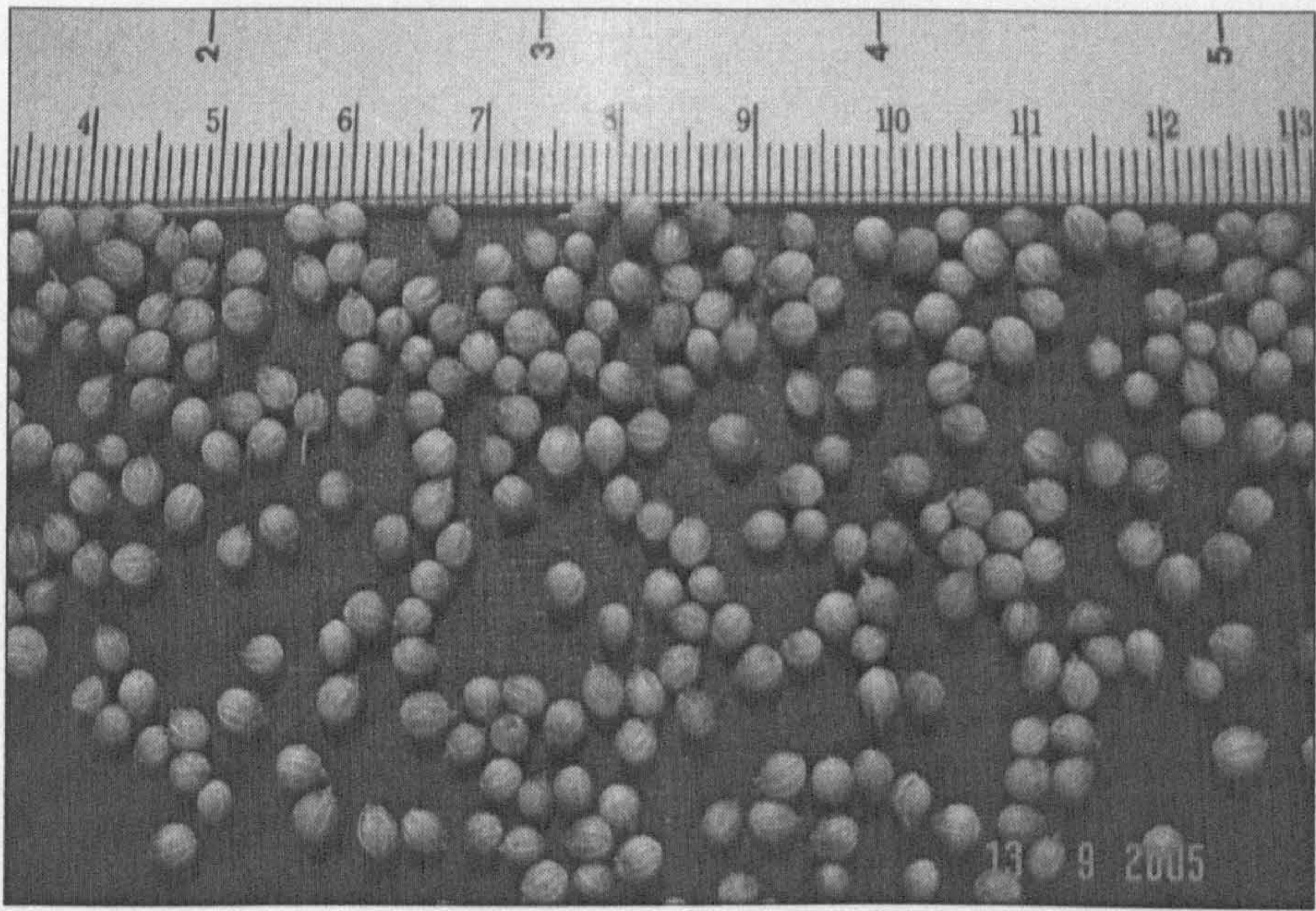


Figure 3.8: Coriander seeds (*Coriandrum sativum*)

Table 3.4: The percentage of residue as a result of firing the seeds at 450°C

Seed type	Dry wt., g	Residue, g	Percentage, %	Mean, %
Poppy	0.2344	0.0081	3.5	4.0
	0.2553	0.0115	4.5	
Coriander	0.0943	0.0033	3.5	3.5
	0.1350	0.0048	3.6	



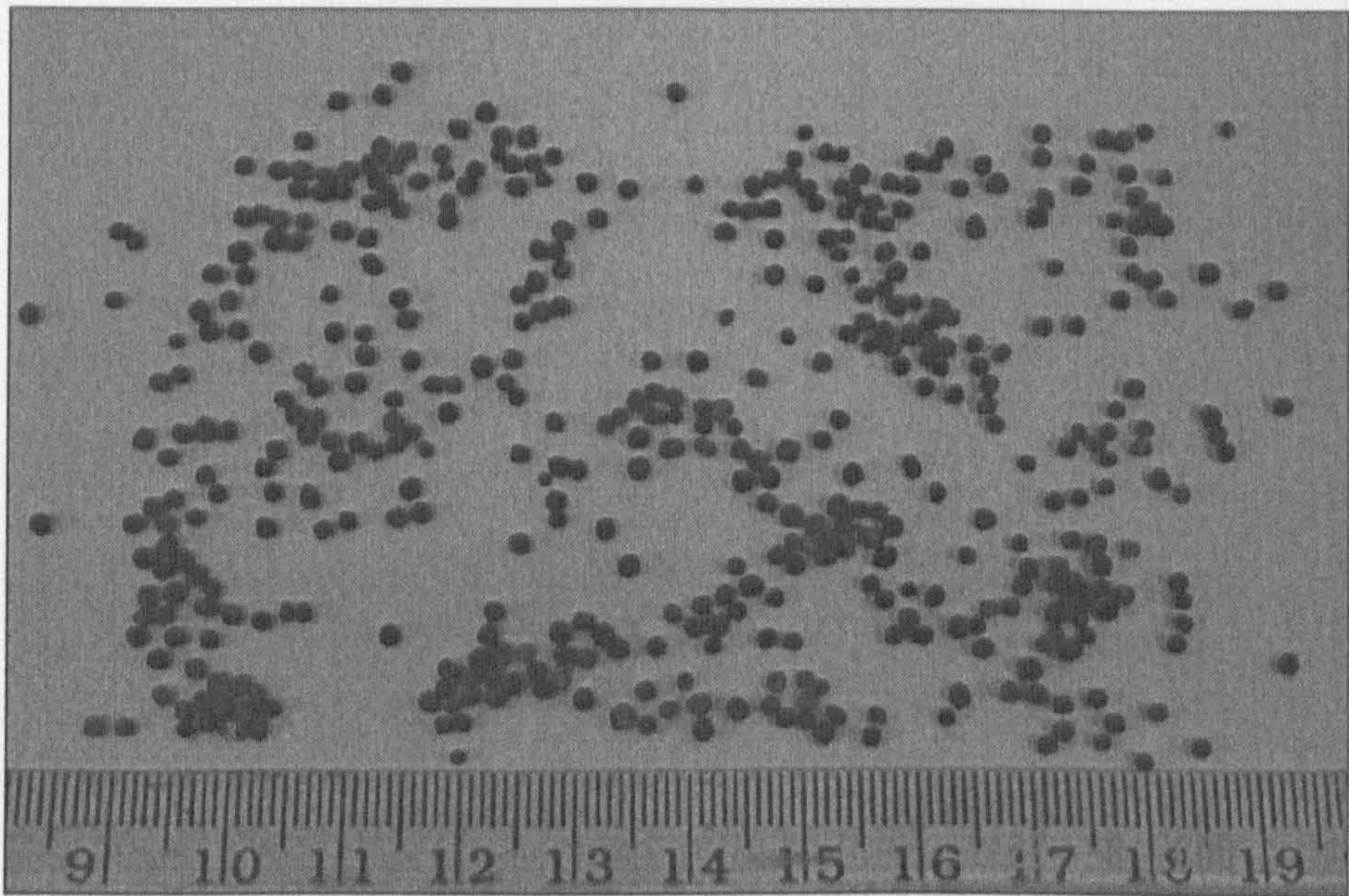


Figure 3.9: Poppy or known as black mustard seeds (*Brassica nigra*)

Table 3.5: The amounts of seeds used in the mixture of sand and kaolin

Seed type	Dry wt., g	Percentage %	Final void ratio, e	Remarks
Poppy	9.0	7.3	n.a	• Produce a lot of smoke
	10.0	8.1		• Sample too brittle and
	11.0	8.9		• Easily broken when handle
Coriander	3.0	2.4	0.877	• Close to the target e = 0.9
	5.0	4.0	0.915	• Not too brittle
	7.0	5.7	0.938	

n.a – not available



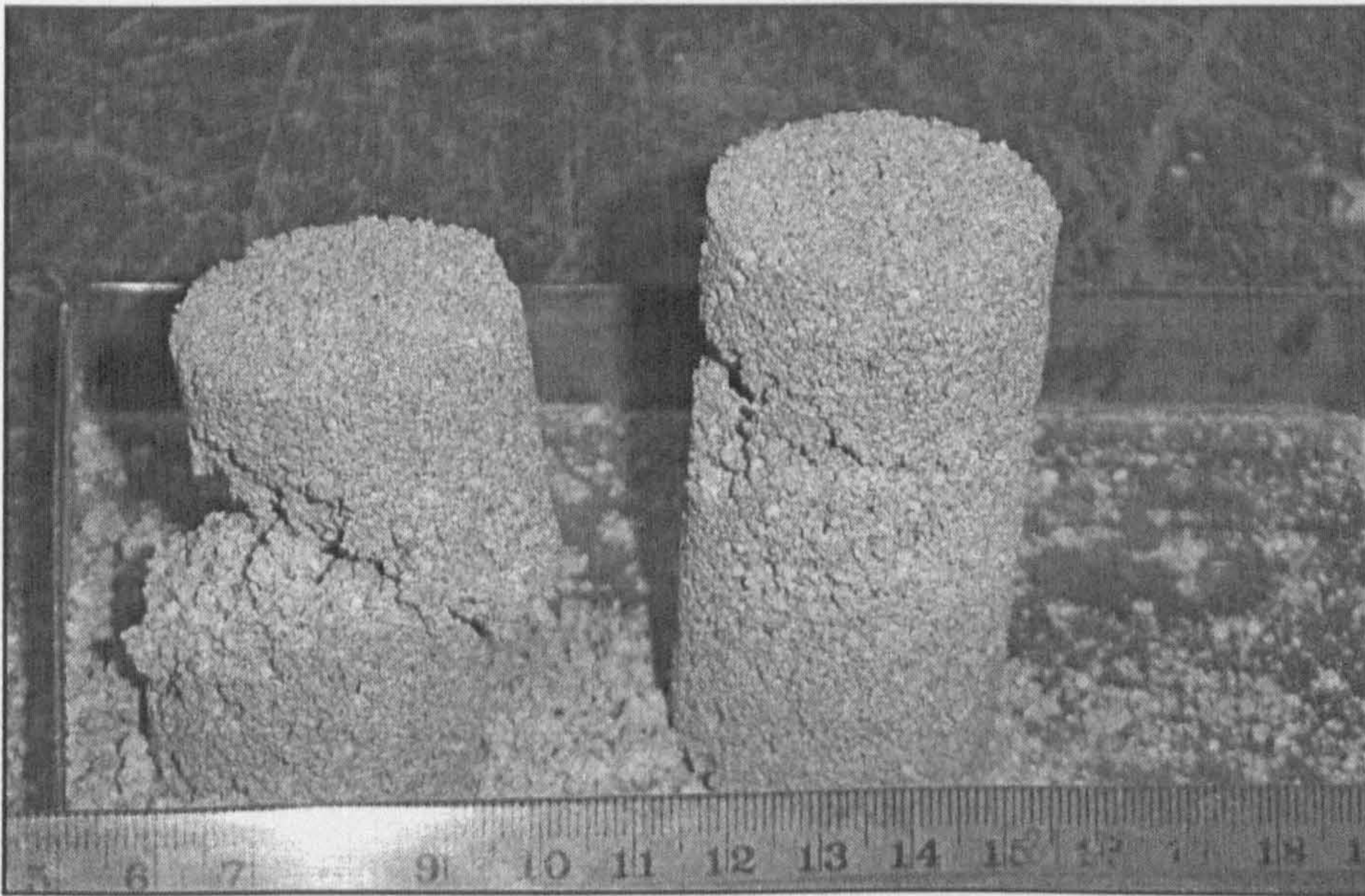


Figure 3.10: Samples prepared using the poppy seeds easily collapsed

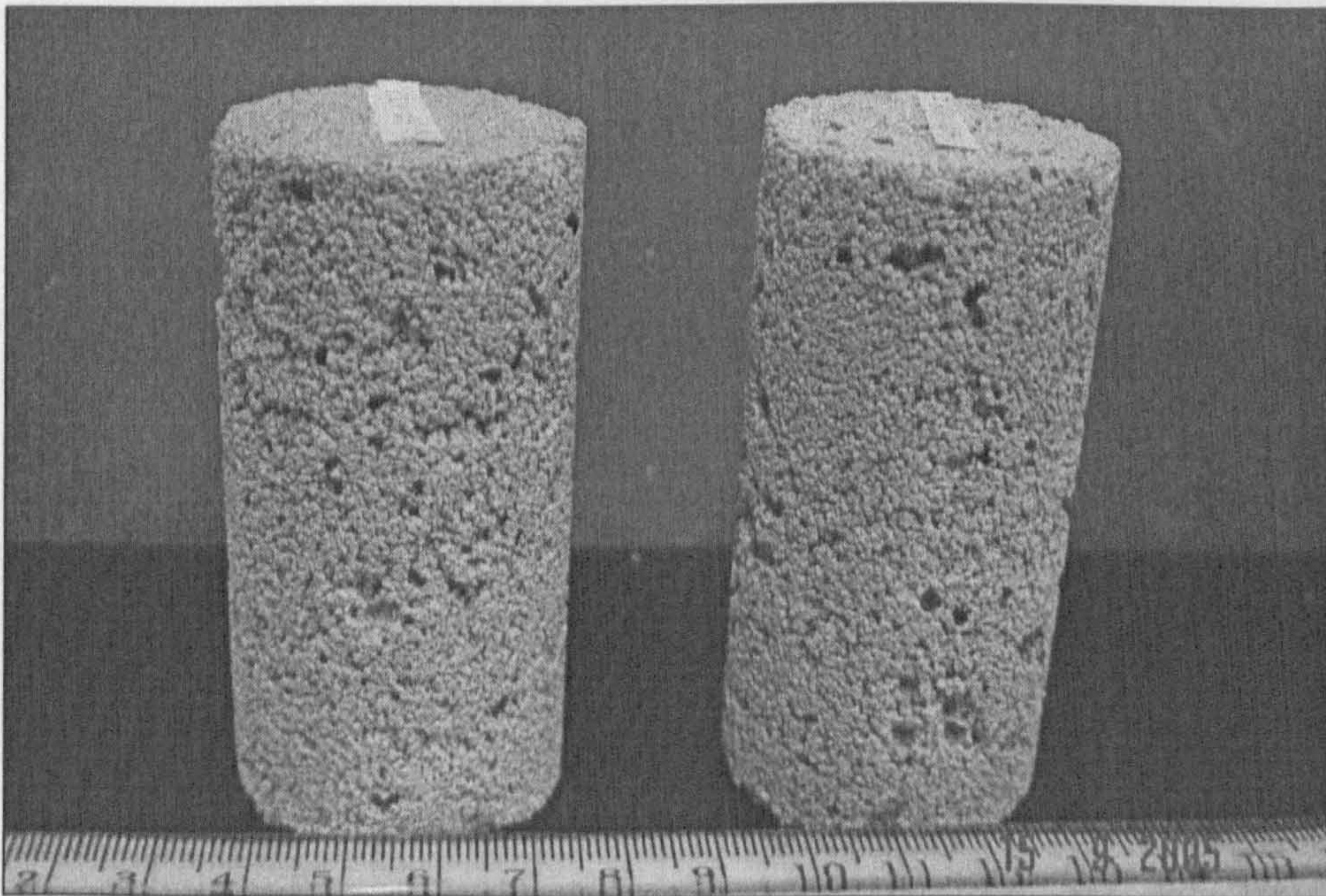


Figure 3.11: Artificial loose samples that were prepared by adding coriander seeds with sand and kaolin mixture



composition and grading (Malandraki 1994). The crushed material was then mixed thoroughly with distilled water (similar amount applied to bonded samples). The wet mixture was transferred into the steel mould in the same procedure as for bonded samples. Each 5 mm layer comprised approximately 10g of wet mixture and was gently levelled using a rubber piston. The final mixture was levelled and pressed using a triaxial loading frame. It was found that the material stuck to the filter paper, which damaged the sample when the mould was opened. In order to avoid this problem, aluminium foil was used instead of a filter paper.

After that, the sample was permitted to dry at room temperature for 24 hours so that the sample was not too wet or too dry. In order to avoid the sample from being broken, a rubber membrane was fitted over the sample with porous low air entry disks on both ends of the sample. At this stage the sample could be transferred and placed easily onto the pedestal. Normally, destructured samples were prepared a day before setting up on the pedestal so that the sample was easier to handle. At this stage the rubber sheath could be fitted without dislodging sand particles from the surface.

### **3.3.3 Microscopic Observation of Artificial Soil**

The main materials used for preparing an artificial sample in this study were predominantly quartz sand and fired kaolin as a bonding agent. Based on previous studies, kaolin could create weak bonds between sand grains when it was fired at high temperature. The procedure of preparing the sample was designed in order to achieve a uniform mixture across the sample.

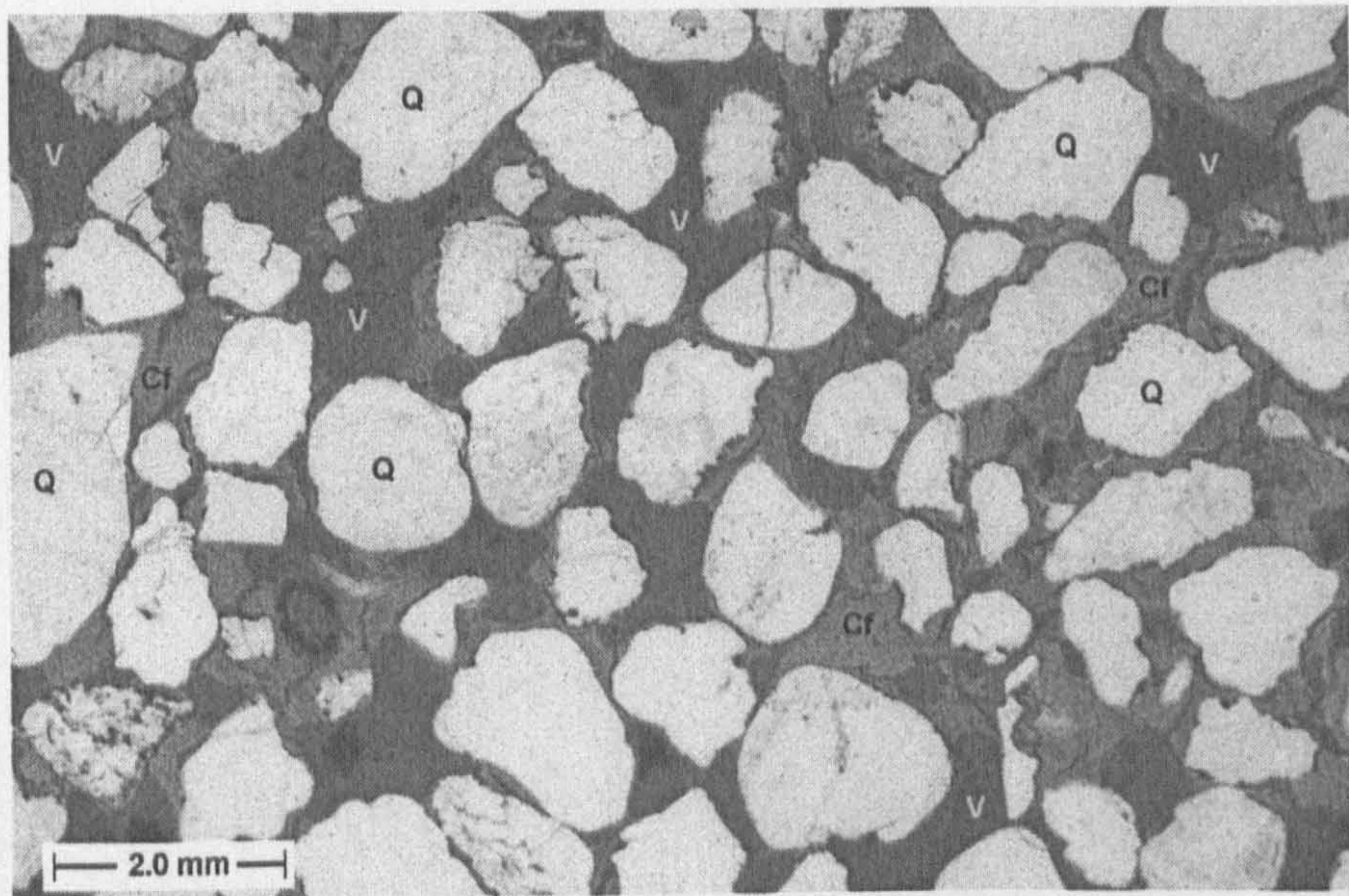
In order to study the physical arrangement of grains and macrostructure (bonds, voids, etc.) of the sample, thin sections were examined by using an optical microscope. Initially the samples were immersed in acetone before being impregnated using Araldite resin under vacuum for about 48 hours at 50°C. Dye was also added to the solution in order to colour the pores within the samples. A Nikon YS100 optical microscope was used which has the capability of magnifying

up to 40X. The thin sections were photographed using the microscope equipped with a camera.

Figure 3.12a and 3.12b were taken from two different samples with void ratio of 0.6 under x2.5 magnification. The presence of quartz sands are identified as white grains meanwhile the fired kaolin is represented by light grey. The majority of the quartz grains are classified as subangular to subrounded according to the IAEG classification (Anon 1979). The black areas are identified as voids. It is clearly seen from the photographs that the fired kaolin has established bridges of bonding whereas in some part of the section the fired kaolin tends to coat the whole sand grains (Figure 3.12a; right side). It also reveals that very few sand grains have direct grain to grain contacts. The occurrences of voids can be isolated (when surrounded by fired kaolin) or connected to each other to form larger voids (Figure 3.12b). A number of fissures were detected in between the bonding and the grains. Since the samples were fired at higher temperature followed by cooling, this could be due to the fired kaolin contracting and causing the development of fissures. This feature was also reported by Bressani (1990) who used similar materials and approach in preparing artificial bonded samples.

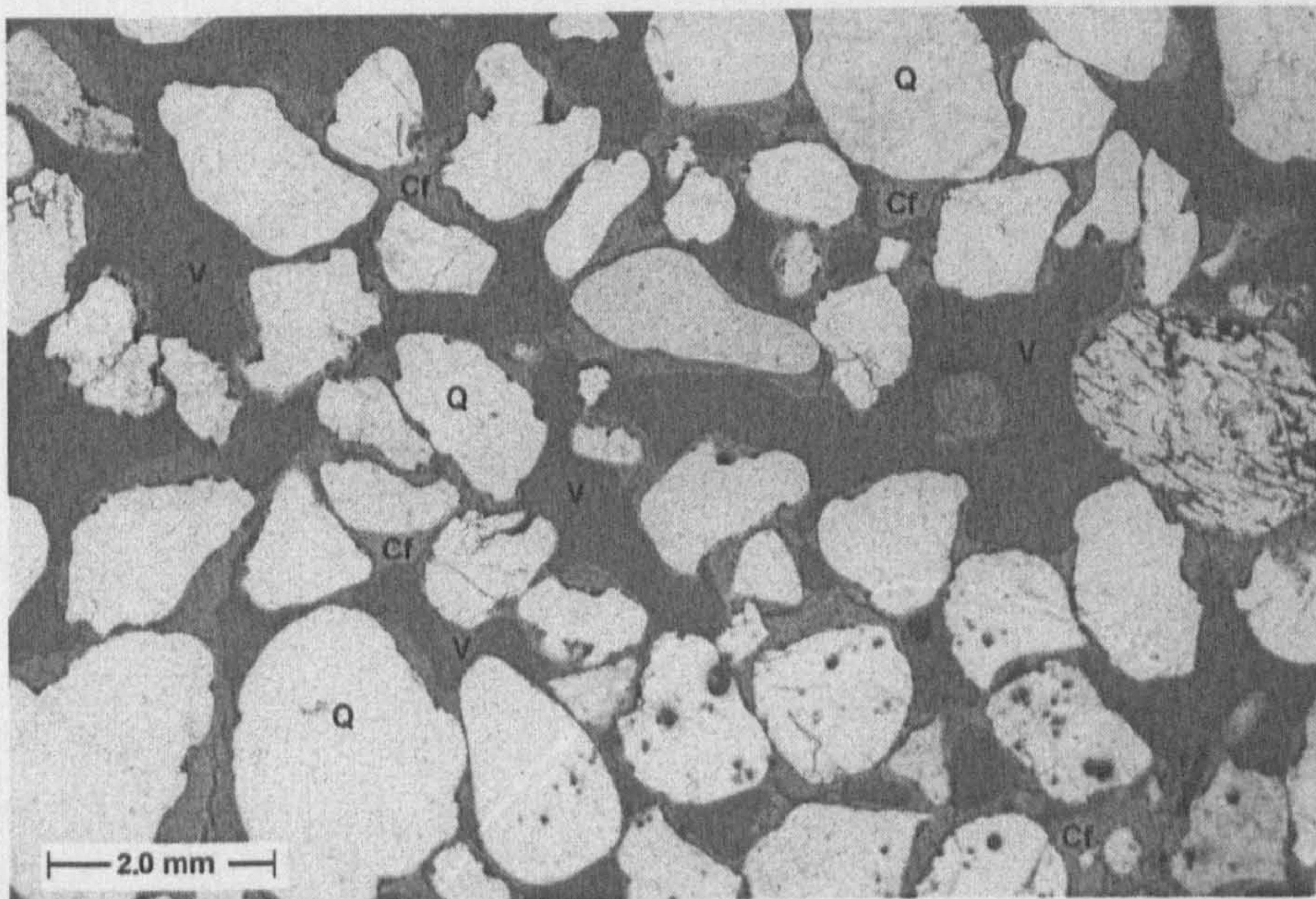
Microscopic studies for loose samples (void ratio = 0.9) were also carried out based on samples that prepared using the coriander seed technique. Figure 3.13a and 3.13b were photographed under the same magnification as the previous photographs. These photographs clearly exhibit the occurrences of larger voids compared to the denser samples. The general characteristics of the artificial samples are still indicated by the bridging of bonds between sand grains and most of the grains are coated by fired kaolin. Figure 3.13b shows a trace of ash possibly from the burning of coriander seeds as a result of firing at higher temperature. This ash residue is trapped at the centre of the largest void of this section. However in the previous photograph, there is no evidence of ash traces. It may be that any residue was washed away during the process of grinding and polishing this thin section.





Notes:  
Q - quartz Cf - fired kaolin V - void

(a)

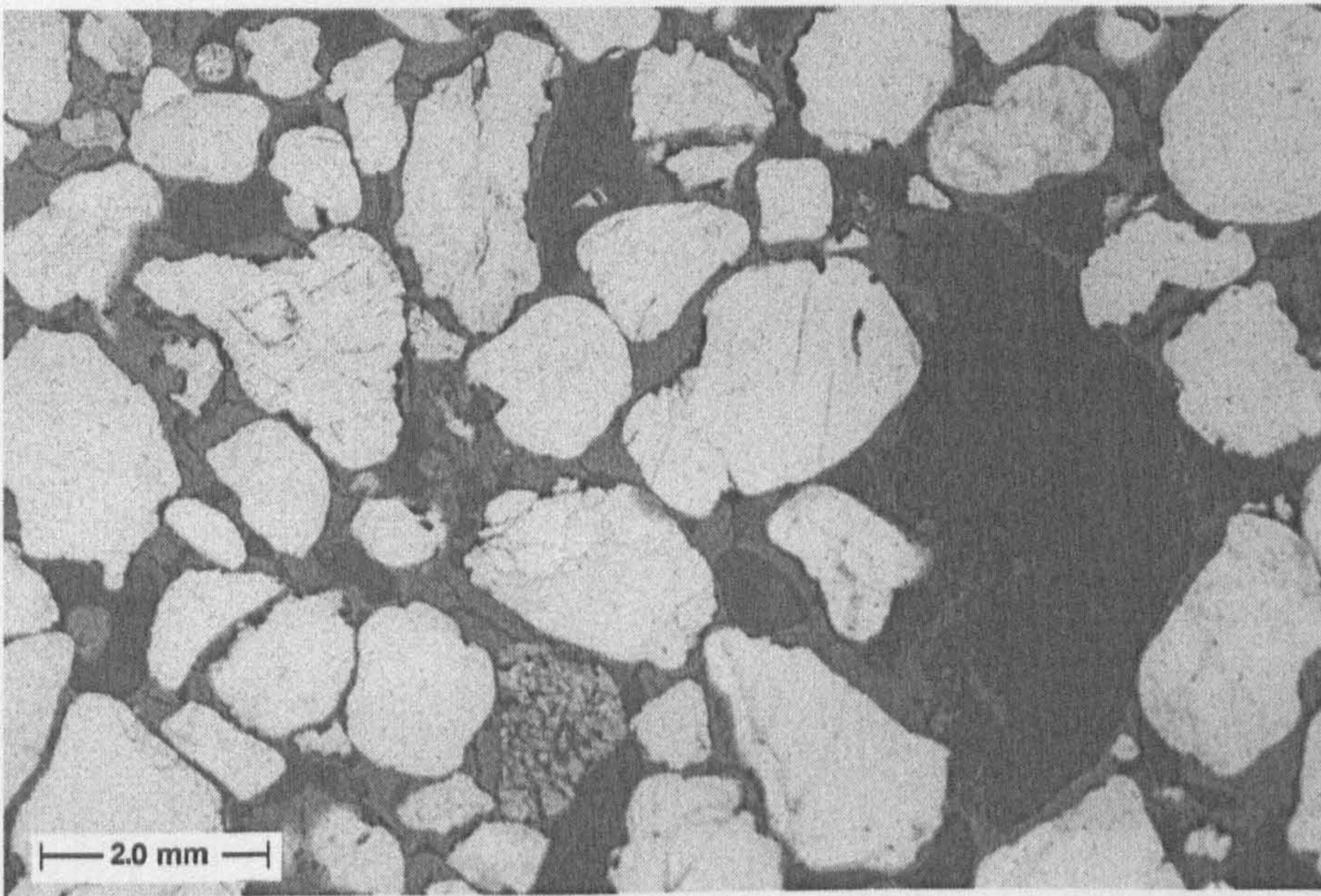


Notes:  
Q - quartz Cf - fired kaolin V - void

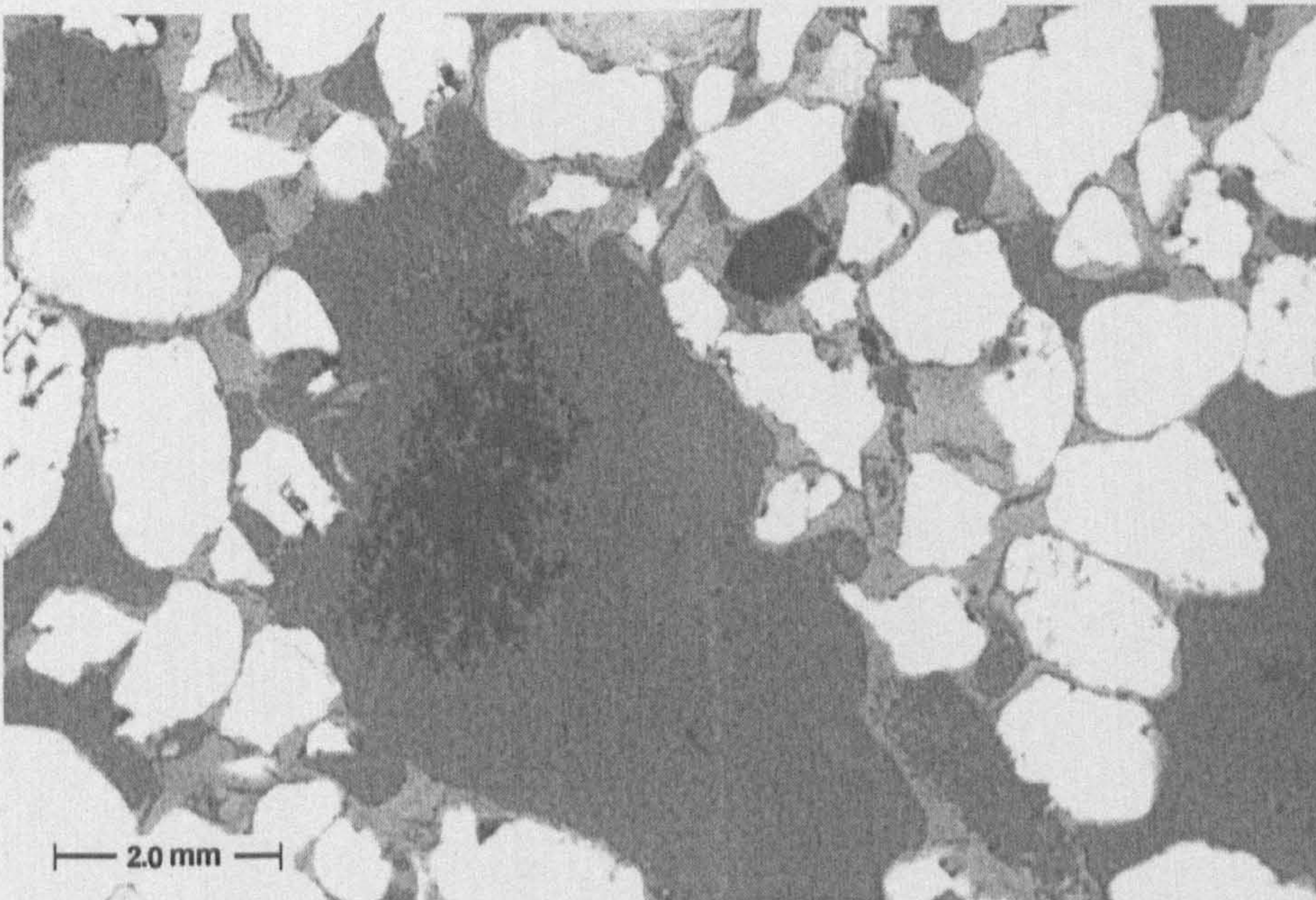
(b)

Figure 3.12: Microscopic photographs of artificially weakly bonded sample with void ratio 0.6 under x2.5 magnification





(a)



(b)

Figure 3.13: Microscopic photographs of artificially weakly bonded sample with void ratio 0.9 under x2.5 magnification



### 3.4 CONCLUSIONS

A number of techniques for preparation of artificial samples have been reviewed. The technique of firing a sand/kaolin mixture was adopted in this study and the detailed procedure used has been described. The technique has the advantage of producing reproducible samples with properties that are not age-dependent.

A new technique for producing looser samples, using coriander seeds has been developed and was used for producing samples with void ratio,  $e = 0.9$ .

Microscopic studies of the thin section show that the fired kaolin forms bridges between the sand grains, as well as coating the grains. Photographs of loose samples produced using coriander seed technique show very small amount of ash residue left after firing at high temperature.

## **CHAPTER 4                      TESTING EQUIPMENT AND PROCEDURES**

### **4.1     INTRODUCTION**

In this study, testing has been carried out using triaxial apparatus to perform the saturated and unsaturated tests. For saturated conditions, conventional undrained and drained tests were performed. Meanwhile for unsaturated conditions, a series of constant water content tests were carried out. The triaxial cell units were supported by a computer control system known as TRIAX (Toll 1999). A brief description of this software will be given in the following section.

### **4.2     BRIEF DESCRIPTION OF CONTROL SYSTEM**

#### **4.2.1: Hardware**

The hardware for setting up a controlling system requires a personal computer (PC), a data acquisition device and controllers that can be digitally controlled. The available computers were supported by Microsoft Window XP. A PCI836A digital input/output card was installed for driving the stepper motor controllers. For data acquisition purpose, a MSL Datascan 7020 manufactured by Measurement Systems Ltd was used as the data logger. This MSL device can handle up to 16 transducers and provides 16-bit A/D conversion, which gives a resolution of  $0.06\mu\text{V}$  for a 100mV range. This device was connected to the computer through a serial (COM1) port. Two types of stepper motor controllers were used in this system, namely stepper motor driven air valve and stepper motor driven piston controller. These devices were originally developed at Imperial College, London. In this case the stepper motor driven air valve was used to control the air pressure



with a pressure range 10 – 820kPa. The pressure could be adjusted in increments of 0.07kPa. Meanwhile the cell pressure was controlled by stepper motor driven piston pump. This piston pump was connected to the 100cc volume gauge in order to measure the volume change of the cell. The stepper motor driven piston and air valve were respectively controlled by the IC Piston controllers (Control Box 1) and IC air valve controllers (Control Box 2), defined as output devices. IC stands for Imperial College.

In order to achieve higher cell pressure for saturated tests, an air ram was connected to the modified piston pump. The air pressure to the air ram was controlled by the stepper motor driven air valve which transferring the air pressure to the piston pump. The internal area of the air ram used in this work was about 4:1 to the area of the piston pump. Hence, an increase of air pressure in the air ram increased the pressure in the piston pump approximately 4 times higher. The setting up of the equipment in saturated and unsaturated tests will be further explained in the following chapter.

#### **4.2.2: Triax Program**

The TRIAX control system software was initially developed at Imperial College Soil Mechanics laboratory (Toll and Ackerley 1988). The PC version was developed at Durham University in 1988 (Toll 1999). In this study, TRIAX version 5.0 was used.

In the software, each transducer connected to an input device is configured as a *Channel* that is assigned a *Variable* name defined by the user. The *Channels* window provides settings option for each transducer such as how the reading is to be displayed. The variable name defined by user should be easily related to the function of the transducer. Thus, the reading from each transducer can be referred to a variable name instead of a channel number. Variables can be grouped into *System* variables, *Channel* variables, *UserInput* variables and *Calculated* variables.



Every test can comprise many different *stages* (up to 100 *stages*) and is controlled by its own control parameters. The control is shifted from one stage to another by a series of *alarms*. The user defines the alarms in the form of conditional equations that triggers an action (Toll 1999). The action can either cancel control or shift to another stage. The option for controlling the cell or/and back pressure can be carried out in *stage* menu Figure 4.1. Once a particular condition has been satisfied, the alarms decide to either abort control or transfer control to another stage. The pressures, displacement etc., can be controlled by control devices connected to the computer and displayed on *Control* window (Figure 4.2). The up and down buttons allow the raising and decreasing the value of the controller, manually. The setting up of the control parameters can be made through a *stages* button and Stage Detail window will be opened (see Figure 4.1).

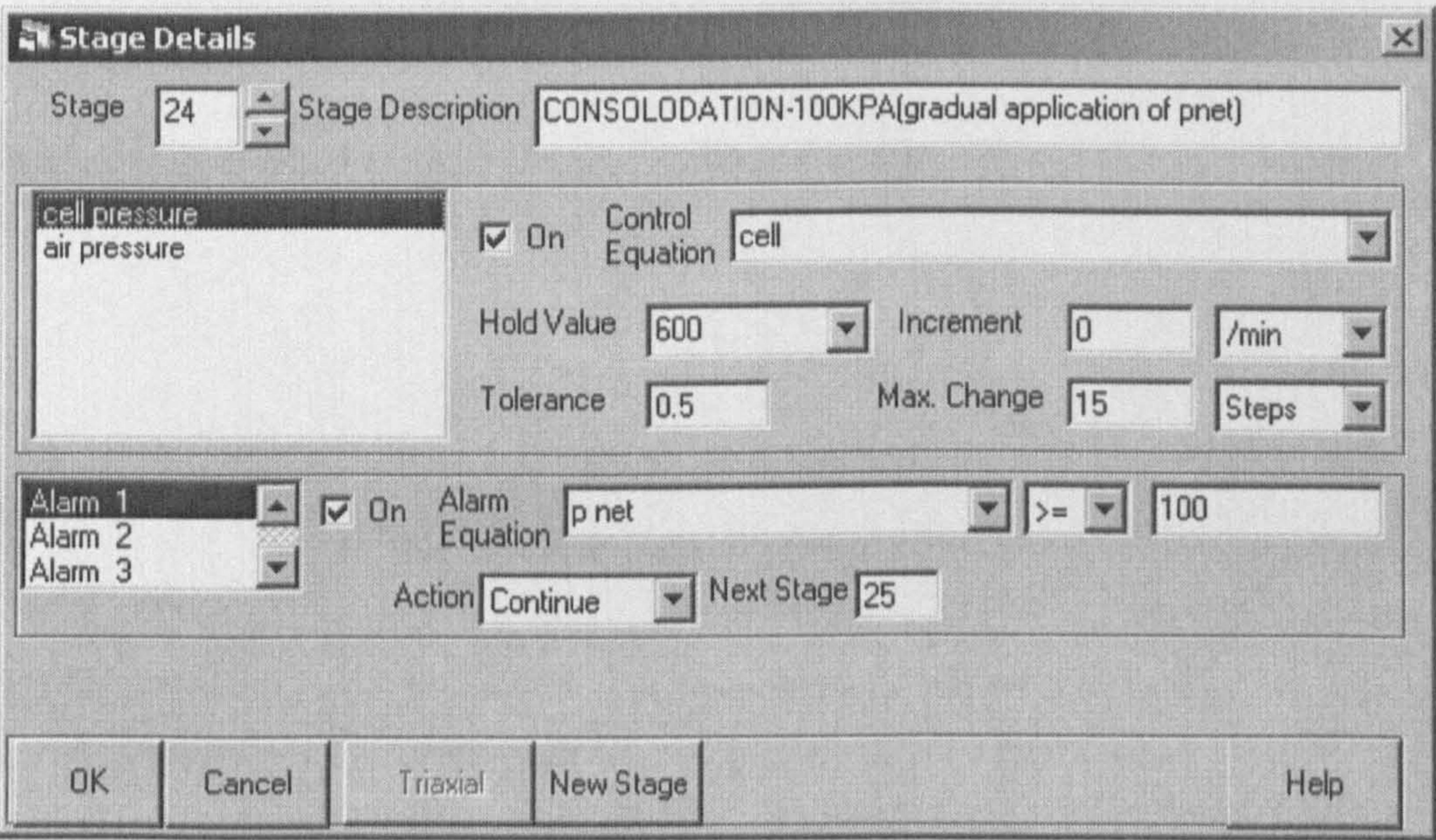


Figure 4.1: The *Stage Detail* for defining the control parameters. Example from the setting up for increasing cell and air pressures during suction equalisation in constant water tests

Calibration must be carried out to all the measurement devices prior to any testing. A certain value of measurement (pressure etc.) is applied to the measurement



device (pressure transducer etc.). The output can be monitored for a while to ensure that they are stable before clicking *Record* button. Normally, several defined values of applied measurement and the corresponding measurement device output are then stored in the calibration file for each channel. A linear regression was fitted to the stored data (non-linear regression options are available but were not required for the transducers used) and was used to convert the voltage to engineering units.

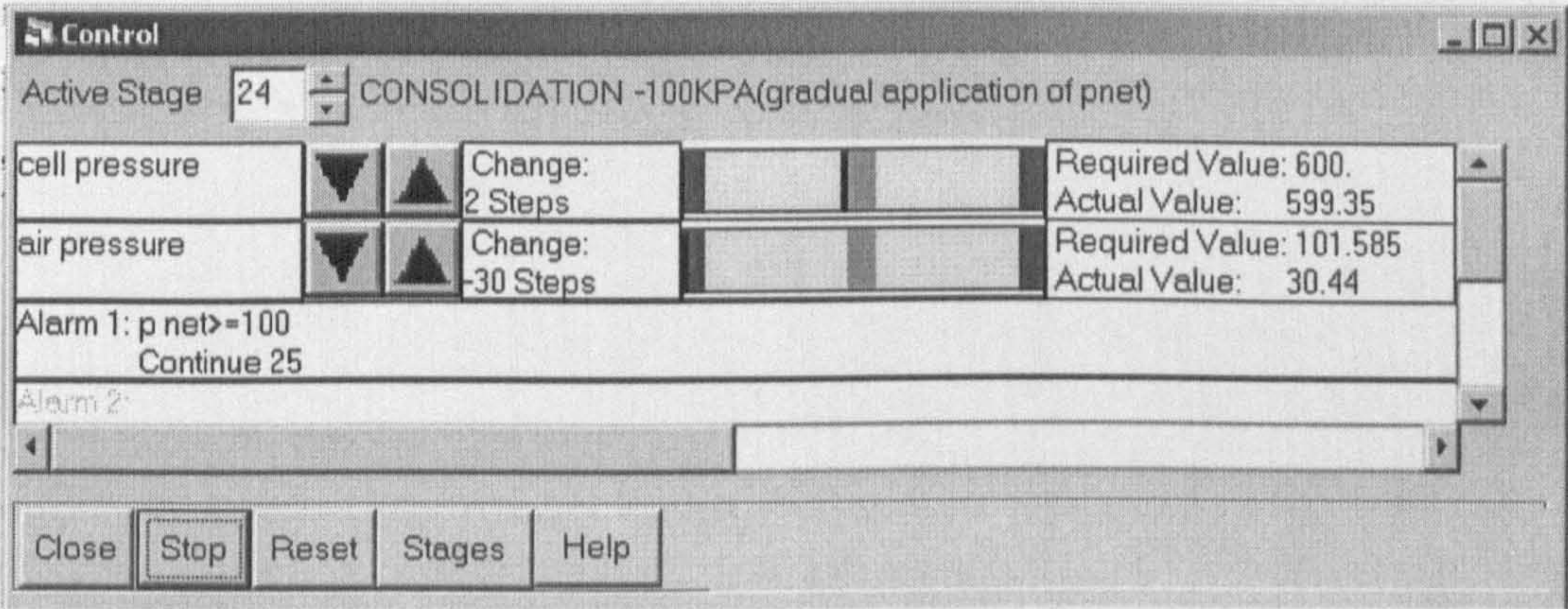


Figure 4.2: The *Control* window for increasing the cell and air pressures during suction equalisation under small mean net stress of 5kPa

4.3 TRIAXIAL INSTRUMENTATION

4.3.1 The Equipment

The equipment consists of a loading frame where load can be applied and a triaxial cell, which allows the control of water and air pressures according to the condition of a test. The schematic layouts of the triaxial control system for saturated and unsaturated tests are shown in Figures 4.3 and 4.5. The set up for the triaxial equipment was slightly different depending on the type of tests (saturated or unsaturated condition). In this study, 38mm diameter and 76 mm tall samples were



used. These samples were sheared by applying axial load (measured by load cell) using compression machines driven by electric motors. The displacement rate during application of loading could be controlled by manually setting the gear combination inside the machine compartment. A new model of triaxial loading frame was also used with digital control function supplied by Wykeham Farrance model Tritech 50kN Digital.

The axial strain (displacement) of the samples for both tests was measured externally using the LVDT (Linear Variable Differential Transformers) displacement transducers with maximum travel of 30mm.

#### **4.3.1.1 Saturated Tests**

The layout of the triaxial control system for saturated tests is shown in Figure 4.3. In this system the cell pressure and back pressure were controlled separately. The back pressure was controlled manually using a monostat air regulator. Air pressure was applied to the bottom part of the bellofram volume gauge and transmitted to water in the upper part of the gauge. The upper part of the volume gauge was filled with deaired water and air bubbles were completely removed. Pressure transducers were attached to the water lines connected to the base and top of the sample. These pressure transducers were used to read the applied pressures to the sample and were used to measure the pore water pressure of the sample by closing the outer valves (c3 and c4).

In saturated tests, the cell pressure was also separately controlled either using manual control of the manostat regulator or automatically using the stepper motor driven air valve. The air valves could operate in the range of 10 to 800 kPa of air pressure and maintain pressure to better than 0.5 kPa. The manual control of cell pressure was used to achieve pressure up to 650 kPa, the limit that could be supplied by the air compressor. An air-water interface was used in order to transmit an applied air pressure to the water in the triaxial cell. A 2 MPa maximum capacity transducer was used in order to cope with the wide range of applied cell pressure.



In order to achieve higher cell pressure beyond that limit, a modification was carried out by connecting a modified piston pump to the air ram pump (Figure 4.3). For a safety reason, pressure test was initially carried out on the piston pump up to 2 MPa. However, for the purpose of this work, the maximum cell pressure used was about 1500 kPa. The stepper motor driven air valve controlled the pressure in the air ram pump. Meanwhile the piston pump was connected directly to the triaxial cell. The tap water was used to fill its compartment water by opening valves b1, b2 and b3 (valve b3 was closed after filling the piston pump). The water used in the piston pump was pressurised during saturation of the samples (cell pressure was set at 305 kPa), allowed air to dissolve into solution before using the automatic cell control. Before using the automatic cell controller, valves a, b3, b4 and d were closed.

Three pressures transducers were installed for measuring the cell pressure, top pore water pressure and back pressure (at the base). The two transducers connected to the base and top of the sample could be used to measure the pore water pressure by closing the outer valves (c3 and c4). A volume gauge was used to measure the change in volume of the sample during the drained tests by recording the amount of water that flowed in to or out of the sample. An external LVDT with maximum travel of 30mm was used to measure the axial displacement during shearing of the sample.

In order to apply isotropic consolidation to the sample, the back pressure was maintained at 300 kPa while the cell pressure was automatically controlled by the computer control system. Cell pressure was increased gradually to the predetermined cell pressure to achieve desired effective confining pressure,  $p_o'$ . For the consistency of all of the tests, cell pressure was set up so that it reached the final pressure within an hour and then cell pressure was maintained up to the end of shearing. Figure 4.4 shows the control window for the controlling the cell pressure.



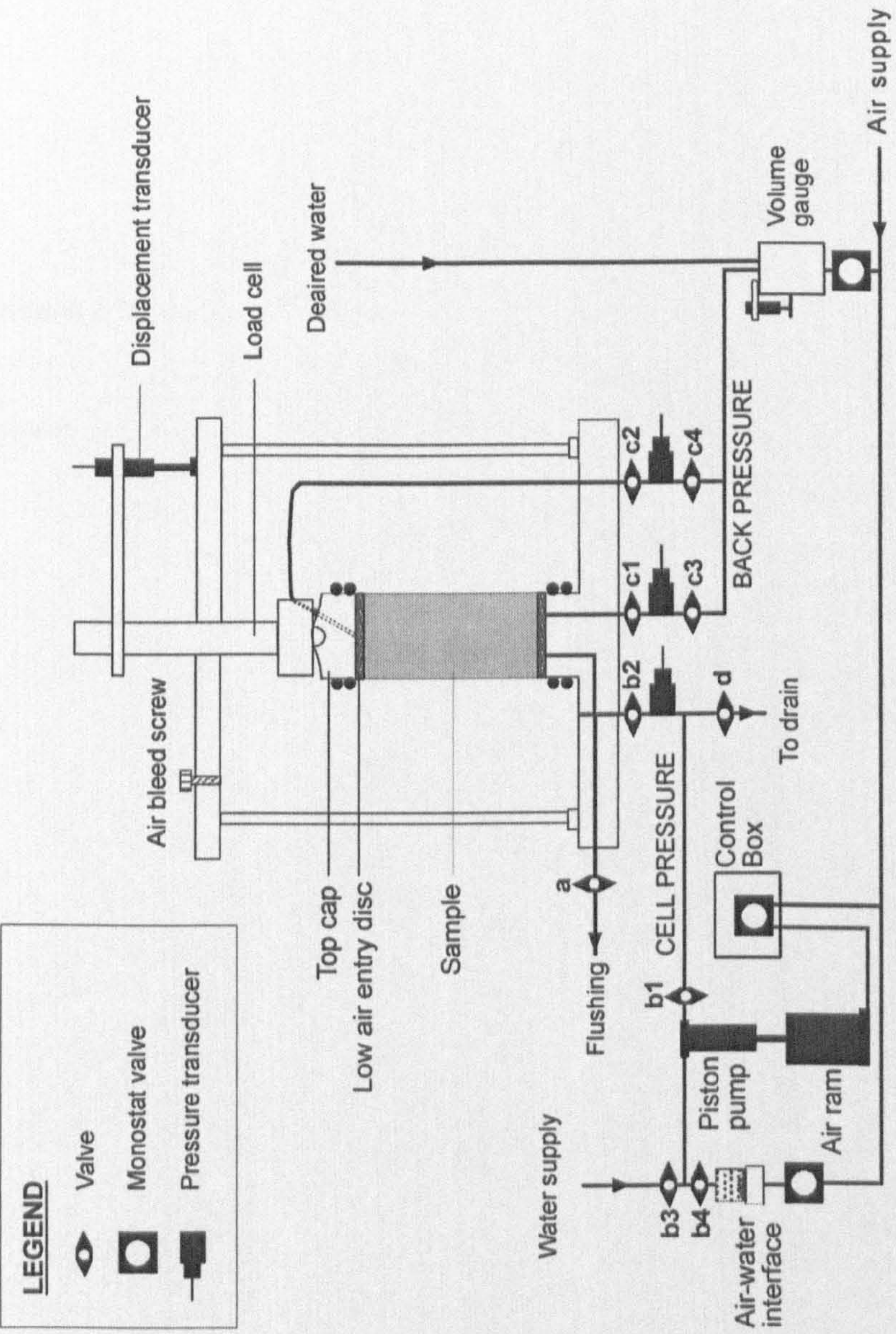


Figure 4.3: The setting of the triaxial controlling system for saturated tests



### 4.3.1.2 Unsaturated Tests

The schematic layout of the control system for the unsaturated tests is shown in Figure 4.5. The cell and air pressures were controlled separately using the computer control system. The control system of the triaxial was intentionally designed in order to perform a constant water content test; however other types of unsaturated tests could also be carried out using this system.

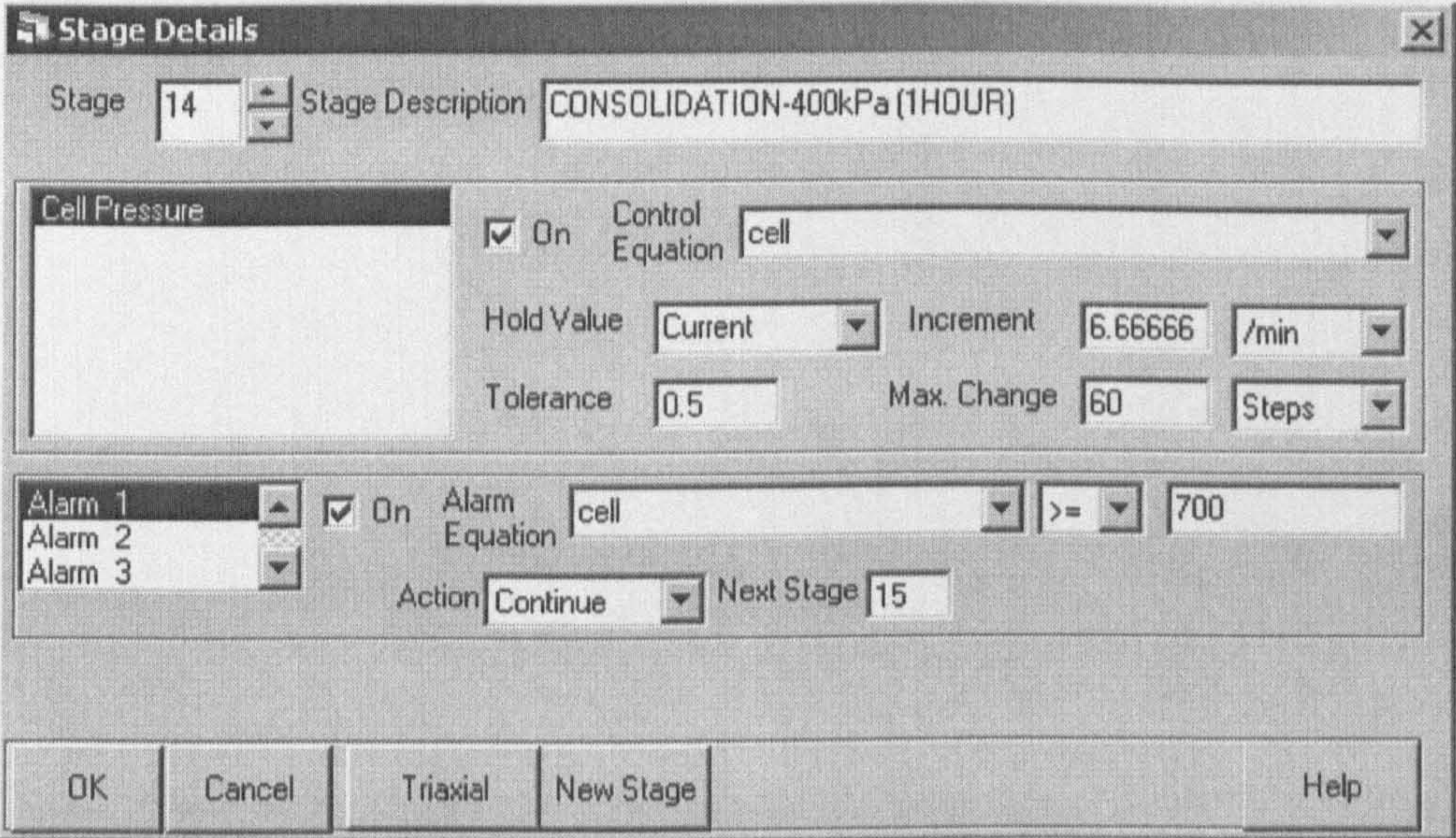


Figure 4.4: Control window for increasing the cell pressure to predetermined pressure to achieve targeted confining pressure

The cell pressure was controlled by a stepper motor driven piston pump. The piston pump was connected to the volume gauge, which was then connected to the cell. This volume gauge was also used for measuring the amount of water that flowed in to or out of the cell. The deaired water was used to fill the upper part of the volume gauge and the cell. The amount of trapped air bubbles was minimised during the filling of the cell with deaired water. The pedestal was fitted with a 500kPa high air entry (h.a.e.) disc to allow independent measurement of pore water pressure. In order to saturate the h.a.e. disc, the cell was filled with deaired water, the cell



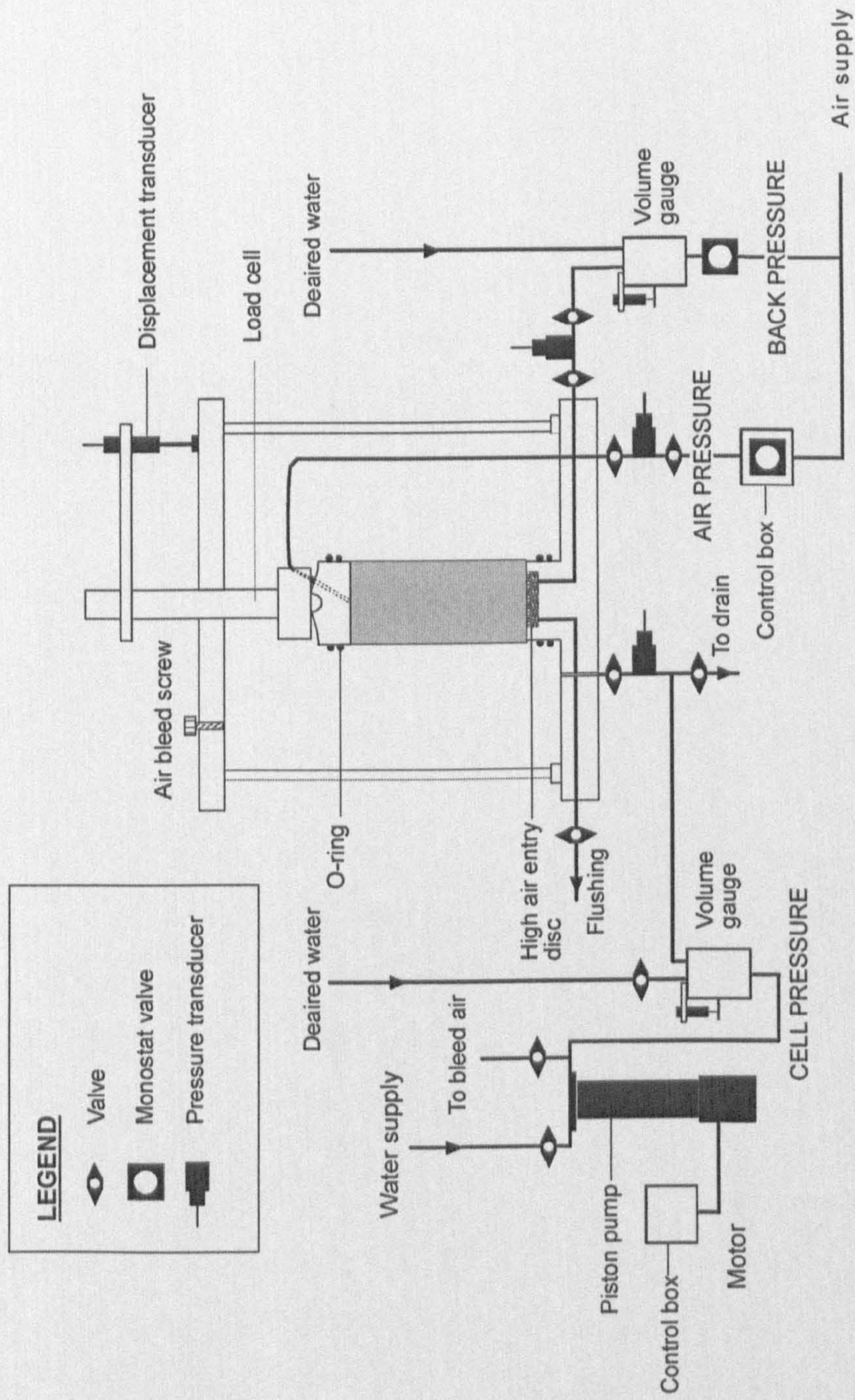


Figure 4.5: The setting of the triaxial controlling system for unsaturated tests



pressure was increase to 600kPa and the back pressure was set at 300 kPa in order to allow water to be flushed through the disc for two days. Then, while maintaining the cell pressure, the back pressure was also increased to the same amount of cell pressure and left for 24 hours. During this stage, water at the base of h.a.e disc was flushed several times.

An air line was connected to the top cap. The air pressure was controlled using the stepper motor driven manostat air regulator. During suction equalisation (SE), air pressure would be increased using the computer control system in order to follow the increase of the cell pressure so as to maintain a small mean net stress,  $p-u_a$  of approximately 5kPa. A detailed description of this procedure will be discussed later in the following section.

In unsaturated tests, three pressure transducers were installed in order to record the cell pressure, air pressure and pore water pressure (or back pressure). Two volume gauges were also used, one connected to the cell and one to the base of the h.a.e disc. The first one was used to measure the volume change of the cell while the latter was used to set a back pressure to the base of h.a.e disc. All the pressure transducers and other measuring systems were fully saturated before installation. The axial displacement was measured externally using a LVDT displacement transducer.

#### **4.3.2 Calibration of the Measurement Devices**

Each measurement transducer was calibrated before fitting to the triaxial system. The pressure transducers were calibrated using the Budenberg dead weight tester. Any air traps were avoided when connecting the transducer to the pressure outlet. Different weight loads were applied in increment and decrement orders. The Triax program allows calibration of a number of transducers simultaneously for the same measurement value. Meanwhile, the load cell transducer was calibrated using dead weights. The load transducer was placed up side down on the frame and a hanger

was mounted to apply a point load. Each weight was converted to Force (N) and the corresponding voltage was then recorded.

The external LVDT displacement transducers were calibrated using a vernier micrometer. The external displacement transducer had maximum travel up to 30mm. The volume change transducers were calibrated by using a 25cm<sup>3</sup> burette. The volume gauges for measuring the changes in volume of the sample and cell during drained loading had capacity of 100cm<sup>3</sup>.

The calibration data of each transducer was stored in calibration data file on the computer. The ranges of calibration errors of each measurement devices used in three cells are summary in Table 4.1a. The regression curves (up to 3<sup>rd</sup> order for internal displacement transducers) were fitted to the stored calibration data and were used to convert the voltage to engineering units. The analyses of errors in measurement were also carried out and are shown in Appendix I. Based on the adopted technique, the maximum error in measurement can be calculated.

#### **4.3.3 Calibration of Volume Change**

The volume change of the cell was measured to represent the change in the volume of the sample in unsaturated tests. Since the perspex cell is expandable due to changes in cell pressure and temperature, calibration of the volume change was carried out at cell pressures of 600kPa, 695kPa and 895kPa in a temperature-controlled room. During suction equalisation of the sample, cell and air pressures were set up at 600kPa and 595kPa, respectively (only a small net stress was allowed at this stage). For samples with low and medium suction (0 – 300kPa), consolidations of the samples at  $p-u_a = 50\text{kPa}$  and  $100\text{kPa}$  were carried out by maintaining the cell pressure and decreasing the air pressure until the target net stress,  $p-u_a$  was achieved. However, this approach generated a cavitation problem to the samples with high suction (more than 300kPa) when consolidated at  $p-u_a = 100$  and  $300\text{kPa}$ . Therefore, cell pressure was gradually brought up to 695kPa or



Table 4.1a: Summary of the ranges of calibration values for the measurement devices used for three triaxial cells

Types of Measurement	Percentage of error calibration (%)		
	Triaxial Cell-1 (saturated tests)	Triaxial Cell-2 (unsaturated tests)	Triaxial Cell-3 (unsaturated tests)
1. Cell pressure	0.00 – 0.17	0.00 – 0.05	0.00 – 0.15
2. Back or pore water pressure at base of sample	0.00 – 0.04	0.00 – 0.18	0.01 – 0.12
3. Pore water pressure at top of sample	0.00 – 0.04	n.a	n.a
4. Air pressure	n.a	0.00 – 0.19	0.02 – 0.10
5. Load	0.01 – 0.04	0.02 – 0.21	0.00 – 0.04
6. Axial displacement	0.00 – 0.12	0.03 – 0.29	0.04 – 0.20
7. Volume change	0.01 – 0.15	0.03 – 0.30	0.02 – 0.10
n.a – not available			

Table 4.1b: Summary of the values of error in measurement,  $E(x)$  for each variable

895kPa and air pressure was maintained until target  $p-u_a$  was achieved. Therefore, pore water pressure within the samples would respond to the increasing cell pressure and equilibrate within the positive region. Thus, cavitation could be avoided during this stage. In order to monitor the temperature change, a thermocouple sensor was located close to the cell. Figure 4.6 shows the temperature variation during one of the tests using cell 2. The temperature initially fluctuated between 18.5°C and 21.2°C. Therefore, in order to minimise the temperature variation, the cells were blanketed with bubble wrap throughout the tests. It is clearly seen that the variation of temperature became smaller ( $<0.5^\circ\text{C}$ ) after the cell was covered. However, there was a prolonged period of cycles which fluctuated within less than 1°C.

Two single wall cells were used for the unsaturated tests and each of them was calibrated individually at the applied cell pressure. In order to minimise errors in volume change of the cell, the calculation of creep rate was carried out for every test (during suction equalisation and consolidation). During suction equalisation, the cell pressure and sample air pressure were monitored at constant values, so the volume changes measured should be due only to volumetric creep of the perspex cell. The volume change of the cell corresponding to temperature variation for cell 3 was calibrated during suction equalisation (cell pressure at 600kPa and air pressure at 595kPa) is shown in Figure 4.7. At early application of cell pressure, large volume change happened due to the expansion of the perspex cell, but then reduced with time. A reasonably constant volume change can be observed after 24 hours. However, since pore water pressure of samples required several days to equilibrate, the cell already achieved its constant creep before consolidation took place. The plot clearly indicates the relationship between volume change of the cell and temperature variation. A variation in temperature inside the temperature controlled room was found to be different between “working days” and “weekend”. It is seen from the plot that temperature began to increase while fluctuated at early morning (around 8 a.m.) until midday and thereafter it started to drop gradually throughout the night. The cycle continued everyday during working days. During weekend, temperature variation fluctuated at lower temperature



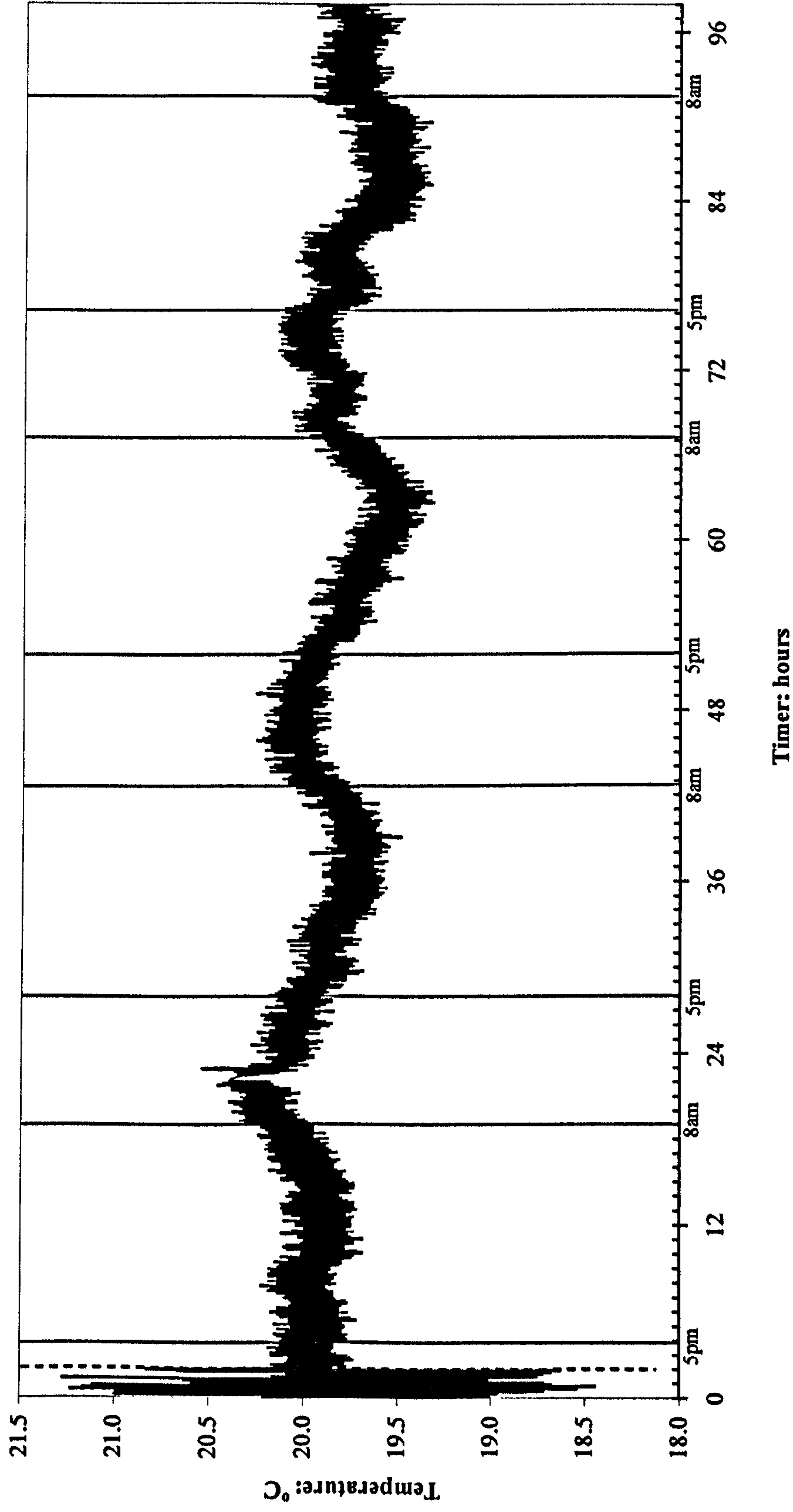


Figure 4.6: The temperature variation of the cell before and after wrapping with bubble wrap (from Cell 2)

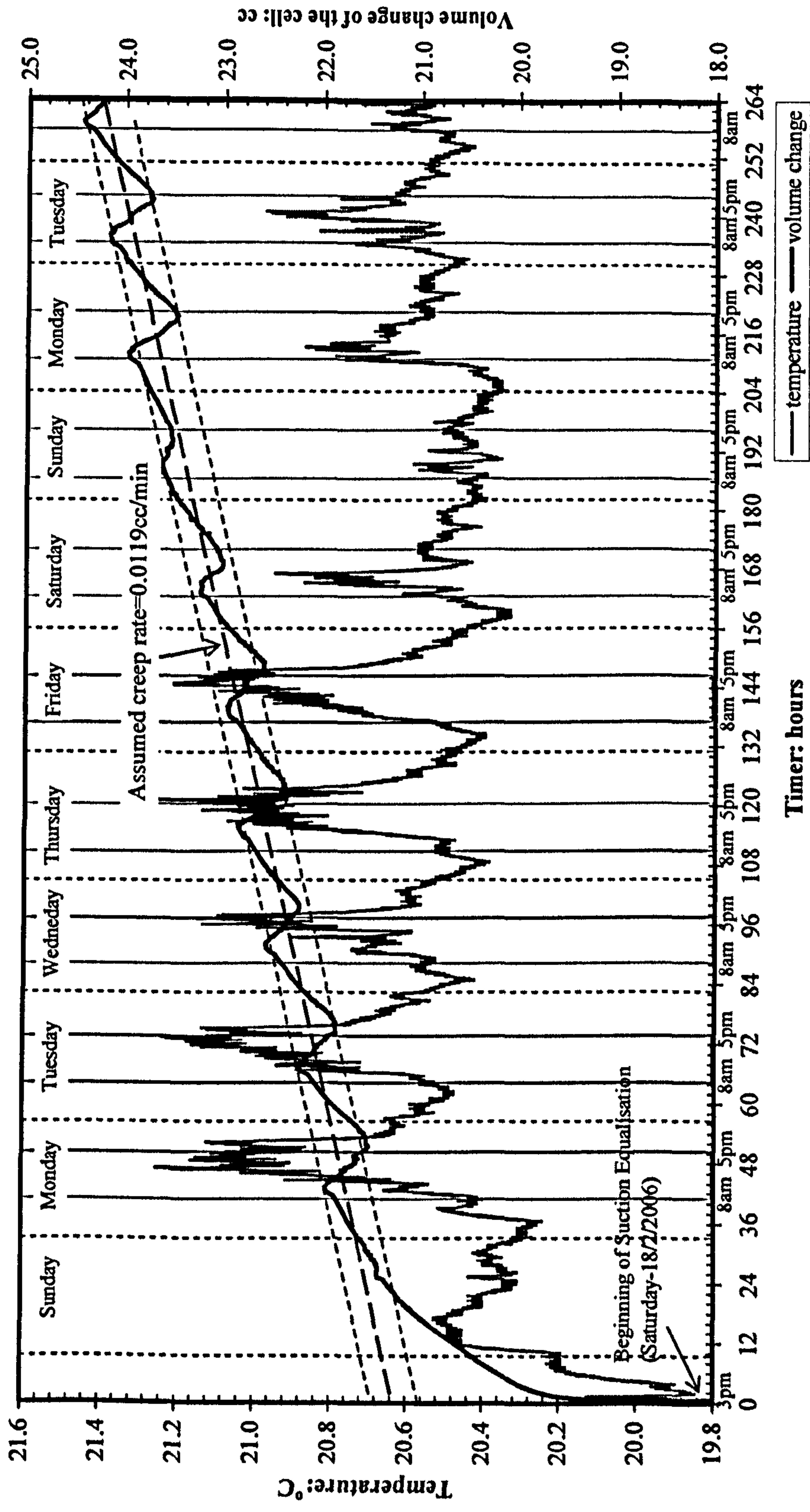


Figure 4.7: The volume change of the cell during suction equalisation under 600kPa of cell pressure (from Cell 3)



(20.3°C to 20.6°C). However a similar pattern of volume change during working days and weekend was observed even though the temperature variation was clearly different. As can be seen from the plot, there was still a small increase in temperature variation particularly at early Sunday morning which corresponding to the decrease of volume change which then increased as temperature dropped again. This also suggested that the increasing section of volume change correlated to the decreasing of temperature variation while the decreasing part of volume change was due to the increasing of temperature variation, independent of magnitude (see Figure 4.7).

As a result of an increase in temperature fluctuation, since water responded quicker than the perspex cell, volume of water in the cell would expand quicker than the creep of the cell. Therefore, water moved out from the cell to the volume gauge and this was indicated by a decreasing in the rate of volume change (down slope section). In a case of increasing volume change (or upslope section) water moved back into the cell due to the contraction of water and creeping of the perspex under cell pressure.

Based on this observation, since the room temperature controller was capable of maintaining room temperature within 1°C, a small fluctuation really poses significant change to volume of a single wall cell for unsaturated tests. Therefore, it is important that the calibration for the volume change must be carried out on each test in order to minimise error. The correction factor for every test was obtained during suction equalisation stage where small net stress (5kPa) was imposed to the sample at cell pressure and air pressure equal to 600kPa and 595kPa, respectively, assuming that the imposed net stress did not consolidate the sample. Therefore, correction factor for volume change for each test was obtained from the same test instead of using universal correction for all tests. The correction factor was calculated from the reasonably constant volume change during the suction equalisation stage. The calibration curves of the volume change for Cell 2 carried out at cell pressures of 695kPa and 900kPa are shown in Figures 4.8 and 4.9. It clearly seen that the effect of temperature variation on volume change was

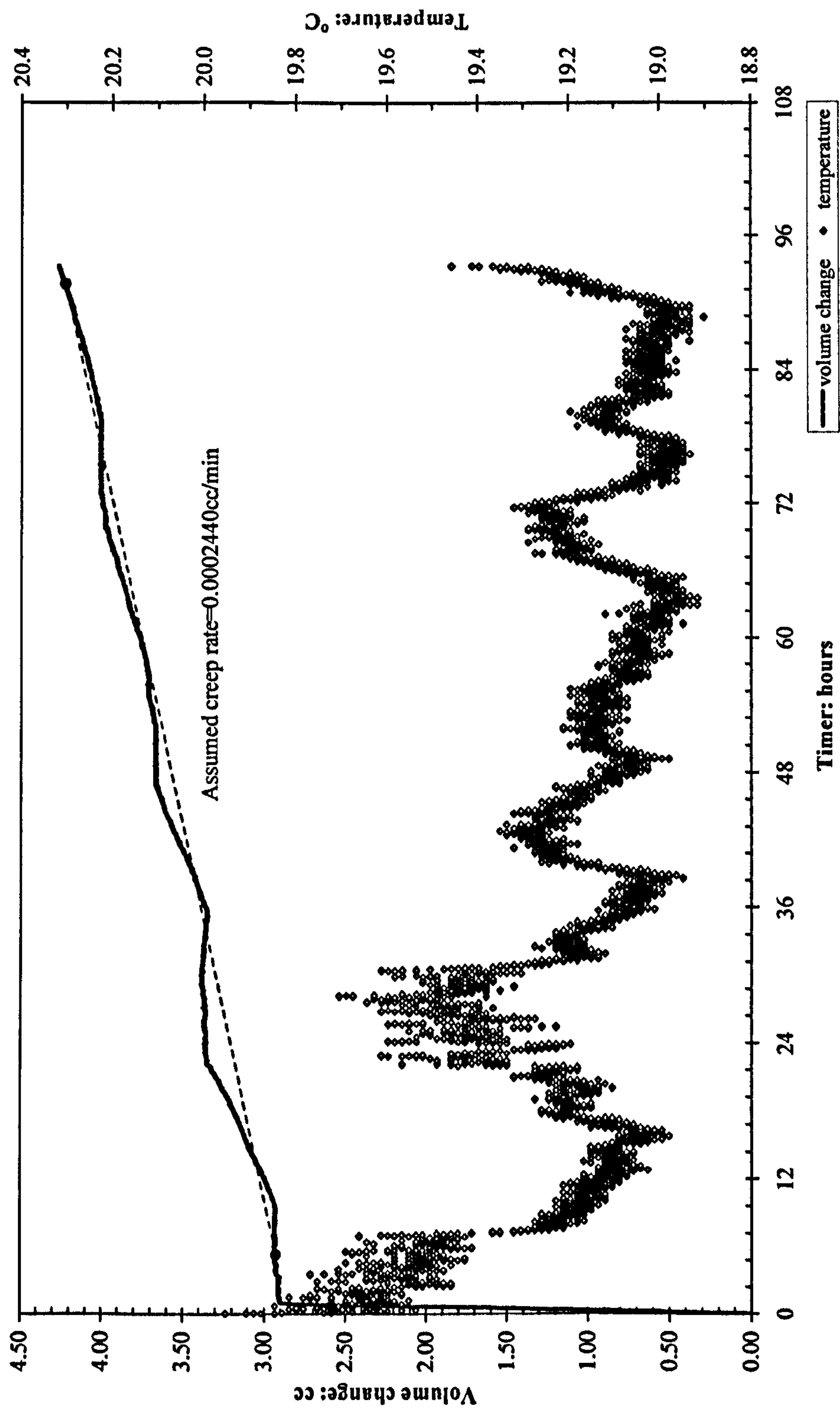


Figure 4.8: The calibration of volume change of the cell under 695kPa of cell pressure (from Cell 2)



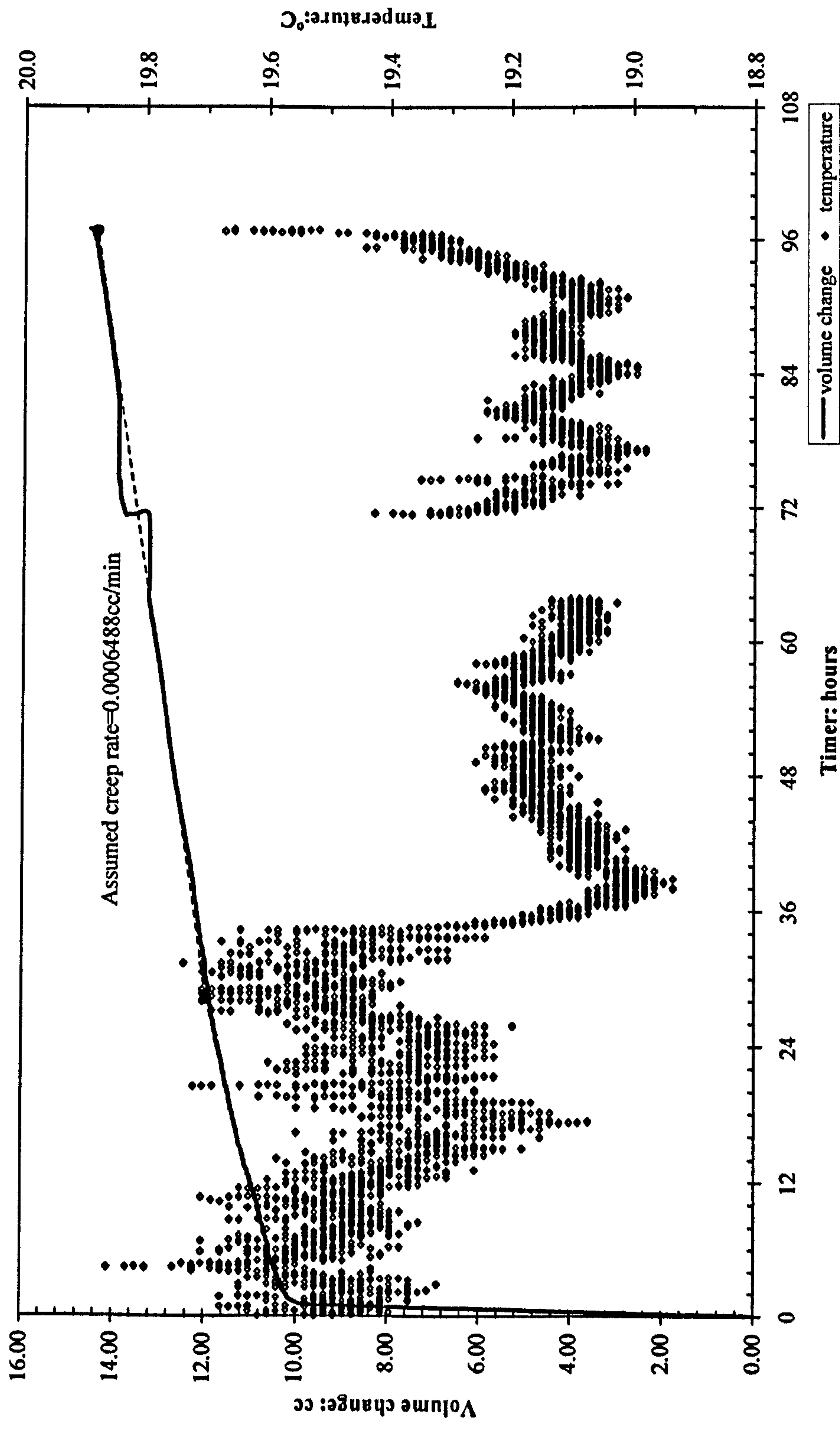


Figure 4.9: The calibration of volume change of the cell under 895kPa of cell pressure (from Cell 2)

negligible under cell pressure of 895kPa. In other hand, at 695kPa cell pressure, fluctuation of volume change corresponding to the variation of room temperature is noticeable (Figure 4.8). This behaviour was also seen in the other cell at 600kPa cell pressure. In the case of samples, which had to be consolidated by increasing cell pressures, a single correction factor for volume change was used. Due to the limitation of air pressure (supplied by air compressor) and the air entry value of high air entry disk, suction equalisation of samples was carried out at a cell pressure of 600kPa. The correction factors gained from the volume change calibrations (Cell 2) were used for the tests that involved an increase of cell pressure (695kPa and 895kPa). The increase of cell pressure in order to achieve predetermined mean net stress was also accompanied by an instantaneous volume change which was then used to correct the actual volume change of the samples during consolidation.

Calibration of the volume change of the cell also took into consideration the volume change caused by the penetration of the loading piston into the cell at cell pressure of 600kPa (Figure 4.10.a and 4.10.b). Since a similar strain rate of 0.019mm/minute was used for all the tests, the calibration value of volume change due to piston movement into the cell would be used and be valid for all the tests providing that a similar strain rate and no changing or swapping of either piston load or cell top. From Figure 4.10.a from cell 2, the correction factor due to piston is -0.0112cc/minute or -0.672cc/hour. Meanwhile, correction factor due to piston for cell 3 is -0.0096cc/minute or -0.576cc/hour (Figure 4.10.b). The negative sign is referred to the sign convention corresponding to the flowing out of water from the cell (dilation). A summary of the correction factor values for the calibration of volume change due to creeping of the perspex cells and penetration of piston load during loading is shown in Table 4.2.

Calculation of sample volume change during consolidation was carried out by taking the volume of flow into or out of the cell, which then corrected to the correction factor due to the creep of the cell based on a linear volume change-timer. Meanwhile for correction of sample volume due to shearing, volume change



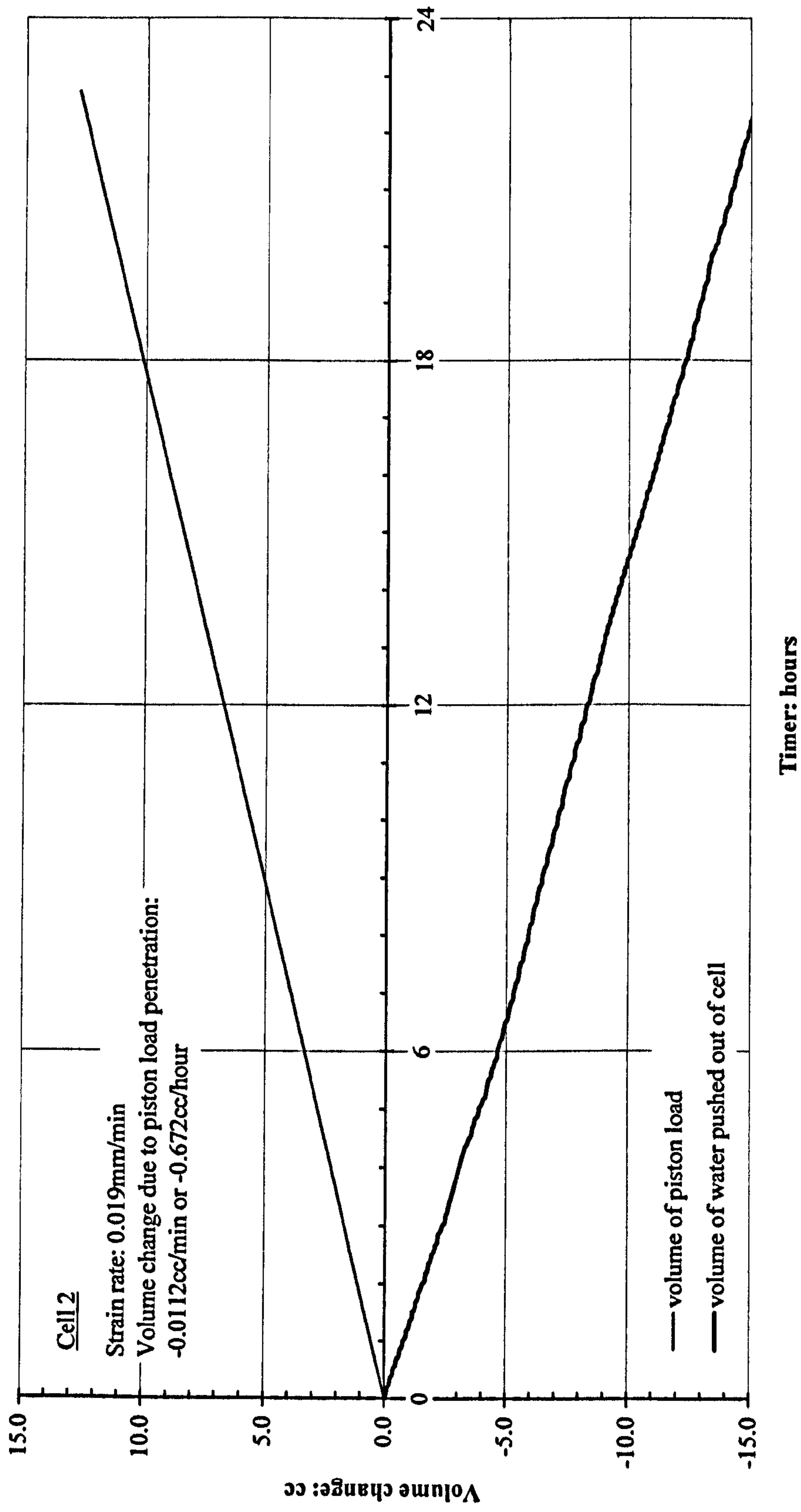


Figure 4.10.a: The volume change of the cell during penetration of piston load into the cell at 600kPa of cell pressure (from Cell 2)

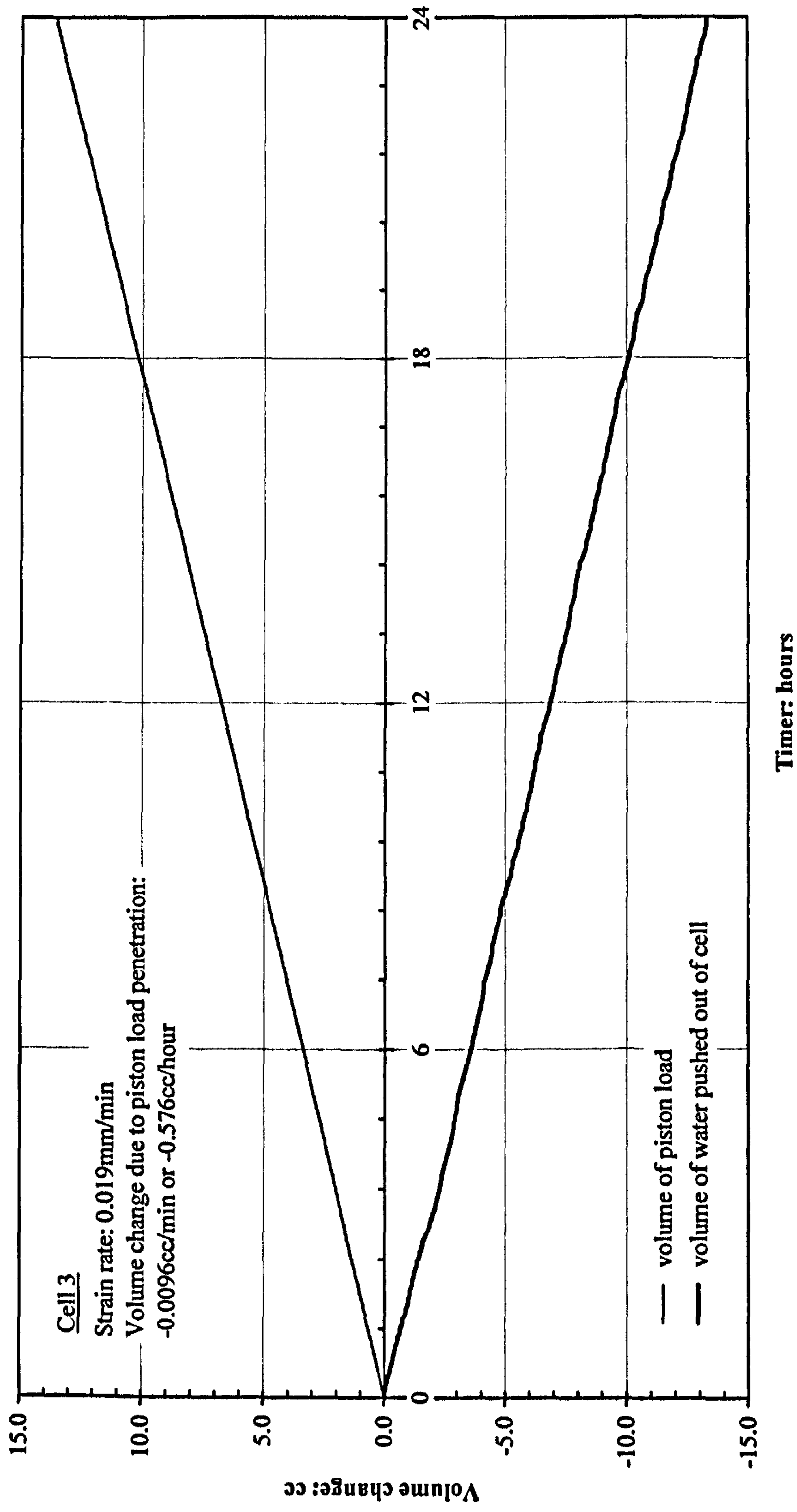


Figure 4.10.b: The volume change of the cell during penetration of piston load into the cell at 600kPa of cell pressure (from Cell 3)



Table 4.2.a: Summary of the correction factors for volume change of the cell for Cell 2

Cell 2: Volume change due to:	Cell Pressures		
	600kPa	695kPa	895kPa
a. Instantaneous volume change	n.a		
b. Creeping of perspex cell	0.0003*	0.00024	0.00065
c. Penetration of piston load	-0.0112	-0.00074	-0.00091

\* - for particular test, each test has own correction factor for volume change due to creep  
n.a - not available

Table 4.2.b: Summary of the correction factors for volume change of the cell for Cell 3

Cell 3: Volume change due to:	Cell Pressures		
	600kPa	695kPa	895kPa
a. Instantaneous volume change	n.a	n.a	n.a
b. Creeping of perspex cell	0.0002*	n.a	n.a
c. Penetration of piston load	-0.0096	n.a	n.a

\* - for particular test, each test has own correction factor for volume change due to creep  
n.a - not available



was corrected due to the creep effect and the penetration of loading ram into the cell.

## **4.4 TRIAXIAL TESTS**

### **4.4.1 Saturation, Suction Equalisation and Consolidation Processes**

#### **4.4.1.1 Saturated tests**

The bonded and destructured samples were initially placed in a latex rubber membrane with low air entry discs fitted at the top and bottom of the samples. Then two O-rings were used to seal the membrane at the base and the top of the sample around the top cap. The cell then was filled with water up to the top with the bleed screw open.

The saturation of samples was carried out in two steps. Firstly, the samples were flushed through using deaired water from the base of the samples. With all the valves to the cell and top and bottom of the sample closed, cell pressure and back pressure were set at approximately 30kPa and 27kPa respectively in order to apply only small effective stress (3 - 5kPa) to the samples (to avoid the swelling of the membrane). Then the valves to the cell and back pressure were opened slowly to avoid any damage to the sample due to instantaneous pressure. By applying a back pressure at the base, any air bubbles were brought up to the top of the samples and driven out to atmosphere through the top line. Once the air had been released from the sample, water started to flow out of the top line. The process would be repeated until no air bubbles were observed. Normally, in order to ensure air had been flushed out from the sample, about 100cc of deaired water was used.

The second stage of saturation involved the application of higher back pressure of 300kPa. The top line was closed and connected back to the back pressure. The cell pressure was set up again slightly higher than the back pressure (3 - 5kPa higher). Then the cell and back pressures were applied to the samples and would be left for



24 hours before checking the B value. The B value is calculated prior to isotropic consolidation in order to determine the degree of the saturation of the sample under applied cell and back pressures. The B value was measured by increasing the cell pressure by about 50kPa from the initial value while the back pressure valve was closed. A B value of at least 0.96 was required before performing the consolidation process. Once the required B value was achieved, the samples were isotropically consolidated by applying different cell pressure and back pressure. During this stage, the volume change was monitored. It was considered that the consolidation had reached an equilibrium condition when there was no longer flow of water from the sample.

#### **4.4.1.2 Unsaturated tests**

In order to start from uniform initial conditions, all the samples were manually saturated before drying. The samples were left to dry naturally at room condition until a particular water content was achieved. By differentiating the water content, a particular suction value could be achieved in the sample.

Initially the dry weight of the samples was determined. Prior to this, samples and rubber membrane were kept for overnight in desiccators containing dry silica gel to absorb any moisture. Then the samples were carefully placed in a rubber membrane with low air entry porous discs attached to the top and base of the sample. The samples were then stood in a beaker of distilled water with the water surface just above the top of the samples. The samples were left in this condition at least overnight. The samples were taken out of the beaker and the low air entry porous discs were removed from the samples. Then the samples were allowed to dry out to a certain value of water content at room temperature. Before placing the sample on to the pedestal, the weight of the sample was determined again in order to ascertain the final water content. The O-rings were used to seal the base and top of the samples.

Once the sample was mounted on the pedestal, the pressure transducer measuring the pore water pressure would start to drop depending on the value of suction in the sample. Therefore the pore water pressure was continuously monitored. If the pore water pressure dropped nearly to  $-70$  kPa, the valve closing off the deaired water line would be opened temporarily in order to permit a small amount of water to enter and bring back the pressure to the atmospheric pressure. In this way, the cavitation problem could be prevented. The pressure could drop again to  $-70$  kPa in a short period for several times during this stage. However the opening of valve to bring pressure back to atmospheric pressure would only permit very small amounts of water to enter the measuring system, which should not give significant changes to the initial water content of the sample. Toll (1988) studied laterite samples and found that samples with suction of 200 kPa or less, the pore water pressure would not fall below  $-50$  kPa within the setting up period (1 to 1.5 hours). Samples with higher suction normally took 30 minutes to fall below  $-70$  kPa. In this study, artificial bonded samples with different degree of saturation were used to achieve different suction. For samples with high suction (500-600kPa), the pore water pressure would drop to  $-70$ kPa between 30 to 45 minutes. Meanwhile sample with low to intermediate suction, pore water pressure could fall to  $-45$ kPa in more than hour.

The cell was then filled with deaired water and any air bubbles would be allowed to bleed out from the cell. Once the cell was full, the load cell was brought down manually close to the top cap with a very small gap. After that the bleed screw on top of the cell was tightly closed. Then a small net stress,  $(p-u_a)$  was applied to the sample during suction equalisation stage. The suction equalisation stage would allow the equilibrium of suction in the sample and the measuring system. It would take time for the suction of the samples to reach equilibrium with the applied air pressure because of low permeability of high air entry (h.a.e.) disc. It is paramount to ensure that no air bubbles present in measuring system by flushing with deaired water several times, otherwise it would affect the equilibrium process of suction. The suction equalisation procedure was achieved by using the computer control system to increase the cell and air pressure together while maintaining the net



stress at approximately 5kPa. The cell and air pressures were gradually increased up to 600kPa and 595kPa, respectively. The process of bringing up the cell and air pressures to predetermined values during suction equalisation stage was scheduled for all the tests within an hour. During suction equalisation under small net stress, there was a significant change in volume of the cell at an early stage as a result of the compression of any trapped air in the cell. Once the air was fully dissolved the volume change was due to the creeping of the perspex cell (Figure 4.7). In this study, a single wall perspex cell was used; therefore creep problems were expected and had been calibrated to correct for this and hence obtain the actual volume change. However, in order to correct the volume change precisely, the actual creeping of the cell was determined for every test. It was assumed that the application of small net stress caused no deformation to the sample during this stage. The suction equalisation was considered complete when the pore water pressure was constant or rate of pore water change became less than 0.002kPa/minute. Figure 4.11 shows the suction equalisation stage from one of constant water content tests. In general, the suction equalisation stage would take about 3-4 weeks depending on the value of the suction of the sample.

The consolidation stage involved either increasing the cell pressure or decreasing the air pressure. The first technique was applied to the samples with low degree of saturation (suction larger than 300kPa) and pore water pressures were close to or below zero. By increasing the cell pressure and maintaining the air pressure at 595kPa, the pore water pressure would be equilibrated within a positive range. Therefore, the cavitation problem would be avoided during application of net stress,  $p-u_a$ . Meanwhile for latter technique was used for samples with low and medium suction (0 – 300kPa) at which the pore water pressures were reasonably close to the imposed air pressure ( $u_a = 595\text{kPa}$ ). The air pressure was gradually decreased and the cell pressure was maintained at 600kPa throughout the tests. The gradual increasing of cell pressure or decrease of air pressure occurred within an hour by setting up the rates of pressure change and applied net stress for the consolidation in the computer control system. By increasing the cell pressure,  $\sigma_3$  or decreasing the air pressure,  $u_a$  the net stress,  $p-u_a$  gradually increased to the target



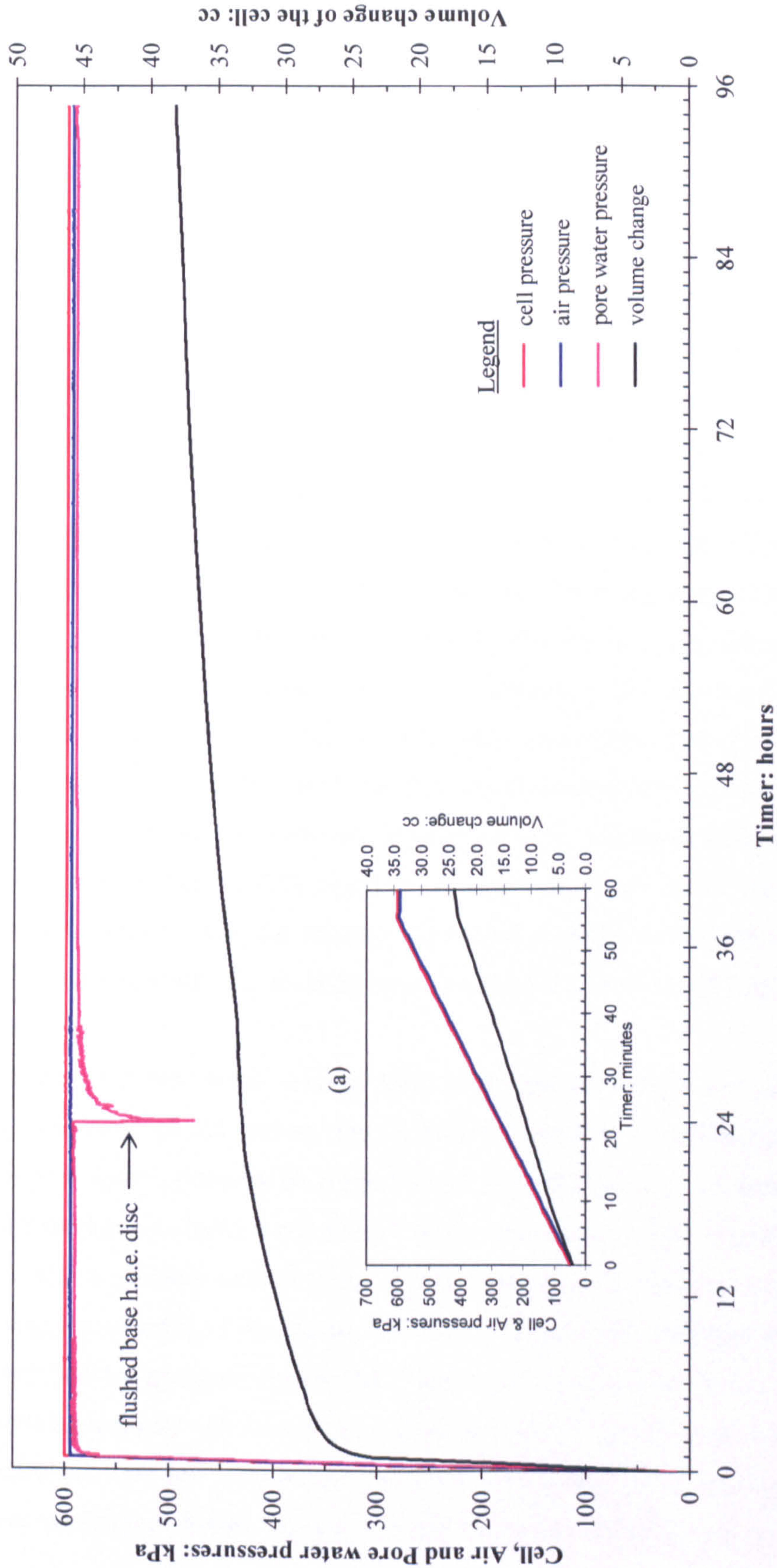


Figure 4.1.1: Suction equalisation stage. (a) increment of cell and air pressures during first hour of suction equalisation under small  $p-u_a$



value. The pore water pressure should response to the increasing of  $p-u_a$ . Then the sample was left under this condition for several days until the suction value became stable.

#### 4.4.2 Shearing Stage

In saturated tests, the samples were sheared under *consolidated drained* (CD) conditions and *consolidated undrained* (CU) conditions. Shearing samples under undrained condition were carried out by closing the drainage line and the changes in pore water pressure were measured throughout this process. Meanwhile, the samples sheared under drained condition were carried out with the drainage line opened. All the samples were sheared at a constant strain rate of 0.025%/minute (0.019mm/minute) similar to the strain rate used by Malandraki (1994). Initially a higher strain rate of 0.08%/min or 0.061mm/min was used in order to speed up the preliminary tests. Based on some of the preliminary drained tests, no significant change of excess pore water pressure were seen, suggesting that this rate was sufficiently slow to allow dissipation of any increasing pore water pressure during loading (Figure 4.12). However, in order to have a uniform procedure with that used by Malandraki (1994), a slower strain rate was used for the later samples. In both CU and CD tests, the samples were sheared until a strain of at least 25% was achieved. Generally, the shearing process carried on for about 20 hours.

Initially, constant water content tests were carried out on several unsaturated samples in which the suction was controlled by imposing a difference between air and pore water pressures. However the samples took about 3 – 4 weeks to achieve their suction equalisation and about 2 weeks for consolidation to equilibrate. There was also a problem related to the cell pressure that was unable to be maintained during the shearing of the sample (previously cell and air pressures were manually controlled by manostat regulators). Then it was decided to set up the computer control system for the triaxial tests, thus the cell and air pressures could be easily controlled. This involved some modification of piping system and leakage checks were performed before starting the actual tests. In addition, due to limited time

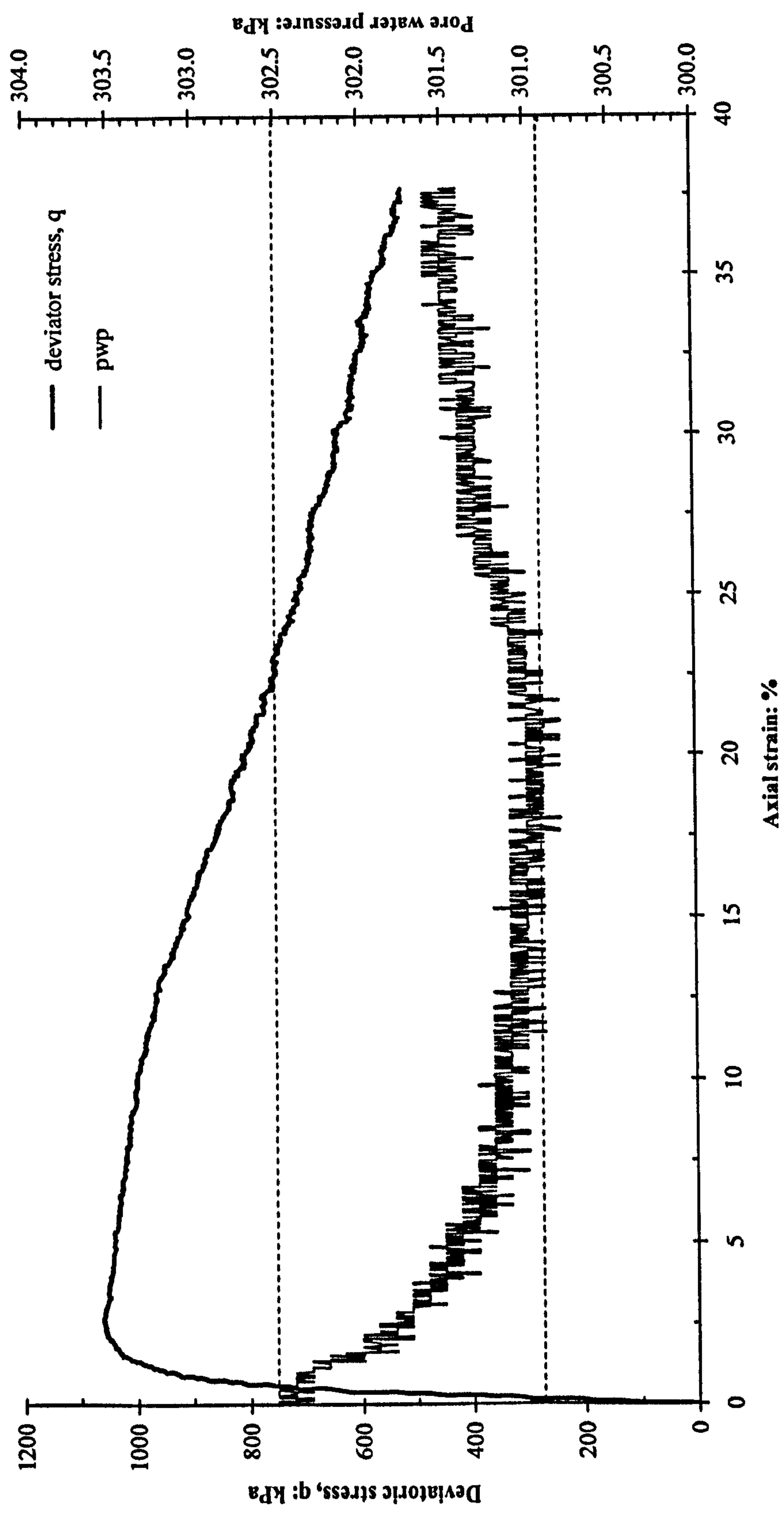


Figure 4.12: Pore water pressure changes during shearing of sample under the drained test



available, it was finally decided to use constant water content tests (CW) for the tests where pore water pressure is measured. This test is quite similar to a saturated undrained test in terms of the water phase. However, in a CW test the air phase is drained while water phase is undrained, thus pore water pressure was measured. The pore air pressure was held constant; this means that the sample can change in volume.

In these tests the water line to the base of the sample was closed and the change in pore water pressure was measured. When the equalisation of pore water pressure had been achieved, the sample was ready for shearing. Prior to that, the load cell was slowly brought close to the top cap using the applied shearing rate. The axial strain transducer and the volume gauge were reset in order to measure the change in volume of the samples during the test. A series of tests were designed using samples having different water content (or degree of saturation) and then were sheared under different applied net stress,  $(p - u_a)$ .

#### 4.5 CONCLUSIONS

Triaxial equipment was used for carrying out drained and undrained tests on saturated, consolidated samples. To carry out tests at higher stress levels, an air piston system was devised capable of applying a cell pressure of up to 2MPa. For unsaturated testing, the triaxial pedestal was fitted with a high air entry disc. To measure volume change of the sample, the volume change due to creep of the perspex cell and penetration of loading ram was investigated, therefore correction factors could be applied. Samples were consolidated at different mean net stresses in two techniques either by maintaining the cell pressure and decreasing the air pressure or by increasing the cell pressure and maintaining the air pressure.

## **CHAPTER 5   SATURATED DESTRUCTURED MATERIAL**

### **5.1   INTRODUCTION**

In this chapter, the results from conventional saturated drained and undrained tests are presented and discussed. The tests were carried out on artificial destructured samples that were prepared with a void ratio of 0.6. These samples were prepared using a similar method to that adopted by Malandraki (1994). A detailed explanation of the method of preparing the destructured samples was given in the Chapter 3. A wide range of effective stresses was applied during the consolidation stage (up to 1 MPa) prior to shearing. The relationship between deviator stress, volumetric strain or excess pore water pressure and maximum  $q/p'$  stress ratio with strain of the drained and undrained tests is discussed. The bounding surfaces of the soils are determined and comparisons are made between the bonded and destructured samples. This series of tests also establishes a benchmark in assisting the interpretation of the test results from the unsaturated tests. The details of the tests are described further in a later section.

### **5.2   DRAINED TRIAXIAL TESTS**

The results of the drained tests on artificial destructured samples are presented and described in this section. The drained behaviour of the artificial samples is discussed in term of stress-strain, volumetric strain, stress ratio and effective stress paths. The bounding surface and phase transformation lines are presented in the stress space for the destructured samples.



### 5.2.1 Description of Testing

Thirteen destructured samples were examined using the conventional drained triaxial compression test. Samples were also prepared with similar void ratio and bond strength (i.e. fired for 5 hours at 500°C) as bonded samples, before being destructured. Prior to shearing, samples were initially isotropically consolidated under different effective confining pressures between 15kPa and 1000kPa. The consolidation stage was applied within an hour and volume change monitored until consolidation was completed. Shearing was started immediately after consolidation was completed. All the samples were sheared at a constant rate of strain of 0.025%/min, the same rate as used for shearing bonded samples. The details of the samples and the confining pressures applied are shown in Table 5.1. The identification of the tests refers to the type of test, the condition of sample and applied effective confining stress prior to shearing. The first two letters “cd” refer to the consolidated drained condition during shearing while the third letter “d” indicates the destructured type of sample being used for the test. Finally the numbers refer the value of confining stress used during isotropic consolidation of the sample.

### 5.2.2 Stress Strain Behaviour

The stress strain curves for all the tests are shown in Figure 5.1. All the tests generally show a linear increment of deviatoric stress,  $q$  at early strain and then the increment of  $q$  gradually decreases until it reaches the peak value. Then the deviator stress decreases gradually with increasing axial strain to the end of shearing. For the tests which were carried out at low confining pressures (cdd15, cddcd20, cdd50, cdd100 and cdd200) the peak values of  $q$  are reached at axial strain around 1%, then followed by a slight decrease in  $q$  with increasing axial strain. Meanwhile, for the rest of the tests that were sheared at higher confining pressures, the stress strain curves indicates an apparent peak in  $q$  and then a gradual decrease with further increase in axial strain. Samples carried out at higher confining pressures are also associated with the development of shear surfaces as a

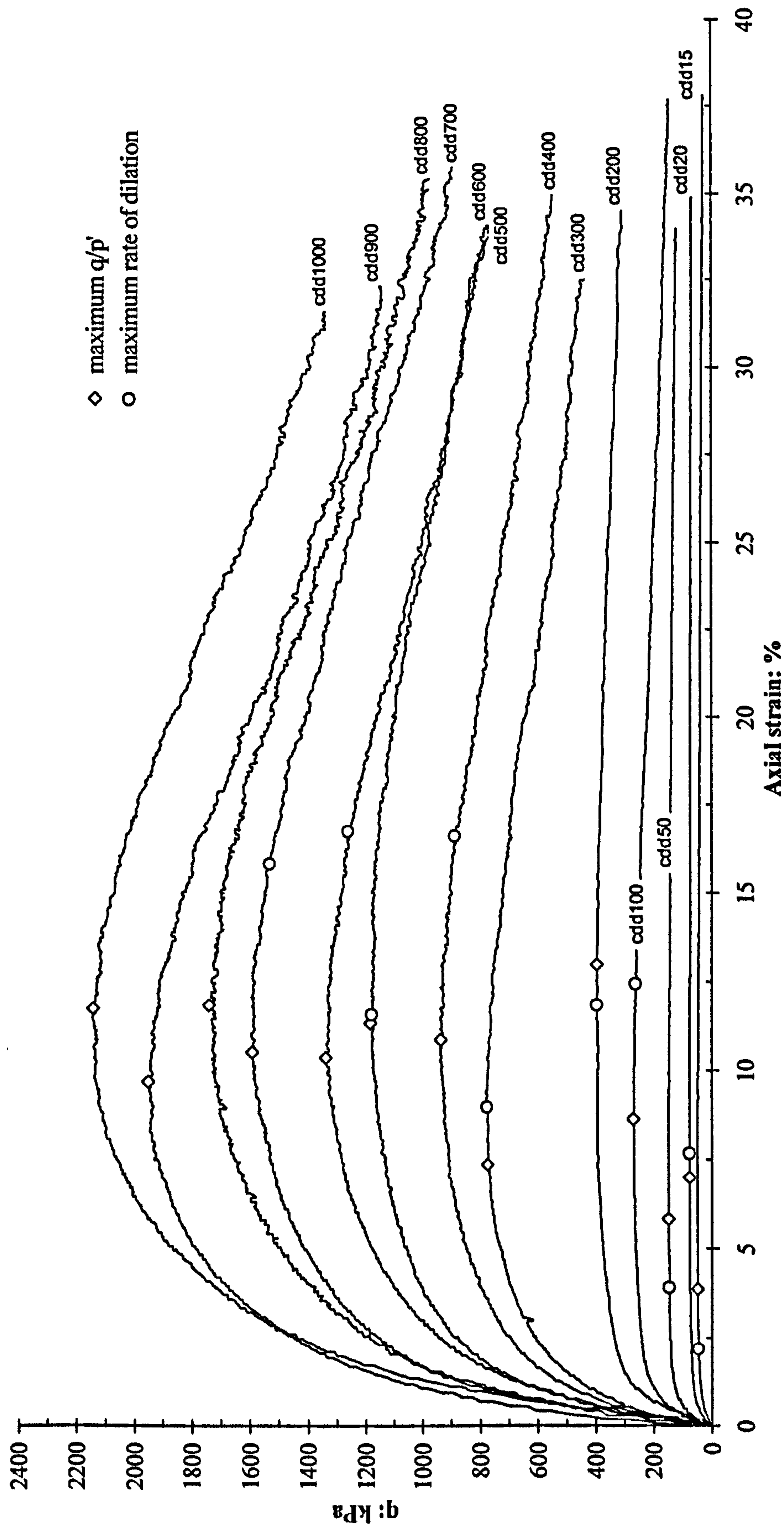


Figure 5.1: Stress-strain curves for the drained tests on destructured soils



result of strain non-uniformity, hence deviator stress continues to decrease to the end of shearing.

**Table 5.1: A series of drained tests on destructured samples**

<b>Test</b>	<b>Initial void ratio, <math>e_0</math></b>	<b>Confining pressure, kPa</b>
cdd15	0.6083	15
cdd20	0.6116	20
cdd50	0.6097	50
cdd100	0.6045	100
cdd200	0.6068	200
cdd300	0.6073	300
cdd400	0.5933	400
cdd500	0.6071	500
cdd600	0.6032	600
cdd700	0.6044	700
cdd800	0.6099	800
cdd900	0.6024	900
cdd1000	0.6017	1000

The volumetric strain curves for the tests are presented in Figure 5.2. Samples examined at lower confining pressures established smaller compression (positive values) at the beginning of the shearing then followed by strong dilation (negative values). Meanwhile, with increasing applied confining pressure, the compression becomes more apparent while on the other hand the degree of dilation gets smaller. The amount of axial strain at which the samples began to change from contraction to dilation behaviour also increased with the increase of confining pressure. Tests carried at lower confining pressures (cdd15, cdd20, cdd50 and cdd100) indicated small compression compared to the rest of the tests. Samples carried out at high confining pressures such as cdd800 and cdd1000 showed virtually no dilation. Many of the tests except tests cdd20, cdd50, cdd100 and cdd200, showed no

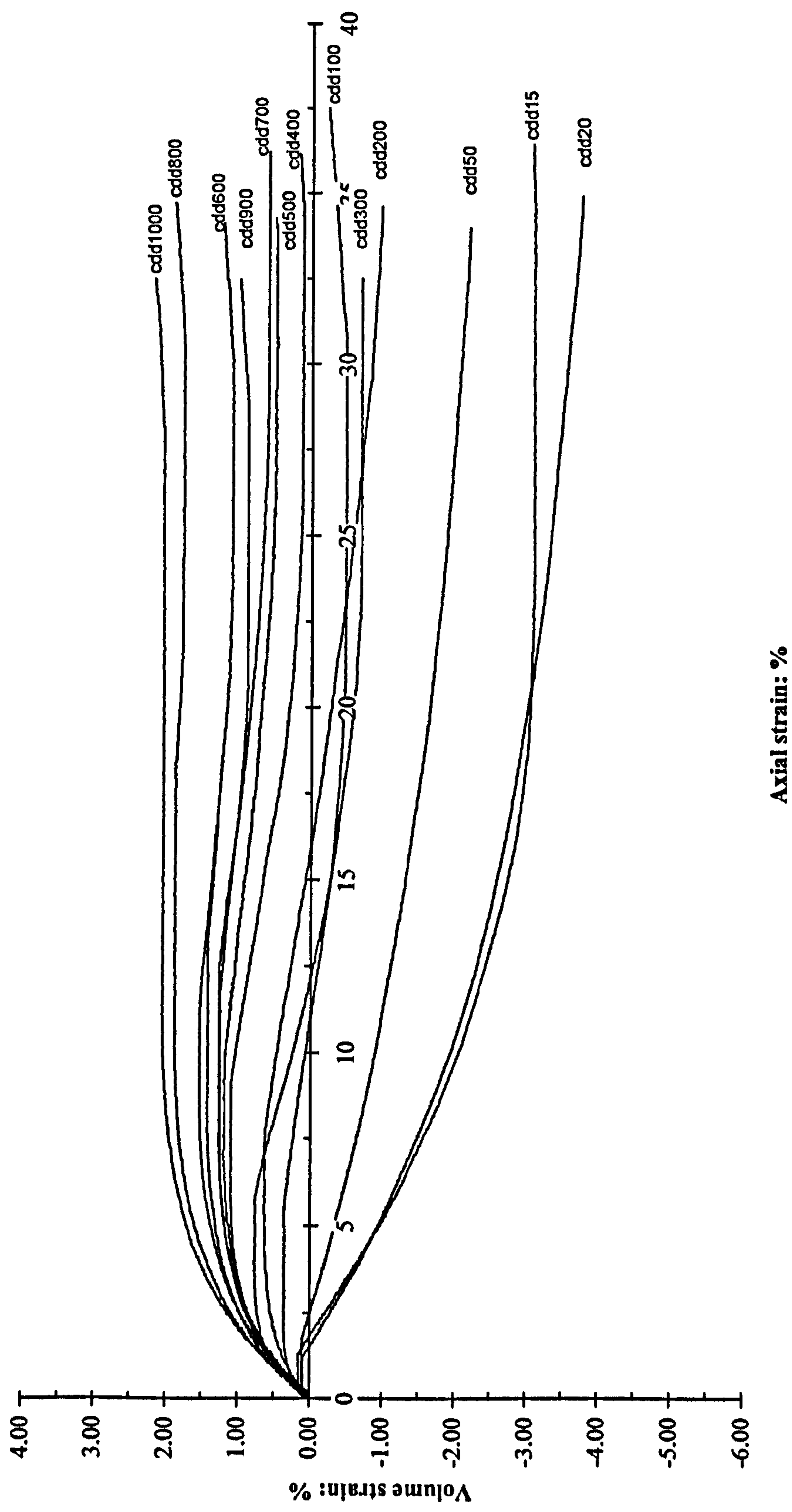


Figure 5.2: Volume strain curves against axial strain for the drained tests on destructured soils



significant change in volume of the samples toward the end of the test (>20% strain), suggesting that the tests achieved their critical state at the end of shearing. However, if compared to the stress strain curves (Figure 5.1) for tests carried out at lower confining pressures, cdd20 up to cdd200 showed constant  $q$  to the end of the tests therefore those tests fulfilled that criteria for the critical state.

### 5.2.3 Peak Strength, Stress Paths and Bounding Surface

As explained in Chapter 2, the peak stress ratio  $q/p'$  is related to the rate of dilation by  $q/p' = M - (\delta\epsilon_v/\delta\epsilon_s)$ . Taylor's equation is easier to understand in its generalised form and was used in this work for qualitative study. The position of the maximum rate of dilation of each test on bonded samples was calculated from  $\delta\epsilon_v/\delta\epsilon_a$  and plotted against axial strain,  $\epsilon_a$  (Figure 5.3). The maximum  $q/p'$  ratio and the maximum rate of dilation points are also marked on the stress strain curves in Figure 5.1. The positions of these two points are not coincident. For tests cdd15, cdd20, cdd50, cdd200, cdd300 and cdd500, the two points are reasonably close to each other. Meanwhile, for the other tests the two points were located further apart. Generally, the two points seem to move apart further with the increase of the confining pressures (except for cdd500). For tests cdd800 and cdd1000, the point for maximum rate of dilation could not be defined because these tests were associated with contraction behaviour up to the end of shearing.

The effective stress paths for the drained tests on destructured samples are presented in Figure 5.4. This figure clearly suggests that the higher the confining pressure, the higher the maximum deviator stress,  $q$  achieved. Meanwhile the bounding surface and the phase transformation lines are shown in Figure 5.5. The bounding surface was constructed from the maximum  $q/p'$  ratio values. The phase transformation line was plotted using the point where the behaviour changed from contraction to a dilative tendency. The plotted values of maximum  $q/p'$  ratio can be fitted with a straight line with  $q/p'=1.25$ . This gives an equivalent angle of friction,  $\phi'$  and cohesion intercept,  $c'$  of  $31^\circ$  and 23kPa, respectively. However

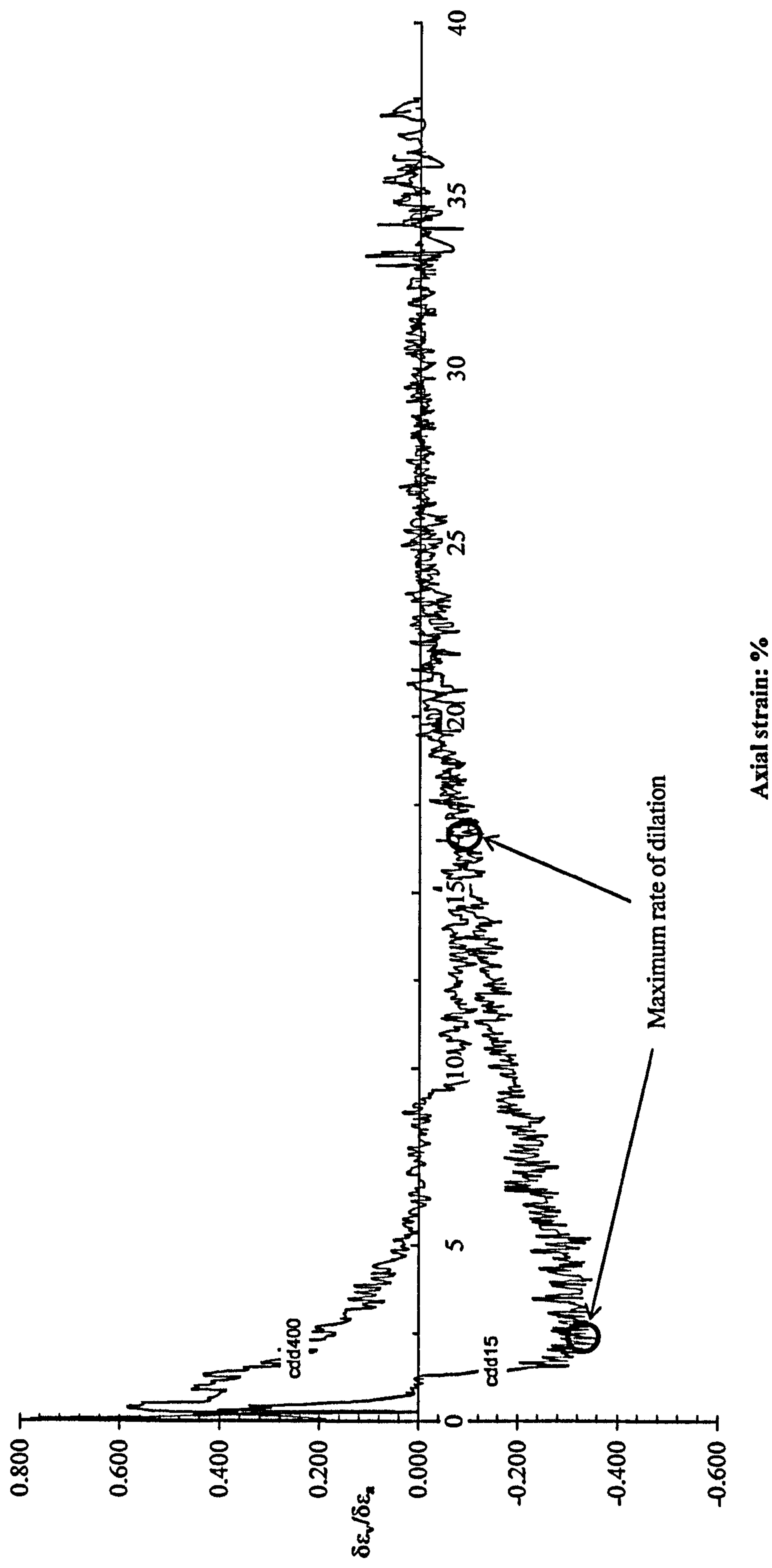


Figure 5.3: The definition of the maximum rate of dilation from the curves (e.g. cdd15 and cdd400)



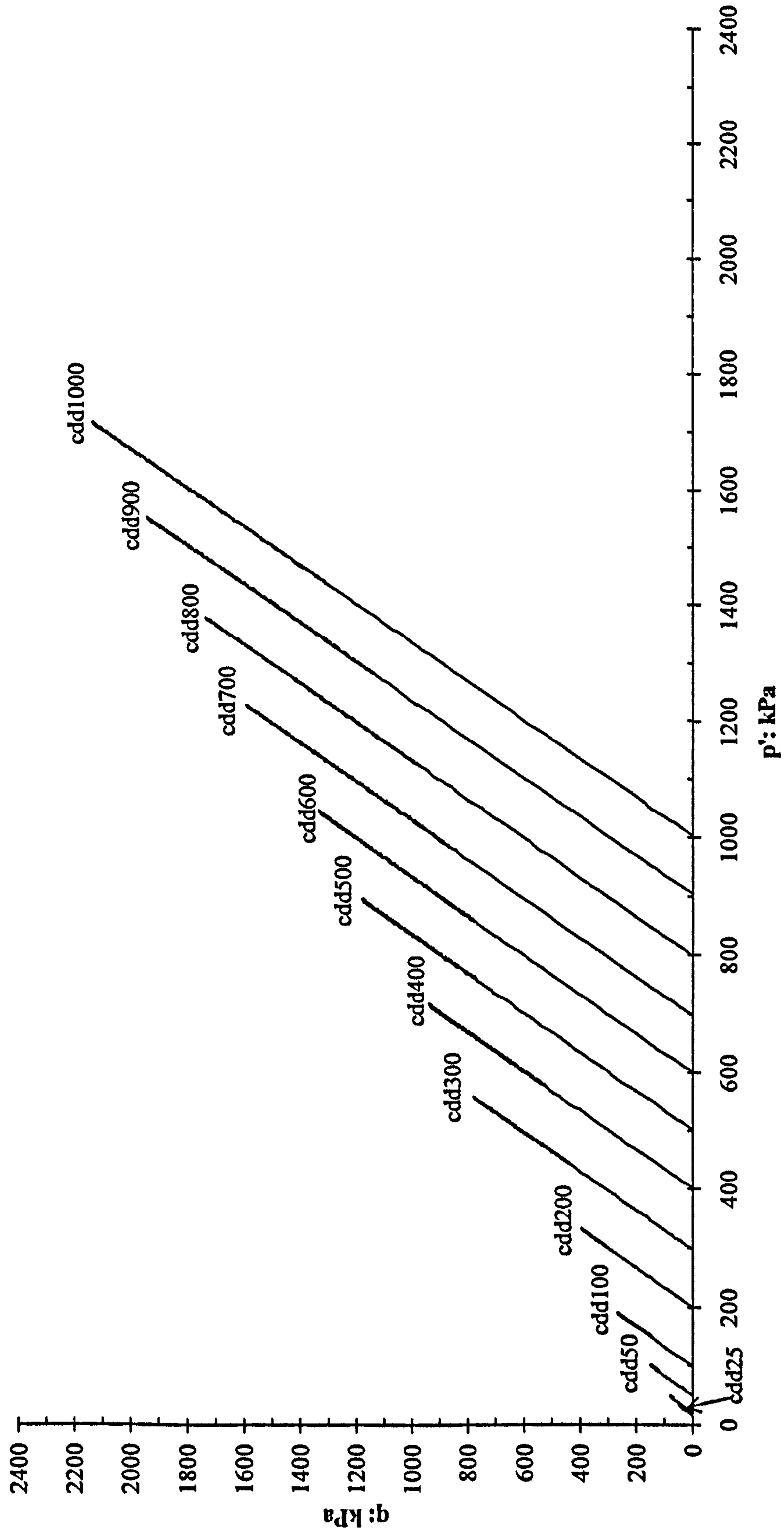


Figure 5.4: Effective stress paths for the drained tests on destructured soils

some curvature can be clearly seen at stress level below 500kPa. The equivalent  $q/p'$  ratio for the bounding surface line is lower than equivalent values achieved from previous tests carried out by Malandraki ( $q/p'=1.32$ ,  $\phi'=33^\circ$  and  $c'=29\text{kPa}$ ). The equivalent value of  $q/p'$  ratio for the phase transformation line is 1.27, slightly higher than the value defined from the bounding surface. However this line is almost parallel to the bounding surface, again showing some curvature below 500kPa.

The  $q/p'$  ratio value against axial strain for the destructured samples is shown in Figure 5.6. The position of the phase transformation and maximum rate of dilation are also marked on each curve. For samples at lower confining stresses, the phase transformation point occurs at lower axial strain ( $<2.5\%$ ) and increases with an increase in confining pressure. Tests carried out at lower confining pressures also achieved higher maximum  $q/p'$  ratios than samples consolidated at higher stress levels. This is consistent with the apparent cohesion intercept shown in Figure 5.5. However, all the tests showed a very similar pattern which did not show any significant peak of  $q/p'$  ratio.

### **5.3 UNDRAINED TRIAXIAL TESTS**

The results of the undrained tests on destructured samples are presented and described in this section. The results from the undrained tests are discussed in terms of deviator stress,  $q/p'$  ratio and pore water pressure against axial strain. The bounding surface and phase transformation line are also presented in the stress space.



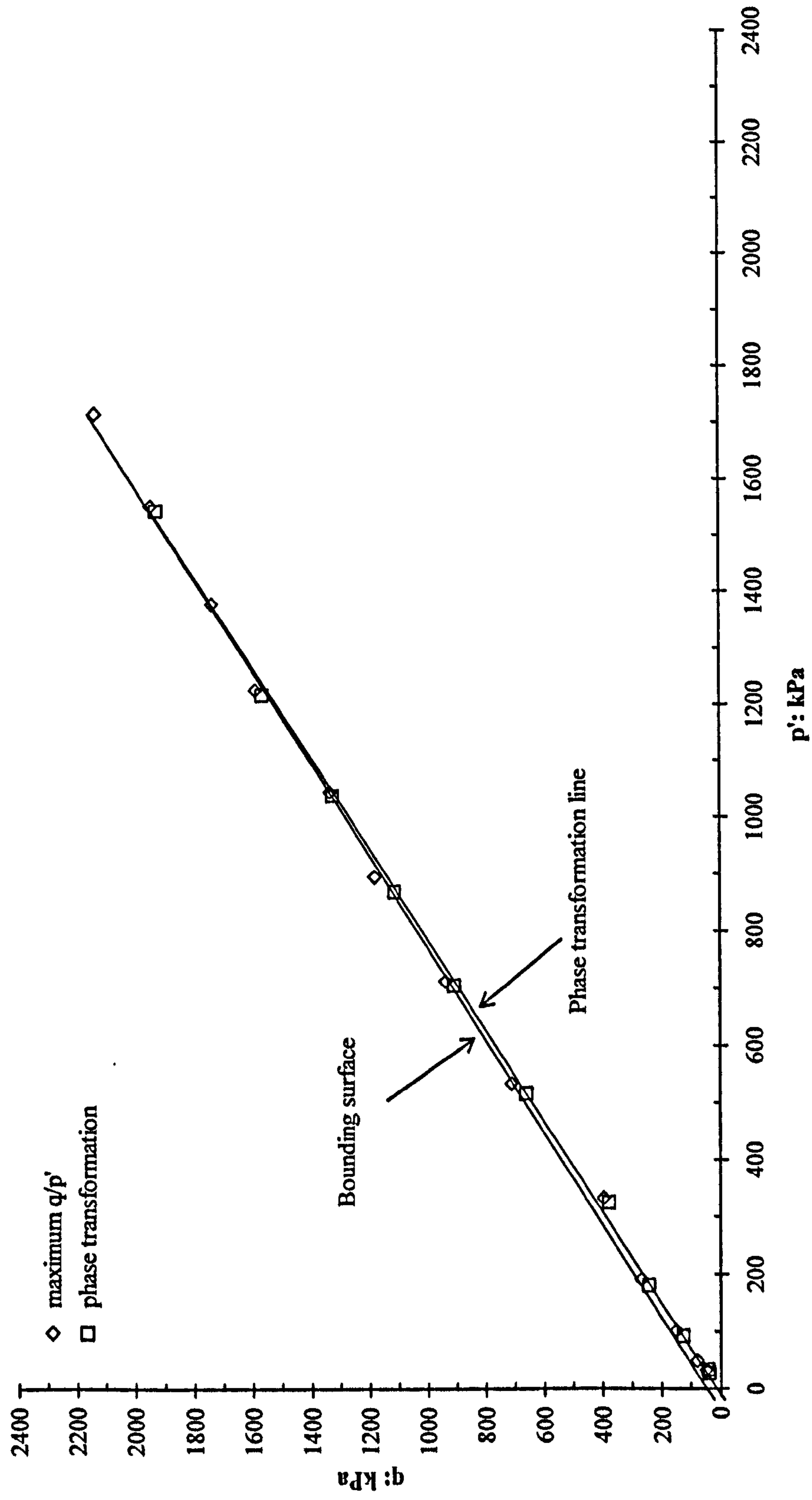


Figure 5.5: Bounding surface and phase transformation lines for the drained tests on destructured soils

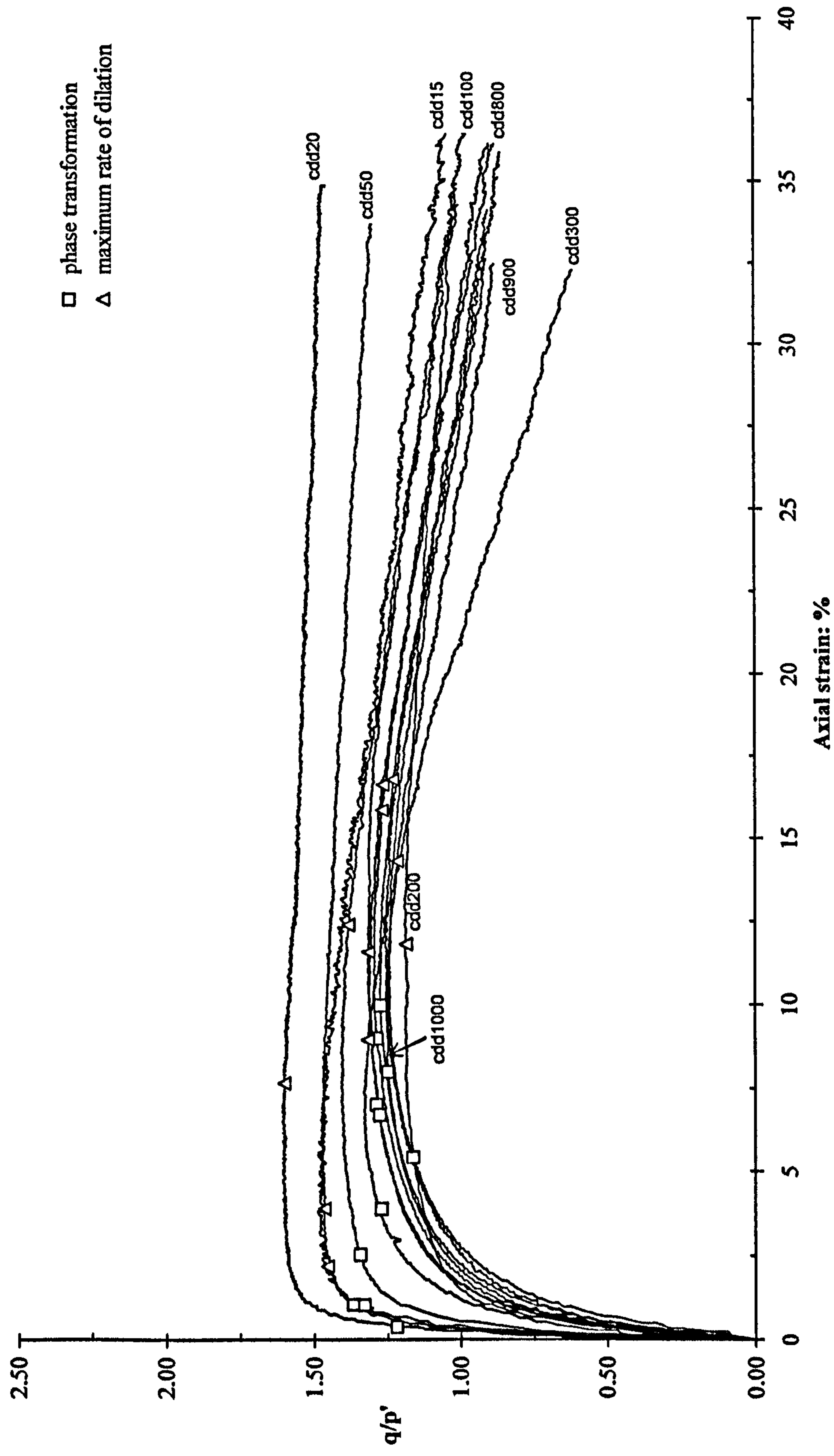


Figure 5.6: Stress ratio,  $q/p'$  against axial strain for the drained tests on destructured soils



### 5.3.1 Description of Testing

Eleven destructured samples were examined using the conventional undrained triaxial compression test. Samples were prepared in the same manner as the drained tests. Prior to shearing, samples were initially isotropically consolidated under different confining pressures from 25 kPa up to 1 MPa. The consolidation procedure and the rate of strain of 0.025%/min, was the same as used for drained testing. The details of the samples and the confining pressures applied are shown in Table 5.2. The identification of the tests was based on type of test, condition of sample and applied confining stress prior to shearing. The first two letters “cu” refer to the consolidated undrained condition during shearing while the third letter “d” indicates the destructured type of sample being used for the test. Finally the numbers refer the value of confining stress used during isotropic consolidation of the sample.

### 5.3.2 Stress Strain Behaviour

The stress strain, pore water pressure change and stress ratio curves for all the tests are shown in Figure 5.7, 5.8 and 5.9. The deviatoric stress values increased up to the maximum shear strength before decreasing gradually to the end of shearing. Failure of the samples was mainly associated with the presence of shear surfaces. There is no sharp peak in deviatoric stress for these tests. Most of the samples reached their maximum shear strength at axial strain,  $\epsilon_a$  approximately at 20% before starting to decrease in deviator stress,  $q$ . Some of the tests showed bulging failure modes during shear (cud-25, 60, 200 and 600).

In terms of pore water pressure, all the tests developed initial positive pore water pressure at the early stage of shearing which reached maximum values at axial strain,  $\epsilon_a$  less than 5% before decreasing to lower values. In general, the amount of the initial positive pore water pressures increased with the increase of applied effective confining pressure. All the samples also showed a renewed increase of pore water pressure after reaching a lowest value (after 20% strain). The samples

that were initially consolidated under confining pressure up to 400 kPa showed a negative pore water pressure before bouncing back up to positive values near the end of shearing (except for cud25, cud60 and cud200). For cud25, cud60 and cud600 the excess pore water pressure continued to decrease right to the end of shearing. Meanwhile for cud500 to cud1000, the pore water pressure only decreased within the positive range before increasing again near to the end of shearing. The pore water pressures for all the tests were still changing up to the end of the shearing suggesting that the samples did not achieve their true critical state or probably were caused by the strain localisation.

Table 5.2: The undrained tests on destructured samples

Test	Initial void ratio, $e_0$	Confining pressure, kPa
cud25	0.6048	25
cud60	0.6103	60
cud100	0.6018	100
cud200	0.6048	200
cud300	0.6103	300
cud400	0.6097	400
cud500	0.6022	500
cud600	0.6152	600
cud700	0.6092	700
cud800	0.6047	800
cud1000	0.6113	1000

The maximum stress ratio,  $q/p'$  and maximum rate of change in excess pore water  $\Delta u/\Delta \epsilon_a$  are also marked on the stress strain curves (Figure 5.7). The occurrences of the two points are not coincident. The maximum rate of pore water pressure change always occurs after the maximum  $q/p'$ . For samples that were isotropically consolidated at lower than 200 kPa, the position of these two points is more distant



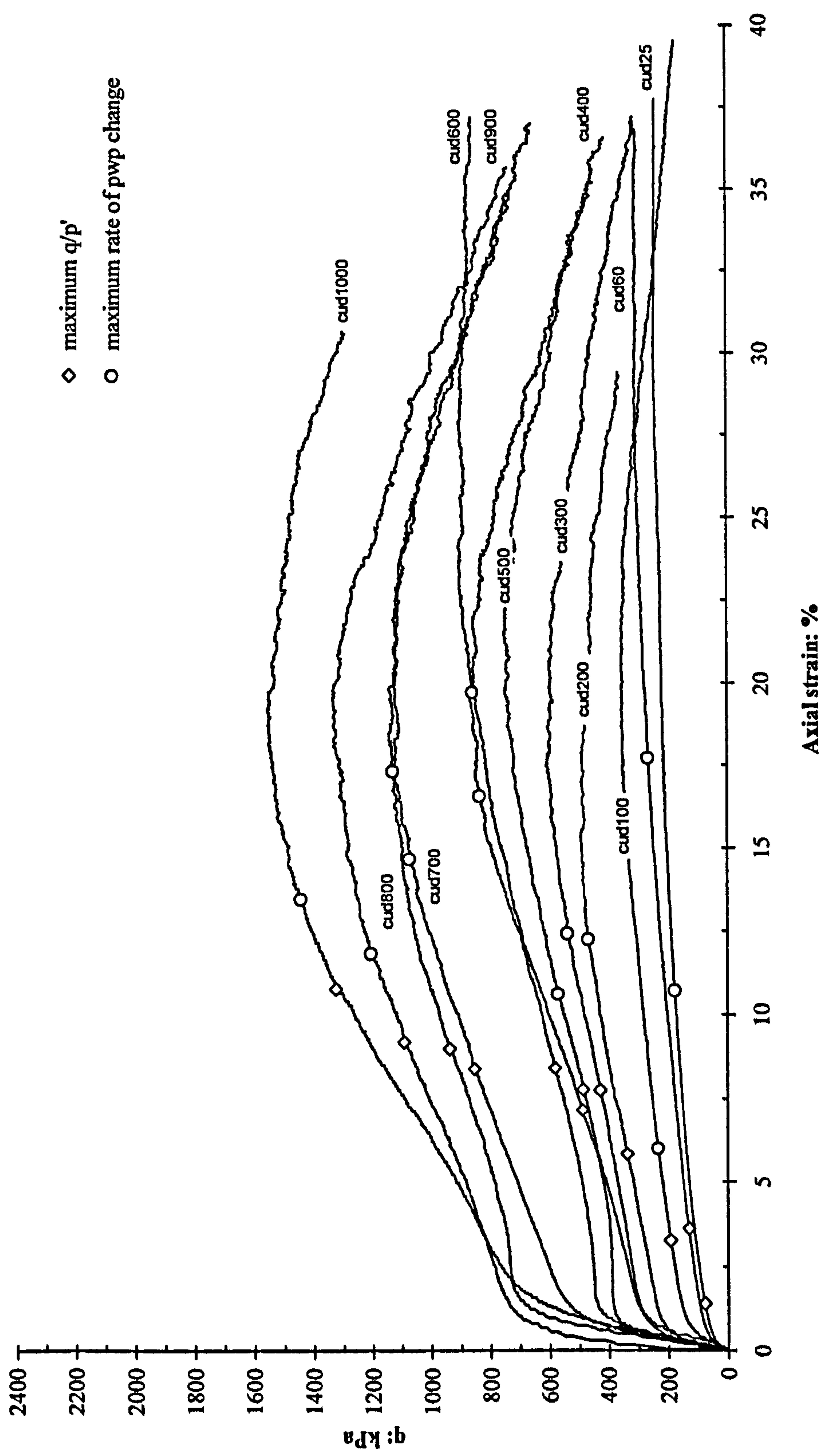


Figure 5.7: Stress-strain curves for the undrained tests on destructured soils

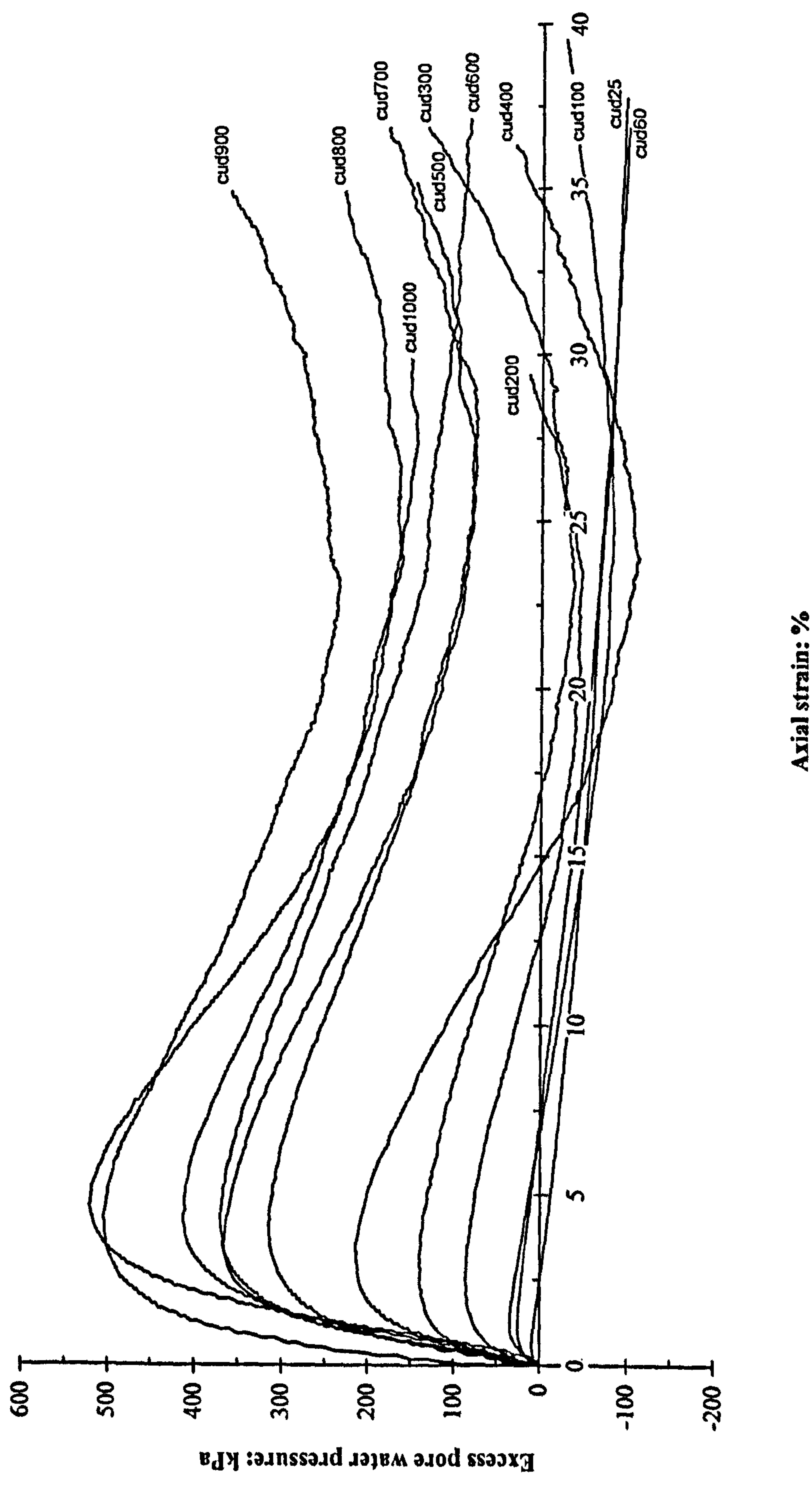


Figure 5.8: Excess pore water pressure against axial strain for the undrained tests on destructured soils



than for samples tested at higher confining pressures. This is particularly true for samples that failed in bulging mode such as cud25, cud60, cud200 and cud600. For the samples that failed due to initiation of shear planes, the stress ratio began to decrease with increasing axial strain (Figure 5.9). From the stress ratio,  $q/p'$  curves it can be seen that samples initially consolidated at lower confining stress (cud25 and cud60) achieved higher maximum  $q/p'$  (1.5 and 1.7, respectively) compared to the rest of the tests (between 1.2 and 1.4). However, the destructured samples consolidated at lower confining stress do not show a significant peak of  $q/p'$  and the values become smaller for samples consolidated at higher confining stress. It was also found that the maximum pore water pressure occurs before the maximum  $q/p'$  ratio and this is then followed by the maximum rate  $\Delta u/\Delta \epsilon_a$  (Figure 5.9). Samples tested at lower confining pressures indicate that the maximum rate of  $\Delta u/\Delta \epsilon_a$  points is even further from the maximum  $q/p'$  ratio (cud25 and cud 60).

### 5.3.3 Stress Paths and Bounding Surfaces

The effective stress paths of the destructured samples are plotted in stress space in Figure 5.10. From the figure, it is clearly seen that almost all the samples follow a similar stress path pattern. For samples tested at lower stresses ( $<200\text{kPa}$ ), stress paths moved to the right corresponding to the increasing negative pore water pressure. Meanwhile for higher stress level, stress paths tend to move to the left, more significantly with increasing confining pressures. After that the paths continue to climb gradually along a fairly constant stress ratio up to failure. The  $q/p'$  stress ratio values started to drop significantly whenever a shear surface developed in the samples. Some of the samples continue to higher stress along the linear line as associated with bulging type of failure (with no initiation of shear surface).

The bounding surface for the destructured samples is plotted in Figure 5.11. The maximum  $q/p'$  points define a straight line representing the bounding surface with

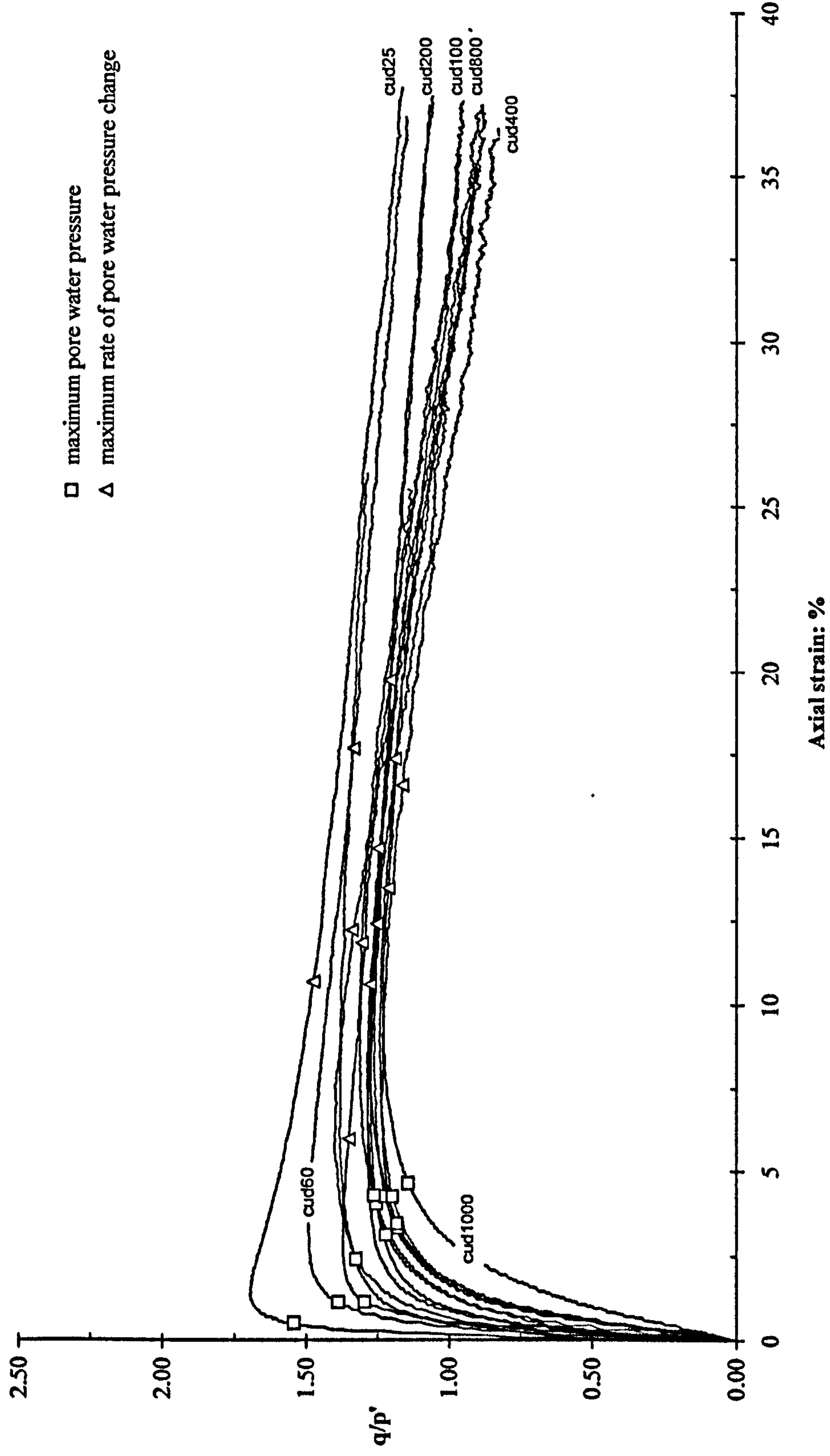


Figure 5.9: Stress ratio,  $q/p'$  against axial strain for the undrained tests on destructured soils



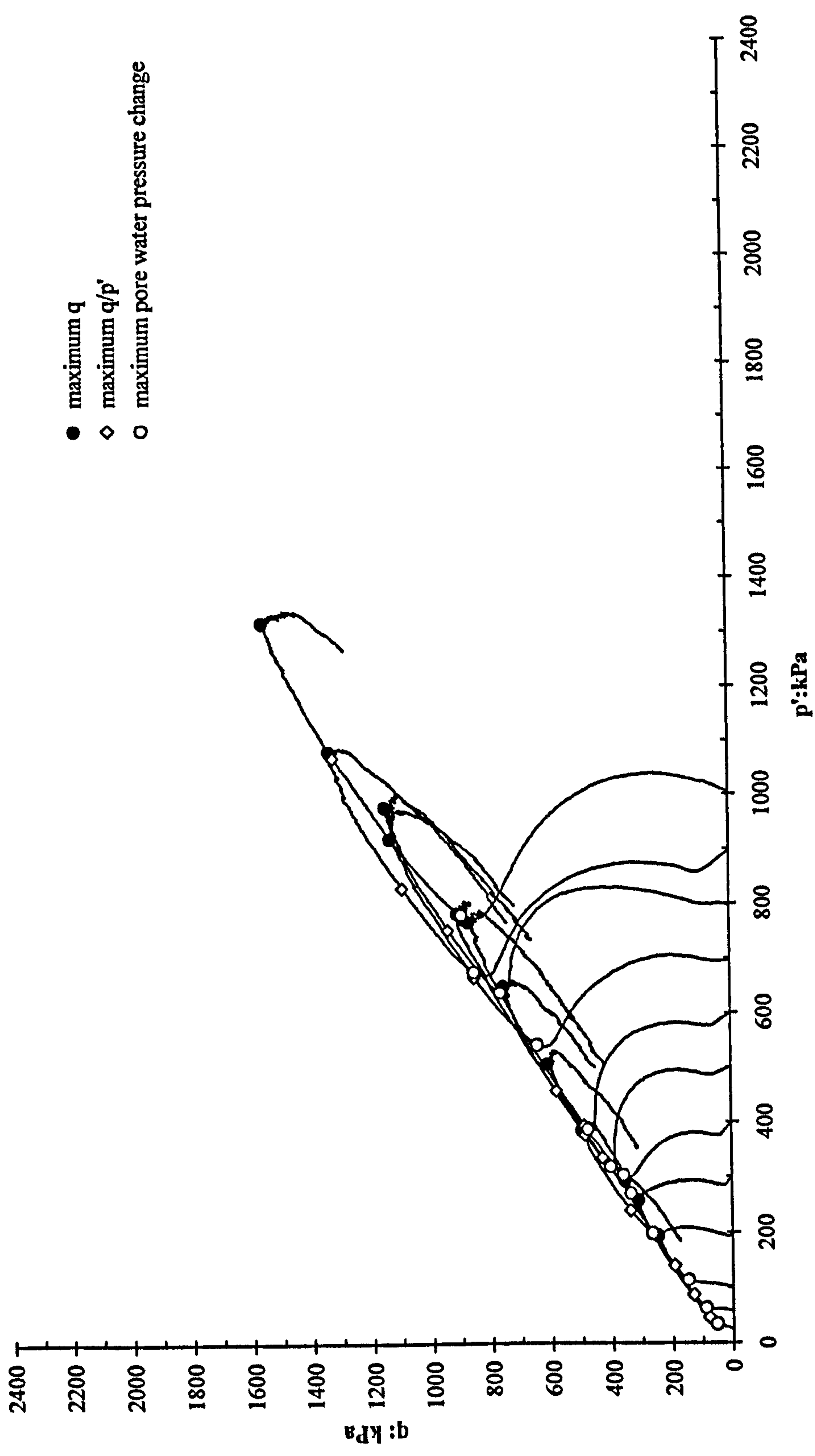


Figure 5.10: Effective stress paths for all the undrained tests on destructured soils

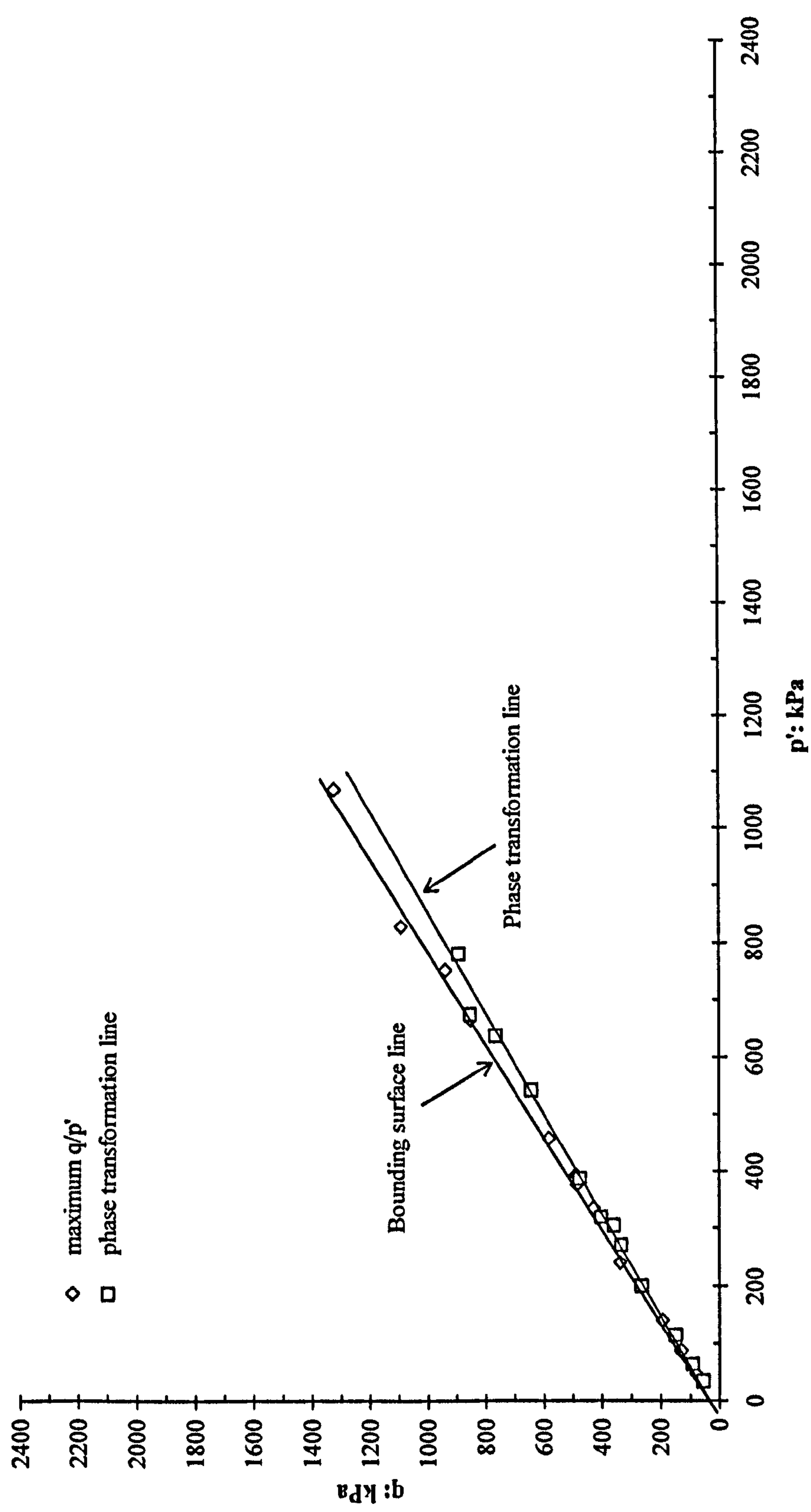


Figure 5.11: Bounding surface and phase transformation lines for the undrained tests on destructured soils



$q/p'$  value equivalent to 1.24. This value is quite close to the value obtained by Malandraki (1994) ( $q/p'=1.26$ ). The equivalent values of angle of friction,  $\phi'$  and cohesion intercept,  $c'$  are  $30.9^\circ$  and 21kPa, respectively. The phase transformation line is also plotted based on the point of maximum pore water pressure. This is the where the behaviour changes from a contractive tendency to a dilative tendency and the pore water pressures start to drop. The phase transformation line has a smaller value of  $q/p'$  equivalent to 1.17.

## **5.4 COMPARISON BETWEEN DRAINED AND UNDRAINED BEHAVIOUR OF DESTRUCTURED SAMPLES**

### **5.4.1 Stress Ratios for Destructured Samples**

The  $q/p'$  ratio values for the destructured samples from the two types of tests are plotted against axial strain. Comparison of the development of  $q/p'$  ratio were carried out at low ( $p_o'=15\text{kPa}$  to  $60\text{kPa}$ ), intermediate ( $p_o'=300\text{kPa}$  to  $500\text{kPa}$ ) and high ( $p_o'=900\text{kPa}$  and  $1000\text{kPa}$ ) confining pressures (Figure 5.12a, 5.12b and 5.12c).

At lower confining pressures, the  $q/p'$  ratio for the destructured samples sustain higher values than that for similar samples at higher confining pressures. Figure 5.12a shows maximum  $q/p'$  ratio between 1.47 and 1.70. The undrained tests indicate a peak  $q/p'$  ratio meanwhile no apparent peak stress ratio was observed from the drained tests (except cdd15). For most of the tests, the maximum  $q/p'$  ratio was achieved at axial strains between 5%-10% (except test cud25). At the end of the shearing, most of the tests (except cdd20 and cdd50) show quite close stress ratio values, while for tests cdd20 and cdd50, the stress ratio values settle at slightly higher  $q/p'$  between 1.32 and 1.50. However in most of the tests, the  $q/p'$  ratios are decreasing towards the end of shearing due to the development of shear surfaces.

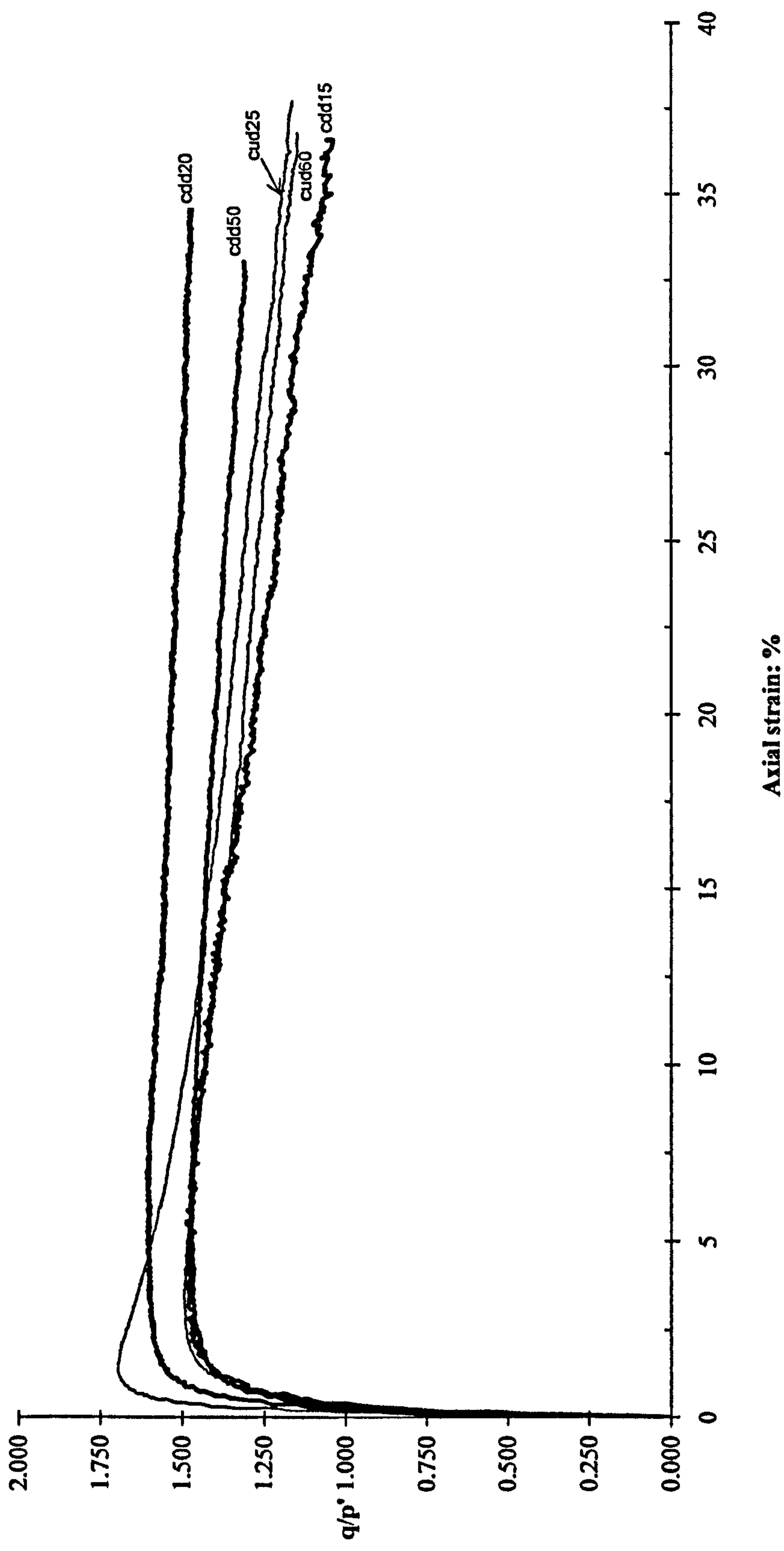


Figure 5.12a: The  $q/p'$  ratio versus axial strain for the drained and undrained tests on destructured soils at lower confining pressures



Figure 5.12b shows the stress ratio against axial strain for similar samples under the drained and undrained tests sheared at 300, 400 and 500kPa confining pressures. It is clearly seen that the maximum  $q/p'$  ratio values fall between 1.32 – 1.33 for the drained and between 1.24 – 1.29 for the undrained tests. These are lower in comparison to the tests carried out at lower confining pressures. From the figure, it can be seen that the maximum  $q/p'$  ratio is also achieved at a similar range of axial strain (around 5%) for the drained and undrained tests sheared at lower confining pressures. Samples sheared at this stress level indicate no clear peak of  $q/p'$  ratio and the stress ratios begin to drop toward the end of the tests. It seems that the  $q/p'$  ratio curve are getting closer to each other (except test cdd300 for which the stress ratio drops significantly to a low value).

Figure 5.12c shows the  $q/p'$  ratio for the drained and undrained test of the destructured samples sheared at high confining pressures of 900kPa and 1000kPa. The maximum  $q/p'$  ratio values for the two types of tests coincide (except cud900, although it is still close to the rest of the tests). At this level of confining pressures, the maximum  $q/p'$  ratio values for the drained and undrained samples are between 1.24 – 1.32 close to the maximum stress ratio for samples that were sheared at the intermediate range of confining pressures (300 – 500kPa). However, the maximum  $q/p'$  ratio values are achieved at higher axial strain (around 10%).

#### 5.4.2 Bounding Surface for Destructured Samples

The bounding surfaces for the destructured samples from the drained and undrained tests are shown in Figure 5.13. The bounding surfaces for both tests represented by a straight line and almost coincide up to the stress level,  $p' = 700$ kPa. At higher stress level, the bounding surfaces for the drained and undrained tests slightly diverge. The equivalent value of the angle of friction,  $\phi'$ , and the cohesion intercept,  $c'$ , for the bounding surface line is  $31^\circ$  and 22kPa, respectively.

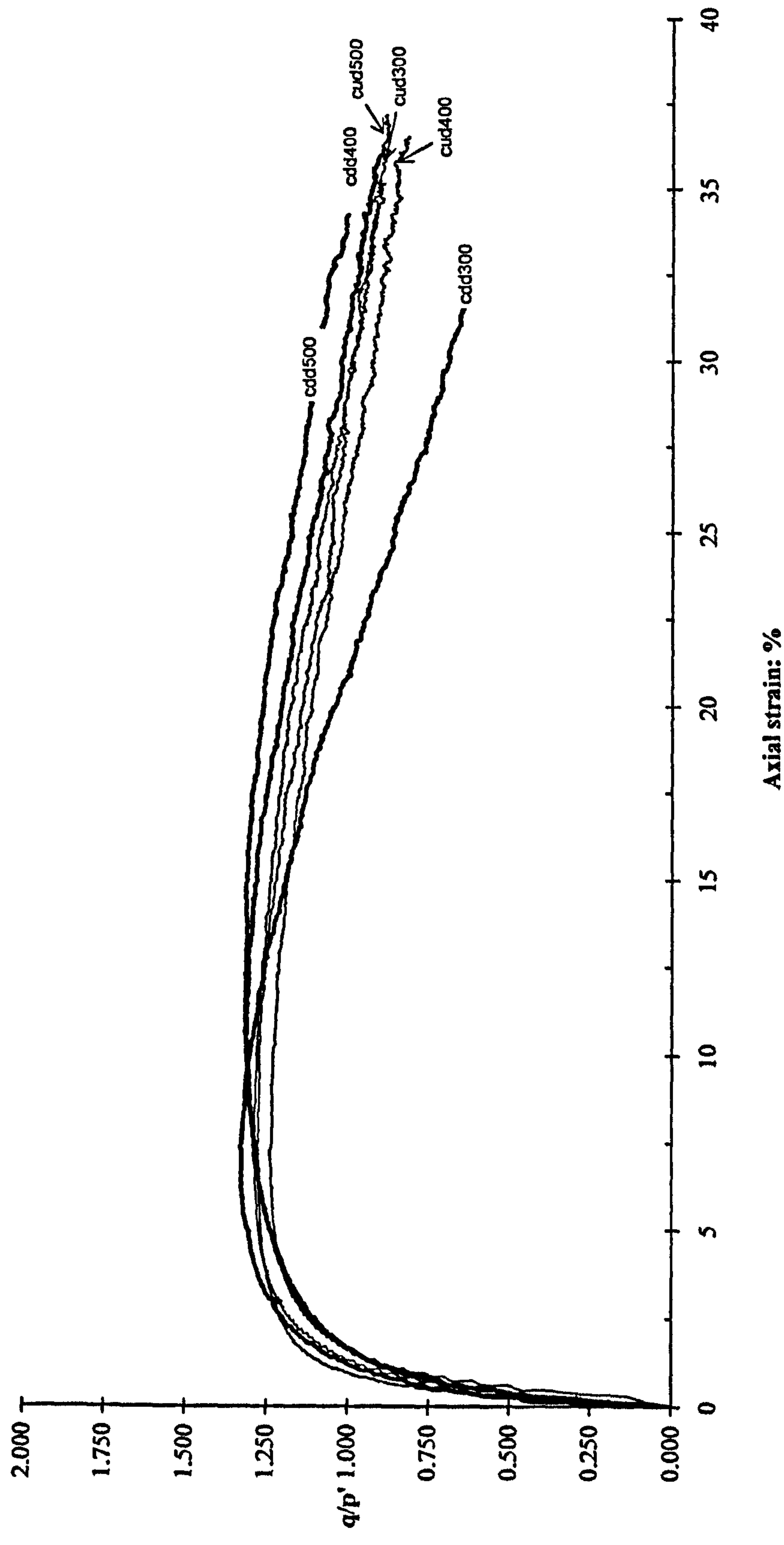


Figure 5.12b: The  $q/p'$  ratio versus axial strain for the drained and undrained tests on destructured soils at intermediate confining pressures



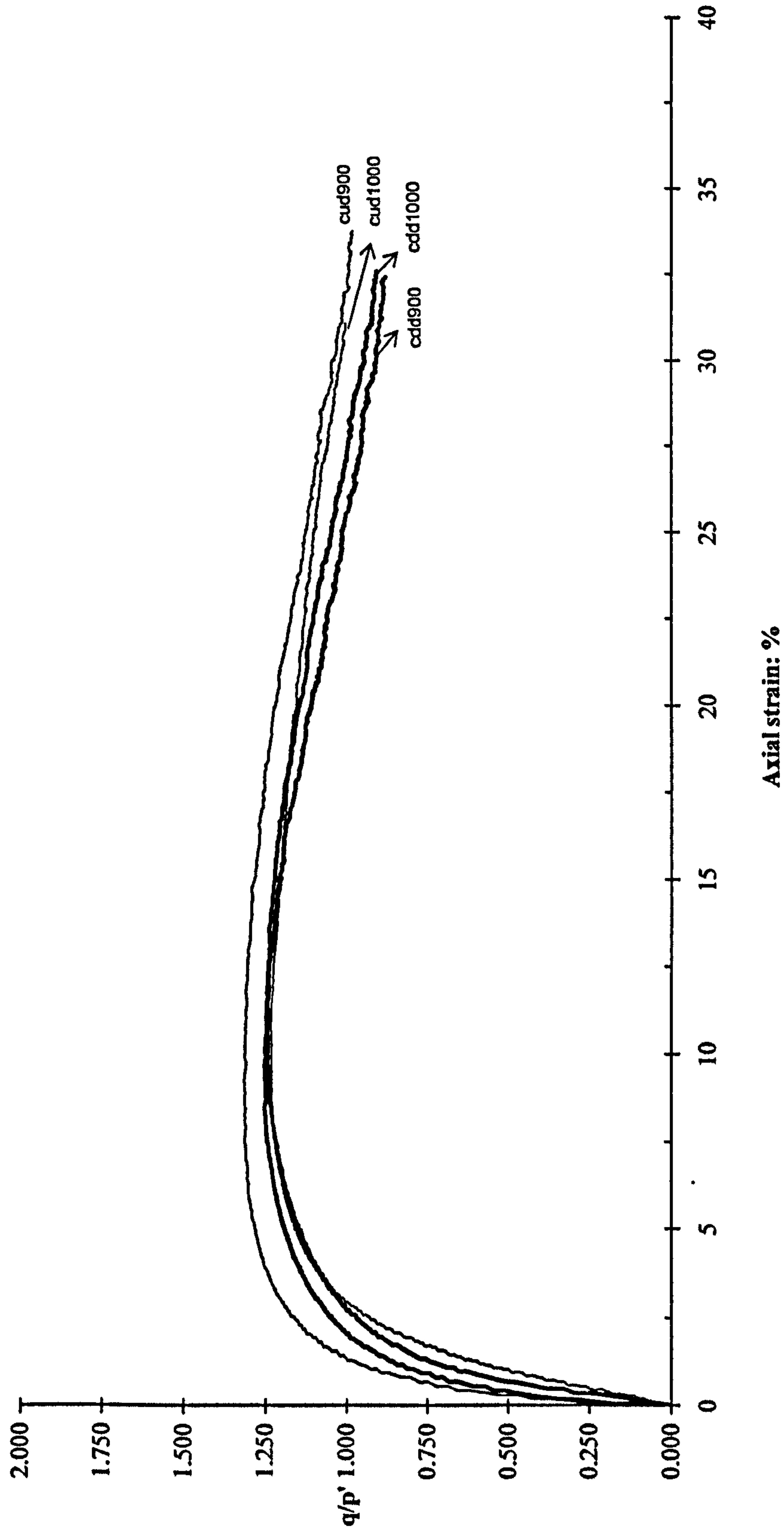


Figure 5.12c: The  $q/p'$  ratio versus axial strain for the drained and undrained tests on destructured soils at high confining pressures

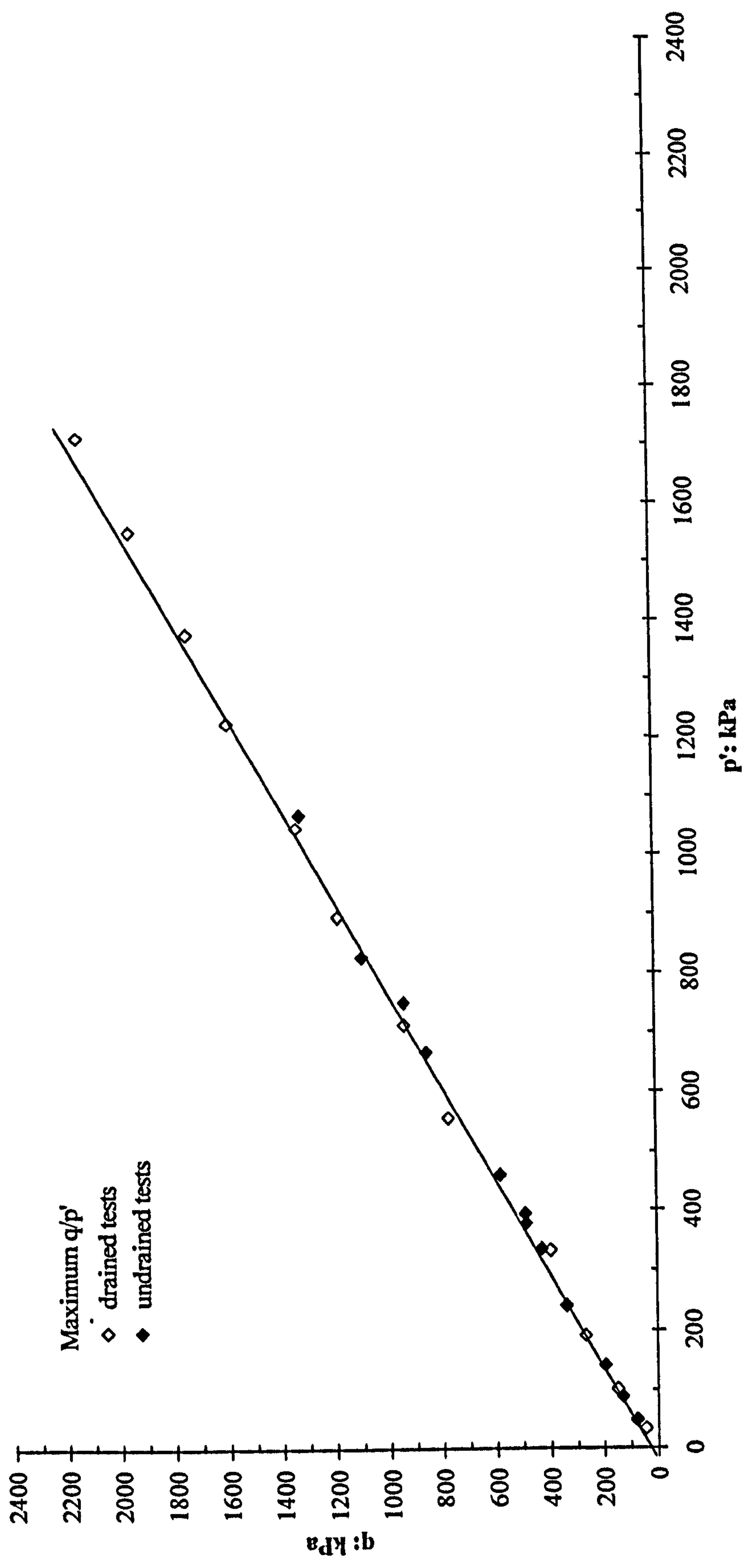


Figure 5.13: Bounding surface lines for the drained and undrained tests on destructured samples



Figure 5.14 shows the phase transformation lines for the drained and undrained tests for the destructured samples. The phase transformation line for the two tests are defined by a straight line and almost coincide at lower stress level,  $p' < 200\text{kPa}$ . At higher stress level of  $p' > 200\text{kPa}$ , these two lines apparently diverge from each other.

## **5.5 CRITICAL STATE OF DESTRUCTURED SAMPLES**

### **5.5.1 The Critical State**

As mentioned in Chapter 2, the definition of the “true” critical state is not always easy. In order to define the critical state for the destructured samples from the saturated triaxial tests, the stress strain, stress path and  $e - p'$  (or  $v - p'$ ) spaces were initially studied carefully. Figure 5.15 shows the curves of the drained tests in  $v - p'$  space. There were some difficulties in defining the critical state from the drained tests. The deviatoric stress,  $q$  and volumetric strain for most of the tests still continue to change up to the end of the tests (Figure 5.16a and Figure 5.16b). Hence, the critical state for the drained tests was defined based on the assessment on the void ratio paths in  $v - p'$  space (Figure 5.15). Based on the assessment of  $v - p'$  curves, for the samples sheared at low and medium range of confining pressures, they indicate initially a contracting behaviour with increasing  $p'$  before switching to dilatant behaviour. Meanwhile, for the samples sheared at high stress levels, they showed contracting behaviour throughout and then failed at the end of shearing. Based on this observation, the selection of critical state should be separated according to these two types of behaviour. Samples associated with

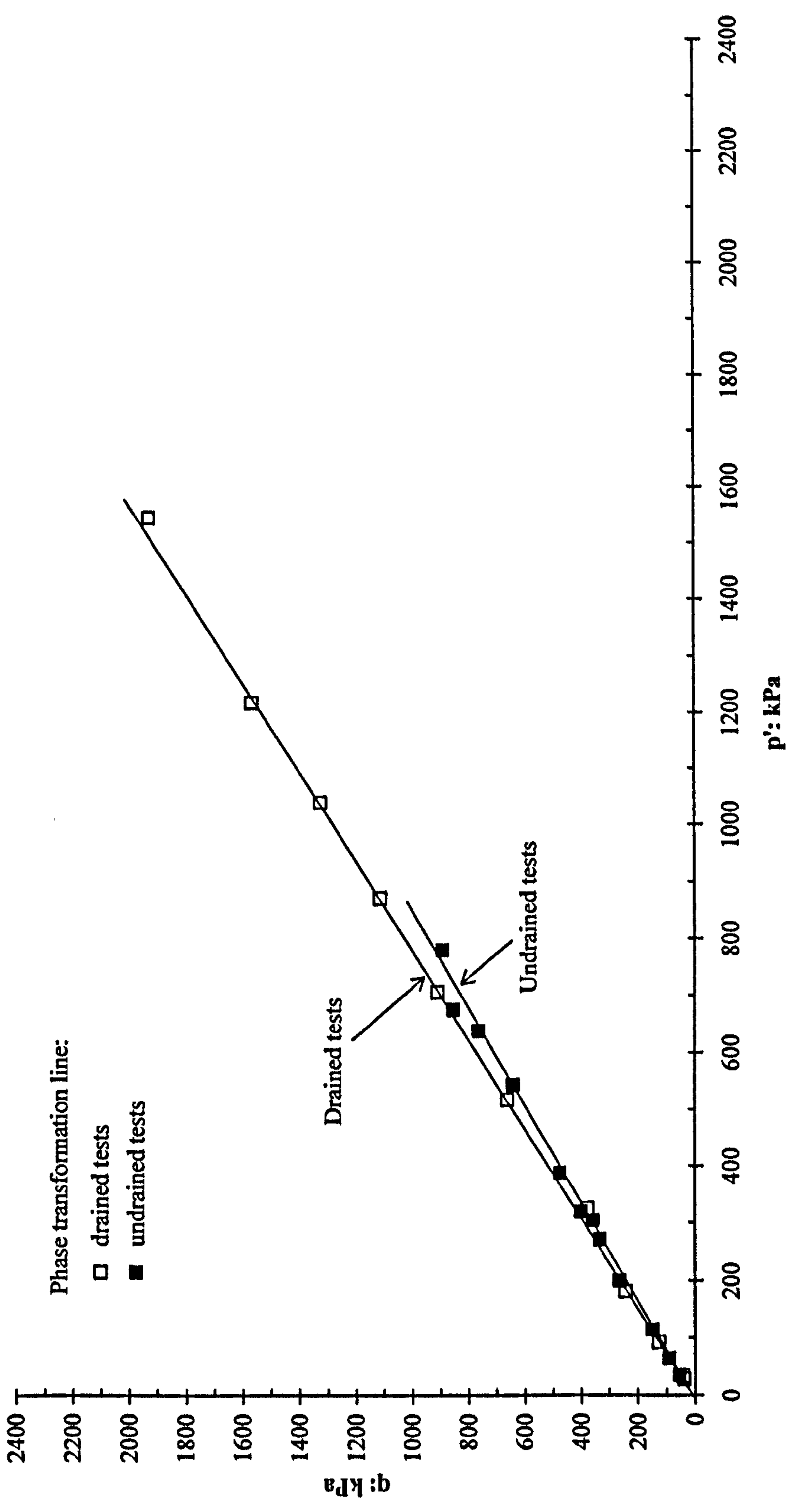


Figure 5.14: Phase transformation lines for the drained and undrained tests on destructured samples



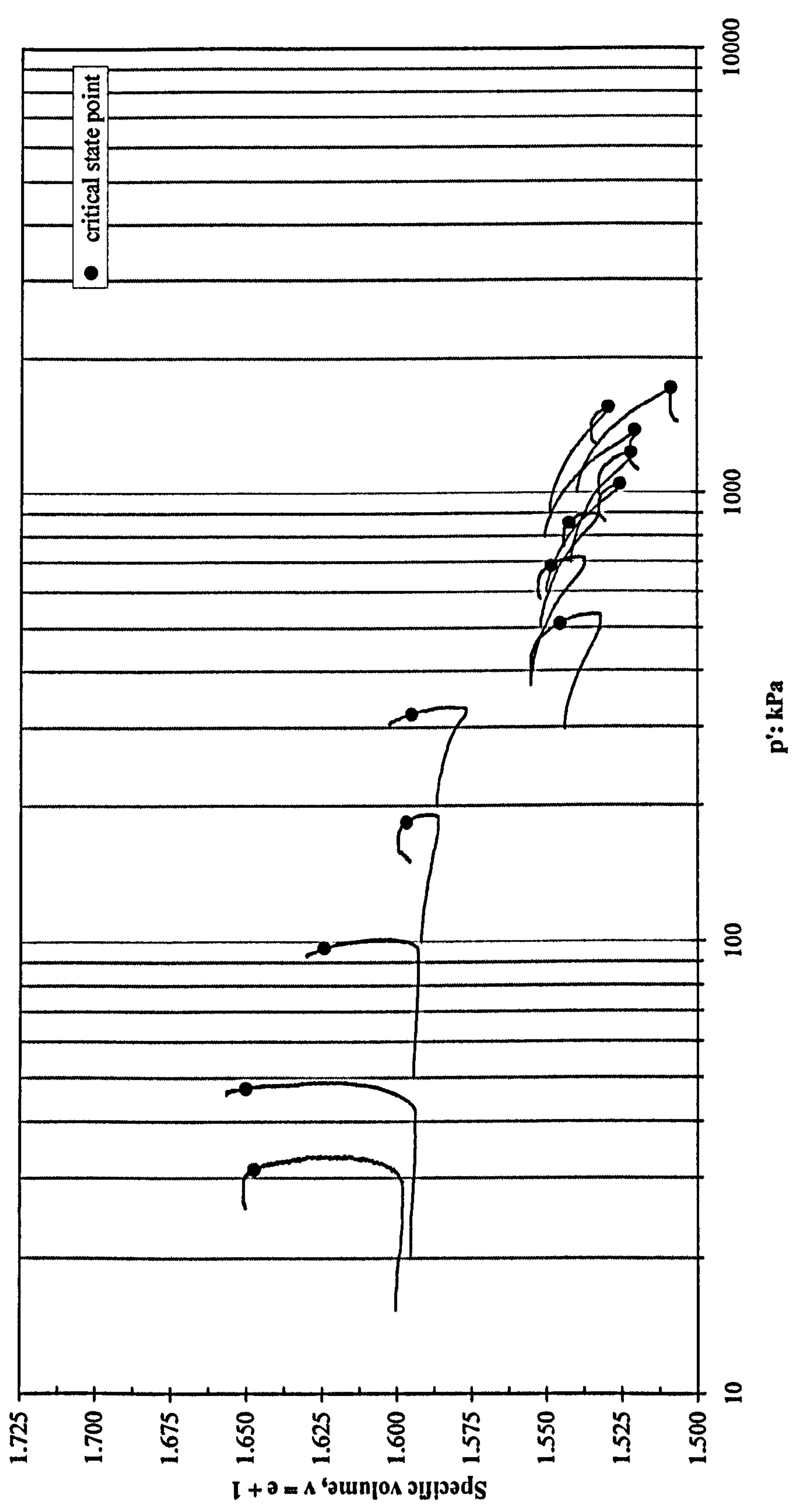


Figure 5.15: Paths followed by drained tests on destructured samples in  $v - p'$  space

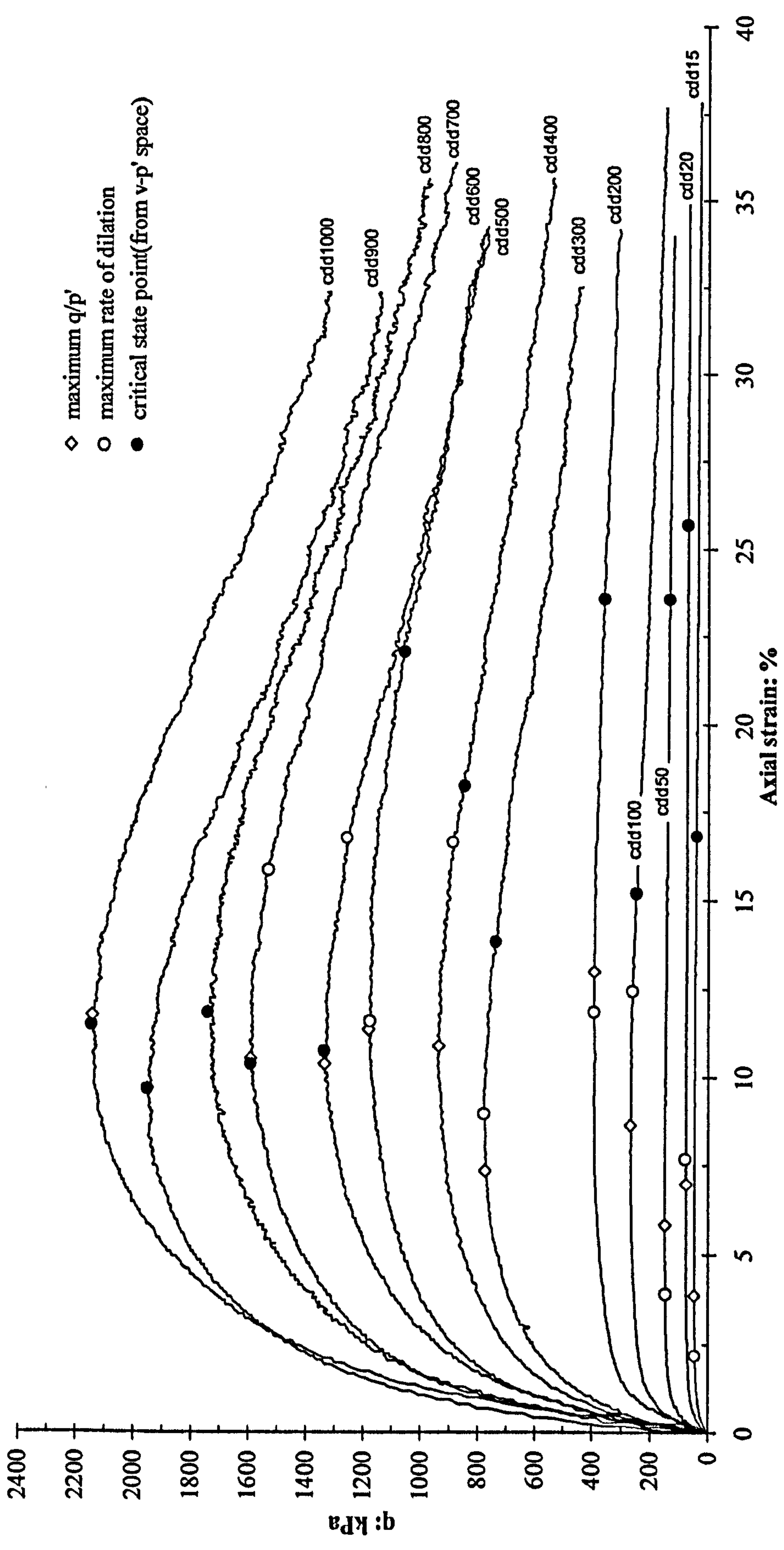


Figure 5.16a: Stress-strain curves for the drained tests on destructured samples



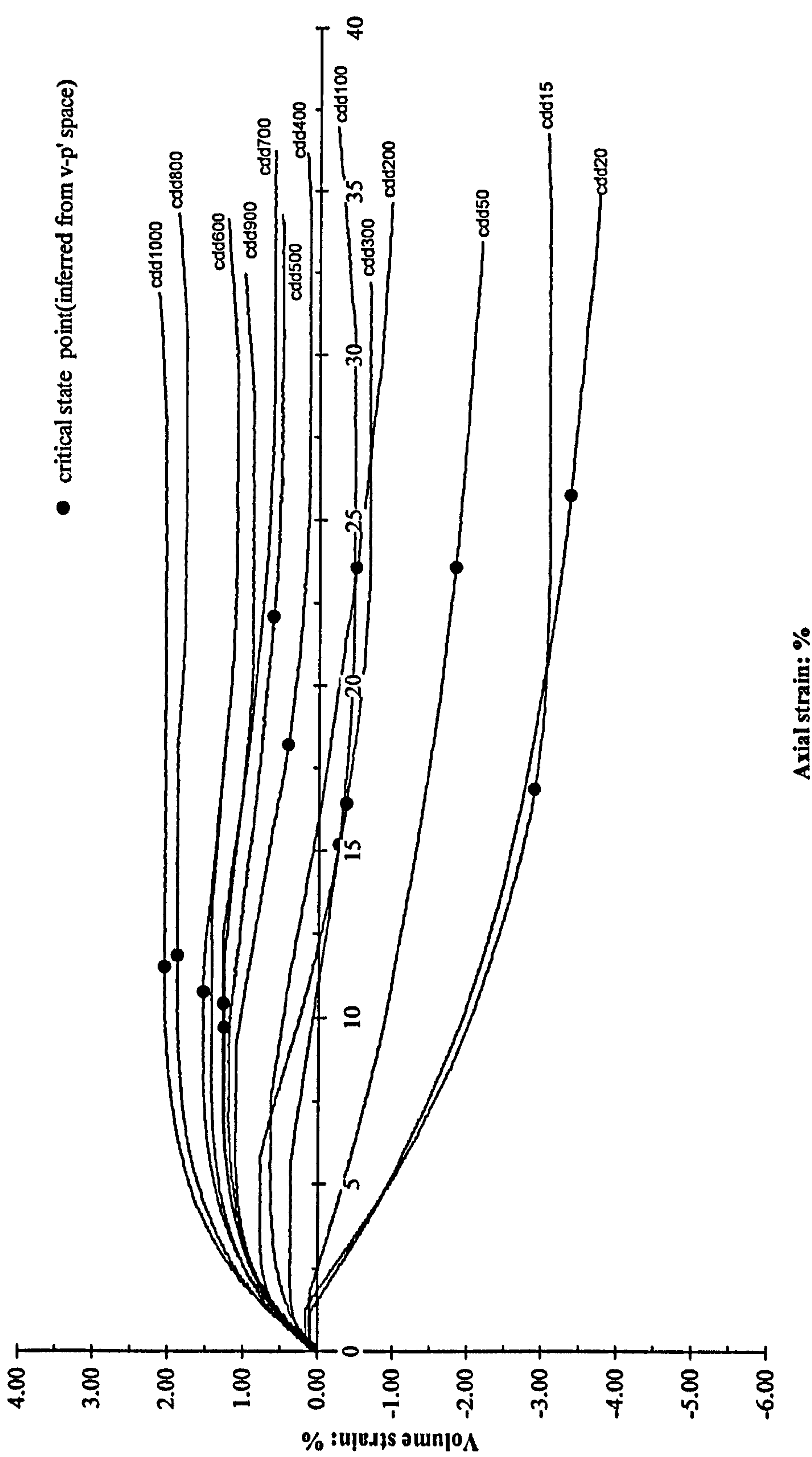


Figure 5.16b: Volumetric strain curves for the drained tests on destructured samples

contracting and dilating behaviour, the position of the critical state was selected at the point where a “discontinuity” could be seen on the dilatant path. At this stage, the behaviour of sample is referred to as the critical state and the change of volume after this is termed a “discontinuity” due to strain localisation. Where samples exhibited contraction behaviour, the critical state was defined at the point where the specific volume,  $v$  path started to deviate to the left with a decrease in  $p'$ .

The  $v - p'$  lines for the undrained tests are shown in Figure 5.17. The selection for the critical state for the undrained tests also used a similar approach. The stress strain and excess pore water pressure curves for the undrained tests with maximum deviator stress,  $q$  points are shown in Figure 5.18a and Figure 5.18b. It is clearly seen that the deviator stress,  $q$  and excess pore water pressure continue to change after the peak to the end of shearing. Due to the difficulty to identify the critical state from stress strain behaviour, alternatively, the effective stress paths of undrained tests has been used. Figure 5.19 shows the effective stress paths for the undrained tests. The stress paths for all the tests follow a similar straight line representing a maximum failure envelope before a “discontinuity” occurs after the maximum deviator stress,  $q$  is reached. Then, based on the stress path behaviour, then it was decided to use the maximum  $q$  straight away to represent the critical state for the undrained samples.

Finally the paths followed by the drained and undrained tests in  $v - p'$  space are shown altogether in Figure 5.20. It is clearly seen that the defined critical state points are scattered and not unique. Similar behaviour was also reported by Hosseini et al. (2005) and many other researchers (e.g.; Konrad 1990; Yamamuro and Lade 1998; Mooney et al. 1998). However, by combining the data for the two types of test in  $v - p'$  space as shown in Figure 5.20, the critical state for destructured material can be defined as a zone with upper and lower bounds. Based on the error analysis, the maximum error in void ratio is in order of 0.008 (refer to Appendix I). These upper and lower limits of the critical state are represented by the following equations in  $v - \ln p'$  space:



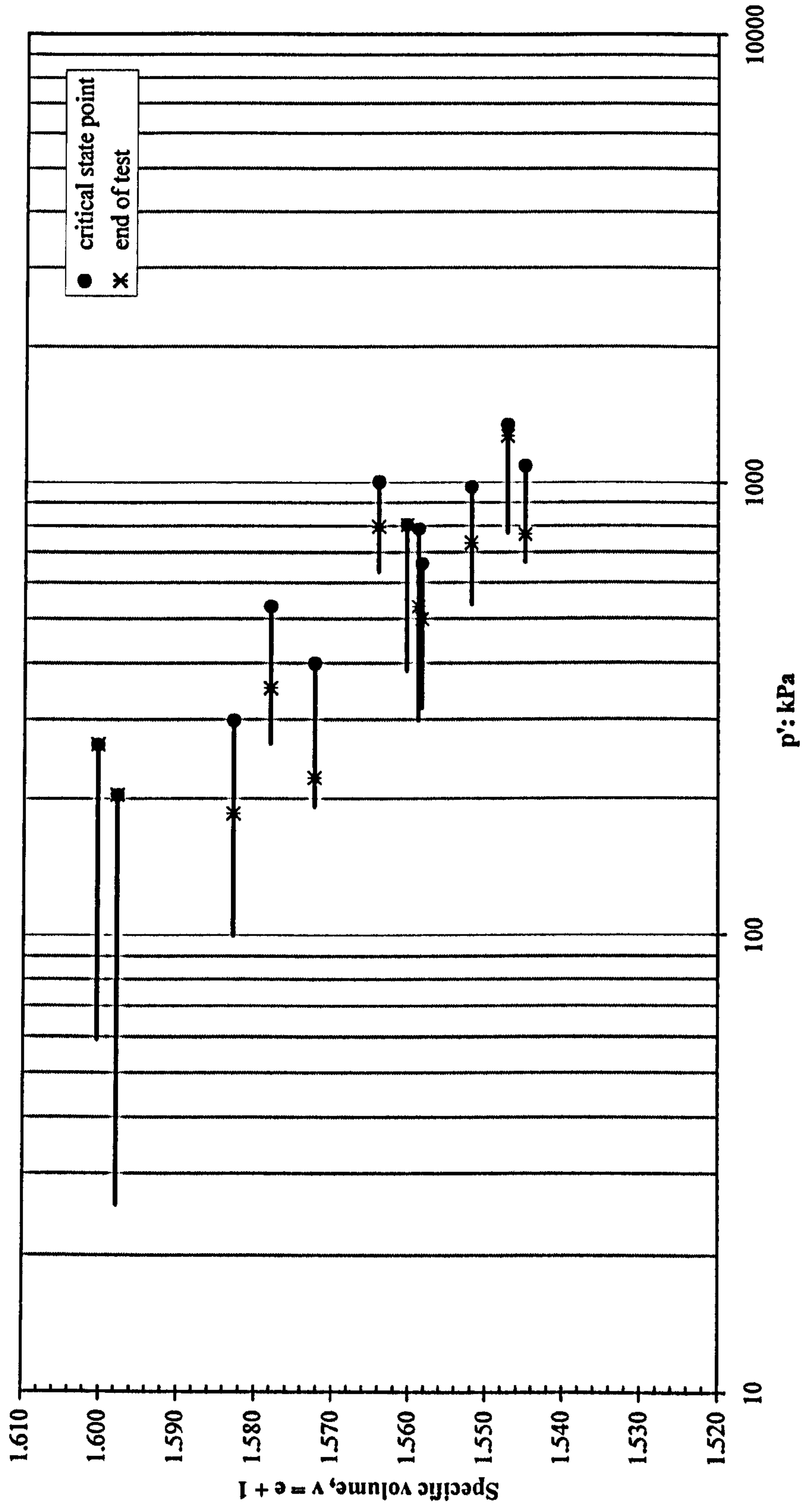


Figure 5.17: Specific volume changes with effective stress,  $p'$  for the undrained tests on destructured samples

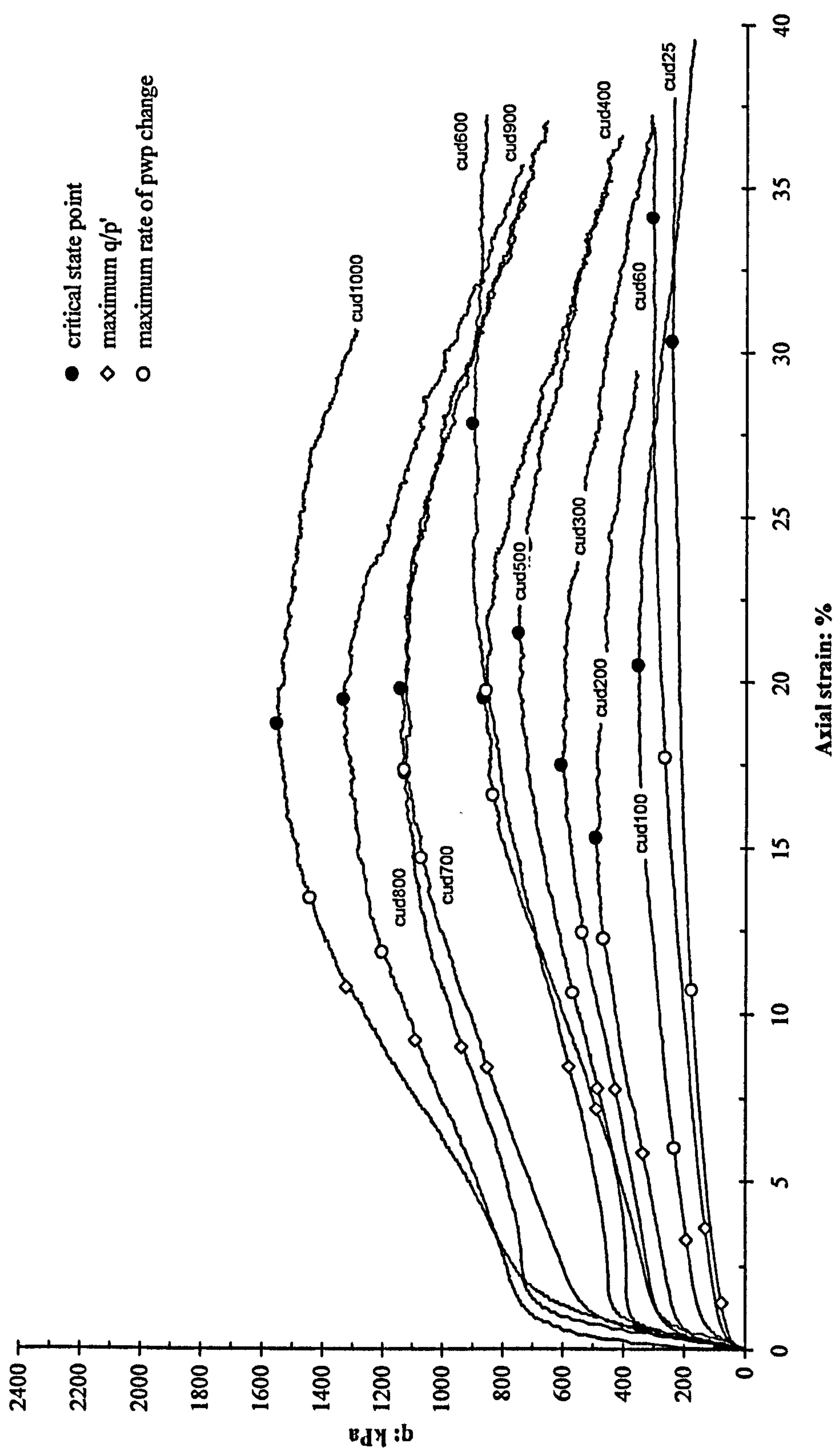


Figure 5.18a: Stress-strain curves for the undrained tests on destructured samples



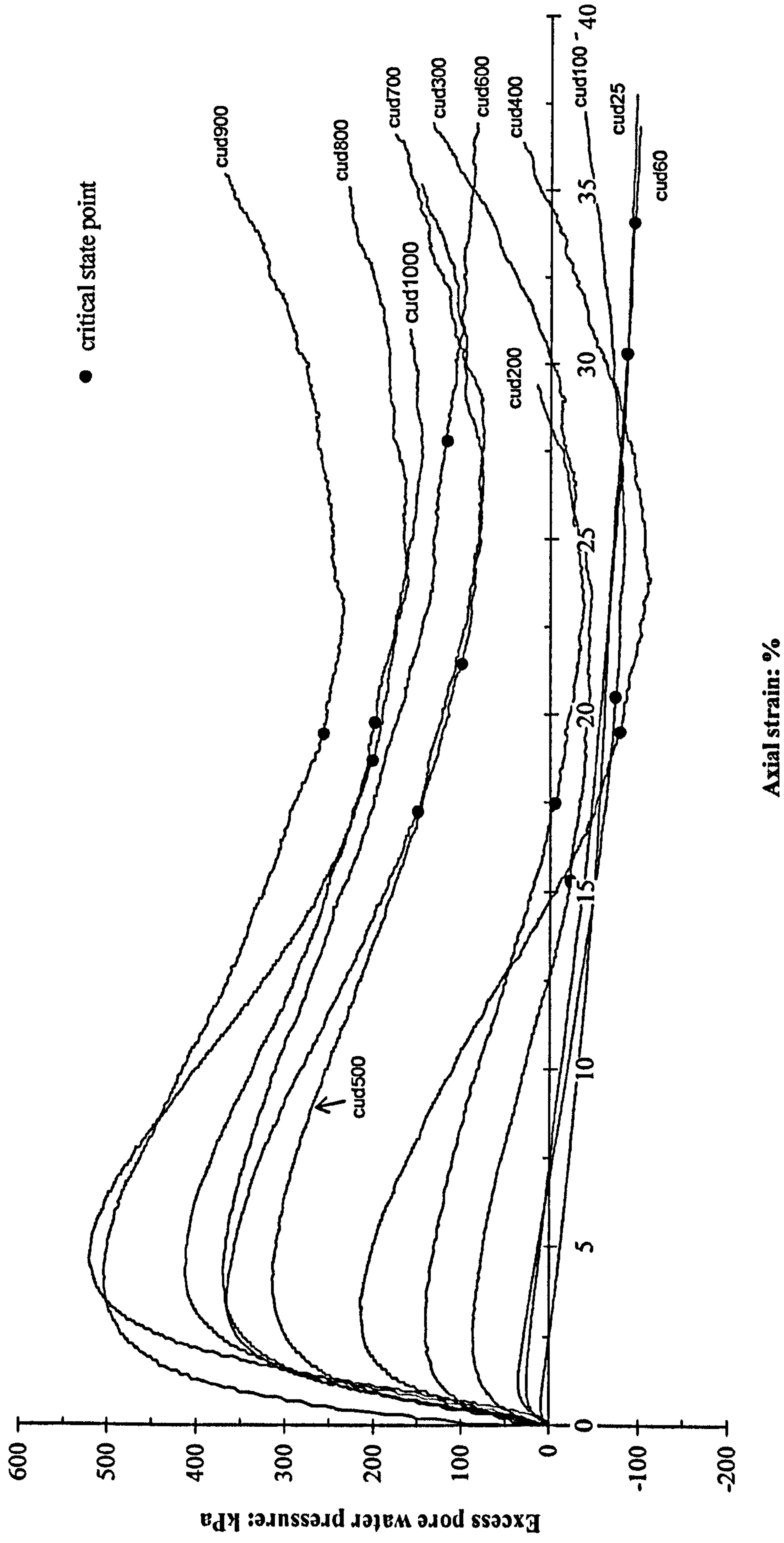


Figure 5.18b: Excess pore water pressure change for the undrained tests on destructured samples

$$v = 1.7991 - 0.034 \ln p' \quad (\text{upper limit}) \quad \dots (5.1)$$

$$v = 1.7581 - 0.034 \ln p' \quad (\text{lower limit}) \quad \dots (5.2)$$

As shown in Figure 5.20, the difference between the upper limit and lower limits represents a variation of  $\pm 0.041$  in terms of specific volume. According to Hosseini et al. (2005), this variation might be due to error in void ratio calculation or most likely caused by the initial fabric and structure, which form during the remoulding of the samples. They found that the difference between upper and lower limit was  $\pm 0.04$ . Therefore, in defining the critical state the effect of error in void ratio measurement and fabric are inevitable and critical state is usually defined by a zone.

A critical state in a  $q - p'$  space was also prepared for comparison with the result from  $v - p'$  space. The  $q$  and  $p'$  values were taken for the same points chosen to represent the critical state. Figure 5.21 shows the critical state for the destructured material in  $q - p'$  space (error bars for  $q$  and  $p'$  are shown). The critical state points are assumed to be defined by a straight line through the origin giving a slope of  $M = 1.24$ . This is equivalent to a critical state angle of friction,  $\phi'$  of  $30.8^\circ$ . However, it is clearly seen that the points are slightly scattered and fan out from origin coinciding with the variation in  $q/p'$  ratio values in both tests (refer to Section 5.4.1). Therefore, the critical state for destructured material is seen to be a reasonably unique line in the  $q - p'$  space in comparison to that in  $v - p'$  space.

### 5.5.2 Normalisation

In order to compare results from different tests, it is convenient to carry out normalisation of the stress paths (Hosseini et al. 2005). In this study, samples with a very similar void ratio were sheared at different stress levels. Three established techniques have been described by Atkinson and Bransby (1978) and Atkinson (1993) for normalisation of the stress path. The three methods use either  $p'_e$ , the equivalent stress on the normal compression line,  $p'_c$ , the equivalent stress on the



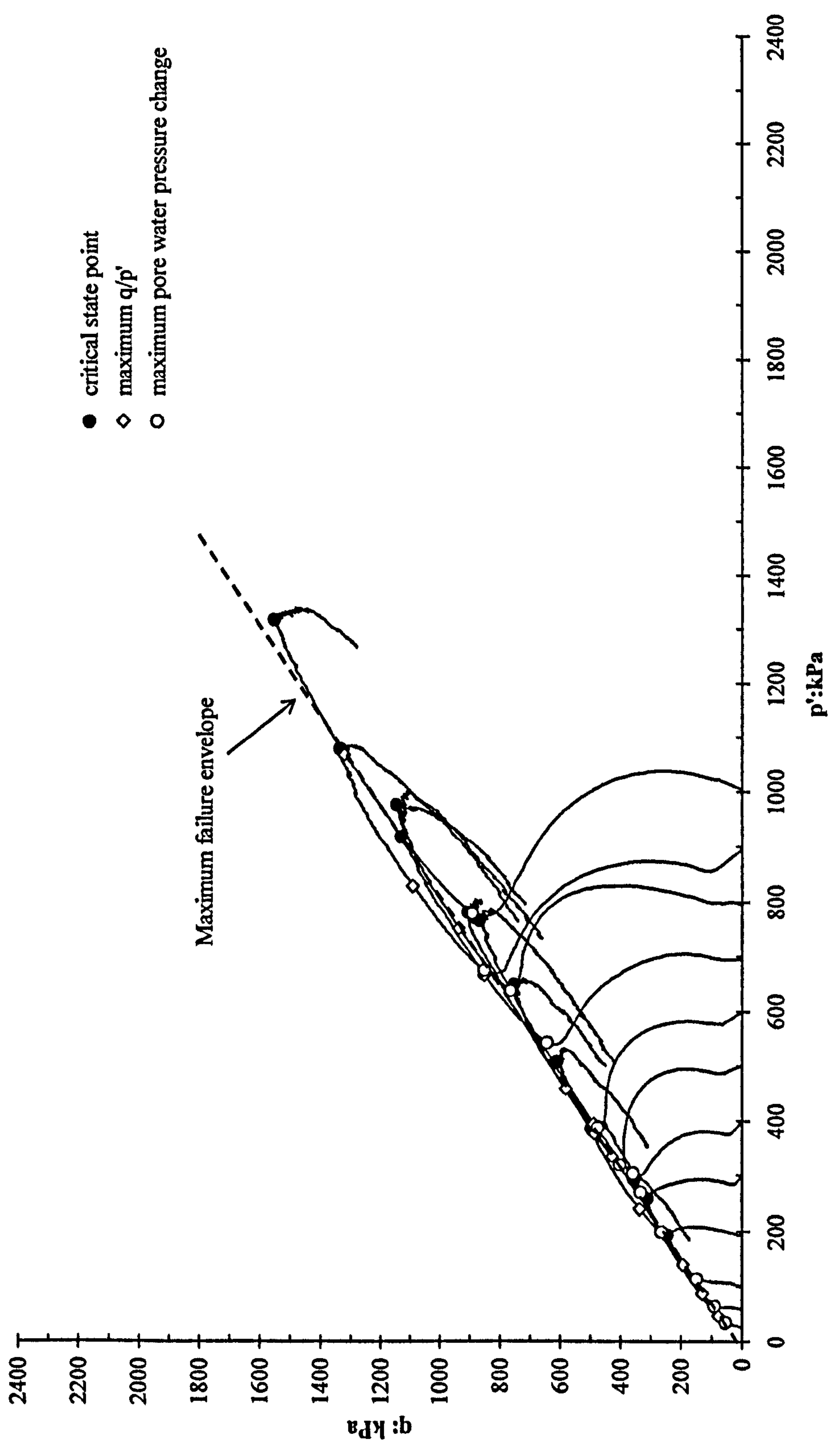


Figure 5.19: Effective stress paths for the undrained tests on destructured samples

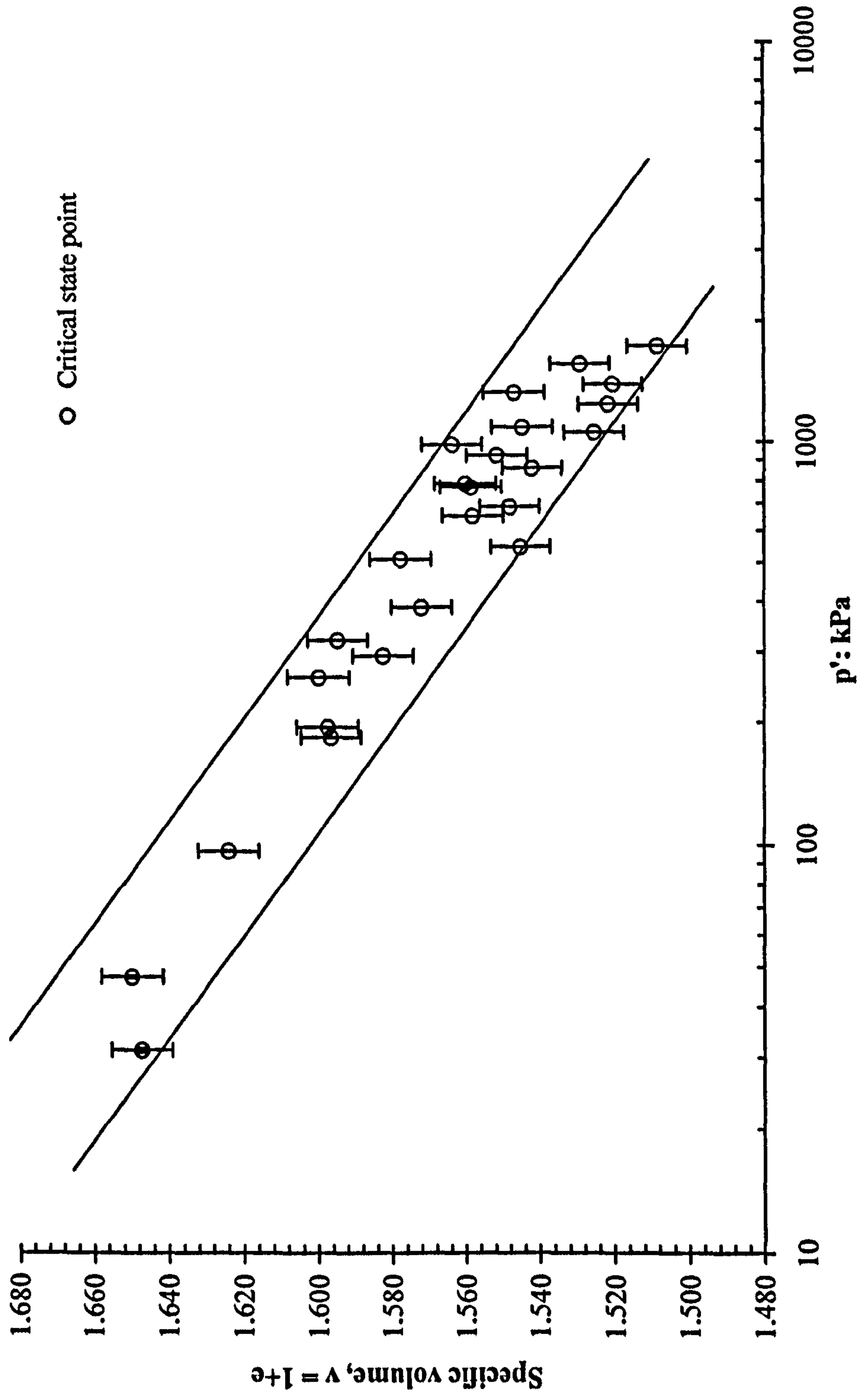


Figure 5.20: Critical state line for drained and undrained tests on destructured samples (error bars were included)



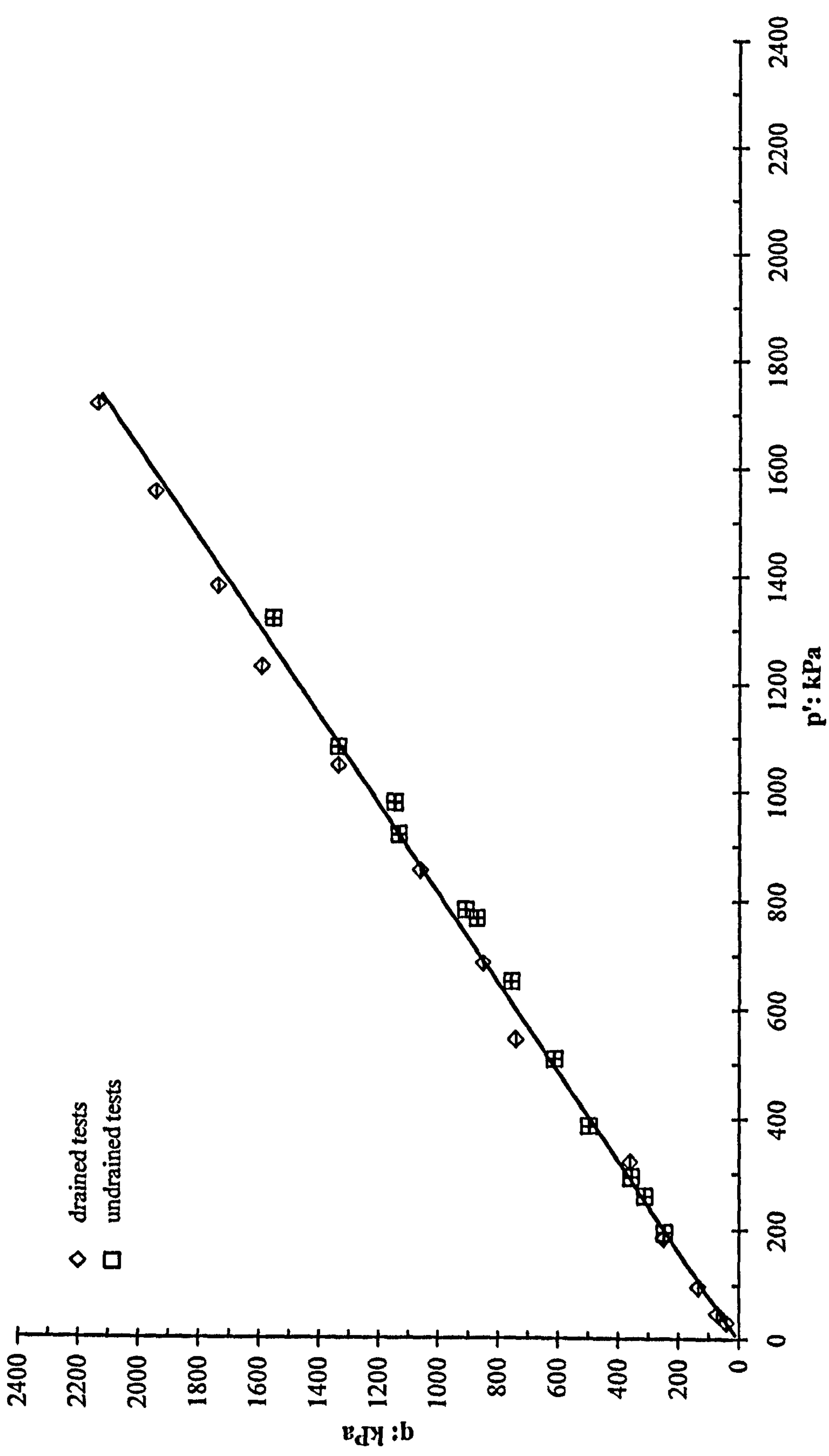


Figure 5.21: Critical state for the drained and undrained tests on destructured samples in  $q - p'$  space (error bars were included)

critical state line or  $v_\lambda$ , the equivalent specific volume intercept. Since the studied material is classified as a coarser material (consisting of medium sand and a small fraction of fired kaolin), the use of the  $p'_e$  approach is not possible because of the difficulty in establishing the position of the normal consolidation line (NCL). The value of  $p'_e$  is referred to the effective mean stress corresponding to the void ratio on the NCL. The second approach is to use  $p'_c$ , which is the effective mean stress corresponding to the void ratio on the critical state line (CSL). However, a unique critical state line was impossible to define for the studied material; as a result a single  $p'_c$  could not be simply defined for any void ratio to be used in normalisation of the stress paths. Hosseini et al. (2005) used a refinement of the second approach to overcome the difficulty of the critical state being a zone rather than a unique line. Hence, the values of  $p'_c$  were observed for each test as the critical state point defined earlier (refer to Section 5.5.1). The normalisation of the stress path based on the critical state value of  $p'_c$ , by definition, should end up with  $p'/p'_c = 1$  and  $q/p'_c = M$ .

Figures 5.22a and 5.22b show the stress paths in normalised  $p'/p'_c - q/p'_c$  spaces for the drained and undrained tests using a second method. It clearly seen that the stress paths reach at different values in of  $q/p'_c$ . Therefore, a refinement for each test in this space for  $q/p'_c$  was carried out by re-normalising with the end values of  $q/p'_c$  where  $(q/p'_c)/(p'/p'_c)$  equal to  $M$ . By doing this the stress path values for  $p'/p'_c$  and  $q/p'_c/M$  will end at the (1, 1) point, which represents the critical state (Figure 5.23a and 5.23b). Figure 5.24 shows a combined stress paths for the drained and undrained tests. In this  $q/p'_c/M - p'/p'_c$  space, a clear boundary surface for the destructured material can be defined. It can be seen that those samples on the dense side of the critical state ( $p'/p'_c < 1$ ) climb to the limiting surface of Hvorslev surface and turn to critical state. Meanwhile, those samples on the loose side ( $p'/p'_c > 1$ ) are limited by the Roscoe surface and move toward the critical state from the right side of the space. It is interesting to acknowledge that those samples on the loose side with value of  $p'/p'_c$  closer to 1 have a tendency to reach critical state without reaching the Roscoe surface. However, based on this type of normalisation, clear



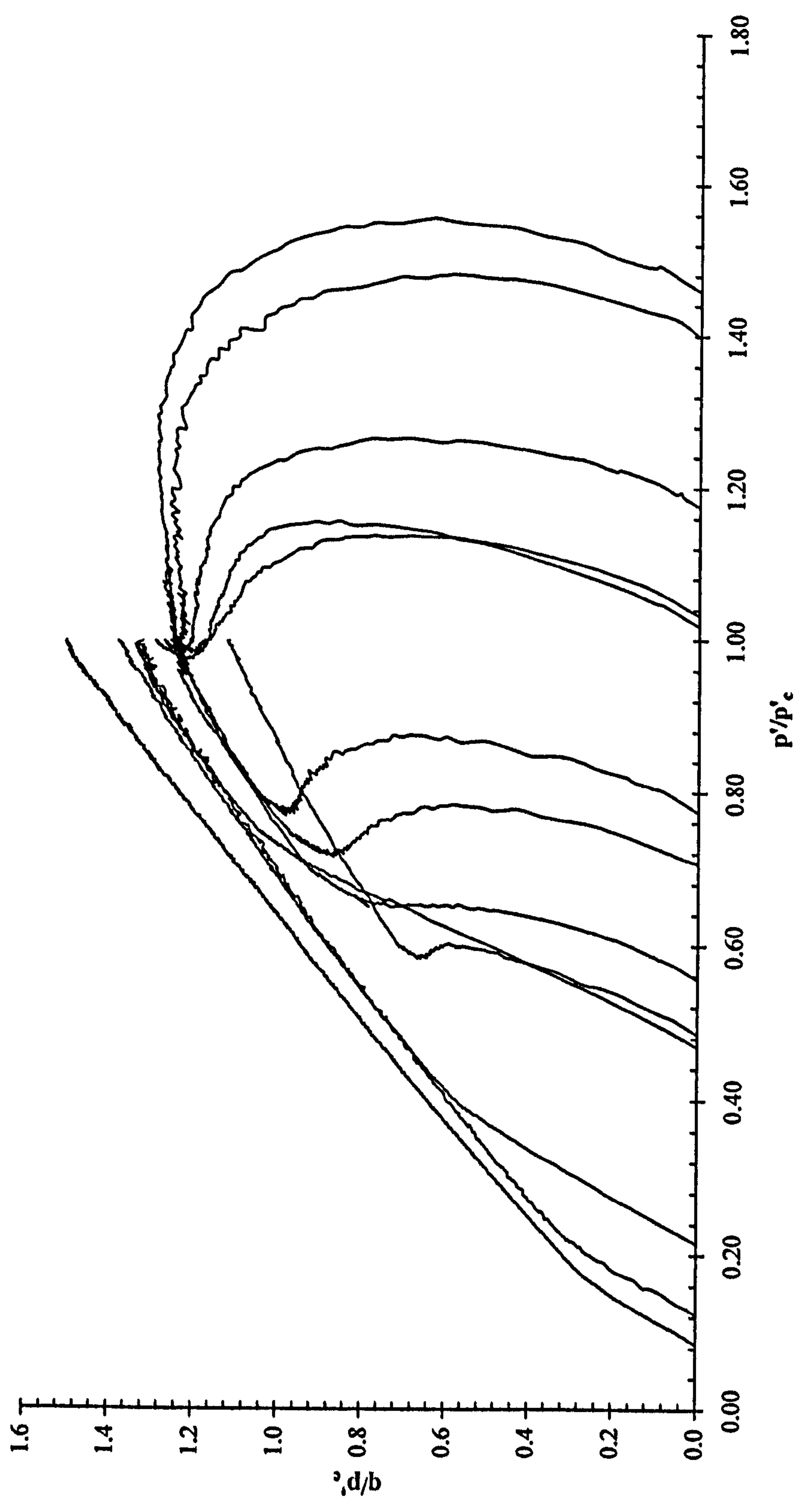


Figure 5.22a: Normalised stress paths in  $q/p'_c - p'/p'_c$  space for drained destructured samples

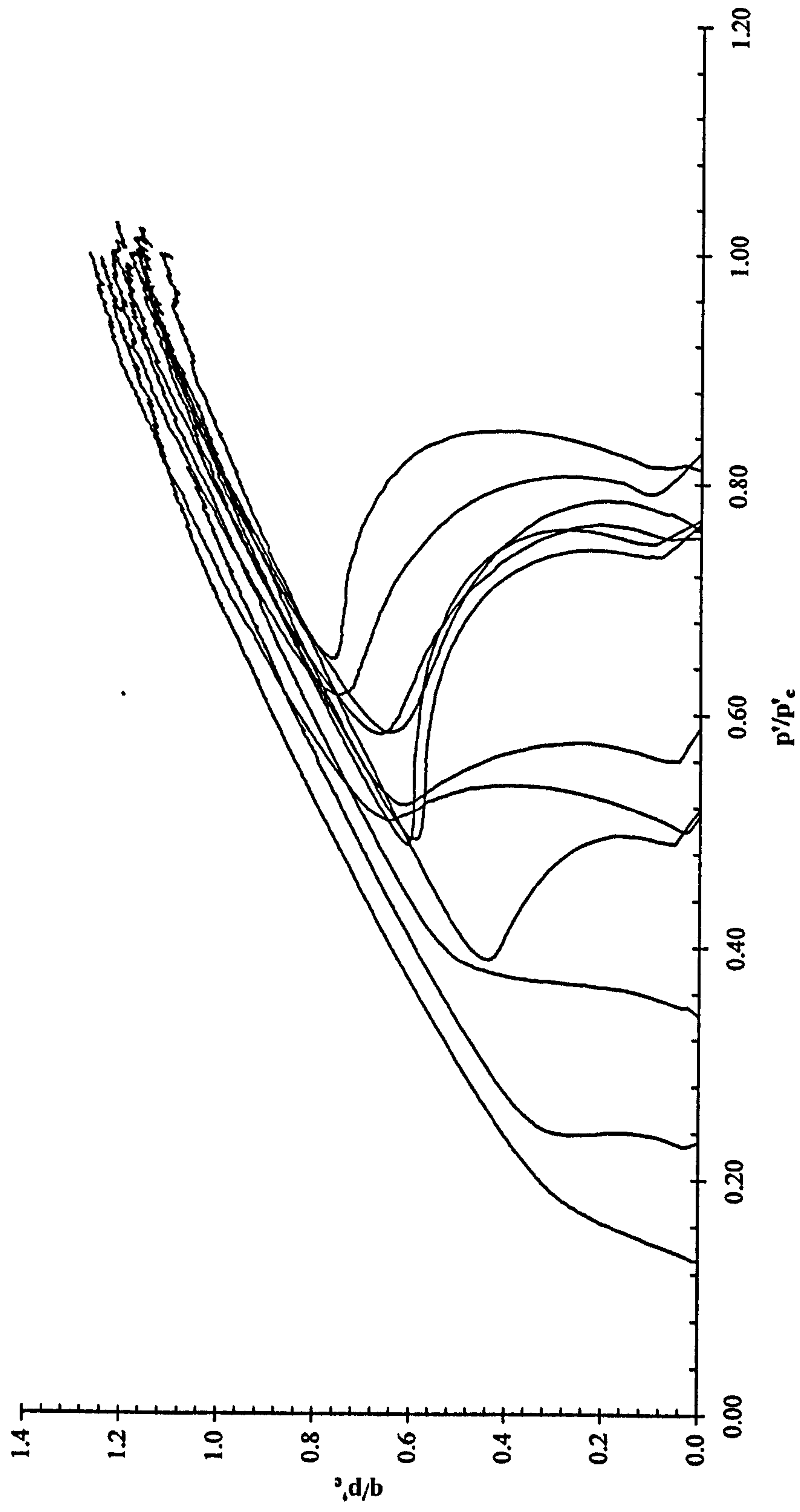


Figure 5.22b: Normalised stress paths in  $q/p'_c - p'/p'_c$  space for undrained destructured samples



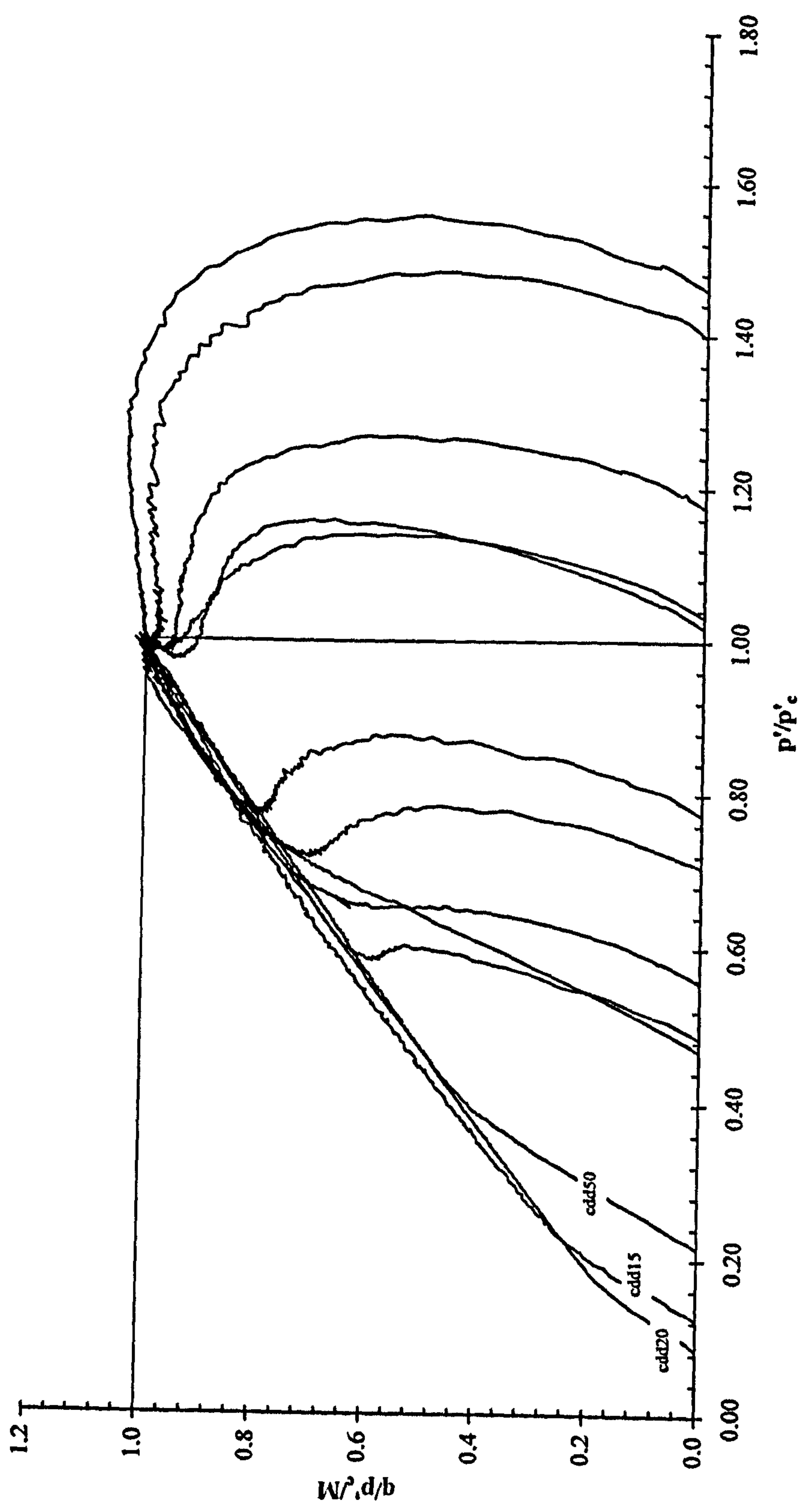


Figure 5.23a : Normalised stress paths for drained tests in  $q/p' - M - p'/p'_e$  space

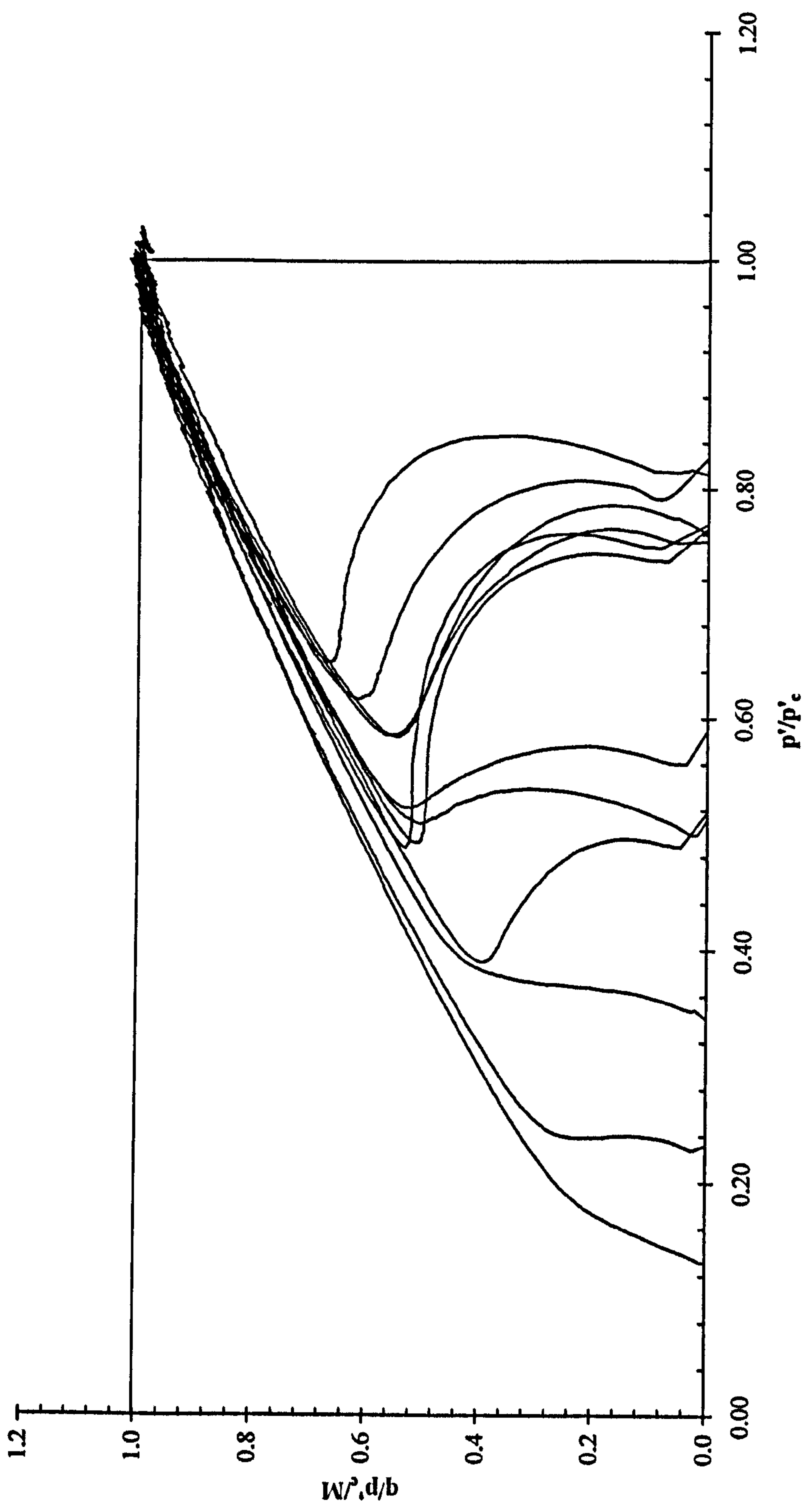


Figure 5.23b: Normalised stress paths for undrained tests in  $q/p'_c/M - p'/p'_c$  space



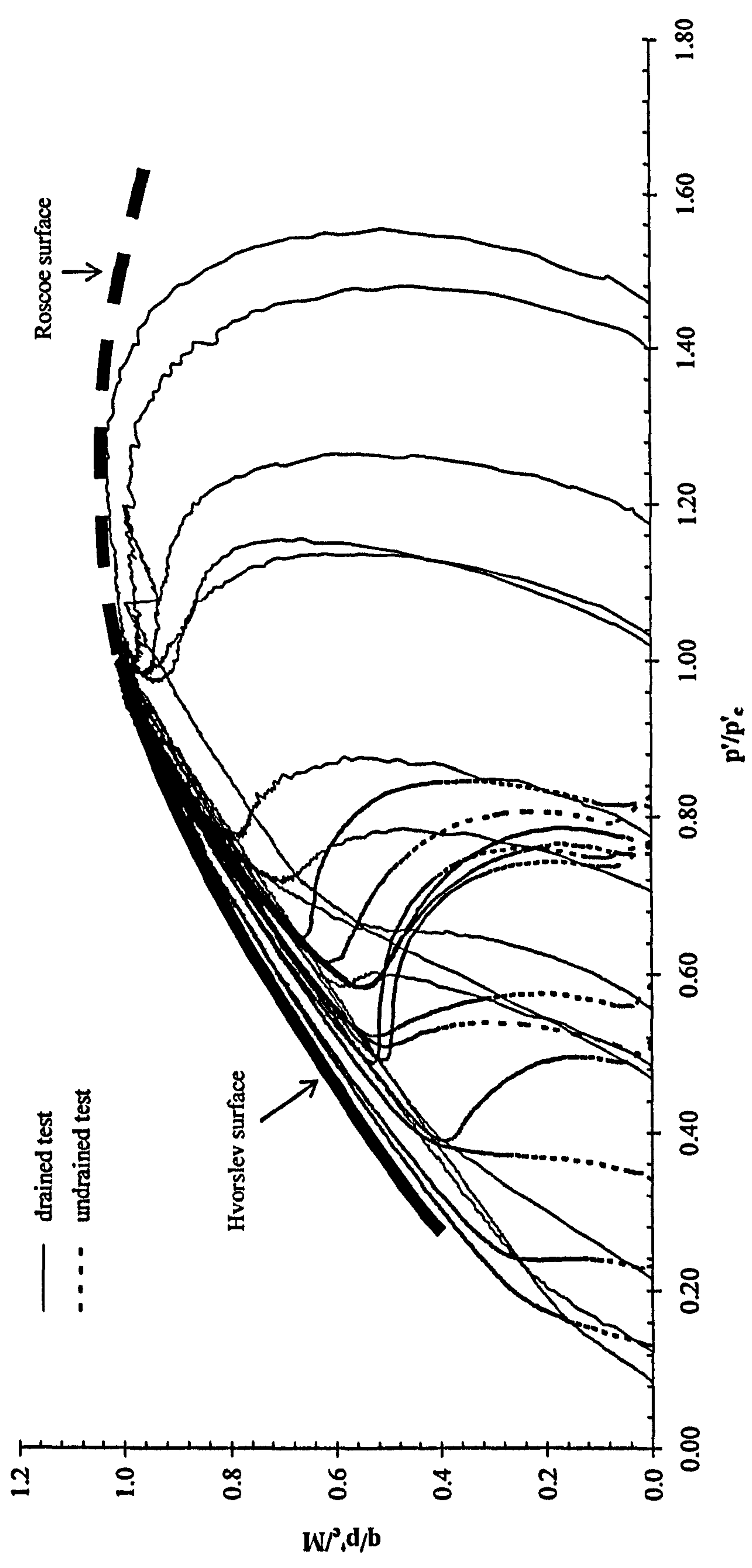


Figure 5.24: Normalised stress paths for drained and undrained tests in  $q/p', d/b$  -  $p'/p'_c$  space

boundary surfaces for the destructured material could be defined irrespective of different type of tests and applied confining pressures.

## 5.6 FINAL REMARKS

Two series of conventional triaxial drained and undrained tests were carried out on the destructured material in saturated conditions. The destructured samples were initially prepared from a fired mixture of sand and kaolin, which were then crushed in order to destroy the bonded structure.

The stress strain behaviour for both tests showed a consistent pattern of behaviour. For drained tests, samples achieved maximum deviator stress which then gradually decreased with increasing axial strain. Similar cases were also present from the undrained tests. However, a quasi-steady state behaviour as suggested by Yamamuro and Lade (1991) was observed in some samples sheared at medium and high confining pressures. Excess pore water change from undrained tests for samples sheared at low confining stresses indicated initial compression followed by dilation. Similarly, the drained samples sheared at low confining stress levels showed compression initially which changed to dilation. It suggests that the behaviour of the destructured material under shearing is similar to the behaviour of dense sand. According to the stress-strain curves and volumetric strain from the drained tests, the destructured samples could be considered to have achieved their critical state. However, for the undrained samples, critical state was difficult to observe based on the stress-strain curves and excess pore water change because both variables still changed up to the end of shearing.

All the tests carried out on the destructured samples showed no significant peak in  $q/p'$  ratio. For most of the tests, the maximum  $q/p'$  ratio is achieved at axial strain between 5%-10%. Destructured samples sheared at lower confining pressures sustain a higher value of  $q/p'$  ratio than those at higher confining pressure. The  $q/p'$  ratio values range from 1.47 to 1.70 for samples sheared at low confining pressures



and between 1.24 – 1.32 for high confining pressures. This suggests that the stress ratio value of the samples depends on the consolidation stress, and is consistent with an apparent cohesion of 22kPa for the peak state.

As a result of the difficulty in defining the critical state for some of the tests, a “discontinuity” approach was used in identifying a sudden change that might be associated with shear surface formation. For drained tests, the critical state was defined based on assessment of the void ratio path in  $v - p'$  space. A similar approach was used for undrained samples, since no clear point could be defined as critical state from the plots of stress-strain, pore water change and void ratio path ( $v - p'$ ), the effective stress paths were studied for that purpose. The critical state line for destructured material was found to be not unique in  $v - p'$  space. Therefore, the critical state is represented by a zone with upper and lower limits. The scatter in void ratio is due to error measurement of in order 0.008. The difference between the upper and lower limit is  $\pm 0.041$ . This scatter might be due to errors in void ratio and/or caused by the initial fabric and structure of the samples. A critical state defined in  $q - p'$  space defined by a fairly straight line with minimum scatter of data points which radiating from the origin coinciding with the variation in  $q/p'$  ratios. Therefore, the critical state for destructured material is seen to be a realistically unique line in the  $q - p'$  space in comparison to that in  $v - p'$  space.

In order to compare results from different tests, normalisation of the stress paths was carried out for each test. Three methods of normalisation were reviewed and second approach was adopted to normalise the stress paths for the destructured material in this study. The normalisation of stress paths in  $q/p'_c - p'/p'_c$  showed a scattered values in  $q/p'_c$ , which corresponding to variation in stress ratio in each test. A further refinement was carried out by re-normalised with the end values of  $q/p'_c$  (equal to  $M$ ). Based on the refined plot in  $q/p'_c/M - p'/p'_c$  space, boundary surfaces could be defined. These normalised stress paths showed a clear limiting surface for different behaviour. Samples on dense side of the critical state exhibit dilative behaviour (bounded by the Hvorslev surface) and those on the loose side of the critical state show contractive behaviour (bounded by the Roscoe surface).

## **CHAPTER 6   SATURATED BONDED MATERIAL**

### **6.1   INTRODUCTION**

In this chapter, the results from conventional drained and undrained tests on saturated bonded samples are presented and discussed. The artificially weakly bonded samples were prepared with a void ratio of 0.6. The details of the preparation of this type of sample were discussed in Chapter 3. A wide range of effective stresses were applied to the samples during the consolidation stage up to 1MPa prior to shearing. The relationships between deviator stress, volume strain or excess pore water pressure and maximum  $q/p'$  stress ratio with axial strain are discussed. The bounding surfaces of the soils are determined and comparisons are made between the bonded and destructured samples. This series of tests also established a benchmark in assisting the interpretation of the test results from the unsaturated tests as will be discussed in a later chapter.

### **6.2   DRAINED TRIAXIAL TESTS**

The results of the drained tests on saturated artificial bonded samples are presented and described in this section. The drained behaviour of the artificial samples is discussed in term of stress-strain, volumetric strain, stress ratio and effective stress paths. The bounding surface and phase transformation line are also presented in the stress space for the bonded samples and compared with those for the destructured material.



### 6.2.1 Description of Testing

Thirteen artificially bonded samples were examined using conventional drained triaxial compression tests. Samples were prepared to have a similar initial void ratio ( $e_0 = 0.6$ ) to the samples tested in a destructured state. The samples were initially consolidated under applied isotropic confining pressure for about an hour, which was sufficient to achieve full consolidation. The samples were sheared under a constant rate of strain of 0.025%/min (or 1.5%/hr). Relevant data were collected using the computer logging system supported by Triax version 5.1 which was set to scan every 2 minutes during shear. The shearing of the samples was carried out up to 30% of strain in order to establish the behaviour of samples toward the critical state, although some samples had already failed before 30% axial strain. The samples for the drained tests are listed in Table 6.1. The identification of the tests was based on the type of test, condition of sample and applied confining stress prior to shearing. For example test cdb15; the first two letters “cd” refers to the consolidated drained condition during shearing while the third letter “b” indicates that a bonded sample is being used for the test. Finally the numbers refer to the value of confining stress applied during isotropic consolidation of the sample.

### 6.2.2 Stress Strain Behaviour

The tests were carried out at different confining pressures ranging from 15kPa up to 1000kPa. The deviatoric stress,  $q$  curves against axial strain for all the tests are shown in Figure 6.1. As can be seen from the stress strain curves, all tests generally indicated an apparently linear increment of deviator stress,  $q$  at early strain then followed by gradual decrease of  $q$  with increasing axial strain. For the tests up to cdb600, the samples initially climb up to their peak state at low axial strain between 1% and 2%. The samples then experienced strain softening when  $q$  decreases with increasing axial strain due to the development of shear surfaces in the samples. It can also be seen that the axial strain at the peak state increases with increasing applied confining pressure (Figure 6.1). Meanwhile for the tests

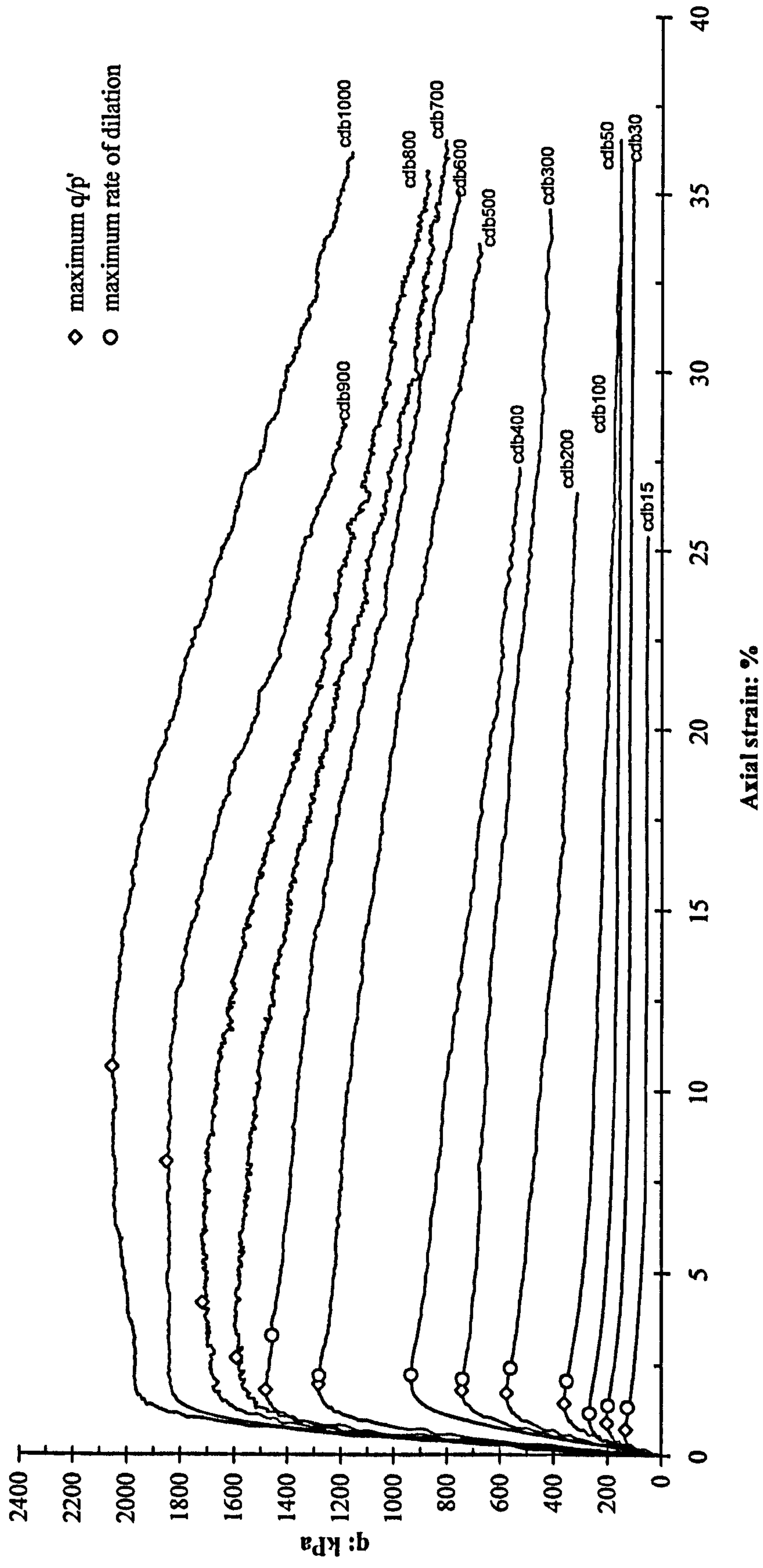


Figure 6.1: Stress-strain curves for the drained tests on bonded soils



between cdb700 and cdb1000 that were consolidated at high confining stresses, samples reach the maximum  $q$  at higher axial strain than those that were consolidated at lower confining pressures. It is clearly seen that the tests sheared at confining pressures,  $p' < 700\text{kPa}$ , show a reasonable peak in the stress-strain curves. On the other hand, for samples sheared at  $p' \geq 700\text{kPa}$ , no noticeable peak can be observed and are represented by almost flat stress-strain curves after reaching maximum  $q$ .

Table 6.1: A series of drained tests on artificial bonded samples

Test	Initial void ratio, $e_0$	Confining pressure, kPa
cdb15	0.6062	15
cdb30	0.6048	30
cdb50	0.6063	50
cdb100	0.5995	100
cdb200	0.6092	200
cdb300	0.6061	300
cdb400	0.6060	400
cdb500	0.6031	500
cdb600	0.6087	600
cdb700	0.6097	700
cdb800	0.6092	800
cdb900	0.6063	900
cdb1000	0.6045	1000

The volumetric strain curves for the tests are presented in Figure 6.2. Samples at lower confining pressures demonstrated smaller compression at the beginning of shearing followed by dilation. This kind of behaviour is that expected of an over consolidated soil. By increasing the applied confining pressure, the compression becomes more apparent, and the degree of dilation becomes smaller.

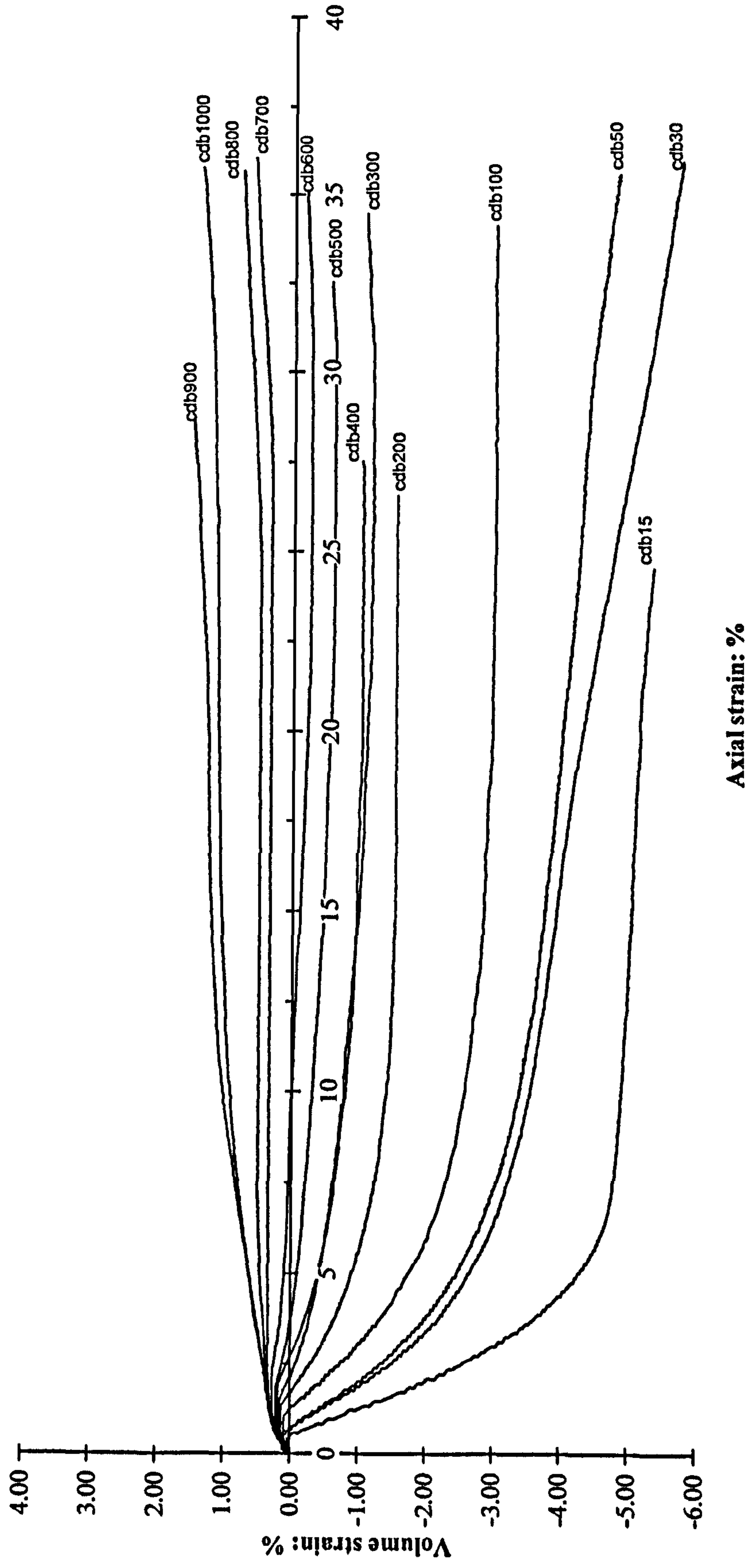


Figure 6.2: Volume strain curves for the drained tests on bonded soils



As seen from the curves, sample cdb15 exhibited very small compression and then started to dilate at low axial strain (less than 1%). In comparison, test cdb100 showed higher initial compression than cdb15 and dilation was initiated at higher axial strain. It was found that dilation was still present in samples which were consolidated up to 600kPa (test cdb600 and onward) however compression was dominant at higher confining pressure ( $p_o' \geq 700\text{kPa}$ ). At confining pressure,  $p_o'$  between 800kPa and 1000kPa, samples simply exhibited compression without any noticeable dilation up to the end of shearing. The state at which the soil changes from compression to dilation can be estimated from the maximum positive values of volume change. Therefore, from the plotted points of maximum positive values of volume change, the curve for the phase transformation line can be defined in  $q$ - $p'$  space (Figure 6.3).

The phase transformation point and maximum rate of dilation points are marked on the plots of stress ratio,  $q/p'$  against axial strain (Figure 6.4). It can be seen that the samples sheared at lower confining pressures are characterised by a clear peak of  $q/p'$  ratio and the maximum  $q/p'$  ratios decrease with increasing confining pressures. At higher confining pressures (cdb700 to cdb1000) no peak in  $q/p'$  ratio is observed. The position of phase transformation occurs before the peak in  $q/p'$  (except cdb15) then followed by the point of maximum rate of dilation.

The points of maximum  $\delta\varepsilon_v/\delta\varepsilon_a$  and maximum value of  $q/p'$  ratios are also marked on the stress-strain curves as shown in Figure 6.1. The maximum  $q/p'$  ratio always occurs earlier than the maximum  $\delta\varepsilon_v/\delta\varepsilon_a$  and the two points occur at quite similar deviator stress indicating a structural contribution to their location. For tests cdb50 and cdb400 the two points almost coincide in the stress-strain curves, suggesting a lack of structural influence. This behaviour was reported by Adams (2000) who studying undisturbed samples of lagoon fly ash. Meanwhile, samples sheared at confining pressures up to  $p'=500\text{kPa}$  (cdb15 to cdb500) show that the two points occur at quite close positions. At this range of stress levels, the maximum strength of samples is mainly influenced by the bond strength and dilation has a minimum

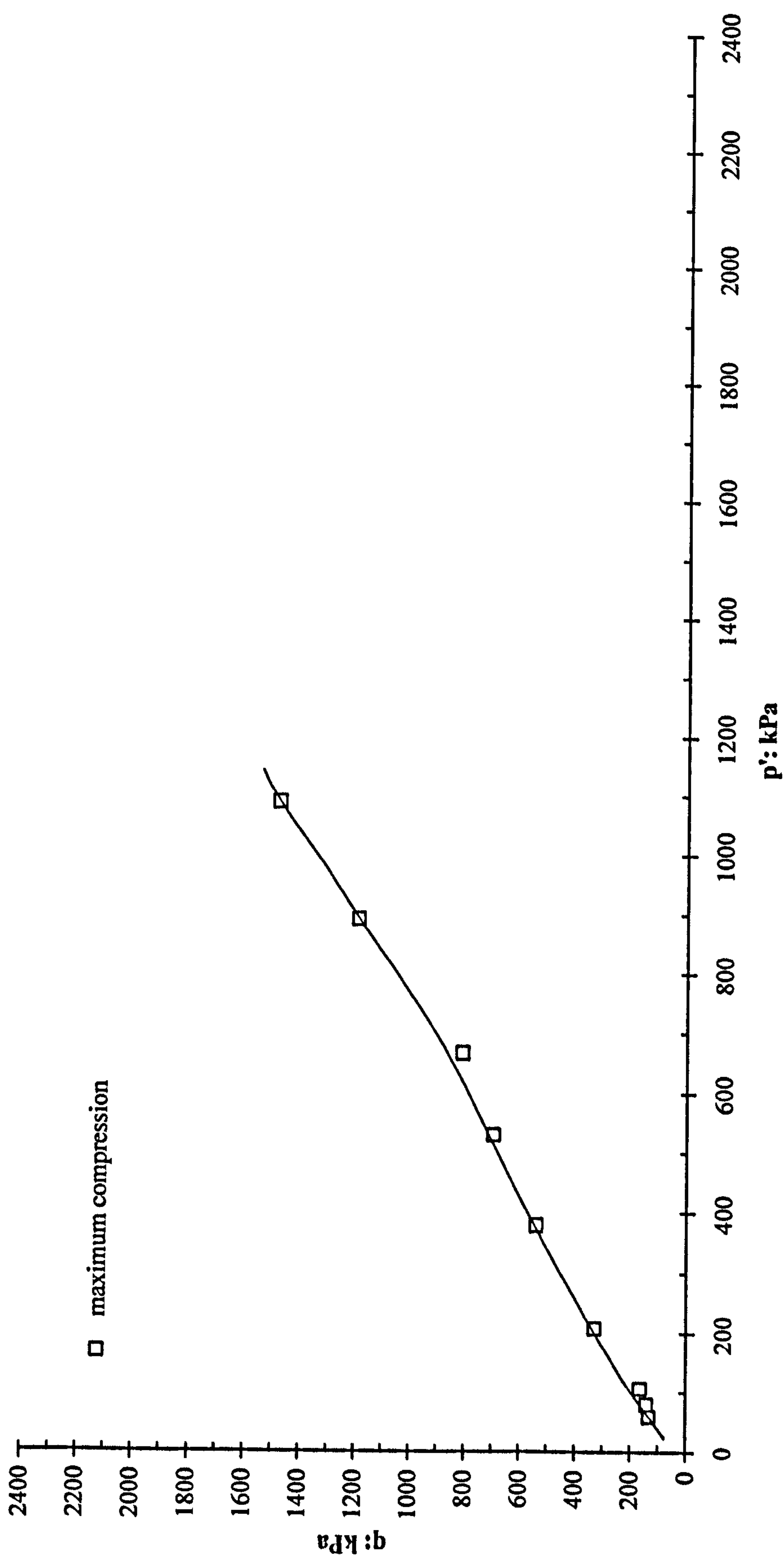


Figure 6.3: Phase transformation curve for the drained tests on bonded soils



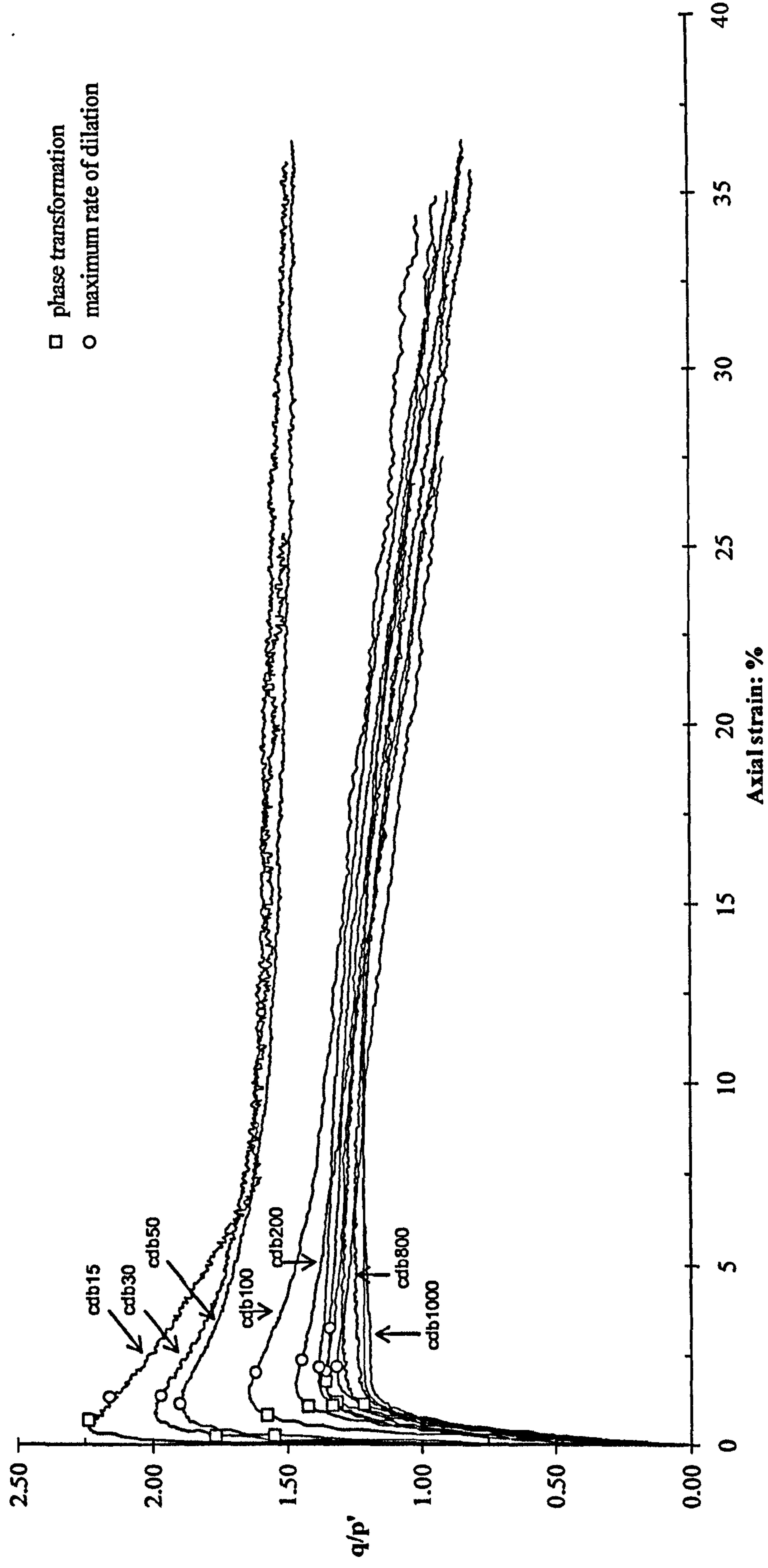


Figure 6.4: Stress ratio,  $q/p'$  against axial strain for the drained tests on bonded soils

effect. It also can be seen that the two points become closer with an increase in applied confining pressure which may correspond to increase in structural breakdown. Samples tested at higher confining pressures above 600kPa also show similar behaviour but the two points were split further. For tests cdb700, cdb800, cdb900 and cdb1000, the behaviour of samples become more ductile and samples contracted up to the end of the test, hence no rate of dilation could be defined. At this stage bonds become less important in governing the maximum strength of the samples.

### 6.2.3 Stress Paths and Bounding Surfaces

The effective stress paths for the drained tests on bonded samples are shown in Figure 6.5. Meanwhile the points representing maximum  $q/p'$  ratio values are presented in Figure 6.6 plotted in stress space in order to delineate the bounding surface of the bonded samples. It can clearly be seen from both figures that the bounding surface has some curvature at a stress level above  $p'=750\text{kPa}$ . At lower stress levels some curvature is also apparent up to stress level about  $p'=200\text{kPa}$ . Then the bounding surface becomes linear up to 750kPa. Based on data from cdb15, cdb30, cdb50 and cdb100, the failure envelope line was defined using conventional linear interpretation with equivalent angle of friction and cohesion intercept of  $\phi'=35^\circ$  and  $c'=55\text{kPa}$ , respectively. Then the gradient of the failure envelope line decreases to a lower value with equivalent friction angle of  $\phi'=29^\circ$  and corresponding cohesion intercept of  $c'=111\text{kPa}$  (tests cdb200, cdb300, and cdb400). Further up to higher stress level (test cdb500 and onward), the maximum  $q/p'$  ratio slightly increases in the region where the bounding surface begins to curve, then the line curves back with increasing stress level. At  $p'=1500\text{kPa}$  the line curves back, toward an envelope where  $c'=0$  and  $\phi'=40^\circ$ .

The change in the gradient of the bounding surface from lower to higher stresses suggests a gradual decrease in the bond strength at failure. This is confirmed by the  $q/p'$  plot in Figure 6.4 where the low confining stresses show maximum  $q/p'$



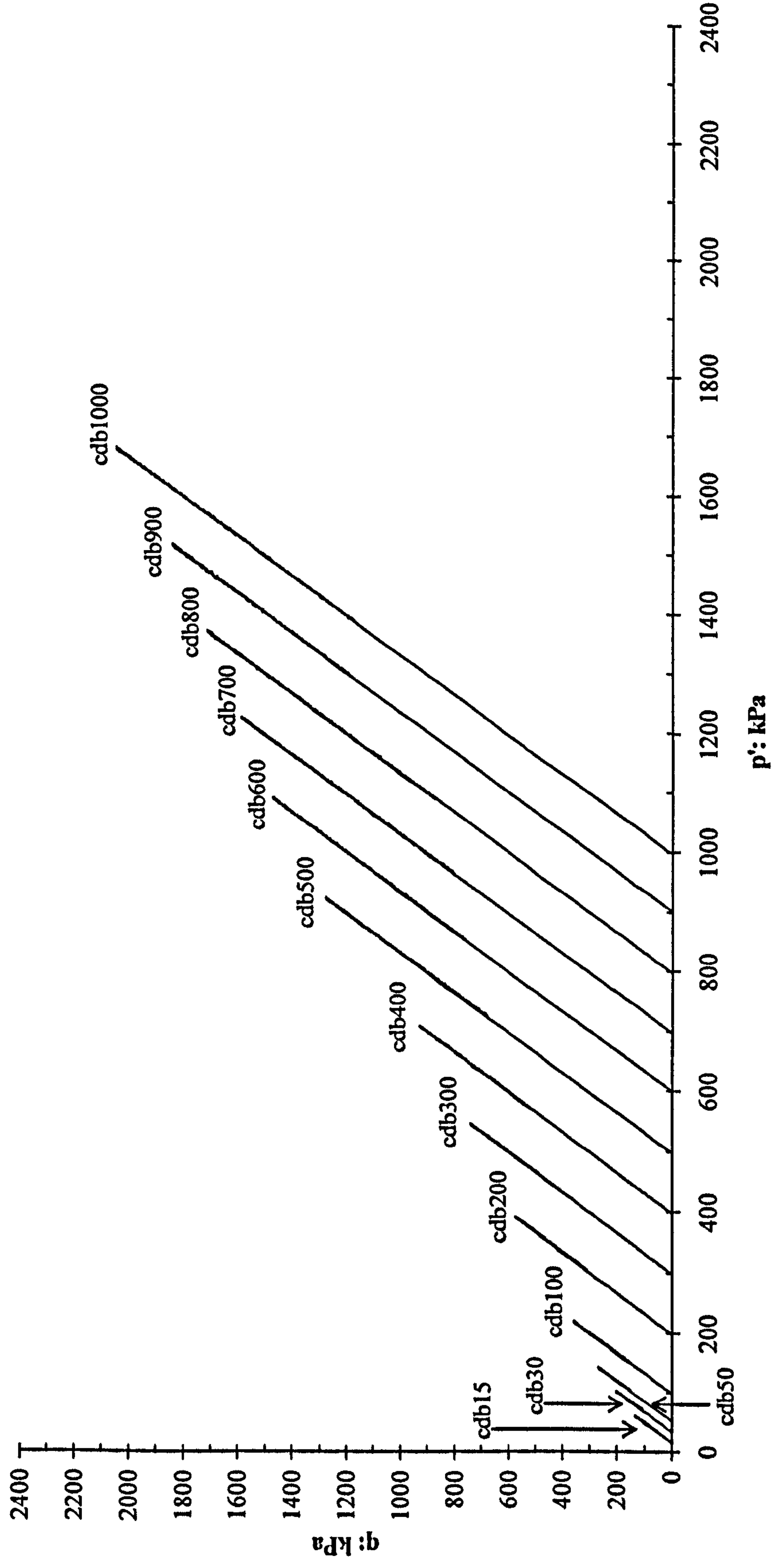


Figure 6.5: Effective stress paths for the drained tests on bonded soils

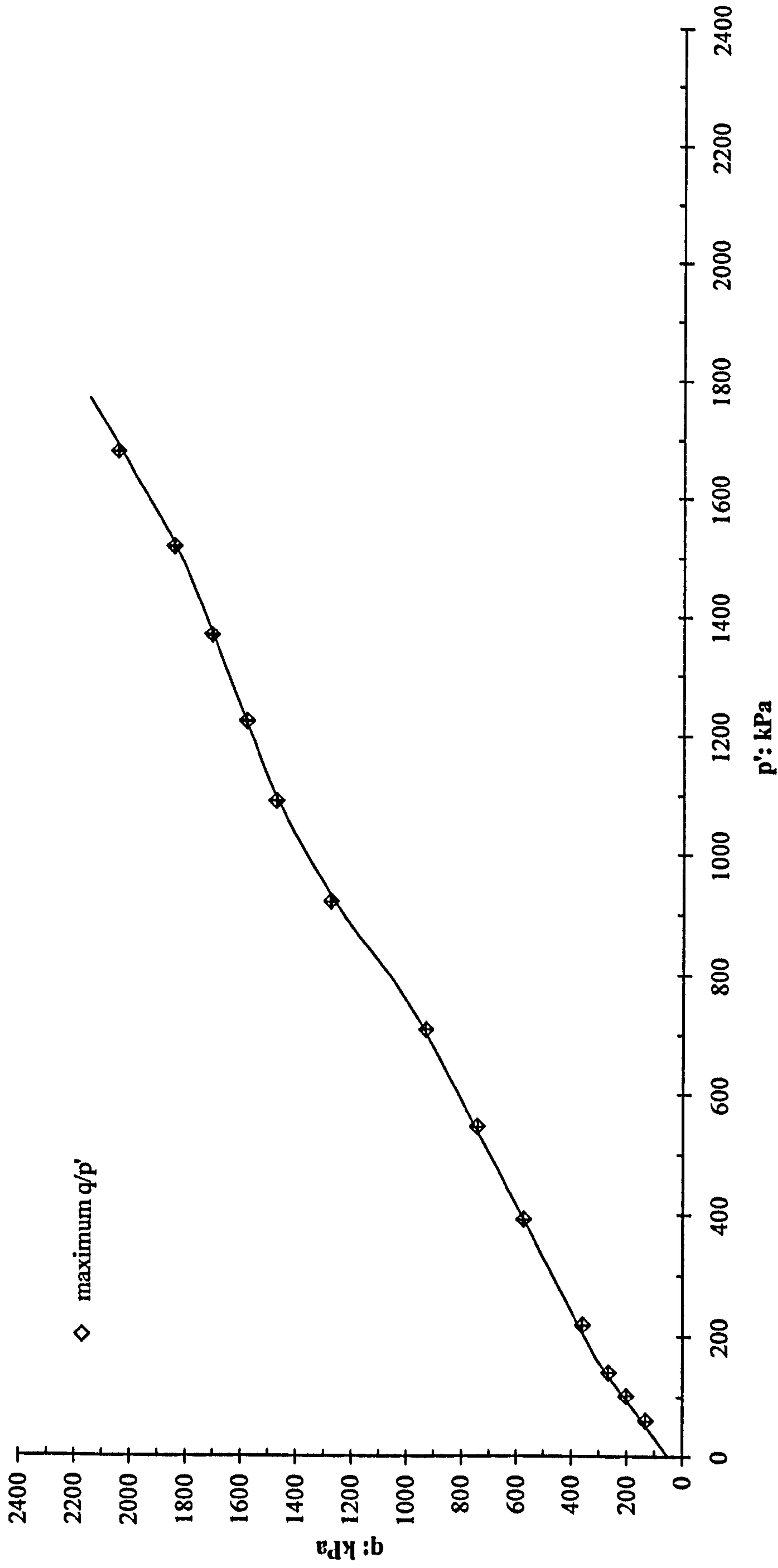


Figure 6.6: Bounding surface represented by maximum  $q/p'$  points for the drained tests on bonded soils (error bars were included)



reaching as high as 2.25. Whereas, samples sheared at effective confining stresses of 900kPa and 1000kPa there is no peak in stress ratio. By increasing the applied initial confining stress, the bond strength decreases as a result of bonds breaking down under the isotropic compressive stresses applied during consolidation. At the highest applied stress level (cdb900 and cdb1000) the strength attributed to bonds is almost destroyed and it behaves close to the destructured material (as will be discussed in more detail later).

#### **6.2.4 Bond Yields and Yield Surfaces**

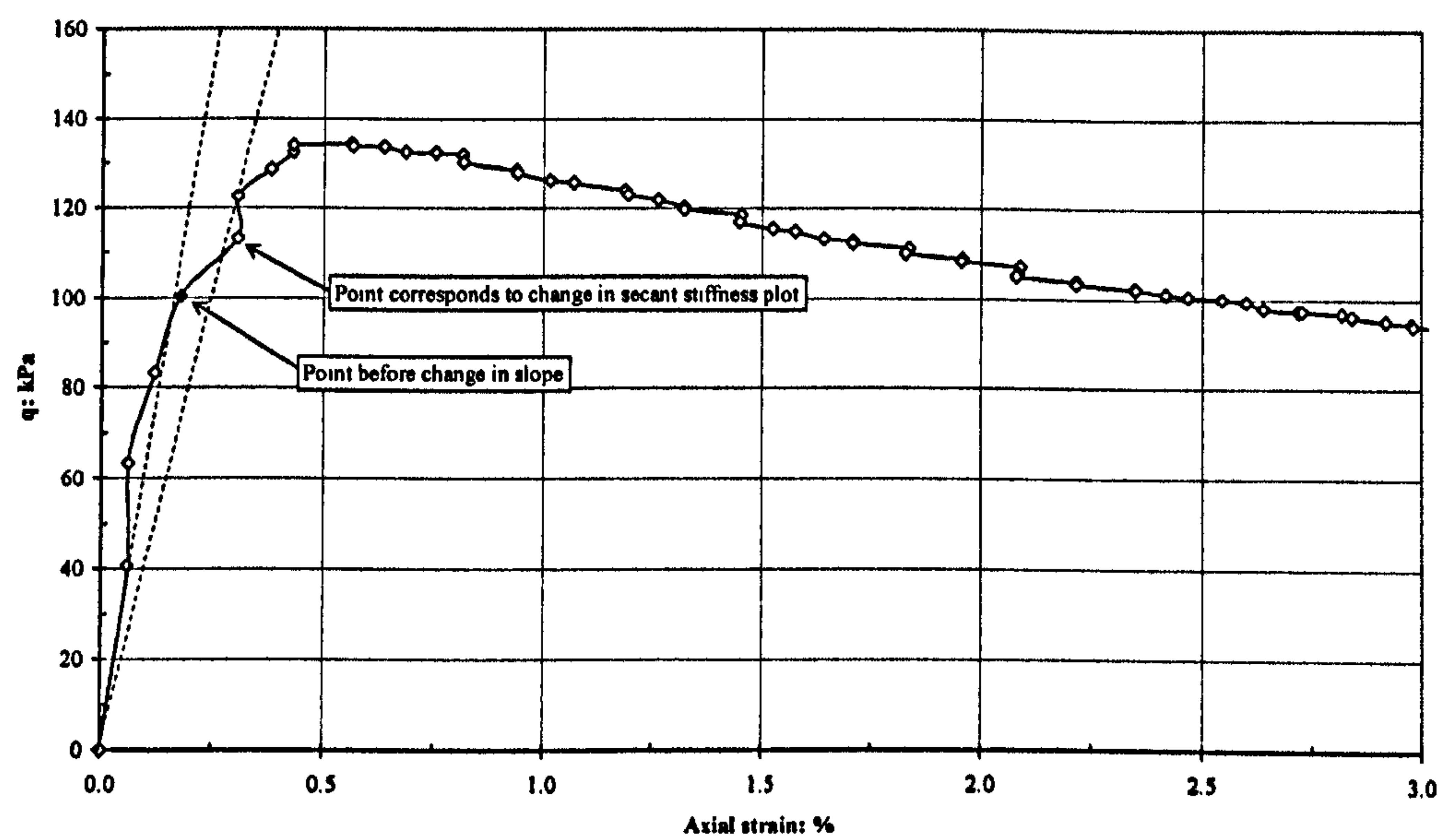
As stated early in Chapter 2, any applied stress to a bonded soil is supported by the bonds and interparticle contacts (Vaughan 1988). At the initial stage, the soil is very stiff predominantly due to the bond structure. When some of the bonds start to break, bonds are at their ultimate strength which is defined as a first yield. A further increase in bond stress, more breakage of bonds occur until at a state the bond strength becomes equal to the increase in bond stress, identified as second yield. From this stage, the bonded soil experiences loss of bond strength and stiffness with a further increase of axial strain.

For identification of the yield points for the bonded material, a technique adopted by Coop and Atkinson (1993) for artificially cemented carbonate sand was applied. Identification of the yield point was carried out based on assessment of stress-strain curves. A discontinuity in the stress-strain curves at early axial strain at a point where it starts to diverge from the linear part was selected as first yield. According to Coop and Atkinson (1993), the identified yield points corresponded to the start of breakage of the cemented bonds. However, in some of the tests the defining of the stress at which yielding occurred was quite difficult and personal judgement had to be exercised in selecting a yield stress. Since the axial strain in this study was measured by an external displacement transducer, errors in measurement readings were expected. In addition, bedding error also made the identification of the bond yield at small strains difficult, therefore only suitable for a qualitative study (Malandraki 1994).

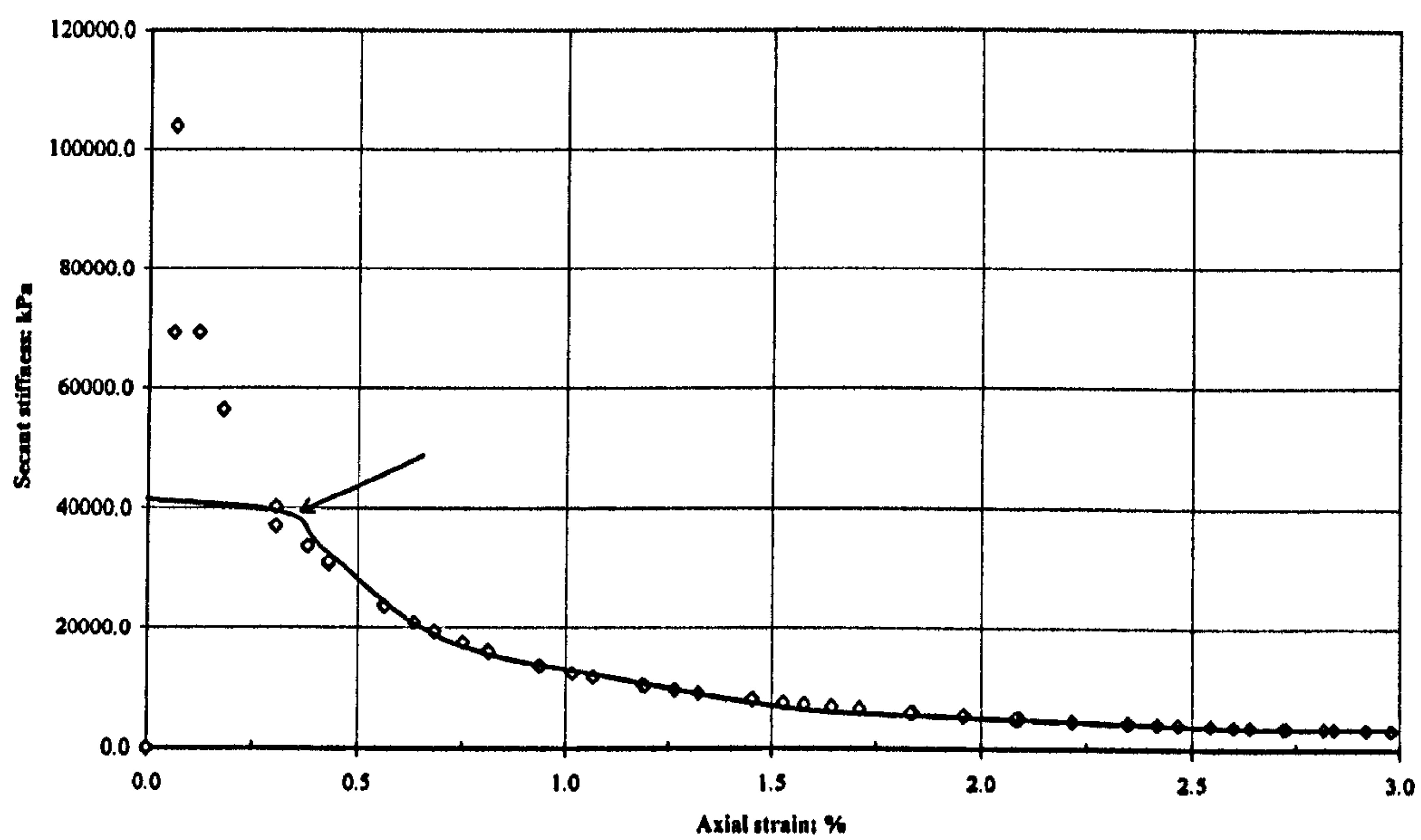
Three examples are shown in Figure 6.7, 6.8 and 6.9 representing the stress-strain and secant stiffness curves from the drained tests cdb15, cdb400 and cdb1000, respectively. The first yield point is identified at the position at point where the stress-strain curves begin to diverge from linearity. In Figure 6.7a, the stress-strain curve for test cdb15 shows linearity up to axial strain,  $\epsilon_a=0.178\%$  with deviator stress,  $q=100\text{kPa}$  (indicated by solid diamond symbol). However, the secant stiffness plot for cdb15 (Figure 6.7b) indicates a drastic change in stiffness can be closely estimated at axial strain,  $\epsilon_a=0.305\%$  corresponding to deviator stress,  $q=113\text{kPa}$ . Meanwhile for test cdb400, the stress-strain plot (Figure 6.8a) shows a straight line until the axial strain,  $\epsilon_a=0.583\%$  with deviatoric stress,  $q=489\text{kPa}$ . These values have a good agreement with the value from the secant stiffness plot as shown in Figure 6.8.b. For cdb1000, the stress-strain curve (Figure 6.9a) also show a straight line up to axial strain,  $\epsilon_a=0.394\%$  with deviatoric stress,  $q=863\text{kPa}$ . The secant stiffness plot in Figure 6.9b, however, indicates some fluctuation in deviator stress,  $q$  during early strain which then eases at axial strain,  $\epsilon_a=0.595\%$ . In this case, the yield stress again has to be estimated by taking into account the fluctuation of the data at early state.

The bond yield points were determined by carefully assessing the stress-strain and volumetric strain curves and stress paths in  $v$ - $p'$  space. From the  $v$ - $p'$  space (Figure 6.10), samples sheared at low stresses indicated clear compressive and dilatant behaviours whilst samples sheared at high stress levels were almost associated with compression behaviour to the end of shearing. Figure 6.10 show that the first yields located on the compression part (flat section) of the stress path in  $v$ - $p'$  space then followed by the bond yield just before samples begin to change in behaviour from compression to dilation. The position of first and final bond yields were also marked on the stress-strain and volumetric strain curves (Figure 6.11a and 6.11b). It can be clearly seen from the volumetric strain curves (Figure 6.11b) that the bond yield points occur at the end of compression behaviour which are apparently seen in samples sheared low to medium stress levels (cdb15 to cdb600). It is also seen that the bond yield points (except for cdb600) always occur at lower



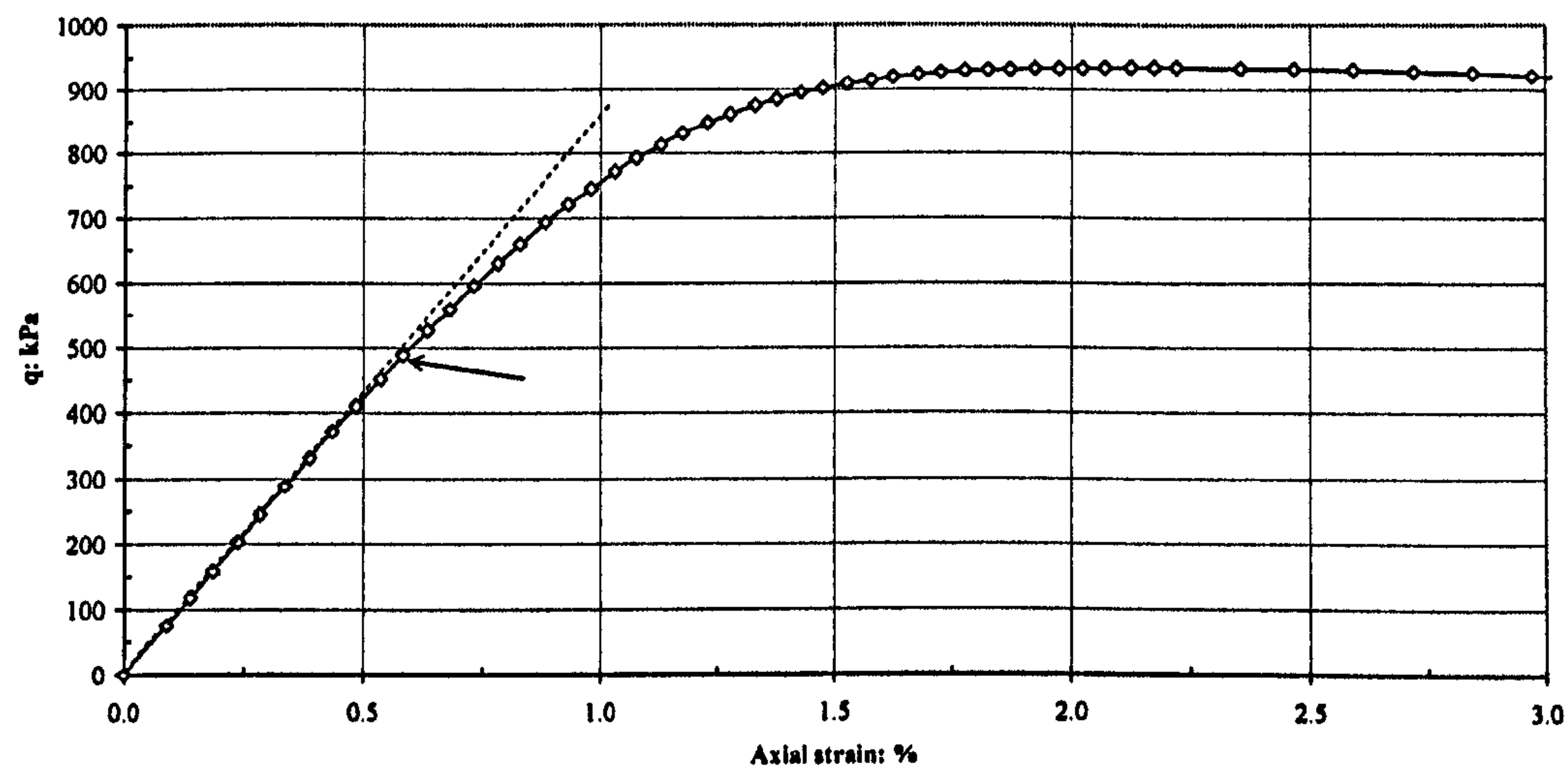


(a)

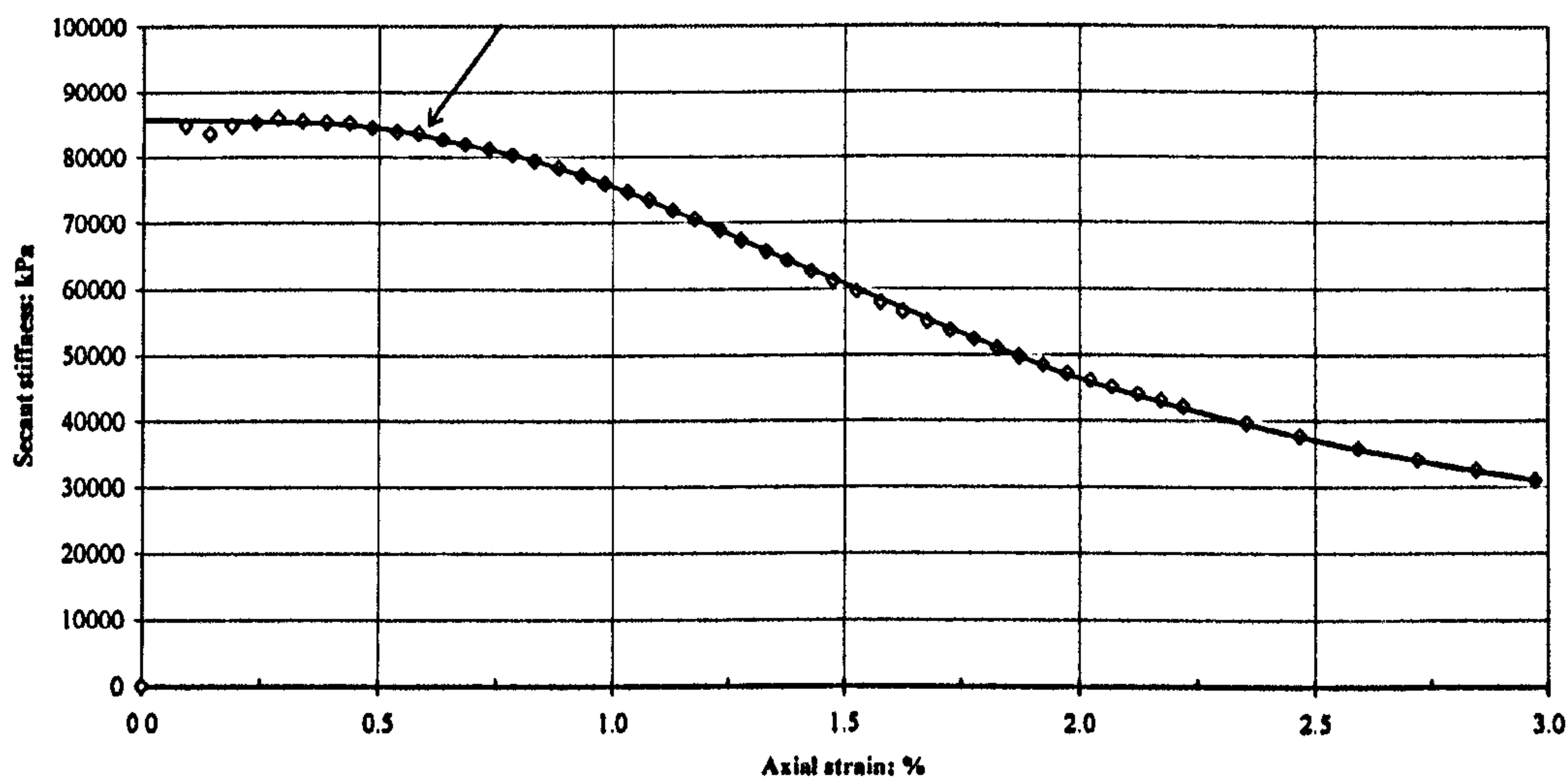


(b)

Figure 6.7: (a) Stress-strain curve and (b) secant stiffness plot for cdb15 sample



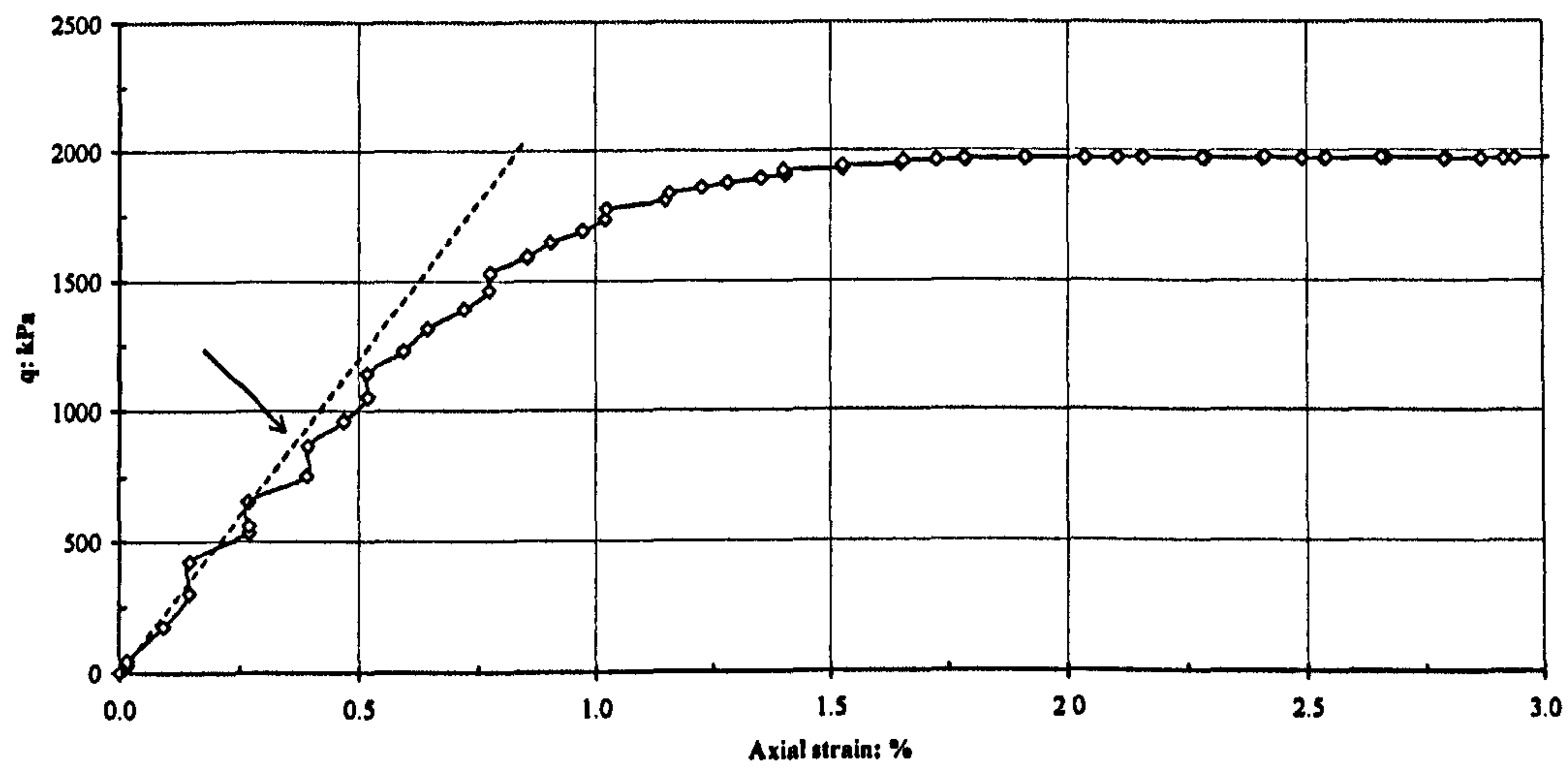
(a)



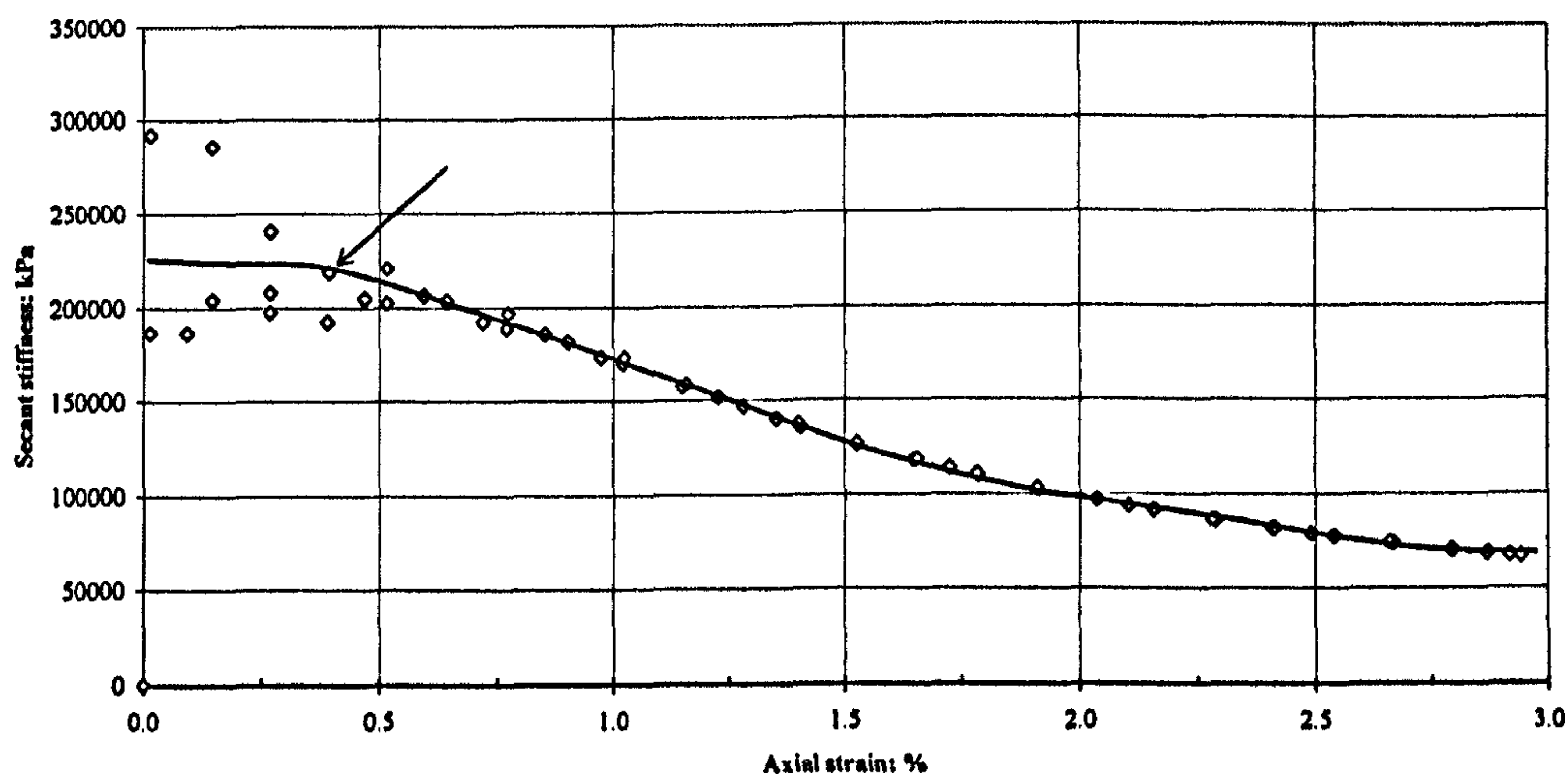
(b)

Figure 6.8: (a) Stress-strain curve and (b) secant stiffness plot for cdb400 sample





(a)



(b)

Figure 6.9: (a) Stress-strain curve and (b) secant stiffness plot for cdb1000 sample

strain levels than the maximum  $q/p'$  ratio point, indicating that bond strength has decreased and however has still contributed to higher stress ratios. In general, the distance between the position of bond yield and the maximum  $q/p'$  ratio increases

with an increase of applied confining pressures. Meanwhile, as seen in Figure 6.1, the distance between the maximum  $q/p'$  ratio and maximum rate of dilation become closer with increase in confining pressures suggesting that the increase in bonding breakdown and less influence of bond structure on the peak shear strength (mainly due to frictional resistance).

The bounding surface and the two yield surfaces for bonded samples are plotted together in the stress space shown in Figure 6.12. The bounding surface for the destructured samples was also plotted on the same axes for comparison. At low and high stress levels (up to 1100kPa), the bounding surface almost coincides with the final bond yield surface. However, at higher stresses ( $p' > 1100\text{kPa}$ ), the final bond yield surface slightly falls below the bounding surface for the bonded samples. The first yield surface is located below the two surfaces in the stress space. At low stress levels, the first yield surface increases linearly from origin and at stresses higher than 1100kPa it curves slightly and becomes parallel with the isotropic axis. However, no data available to prove a further trend of the first yield surface at higher stress levels indicating that bond strength has decreased but still contribute to higher stress ratios. In general, the distance between the position of final bond yield and the maximum  $q/p'$  ratio increases with an increase of applied confining pressures. Meanwhile, as seen in Figure 6.10a, the distance between the maximum  $q/p'$  ratio and maximum rate of dilation become closer with increase in confining pressures suggesting that the increase in bonding breakdown and less influence of bond structure on the peak shear strength (mainly due to frictional resistance).



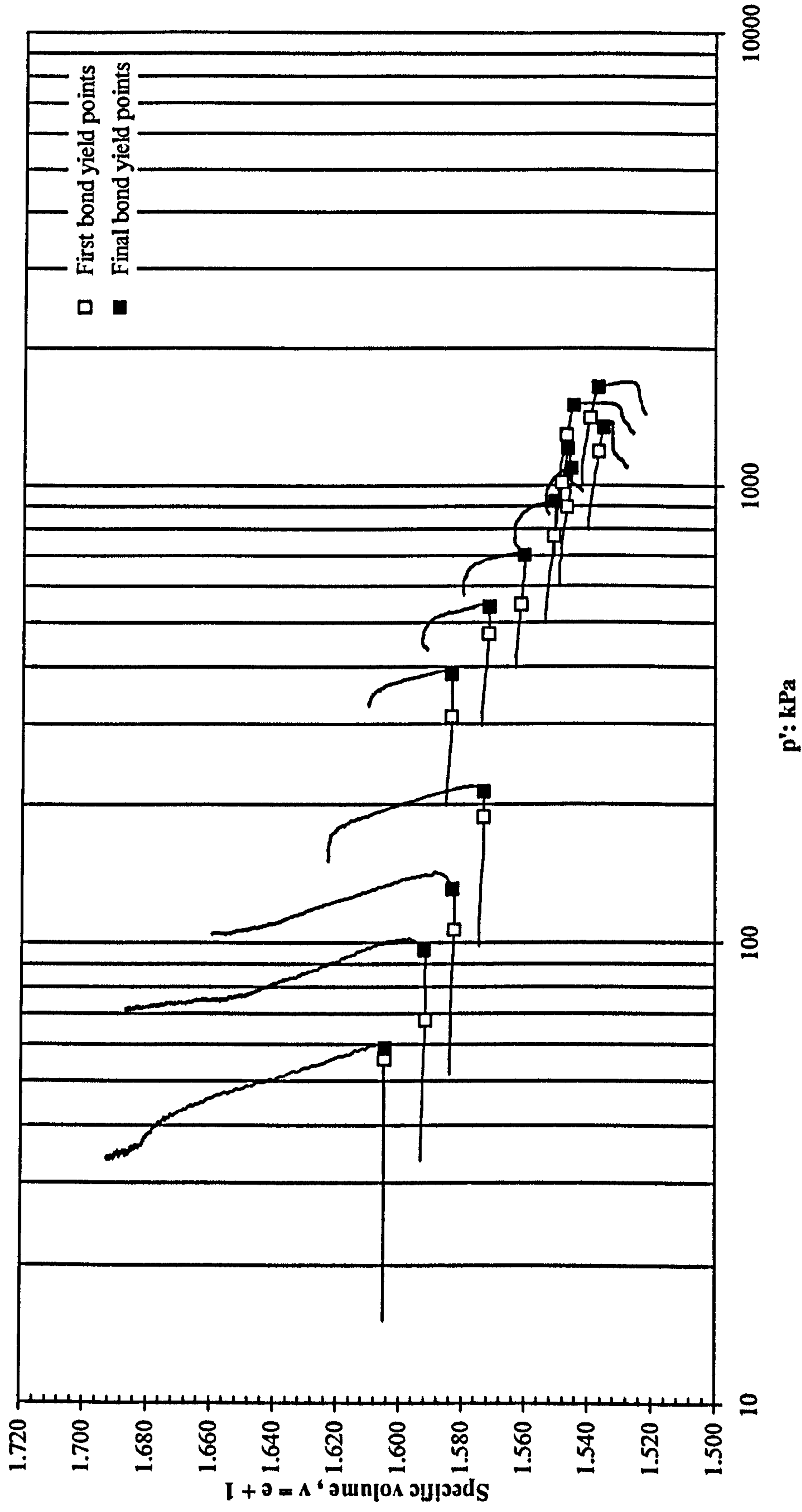
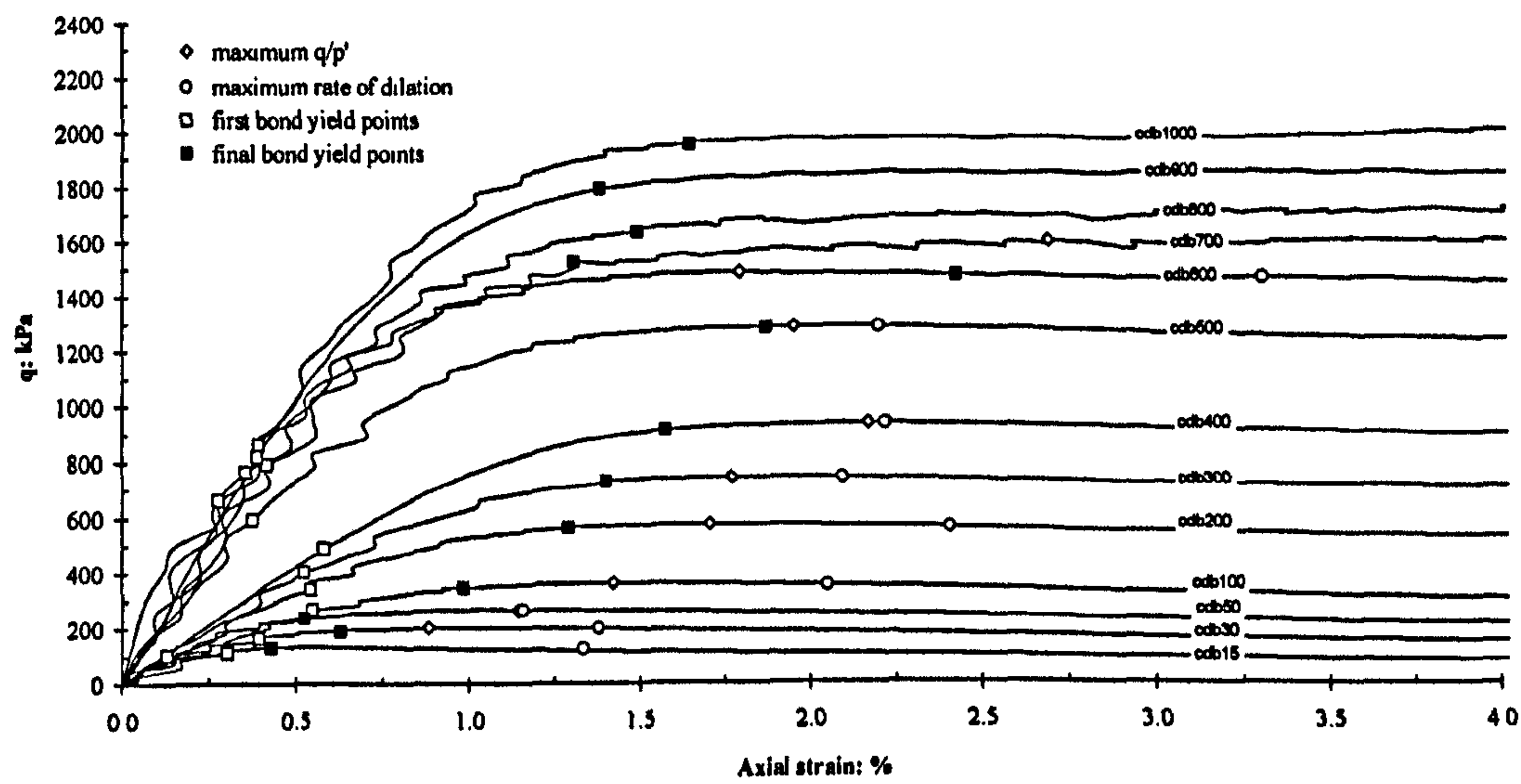
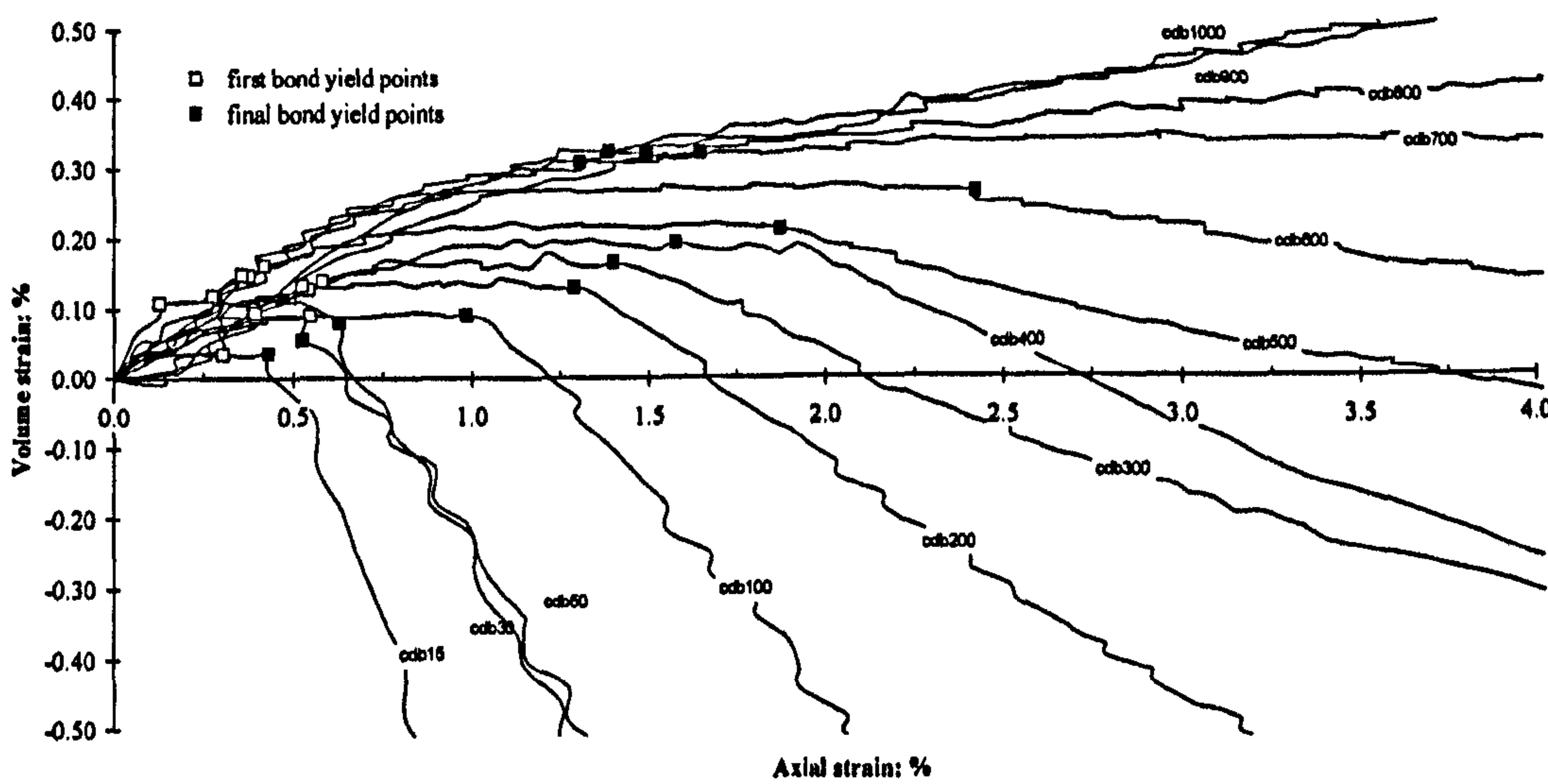


Figure 6.10: Specific volume curves for the drained tests showing the position of yield points



(a)



(b)

Figure 6.11: (a) Stress-strain curve and (b) volumetric strain curves for drained tests



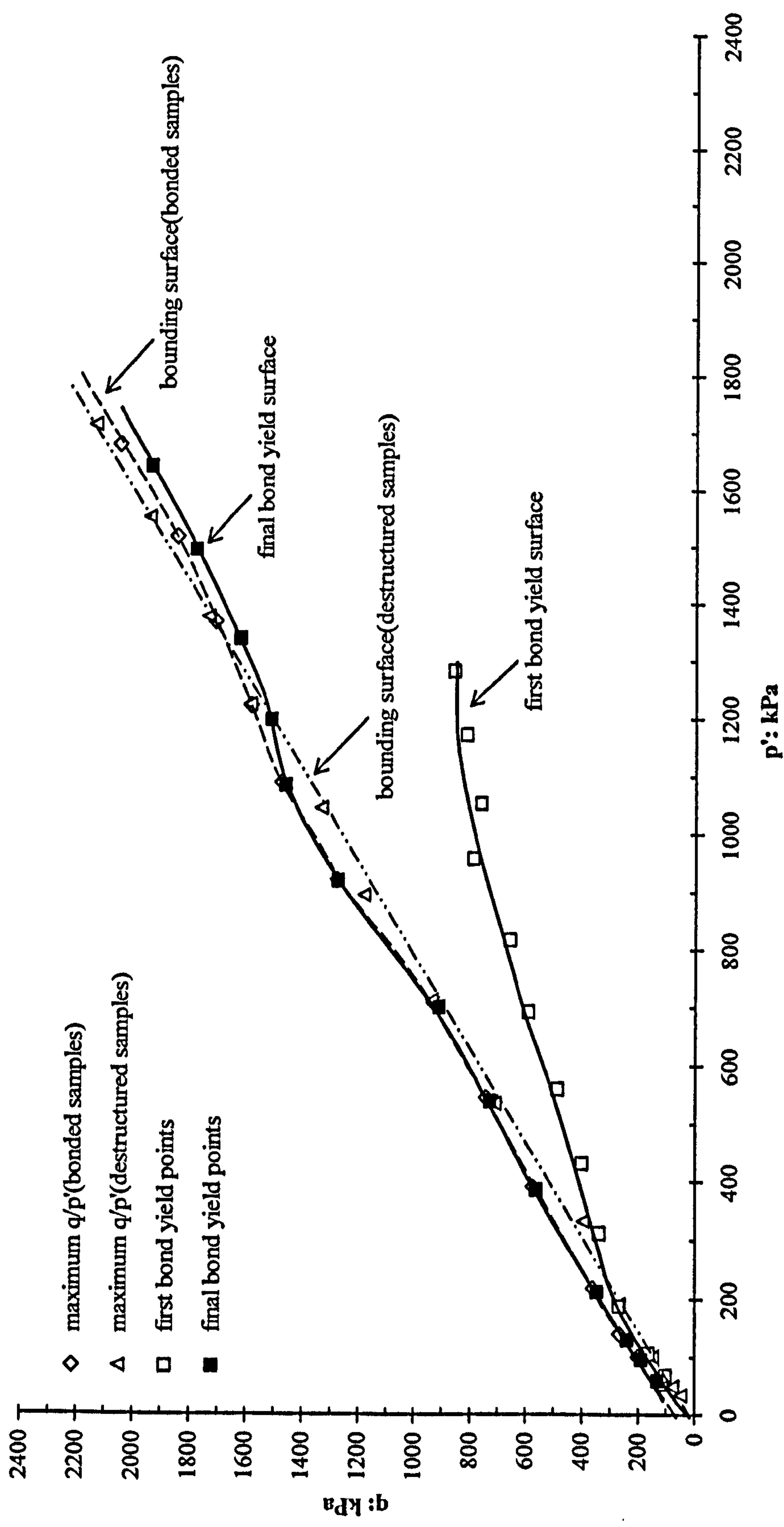


Figure 6.12: The first and bond yields surfaces for the drained tests on bonded samples

### 6.3 UNDRAINED TRIAXIAL TESTS

The results of the undrained tests on bonded samples are presented and described in this section. The results from the undrained tests are discussed in terms of deviator stress,  $q/p'$  ratio-strain and pore water pressure against axial strain. The bounding surface and phase transformation line are also presented in the stress space.

#### 6.3.1 Description of Testing

Thirteen artificially weakly bonded samples were tested using conventional undrained triaxial compression tests. Samples all had similar initial void ratio of 0.6 and were fired in the same way to produce consistent bond strength. The samples were initially consolidated under isotropic confining pressures, for an hour, which was sufficient to achieve full consolidation. All the samples were sheared under a constant rate of strain of 0.025%/min (or 1.5%/hr) the same as for drained tests. The shearing of the samples was carried out up to 30% of strain in order to establish the behaviour of samples towards the critical state. The samples used for the undrained tests are shown in Table 6.2. The identification of the tests was based on the type of test, condition of sample and applied confining stress prior to shearing. The first two letters “cu” refer to the consolidated undrained condition during shearing while the third letter “b” indicates a bonded type of sample was being used for the test. Finally the numbers refer to the value of confining stress used during isotropic consolidation of the sample.

#### 6.3.2 Stress Strain Behaviour

The deviatoric stress  $q$ , excess pore water pressure  $u$  and stress ratio  $q/p'$  are plotted against axial strain  $\epsilon_a$  in Figure 6.13, 6.14 and 6.15, respectively. The position of maximum  $(q/p')$ , maximum  $q$  and maximum rate of excess pore water pressure



change ( $\Delta_u/\Delta\epsilon_a$ ) are also marked on the stress-strain curves. The maximum rate of  $\Delta_u/\Delta\epsilon_a$  in an undrained test is equivalent to the maximum rate of dilation in a drained test as described in the previous chapter (5.2.1.3). All the samples showed a brittle failure mode associated with the development of shear planes where the stress ratio begun to decrease with increasing axial strain.

Table 6.2: The undrained tests on bonded samples

Test	Initial void ratio, $e_0$	Applied confining pressure, $p_o'$ , kPa
cub25	0.6100	25
cub30	0.6015	30
cub50	0.6077	50
cub100	0.6135	100
cub200	0.6083	200
cub300	0.6044	300
cub400	0.6012	400
cub500	0.5998	500
cub600	0.6035	600
cub700	0.6015	700
cub800	0.6081	800
cub900	0.6085	900
cub1000	0.6035	1000

All the bonded samples show an increase in deviatoric stress at early axial strain before achieving maximum  $q$  followed by a decrease in  $q$  with increasing strain. From Figure 6.13, the stress-strain curves indicate an apparent linear increment of stress with strain up to 1.5% - 2% before achieving their maximum strength. It can be seen that samples consolidated at higher confining stress have a more defined, apparently linear portion of stress-strain increment at earlier axial strain than samples at lower confining stresses ( $p_o' \leq 300\text{kPa}$ ). It can also be seen that the maximum deviatoric stress increases with the increase in applied confining stress

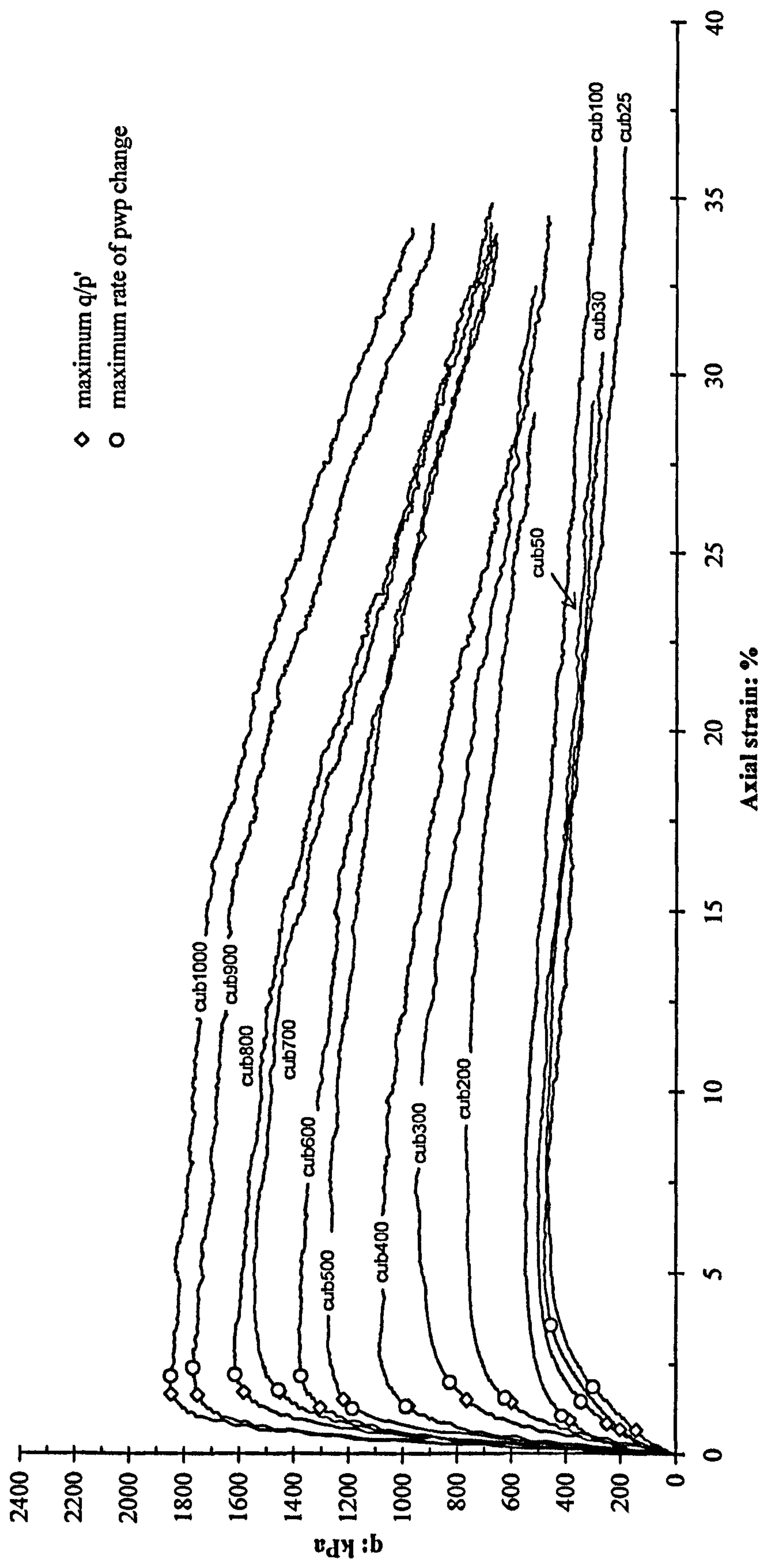


Figure 6.13: Stress-strain curves for the undrained tests on bonded soils



to the samples. The curves for the change in excess pore water pressure versus axial strain are shown in Figure 6.14. In most of the tests, the pore water pressure (pwp) reached a peak at approximately 1% of axial strain. The development of initial positive pore water pressure is associated with the tendency to compress of the bonded sample during shearing. The amount of initial positive pore water pressure corresponds to the amount of applied confining pressure. The pore water pressures gradually increase during early shearing up to maximum values then decrease with increasing axial strain. The development of negative pore water pressures occurred in most of the bonded samples which were consolidated at lower confining pressure (up to 500kPa). Samples with higher confining pressures between 600kPa and 1000kPa also developed positive pore water pressure which corresponds to a tendency to compress, and then followed by decreasing pore water pressure, but still in the positive range. It was found that the excess pwp continue to change up to the end of shearing. These indicated that all the tests did not achieve a true critical state.

It can also be seen from Figure 6.13, that the maximum  $q/p'$  ratio occurs at low strain (1% - 2%) then followed by the maximum rate of pore water pressure change. These two points become closer with increasing confining pressure. For tests cub400 and cub700, these two points almost coincide. It suggests that samples sheared at lower effective confining pressures, the peak strength is almost entirely due to bonding. By increasing the effective confining pressures, the peak strength is less dominated by bonding and this is indicated by the closeness of these two points in stress-strain curves (Figure 6.13). Once the maximum  $q/p'$  has been reached, deviator stress,  $q$  continues to increase slowly up to a maximum value before the initiation of a shear plane (except tests cub900 and cub1000). When shear planes developed in the samples, the stress ratio,  $q/p'$  begins to drop. The  $q/p'$  ratio curves shown in Figure 6.15 indicates that the stress ratios of the samples decrease with an increase in confining stress. Samples at low confining stress show a clear peak of  $q/p'$  but this becomes less significant for samples consolidated at

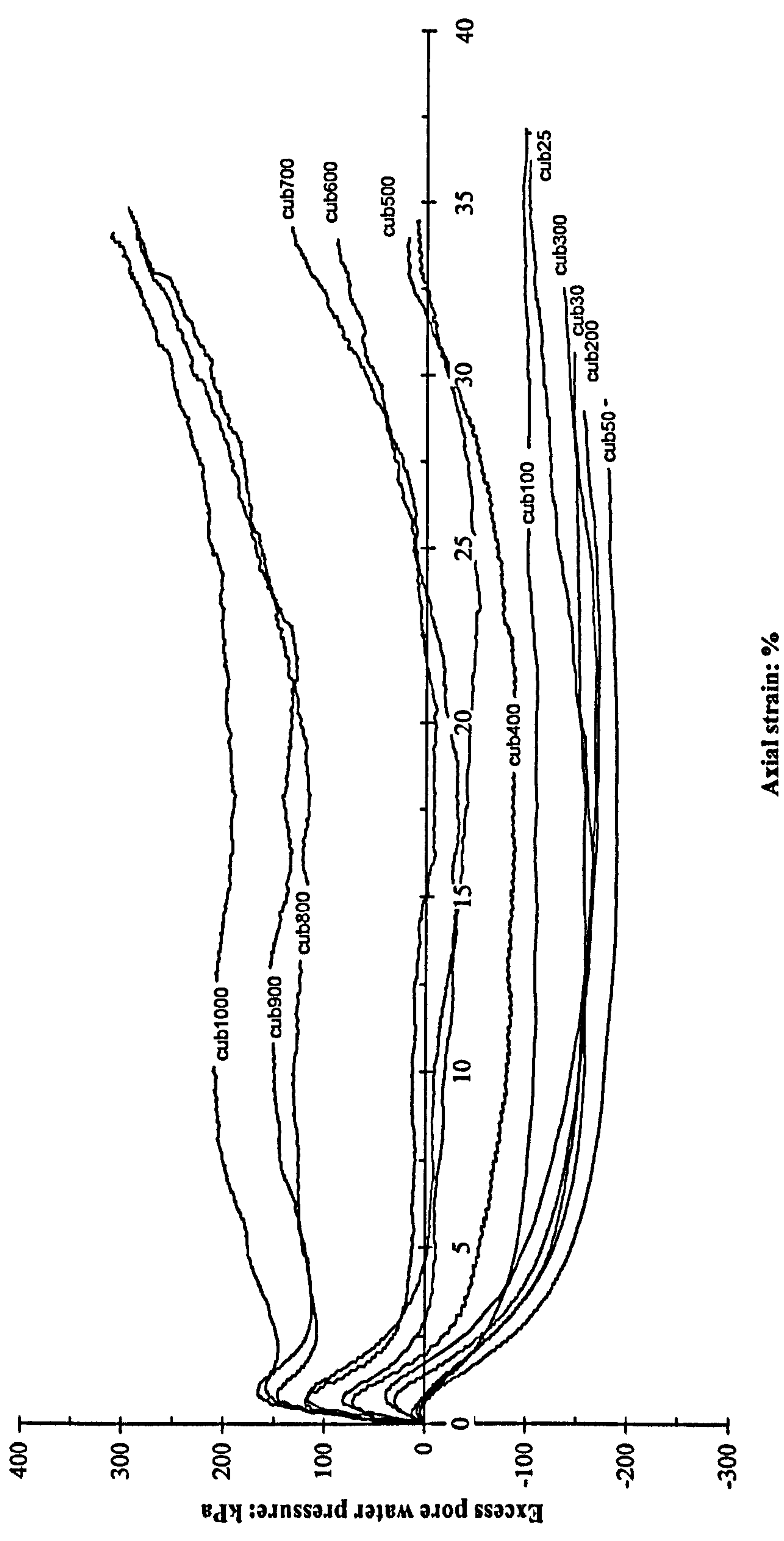


Figure 6.14: Excess pore water pressure against axial strain for the undrained tests on bonded soils



higher confining stress. The maximum pore water pressure and maximum rate of  $\Delta_u/\Delta\epsilon_a$  are also marked on the stress ratio curves in Figure 6.15. The point of maximum pore water pressure always occurs at earlier axial strain then followed by maximum rate of  $\Delta_u/\Delta\epsilon_a$ . Samples carried out at lower confining stresses (cub25-200) indicate that the maximum rate of  $\Delta_u/\Delta\epsilon_a$  occur after the peak in  $q/p'$  ratio. Meanwhile for samples consolidated at higher confining pressures ( $p_o' > 200\text{kPa}$ ) the maximum rate of  $\Delta_u/\Delta\epsilon_a$  becomes closer to the peak of  $q/p'$  ratio. As confining stress increases, a clear maximum stress ratio becomes more difficult to identify on the stress ratio-strain curves (becomes flat). However, it is seen that the position of maximum rate of  $\Delta_u/\Delta\epsilon_a$  points for cub700 to cub1000 are located close to the highest values of  $q/p'$  ratio on the flat section. This indicates that the maximum strength of those samples is dominantly due to friction rather than the effect of bonds. However, a peak of  $q/p'$  ratio still can be seen for samples sheared at confining stresses,  $p_o'$  between 400kPa and 600kPa.

### 6.3.3 Stress Paths and Bounding Surfaces

The effective stress paths for the undrained tests on bonded samples are plotted in stress space in Figure 6.16. The position of the maximum  $q/p'$  ratio, maximum rate of pwp change and maximum deviatoric stress,  $q$  is also located on the stress path curves. From the figure, each individual effective stress path initially defines nearly a straight line. For the tests carried out at low stresses (cub25 to cub300), the stress paths linearly increased, reached the maximum  $q/p'$  ratio and then changing in direction with  $q$  continued to increase. The stress paths begin to reverse their direction after maximum  $q$  is reached, followed by a decrease in  $q$  and  $p'$ . This is most probably associated with the development of shear planes. For these tests, the maximum  $q/p'$  ratio is achieved at lower deviator stresses than the point at which the maximum rate of pwp change occurs.

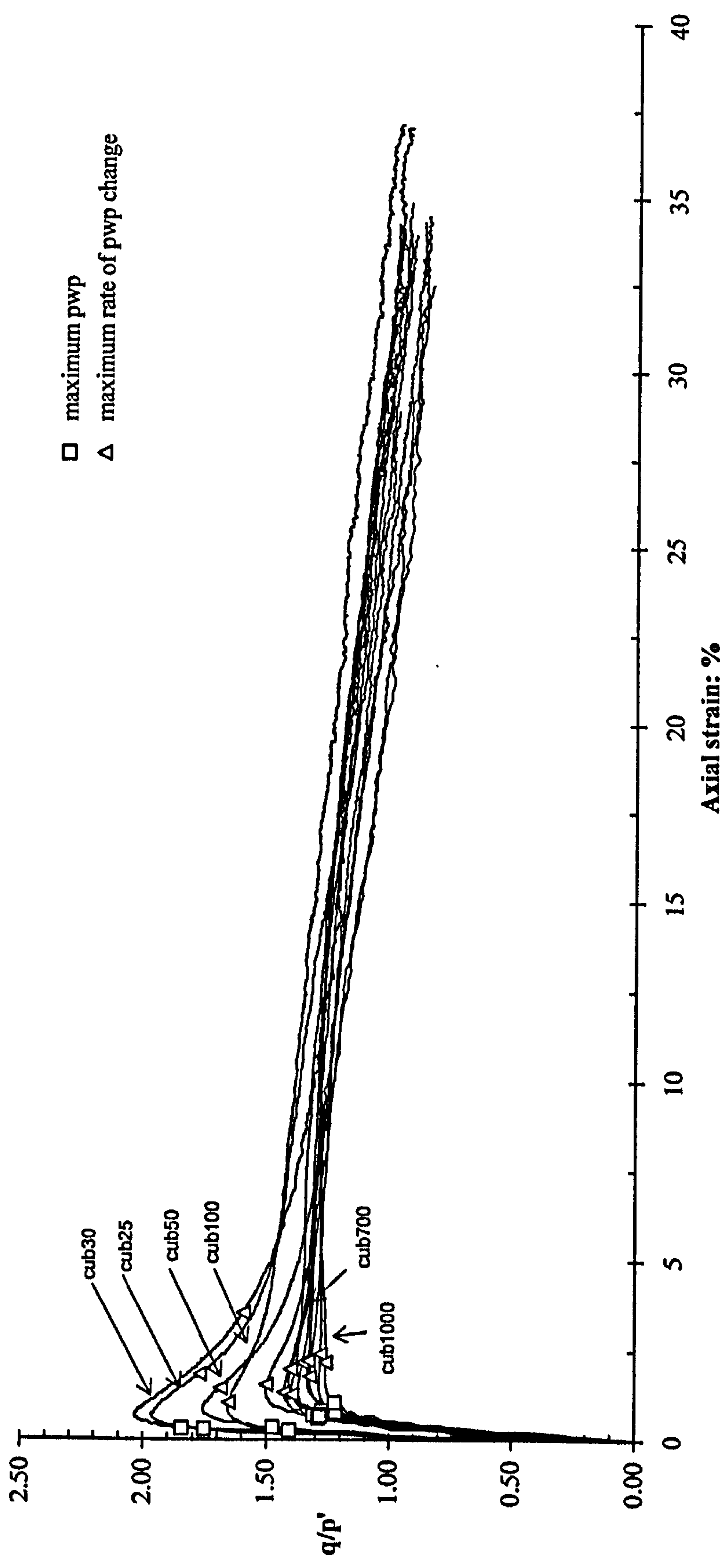


Figure 6.15: Stress ratio,  $q/p'$  against axial strain for the undrained tests on bonded soils



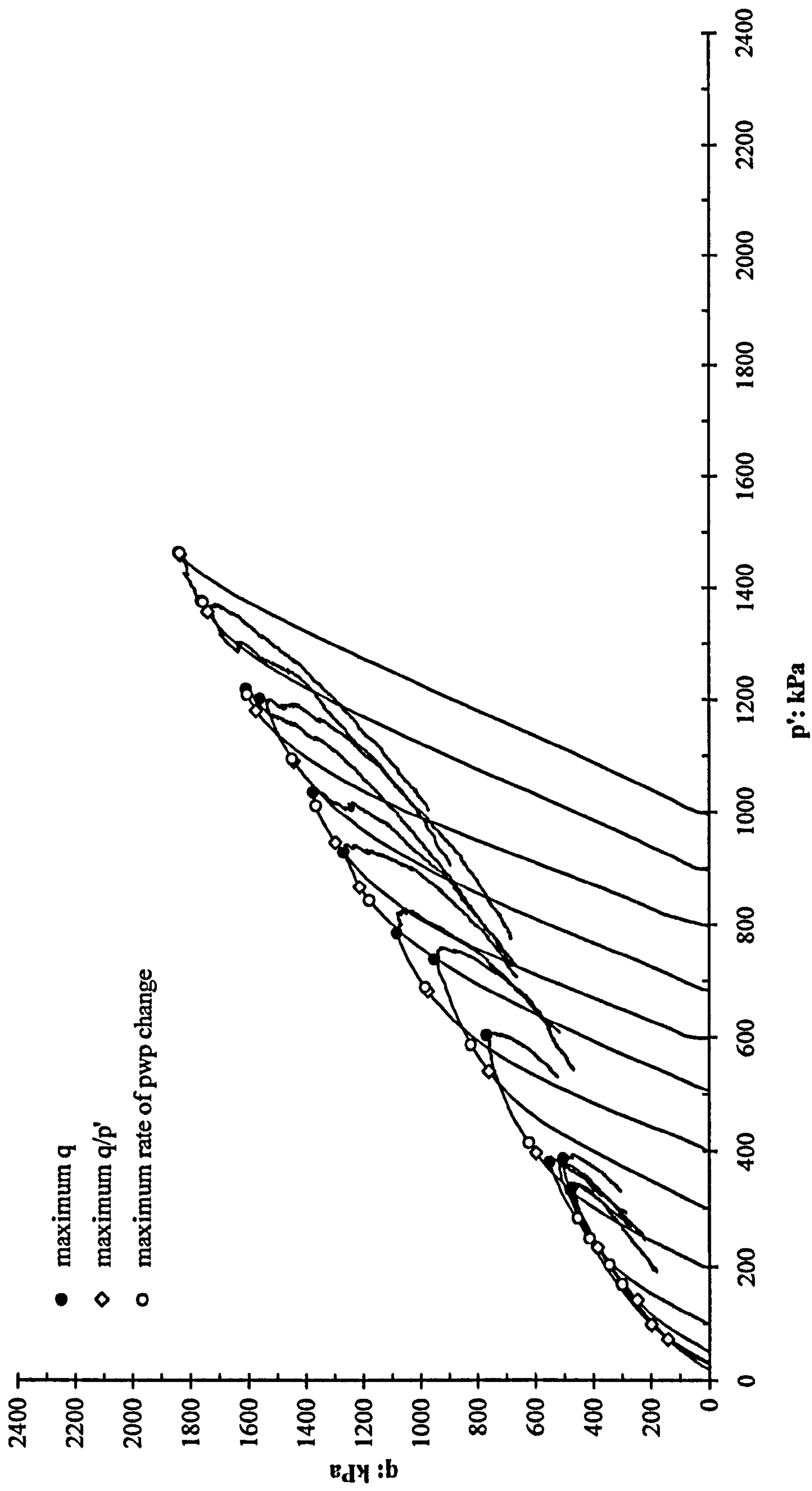


Figure 6.16: Effective stress paths for all the undrained tests on bonded soils

Meanwhile, at higher stresses (tests cub400 to cub800), the maximum  $q/p'$  ratio is closer to the point of maximum rate of pwp change. The stress paths linearly increase, reach the maximum  $q/p'$  ratio and  $q$  continued to increase under lower stress ratio. At  $p_o' > 800\text{kPa}$  (cub900 and cub1000), the stress paths of the samples reach the maximum  $q/p'$  ratio and continue with decreasing stress ratio before the stress paths change in direction as a result of increasing positive pore water pressure during shearing. It can clearly be seen that for test cub1000 the change of stress path is more apparent than test cub900.

The bounding surfaces and phase transformation lines for the bonded samples were defined from the values of maximum  $q/p'$  ratio and maximum pore water pressure. The bounding surface is re-plotted in Figure 6.17. It can be clearly seen from the figure that the bounding surface indicates some curvature above  $p' = 750\text{kPa}$  which is also obvious at lower stresses. This condition was also found by Malandraki (1994) who suggesting that the decrease in the slope of the bounding surface indicates the loss of the bond strength of the samples at failure. For the phase transformation line, it shows a very similar pattern with some curvature up to  $p' = 800\text{kPa}$ . Therefore, it is suggested that the behaviour of the samples is influenced by the presence of bonds.

#### 6.3.4 Bond Yield and Yield Surface

A similar approach was applied in order to define the first bond yield points for the bonded material under undrained tests. The first bond yield was identified from the stress-strain curves at a point where it begun to diverge from linear. Figure 6.18, 6.19 and 6.20 are examples from the undrained test cub30, cub100 and cub1000, sheared at 30, 100 and 1000kPa of effective confining pressures, respectively. As seen in Figure 6.18.a, the first bond yield point was best identified at axial strain,  $\epsilon_a = 0.196\%$  with deviator stress,  $q = 97\text{kPa}$ .



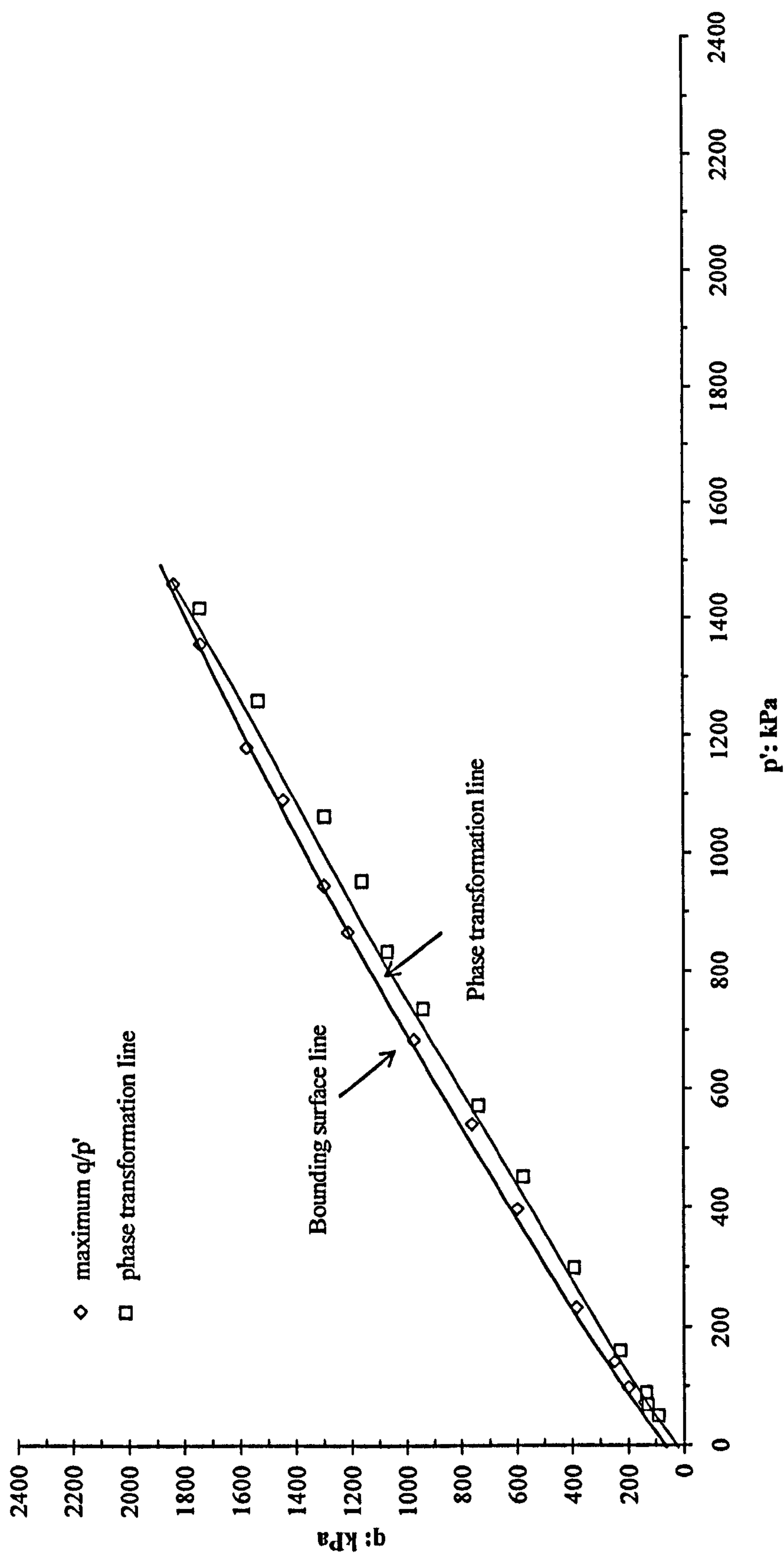


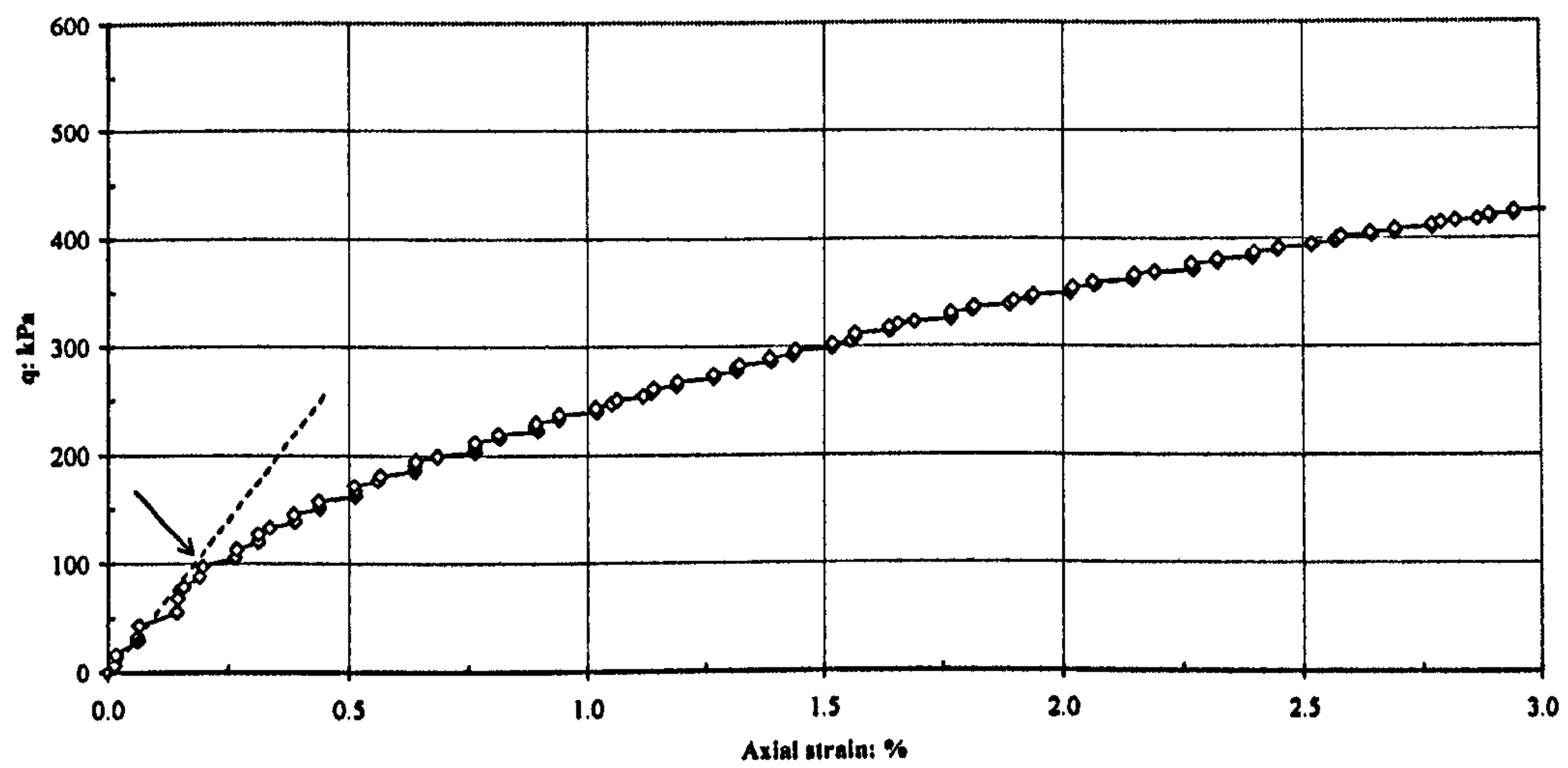
Figure 6.17: Bounding surface and phase transformation lines for the undrained tests on bonded soils

As can be seen from the secant stiffness plot in Figure 6.18b, the chosen values correspond to the best-fit curve delineated across the scattered data point of secant stiffness at early axial strain. Meanwhile for the cub100, the stress-strain curve exhibits a clear linear increase of deviatoric stress,  $q$  up to axial strain,  $\epsilon_a=0.079\%$  (as shown by arrow in Figure 6.19a) and this agree with the secant stiffness plot (Figure 6.19b). For cub1000 (Figure 6.20a), the first yield was defined at axial strain,  $\epsilon_a=0.530\%$  with deviator stress,  $q=1250\text{kPa}$ . Figure 6.20b shows the correspond plot of secant stiffness against axial strain. It is clearly show that the secant stiffness drops after the first bond yields were achieved.

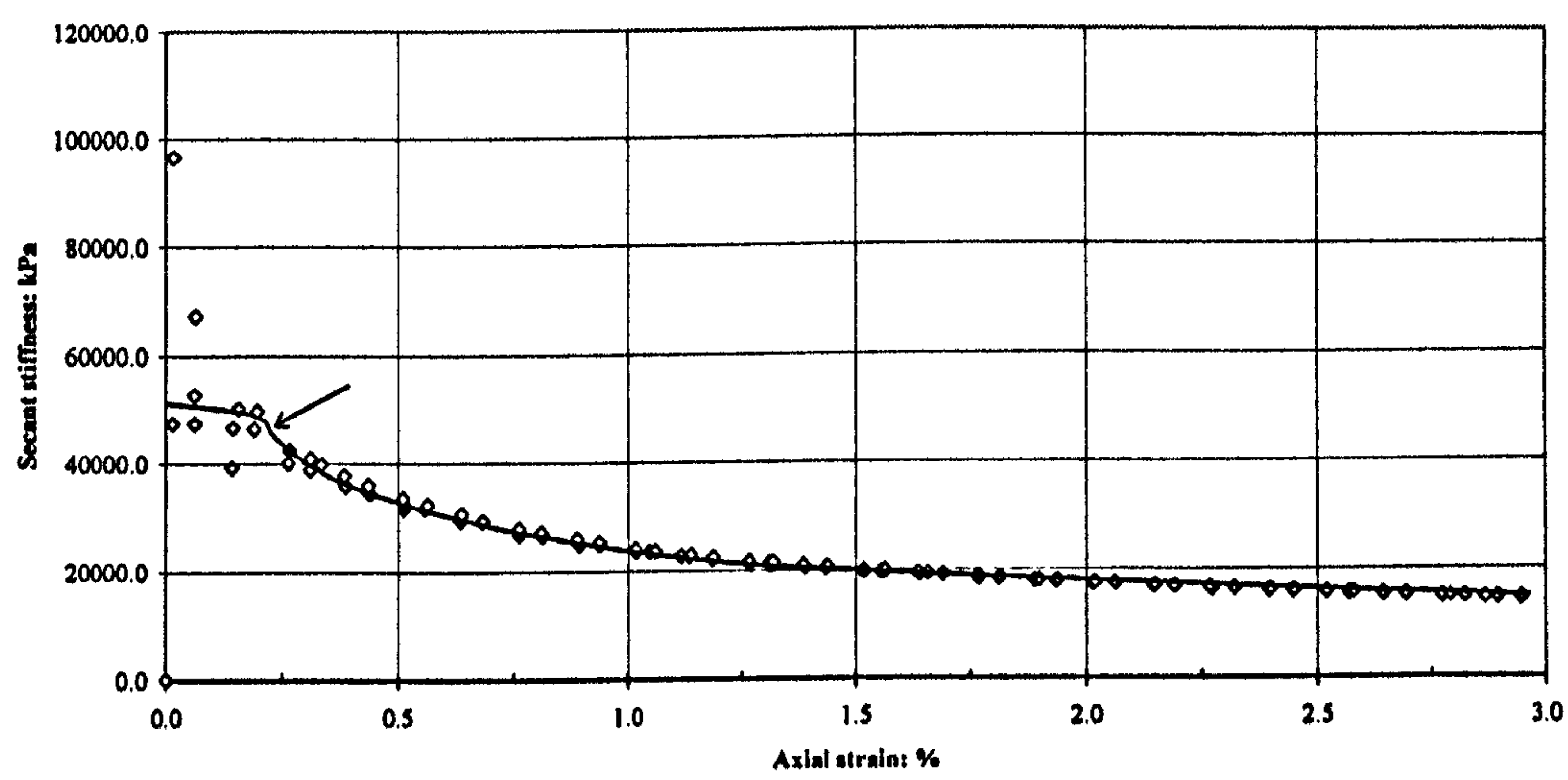
The final bond yield points were identified by carrying out assessment on the stress-strain and excess pwp-axial strain curves. The positions of first and final bond yields were marked on the stress-strain and excess pwp against axial strain curves (Figure 6.21a and 6.21b). In drained tests, the position of final bond yield was located at the end of compression behaviour. In undrained tests, the position of final bond yield is defined at the point where excess pwp starts to drop indicating the beginning of the dilation behaviour (Figure 6.21b). The final bond yield points are also plotted in  $q$ - $p'$  space as shown in Figure 6.22. The final bond yield points always occur at lower axial strain than the maximum  $q/p'$  ratio points, suggesting that the bond strength has decreased, however still contributes to higher stress ratios. The distance between the bond yield points and maximum  $q/p'$  ratios also increases with an increase in applied confining pressures suggesting that the increase in bonding breakdown results in less influence of bond structure on the peak shear strength. This is also clearly shown in the stress-strain curves as the distance between the bond yield and maximum  $q/p'$  ratio points increases with an increase in confining pressures (Figure 6.21a).

The bounding surface and the two yield surfaces for bonded samples are plotted together in the stress space shown in Figure 6.23. The bounding surface is slightly higher than the bond yield surface for the bonded samples. However, the bounding



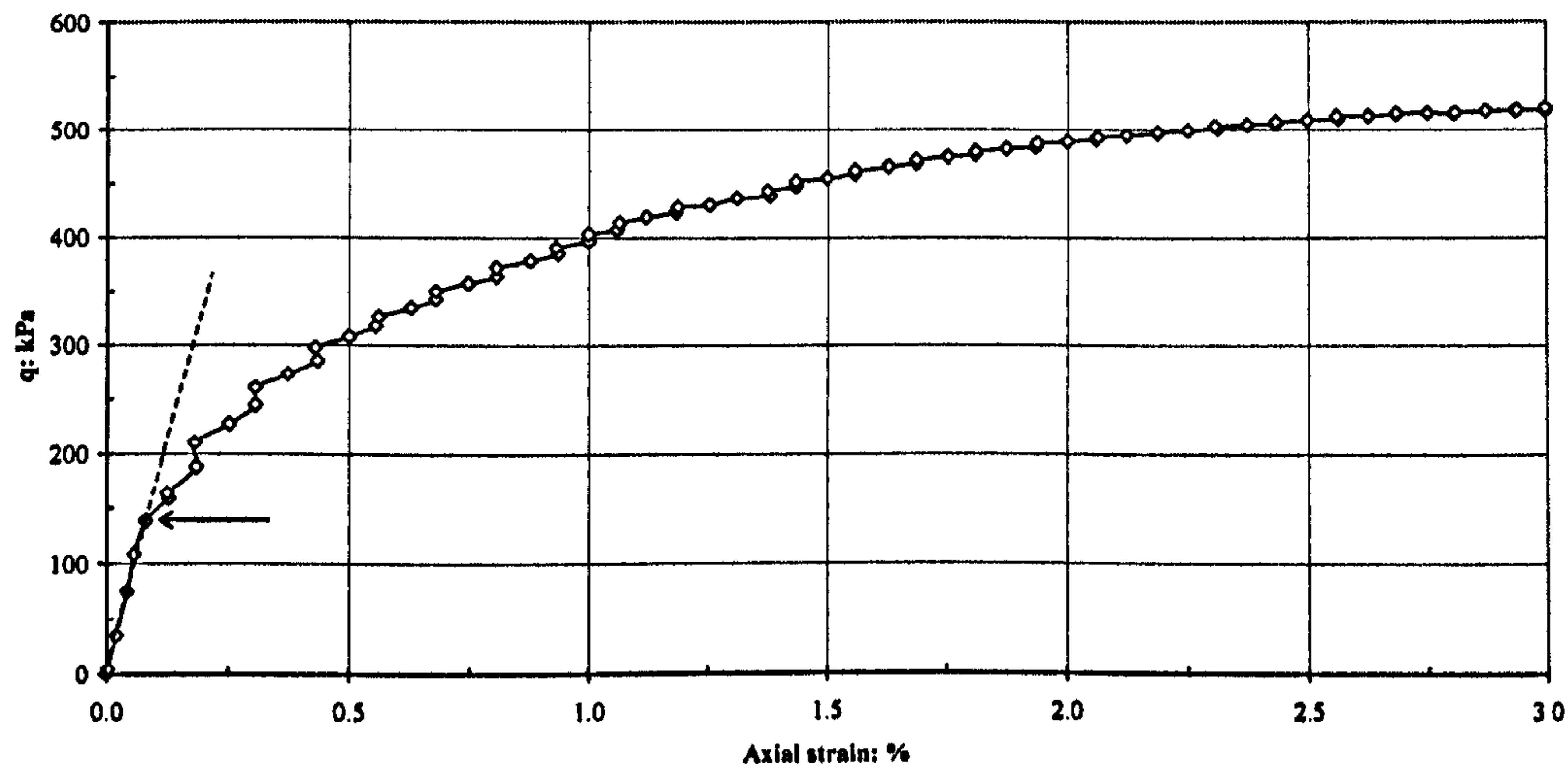


(a)

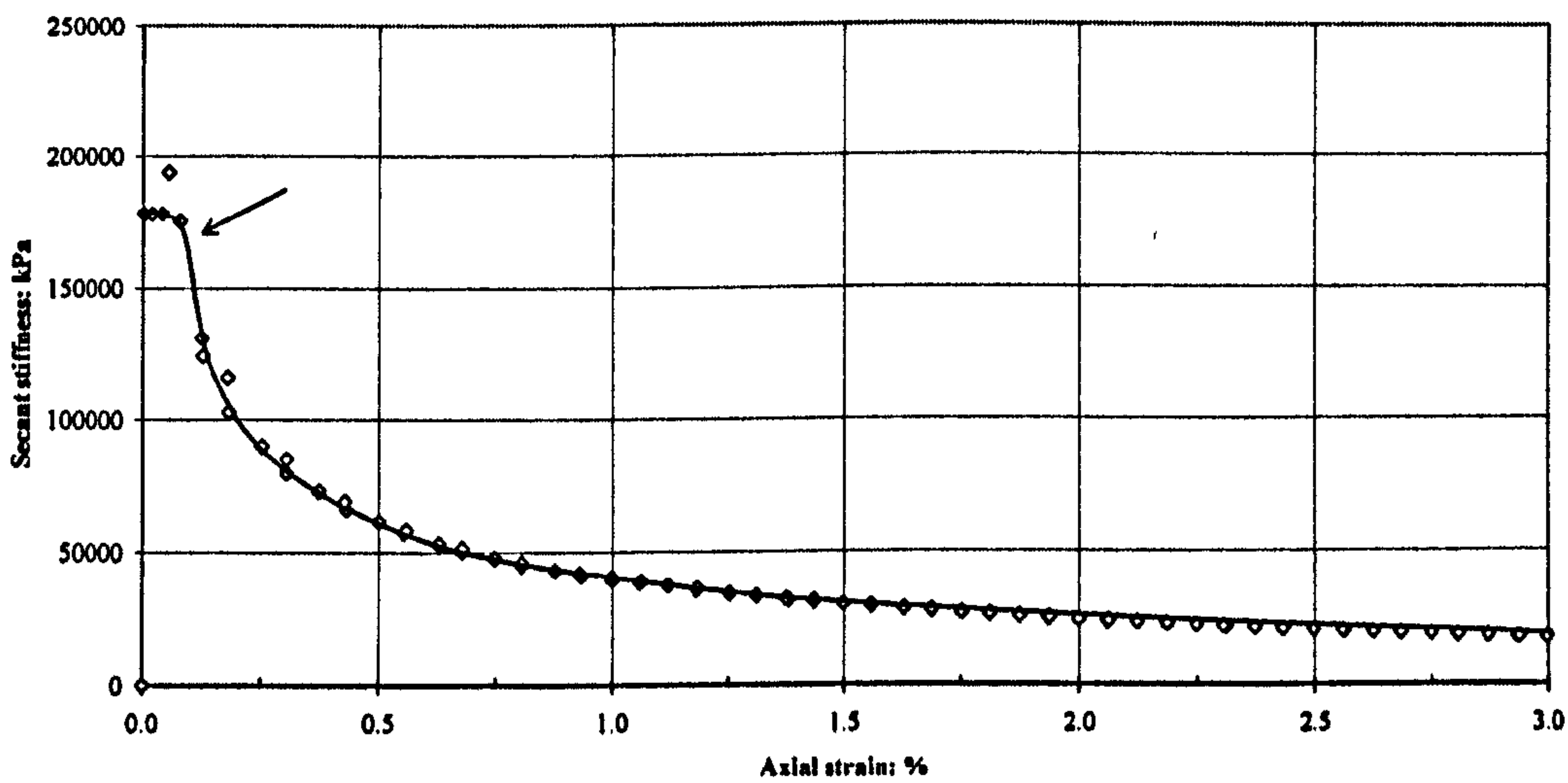


(b)

Figure 6.18: (a) Stress-strain curve and (b) secant stiffness plot for cub30 sample



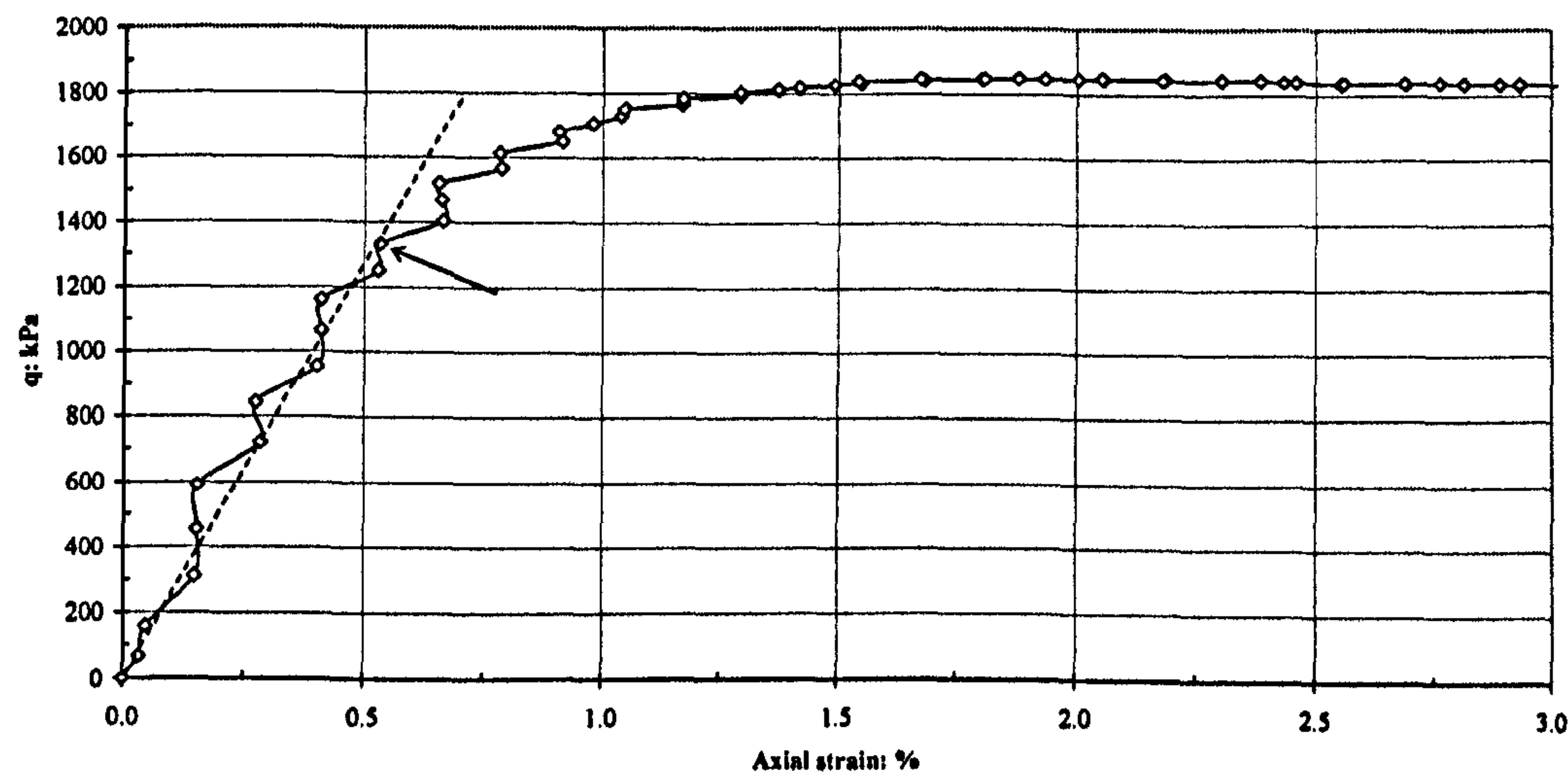
(a)



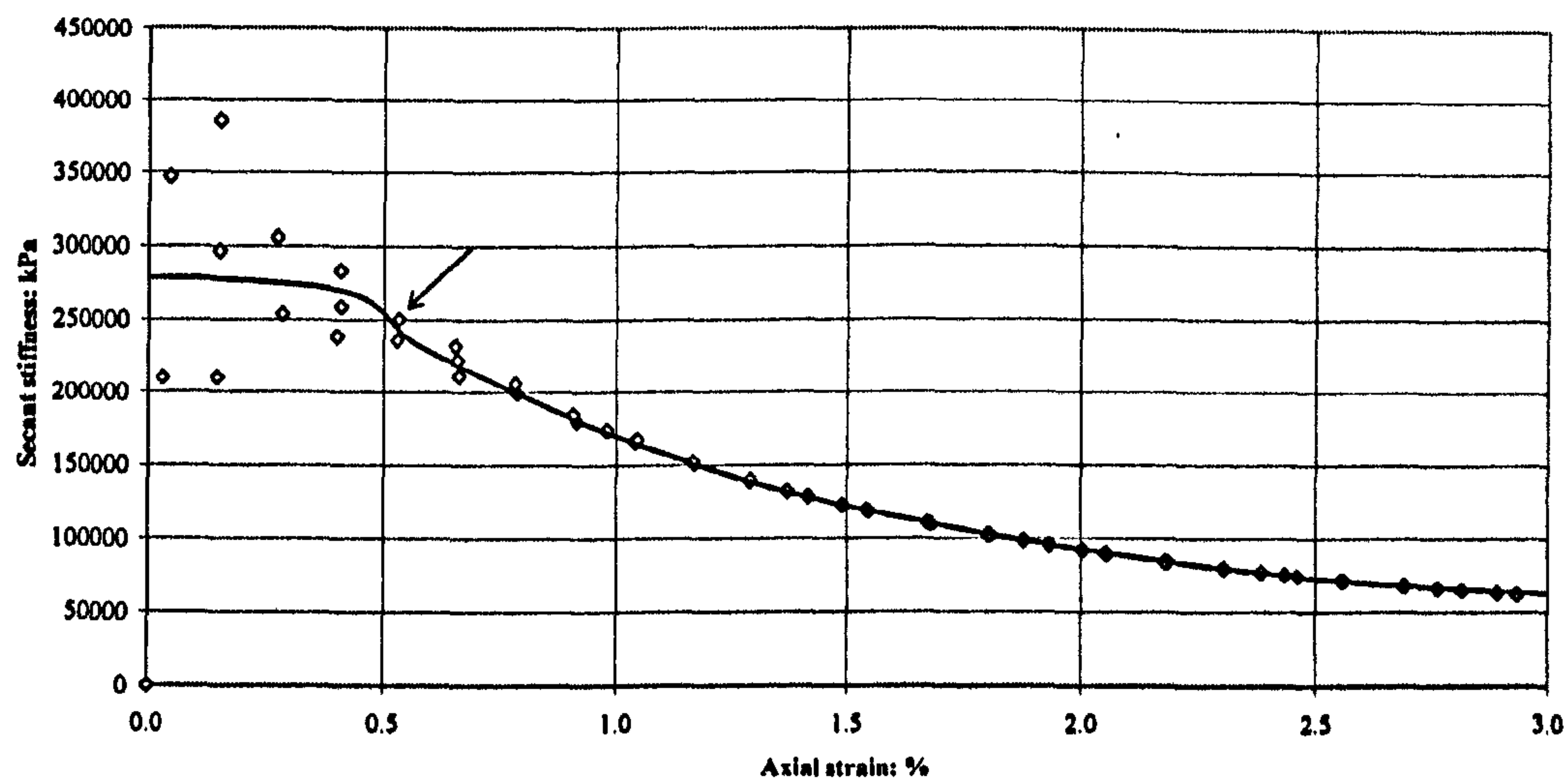
(b)

Figure 6.19: (a) Stress-strain curve and (b) secant stiffness plot for cub100 sample



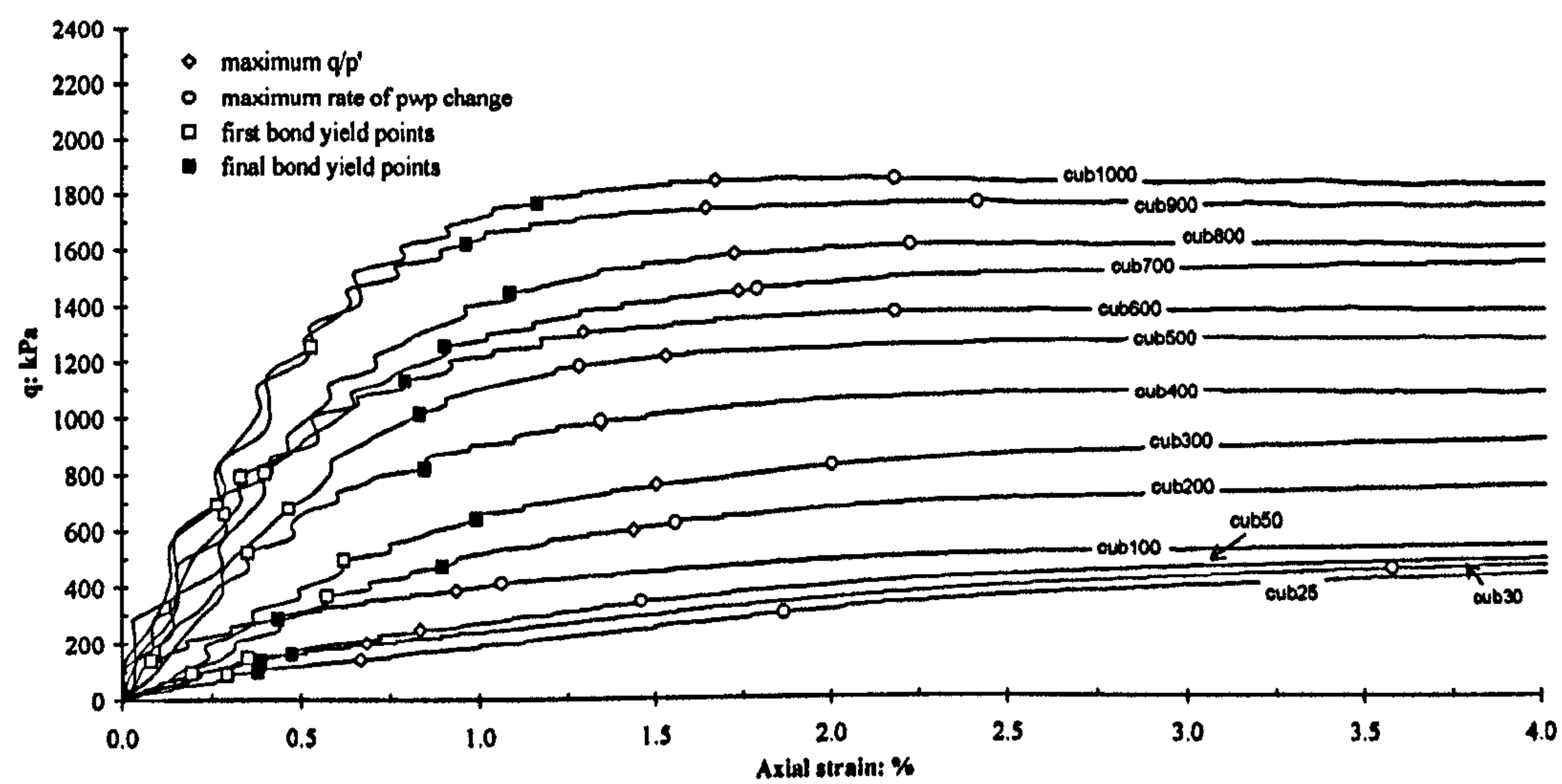


(a)

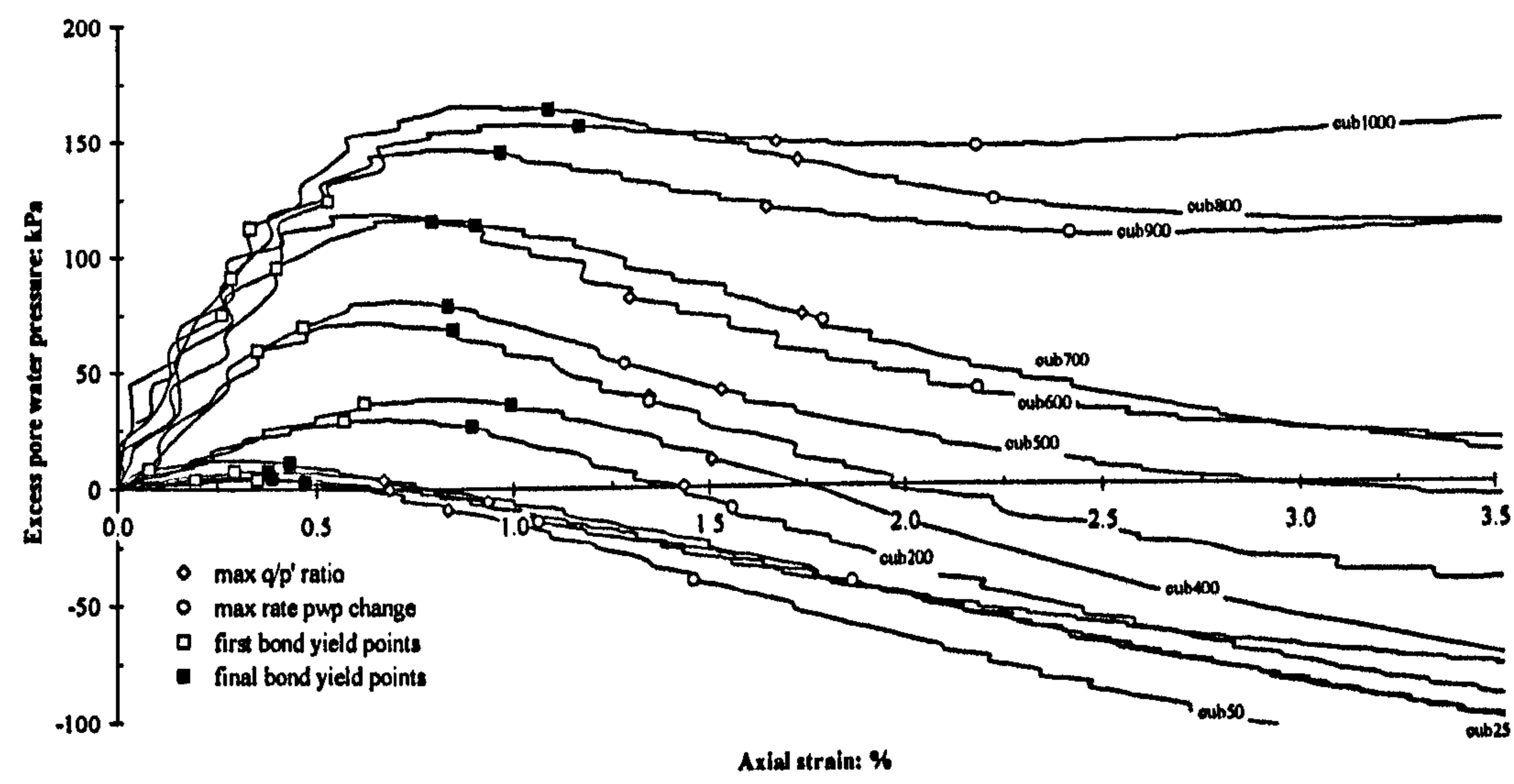


(b)

Figure 6.20: (a) Stress-strain curve and (b) secant stiffness plot for cub1000 sample



(a)



(b)

Figure 6.21: (a) Stress-strain curve and (b) volumetric strain curves for undrained tests



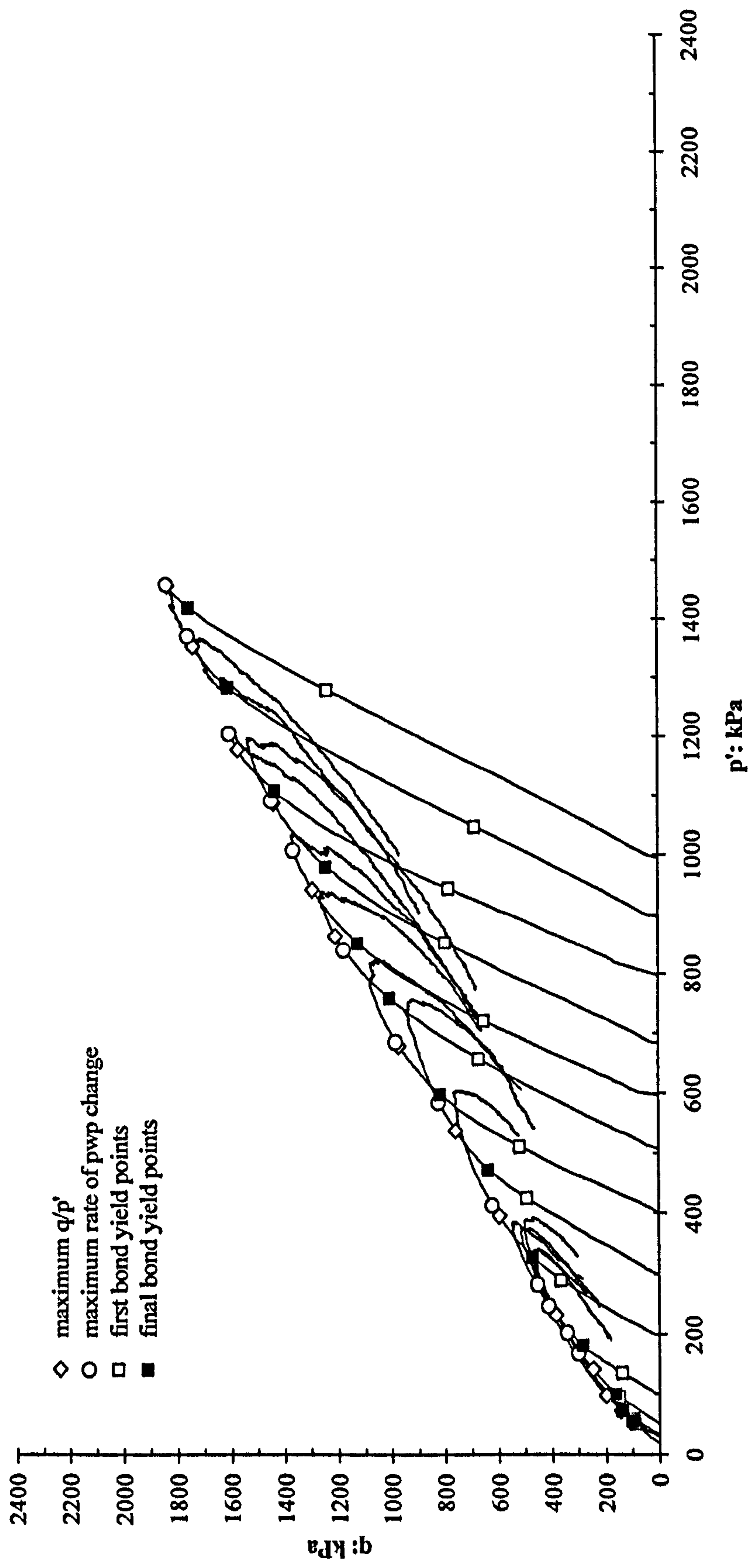


Figure 6.22: Effective stress paths for the undrained tests showing the position of yield points

surface tends to curve towards the bond yield surface at higher stresses ( $p' > 1100\text{kPa}$ ).

The first yield surface is located below the two surfaces in the stress space. At low stress levels, the first yield surface increases linearly from origin and almost coincides with bounding surface for the destructured samples. At stresses level higher than  $1100\text{kPa}$  it curves slightly and becomes parallel with the isotropic axis. There are no data available to prove a further trend of the first yield surface at higher stress levels.

## **6.4 COMPARISON BEHAVIOUR BETWEEN DRAINED AND UNDRAINED BEHAVIOUR ON BONDED SAMPLES**

### **6.4.1 Stress Ratios for Bonded Samples**

The  $q/p'$  ratio values for the destructured samples from the two types of tests are plotted against the axial strain (Figures 6.24a, 6.24b and 6.24c). Comparison of the development of  $q/p'$  ratio were carried out at low ( $p_o' = 15\text{kPa}$  to  $50\text{kPa}$ ), intermediate ( $p_o' = 300\text{kPa}$  to  $500\text{kPa}$ ) and high ( $p_o' = 900\text{kPa}$  to  $1000\text{kPa}$ ) confining pressures, similar stress ranges to those used to analyse the saturated destructured samples.

Figure 6.24a presents the  $q/p'$  ratio plotted against axial strain for the bonded samples sheared at low confining pressures from the drained and undrained tests. From the figure, it is clearly seen that the stress ratio curves from both tests indicate significant peaks at lower axial strain (0.5% to 1.0%) before decreasing with increasing strain. All samples for the drained tests show an increase in maximum  $q/p'$  ratio values with increasing confining pressures, but then level off at a very similar stress ratio at the end of shearing (approximately  $q/p' = 1.50$ ). Meanwhile for the bonded samples sheared under undrained condition, the maximum  $q/p'$  ratio for cub25 and cub30 is very close ( $q/p' = 1.97$ - $2.00$ ) which then decrease to the end of the tests. Sample cub50 achieves a lower value of maximum  $q/p'$  ratio ( $q/p' = 1.76$ ) which also then decreases to a slightly lower value than the two samples.



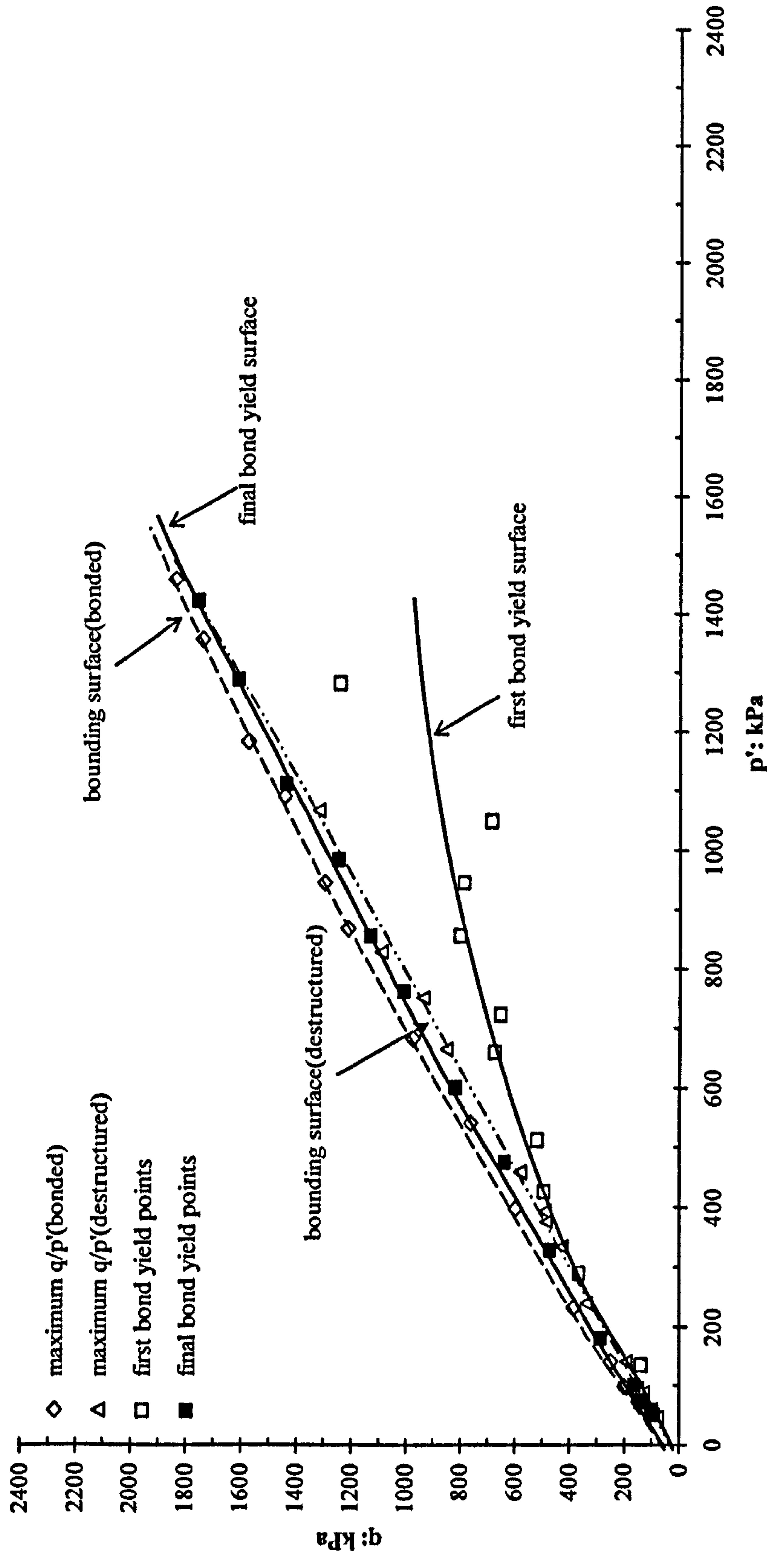


Figure 6.23: The first and bond yields surfaces for the undrained tests on bonded samples

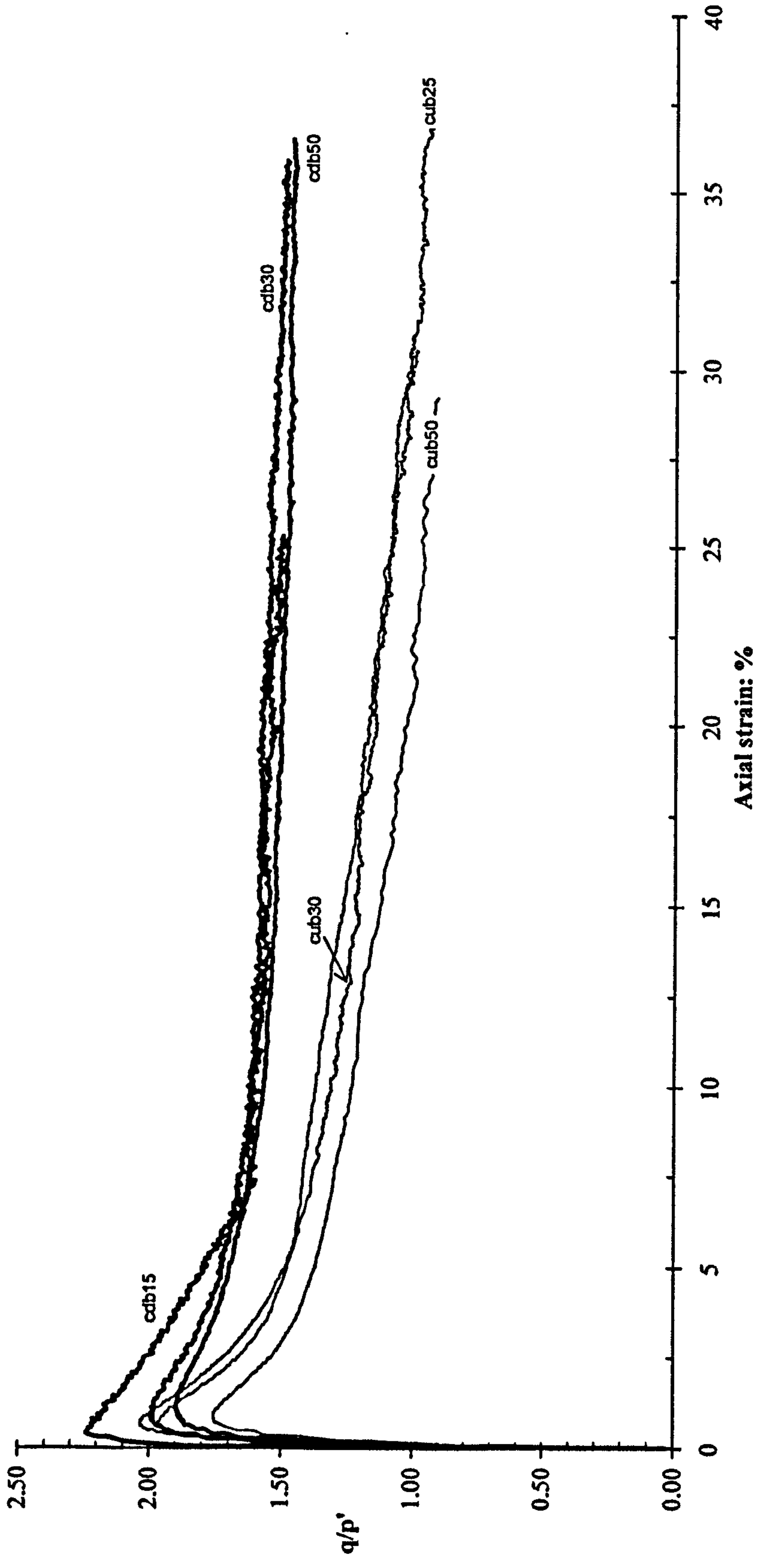


Figure 6.24a: The  $q/p'$  ratio versus axial strain for the drained and undrained tests on bonded soils at low confining pressures



Figure 6.24b shows the stress ratio curves for bonded samples sheared at the medium range of confining pressures under drained and undrained conditions. At this stress level, the maximum  $q/p'$  ratios for all the tests are dramatically lower in comparison to those of the bonded samples sheared at lower confining pressures. The bonded samples sheared under both drained and undrained conditions still indicate a peak in  $q/p'$  ratio, but less significant at earlier axial strain. It can be seen clearly that the maximum  $q/p'$  ratio for all the tests is quite close, between 1.36 and 1.39 for drained tests and between 1.40 and 1.41 for the undrained tests. The stress ratio for all the tests shows a tendency to decrease to the end of shearing due to initiation of shear surfaces.

The  $q/p'$  ratio curves for bonded samples sheared at higher confining pressure under drained and undrained conditions (900kPa and 1000kPa) are shown in Figure 6.24c. It can be seen that the maximum  $q/p'$  ratio for all tests shows lower values between 1.22 and 1.23 for the drained tests and between 1.26 and 1.29 for the undrained tests. However, these  $q/p'$  ratio values are close and apparently all the tests show a similar pattern of curves without the presence of a distinguished peak. The  $q/p'$  ratio increases rapidly up to the maximum value at early strain, and then the stress ratio tends to decrease to the end of the test.

#### **6.4.2 Bounding Surface for Bonded Samples**

The bounding surfaces for the bonded samples in drained and undrained tests are shown in Figure 6.25a. The two bounding surfaces clearly show some curvature at low and high stress levels. However, the curvature in the bounding surface for the drained tests is more prominent in comparison with the bounding surface for the undrained tests.

At low stress level up to  $p'=150\text{kPa}$ , the bounding surface for the drained test is curved and then it becomes linear up to  $p'=750\text{kPa}$  before it continues to curve again at higher stress levels. Then at stress level of  $p'=1100\text{kPa}$ , the bounding

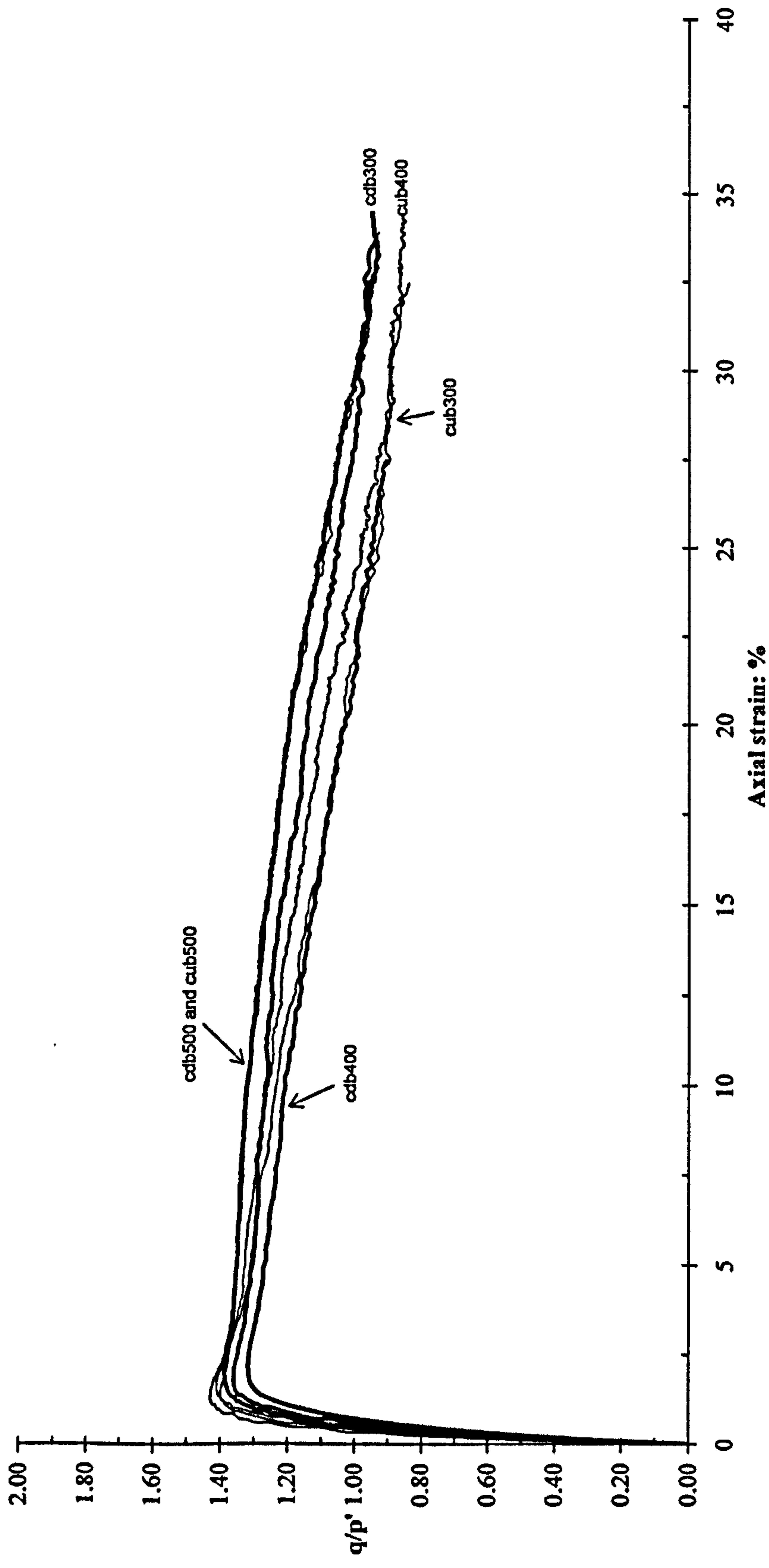


Figure 6.24b: The  $q/p'$  ratio versus axial strain for the drained and undrained tests on bonded soils at intermediate confining pressures



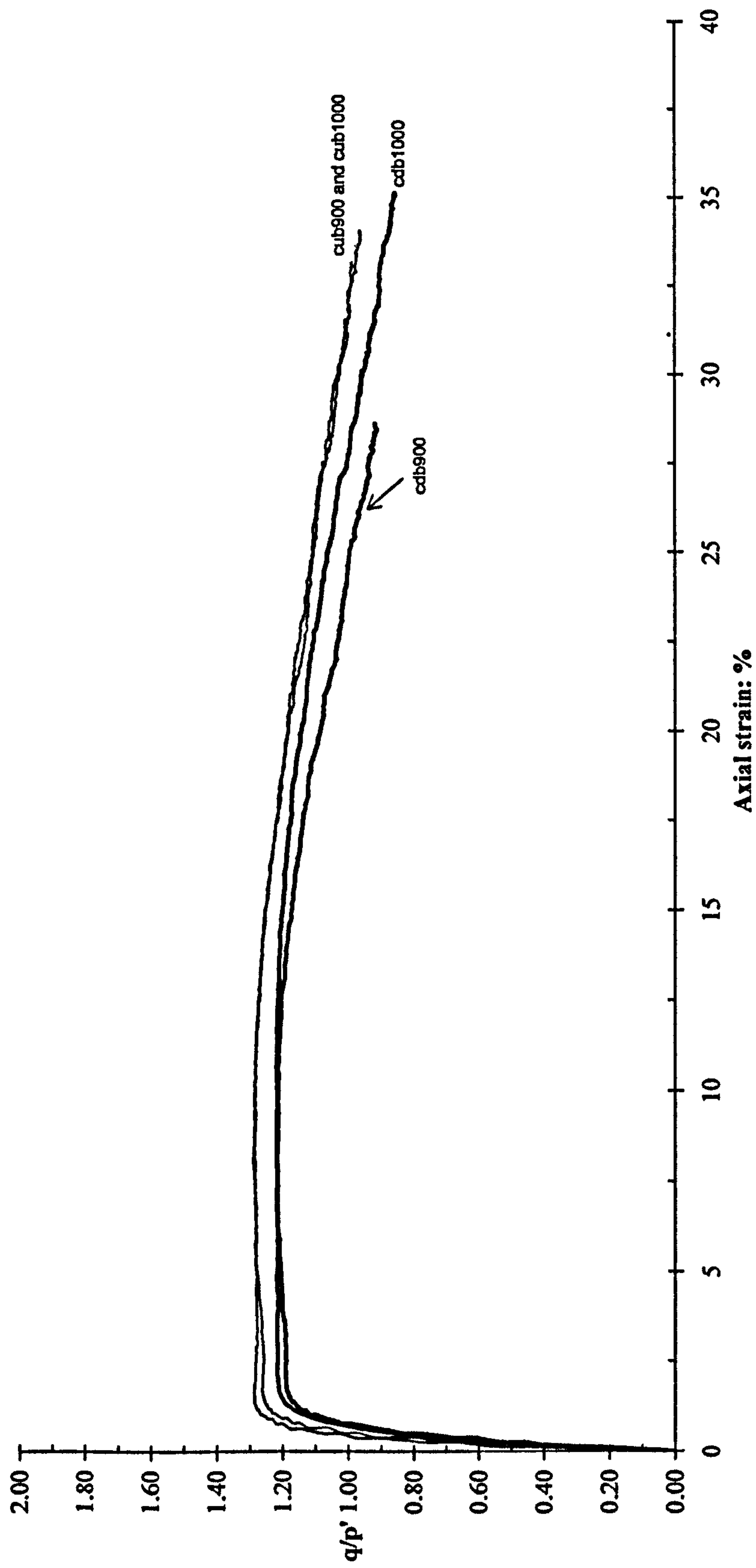


Figure 6.24c: The  $q/p'$  ratio versus axial strain for the drained and undrained tests on bonded soils at high confining pressures

surface turns down and become linear. The bounding surface for the undrained tests also indicates curvature up to  $p'=200\text{kPa}$  which then becomes linear up to  $p'=500\text{kPa}$ . At  $p'>500\text{kPa}$ , the bounding surface curves again until it turns back and becomes linear at higher stress level of  $p'>1100\text{kPa}$ . The two test types clearly show a very similar behaviour of bonded samples, as seen from Figure 6.25b, all the data points could be represented by a straight line up to stress level,  $p'=1400\text{kPa}$ .

Figure 6.26 shows the phase transformation line for the drained and undrained tests on the bonded samples. The phase transformation line for the undrained tests is seen to be very linear in the  $q$ - $p$  space. The line for the drained tests is in a good agreement over most of the stress range, although it does seem to deviate away from the linear relationship above  $800\text{kPa}$ .

#### 6.4.3 First and Final Bond Yield Surfaces for Bonded Samples

The first and final bond yields gathered from the drained and undrained tests on the bonded samples are plotted together as shown in Figure 6.27. It is found that the first bond yield surface from the undrained tests is located slightly higher than that obtained from the drained tests. Malandraki (1994) also noticed that the first yield surface from undrained tests was slightly higher than that from the drained tests, however the differences were not large and could be accepted within the range of experimental discrepancy. It seems that the yielding of bonds is largely unaffected by the type of drainage during shearing of the bonded samples. Meanwhile the final bond yield surfaces show a quite good agreement from the drained and undrained tests. However, the final bond yield surface from the undrained tests is slightly higher especially at higher stress levels of  $p'>1200\text{kPa}$  but seems to turn back to the yield surface for the drained tests.



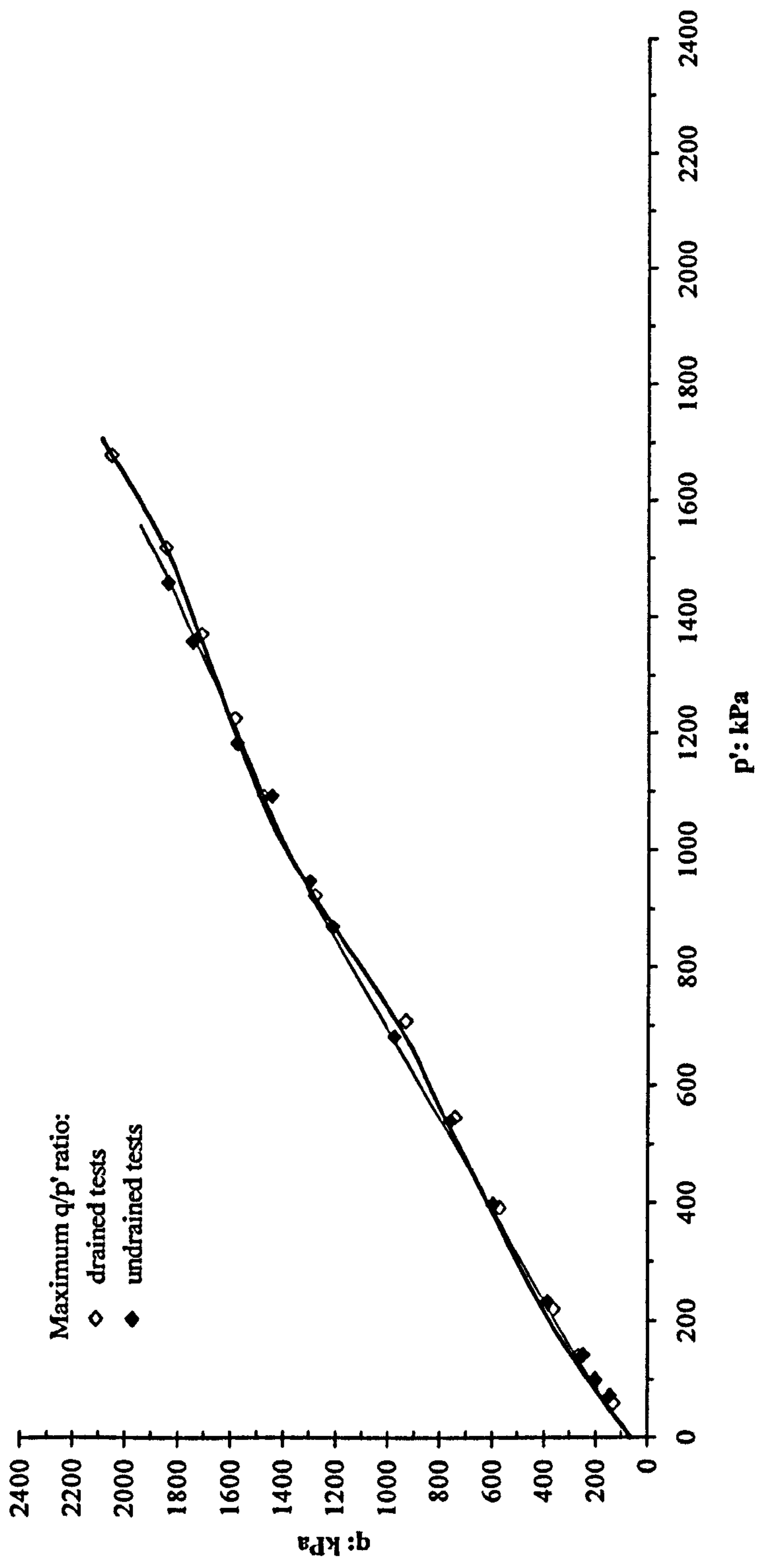


Figure 6.25a: Bounding surface lines for the drained and undrained tests on bonded samples

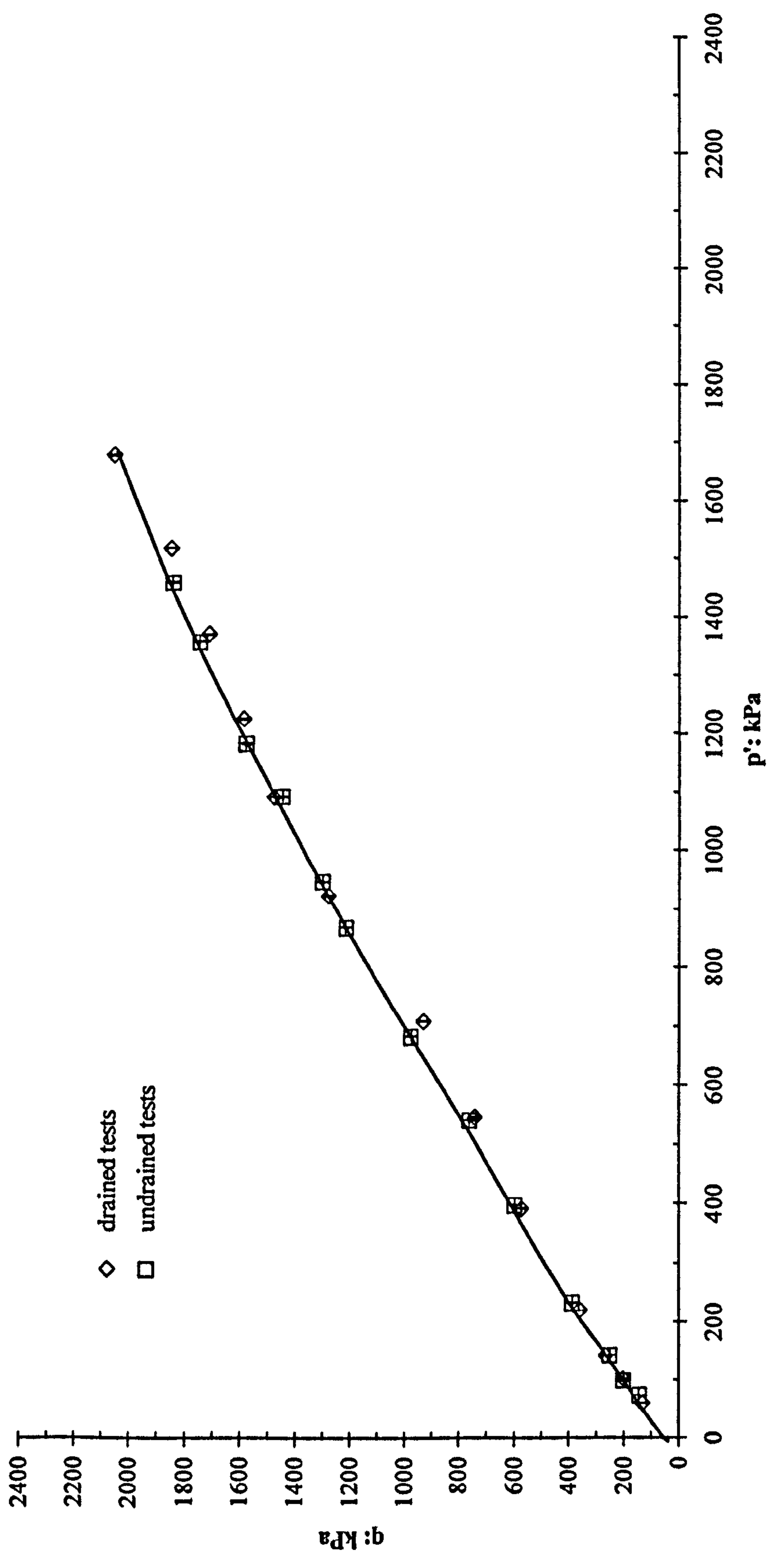


Figure 6.25b: A single line to represent the bounding surface from the drained and undrained tests bonded samples (error bars included)



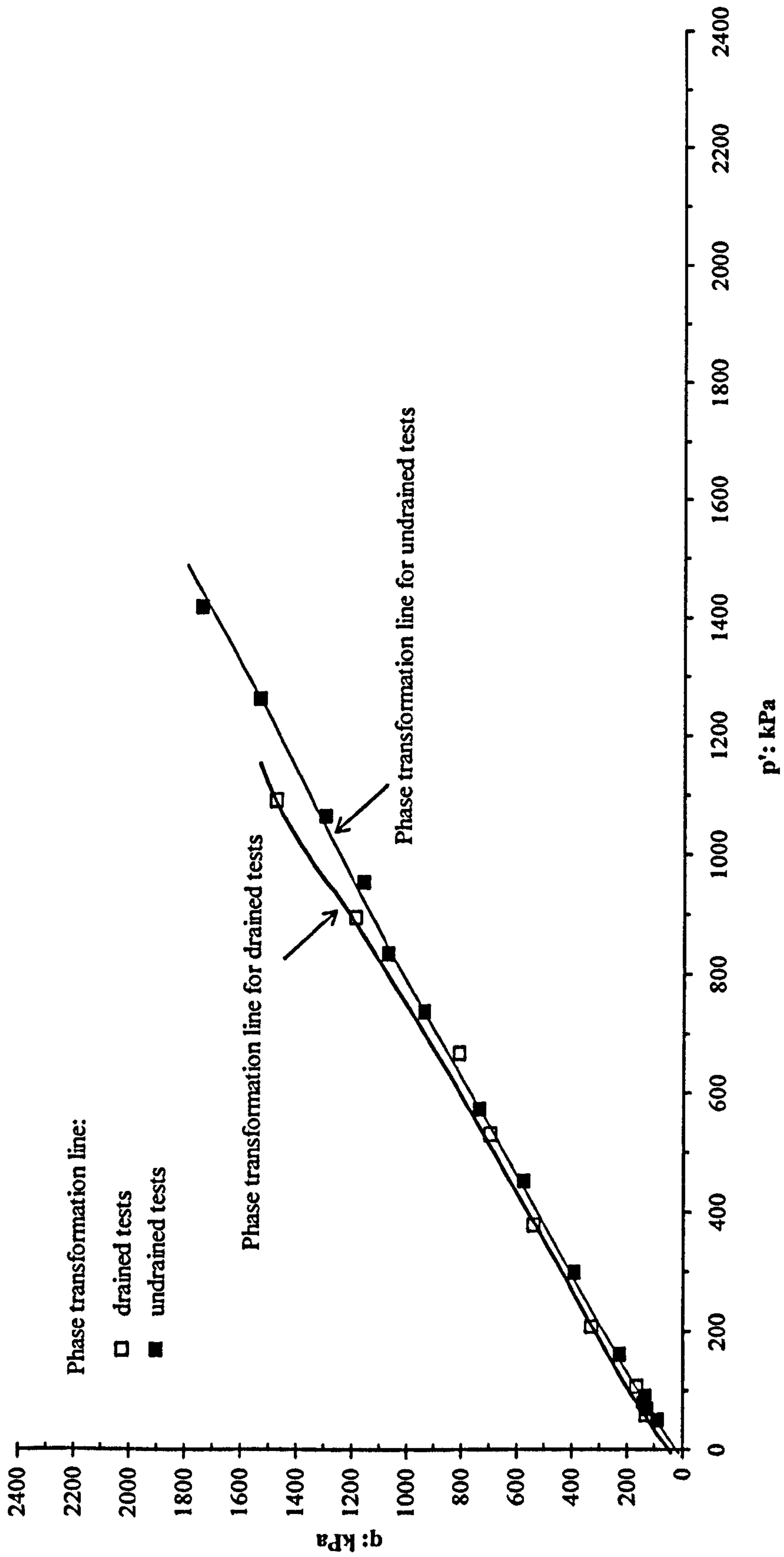


Figure 6.26: Phase transformation lines for the drained and undrained tests on bonded samples

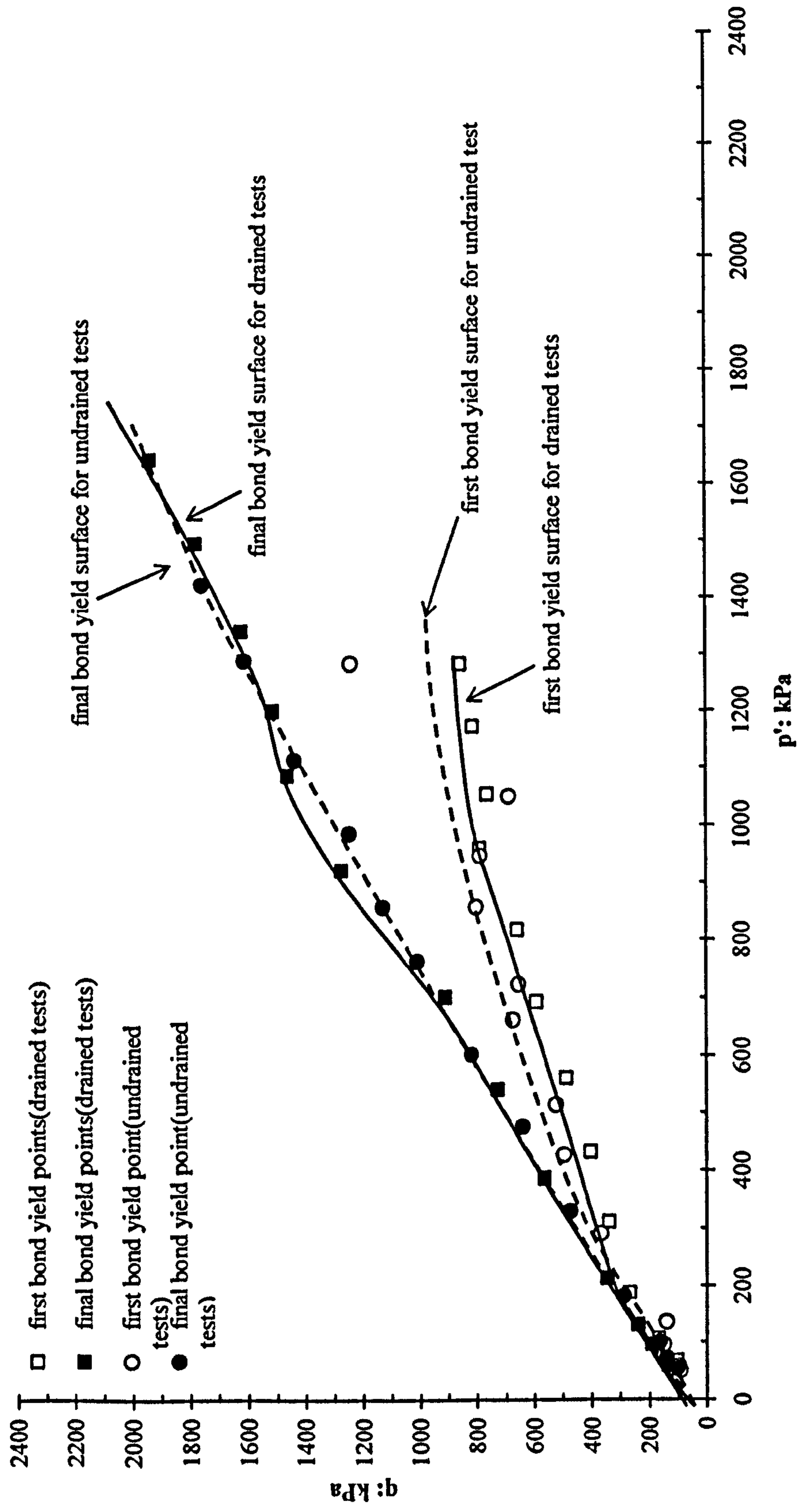


Figure 6.27: The yield surfaces for the drained and undrained tests



## 6.5 COMPARISON BETWEEN BONDED AND DESTRUCTURED SAMPLES IN DRAINED AND UNDRAINED TESTS

### 6.5.1 Stress Ratios in Drained Tests

The  $q/p'$  ratio value for bonded and destructured samples was plotted against axial strain (Figure 6.28a, 6.28b and 6.28c). Comparison of the  $q/p'$  ratios has been carried out at low ( $p_o' = 15, 20, 30$  and  $50\text{kPa}$ ), intermediate ( $p_o' = 300, 400$  and  $500\text{kPa}$ ) and high ( $p_o' = 900$  and  $1000\text{kPa}$ ) values of confining pressures.

Figure 6.28a clearly shows that the bonded samples sheared under low confining pressures achieve higher  $q/p'$  ratios than the destructured samples at similar range of stress level. The maximum  $q/p'$  ratio for the bonded samples was achieved at lower axial strain than for destructured samples. In addition, the bonded samples present a significant peak of  $q/p'$  ratio while no clear peak in the stress ratio was observed from the destructured samples. At the end of shearing, the destructured sample, cdd20 shows a very similar stress ratio to the bonded samples. For the other two destructured samples, cdd15 and cdd50 tests, the stress ratio values gradually decrease to the end of shearing due to the development of shear surfaces.

Figure 6.28b presents the stress ratio against axial strain for bonded and destructured samples sheared at  $300, 400$  and  $500\text{kPa}$  of confining pressures. The maximum  $q/p'$  ratio for bonded samples has dropped significantly in comparison with bonded samples that were sheared at low stress levels. The maximum  $q/p'$  ratio of bonded samples is achieved at a lower axial strain and also is closer to the value of the destructured samples. It can be clearly seen that the bonded samples sheared at these stress levels show a peak suggesting that the bonds still contribute to a higher stress ratio value. For the destructured samples, no obvious peak of  $q/p'$  ratio is observed. The stress ratio for the tests decreases to the end of shearing due to the initiation of shear surfaces. This behaviour is similar in both bonded and destructured samples.

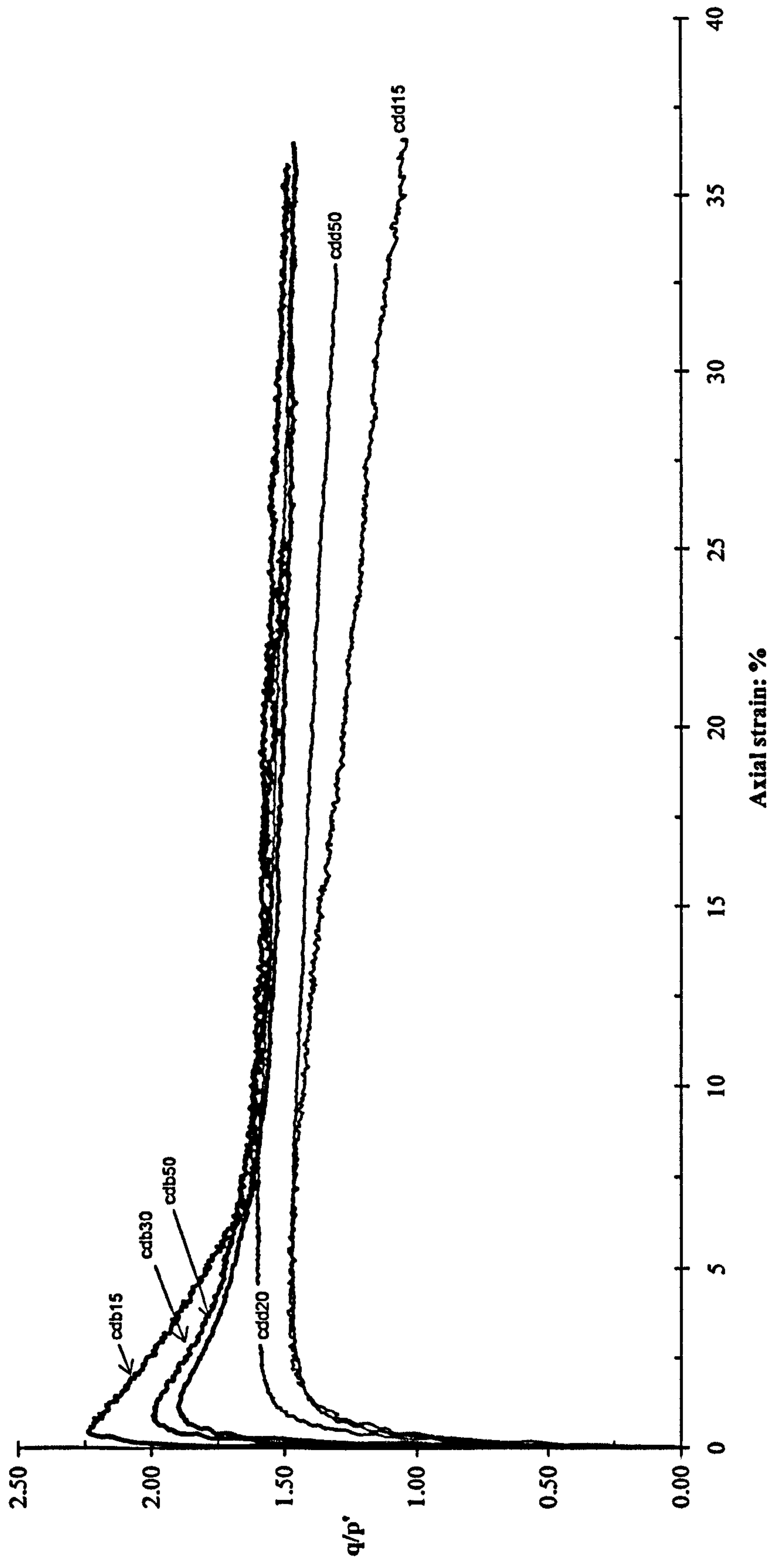


Figure 6.28a: The  $q/p'$  ratio versus axial strain for drained tests on bonded and destructured soils at lower confining pressures



The  $q/p'$  ratios for tests cdb900 and cdb1000 and cdd900 and cdd1000 are shown in Figure 6.28c. The maximum  $q/p'$  ratio of the bonded samples is very close to that of the destructured samples. However the maximum  $q/p'$  ratio for the bonded samples is achieved at a lower axial strain than the destructured samples. The stress ratio value (1.20-1.25) is slightly lower than that bonded and destructured samples sheared at lower confining pressures ( $q/p'=1.30-1.39$  for tests cdb300, cdb400 and cdb500). For the bonded samples, the  $q/p'$  ratios increase quickly then curves after the peak stress ratio to follow values that are very close to those of the destructured samples to the end of shearing. The closeness of the maximum  $q/p'$  ratio between the two samples indicates that the behaviour of bonded samples is becoming closer to that of the destructured sample at these stress levels. The bonded structure of the bonded samples has almost been destroyed at these stress levels and this results in a lower stress ratio similar to that of the destructured samples.

### 6.5.2 Stress Ratios in Undrained Tests

The  $q/p'$  ratio values for bonded and destructured samples from undrained tests are plotted against axial strain (Figure 6.29a, 6.29b and 6.29c). Comparison of the  $q/p'$  ratios has been carried out at low ( $p_o'=25, 30, 50$  and  $60\text{kPa}$ ), intermediate ( $p_o'=300, 400$  and  $500\text{kPa}$ ) and high ( $p_o'=900$  and  $1000\text{kPa}$ ) values of confining pressures.

It is apparent that the bonded samples sheared at low confining pressures sustain a higher  $q/p'$  ratio than that of destructured samples at a similar range of stress level (Figure 6.29a). The maximum  $q/p'$  ratio for the bonded samples was also achieved at lower axial strain than that of destructured samples. The bonded samples indicate a significant peak of  $q/p'$  ratio, while no apparent peak in the stress ratio is observed from the destructured samples. At the end of shearing, the bonded samples, cub25 and cub30 show almost similar stress ratio while cub50 settles at a slightly lower value. For cud25 and cud60 tests, the stress ratio values gradually decrease to the end of shearing but remain higher than the bonded samples.

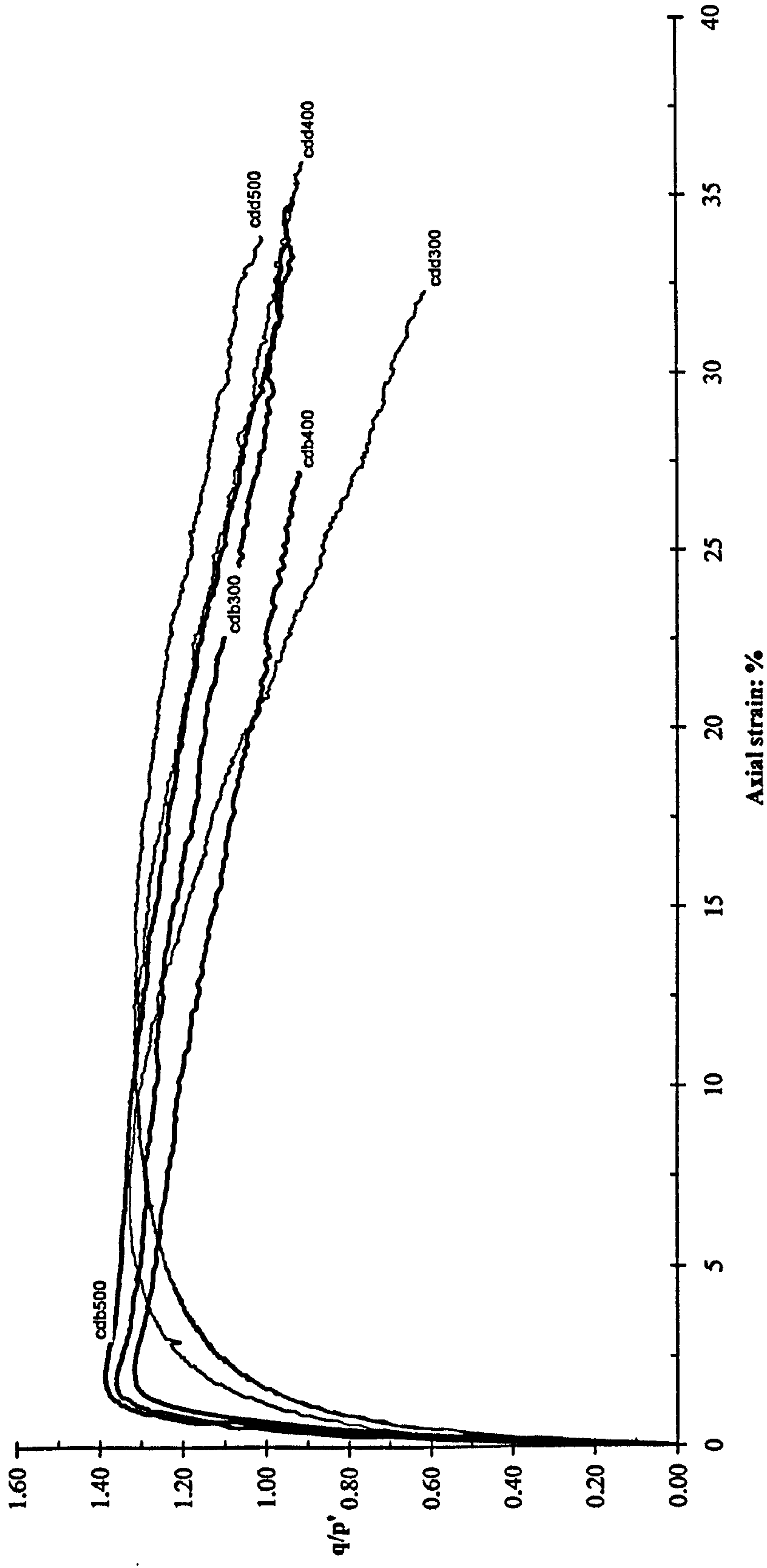


Figure 6.28b: The  $q/p'$  ratio versus axial strain for drained test on bonded and destructured soils at intermediate confining pressures



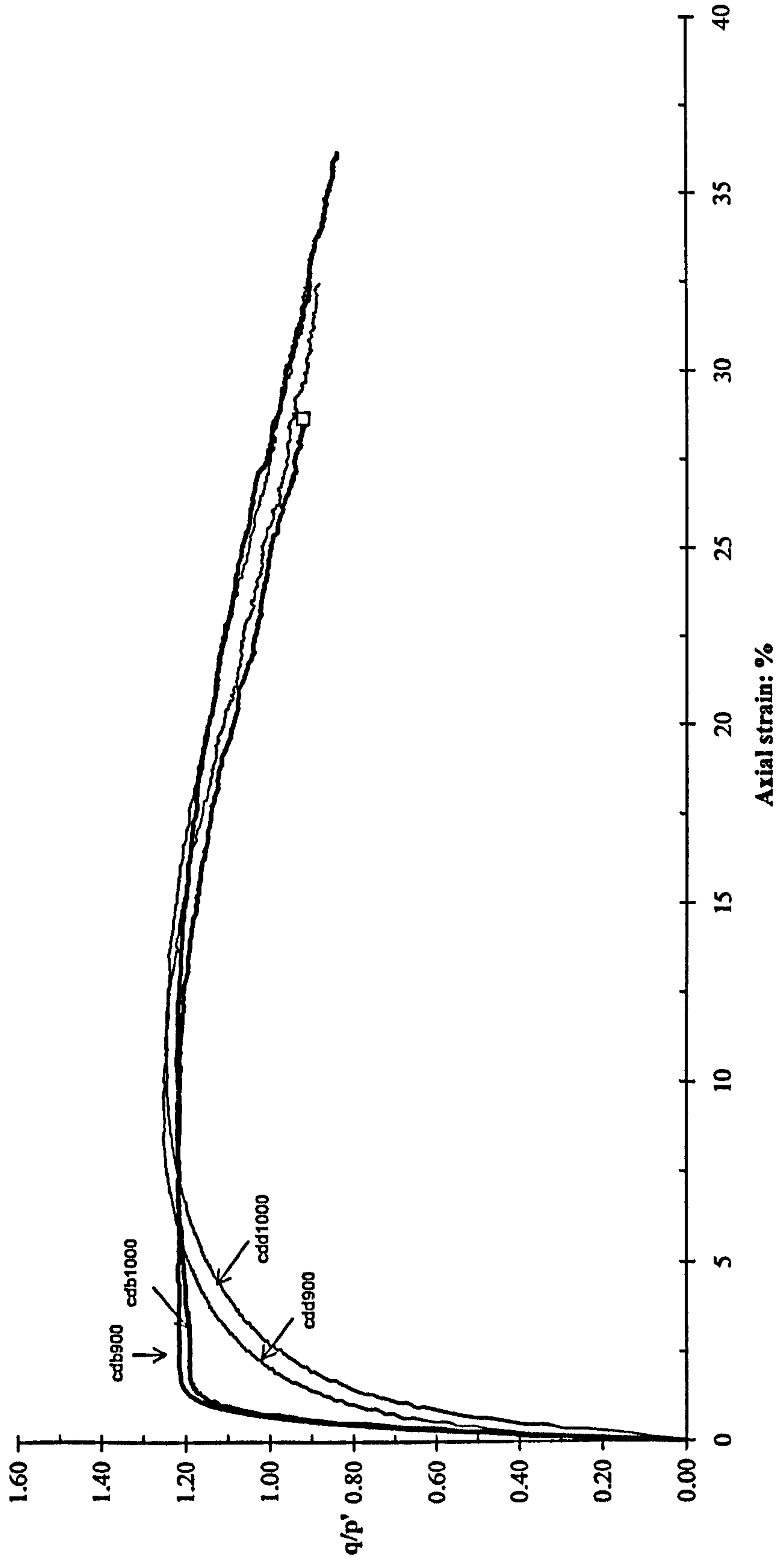


Figure 6.28c: The  $q/p'$  ratio versus axial strain for drained tests on bonded and destructured soils at high confining pressures

Figure 6.29b shows stress ratios against axial strain for bonded and destructured samples sheared under undrained conditions at 300, 400 and 500kPa of confining pressures. The maximum  $q/p'$  ratio for bonded samples has dropped significantly in comparison to bonded samples that were sheared at low stress levels. The maximum  $q/p'$  ratio of bonded samples is achieved at a lower axial strain and also is closer to the value of the destructured samples. The bonded samples sheared at this stress levels still show a peak suggesting that the bond still contributes to a higher stress ratio value. The stress ratio for the bonded samples decreases and the stress ratios for all the tests become close to each other towards to the end of shearing.

The  $q/p'$  ratios for tests on bonded and destructured samples sheared at 900kPa and 1000kPa of confining pressures are shown in Figure 6.29c. The maximum  $q/p'$  ratio of the bonded samples is very close to that of the destructured samples. However the maximum  $q/p'$  ratio for the bonded samples is achieved at a lower axial strain than the destructured samples. The stress ratio values for these tests ( $q/p'=1.29-1.31$ ) are slightly lower than that bonded and destructured samples sheared at lower confining pressures ( $q/p'=1.39-1.43$  for tests cdb300, cdb400 and cdb500). For the bonded samples, the  $q/p'$  ratios increase rapidly then after the peak, the stress ratios become very close to that of the destructured samples. At the end of shearing, the stress ratios for the bonded and destructured samples almost coincide. The closeness of the maximum  $q/p'$  ratio between the two samples indicates that the behaviour of bonded samples has become similar to that of the destructured samples at these stress levels. The bonded structure of the bonded samples has almost been destroyed at these stress levels and shows a lower stress ratio similar to that of the destructured samples.



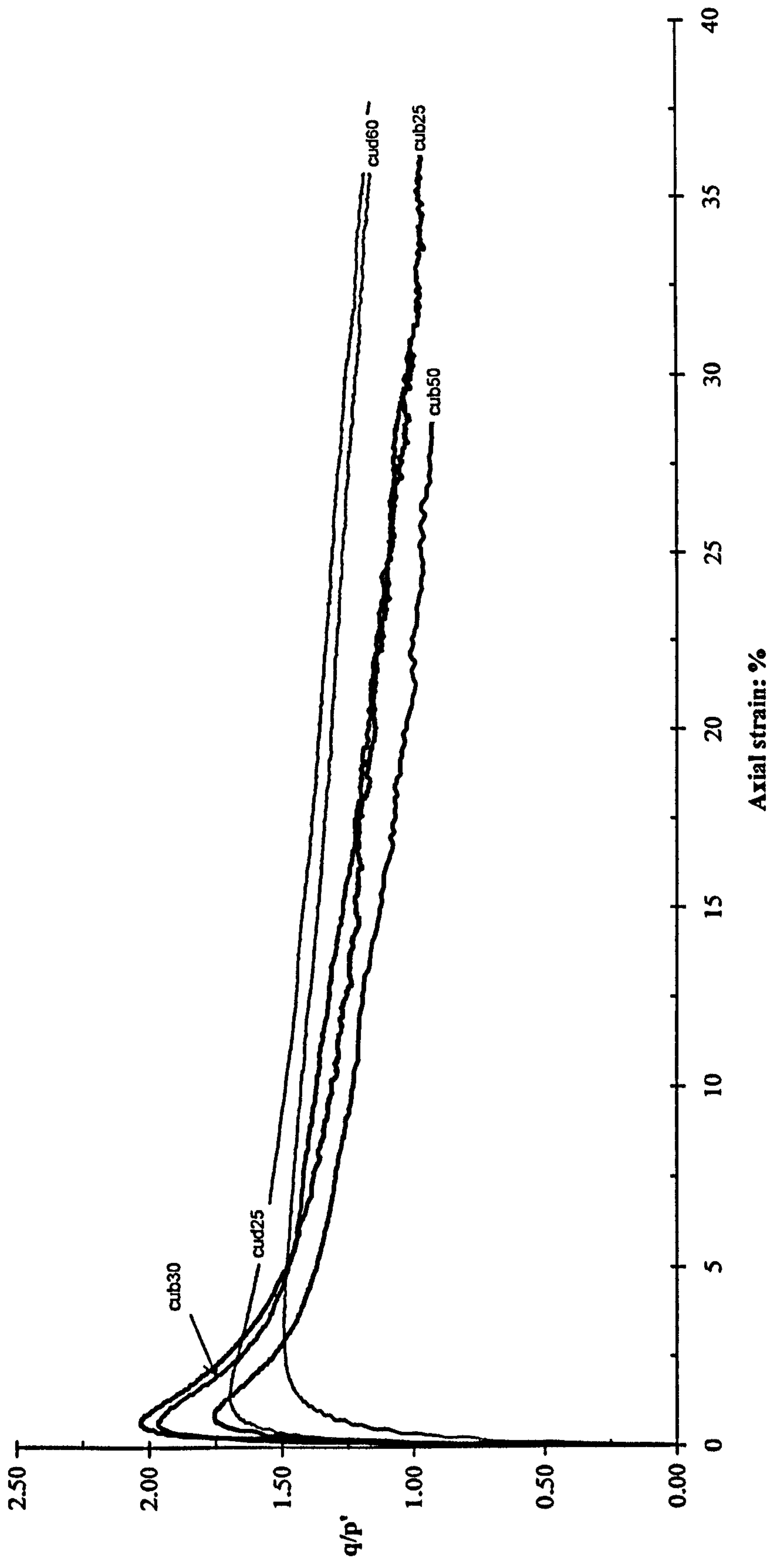


Figure 6.29a: The  $q/p'$  ratio versus axial strain for undrained tests on bonded and destructured soils at lower confining pressures

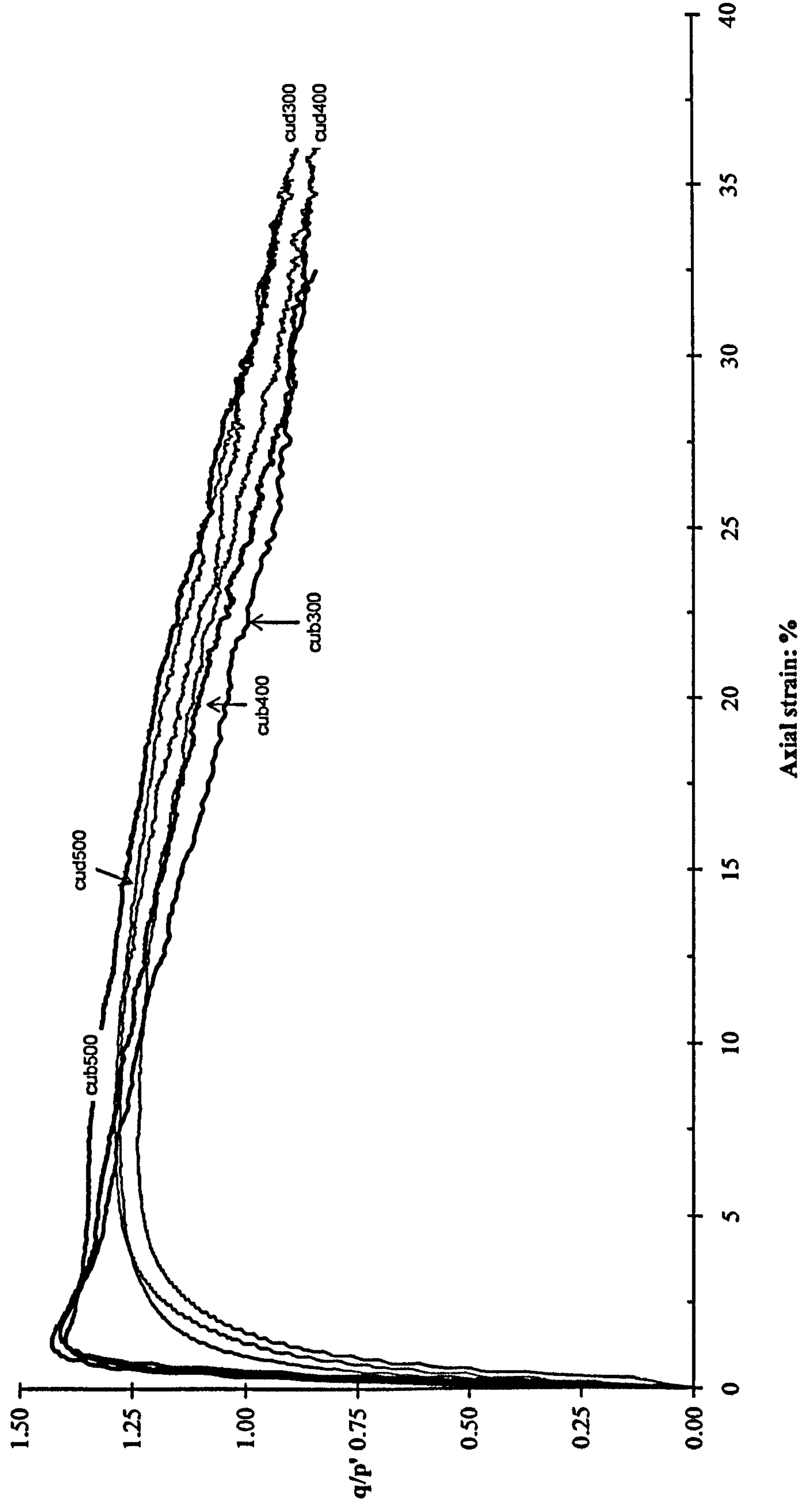


Figure 6.29b: The  $q/p'$  ratio versus axial strain for undrained tests on bonded and destructured soils at intermediate confining pressures



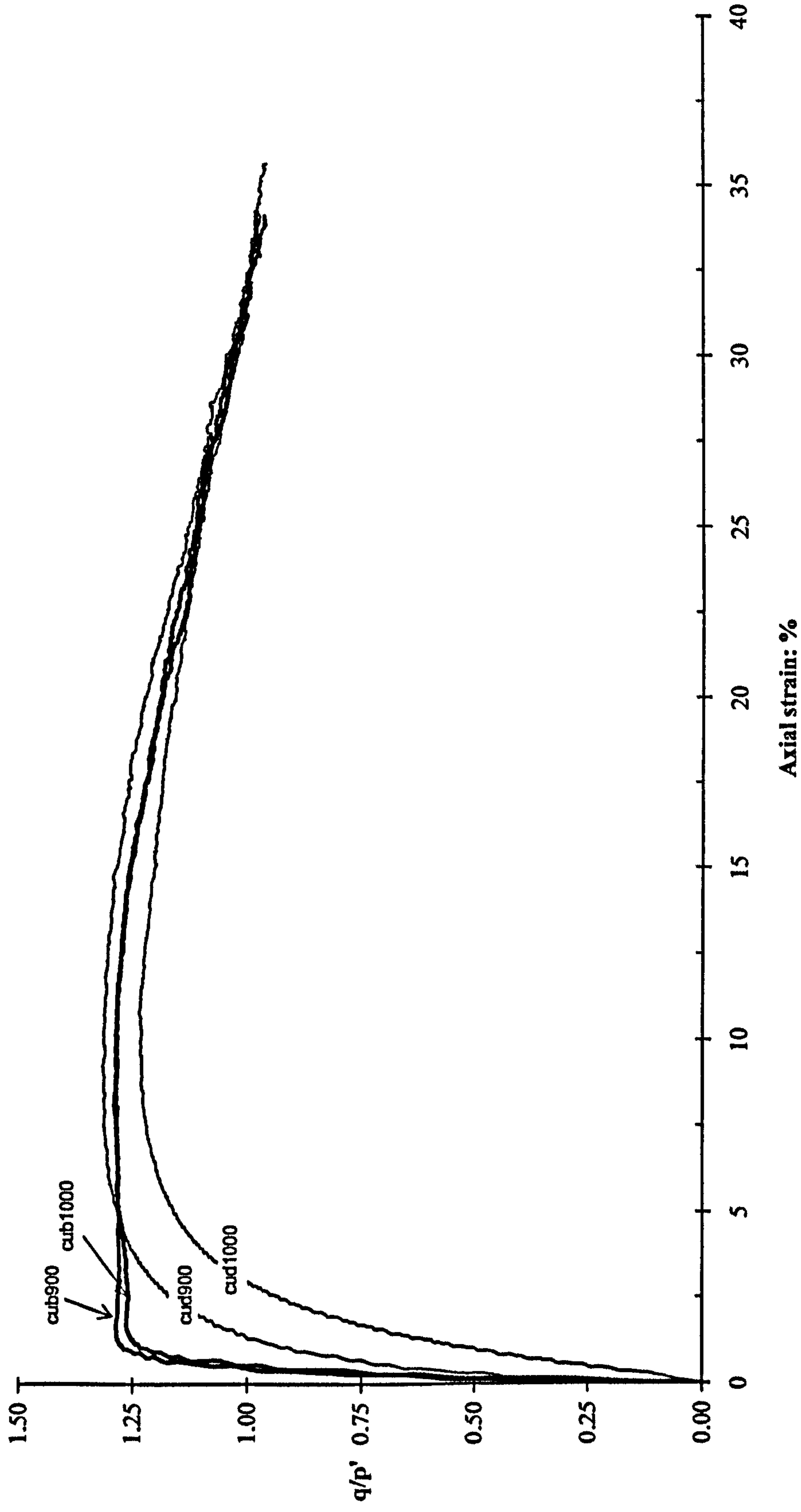


Figure 6.29c: The  $q/p'$  ratio versus axial strain for undrained tests on bonded and destructured soils at intermediate confining pressures

### 6.5.3 Bounding Surfaces in Drained and Undrained Tests

The bounding surfaces for drained tests on the bonded and destructured samples are shown in Figure 6.30. It is clearly seen that the bounding surface for the bonded samples indicates some curvature at low stresses (up to  $p'=150\text{kPa}$ ) and there is apparent kink at higher stresses at about  $p'=750\text{kPa}$ . Meanwhile the bounding surface for the destructured samples is more linear and falls below that for the bonded samples. The bounding surfaces for the two types of sample almost coincide at high stress levels. This suggests that the bonding in the bonded samples contributes to achieving higher stress ratios than the destructured samples up to a stress level of about  $p'=1500\text{kPa}$ .

At low stress levels up to  $p'=150\text{kPa}$ , the bounding surfaces for the two samples are closer to each other. However the bounding surface for the bonded samples is still slightly higher than the destructured samples. At  $p'>150\text{kPa}$ , the bounding surface for bonded samples slightly changes its slope gradient and becomes linear again up to  $750\text{kPa}$ . Bonded samples sheared at higher stresses (cdb500 and cdb600) achieve higher maximum  $q/p'$  ratio than the destructured samples. The bounding surface line for bonded samples curves up, then at stress level of  $p'=1100\text{kPa}$  it turns back to that of the destructured samples. The turning point of this behaviour can be seen after test cdb600 at which the  $q/p'$  ratio begins to decrease.

The bounding surfaces for undrained tests on the bonded and destructured samples are shown in Figure 6.31. The bounding surface for the bonded samples also shows some curvature at high stress level above  $p'=750\text{kPa}$  and curvature can also be observed at lower stresses. Meanwhile, the bounding surface for destructured samples is represented by an almost linear surface that exists at lower stresses than that of the bonded samples. The bounding surface for the bonded samples turns toward the destructured samples starting at high stress of about  $p'=800\text{kPa}$  and then the two lines coincide at  $p'=1500\text{kPa}$ . For a particular range of stresses, it is found



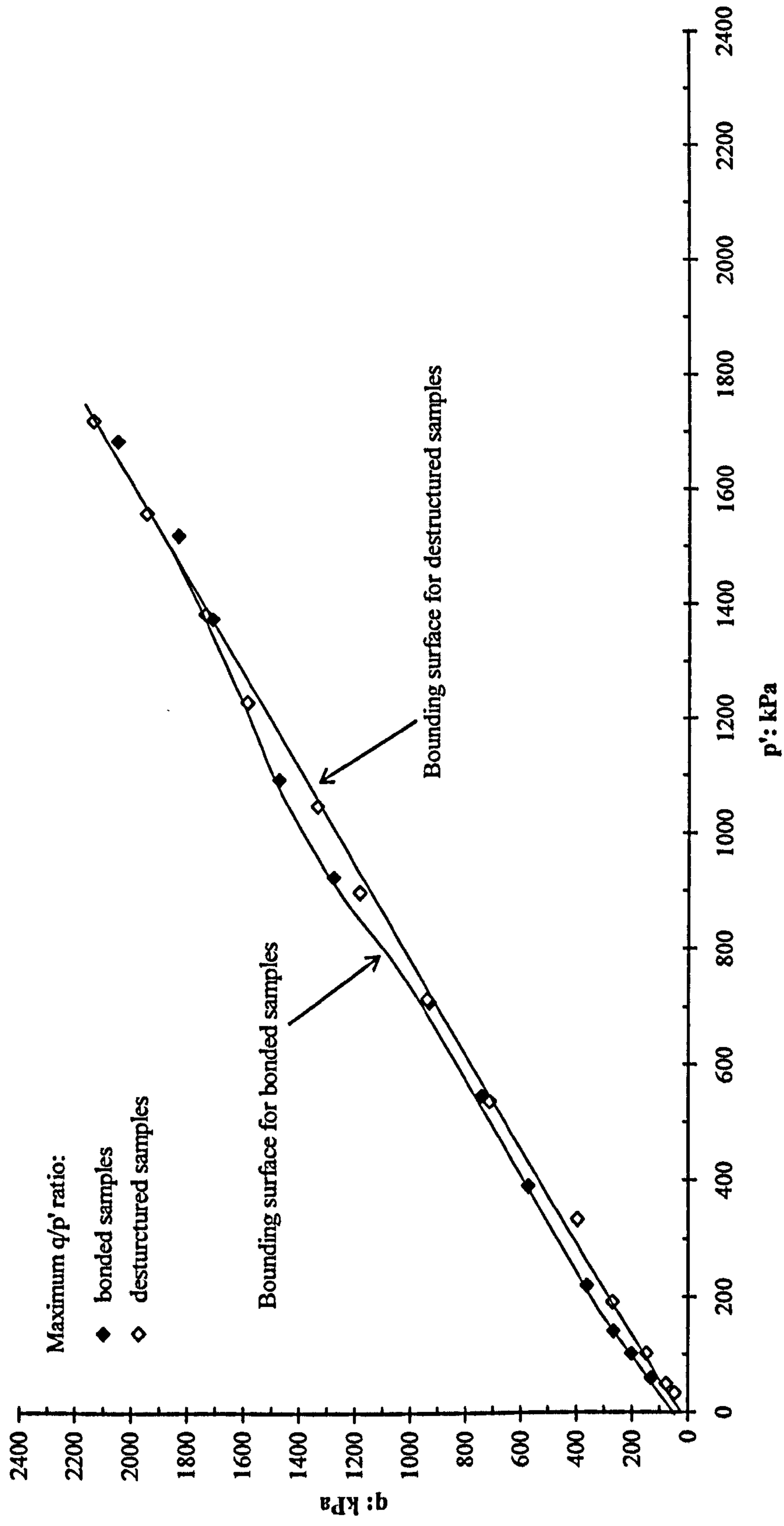


Figure 6.30: Bounding surfaces for the drained bonded and destructured samples

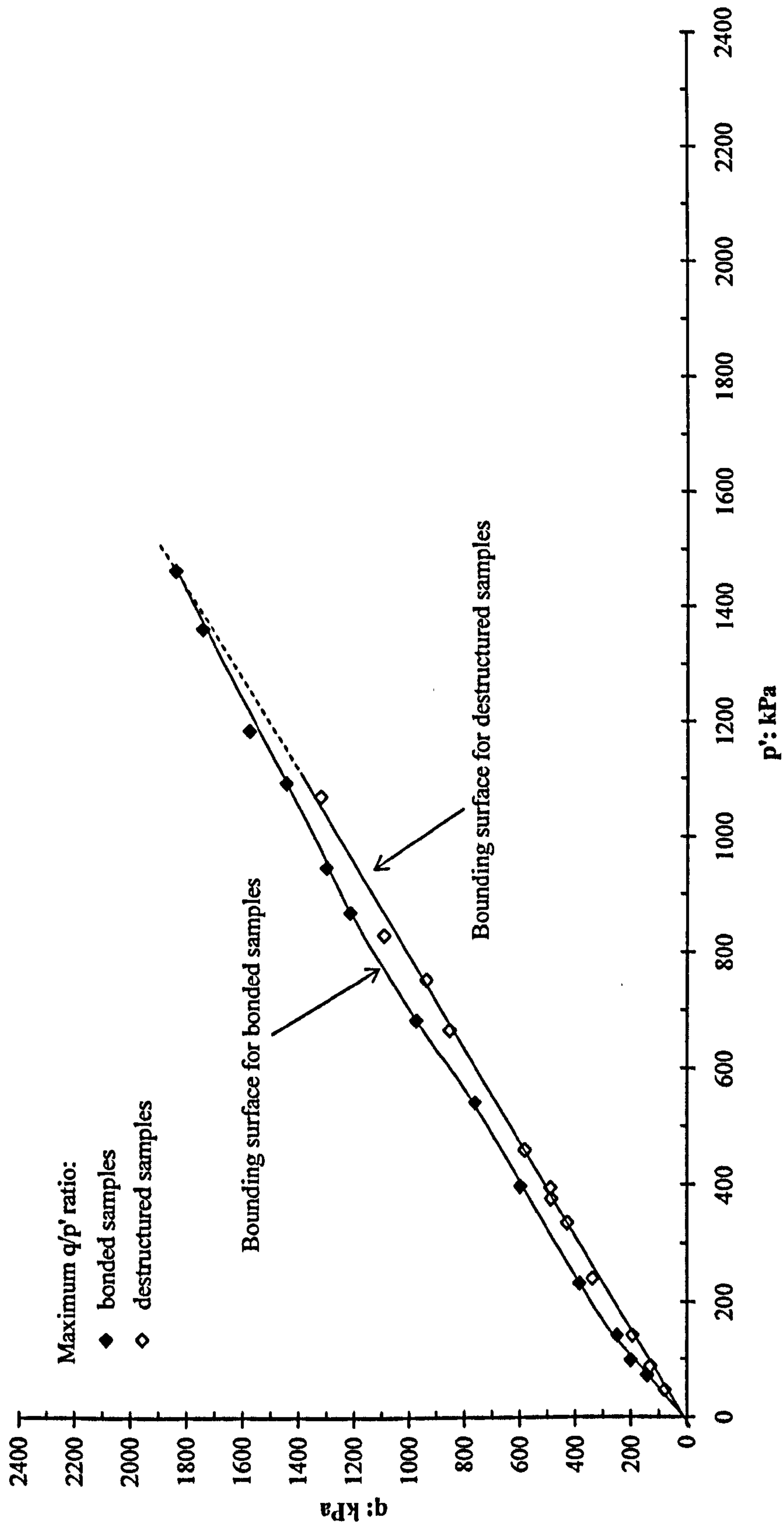


Figure 6.31: Bounding surfaces for the undrained bonded and destructured samples



that the bonded samples sustain a higher stress ratio compared to the destructured samples. This is clearly as a result of the influence of bonding.

At low stress level of about  $p' < 150 \text{ kPa}$ , the maximum  $q/p'$  ratio values of bonded samples are close to the destructured samples. The destructured samples sheared at this low stress level achieved high negative pore water pressure (Figure 5.8). However at higher stress level ( $p' > 150 \text{ kPa}$ ) the bonded samples experienced a higher negative pore water pressure than that of the destructured samples and shifted up the bounding surface of the bonded samples. Further up to about  $p' = 500 \text{ kPa}$ , the bounding surface seem linear for the two samples. For  $p' > 500 \text{ kPa}$  the bonding surface for bonded samples again begins to curve up and become linear up to  $p' = 850 \text{ kPa}$ . At higher stress ( $p' > 850 \text{ kPa}$ ) the bounding surface curves down until the lines become coincident. The bonded samples clearly sustain a higher limiting stress ratio than the destructured samples at intermediate stress levels. However by increasing the stress levels, the strength of the bonds at failure start to degrade and for  $p' > 1100 \text{ kPa}$  the bounding surface turns toward to that of the destructured samples.

The phase transformation line for drained tests on the bonded and destructured samples is shown in Figure 6.32. The line represents the bonded samples shows some curvature at high stress and exists at higher stresses than the destructured samples. At low stresses, the line is quite linear up to a stress level of  $p' = 700 \text{ kPa}$ . The phase transformation line then curves up to stress level of  $p' = 1100 \text{ kPa}$  before the line turns towards that of the destructured samples. Since no dilation occurred in bonded samples sheared at higher stresses ( $p_o \geq 700 \text{ kPa}$ ), no data are available to prove this trend (dash line represents a possible trend at higher stress levels).

Figure 6.33 shows the phase transformation lines for undrained tests on the bonded and destructured samples in  $q - p'$  space. The phase transformation line for the bonded samples exists at higher stresses than the destructured samples and exhibits some curvature for  $p' < 800 \text{ kPa}$ . At low stress levels, these two lines almost coincide. For  $p' > 1000 \text{ kPa}$  the lines for the bonded samples turn close to that of the

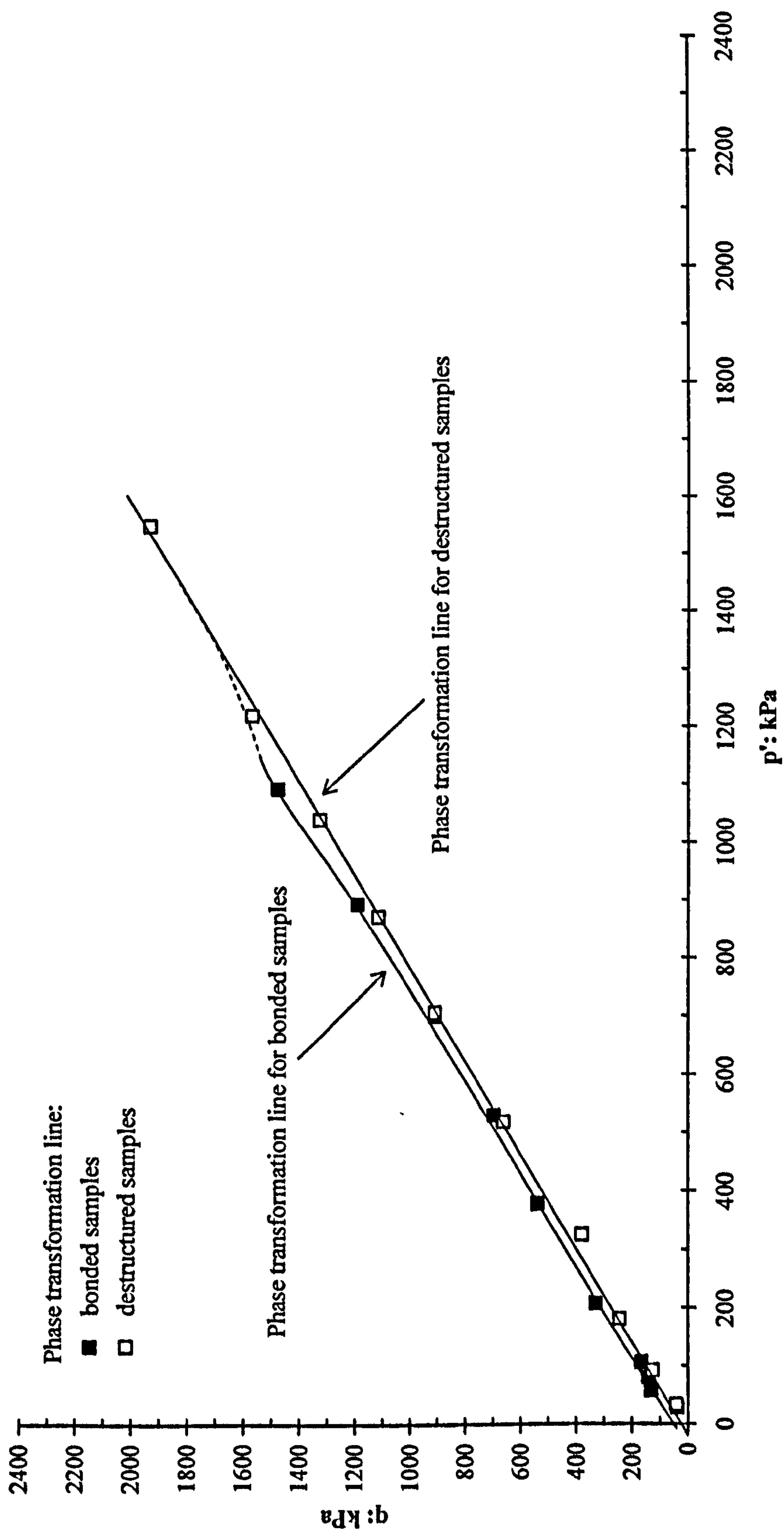


Figure 6.32: Phase transformation lines for drained bonded and destructured samples



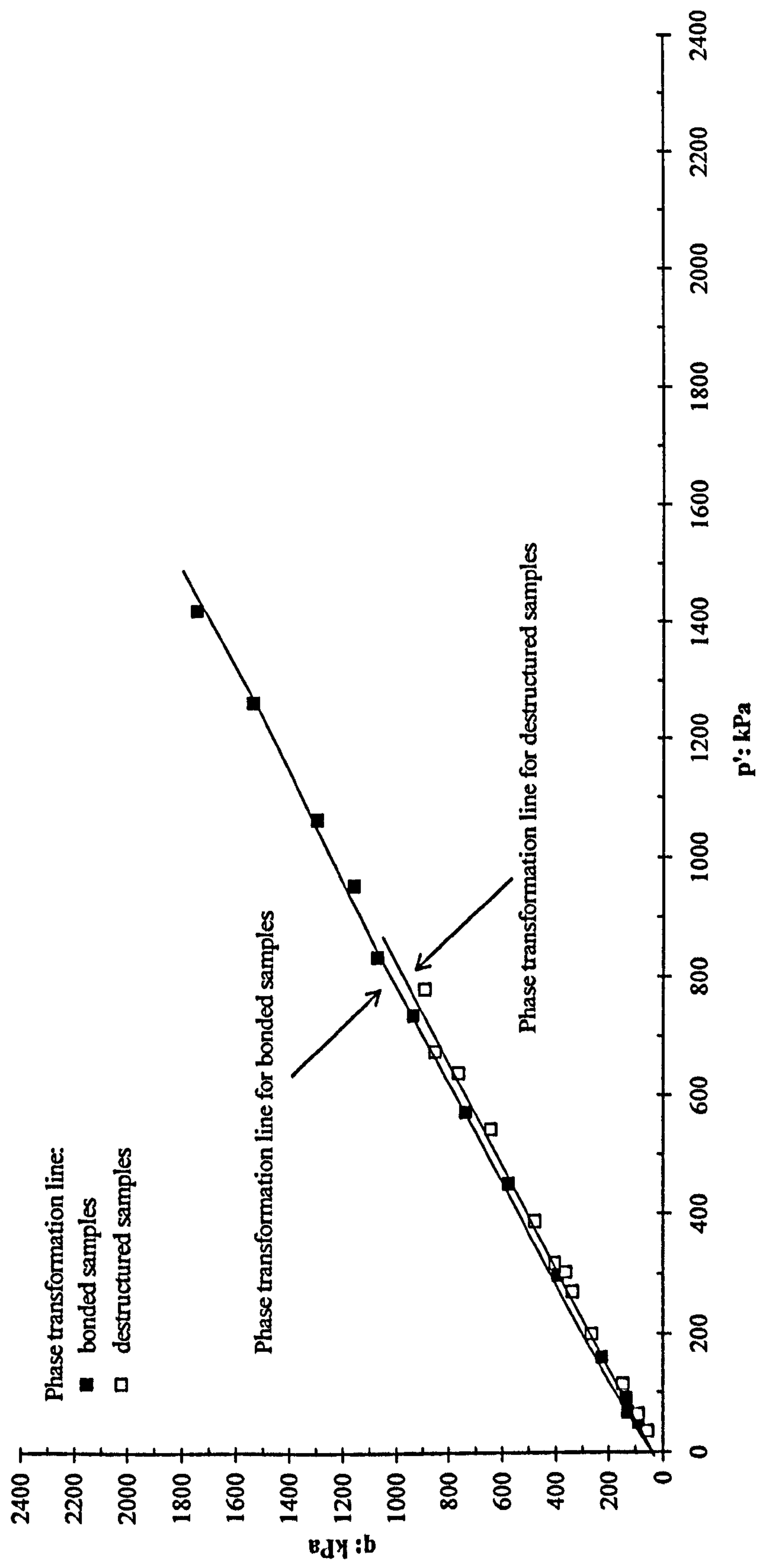


Figure 6.33: Phase transformation lines for the undrained bonded and destructured samples

destructured samples. This indicates that the presence of a bonded structure affects the development of pore water pressure within the bonded samples during shearing, where the change from contraction to dilation occurs at a higher stress ratio than that of the destructured samples. The explanation of this behaviour is due to the presence of bonds which could be acting to separate the sand particles. Once the bonds are broken, sand particles and broken materials move together and the effect is to produce a pore water pressure change. Meanwhile in the destructured material, the fine material from the broken bonds could be present in pore space between the sand particles, rather than separating the particles, therefore more inter-particles contact from the beginning and hence less pore water pressure development.

## **6.6 THE CRITICAL STATE OF BONDED SAMPLES**

### **6.6.1 The Critical State**

A critical state for the bonded material for each test was defined using a similar approach as used for the destructured material. Figure 6.34 shows the paths followed by the bonded drained samples in  $v - p'$  space. Some difficulties were encountered in defining the critical state from the two types of test. As shown in Figure 6.35.a and Figure 6.35.b from the drained tests, the deviator stress,  $q$  and volume strain,  $\epsilon_v$  still continue to change to the end of shearing. In order to define the critical state more accurately from the drained and undrained tests, an assessment had been carried out based on the  $v - p'$  curves. A defined critical state point was ensured located on a reasonably flat section on stress-strain and volumetric strain curves. From Figure 6.36.a and Figure 6.36.b, the critical state points are located approximately between 10% - 15% of axial strain. Assessment of the  $v - p'$  curves for the bonded samples in drained tests indicate two types of behaviours. Bonded samples sheared up to 600kPa show contraction and dilation



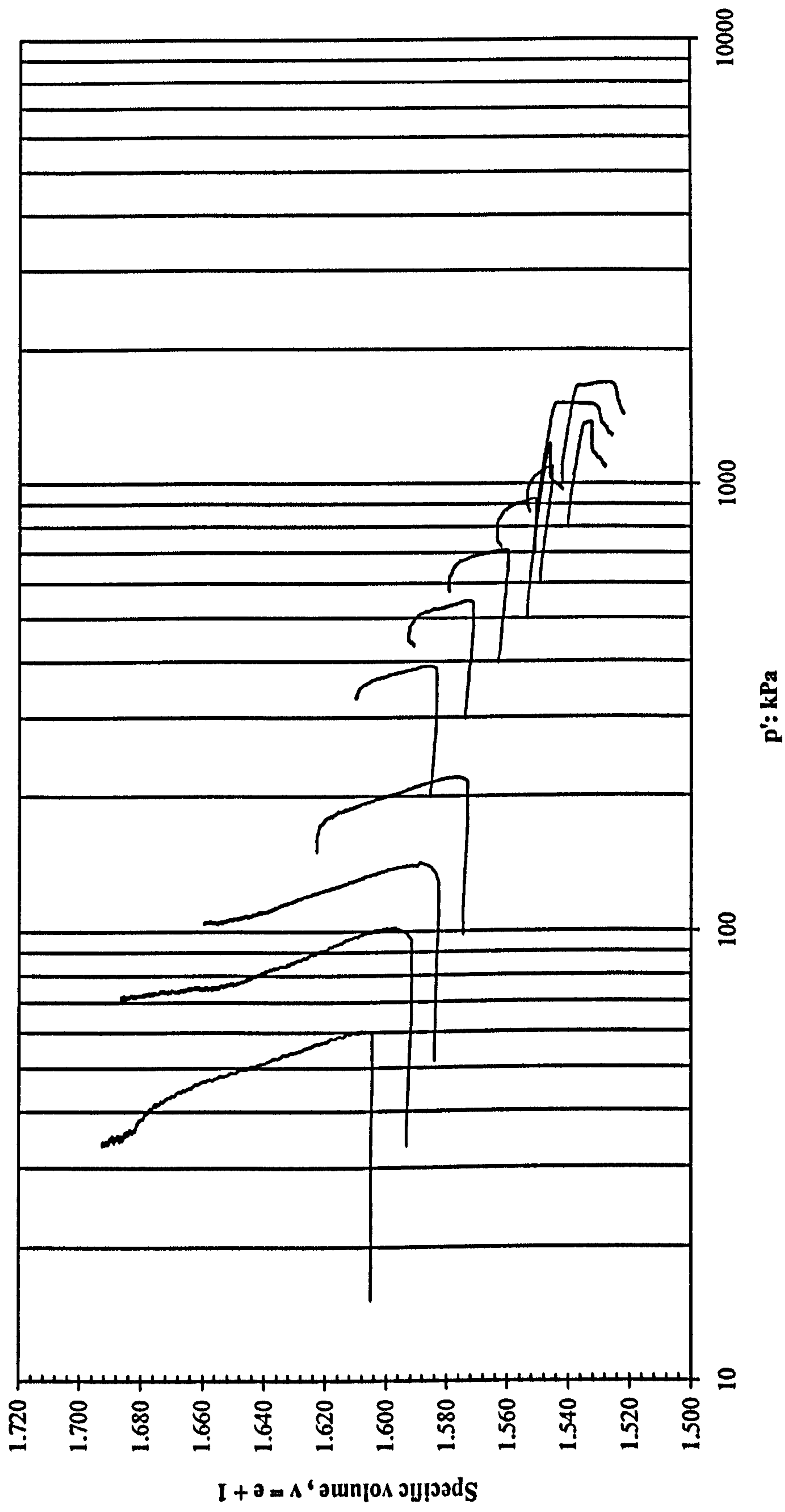


Figure 6.34: Paths followed by drained tests on bonded samples in  $v - p'$  space

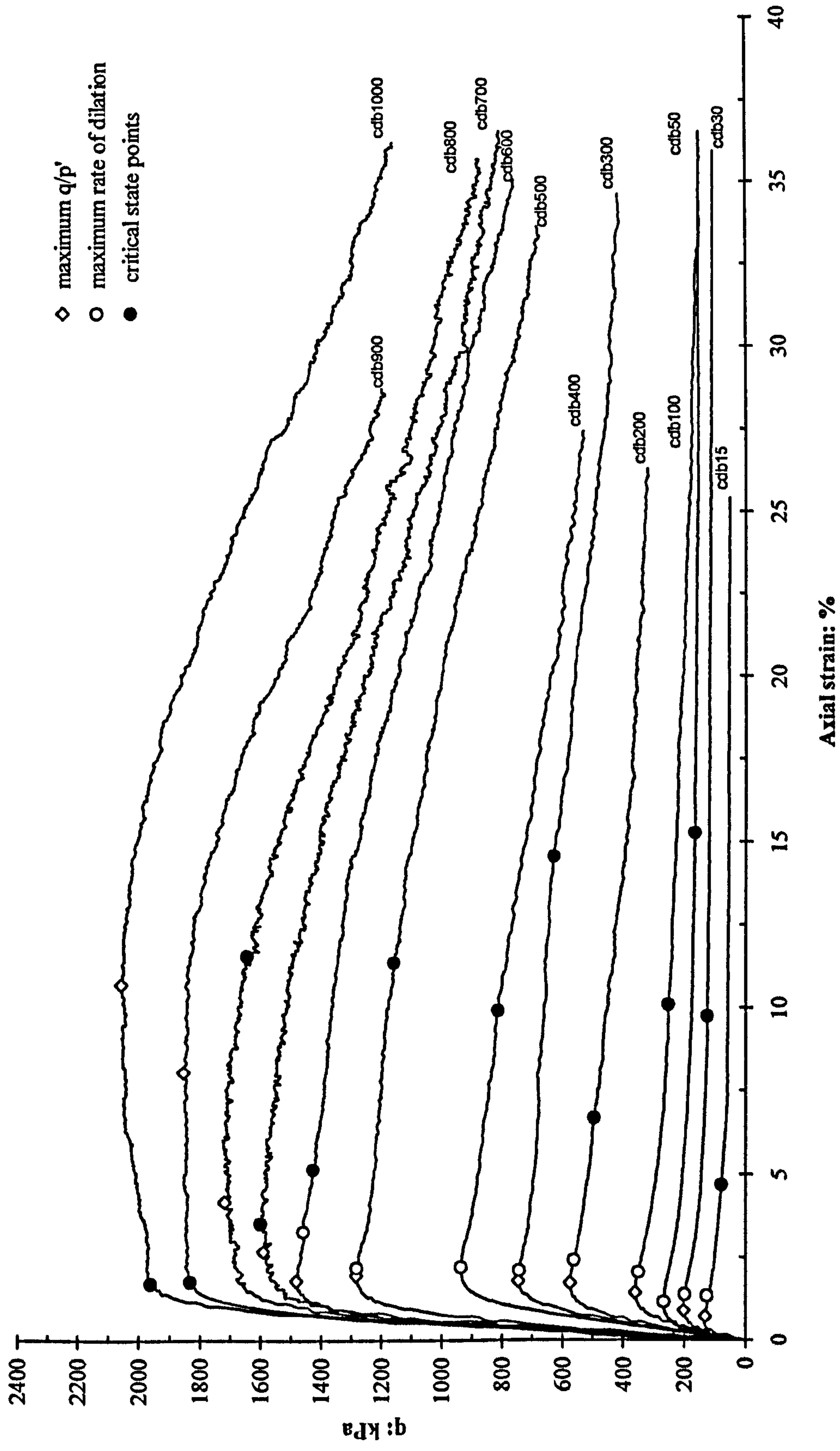


Figure 6.35a: Stress strain curves for the drained tests on bonded samples with critical state points defined using early approach

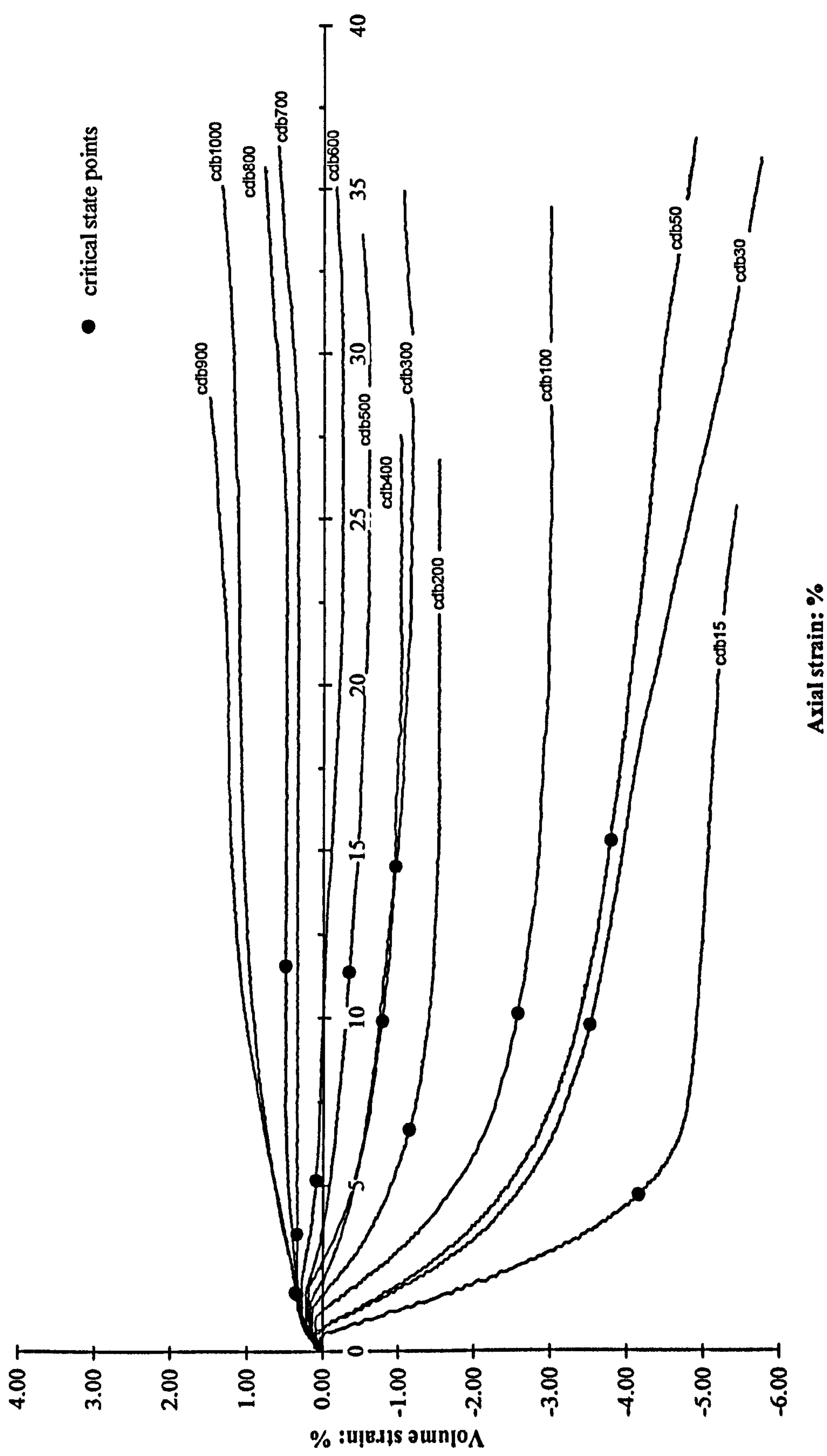


Figure 6.35b: Volumetric strain curves for the drained tests on bonded samples with critical state defined using early approach



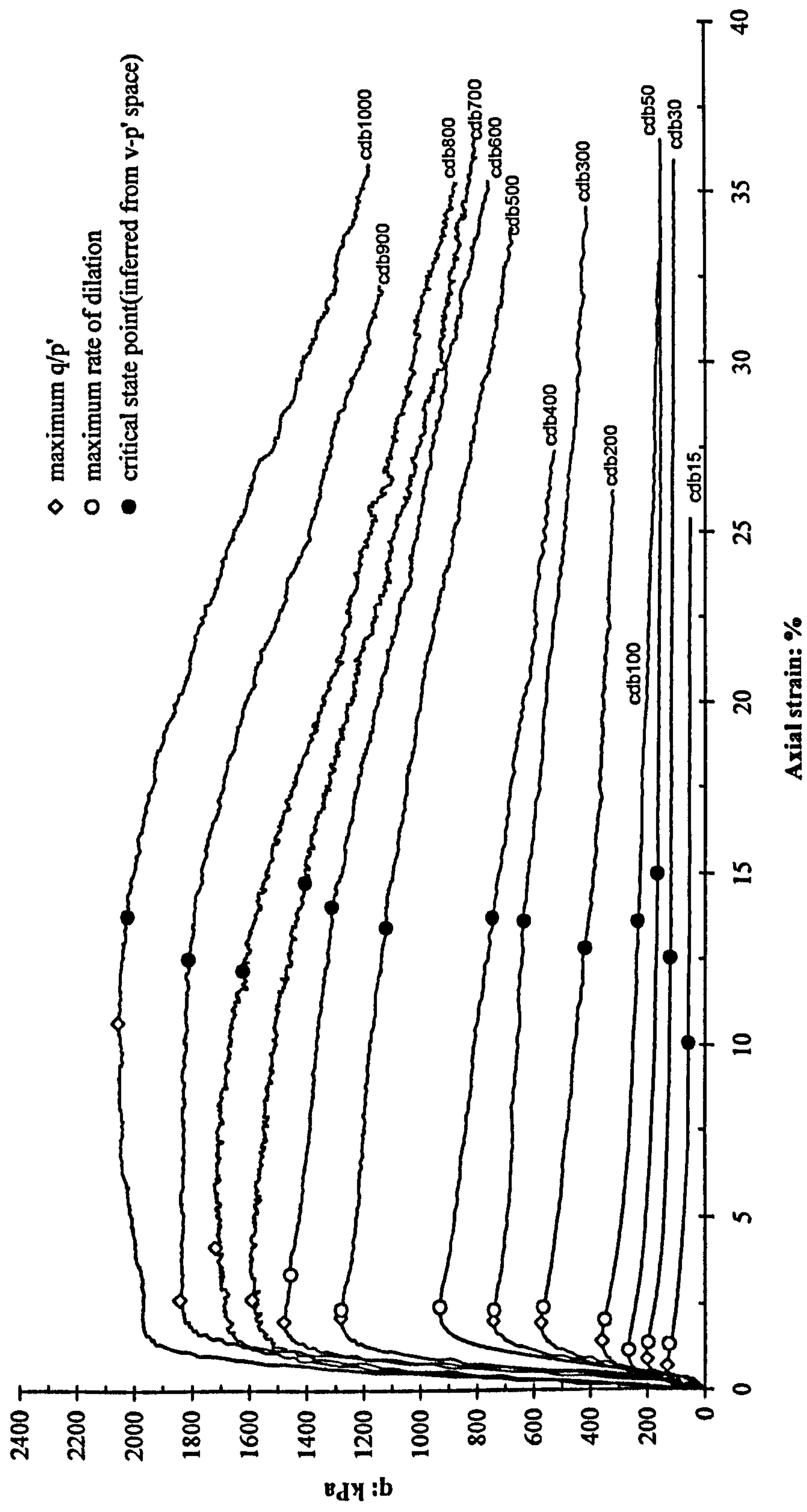


Figure 6.36a: Stress strain curves for the drained tests on bonded samples

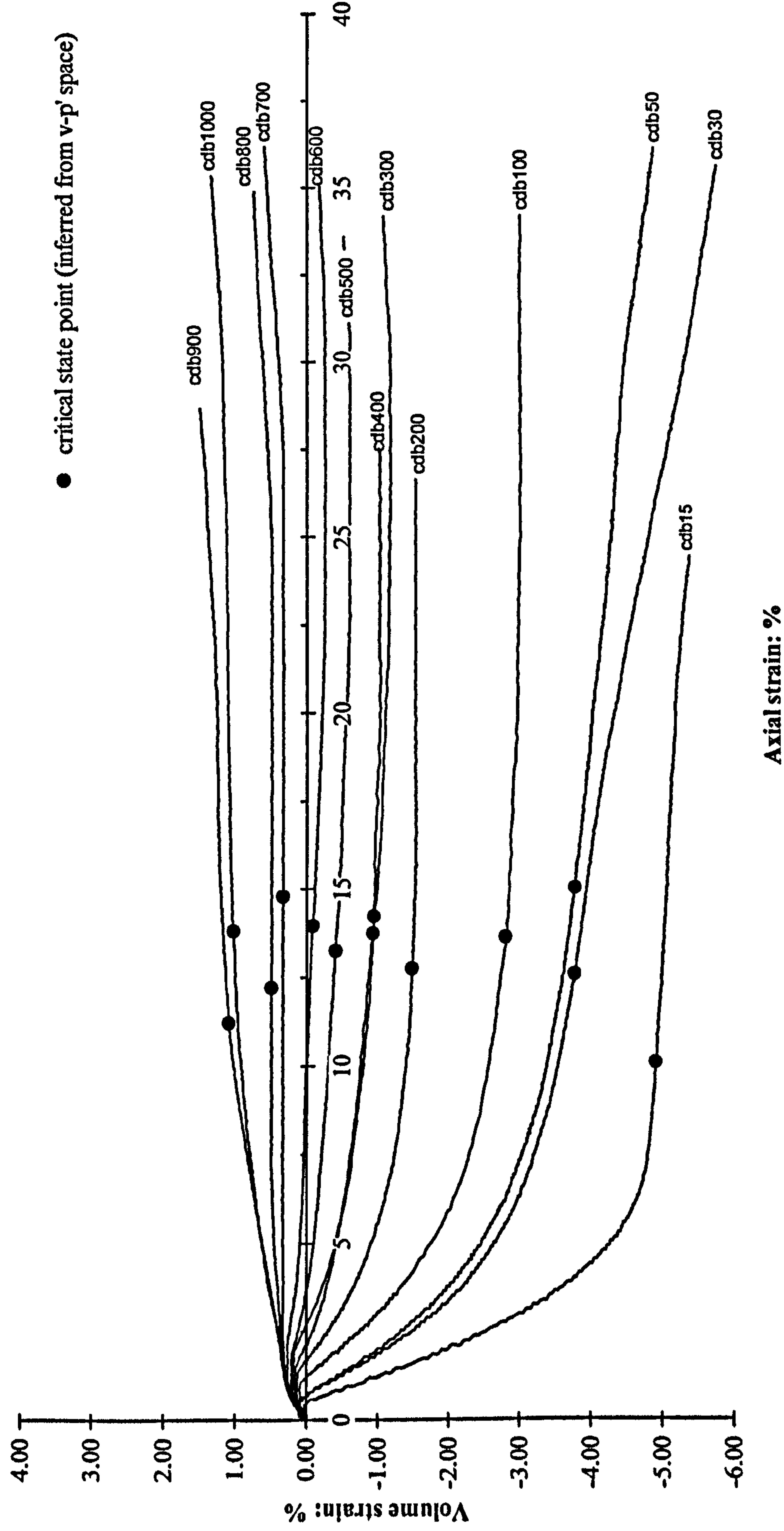


Figure 6.36b: Volumetric strain curves for the drained tests on bonded samples

behaviours whereas samples sheared higher than that ( $p' > 600 \text{ kPa}$ ) are associated with contraction behaviour up to the end of the tests (Figure 6.34). It is clearly seen that for the bonded samples sheared at  $p' \geq 700 \text{ kPa}$ , the specific volume,  $v$  initially decrease gradually with an increase of effective stress,  $p'$  before dropping abruptly at a particular stress. Meanwhile for samples sheared at  $p' < 700 \text{ kPa}$ , samples initially show contraction then change to dilation behaviour. This dilation behaviour continues up to a certain stress,  $p'$  which then start to show a “discontinuity”. This “discontinuity” is believed to be associated with strain localisation.

A similar approach was also performed for the bonded undrained samples using the earlier approach. However the critical state point defined using this approach does not represent a true critical state. As seen in Figure 6.37a and Figure 6.37b show the critical state points are too early which represent the bond yield points and apparently do not satisfy the definition of critical state. Therefore, assessments of the stress-strain and excess pore water pressure-strain plots were then reconsidered in order to define the critical state of the undrained bonded samples. It is clearly seen that the deviator stress (Figure 6.37a) and excess pore water pressure (Figure 6.37b) are still changing with the increase of axial strain. As a result, it is difficult to define the critical state point straightforwardly from the stress path for the undrained destructured material. A careful study of each stress-strain curve and excess pore water pressure-strain curve was carried out in order to define the critical state points. A reasonably flat section of stress-strain curve was identified and compared with the excess pore water pressure-strain curve. According to the critical state definition, both variables must be constant (no change in  $q$  and pore water pressure with the increase of strain), however in some tests, neither is fulfilled. Figure 6.38a and Figure 6.38b show the critical state points on stress-strain curves and pore water pressure-strain curves. It can be seen that the critical state points are located on the reasonably flat section of the curves between 10% - 15% of axial strain. Since the deviatoric stress,  $q$  is steadily changing to the end of shearing, a critical judgement has to be made to define the critical state point on the reasonably flat section before  $q$  drops and pore water pressure changes



significantly. The critical state points were also marked on the effective stress paths for the undrained tests as presented in Figure 6.39. It is found that the critical state points for bonded undrained tests occur after the reversal of the stress paths and are reasonably well represented by straight line from the origin with a minimum scatter ( $M=1.24$ ). This is equivalent to an undrained critical state angle of friction,  $\phi'$  of  $31^\circ$ .

The paths followed by the drained and undrained tests in  $v - p'$  space are shown in Figure 6.40. As expected, the points taken to represent the critical state do not show a unique line, as was found for the destructured material. Fourie and Papageorgiou (2001) insisted the difficulty in defining the void ratio due to error arouse from measurement of samples. Therefore, it would be preferable to accept a “confident zone” instead of a single line, as a result of inevitable errors. As seen in Figure 6.41, the critical state for bonded material is defined by a zone with upper and lower limits. From error analysis, the maximum error in determination of void ratio is in order of 0.08 (Appendix I and III). These upper and lower limits of the critical state are represented by the following equation in  $v - \ln p'$  space:

$$v = 1.8399 - 0.039 \ln p' \quad (\text{upper limit}) \quad \dots (6.1)$$

$$v = 1.8125 - 0.039 \ln p' \quad (\text{lower limit}) \quad \dots (6.2)$$

The difference between the upper limit and lower limit represents a variation of  $\pm 0.0274$ . In comparison with the destructured material, the upper and lower limits of the critical state lines are given by these following equations:

$$v = 1.7991 - 0.034 \ln p' \quad (\text{upper limit}) \quad \dots (6.3)$$

$$v = 1.7581 - 0.034 \ln p' \quad (\text{lower limit}) \quad \dots (6.4)$$

The different between the upper and lower limit calculated from equation (6.3) and (6.4) is  $\pm 0.041$ . It also found that the slope of critical state line,  $\lambda$  for destructured material ( $\lambda=0.034$ ) is slightly smaller than the value for bonded material ( $\lambda=0.039$ ).

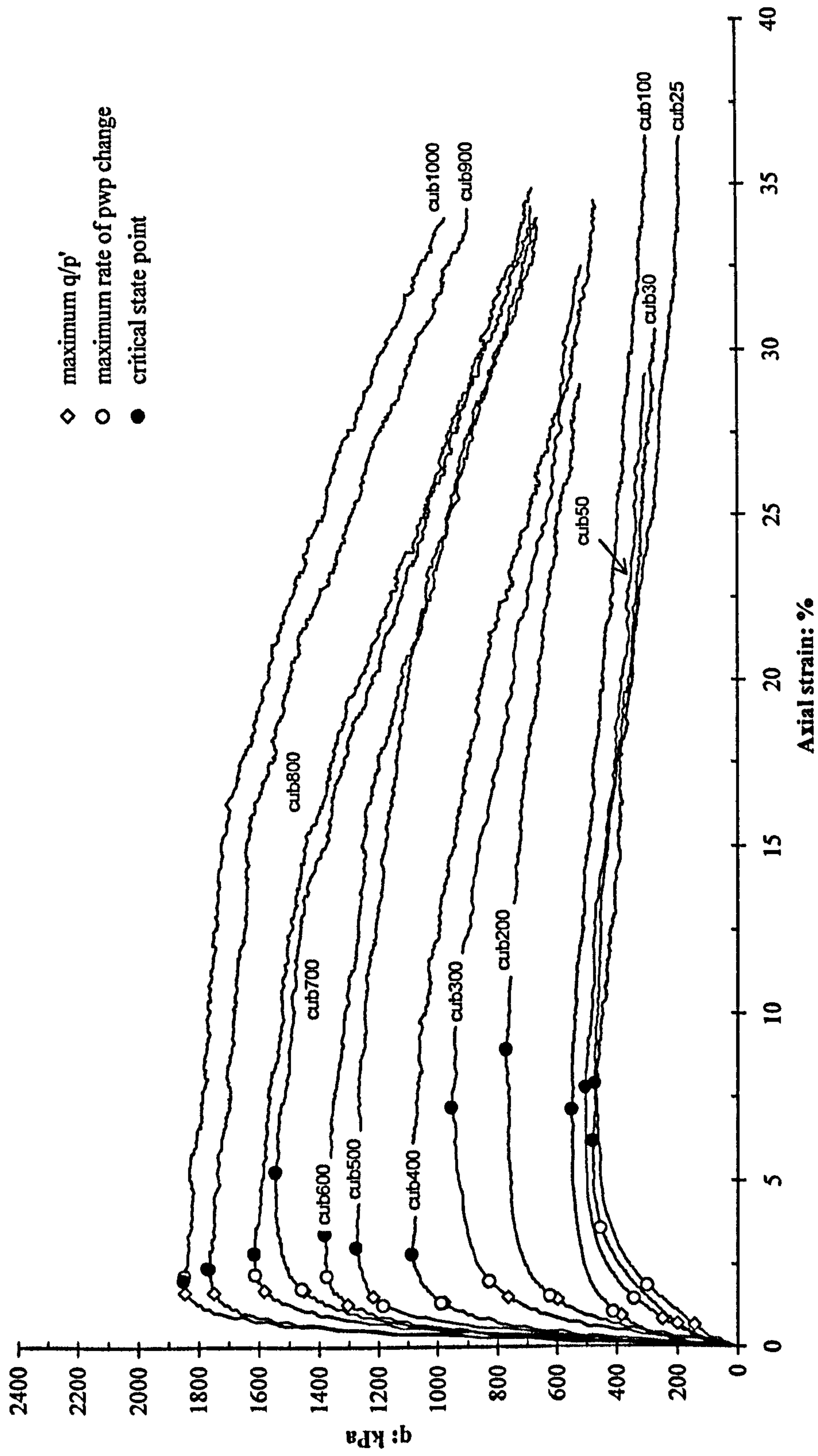


Figure 6.37a: Stress strain curves for the undrained tests on bonded samples with critical points defined using early approach

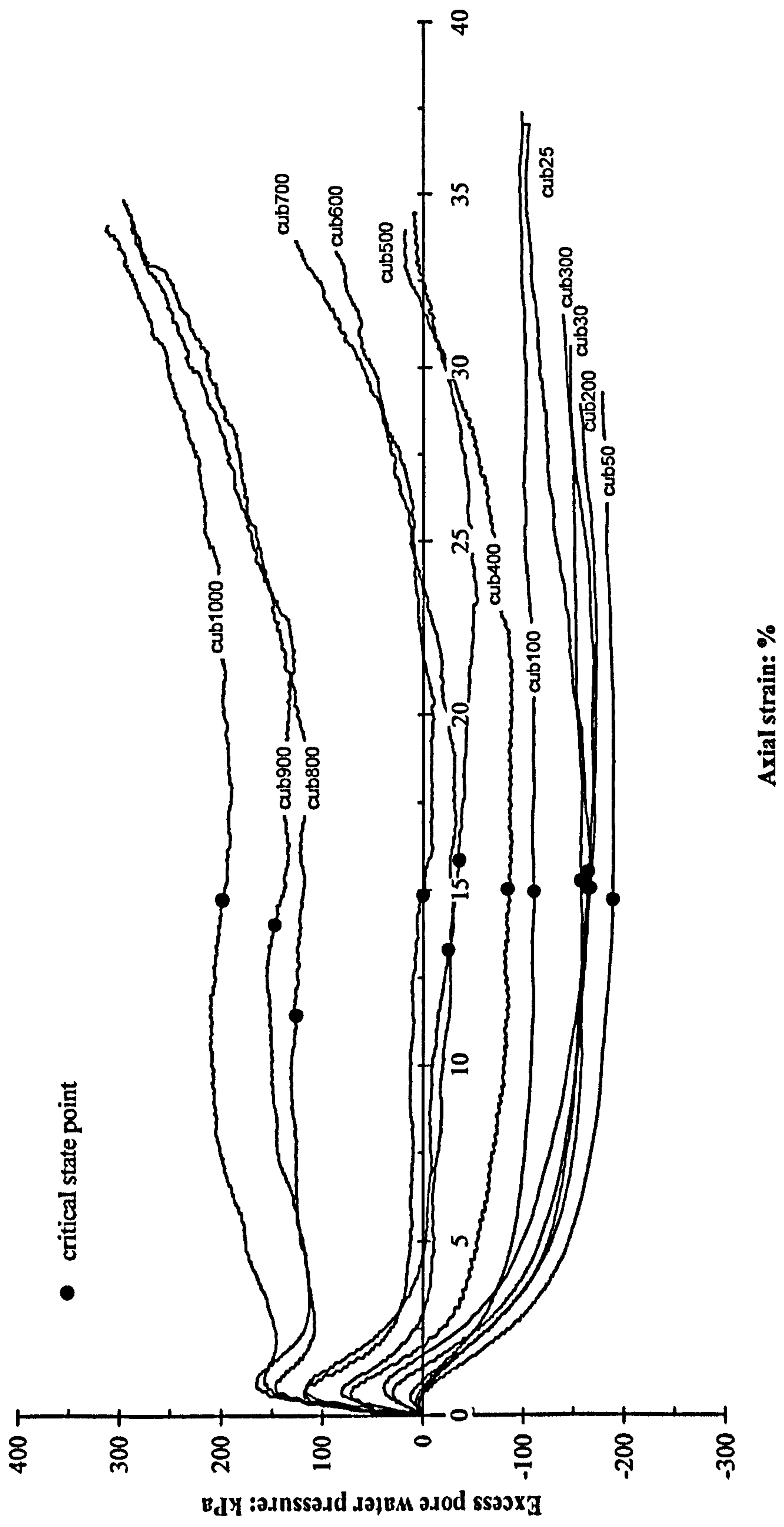


Figure 6.37b: Excess pore water pressure change curves for the undrained tests on bonded samples with critical state points defined using early approach



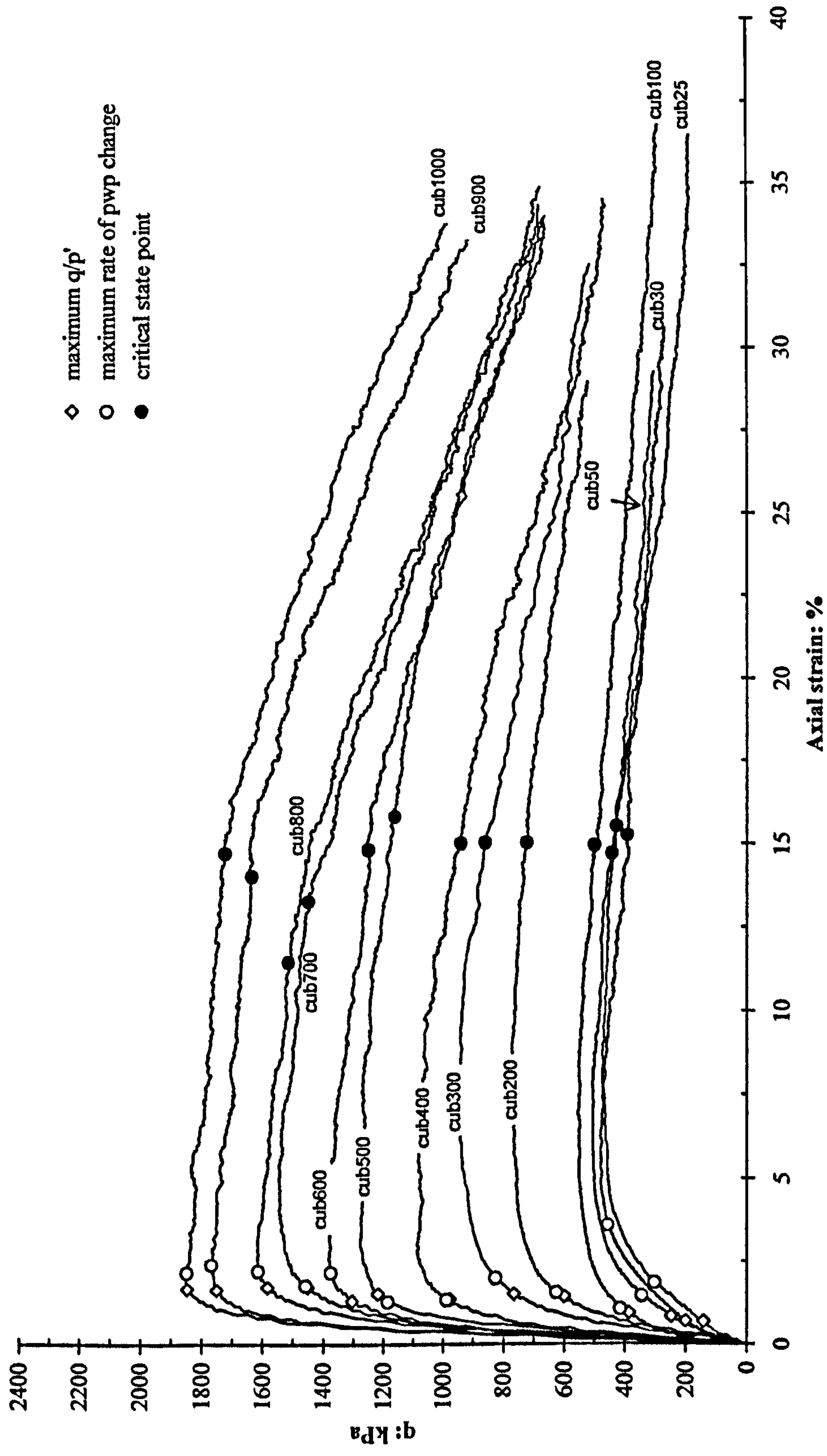


Figure 6.38a: Stress strain curves for the undrained tests on bonded samples

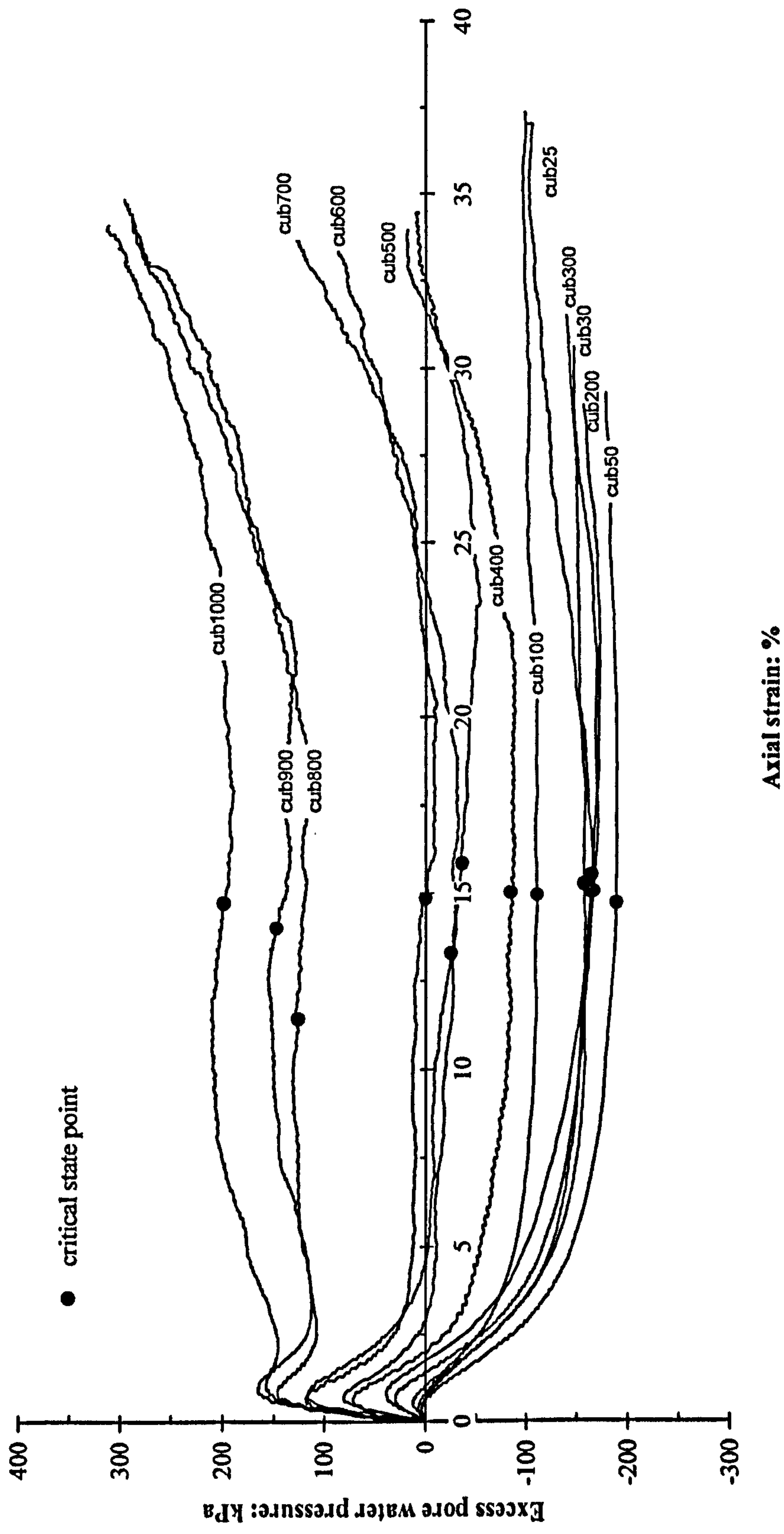


Figure 6.38b: Excess pore water pressure change curves for the undrained tests on bonded samples

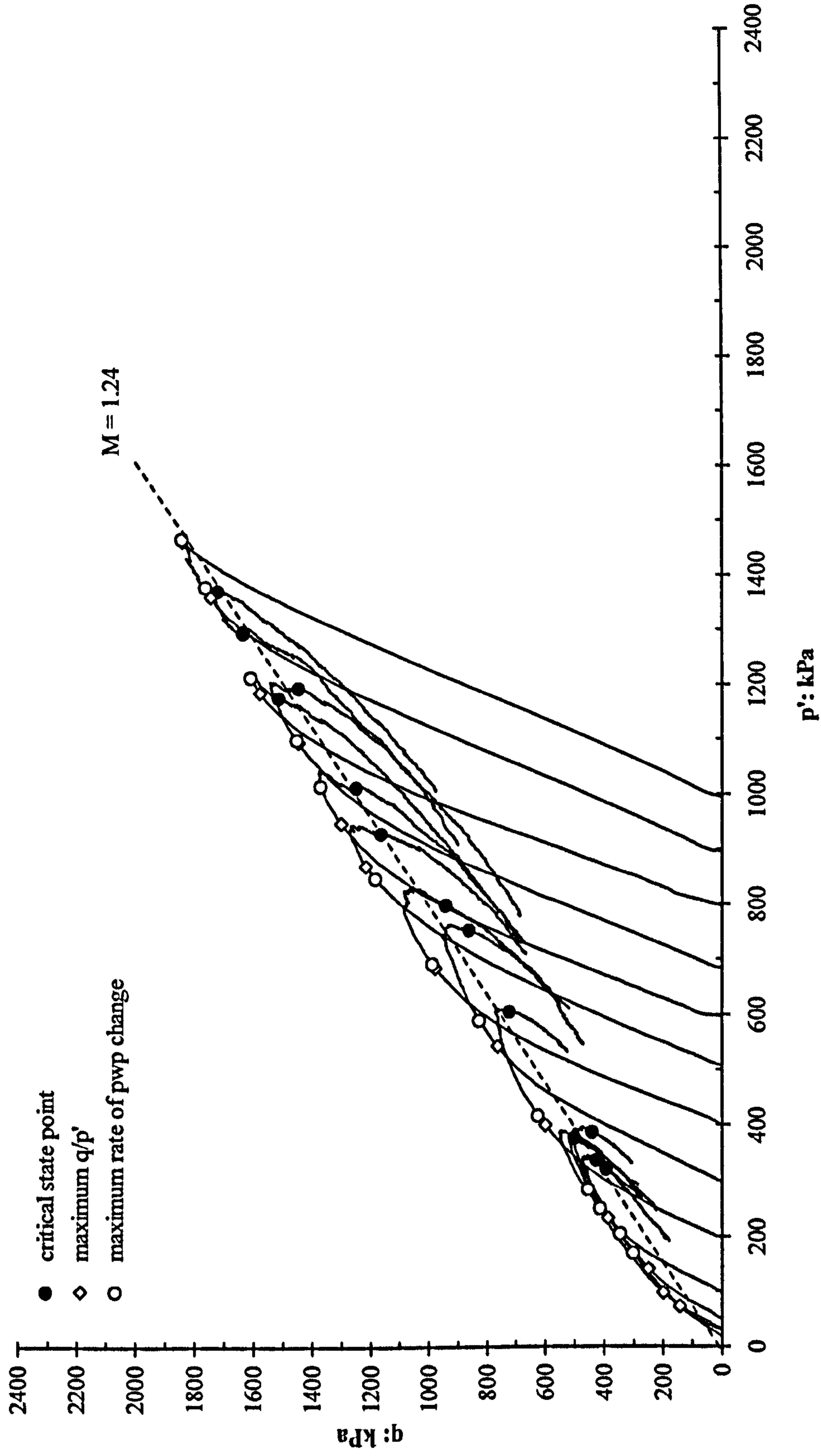


Figure 6.39: Effective stress paths for the undrained tests on bonded samples



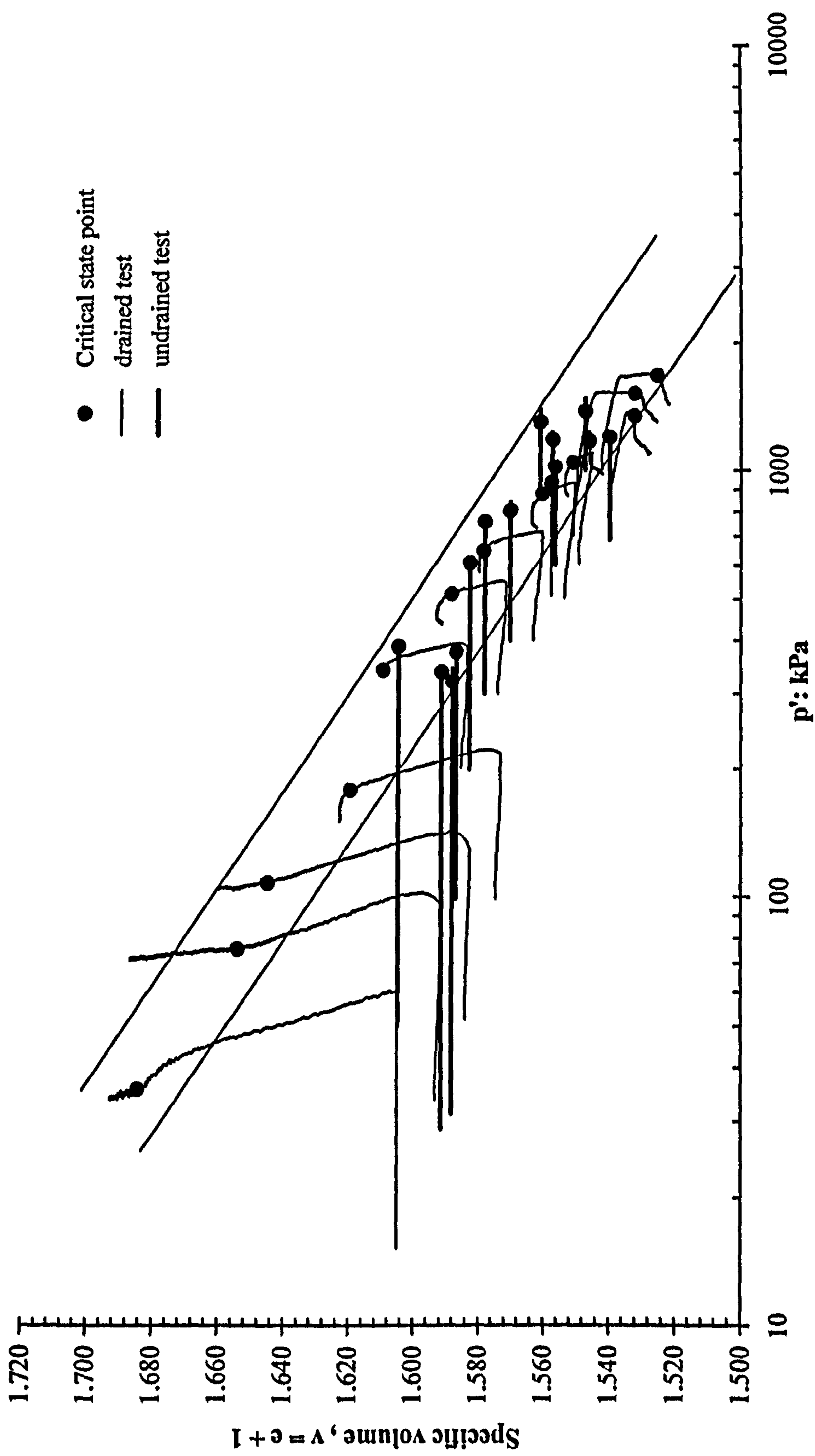


Figure 6.40: Specific volume changes with effective stress,  $p'$  for the drained and undrained tests on bonded samples

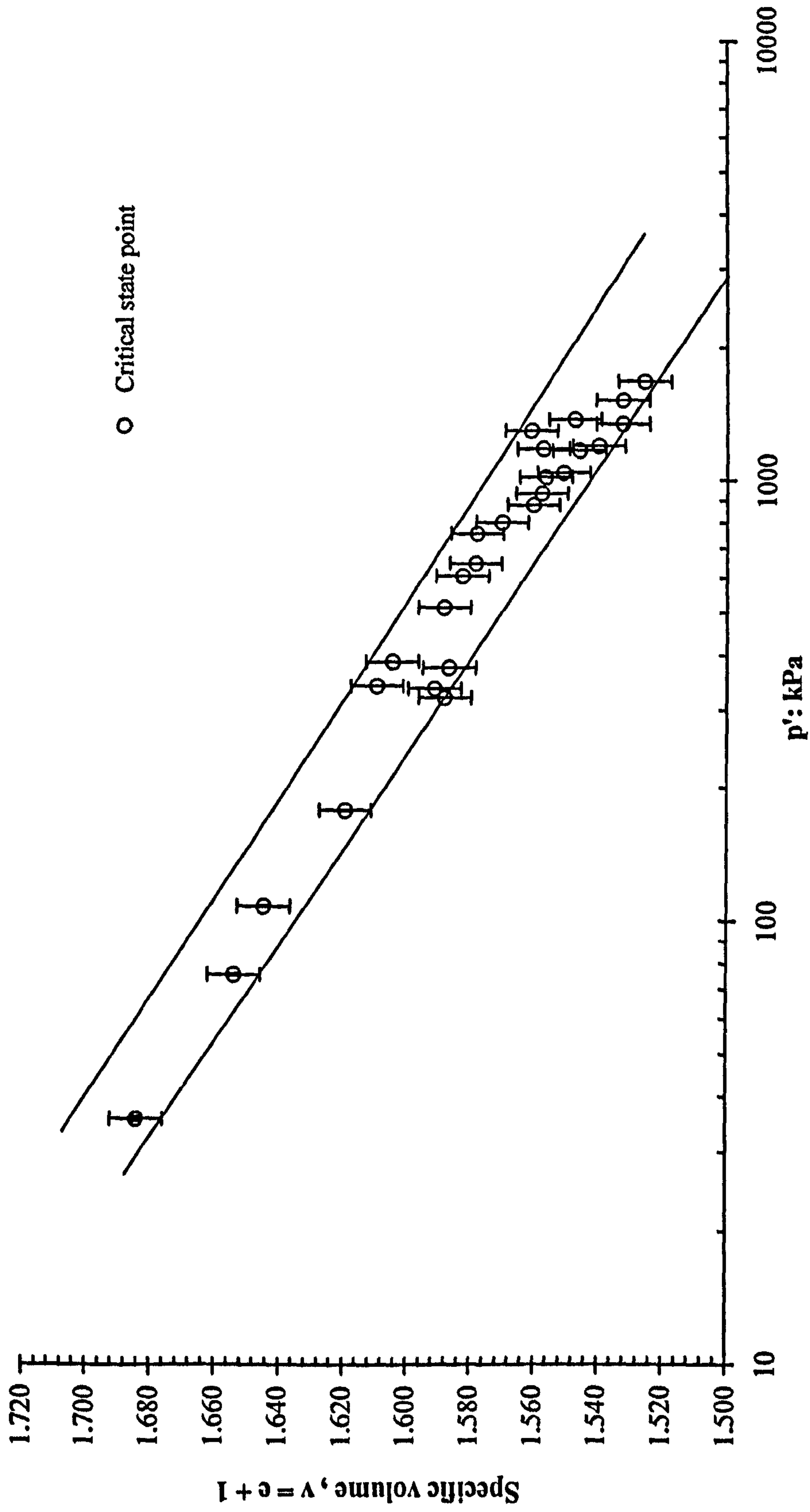


Figure 6.41: Critical state for drained and undrained tests on bonded samples with upper and lower limits (error bars included)

The critical state points are also plotted in a  $q - p'$  space (Figure 6.42). The critical state for the bonded material defines a fairly straight line through the origin with some scatter of the data. The slope of the critical state line is defined by  $M = 1.23$  which is slightly smaller than the destructured material ( $M = 1.24$ ). This is equivalent to a critical state angle of friction,  $\phi'$  of  $30.7^\circ$ . Coop and Atkinson (1993) also found the angle of friction,  $\phi'$  for cemented carbonate sands slightly lower than uncemented samples due to the influenced of cement coating the sand particles. It can be seen from the plot in  $q - p'$  space, the critical state points are scattered mainly at  $p' > 400 \text{ kPa}$  with  $M_c$  ranges from 1.14 to 1.62 corresponding to the variation in  $q/p'$  ratio values. In comparison with the destructured material, the scatter in  $M$  ranges between 1.12 and 1.51, which are quite close to the scatter in  $M$  value for the critical state points for the bonded material.



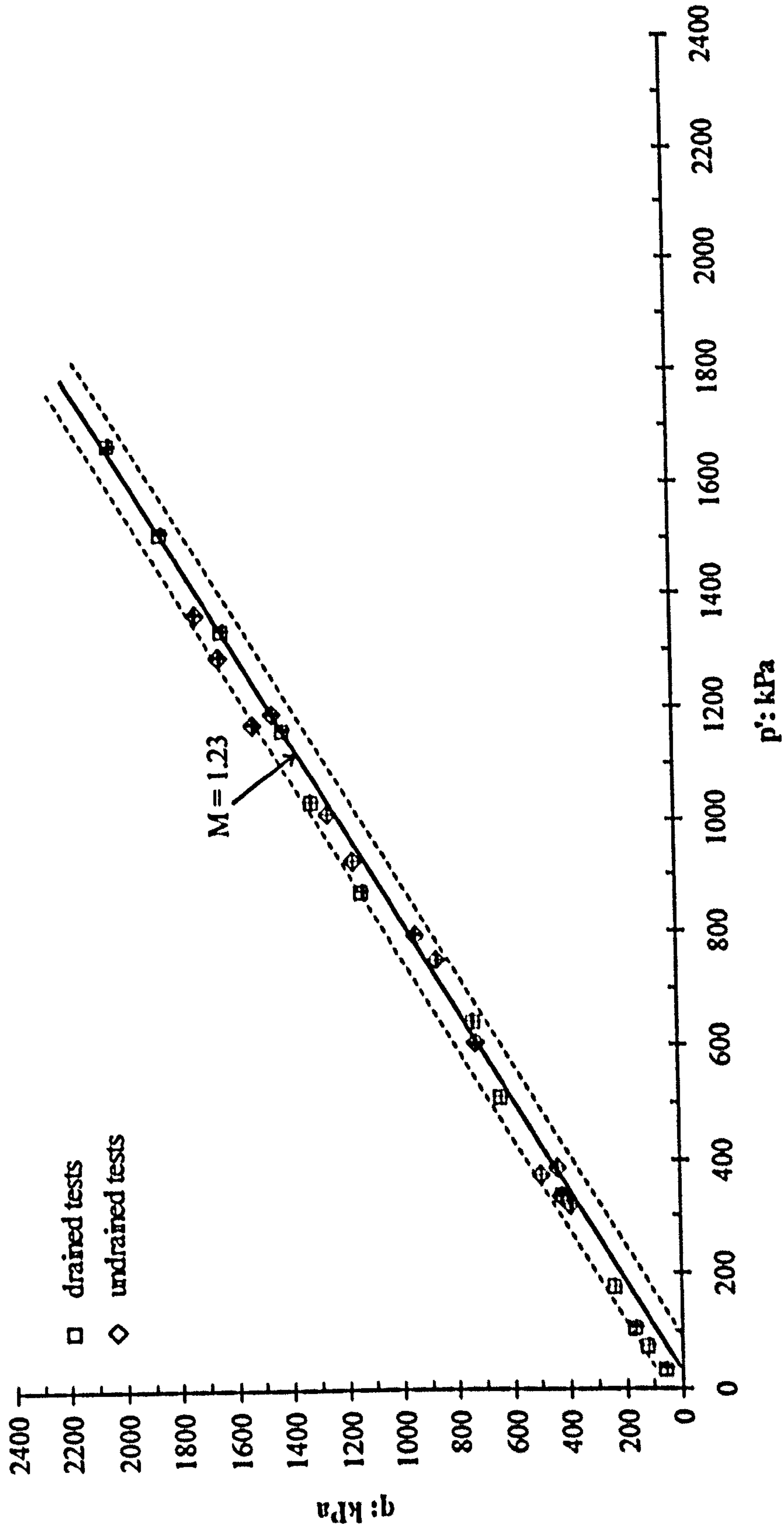


Figure 6.42: Critical state line for the drained and undrained tests on bonded samples in  $q - p'$  space (error bars included)

### 6.6.2 Normalisation

The normalised stress paths in  $p'/p'_c - q/p'_c$  spaces for the drained and undrained tests are shown in Figure 6.43a and 6.43b. It is clear that the normalised stress paths for both types of tests reach a different value of  $q/p'_c$ . A further refinement for each test in this space for  $q/p'_c$  was carried out by re-normalising with the end values of  $q/p'_c$  (equal to  $M$ ). Therefore, the stress path values for  $p'/p'_c$  and  $q/p'_c/M$  will end at the (1, 1) point, which represents the critical state (Figures 6.44a and 6.44b). The refined stress paths for the bonded drained and undrained tests are shown in Figure 6.45. From the normalised stress paths plotted in  $q/p'_c/M - p'/p'_c$  space, drained and undrained samples with  $p'/p'_c < 0.6$  climb up to the limiting surface from the left side of the space towards the critical state. For undrained samples, the stress paths achieve a peak strength before turning down to the critical state. However, the drained samples do not clearly indicate this kind of behaviour. Meanwhile for those samples with  $p'/p'_c > 0.6$ , stress paths move up passing below the critical state to reach the maximum strength then turn down to the critical state. This behaviour is clearly observed from the drained samples sheared at  $p'_o = 900\text{kPa}$  and  $1000\text{kPa}$  (cdb900 and cdb1000) (Figure 6.44a).

Comparison has been made between the normalised drained and undrained stress paths of bonded samples and the destructured material. The boundary surface from the destructured material is marked on the normalised stress paths for the drained and undrained tests on bonded material (Figure 6.46). It is clearly seen that even samples which begin at lower  $p'/p'_c$  reached states outside the state boundary surface of the destructured material. This is particularly true for undrained tests; in fact the drained tests approaching the Hvorslev surface show little difference with the destructured surface. However, the drained tests on bonded material go well beyond the Roscoe surface defined from the destructured material. Therefore, the effect of bonding can be clearly presented on the normalised stress paths.

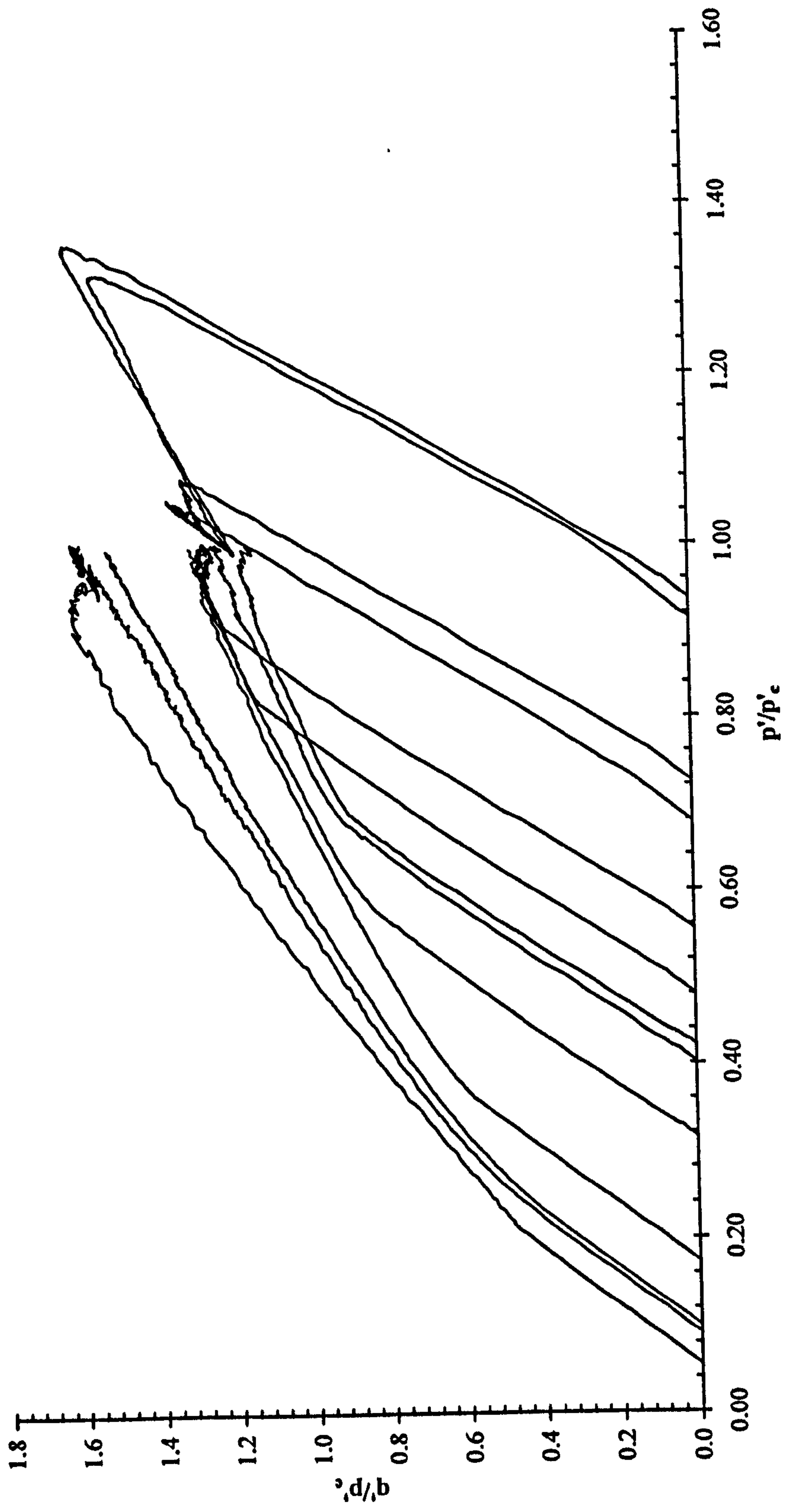


Figure 6.43a: Normalised stress paths in  $q/p' - p'/p'_c$  space for the drained tests on bonded samples



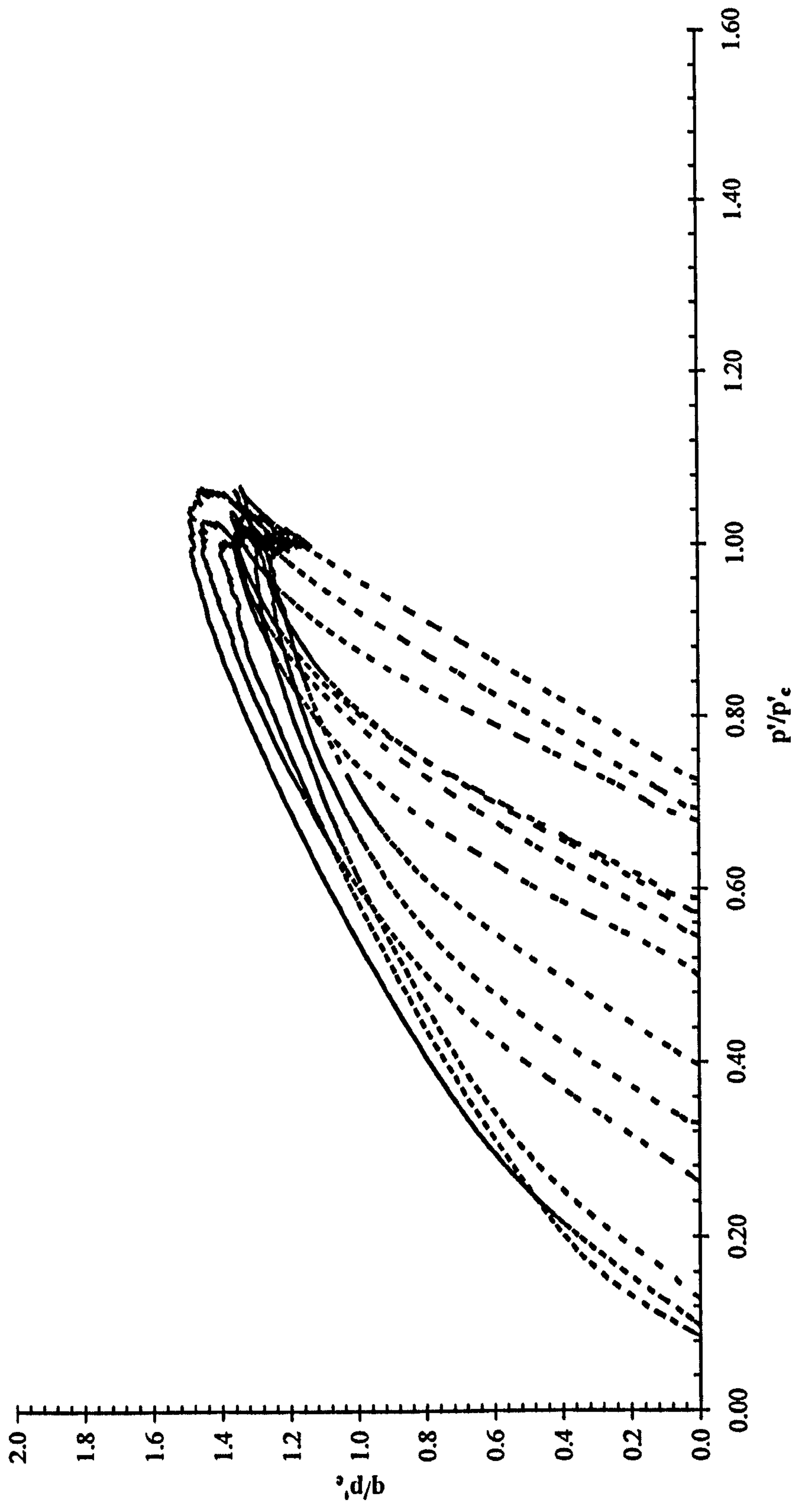


Figure 6.43b: Normalised stress paths in  $q/p' - p'/p'_e$  space for the undrained tests on bonded samples

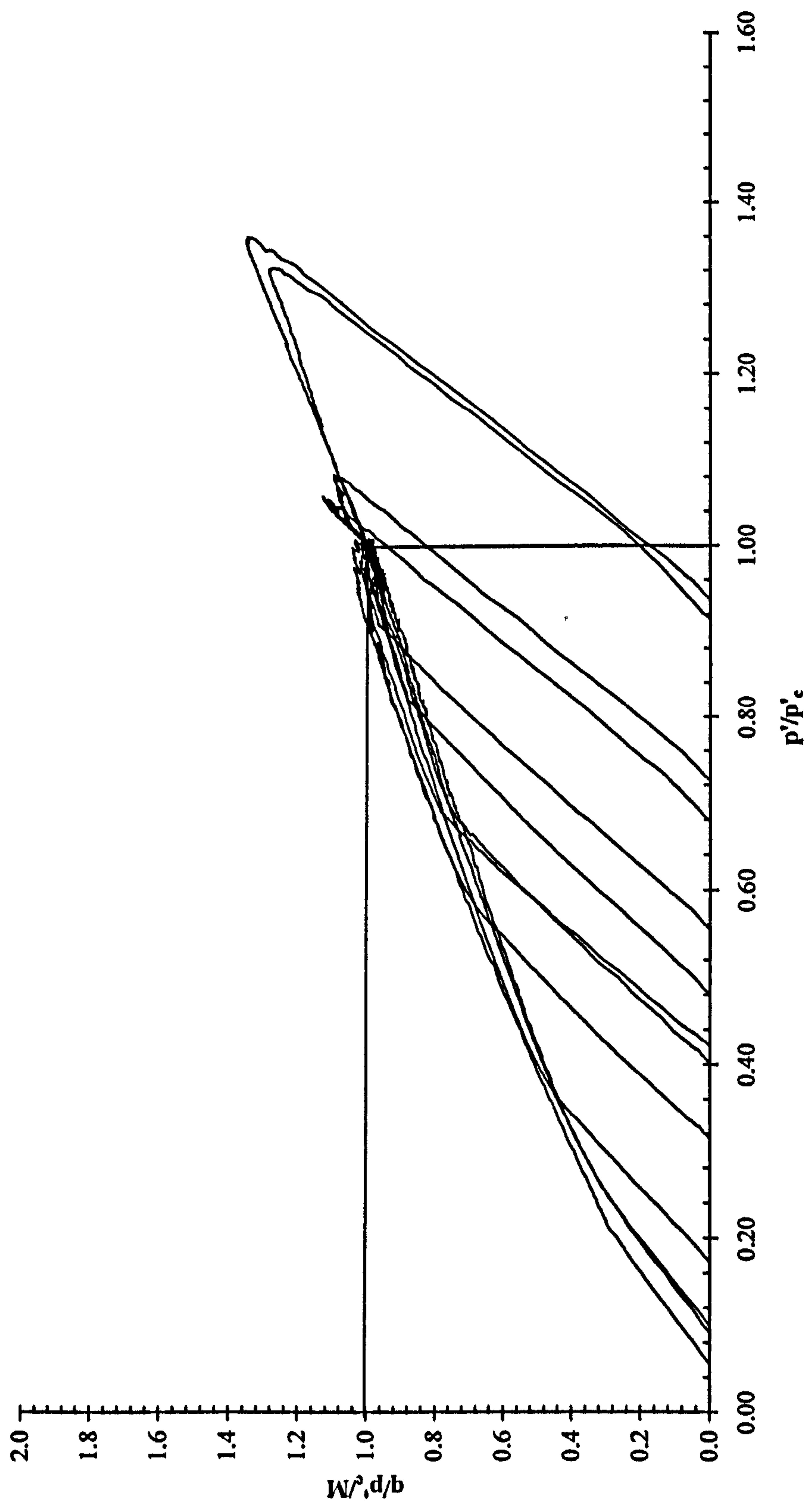


Figure 6.44a: Normalised stress paths in  $q/p'-M - p'/p'_c$  space for the drained tests on bonded samples

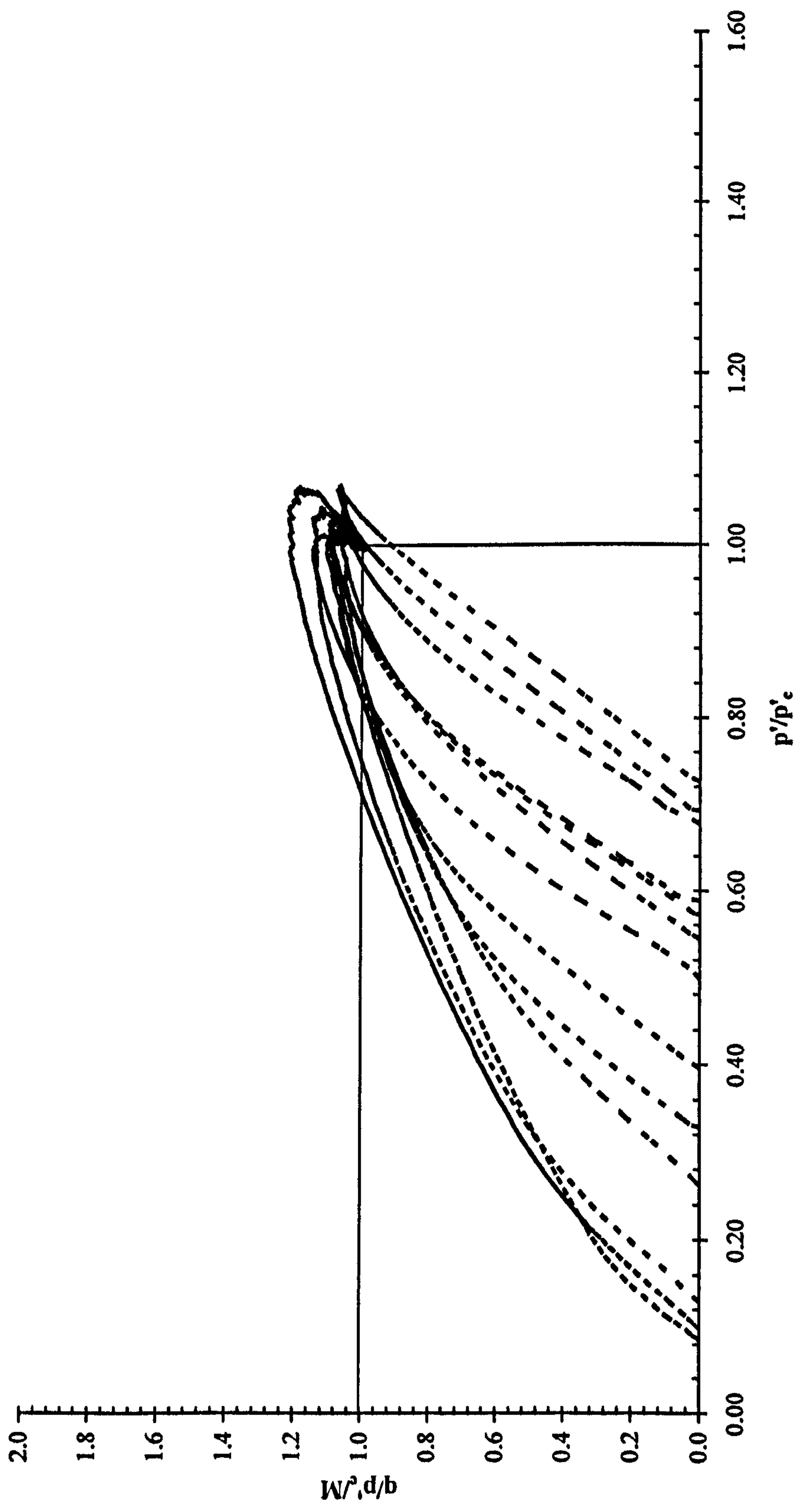


Figure 6.44b: Normalised stress paths in  $q/p'_M - p'/p'_c$  space for the undrained tests on bonded samples



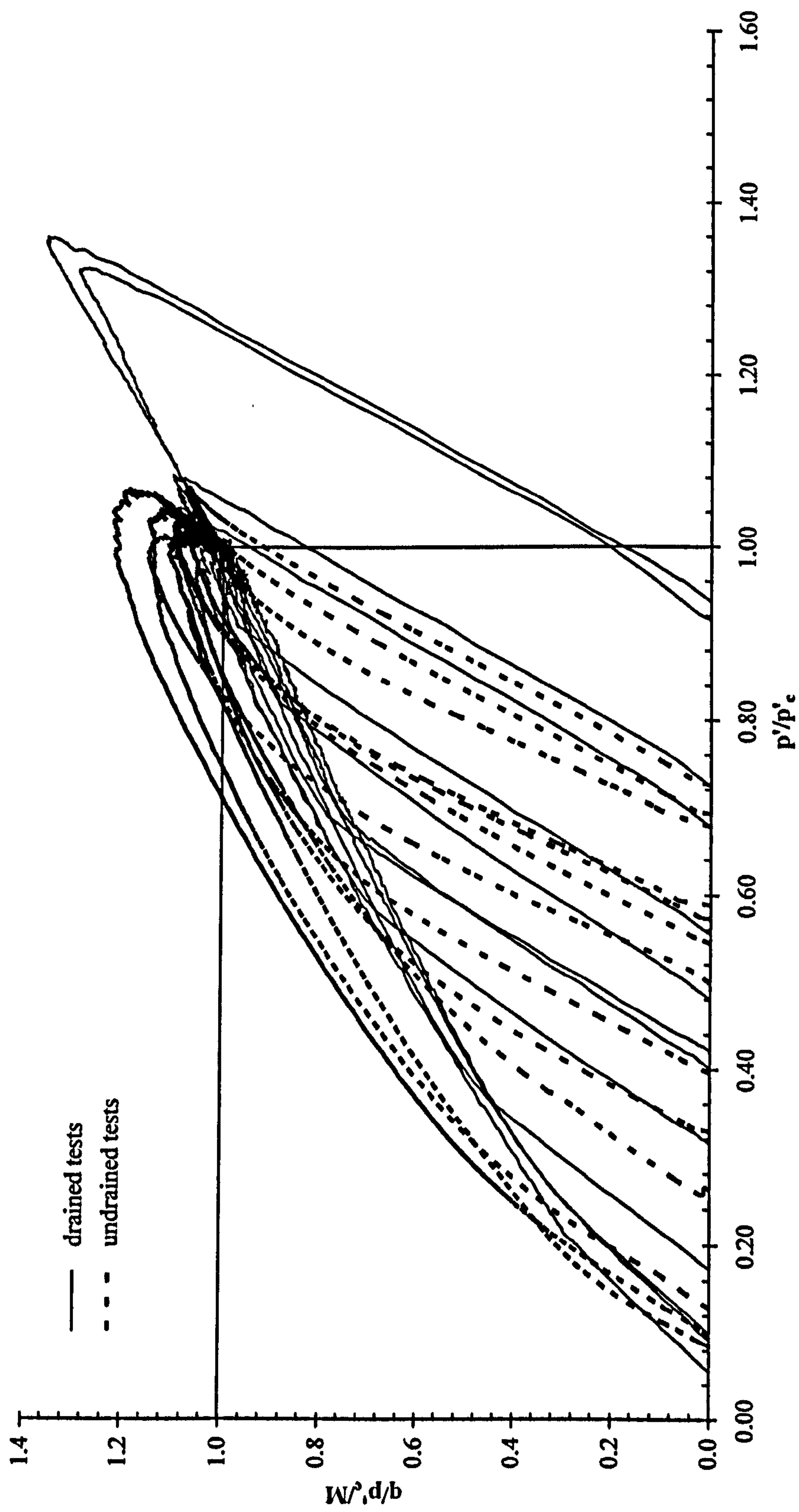


Figure 6.45: Normalised stress paths in  $q/p/M - p'/p'_c$  space for bonded materials

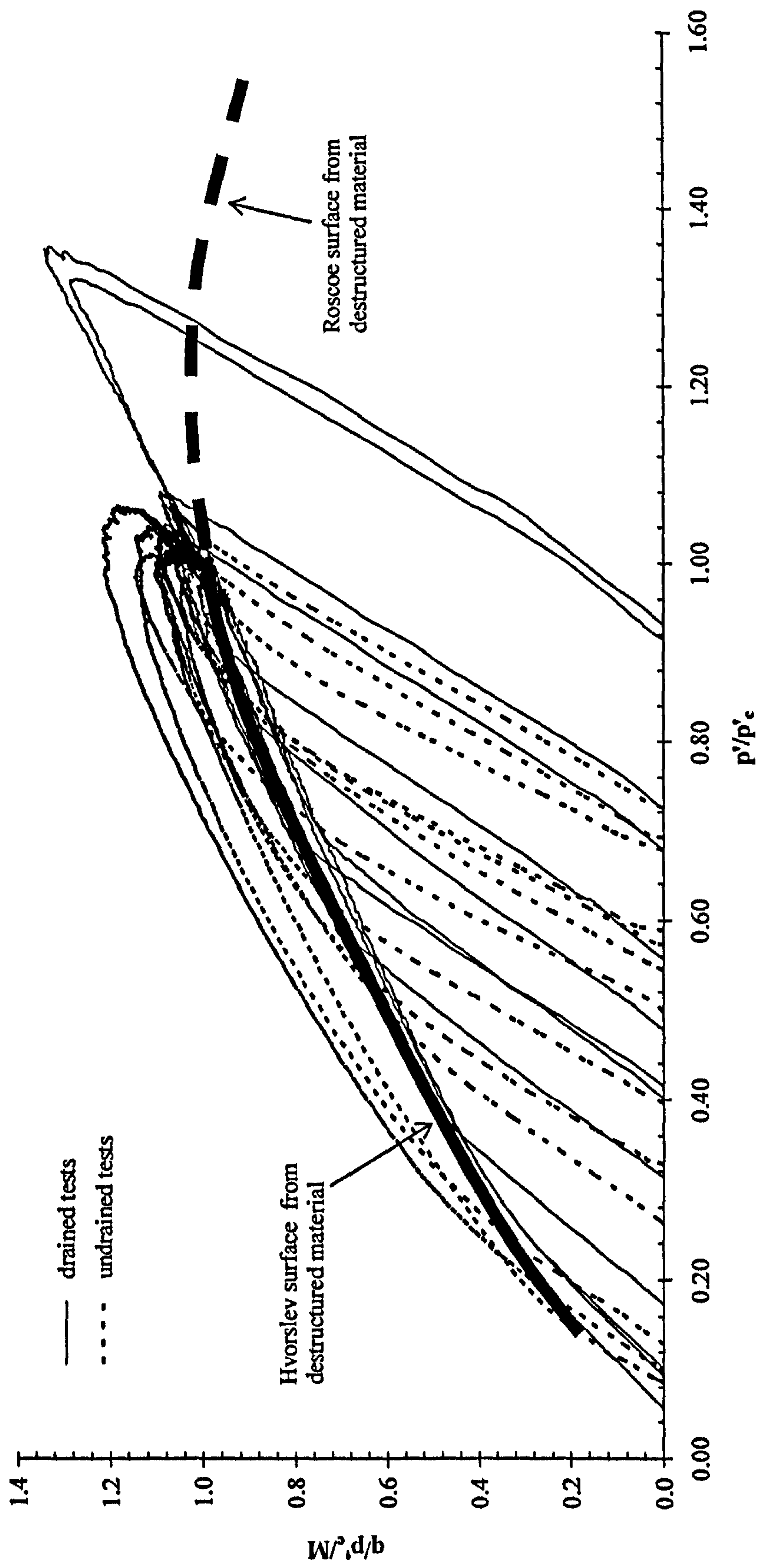


Figure 6.46: Comparison between normalised stress paths in  $q/p'/M - p'/p'_c$  space between bonded and destructured materials

According to Coop and Atkinson (1993), the presence of the bonded structure allows the soil to achieve unstable peak states outside the state boundary surface of uncemented soil followed by rapid strain softening.

## 6.7 FINAL REMARKS

A series of conventional drained and undrained triaxial tests were carried out on the artificially bonded material in saturated conditions. The bonded samples were prepared from a mixture of sand and kaolin which was then fired at 500°C for 5 hours in order to create a weakly bonded structure. All the samples were prepared with initial void ratio of 0.6.

The stress strain behaviour for both types of tests showed a consistent pattern of behaviour. The samples initially climbed up to maximum deviator stress then gradually decreased with increasing axial strain. The drained samples sheared at low confining stress levels showed smaller compression initially then changed to dilative behaviour. Similar behaviour was also observed from the undrained tests for samples sheared at low confining stresses. The undrained samples initially developed positive pore water pressure (tendency to compression) and then excess pore water decreased (tendency to dilation behaviour) with further axial strain. The maximum  $q/p'$  ratio was achieved at low axial strain between 1% and 2% for both types of test. Tests sheared at low confining stresses showed a clear peak of  $q/p'$  ratio and this became less significant with increasing confining stress. The behaviour between the bonded drained and undrained samples was compared at three different stress levels. At low stress levels ( $p_o'=25-50\text{kPa}$ ), the bonded drained samples achieved higher maximum  $q/p'$  ratios (1.90-2.24) than the bonded undrained samples (maximum  $q/p'$  ratio=1.76-2.00). At medium stress levels ( $p_o'=300-500\text{kPa}$ ), the bonded drained samples achieved maximum  $q/p'$  ratios between 1.32 and 1.39, lower than values achieved by the bonded undrained samples (maximum  $q/p'$  ratio=1.40-1.43). For the bonded drained samples sheared at high stress levels ( $p_o'=900-1000\text{kPa}$ ), the maximum  $q/p'$  ratio values range from



1.22-1.23 while the bonded undrained samples achieved higher maximum  $q/p'$  ratios between 1.26 and 1.29. The bounding surface for the bonded drained and undrained samples indicated some curvature at low and high stress levels. However the data points from the two types of test are best represented by a straight line up to stress level,  $p'=1400\text{kPa}$ , suggesting that the drained and undrained samples have a fairly similar behaviour. The phase transformation line for the bonded drained and undrained tests also exhibited some curvature at higher stress level. The yield surfaces from the drained and undrained tests on bonded samples were compared. It was found that the first yield surface from the undrained tests was slightly above than that obtained from the drained tests. However the difference was within the range of experimental discrepancy. It can be concluded that the yielding of bonds was unaffected by the drainage condition during shearing of the bonded samples. The final bond yield surfaces exhibited a good agreement between the drained and undrained tests. However, the final bond yield surface from the undrained tests was slightly above the final bond yield for drained tests especially at higher stress levels of  $p' > 1200\text{kPa}$  but seems turns back to the final bond yield surface for the drained tests.

The behaviour between the bonded samples and destructured samples was also compared. The bonded samples presented higher maximum  $q/p'$  ratio values in comparison to those of the destructured samples. However, by increasing the confining stress, the bond strength decreases progressively at failure, thus the peak in stress ratio drops closer to that of the destructured material. This suggests that the high limiting stress ratios are due to bonding, but by consolidating to high stress levels the bonding is destroyed so the behaviour approaches that of the destructured material.

Due to difficulties in defining the critical state from the drained and undrained tests (because of strain localisation and non-uniformity towards the end of the tests) a similar “discontinuity” approach (as used for destructured material) was applied to the bonded material. In order to define the critical state more accurately from the tests, assessment was carried out based on the  $v - p'$  curves. Since the deviatoric

stress,  $q$  is steadily changing to the end of shearing, a critical judgement has to be made to define the critical state point on the reasonably flat section on stress-strain and volumetric strain or excess pore water pressure curves before these variables change significantly. The defined critical state points are located between 8% - 15% of axial strain for the drained tests and between 10% - 15% of axial strain for the undrained tests. The critical state points thus defined did not show a unique line in  $v - p'$  space (as was found for the destructured material) with the difference between the upper and lower limits of  $\pm 0.0274$ , slightly smaller than the range for the destructured material ( $\pm 0.041$ ). On the other hand, the critical state defined in  $q - p'$  space was represented by a fairly well defined straight line passing through the origin with some scatter of the data. It was found that the critical state points for bonded material were scattered mainly at  $p' > 400 \text{ kPa}$  with  $M$  ranging from 1.14 to 1.62 corresponding to the variation in  $q/p'$  ratio values. In comparison, the destructured material also showed some scatter in data points with  $M$  ranging between 1.12 and 1.51, which are quite close to the scatter in  $M$  value for the critical state points for the bonded material.

The normalised stress paths in  $p'/p'_c - q/p'_c$  spaces for the drained and undrained tests were presented. A refinement for each test in this space for  $q/p'_c$  was carried since  $q/p'_c$  reached different values. It is clear that the normalised stress paths for both types of tests reach a different value of  $q/p'_c$ . It was clearly seen that for samples with  $p'/p'_c < 0.6$  climbed up to the limiting surface from the left side of the space towards the critical state. For undrained samples, the stress paths achieve the peak strength before turning down to the critical state. Meanwhile, the drained samples did not clearly exhibit this kind of behaviour. For those samples with  $p'/p'_c > 0.6$ , the stress paths moved up passing below the critical state to reach the maximum strength then turned down to the critical state. This behaviour was clearly observed from the drained samples sheared at high confining pressures ( $p'_0 = 900 \text{ kPa}$  and  $1000 \text{ kPa}$ ).

Comparison had been carried out between the normalised drained and undrained stress paths of bonded samples and the destructured material. It found that even



samples that started at lower  $p'/p'_c$  reached states outside the state boundary surface of the destructured material. The effect of bonding was clearly presented from the normalised stress paths. According to Coop and Atkinson (1993), the presence of the bond structure permitted the soil to attain unstable peak states outside the state boundary surface of the uncemented soil followed by rapid strain softening.



## **CHAPTER 7    BEHAVIOUR OF BONDED MATERIAL IN UNSATURATED STATE**

### **7.1    INTRODUCTION**

In this chapter, the results from triaxial tests on unsaturated samples are presented. The tests were carried out on artificially bonded samples that were prepared using the same method and void ratio of 0.6 as that used in the previous saturated tests. In pilot studies, the axis-translation technique was used in order to bring the suction to a particular value in the samples. As a result of the long time required in order to achieve suction equalisation within the samples (and limited available time to accomplish the required numbers of unsaturated tests) constant water content testing was finally decided upon for the unsaturated tests. In this type of test, suctions are measured (not controlled), therefore water content had to be predetermined before setting up in the triaxial cell. The bonded samples were fully submerged in a beaker of distilled water and allowed to saturate overnight before being allowed to dry naturally under room conditions. Once each sample had achieved the desired water content, the sample was ready to be set up in the triaxial cell. Each sample was left in the cell until suction equalised within the sample under a small mean net stress,  $p-u_a$  (5kPa). The suction value at the end of this stage was used in defining the water retention curve for the unsaturated bonded samples used in this study. Several samples were dried to different water contents and the related suction was measured (at the end of suction equalisation) in order to construct a water retention curve for the studied material.

The artificially bonded samples with different suction values were then consolidated at different mean net stresses,  $p-u_a$  of 50, 100 and 300kPa and were then sheared after suction equalisation was achieved. The results from the constant

water content tests on bonded samples are presented in terms of stress-strain behaviour, stress paths and bounding surfaces. The critical state for the unsaturated bonded material is presented in a later section.

## **7.2 CONSTANT WATER CONTENT TRIAXIAL TESTS**

### **7.2.1 Description of Testing**

A series of triaxial tests was carried out on artificially bonded samples under constant water content (cw) conditions. These artificially bonded samples were prepared in the same manner as samples that had been used in the conventional triaxial tests in saturated conditions. All samples were sheared at a constant rate of strain of 0.025%/min (or 1.5%/hr) after the suction had equalised within the samples. For samples with low suction, equalisation took less than a week. However, for the samples with high suction values (smaller water content, w) the pore water pressure still continued to change for a longer period. In such drier samples with small water content, it could be that the continuity of the liquid phase is lost and therefore water has to move as vapour through the sample. The migration of water then becomes very slow. For a constant water test, it would not be expected to have movement of water between the drainage system and the sample. Nevertheless, in order to achieve suction equalisation, it is necessary that some water (although very small in quantity) has to move from the sample into the drainage system in order for the pressure transducer diaphragm to deflect. The movement of this minuscule quantity of water through the sample during suction equalisation is very slow as continuity of liquid phase is absent and it happens in the vapour phase. Due to the slow nature of equalisation in some samples, suction equalisation was assumed to be complete after the rate of pore water pressure change became less than 0.002kPa/min.



The shearing of the samples was carried out up to 30% of axial strain in order to achieve the behaviour of samples toward the critical state.

The series of tests and descriptions of the unsaturated bonded samples for the constant water content tests are shown in Table 7.1. The identification of the tested sample is referred to the type of test, type of sample, applied net stress,  $p-u_a$  and suction value. The first three letters "cwb" refer to the constant water content test (cw) on bonded sample (b) which is then followed by applied ( $p-u_a$ ) and suction value (at the end of suction equalisation) and the value in bracket refers to the degree of saturation,  $S_r$  (e.g., cwb50/100(0.15)).

### 7.2.2 Water Retention Curve

The water retention curve for the unsaturated bonded samples is presented as suction,  $(u_a-u_w)$  against degree of saturation,  $S_r$  and gravimetric water content,  $w$  (Figure 7.1 and Figure 7.2). The values of suction are those recorded at the end of the suction equalisation stage. The values of degree of saturation were calculated based on the water content measured before samples were set up in the triaxial cell. An assumption had to be made that the void ratio of the bonded samples would not change (no deformation) during the stage of suction equalisation since the applied mean net stress,  $(p-u_a)$  was 5kPa. The creep of the perspex cell during application of the small  $(p-u_a)$  was assumed to be nil. In addition, it was always assumed that there was no loss of mass during handling the sample therefore the degree of saturation,  $S_r$  or water content,  $w$  could be determined from the measured dry mass of samples. The calculations of water content of the samples were based on the water content at the end of tests (since the water content remains constant throughout).

The water retention curves represent the drying paths for the artificial samples (Figure 7.1 and Figure 7.2). It can be observed that both retention curves change very rapidly in the suction range 2kPa to 4kPa, (with some scatter in the data,



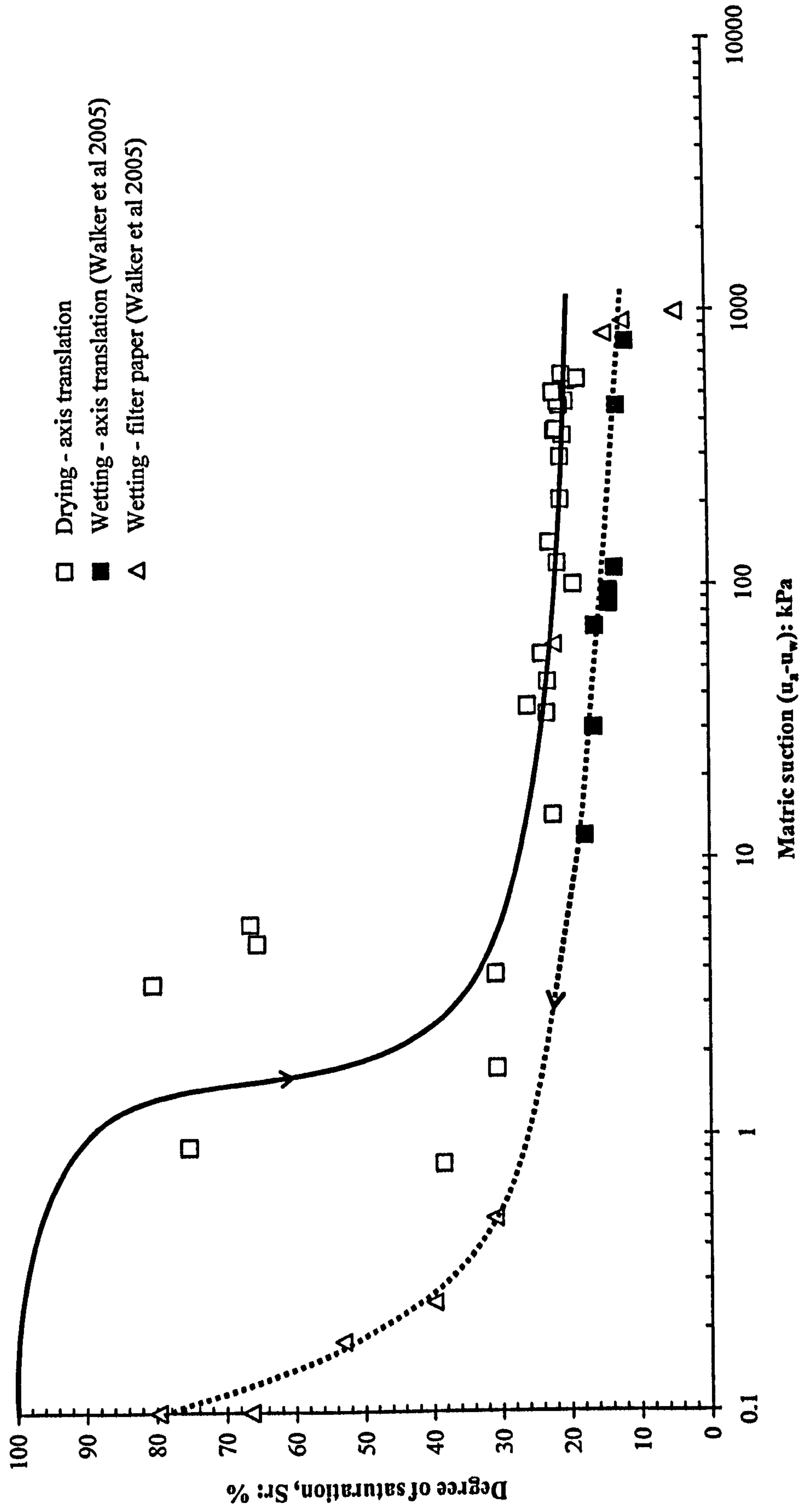


Figure 7.1: The water retention curve in degree of saturation against matric suction

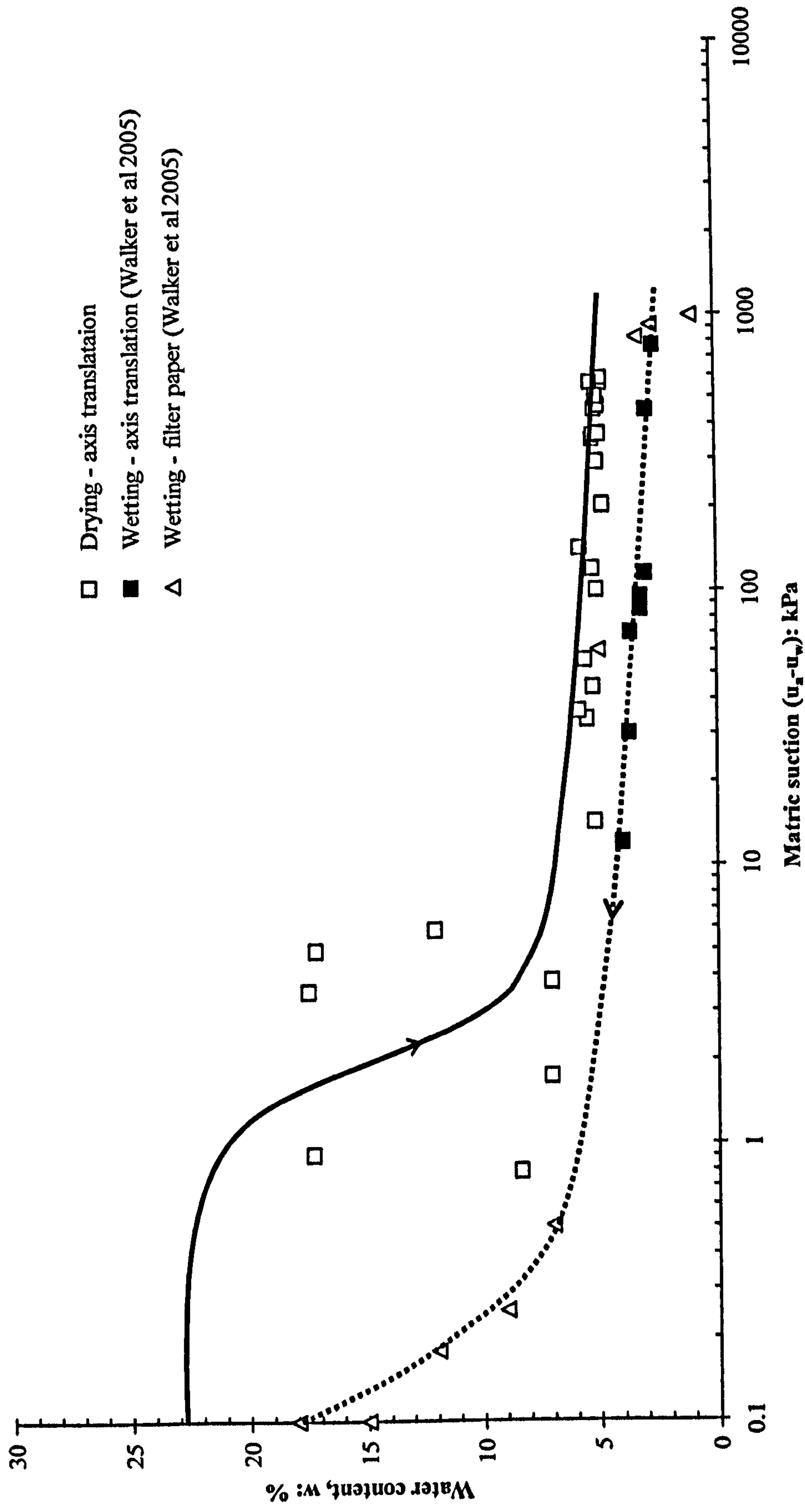


Figure 7.2: The water retention curve in water content against matric suction

which is emphasised by the logarithmic scale), then followed by an almost flat portion once the degree of saturation,  $S_r$  drops below 25% (or about 6% of water content) (Figure 7.1 and Figure 7.2). The saturated water content,  $w_{sat}$  of the studied bonded samples is equal to 22.6% ( $e = 0.6$  and  $G_s = 2.66$ ). The medium range of suction (1 to 10kPa) was very difficult to achieve since a small change in  $S_r$ , led to a significant change in suction.

Table 7.1: Initial values of the matric suction ( $u_a - u_w$ ), water content ( $w$ ), degree of saturation ( $S_r$ ) and void ratio ( $e$ ) of the bonded samples tested in constant water content tests (cw) under various mean net stresses ( $p - u_a$ )

$p - u_a$ , (kPa)	Test	Initial $u_a - u_w$ (kPa)	Initial $w$ (%)	Initial $S_r$ (%)	Initial $e$
50	cwb50/0(0.75)	0	18.0	75.3	0.6074
	cwb50/5(0.66)	5	15.8	66.4	0.6104
	cwb50/1(0.51)	1	12.0	50.6	0.5990
	cwb50/46(0.23)	46	5.3	23.0	0.6109
	cwb50/55(0.24)	55	5.5	23.9	0.6092
	cwb50/124(0.22)	124	5.3	21.5	0.6098
	cwb50/350(0.21)	350	5.2	21.1	0.6091
	cwb50/426(0.20)	426	5.1	20.3	0.5979
	cwb50/507(0.20)	507	4.9	20.0	0.6092
	cwb50/514(0.20)	514	4.9	19.5	0.6088
100	cwb100/1(0.80)	1	18.5	80.4	0.6031
	cwb100/5(0.66)	5	14.8	65.5	0.5929
	cwb100/22(0.22)	22	5.2	22.3	0.6076
	cwb100/34(0.23)	34	5.6	23.2	0.6087
	cwb100/248(0.19)	248	5.2	19.3	0.6094
	cwb100/391(0.21)	391	5.1	21.1	0.6098
	cwb100/560(0.21)	560	5.1	18.5	0.6099
300	cwb300/0(0.53)	0	12.1	53.3	0.6112
	cwb300/0(0.38)	0	8.5	38.4	0.6020
	cwb300/0(0.31)	0	7.0	30.6	0.6082
	cwb300/123(0.23)	123	5.8	22.7	0.6055
	cwb300/290(0.21)	290	5.0	21.0	0.6094

Comparison was also carried out with the data presented by Walker et al. (2005) since they used a similar method and material in preparation of their unsaturated artificial samples. Axis translation and filter paper techniques were used to measure the suction. Figure 7.1 and 7.2 show the drying curves obtained in this study with the wetting curve data obtained from Walker et al (2005). It is clearly seen that the data points gained from Walker et al (2005) fall lower than the data



points obtained from the current study, exhibiting the expected hysteresis between wetting and drying.

### 7.2.3 Volume and Suction Behaviour during Consolidation Stage

#### 7.2.3.1 Volume change

Consolidation was carried out by an increase in mean net stress,  $p-u_a$  under constant water content conditions. The specific volume,  $v$  against time (minutes) for the samples were plotted in order to see the trend during the consolidation stages. Figure 7.3a and Figure 7.3b show the volume changes of the samples consolidated under mean net stress,  $p-u_a$  of 50kPa with zero and low suctions and with low  $S_r$ . All samples showed compression when mean net stress was applied to the samples. For sample cwb50/0(0.75) the volume increases gradually for about two days before it was decided to shear the sample when the pwp became constant. Samples cwb50/5(0.66) and cwb50/1(0.51) also showed an initial drop in volume, the latter experienced a higher compression than sample cwb50/5(0.66) and cwb50/0(0.75). For the samples with low  $S_r$ , a similar picture can be observed in Figure 7.3b. Samples experienced initial compression which then either increased or levelled off prior to shearing. For the tests of cwb50/55(0.24), cwb50/426(0.20), cwb50/507(0.20) and cwb50/514(0.20), volume change became constant after two days. Sample cwb50/507(0.20) showed an initial compression before increasing in volume then levelling off within less than a day. Meanwhile samples cwb50/46(0.23), cwb50/124(0.22) and cwb50/350(0.21) indicated an increase in volume after initial compression. However for cwb50/124(0.22) test, there was a power cut during the consolidation stage (marked by no data recorded as shown in Figure 7.3b). This led to a slight decrease in applied mean net stress (42kPa) causing an increase in volume of the samples. However the suction showed a gradual increase during the consolidation (Figure 7.3c).

Figure 7.4a shows the specific volume,  $v$  against time for samples consolidated under mean net stress,  $p-u_a$  of 100kPa. Samples with low suction, cwb100/1(0.80)

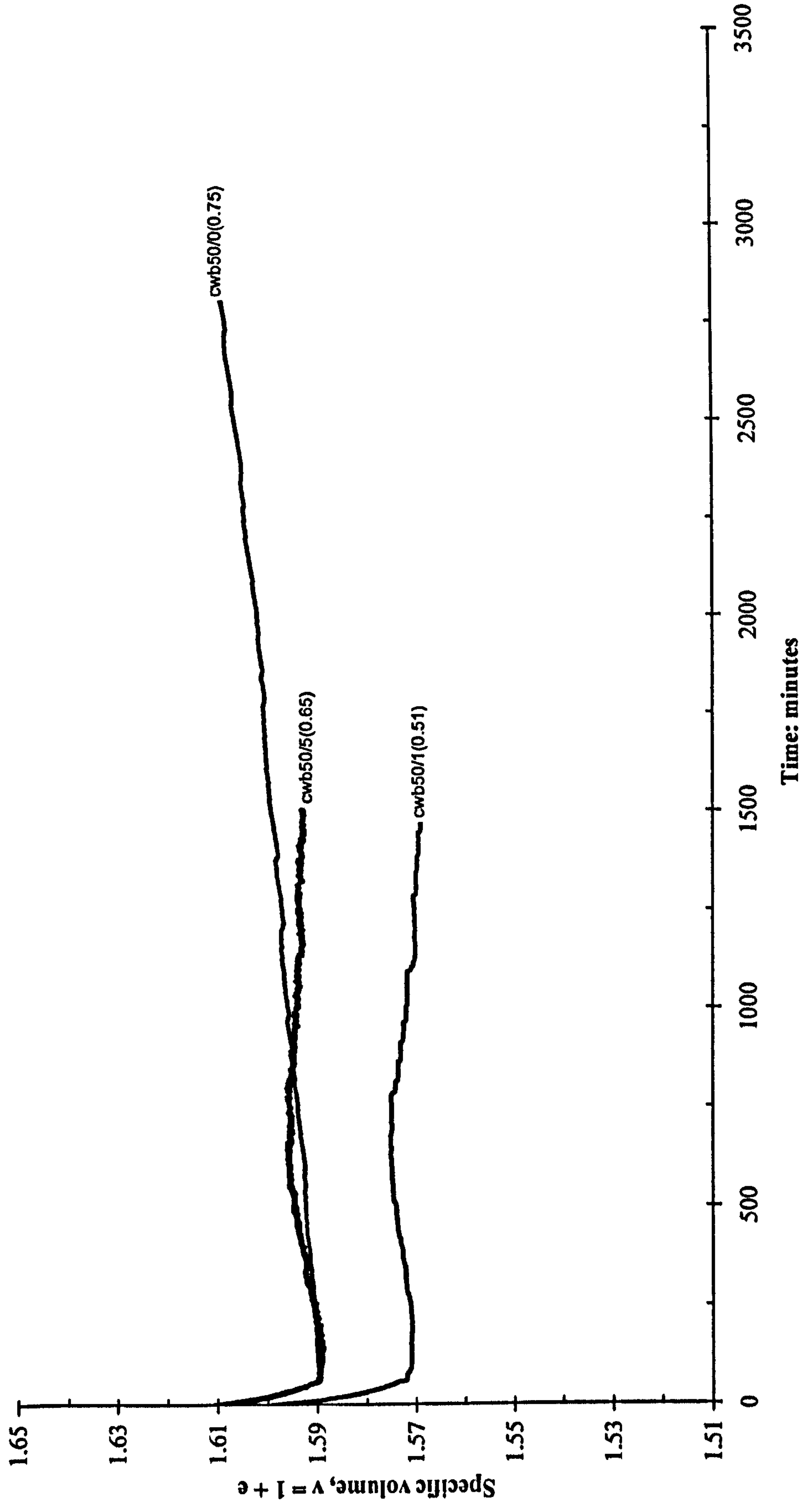


Figure 7.3a: Specific volume against time for cwb samples consolidated at  $p-u_a = 50\text{kPa}$  with zero and low suctions



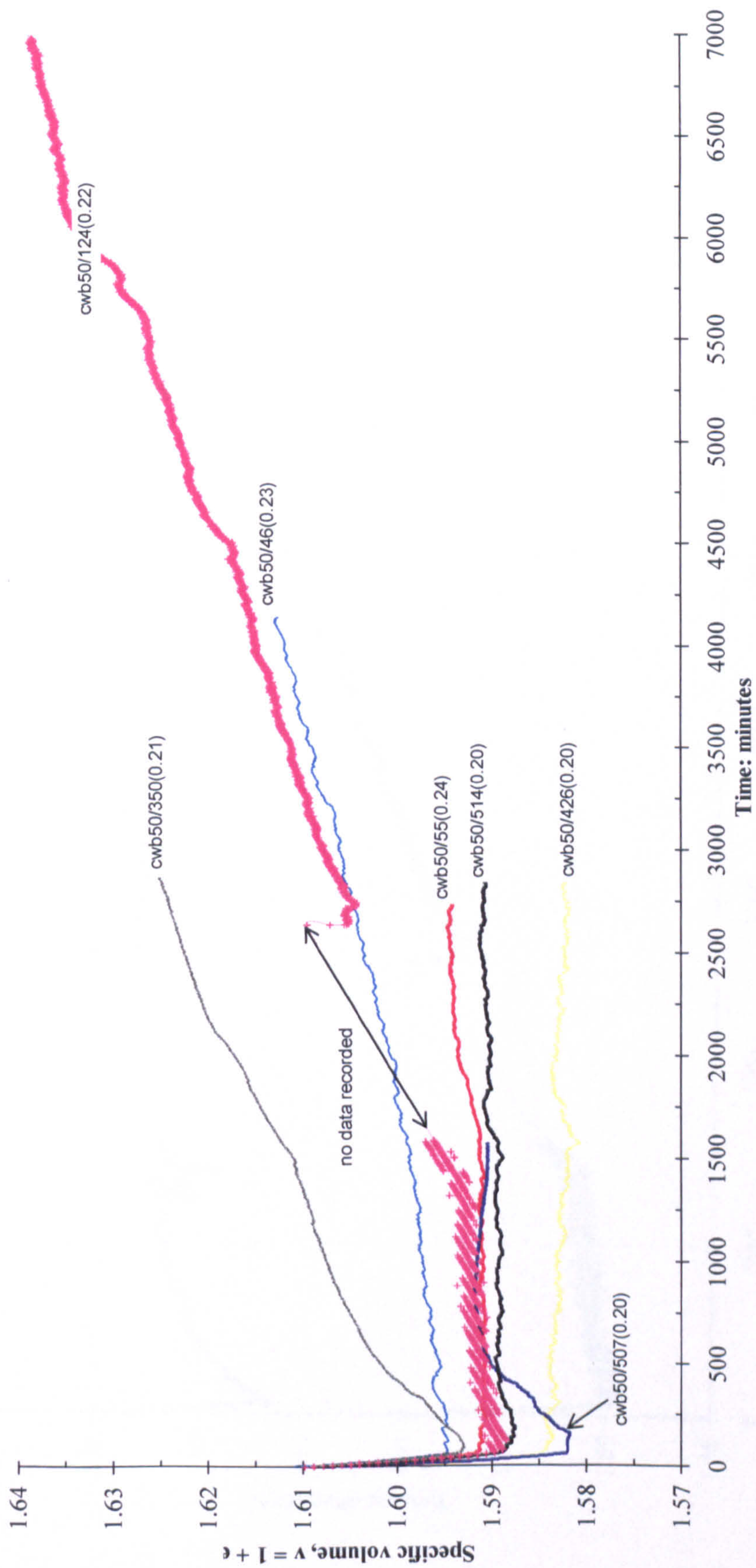


Figure 7.3b: Specific volume against time for cwb samples consolidated at  $p-u_a = 50\text{kPa}$  with low  $S_r$



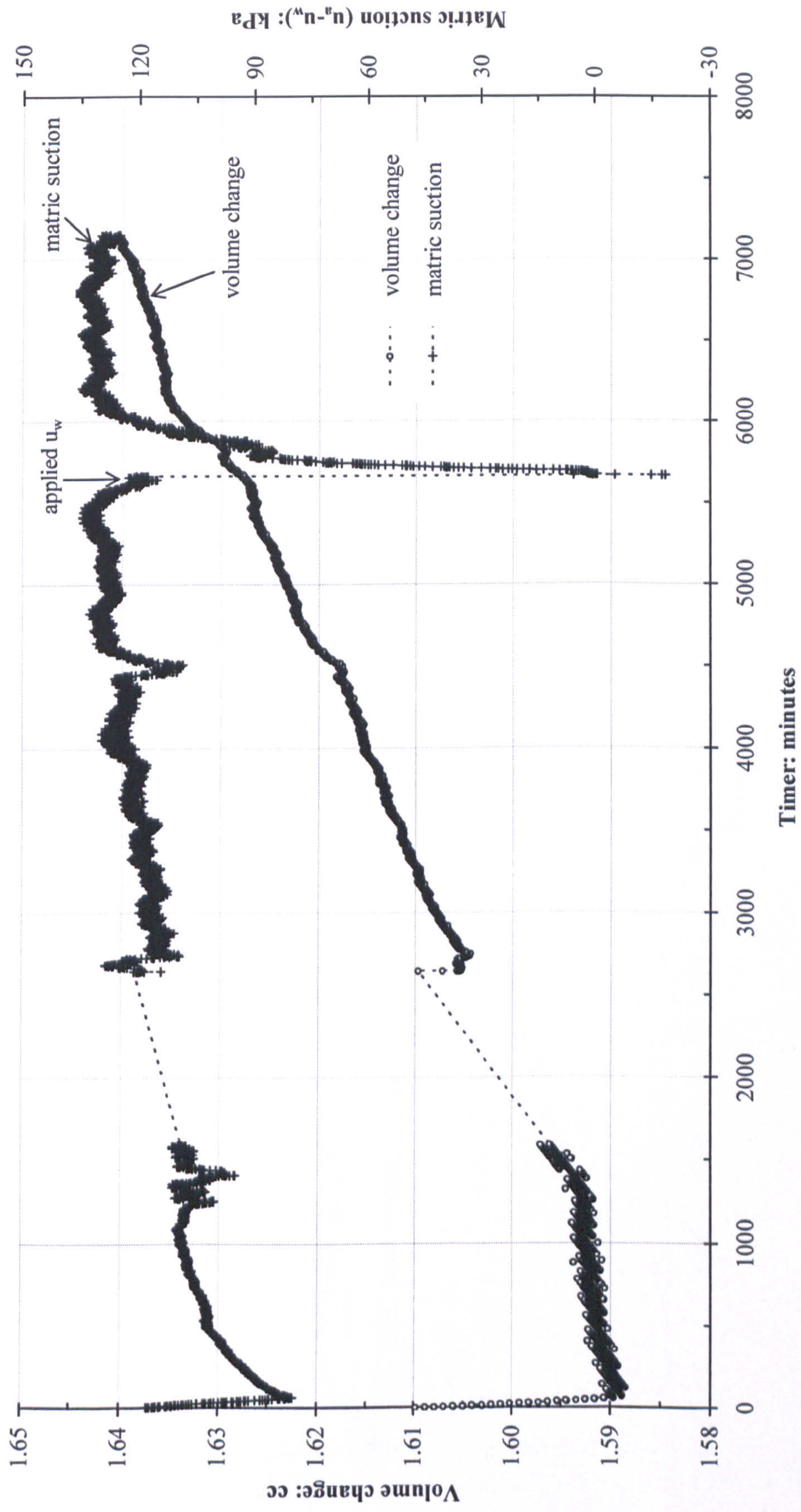


Figure 7.3c: Volume change and suction during consolidation under  $p - u_a = 50 \text{ kPa}$  for cwb50/124(0.22) test



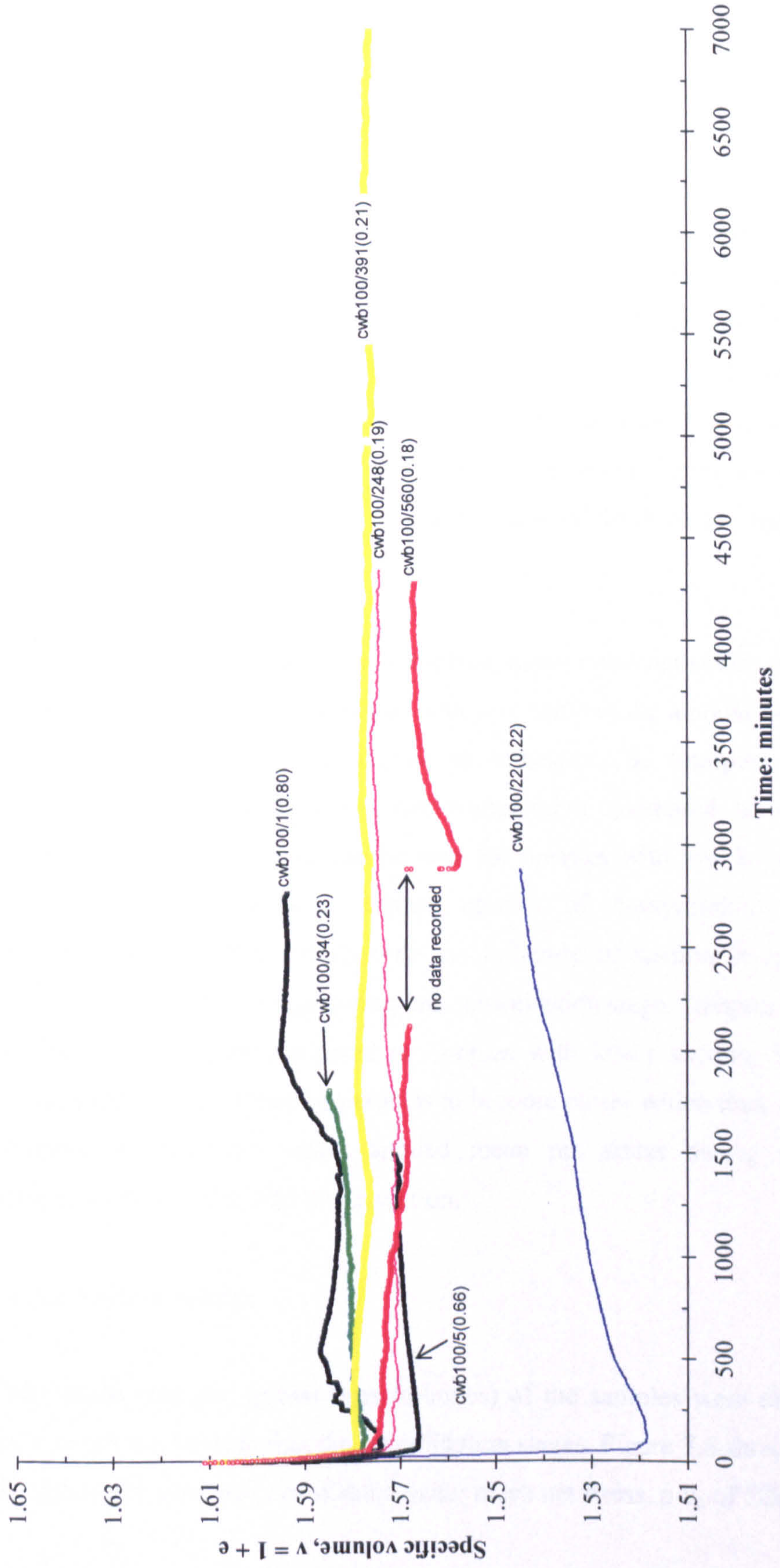


Figure 7.4a: Specific volume against time for cwb samples consolidated at  $p-u_a = 100\text{kPa}$



and cwb100/5(0.66) showed an initial compression followed by an increase in volume. The further increase in volume for cwb100/1(0.80) was due to the problem with the connection between the probe and the data logger. Therefore the probe was disconnected temporarily and reconnected to a new channel causing some wobbly readings (Figure 7.4b). It was seen that the volume change climbed up for about eight hours before levelling off. For samples with low  $S_r$ , all samples experienced an initial compression which was then followed by almost constant volume except for cwb100/22(0.22) and cwb100/34(0.23). Test cwb100/22(0.22) showed the highest compression compared to the rest of the tests in this series. Test cwb100/560(0.18) experienced a power disconnection during the consolidation process (Figure 7.4c) but volume change returned back to the same level with consistent pwp reading (or suction).

The volume change of samples consolidated under mean net stress,  $p-u_a$  of 300kPa is shown in Figure 7.5. For samples with zero suction, the amount of compression is clearly controlled by the degree of saturation,  $S_r$ . Samples with less  $S_r$  (cwb300/0(0.31)) experienced lesser compression compared to samples with higher  $S_r$ . A similar picture can be seen for samples with low  $S_r$ , where sample cwb300/123(0.23) shows a higher amount of compression than sample cwb300/290(0.21). It is clearly seen the influence of suction in controlling the behaviour of volume change during this consolidation stage. Samples with a higher suction compress less compared to samples with lower suction. Samples with higher suction holds group of particles to become closer which then will have less compressive behaviour under applied mean net stress during consolidation comparing to samples with lower suction.

### 7.2.3.2 Suction change

The suction changes against time (minutes) of the samples were also plotted in order to see the trend during the consolidation stages. Figure 7.6 shows the suction changes of the samples consolidated under mean net stress,  $p-u_a$  of 50kPa with zero



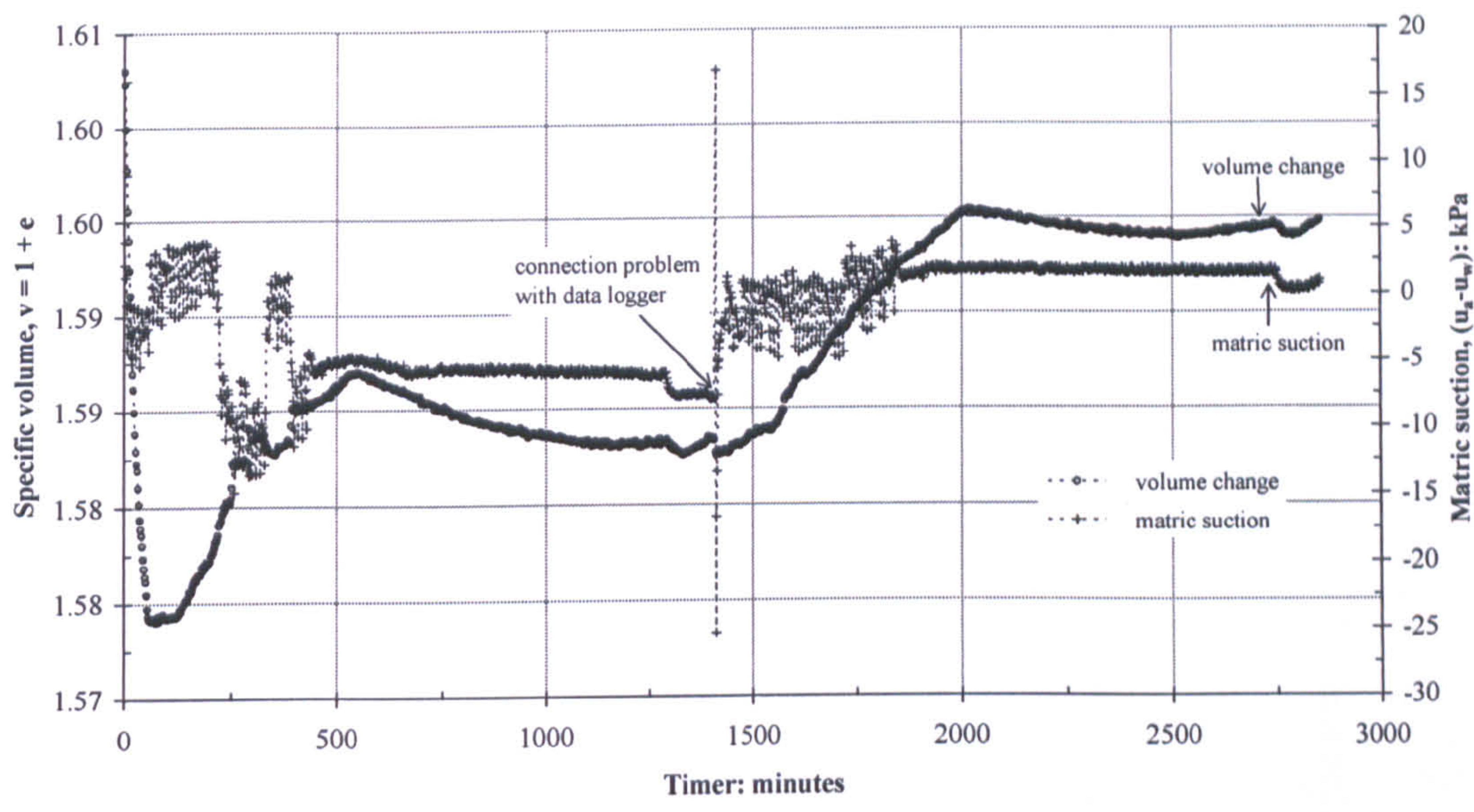


Figure 7.4b: Volume change and suction during consolidation under  $p-u_a= 100\text{kPa}$  for cwb100/ 1(0.80) test

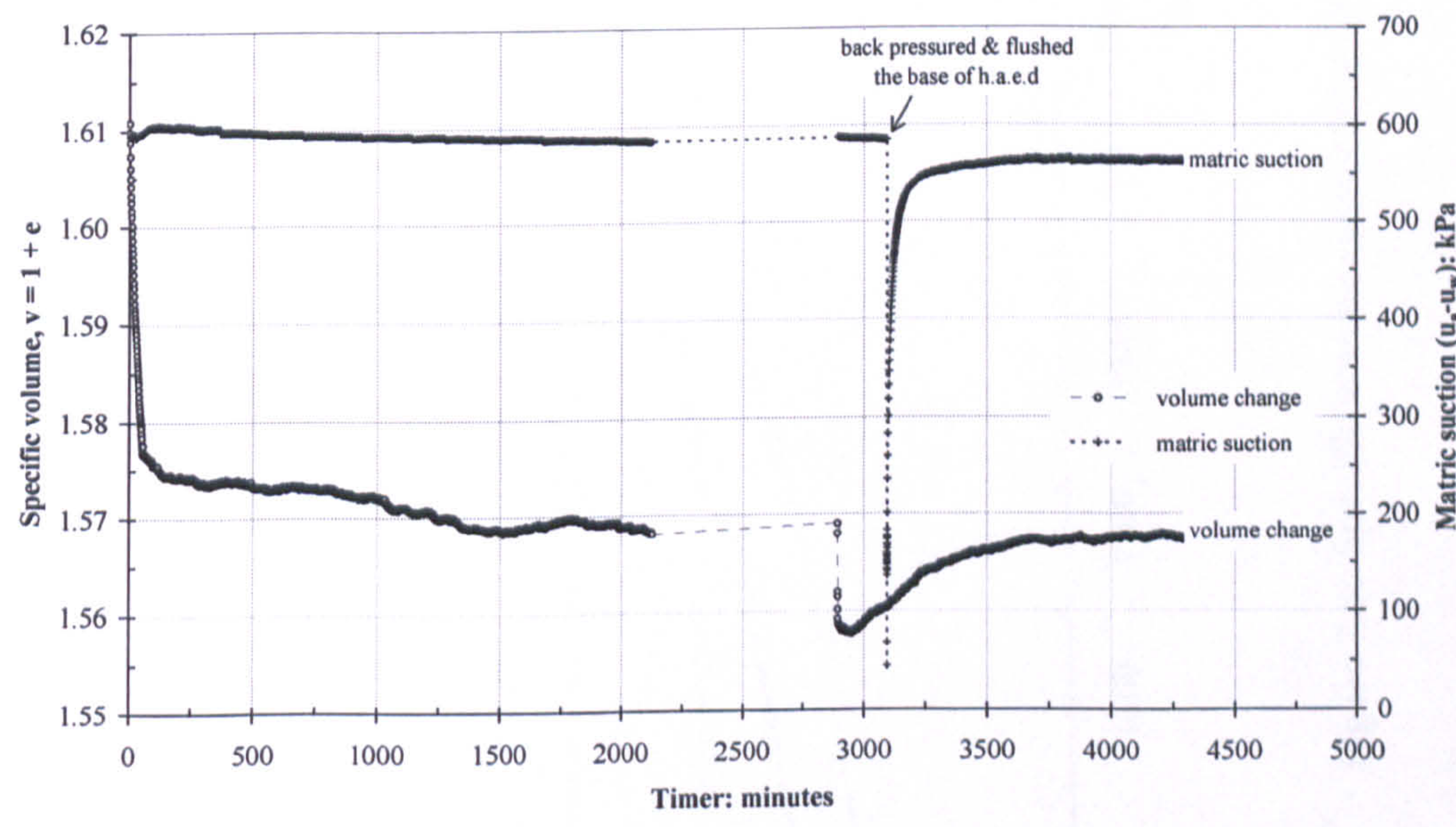


Figure 7.4c: Volume change and suction during consolidation under  $p-u_a= 100\text{kPa}$  for cwb100/560(0.18) test



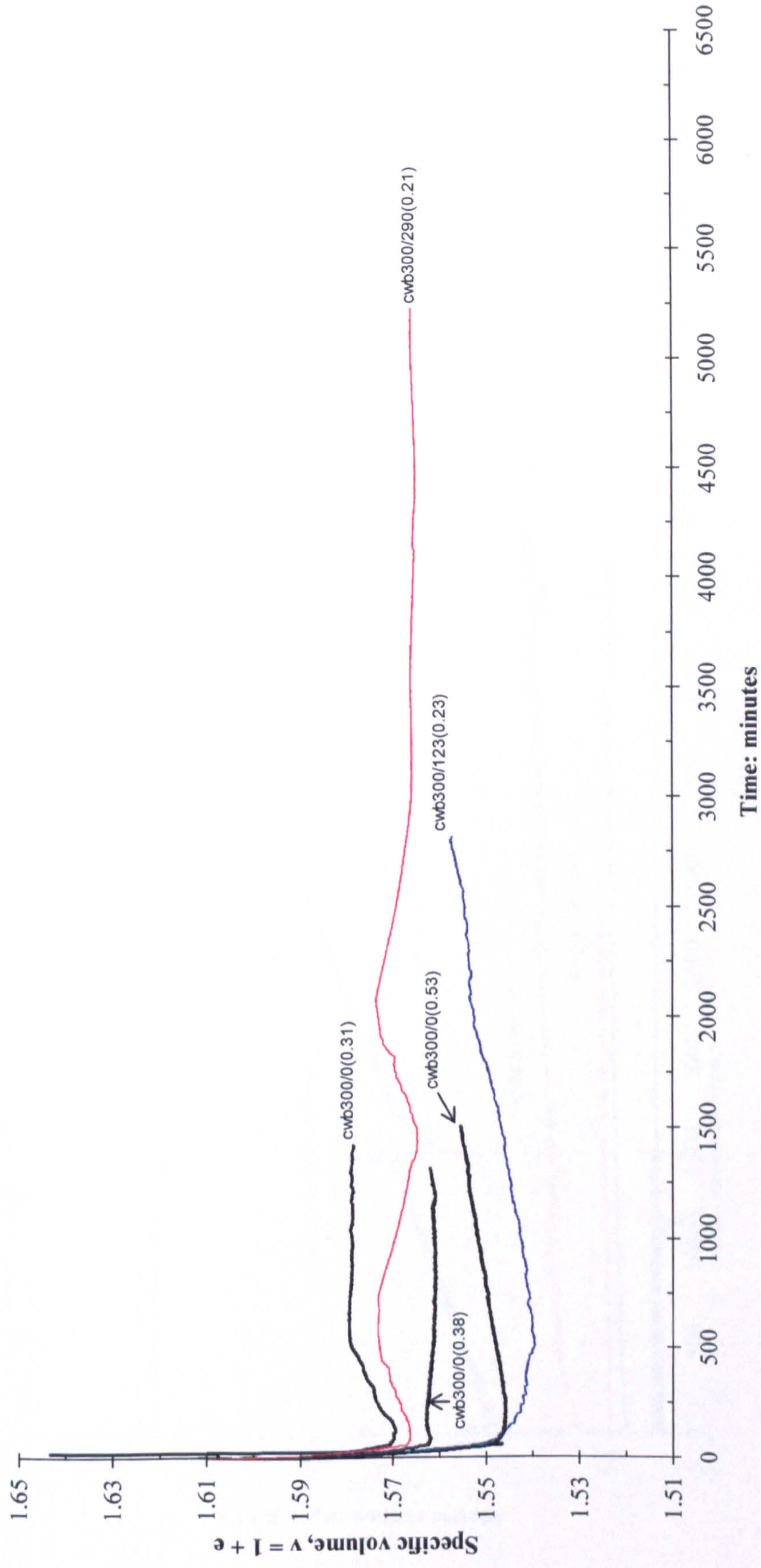


Figure 7.5: Specific volume against time for cw b samples consolidated at  $p-u_a = 300\text{kPa}$



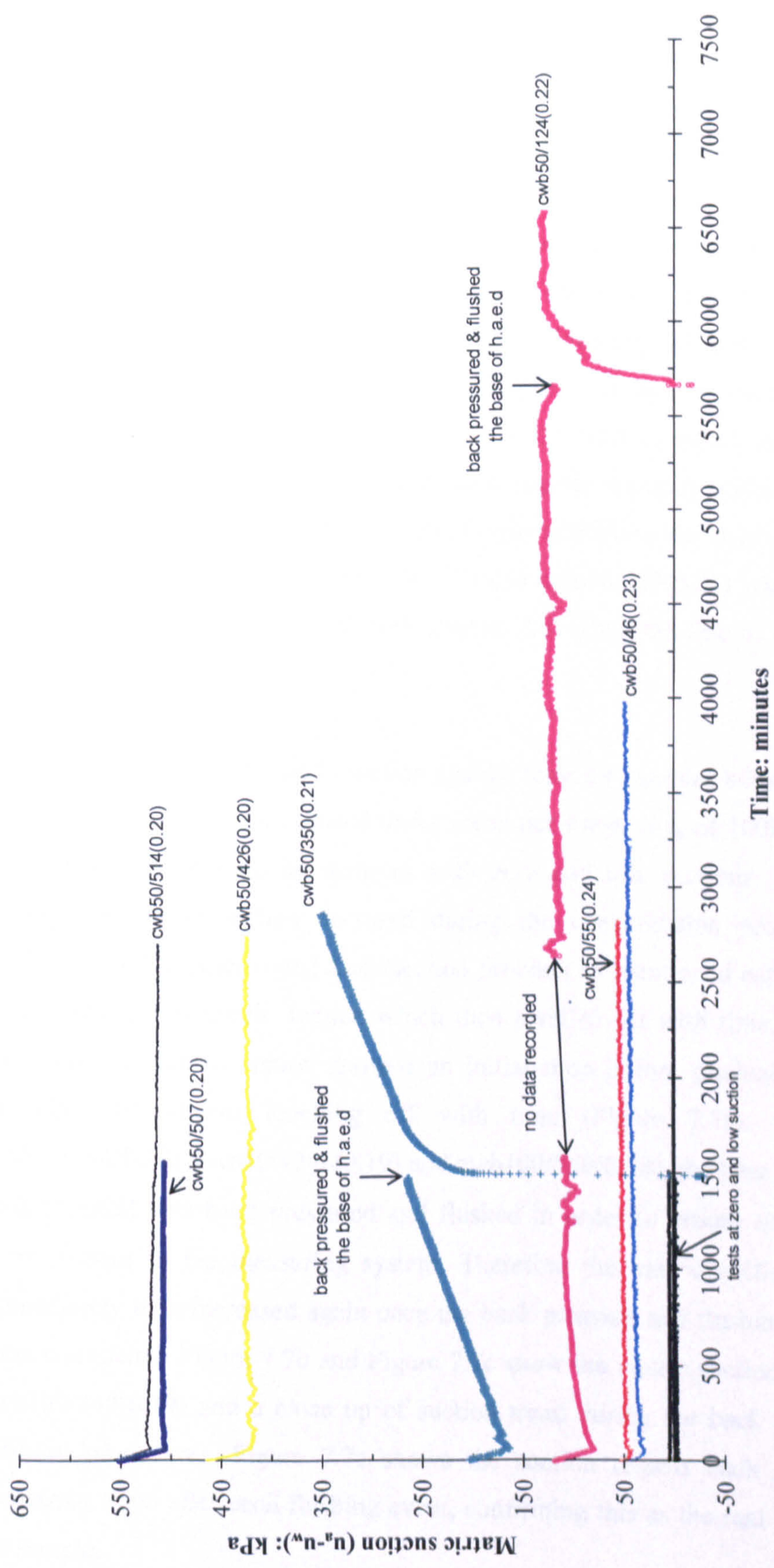


Figure 7.6: Matric suction against time for cwb samples consolidated at  $p-u_a = 50\text{kPa}$



and low suctions and with low  $S_r$ . All samples with zero and low suctions showed very small change in matric suction throughout the consolidation process. A fluctuation in suction readings was studied earlier due to variation in volume change caused by the temperature variation in the temperature controlled room ( $\pm 1^\circ\text{C}$ ). Samples with low  $S_r$  presented an initial drop in matric suction when mean net stress,  $p-u_a$  was applied to the samples. The matric suction in the samples gradually increased again followed by almost levelling off with time except for sample cwb50/350(0.21). Sample cwb50/350(0.21) showed a constant increase in matric suction up to the end of consolidation. In order to ensure that the pressure transducer was measuring the actual pwp (matric suction) within the samples, water pressure (back pressure) was temporarily applied to the base of sample. This can be seen in samples cwb50/124(0.22) and cwb50/350(0.21) where the matric suction dropped and increased back (Figure 7.6) when the line to water pressure was closed again.

Figure 7.7a shows the matric suction against time for samples with zero and low suctions and low  $S_r$  consolidated under mean net stress,  $p-u_a$  of 100kPa. A similar behaviour can be seen for samples with zero and low suctions. A very small change in matric suction occurred during the consolidation process. Sample cwb100/1(0.80) experienced a connection problem as mentioned earlier showed a slight increase in matric suction which then levelled off with time. For samples with low  $S_r$ , matric suction showed an initial drop before gradually increasing slightly then almost levelling off with time (Figure 7.7a). For samples cwb100/34(0.23), cwb100/248(0.19) and cwb100/560(0.18), the base of high entry disk (h.a.e.d) was back pressured and flushed in order to ensure no air bubbles were present in the measuring system. Therefore the matric suction decreased immediately then increased again once the back pressure and flushing procedures were completed. Figure 7.7b and Figure 7.7c show the matric suction for samples cwb100/248(0.19) and a close up of suction trend during the back pressure and flushing procedures. Figure 7.7c shows the suction returns back to the same increasing trend after each flushing event, confirming this as the real behaviour of the sample.



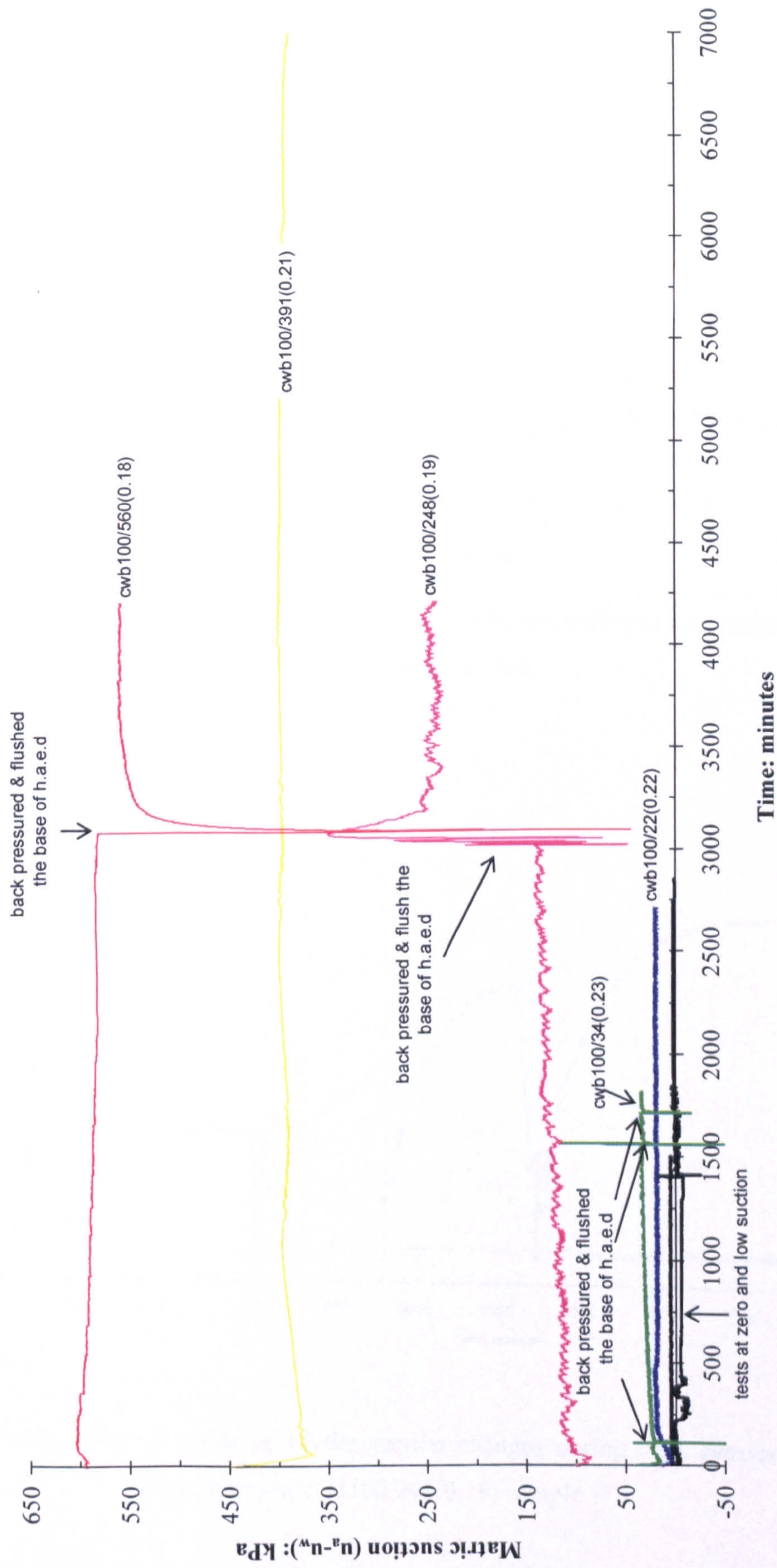


Figure 7.7a: Matric suction against time for cwb samples consolidated at  $p - u_a = 100 \text{ kPa}$



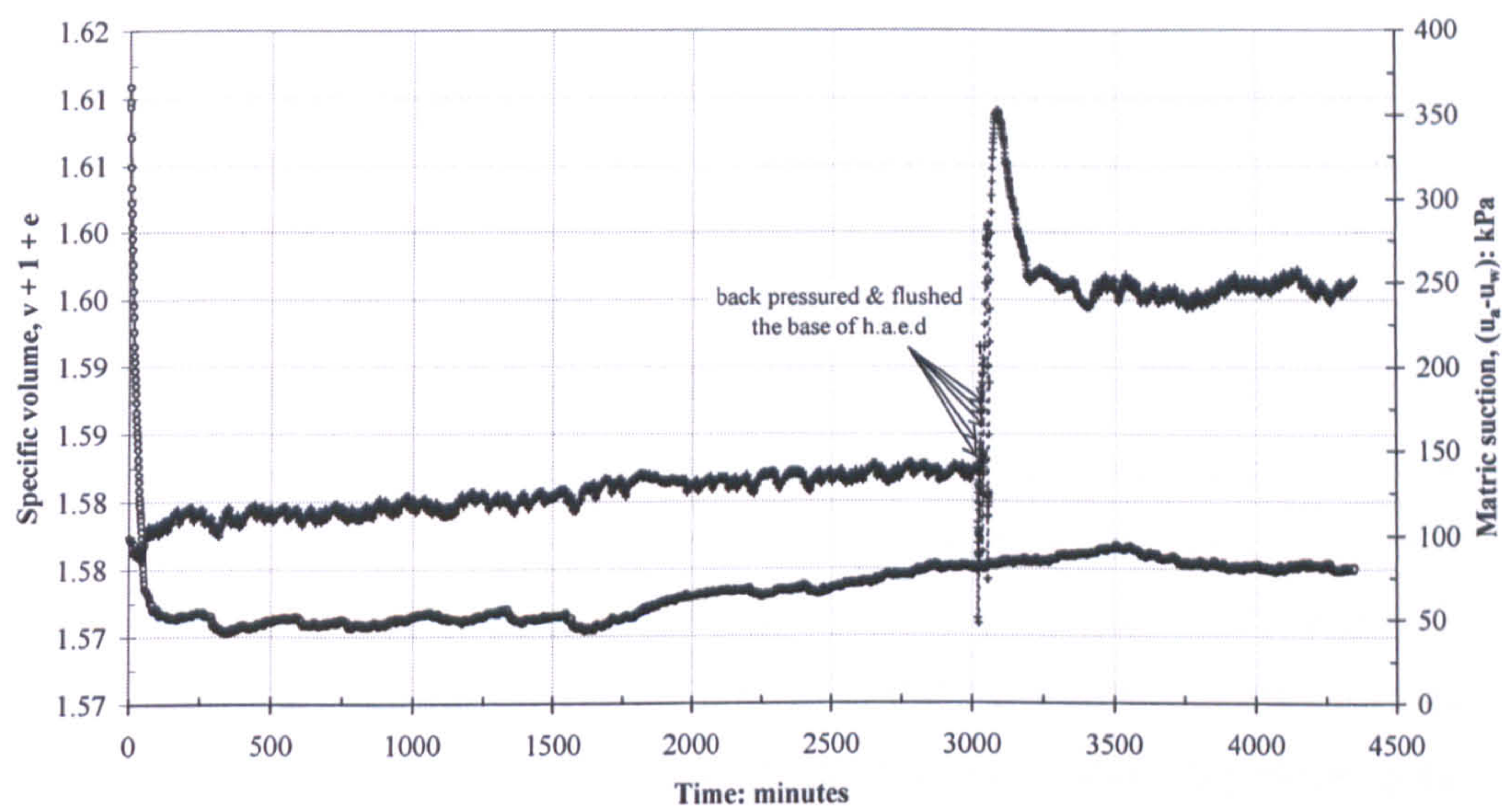


Figure 7.7b: Specific volume and suction changes during consolidation under  $p-u_a = 100\text{kPa}$  for cwb100/248(0.19) test

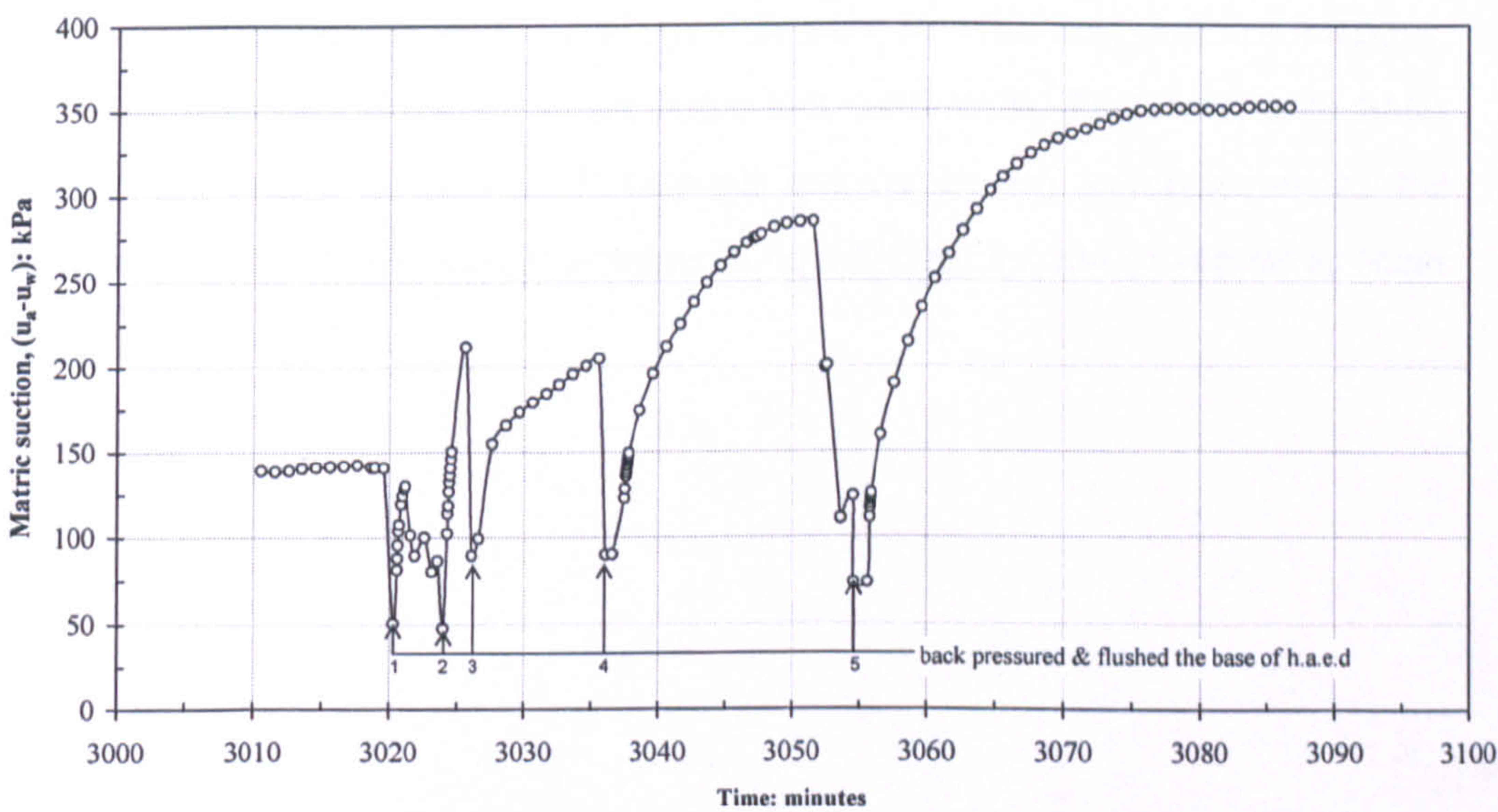


Figure 7.7c: A close up of the suction changes during back pressure and flushing procedures of cwb100/248(0.19) sample



Figure 7.8 shows the matric suction against time for samples with zero and low suctions and low  $S_r$  consolidated under mean net stress,  $p-u_a$  of 300kPa. Samples cwb300/0(0.53), cwb300/0(0.38) and cwb300/0(0.31) showed an unnoticeable change in matric suction. For cwb300/0(0.31), the control system for the air pressure had a problem and was not able to control the cell and air pressures according to the predetermined setup in the computer. However, all valves to the cell and samples were closed in order to keep the samples from higher pressures. The control system returned back to normal after releasing the excess pressure developed in the piston pump. Meanwhile for the samples with lower  $S_r$  (cwb300/123(0.23) and cwb300/290(0.21)), a similar trend can be seen where an initial drop in matric suction occurs due to application of mean net stress,  $p-u_a$ . Then the matric suction gradually increased before levelling off with time.

In conclusion, for samples with zero and low suction values, the change in suctions after imposing mean net stress was not significant and matric suction achieved its equilibrium quite fast if compared to samples with low degree of saturation,  $S_r$ . A longer suction equalisation for samples with suction would be due to the scatter of water menisci across the samples. Meanwhile samples with zero and low suctions, the occurrences of water menisci are larger and continuous. Therefore, pore water pressure (or matric suction) will respond quicker to any compression of the samples and suction equilibrium happens in liquid phase instead of vapour as occur in sample with low  $S_r$ .



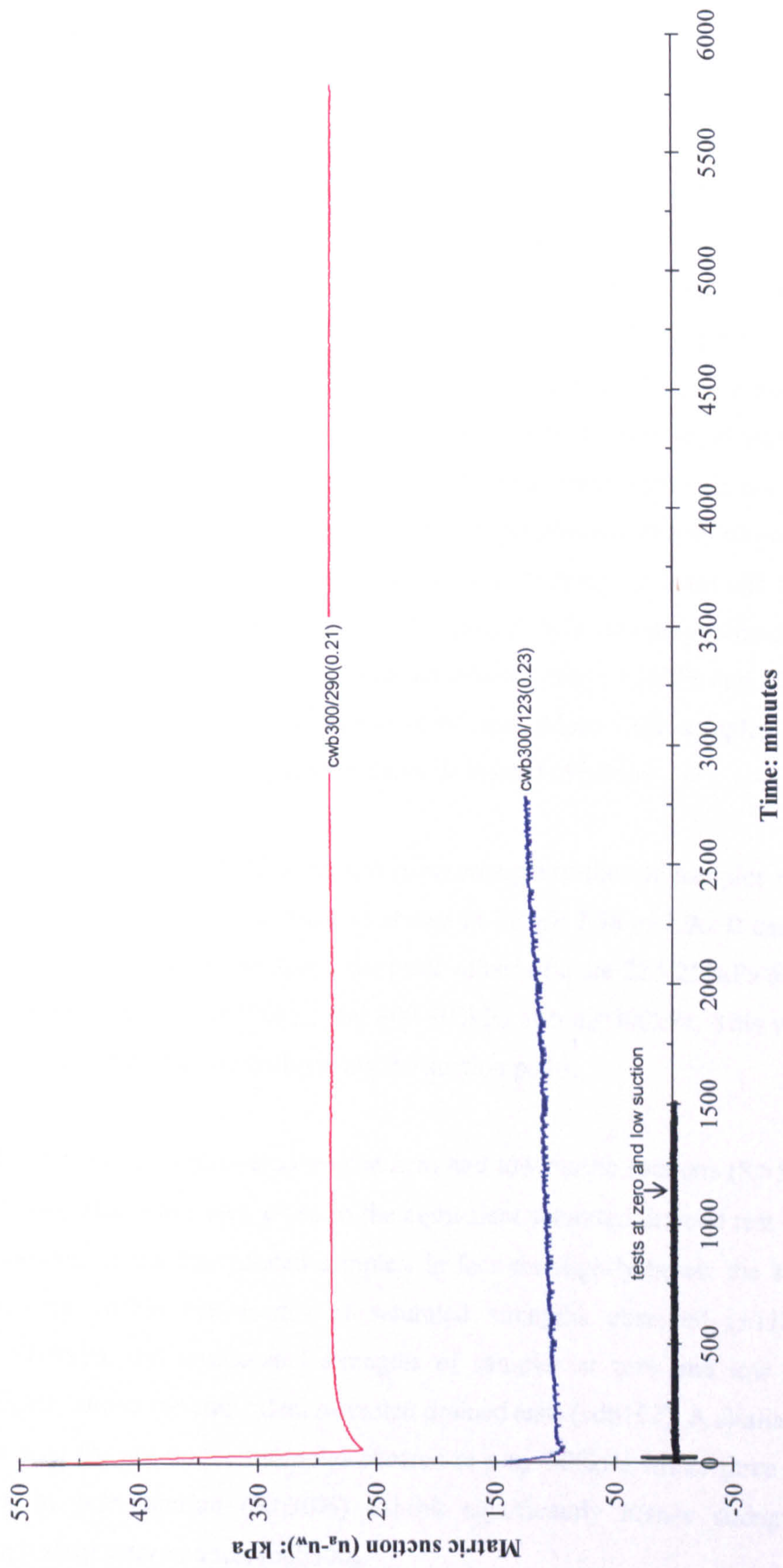


Figure 7.8: Matric suction against time for cwb samples consolidated at  $p-u_a = 300\text{kPa}$



## 7.2.4 Stress Strain Behaviour

The stress-strain curves for the three sets of the constant water content tests (cw) are presented in Figure 7.9a, Figure 7.9b and Figure 7.9c. These three sets of tests represent samples that were initially consolidated under mean net stress,  $p-u_a$  of 50kPa, 100kPa and 300kPa. An equivalent saturated bonded drained (cdb) test is also shown in each of the cw plots. Tests at  $p-u_a=50$ kPa (Figure 7.9a) and tests at  $p-u_a=100$ kPa (Figure 7.9b) show a distinctive peak in the stress-strain curves irrespective of the suction values usually around 2.5% of axial strain. Meanwhile for samples sheared at  $p-u_a=300$ kPa, the stress-strain curves do not exhibit such a distinct peak. It is also seen that for samples sheared at low mean net stress ( $p-u_a=50$ kPa), the stress-strain curves have a tendency to level off by 15% strain whereas the samples sheared at higher  $p-u_a$  show a tendency to continue dropping to the end of the test. At low mean net stresses of  $p-u_a=50$ kPa and 100kPa, the soil behaves more like an overconsolidated soil. Meanwhile samples sheared at  $p-u_a=300$ kPa show more ductile behaviour instead of brittle.

It was found that the stiffness and shear strength of the soil samples increased with an increase in mean net stress as shown in Figure 7.9a to 7.9c. It can be observed from the tests at low suctions, the peak values of  $q$  are 225-250kPa at  $p-u_a=50$ kPa, 390-440kPa at  $p-u_a=100$ kPa and 800-900kPa at  $p-u_a=300$ kPa. This will be shown more clearly later when observing the suction paths.

The curves for unsaturated tests at zero and low matric suctions ( $S_r > 50\%$ ) sheared at  $p-u_a=50$ kPa are very close to the equivalent saturated drained test (cdb50). The strengths of the unsaturated samples, in fact are slightly below the saturated test, but are within the scatter of saturated strengths observed ( $\pm 11$ kPa). At  $p-u_a=100$ kPa, the unsaturated strengths of samples at zero and low suctions are slightly above the equivalent saturated drained tests (cdb100). A similar picture can be seen for unsaturated samples sheared at  $p-u_a=300$ kPa where three tests carried out at zero suction ( $S_r > 30\%$ ) exhibit significantly higher strength than the equivalent saturated test (cdb300).



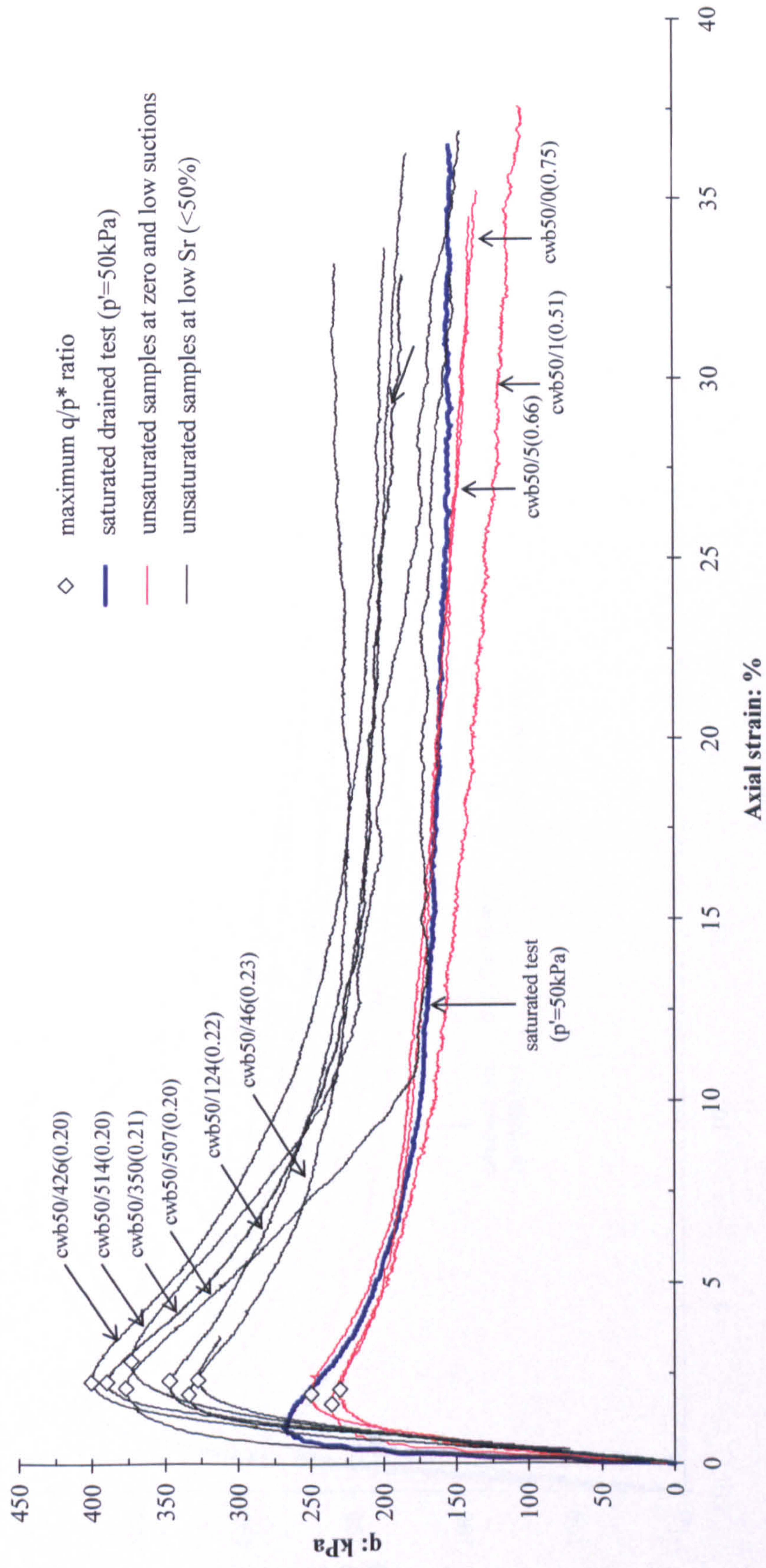


Figure 7.9a: Stress-strain curves for  $p-u_a$  of 50kPa for bonded samples



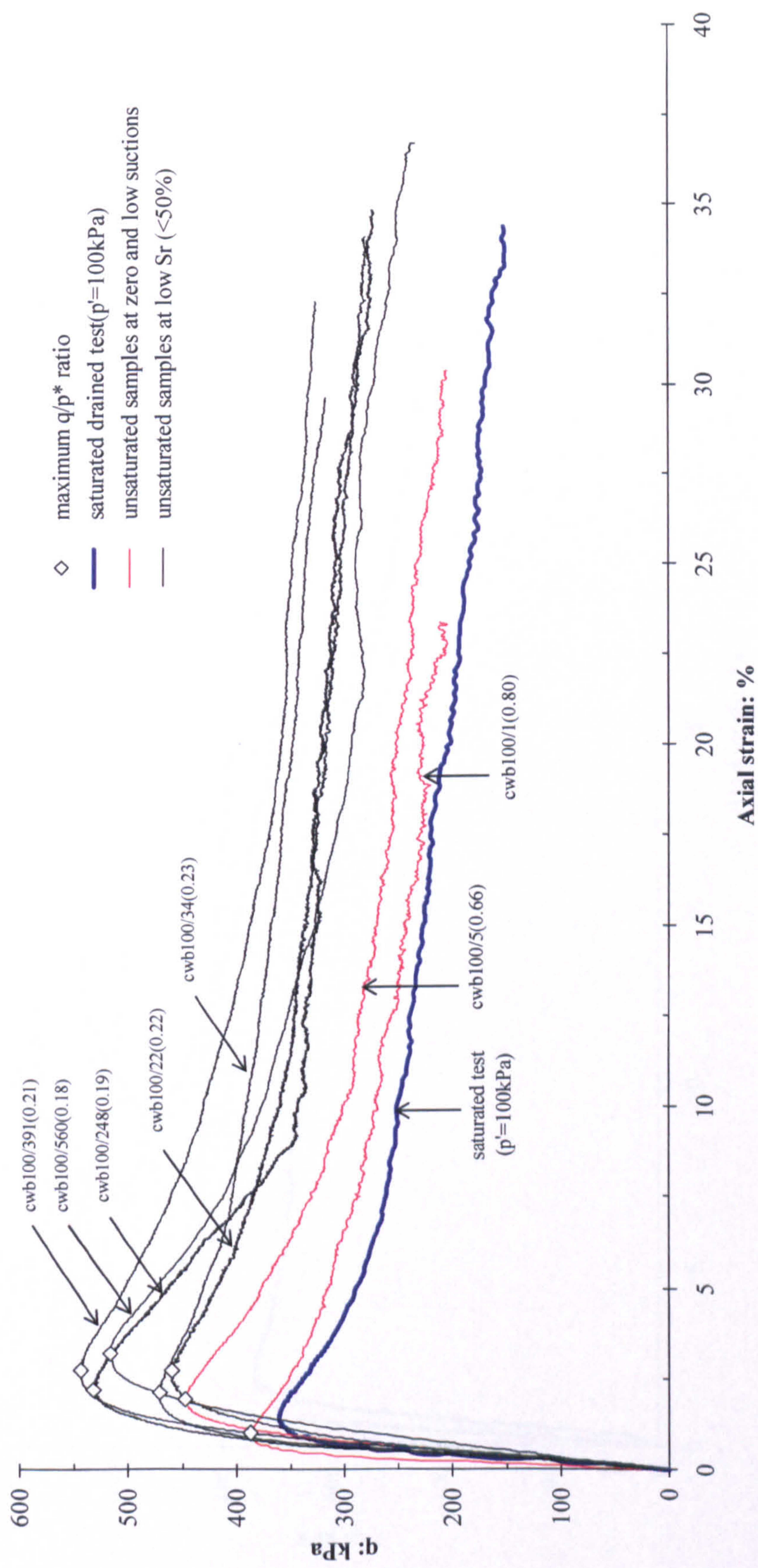


Figure 7.9b: Stress-strain curves for  $p-u_a$  of 100kPa for bonded samples



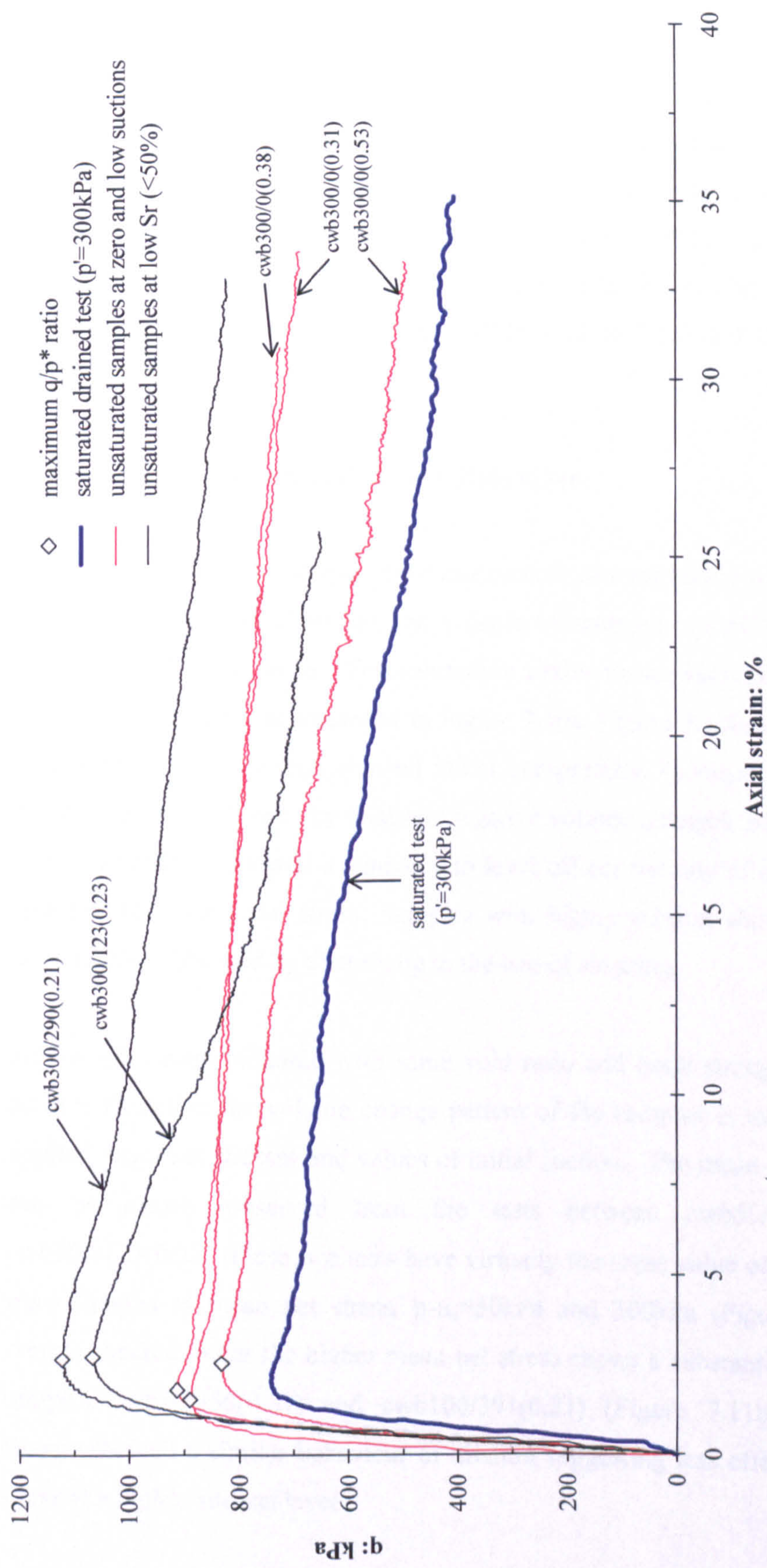


Figure 7.9c: Stress-strain curves for  $p-u_a$  of 300kPa for bonded samples



It is found that the strength of unsaturated samples continue to increase as suction increases. For example, at  $p-u_a=50\text{kPa}$  (Figure 7.9a) the peak value of  $q$  at low suction is 225-250kPa rising to 325-350kPa for suctions of 46-124kPa and to 375-400kPa for suctions greater than 350kPa. However, it can be seen that the increase in strength is generally small at suctions between 350kPa and 514kPa (Figure 7.9a). Samples sheared at  $p-u_a=100\text{kPa}$  and 300kPa also exhibit a little difference in strength at suctions of 248kPa to 560kPa (Figure 7.9b) and 123kPa to 290kPa (Figure 7.9c).

### 7.2.5 Volume Change and Suction Behaviour

In constant water content tests, the water content of samples (or water phase) is not permitted to change. However, the volume of samples can still change through expelling and taking in air. The volumetric strains versus axial strain for the three sets of the cw tests are presented in Figure 7.10a, Figure 7.10b and Figure 7.10c. Generally, all the cw tests showed initial compression (positive volume change) which was then followed by dilation (negative volume change). Samples with zero and low suctions, showed a tendency to level off (or the rate of dilation becomes smaller) at larger axial strain. Samples with higher suction showed little or no compression followed by dilation up to the end of shearing.

All samples were prepared with same void ratio and bond strength as described earlier. Therefore the volume change pattern of the samples is influenced by the applied mean net stresses and values of initial suction. The mean net stress affect can be clearly observed from the tests between cwb50/124(0.22) and cwb300/123(0.23) (these two tests have virtually the same value of suction) which were sheared at mean net stress,  $p-u_a=50\text{kPa}$  and 300kPa (Figure 7.11a). The sample sheared under the higher mean net stress shows a substantial dilation. For samples cwb50/350(0.21) and cwb100/391(0.21) (Figure 7.11b), the volume change showed a similar behaviour of dilation suggesting less effect of mean net stress at a higher suction level.

The effect of suction can be seen in each of the series of cwb tests. In Figure 7.10a, samples with high matric suctions (350kPa, 426kPa, 507kPa and 514kPa) show a larger rate of dilation than the tests with zero and low suctions. A similar trend can also be seen clearly in cwb tests sheared under  $p-u_a=100\text{kPa}$  and  $300\text{kPa}$ . In Figure 7.10b, samples cwb100/248, cwb100/391 and cwb100/560 exhibit greater degree of dilatancy in comparison with the samples having zero and low suctions. A greater degree of dilation can be observed in cwb300 tests for samples with high matric suctions (123kPa and 290kPa) as shown in Figure 7.10c. The same behaviour was also acknowledged by Toll (1988). He noted that this was the opposite to what would be expected if the suction was to be considered as an equivalent to effective stress in saturated condition. In saturated condition, samples consolidated at higher effective stress,  $p'$  tend to have less dilatancy. Toll (1998) noted that this apparently opposite effect could be explained by considering the fabric of an unsaturated soil i.e. suction can act to hold groups of particles together, making the soil behave as if has a larger particle, and hence is more dilatant.



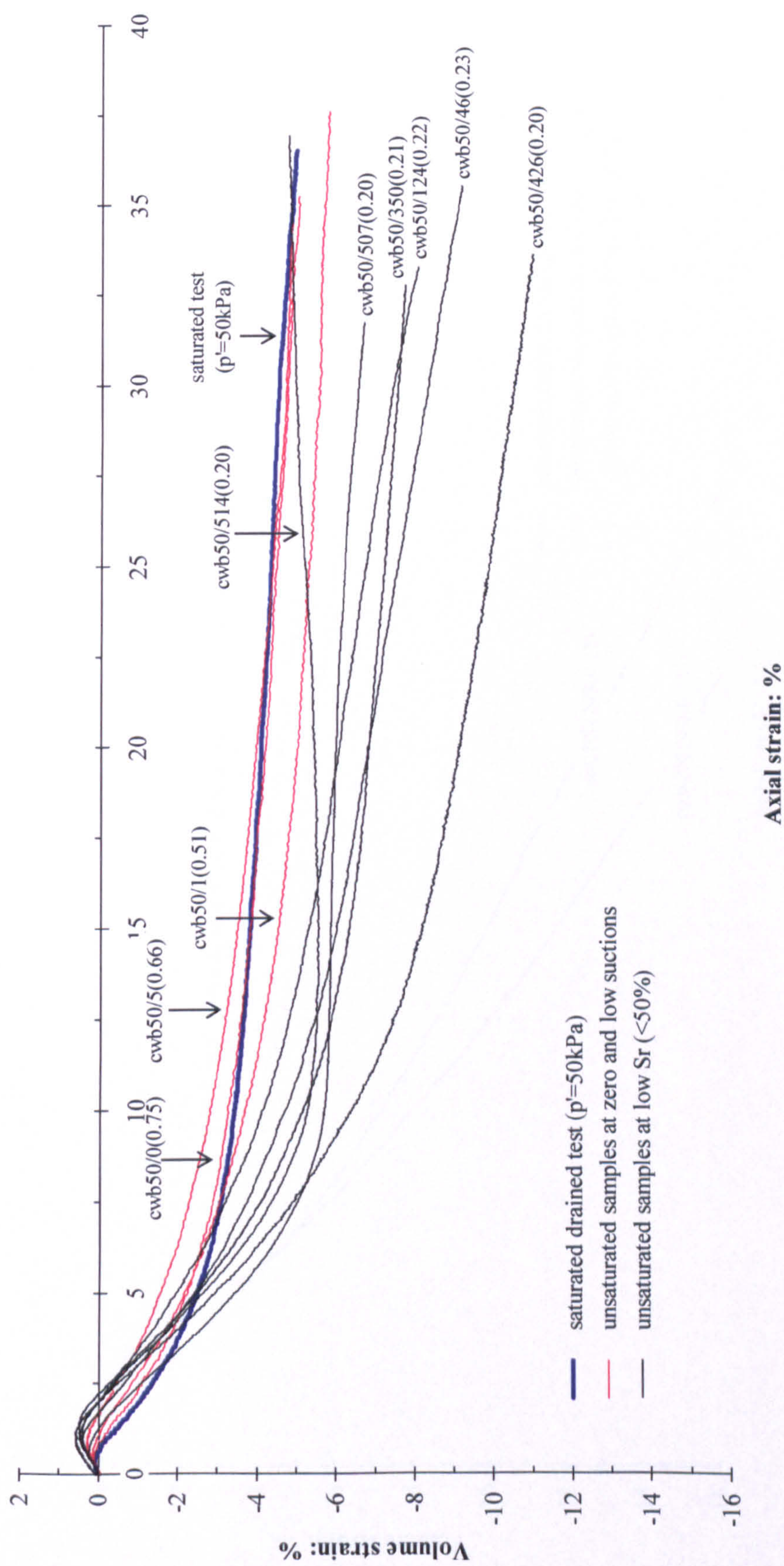


Figure 7.10a: Volume strain against axial strain for  $p-u_a$  of 50kPa



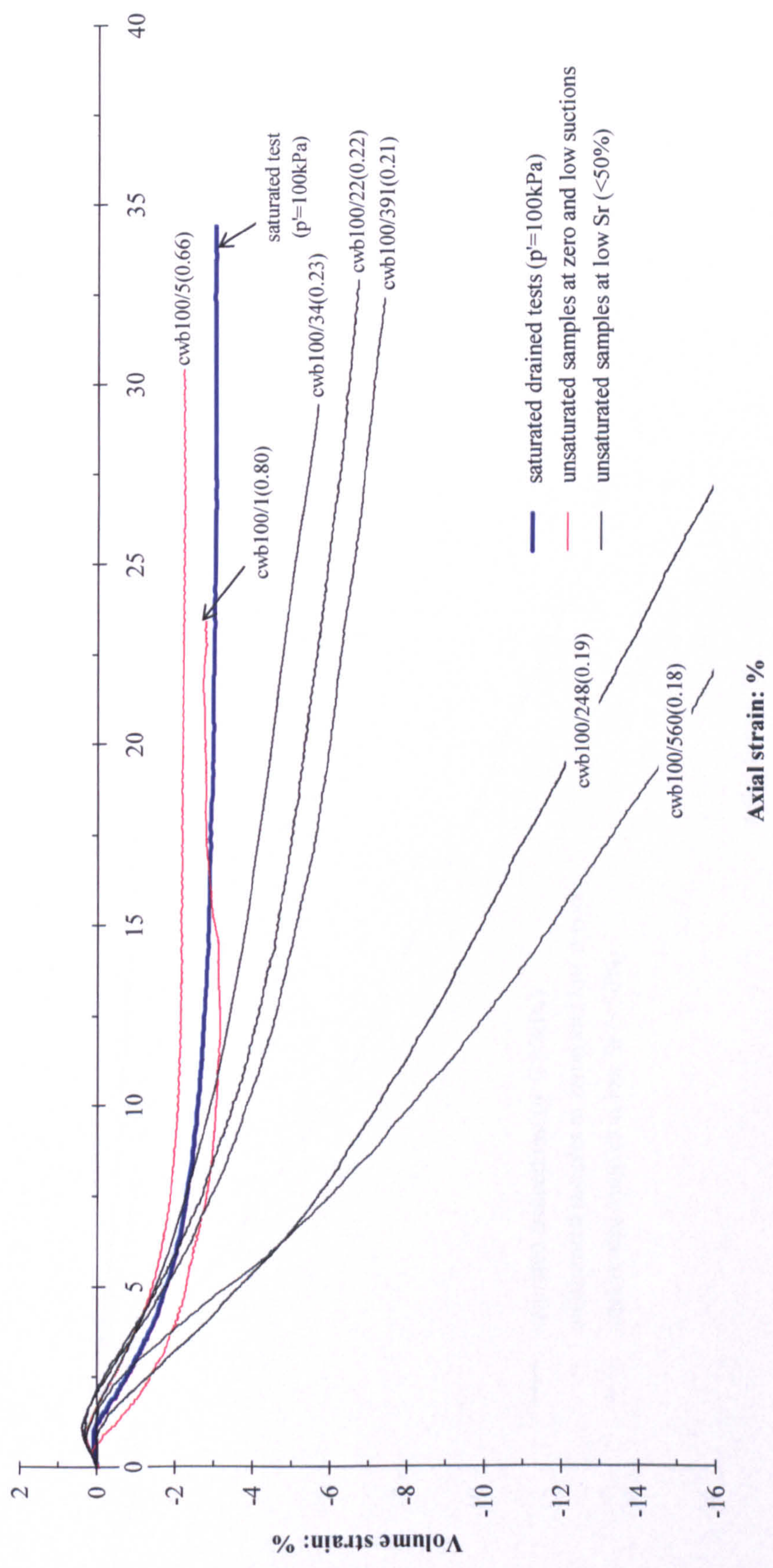


Figure 7.10b: Volume strain against axial strain for  $p-u_a$  of 100kPa



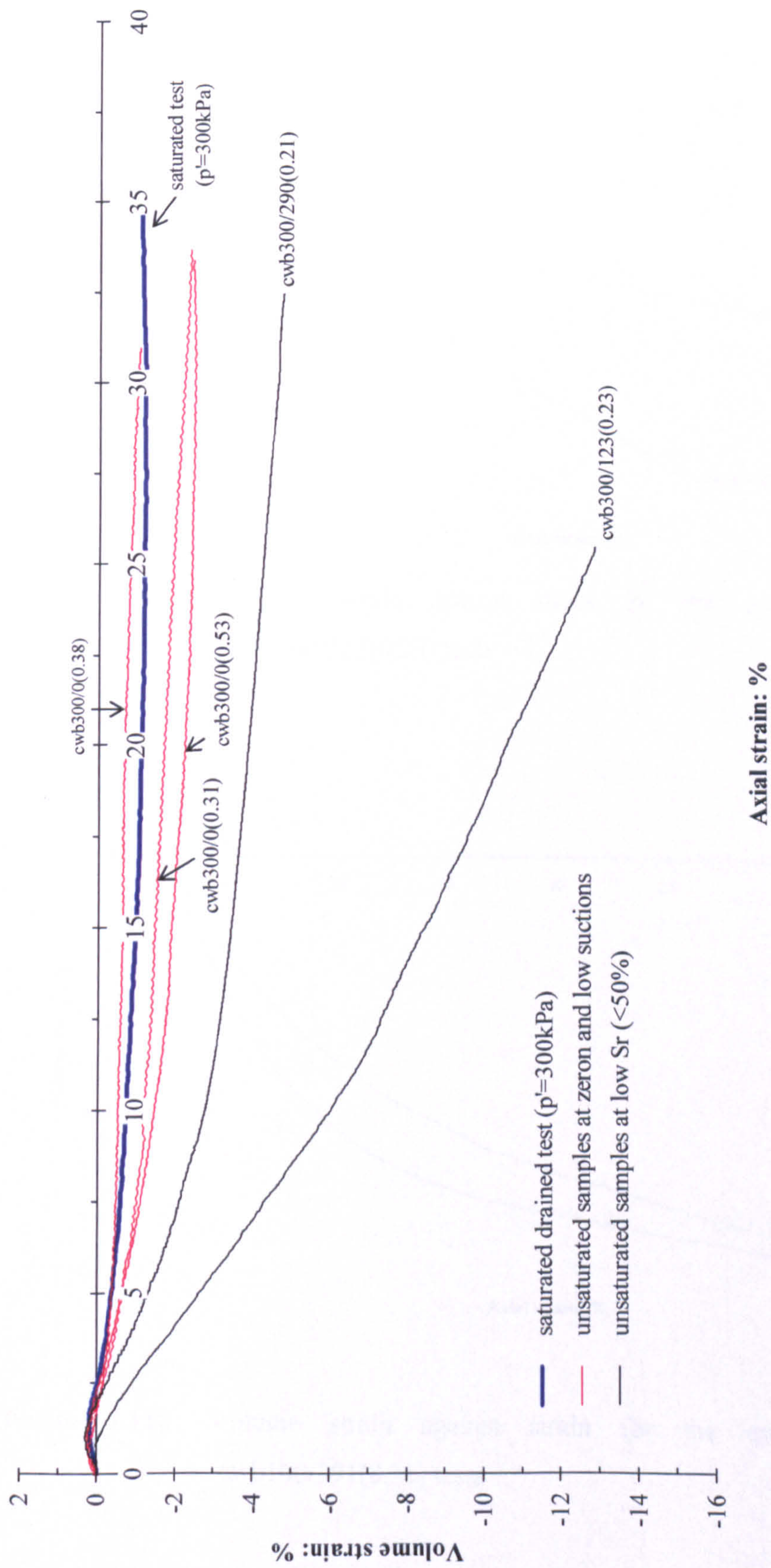


Figure 7.10c: Volume strain against axial strain for  $p-u_a$  of 300kPa



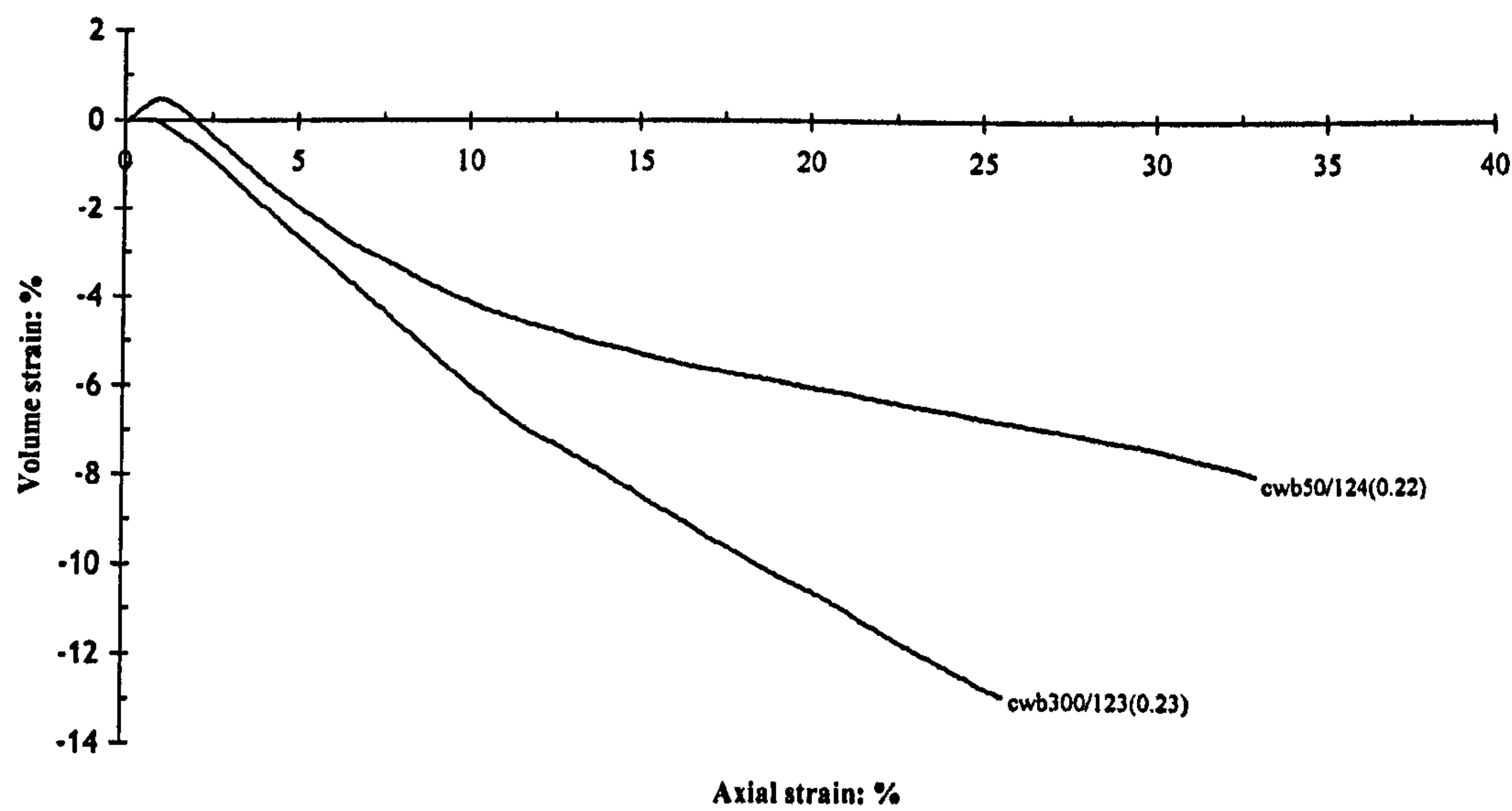


Figure 7.11a: Volume strain against strain for the cwb50/124(0.22) and cwb300/123(0.23) tests

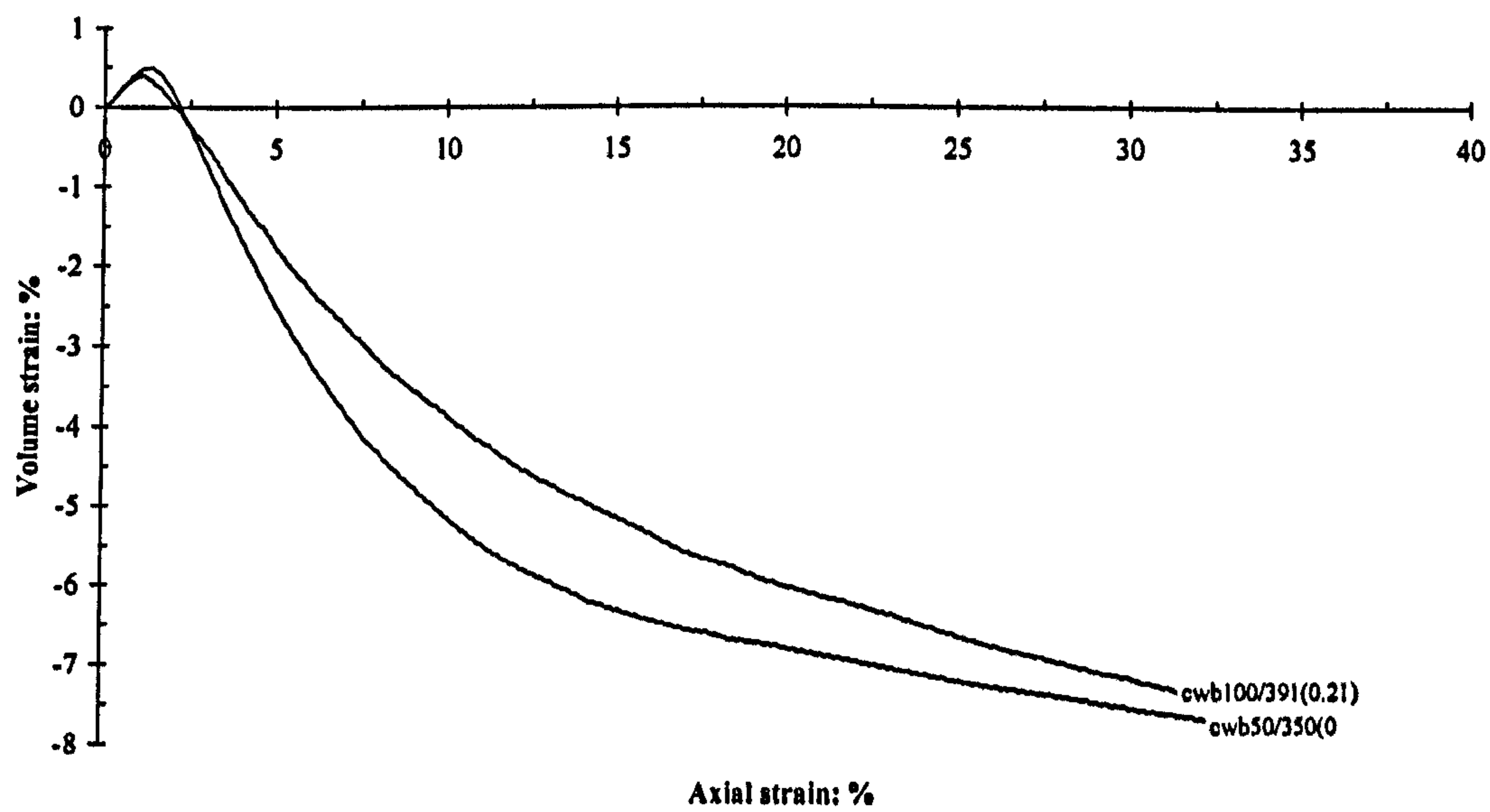


Figure 7.11b: Volume strain against strain for the cwb50/350(0.21) and cwb100/391(0.21) tests



The excess pwp,  $\Delta u$  against axial strain,  $\epsilon_a$  for the cwb tests are plotted in Figure 7.12a, 7.12b and 7.12c. From these figures, the pwp for samples with zero initial matric suction show almost no change up to the end of shearing. Figure 7.12a presents the curves for the cwb samples sheared under  $p-u_a=50\text{kPa}$ . The excess pwp,  $\Delta u$  for cwb50/124(0.22) and cwb50/350(0.21), indicate an initial increase in pore water pressure before decreasing again up to the end of tests. Samples cwb50/46(0.23) did not exhibit a clear initial increase in excess pwp but present a high rate in  $\Delta u$  up to axial strain,  $\epsilon_a=1.5\%$ . Meanwhile for samples with higher suction such as cwb50/426(0.20), cwb50/507(0.20) and cwb50/514(0.20) show an increase in excess pwp which then almost levels off up to the end of shearing. The increase and decrease in pwp coincide with the compression and dilation of the samples. The positive excess pwp of samples is greater for larger suction until the initial suction reaches 426kPa (test cwb50/426(0.20); Figure 7.12a). However for samples with higher initial suction ( $s>426\text{kPa}$ ), the peak of excess pwp is lower than the cwb50/426(0.20) which then almost level off as seen for samples cwb50/507(0.20) and cwb50/514(0.20) tests. A similar trend can be seen for cwb samples sheared under higher  $p-u_a$  (100kPa) (Figure 7.12b). The pwp for samples with zero initial matric suction show almost no change up to the end of shearing. Samples cwb100/22(0.22) and cwb100/34(0.23) exhibited unnoticeable peak of excess pwp but showed a high rate in  $\Delta u$  up to axial strain,  $\epsilon_a=1.7\%$  and  $1.2\%$ , respectively. For sample with higher initial suction (up to 391kPa), samples initially show positive excess pwp followed by a decrease in excess pwp up to the end of tests (Figure 7.12b). The rates of decreasing in excess pwp, however, are getting smaller to the end of shearing. It is clear that the peak of excess pwp is suction dependant. Meanwhile cwb100/560(0.18) shows positive excess pwp up to axial strain,  $\epsilon_a=5\%$ , which then levels off to the end of shearing. For samples sheared under  $p-u_a=300\text{kPa}$ , only cwb300/123(0.28) shows a significant peak of excess pwp (Figure 7.12c). Meanwhile sample cwb300/290(0.21) exhibits very small excess pwp followed by gradual decrease in excess pwp to the end of the test.

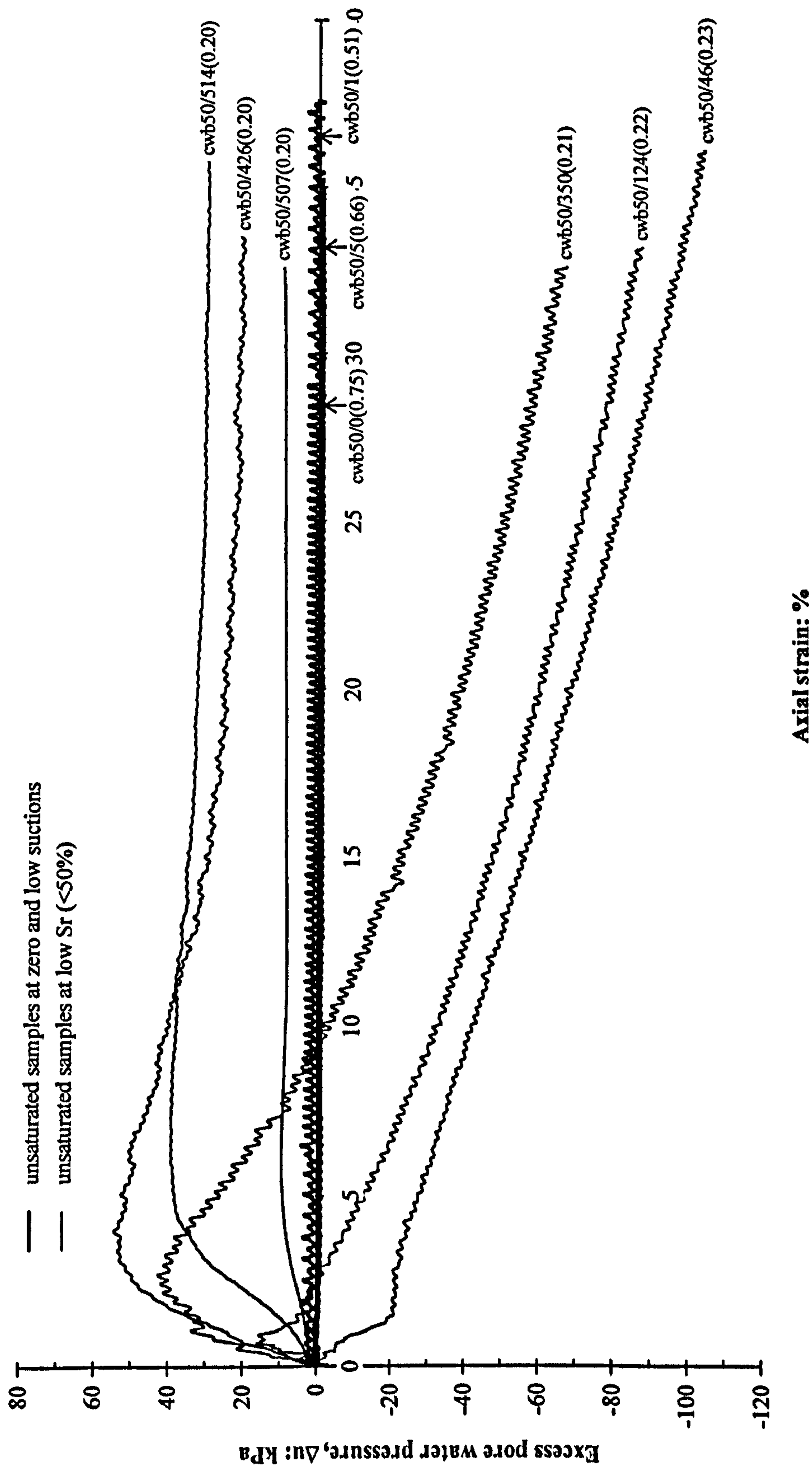


Figure 7.12a: Excess pwp against axial strain for  $p-u_a$  of 50kPa



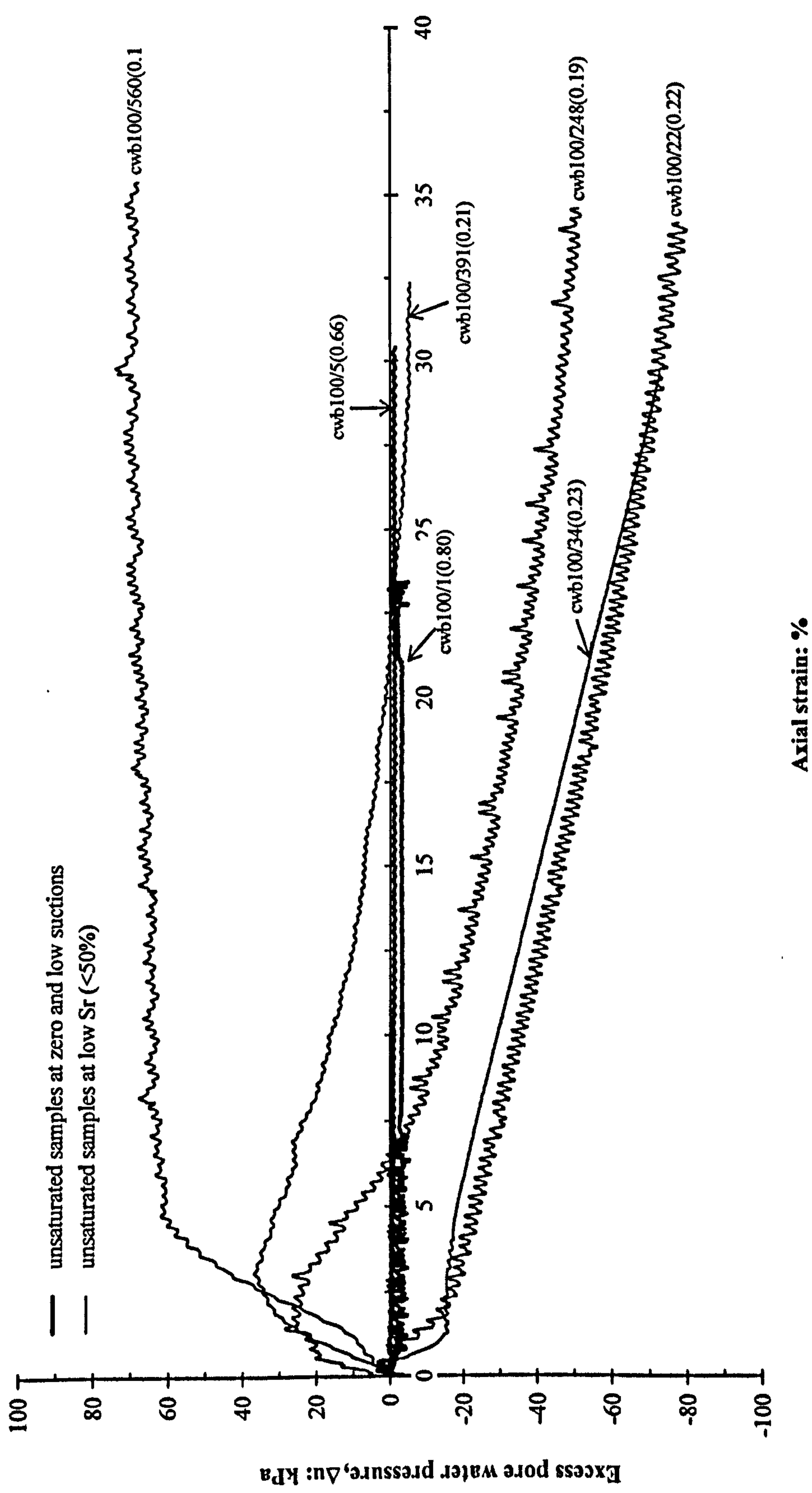


Figure 7.12b: Excess pwp against axial strain for  $p-u_a$  of 100kPa

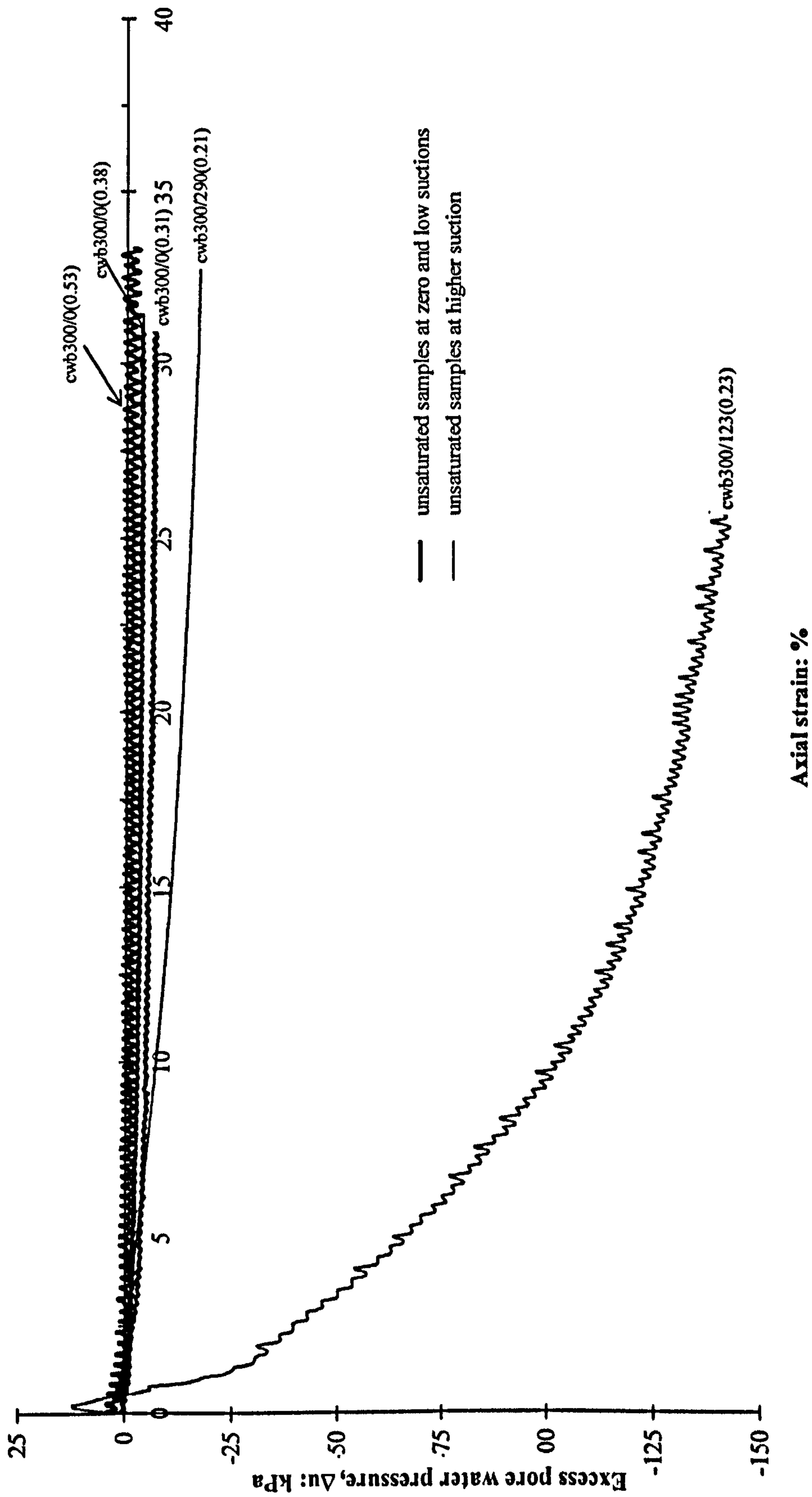


Figure 7.12c: Excess pwp against axial strain for  $p-u_a$  of 300kPa



### 7.2.6 Suction Path

In order to observe more clearly the influence of suction on strength, the deviatoric stress,  $q$  is plotted against suction for each of the three mean net stresses (Figure 7.13a, 7.13b and 7.13c). For mean net stress of 50kPa, the strength increases sharply from zero to 70kPa of suction, steadily increases for suctions up to 400kPa and then decreases at higher values of suction (Figure 7.13a). At mean net stress of 100kPa, the same trend can be observed but the increase in strength is sharper at low suctions (Figure 7.13b) than the lower mean net stress of 50kPa. The strengths for samples with suctions of 1kPa and 5kPa increase dramatically (almost vertically) and exhibit greater strength than the saturated test as seen in Figure 7.9b ( $q_{\max} = 361\text{kPa}$ ). The tests at higher mean net stress of 300kPa (Figure 7.13c) for three samples at zero suction also show a significant increase in strength compared to the equivalent saturated test as shown in Figure 7.9c ( $q_{\max} = 743\text{kPa}$ ).

It is also interesting to observe the suction changes during the cwb tests. Tests at low suction show very little change in suction throughout the test. For samples with medium ranges of initial suction, matric suction seems to increase with increase in deviatoric stress. An increase in suction is also seen post-peak. However, for samples with higher initial suction, the suction tends to decrease up to peak state. They also show a decrease in suction post-peak (Figure 7.13a and 7.13b). A similar trend is likely to be true for cwb300 at higher initial suctions ( $>300\text{kPa}$ ) but no data are available to confirm that trend.

The suction paths for all the cwb tests are plotted together as deviatoric stress,  $q$  against suction in Figure 7.14. It is clearly seen from this figure that peak strengths for each group show very similar behaviour although the applied mean net stress,  $p-u_a$  affects the position of inferred peak strength boundary. The peak strength boundary seems to increase sharply from the saturated condition to an unsaturated condition in the low suction range as described previously. As suction continues to increase to higher values, the strength begins to reduce and the peak boundary curves down especially for cwb50 and cwb100. For samples cwb300, the peak

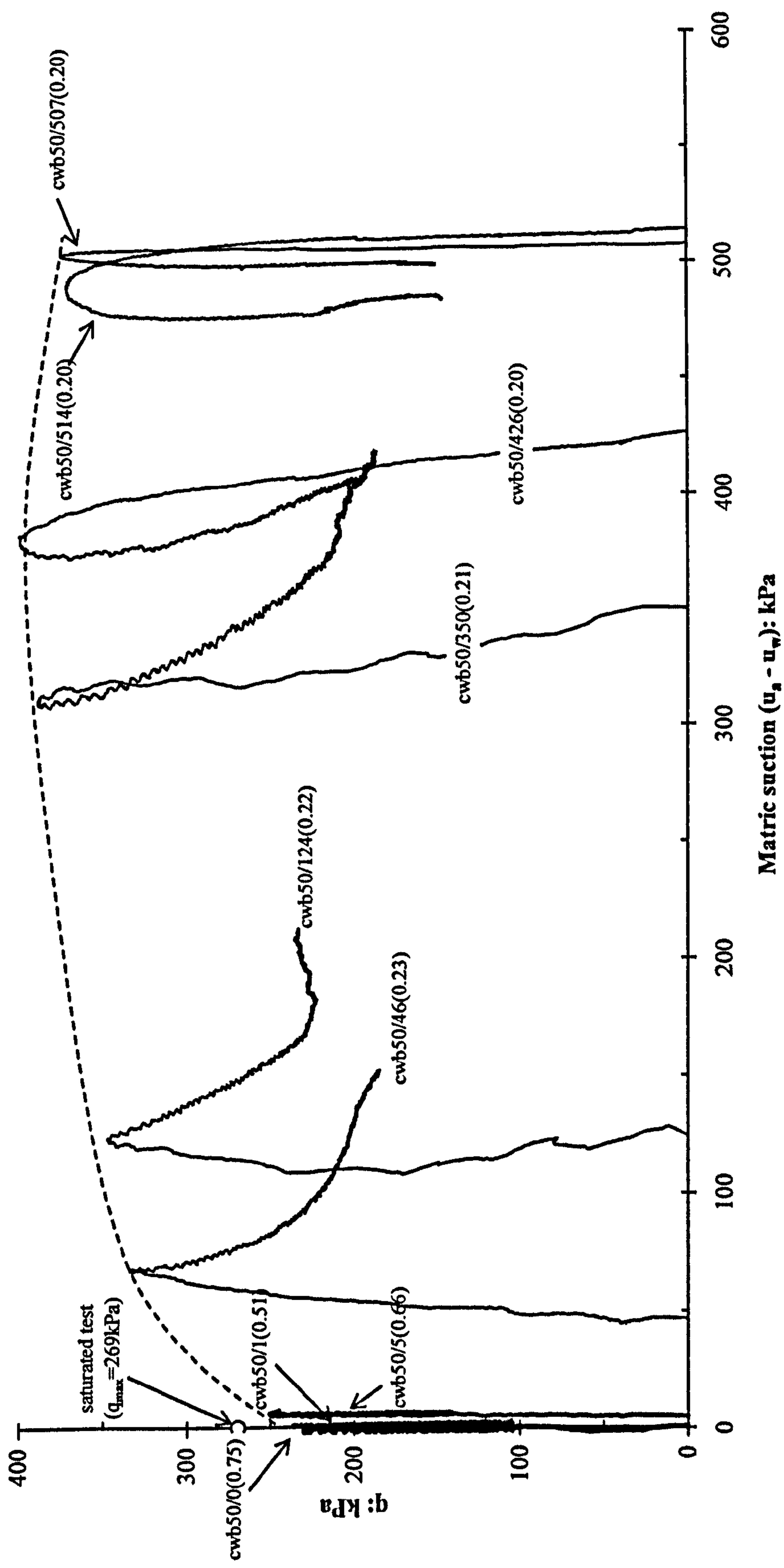


Figure 7.13a: The variation in deviator stress with suction for  $p-u_a$  of 50kPa



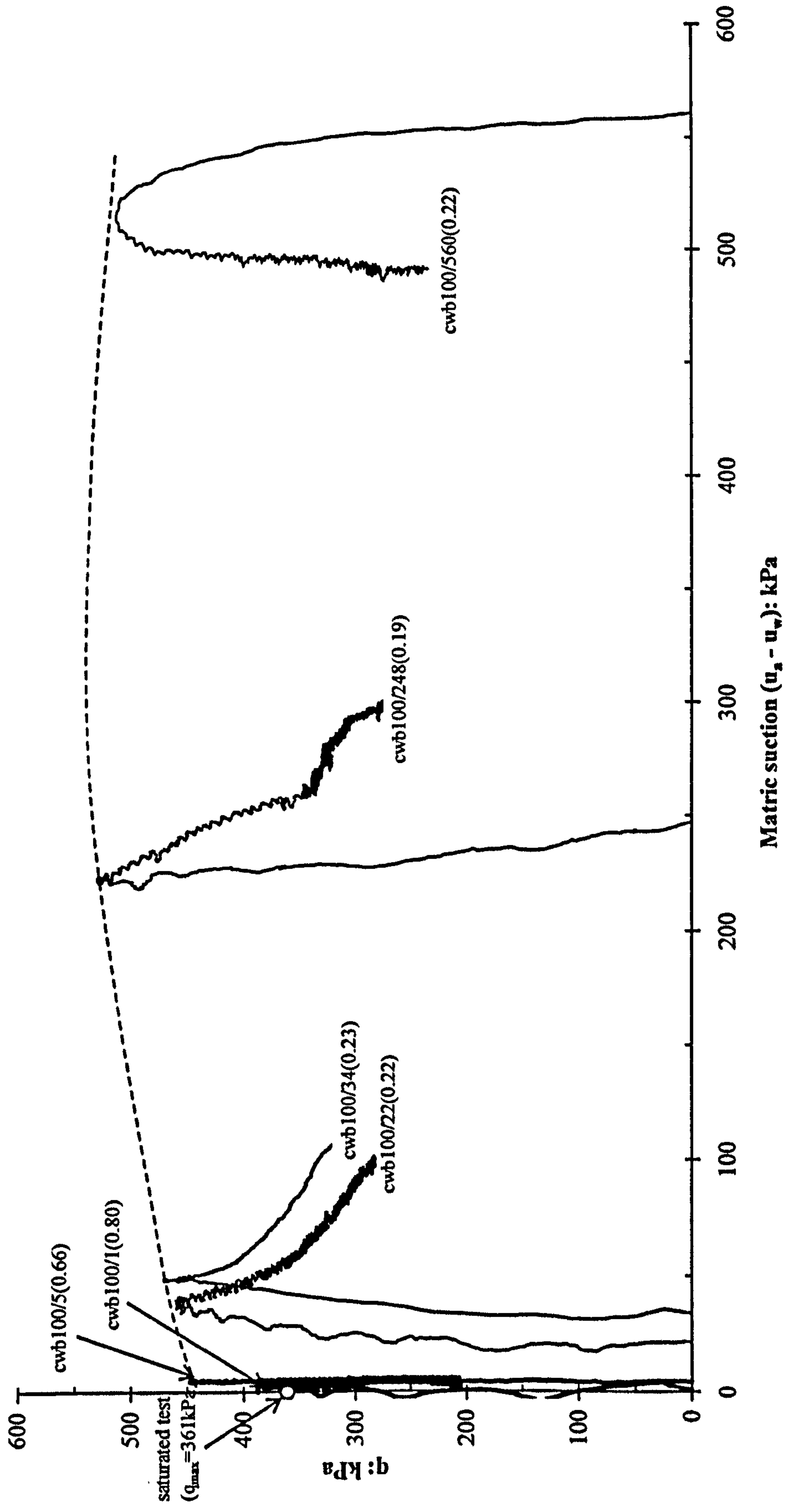


Figure 7.13b: The variation in deviator stress with suction for  $p-u_a$  of 100kPa

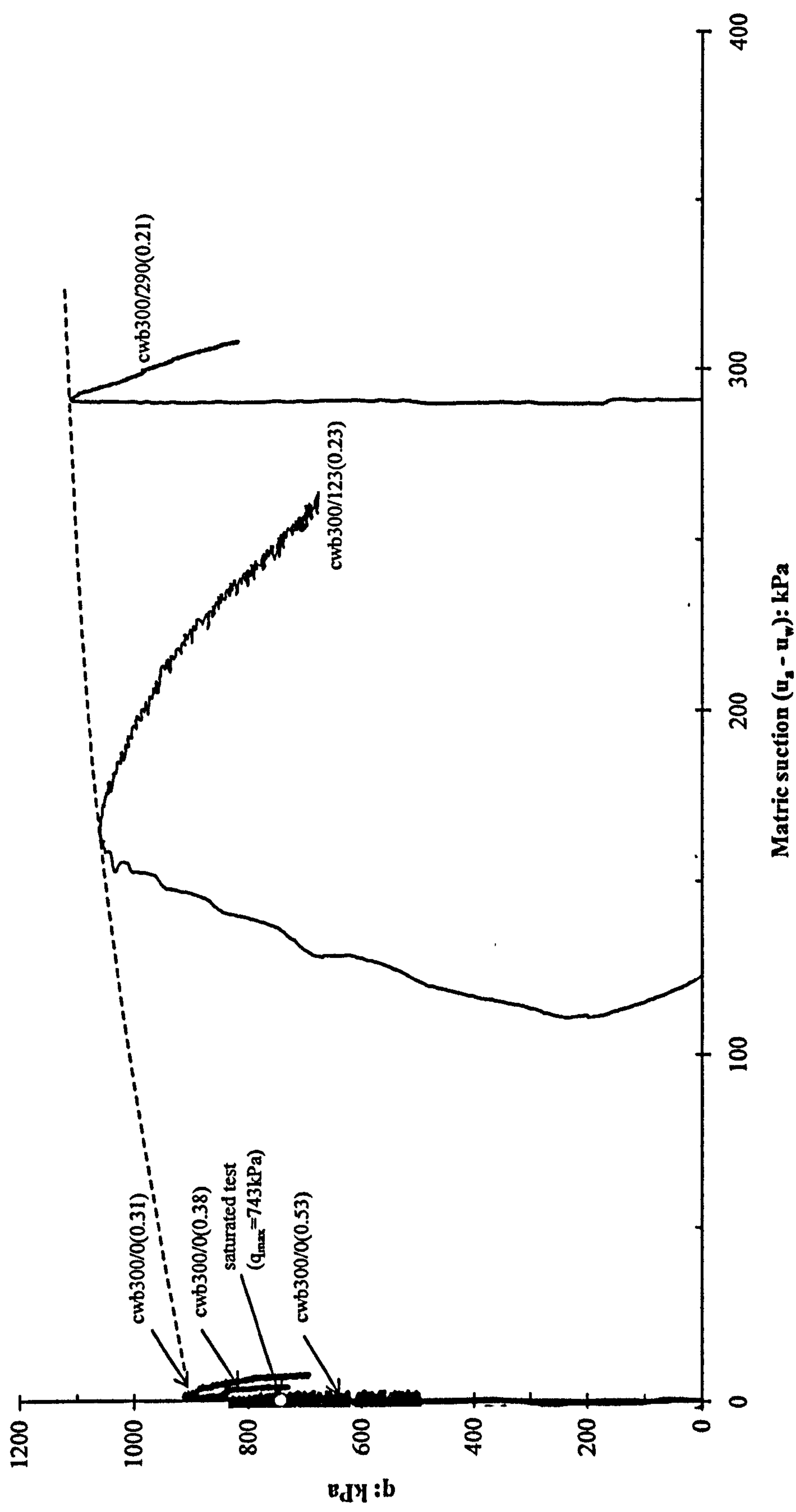


Figure 7.13c: The variation in deviator stress with suction for  $p-u_a$  of 300kPa



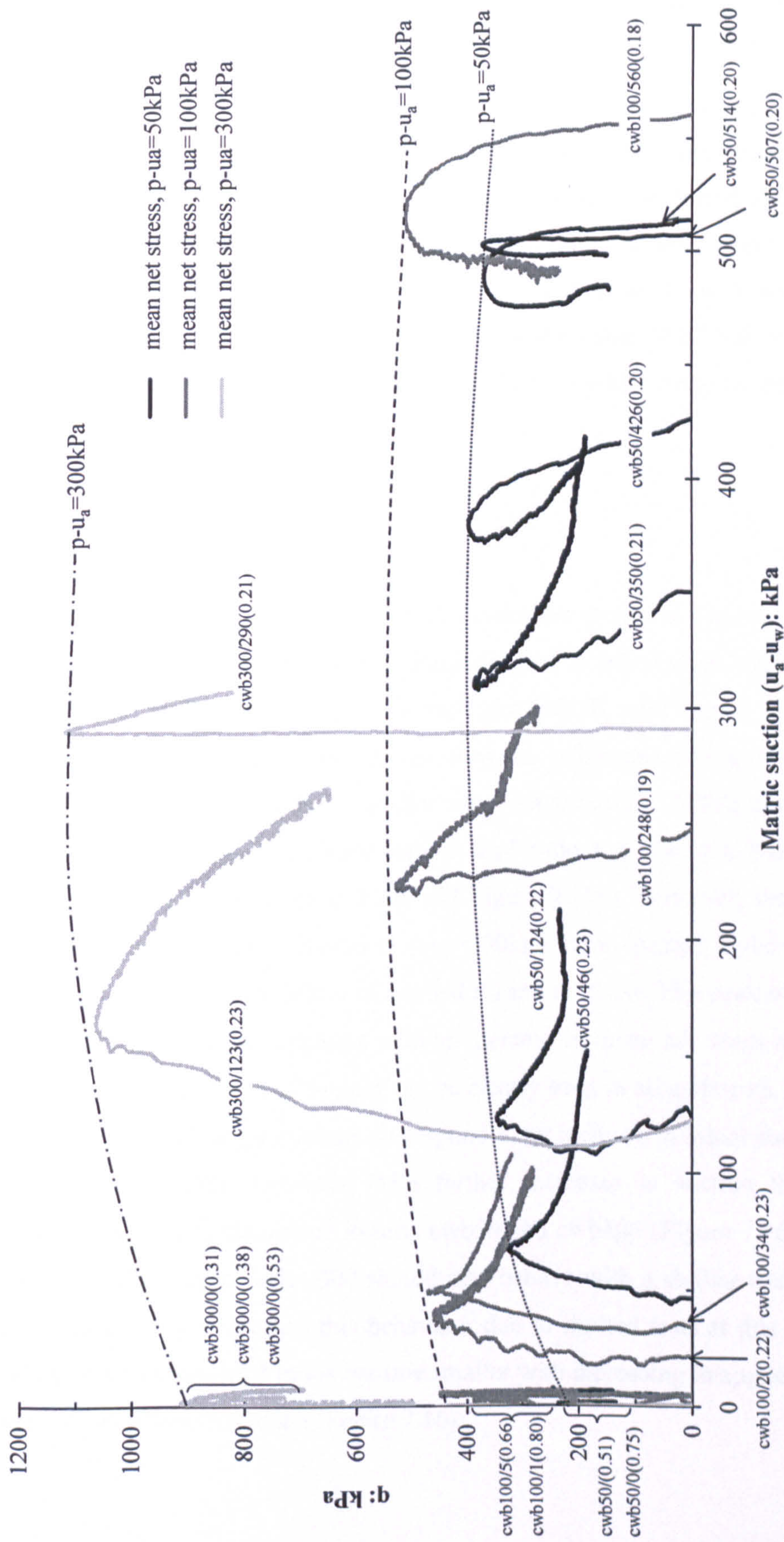


Figure 7.14: The peak strength boundary for  $p-u_a$  of 50kPa , 100kPa and 300kPa



strength seems to increase steadily with increasing suction but at a small increment. The lines of peak strength for all cw tests look quite parallel to each group and indicate some curvature. This behaviour was also found by Escario and Saez (1986) and Gan and Fredlund (1988) performing a series of direct shear tests on remoulded soils. The curvature of shear strength against matric suction graph occurring mainly at low suction suggested that the value of  $\phi^b$  was not constant. This became obvious when soils were studied over a wider range of matric suction (Fredlund and Rahardjo 1993).

### 7.2.7 Stress Ratio

The stress ratio,  $q/p^*$  against axial strain curves are shown in Figure 7.15a, 7.15b and 7.15c. The equivalent saturated drained test at an initial mean stress of 50kPa, 100kPa and 300kPa is also shown in each plot (cdb50, cdb100 and cdb300). It is clearly seen that the stress ratio curves show the influence of mean net stress and suction. Samples sheared under smaller mean net stresses of 50kPa and 100kPa at zero suction showed a significant peak of  $q/p^*$  ratio and closest to the equivalent saturated drained tests (Figure 7.15a and Figure 7.15b). However, the  $q/p^*$  ratio curves for cwb samples sheared at  $p-u_a=300$ kPa were located higher above the saturated tests due to the affect of applied mean net stress. The peak of  $q/p^*$  ratio curves also become less apparent with an increase in mean net stress as shown in Figure 7.15c. The effect of suction can be clearly seen in all cwb tests. The values of maximum  $q/p^*$  ratios increase correspond to an increase in initial suction of the unsaturated samples. However, with further increases in suction the strength decreases as clearly illustrated in tests cwb50 and cwb100 (Figure 7.16). It would be expected that tests series 300 should also behave with a similar trend however no available data to support this behaviour due to limited tests at this series. The values of maximum  $q/p^*$  ratios became smaller with increasing in applied mean net stress from 50kPa to 300kPa (Figure 7.16).



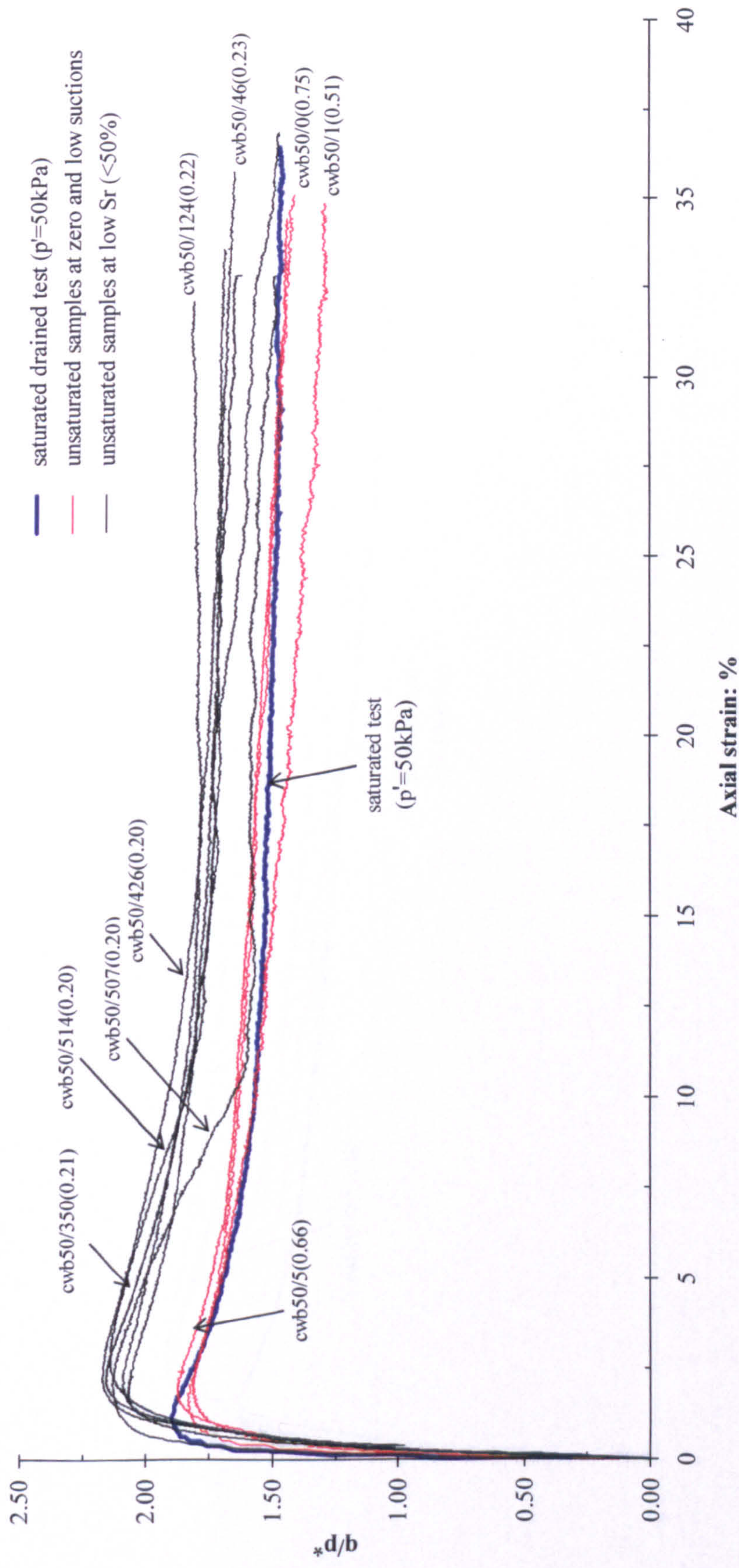


Figure 7.15a: Stress ratio,  $q/p^*$  against axial strain for  $p - u_a$  of 50 kPa



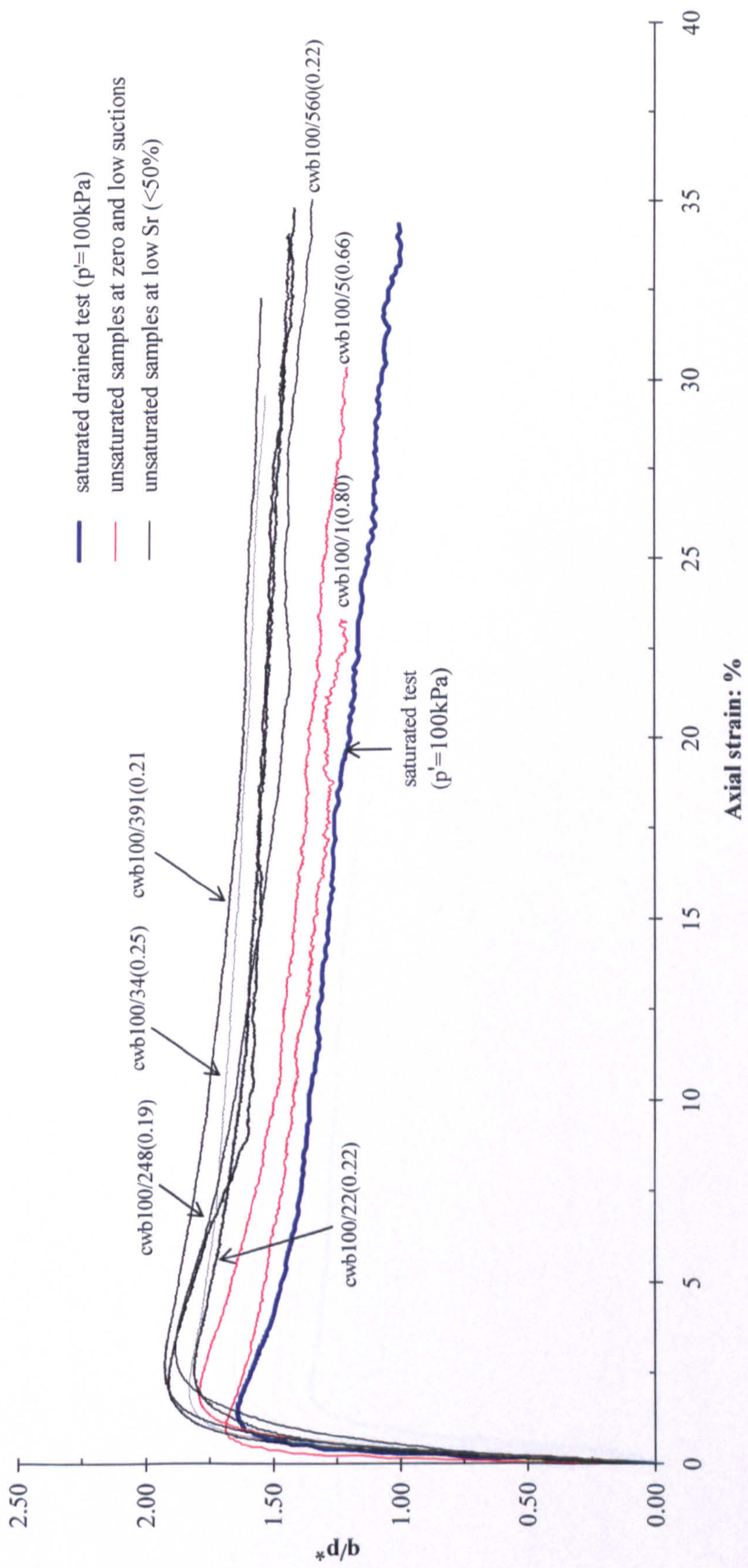


Figure 7.15b: Stress ratio,  $q/p^*$  against axial strain for  $p-u_a$  of 100kPa



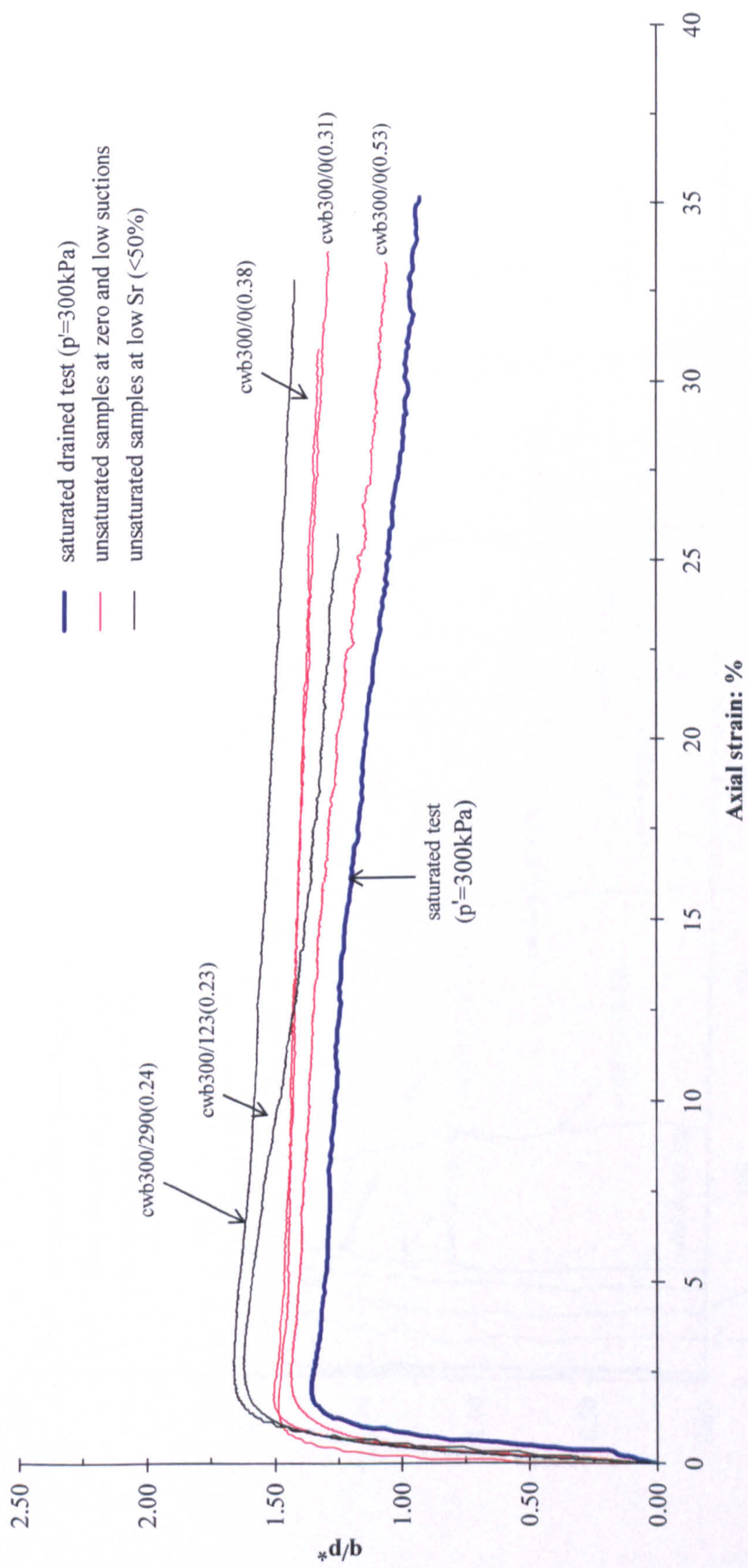


Figure 7.15c: Stress ratio,  $q/p^*$  against axial strain for  $p-u_a$  of 300kPa



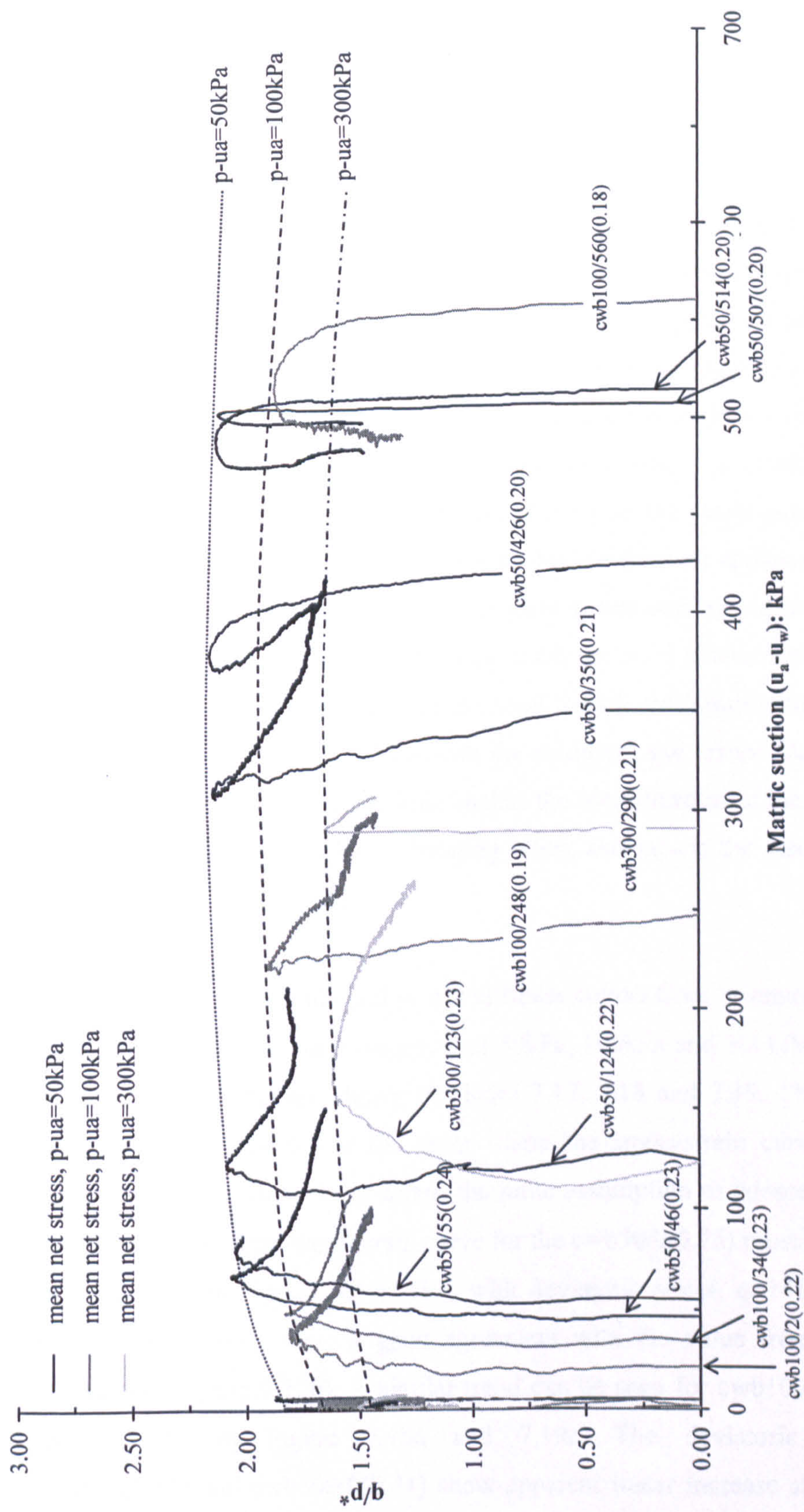


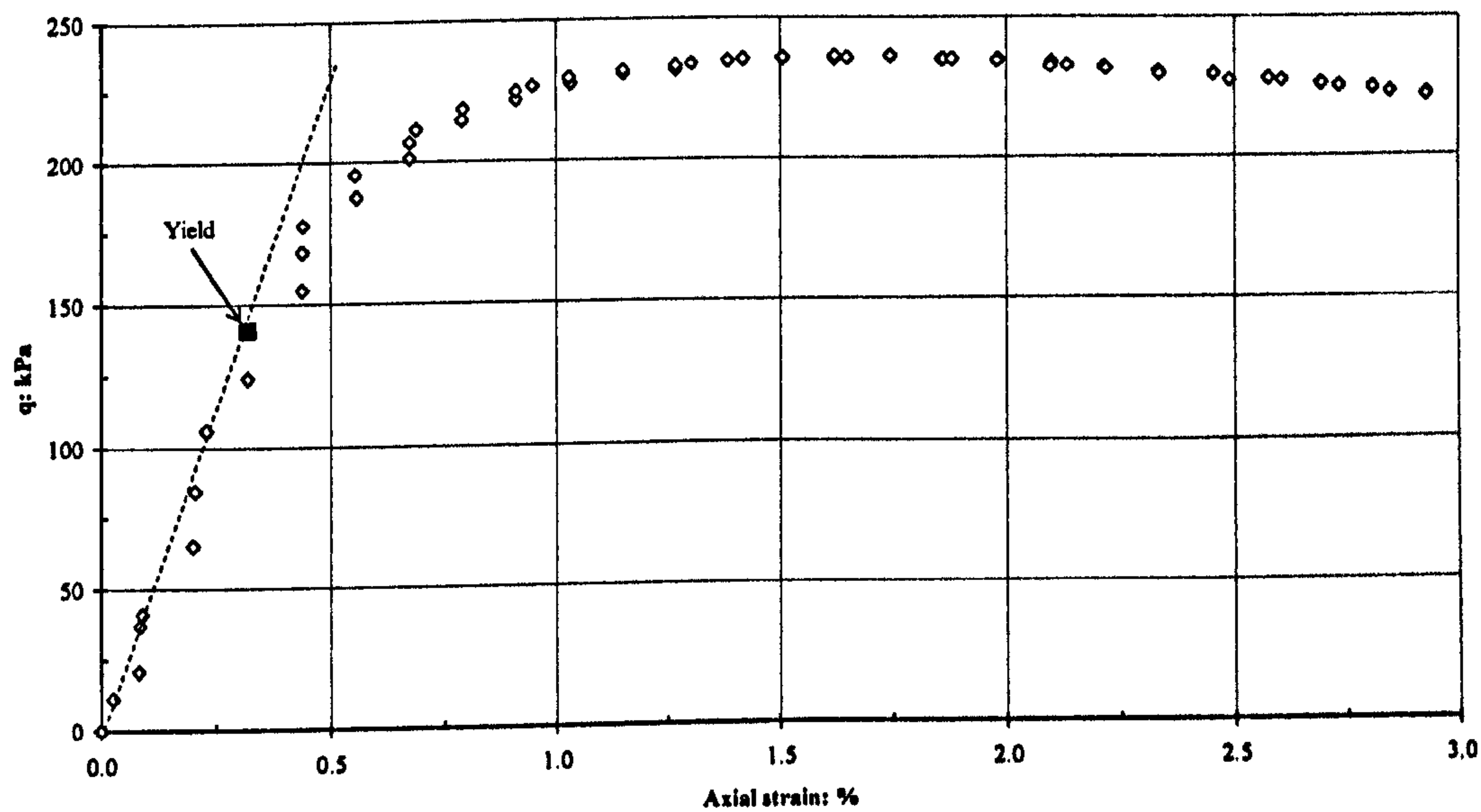
Figure 7.16: Maximum stress ratio,  $q/p^*$  against mean net stress  $p-u_a$  for all series of mean net stresses



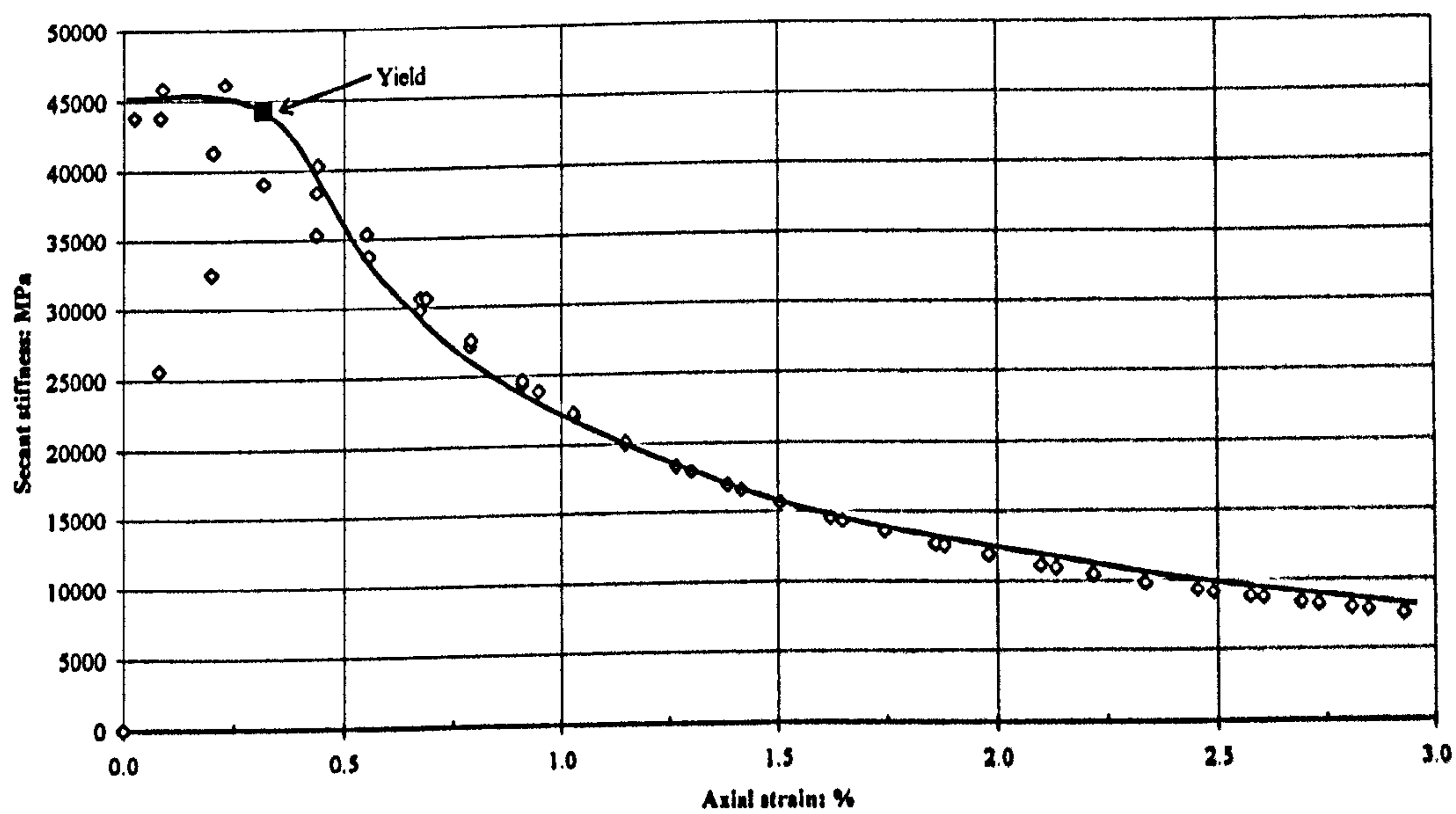
### 7.2.8 Bond Yield and Yield Surfaces

For the identification of the yield points, a similar technique to that adopted by Coop and Atkinson (1993) was applied for the unsaturated bonded material. In unsaturated tests, the volume and pore water pressure are both changing and both variables need to be examined in order to determine the positions of bond yield points. Therefore, for unsaturated samples a thorough investigation was carried out on the stress-strain and volumetric strain curves and the paths in  $v - (p-u_a)$  and  $q - (u_a-u_w)$  spaces. Firstly, an assessment of stress-strain plots was carefully made in order to define a bond yield point. A discontinuity in the stress-strain curves at early axial strain at a point where it starts to deviate from an apparent linear part was chosen as first bond yield. First bond yield points correspond to the start of breakage of the cemented bonds. In all cw tests, the axial strains during shearing were measured using an external displacement transducer (sample mounted lvdt's were used, but there were problems with the readings) and errors due to external measurement are likely to occur. Thus makes the identification of the bond yields at small strains difficult owing to bedding errors and means the results are only suitable for a qualitative study.

Examples of the stress-strain and secant stiffness curves from unsaturated tests on bonded samples at mean net stresses,  $p$  of 50kPa, 100kPa and 300kPa at zero and low suctions ( $S_r > 50\%$ ) are shown in Figure 7.17, 7.18 and 7.19. The first bond yield points were selected at the point where the stress-strain curves begin to diverge from an apparent linear trend (the same assumption as adopted earlier for saturated samples). The stress-strain curve for the cwb50/0(0.75) presents a straight line up to the axial strain,  $\epsilon_a = 0.318\%$  with deviatoric stress,  $q = 141\text{kPa}$  (Figure 7.17a). These values have a good agreement with the value from the secant stiffness plot (Figure 7.17b). A similar trend can be seen for cwb100/1(0.80) and cwb300/0(0.38) in Figure 7.18a and 7.19a. The deviatoric stress for cwb100/1(0.80) and cwb300/0(0.31) show apparent linear increase at early strain up to  $\epsilon_a = 0.178\%$  and  $\epsilon_a = 0.180\%$  respectively before starting to deviate away from the linear trend. The secant stiffness plots exhibited some fluctuation in deviatoric



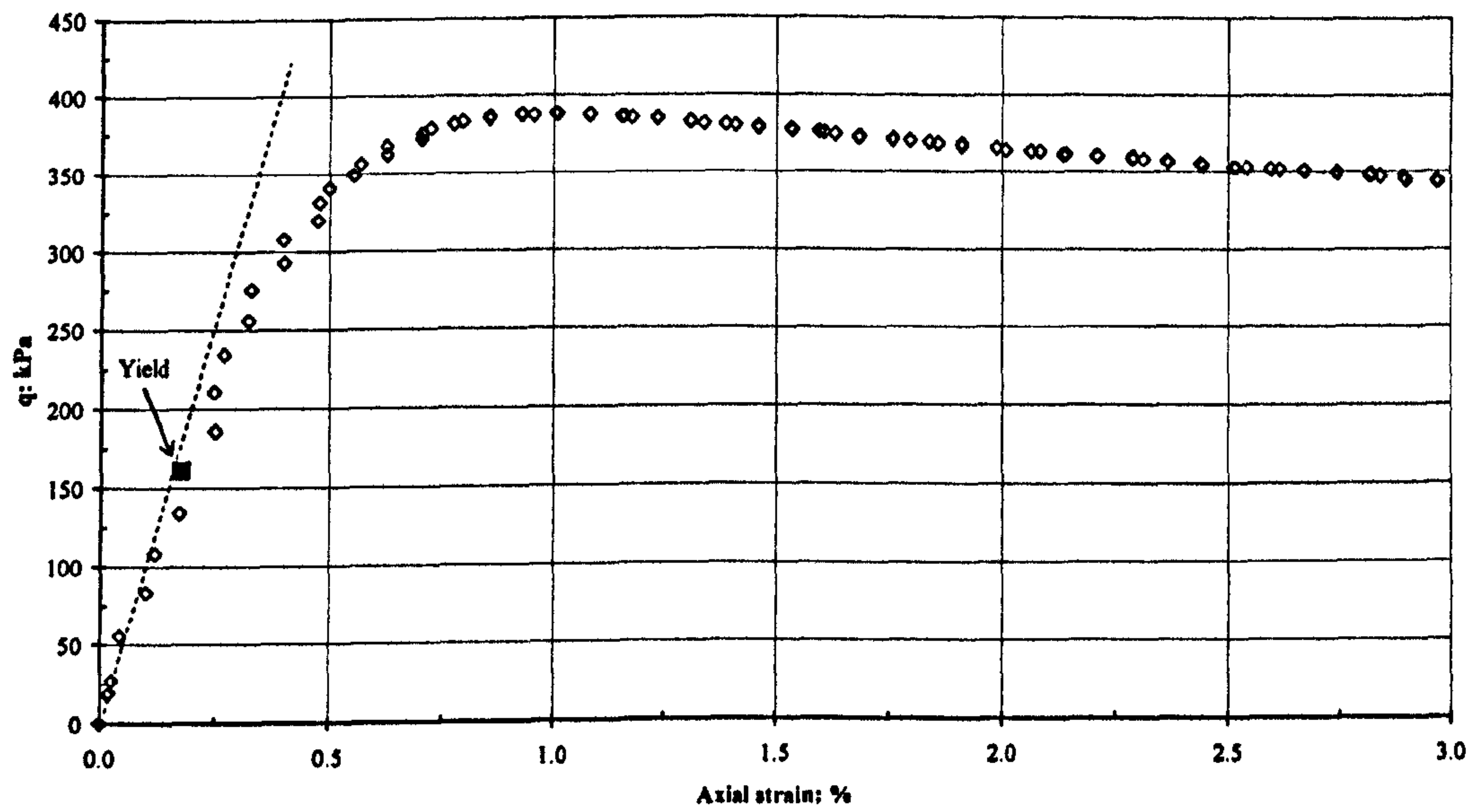
(a)



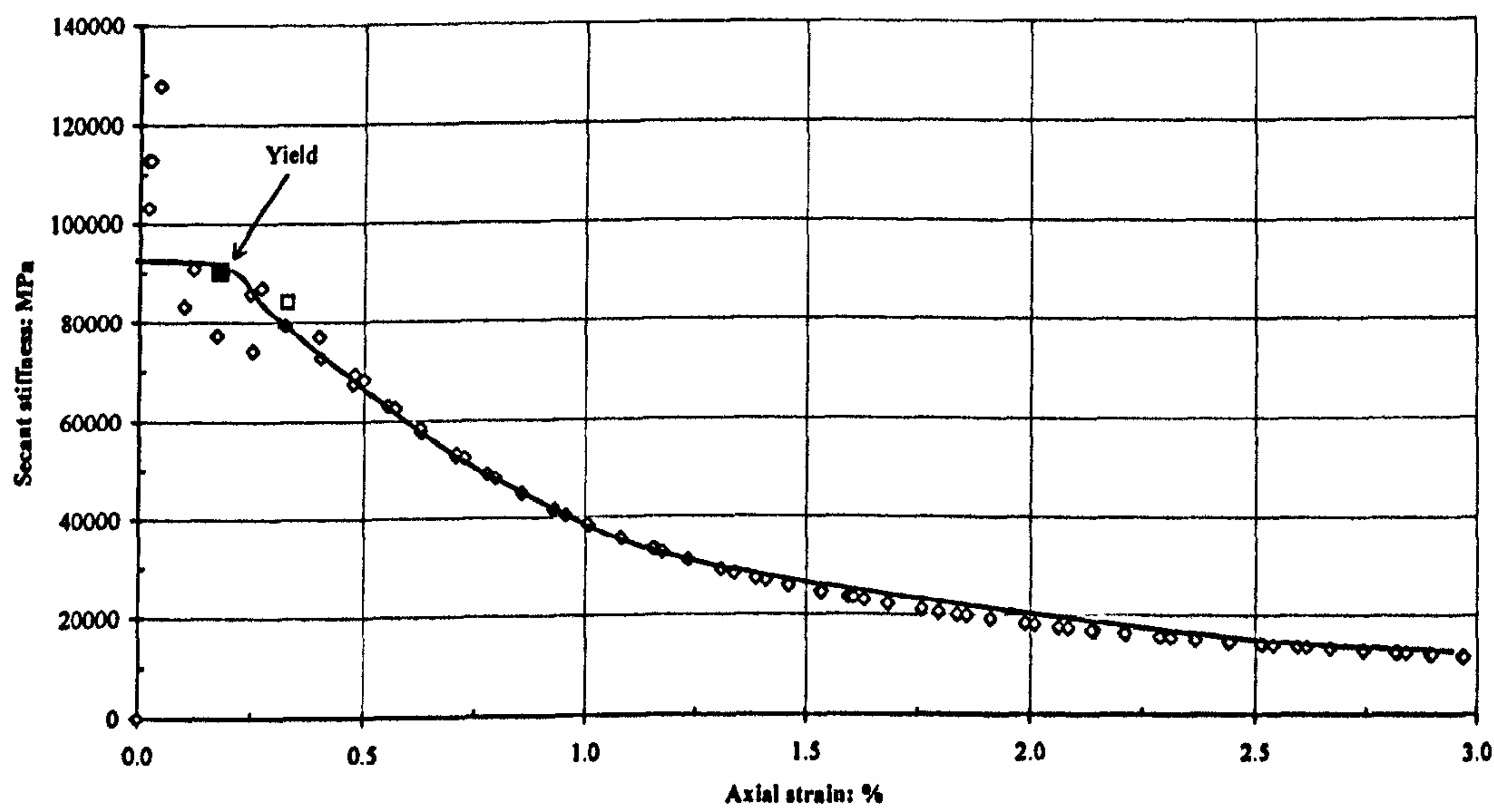
(b)

Figure 7:17: (a) Stress-strain curve and (b) secant stiffness plot for sample cwb50/0(0.75)



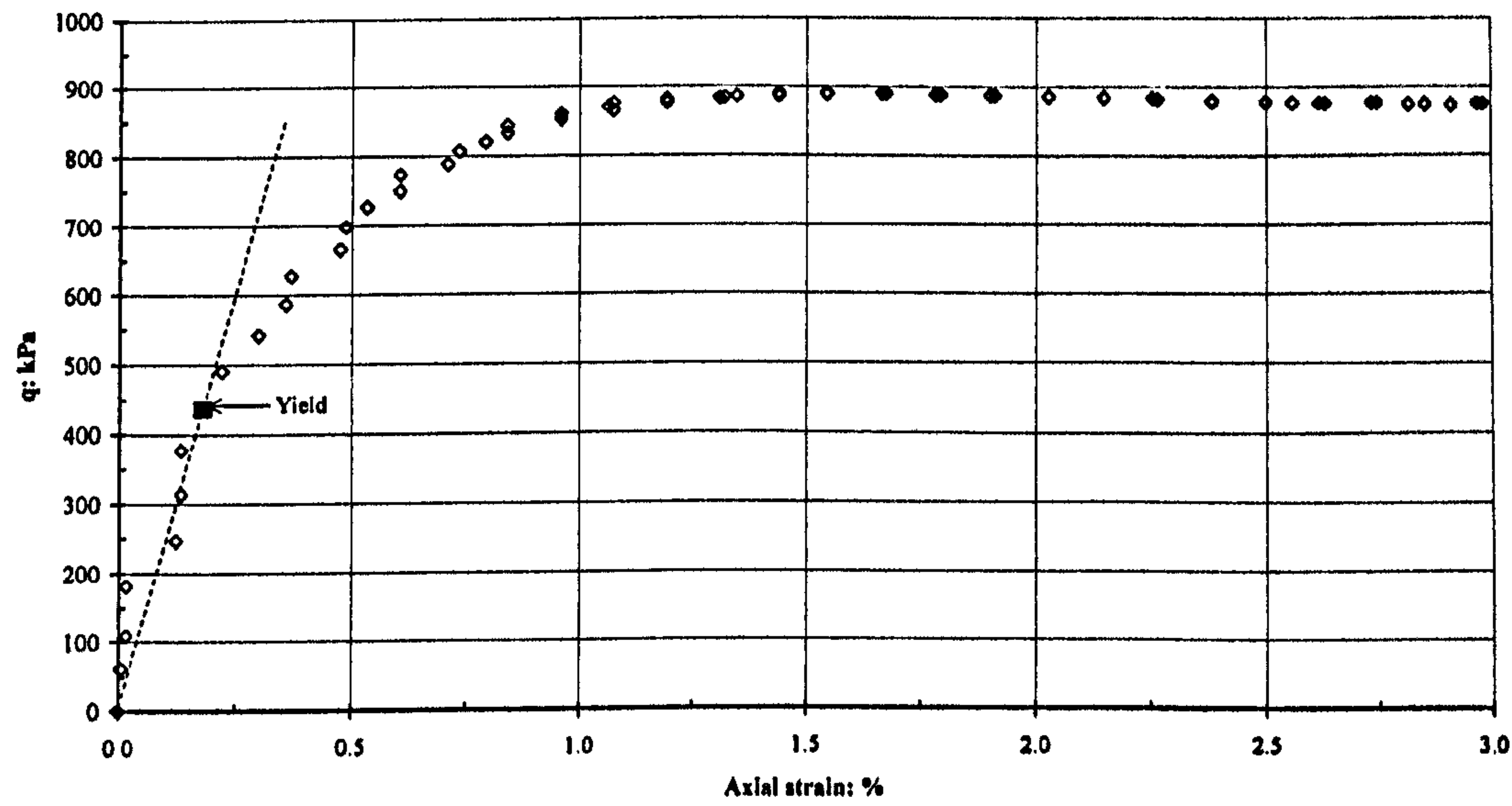


(a)

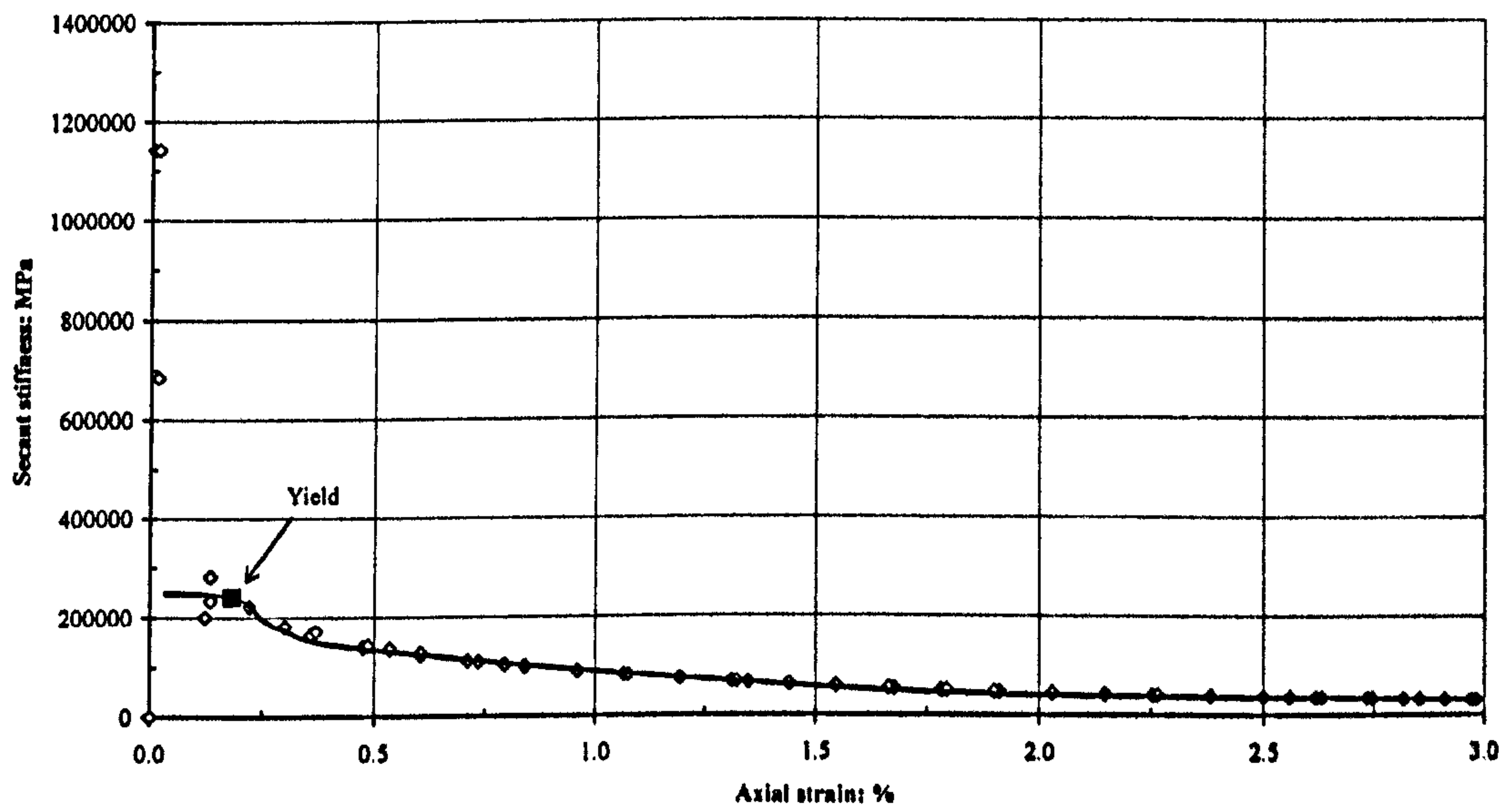


(b)

Figure 7:18: (a) Stress-strain curve and (b) secant stiffness plot for sample cwb100/1(0.80)



(a)



(b)

Figure 7:19: (a) Stress-strain curve and (b) secant stiffness plot for sample cwb300/0(0.38)



stress especially during early axial strain (Figure 7.18b and 7.19b). Therefore, the yield stress has to be estimated by taking into account the fluctuation of the secant stiffness point.

A further assessment was carried out by carefully examining the stress-strain, volumetric strain, excess suction curves and  $v - (p-u_a)$  and  $q - (u_a-u_w)$  paths. The  $v - (p-u_a)$  space for samples with zero and low suctions sheared at mean net stress,  $p-u_a=50\text{kPa}$ ,  $100\text{kPa}$  and  $300\text{kPa}$  exhibited initial compression that was followed by dilatant behaviour (Figure 7.20a – c). The first bond yields were located on the compression part (flat section) of the stress path in  $v - (p-u_a)$  space then followed by a gross yield (denoted as  $Y_{bf}$  or final bond yield) just before samples start to change in behaviour from compression to dilation. The positions of first and final bond yield points for samples with high suction also marked on the  $v - (p-u_a)$  plots shown in Figure 7.21a – c.

Identification of bond yield points was not always straightforward. A point of change in one variable did not always exactly coincide with the change in another. Therefore, personal judgement had to be exercised in order to identify points that could satisfy the change in all variables, with some compromise being necessary.

The positions of first and final bond yields for mean net stress,  $p-u_a=50\text{kPa}$ ,  $100\text{kPa}$  and  $300\text{kPa}$  are also marked on the stress-strain and volumetric strain curves (Figure 7.22, 7.23 and 7.24). As can be seen in volumetric strain plot for mean net stress of  $50\text{kPa}$  (Figure 7.22b), the position of first bond yield points generally concur with the onset of dilation behaviour. Final yield points correspond to peaks in stress strain behaviours. A similar picture can be seen for  $p-u_a=100\text{kPa}$  and  $300\text{kPa}$  (Figure 7.23b and 7.24b).

The excess suction,  $\Delta(u_a-u_w)$  against axial strain curves for cw tests for all three mean net stresses were plotted and were examined in order to help identify the position of final bond yield (Figure 7.25a - c). In Figure 7.25a, the final bond yield

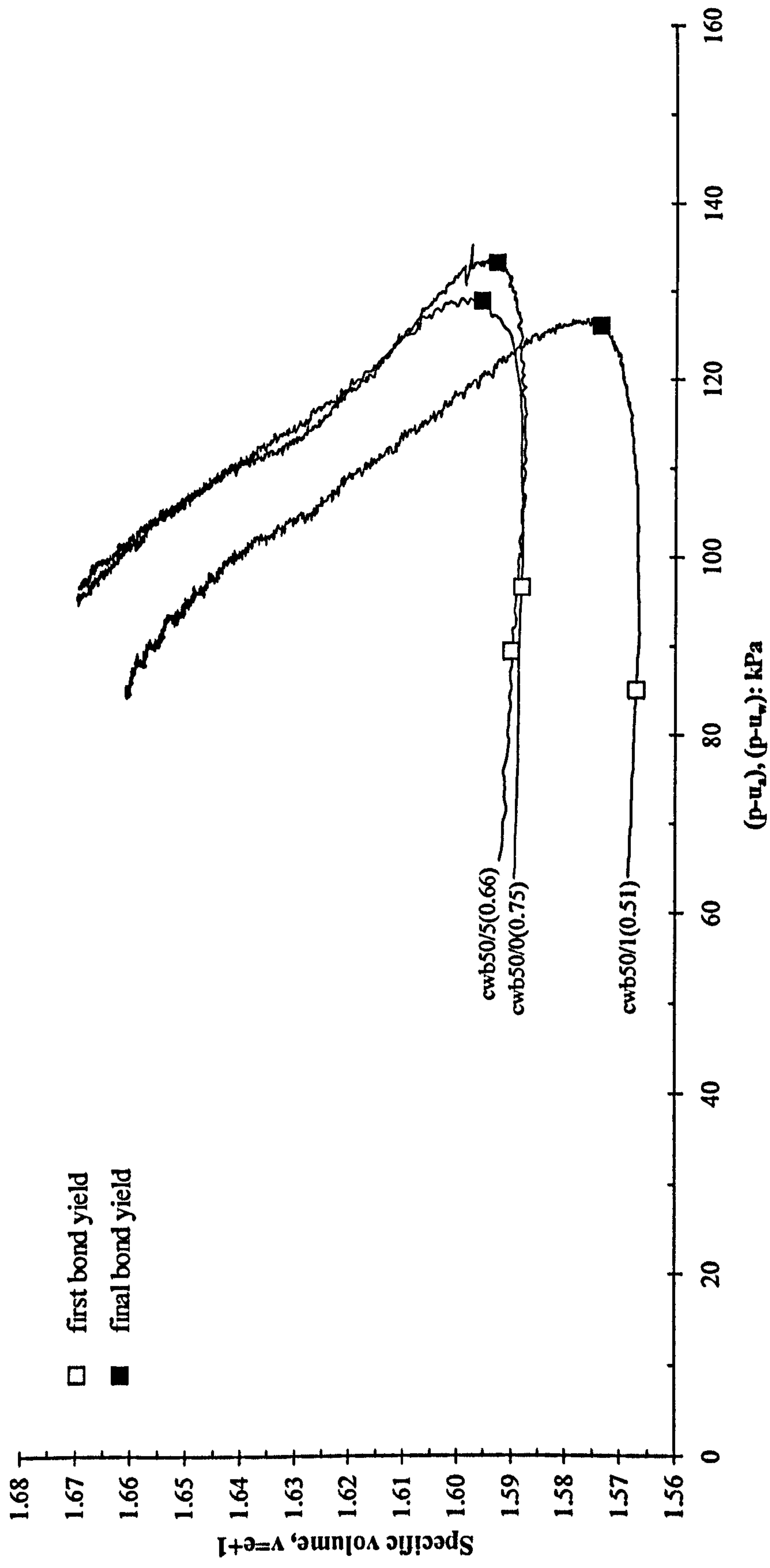


Figure 7.20a: Stress path in  $v - (p-u_w)$  space for samples with zero and low suctions at mean net stress,  $p-u_w = 50 \text{ kPa}$



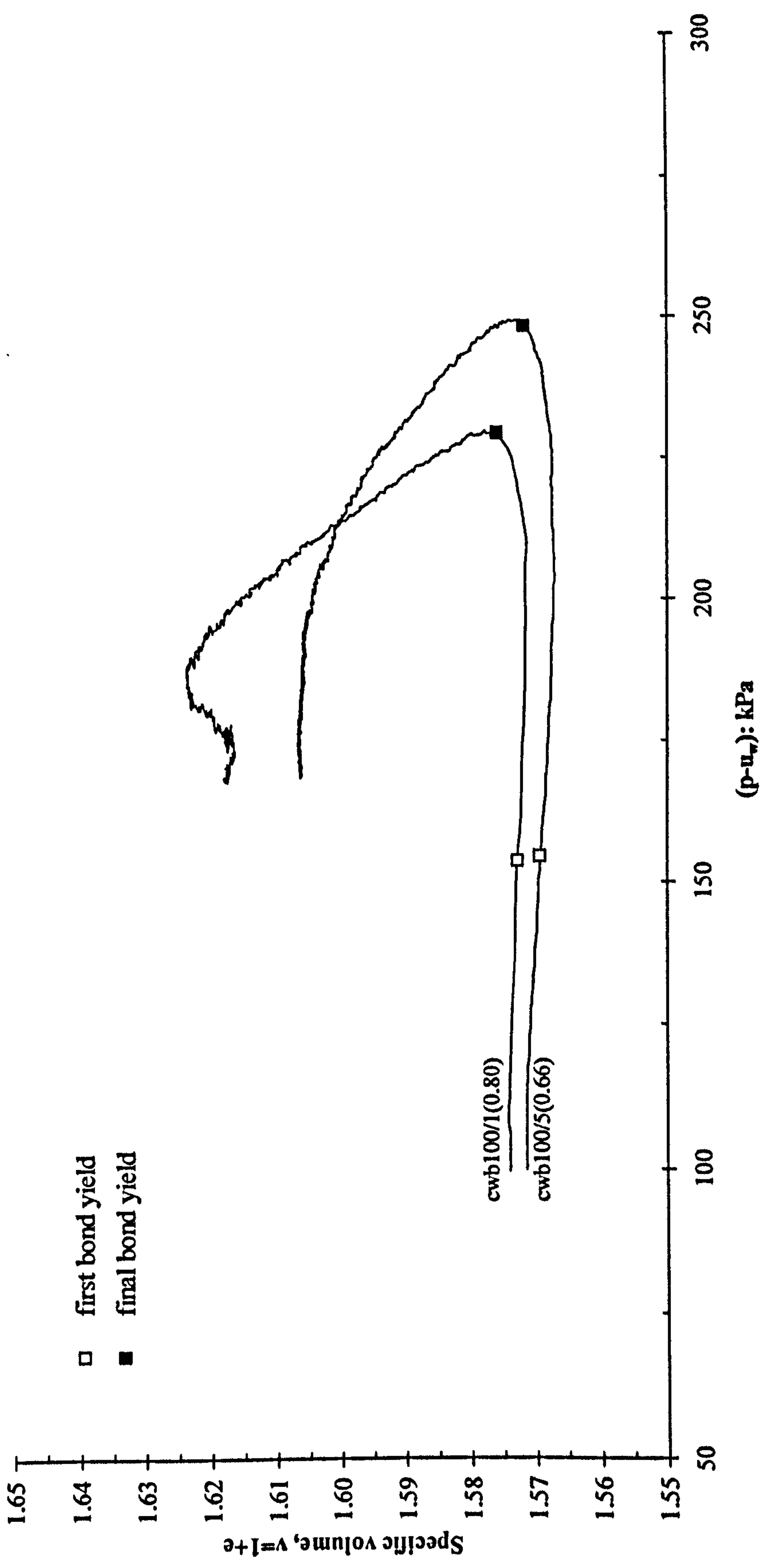


Figure 7.20b: Stress path in  $v - (p-u_w)$  space for samples with zero and low suctions at mean net stress,  $p-u_w = 100\text{kPa}$

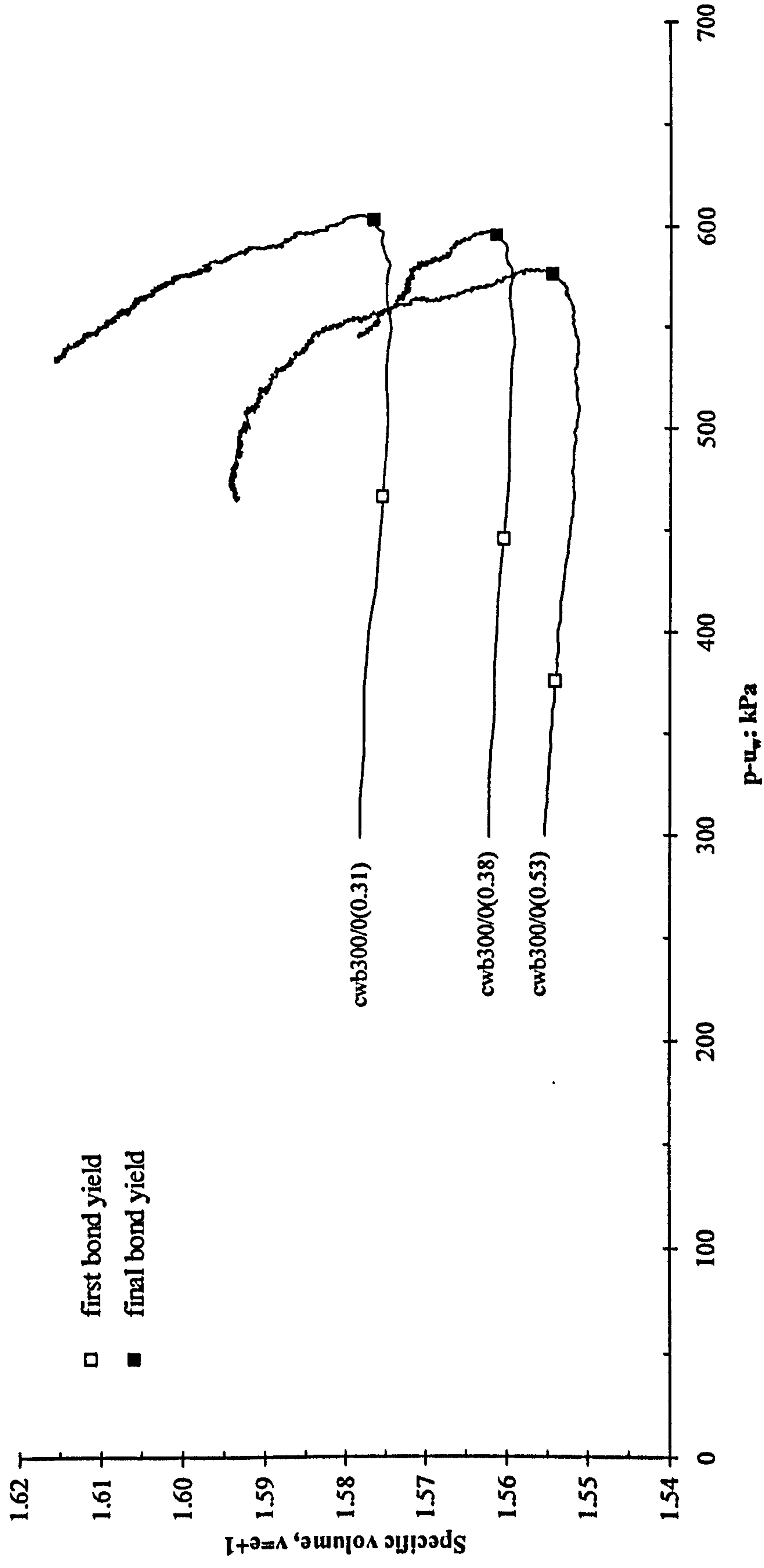


Figure 7.20c: Stress path in  $v - (p-u_w)$  space for samples with zero and low suctions at mean net stress,  $p-u_w = 300\text{kPa}$



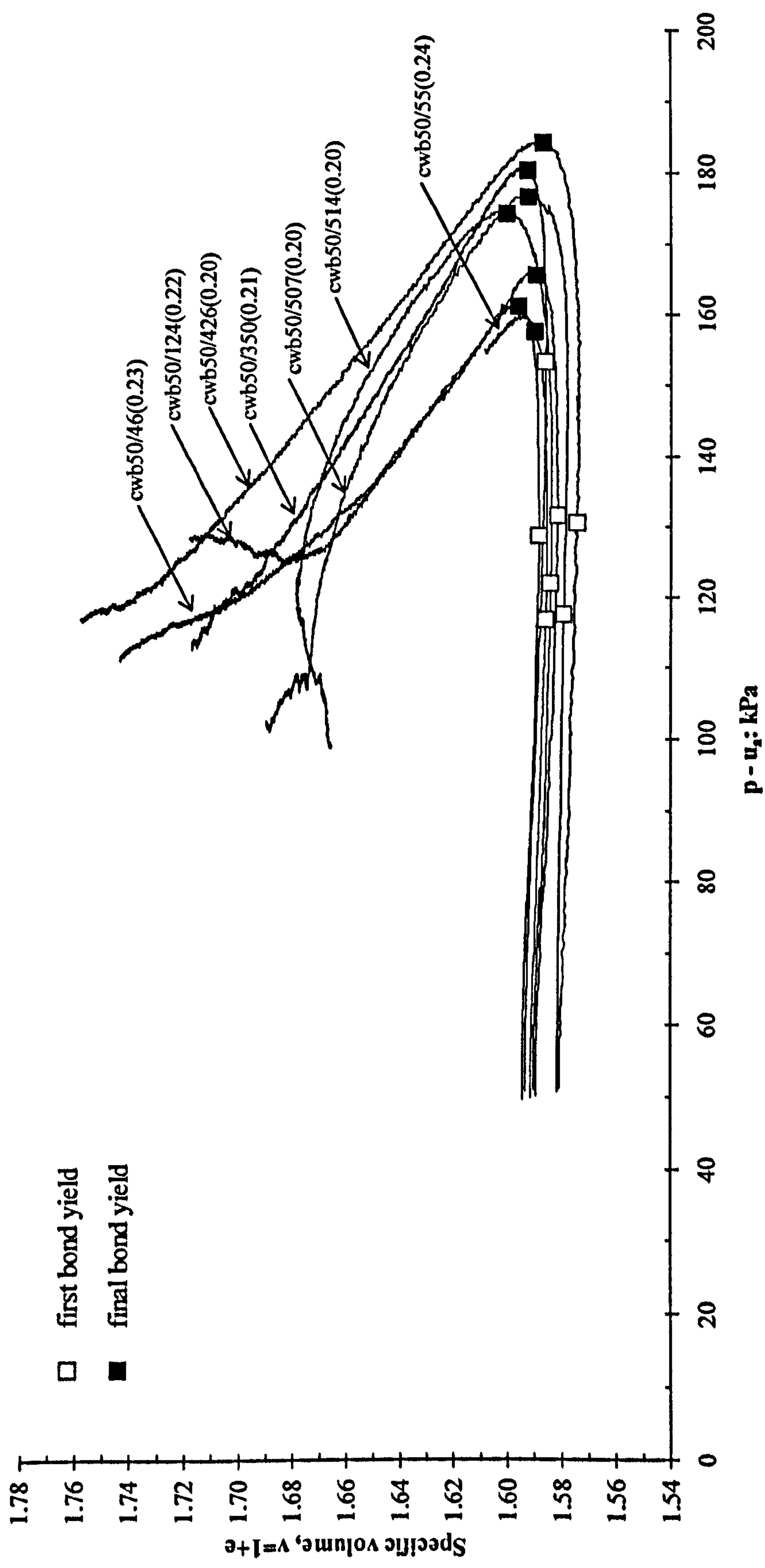


Figure 7.21a: Stress path in  $v - (p - u_w)$  space for samples with low  $S_r$  at mean net stress,  $p - u_w = 50$  kPa

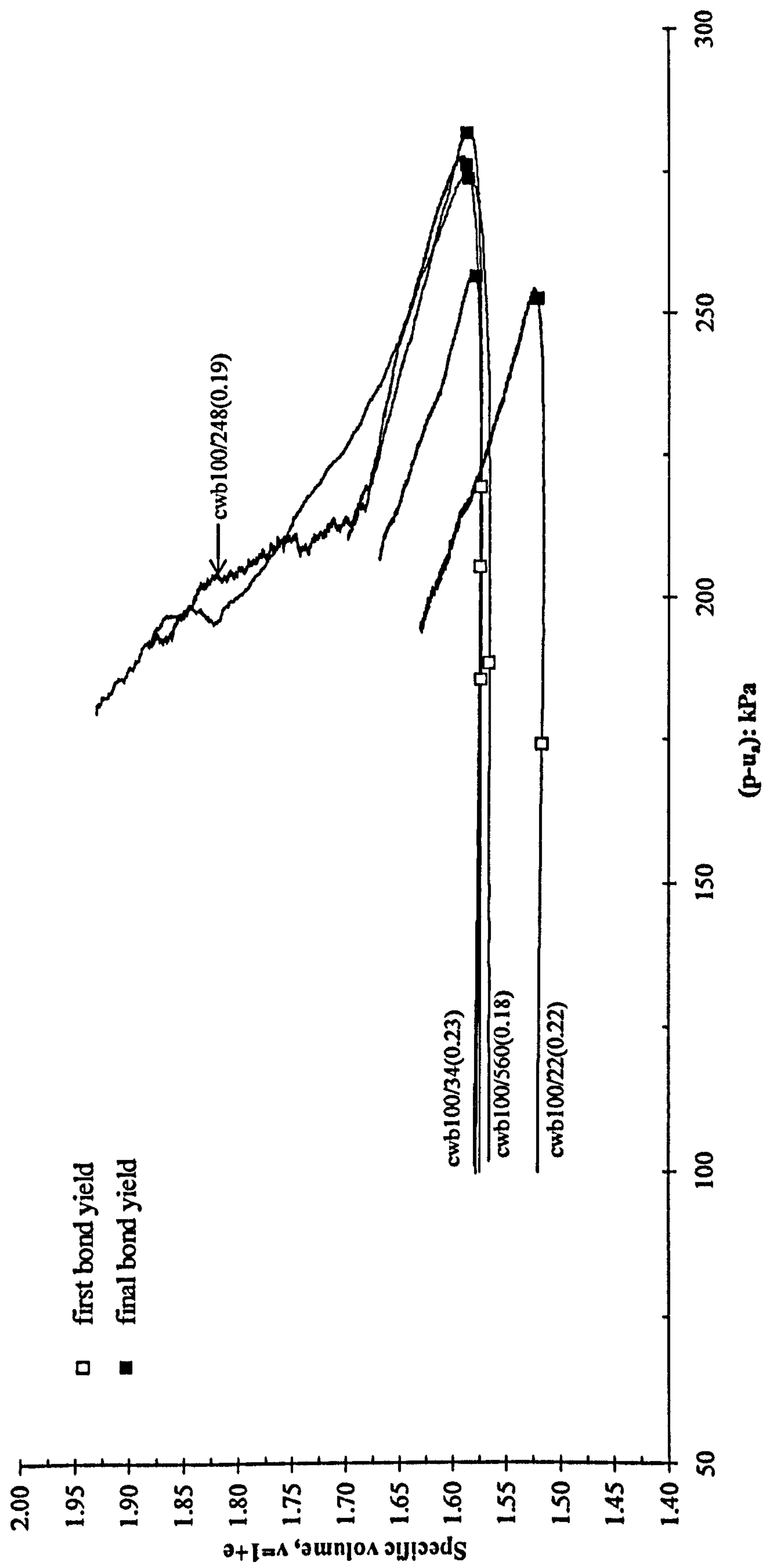


Figure 7.21b: Stress path in  $v - (p-u_w)$  space for samples with low  $S_r$  at mean net stress,  $p-u_w = 100\text{kPa}$



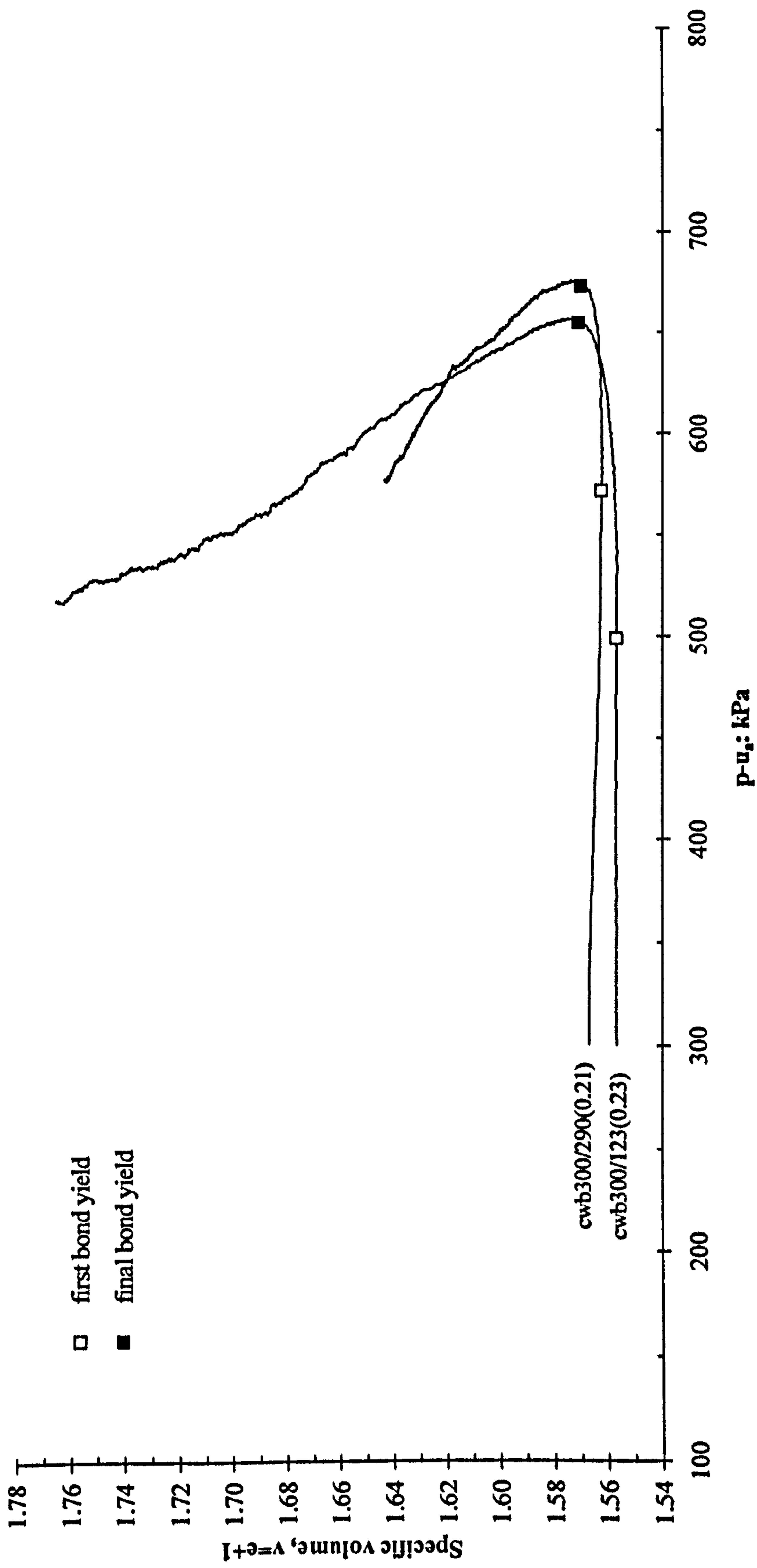
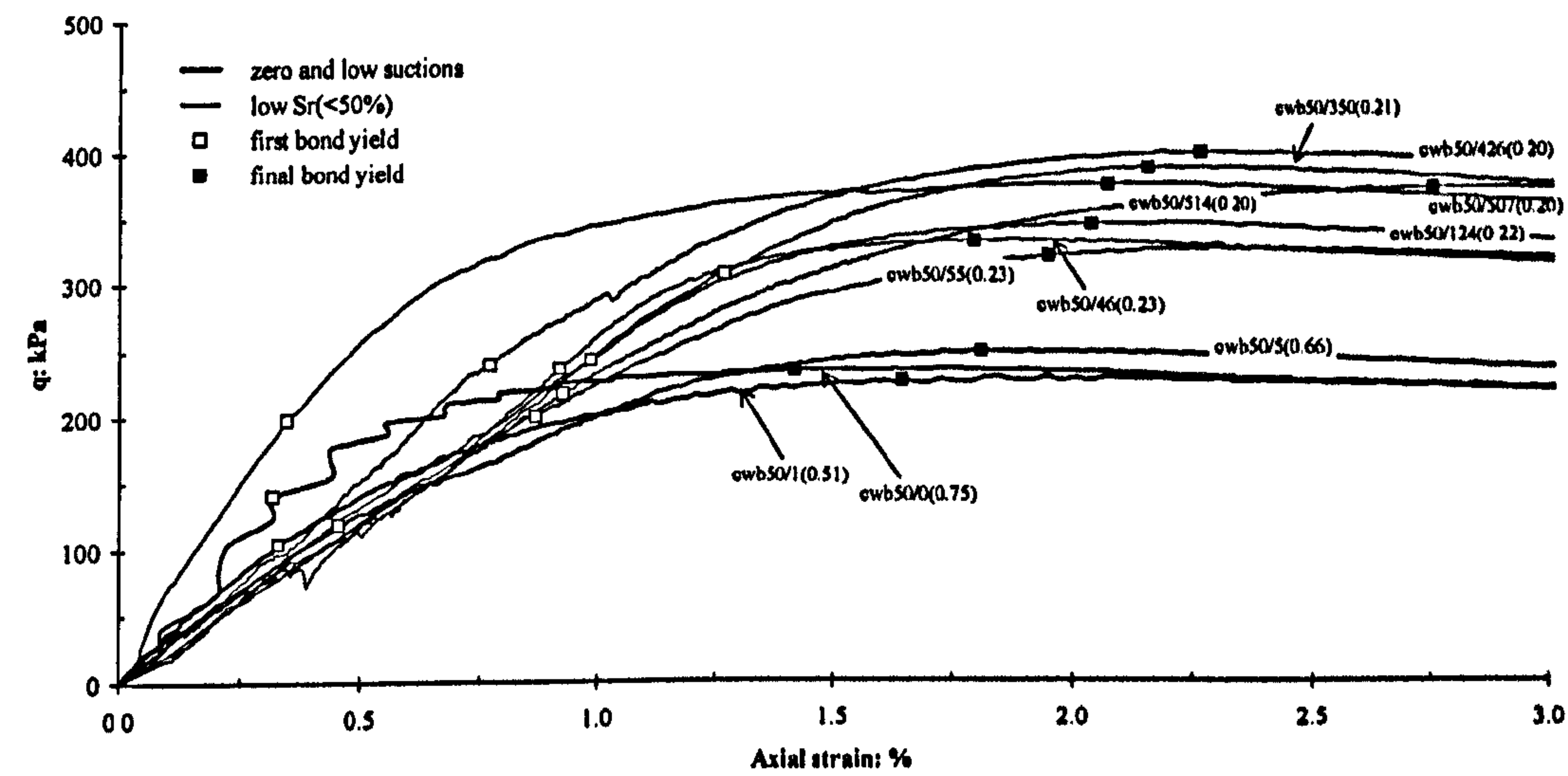
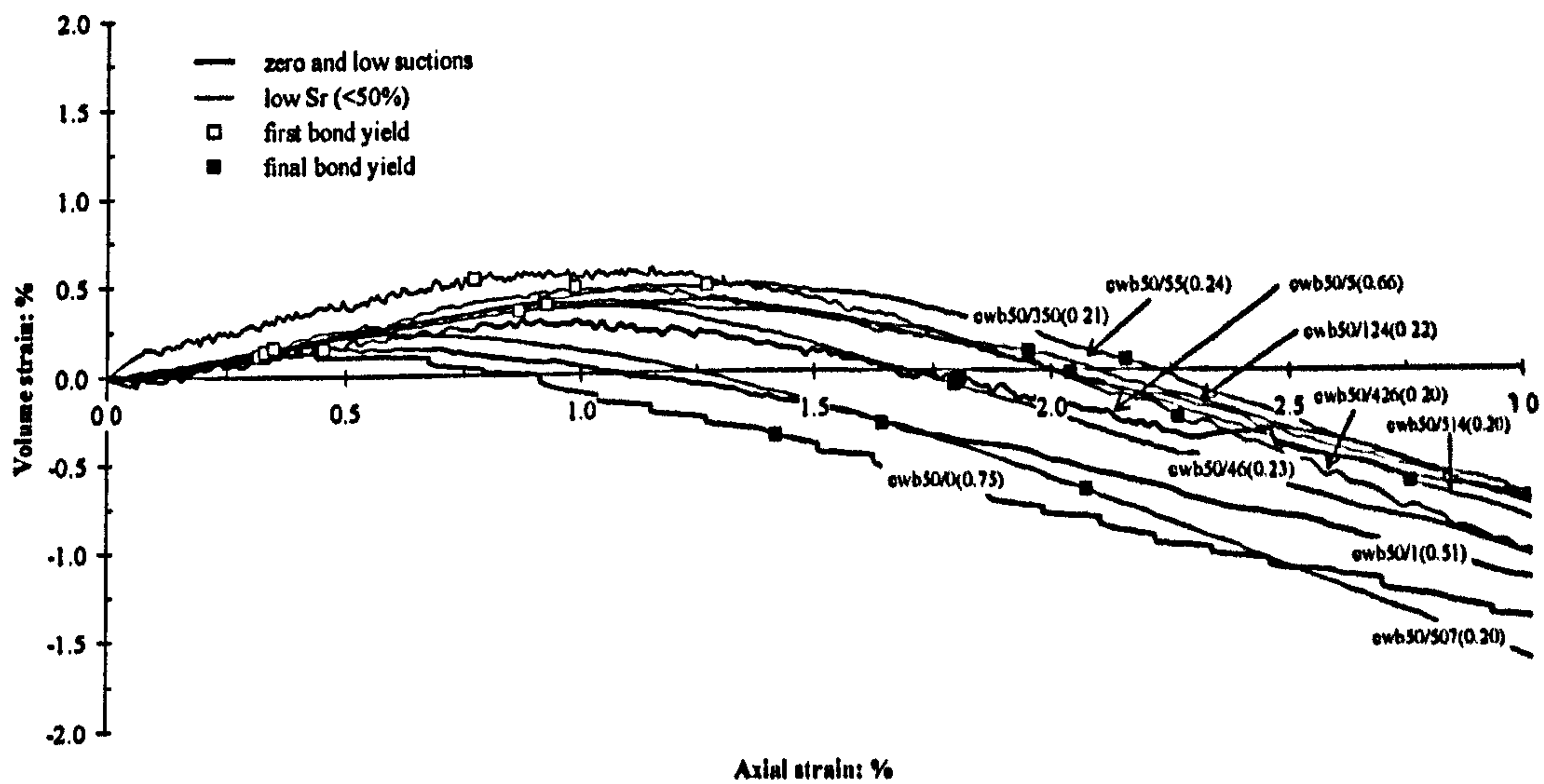


Figure 7.21c: Stress path in  $v - (p-u_w)$  space for samples with low  $S_r$  at mean net stress,  $p-u_w = 300\text{kPa}$



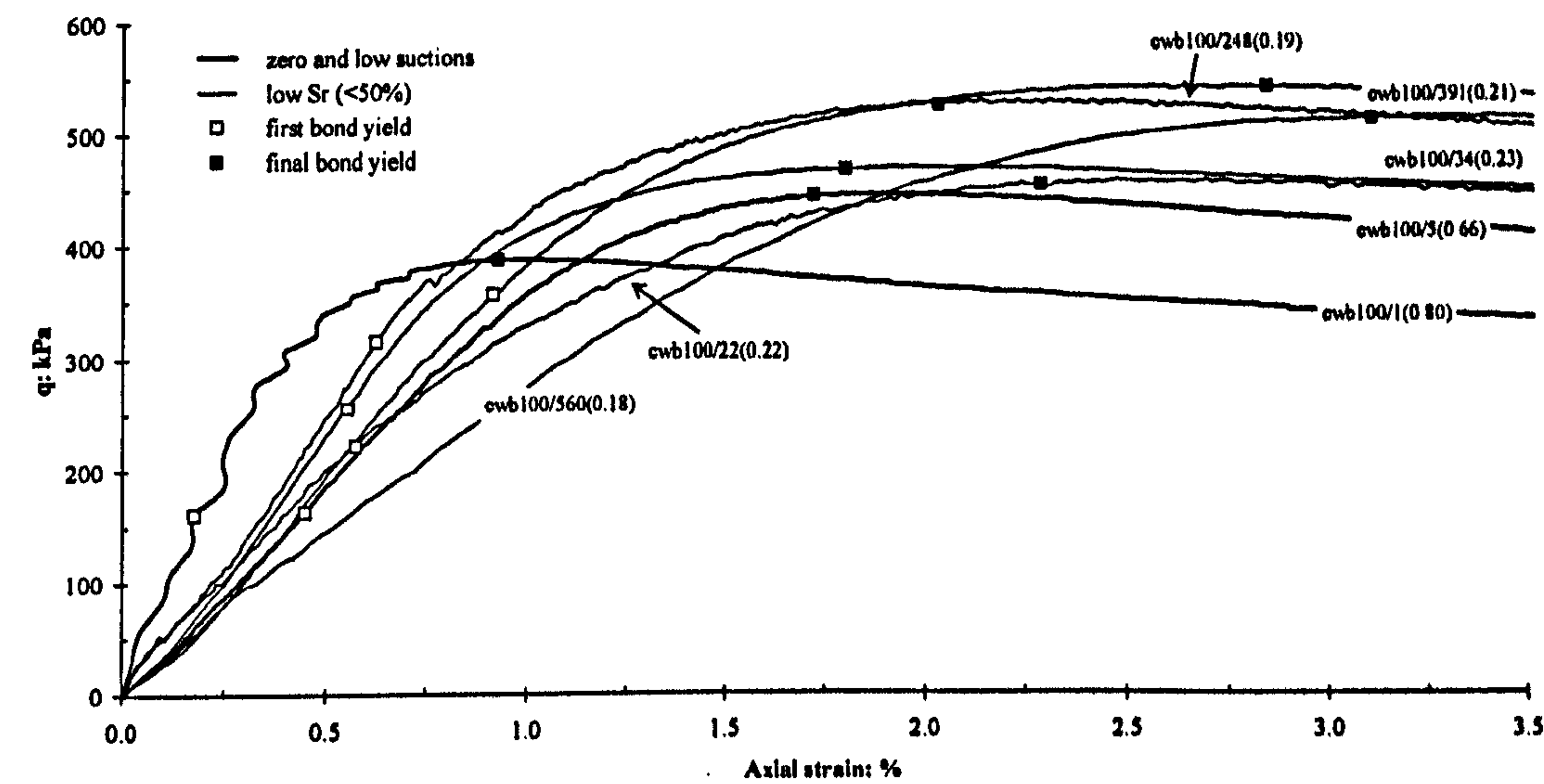
(a)



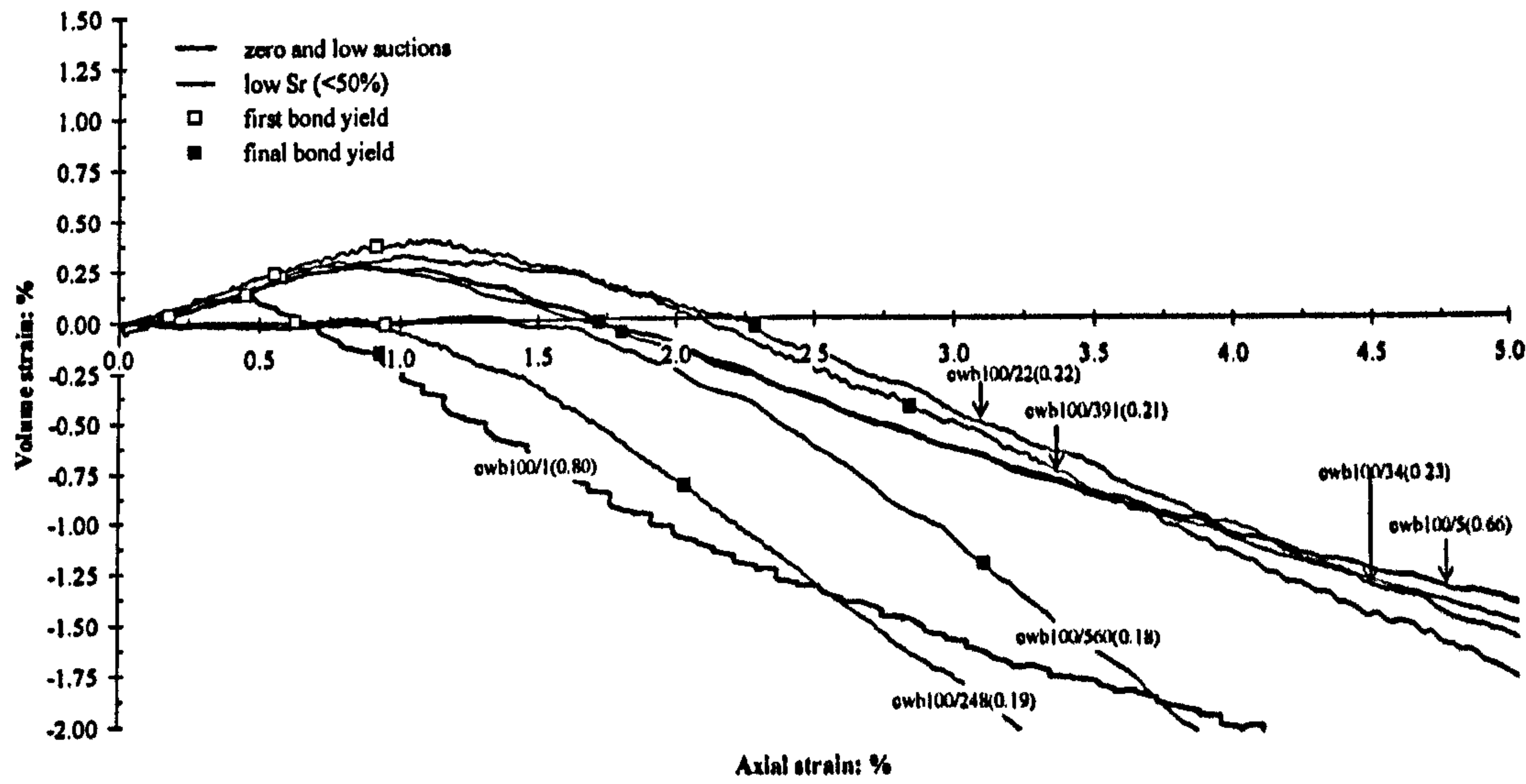
(b)

Figure 7.22: Mean net stress of 50kPa (a) stress-strain curves (b) volume strain-axial strain curves



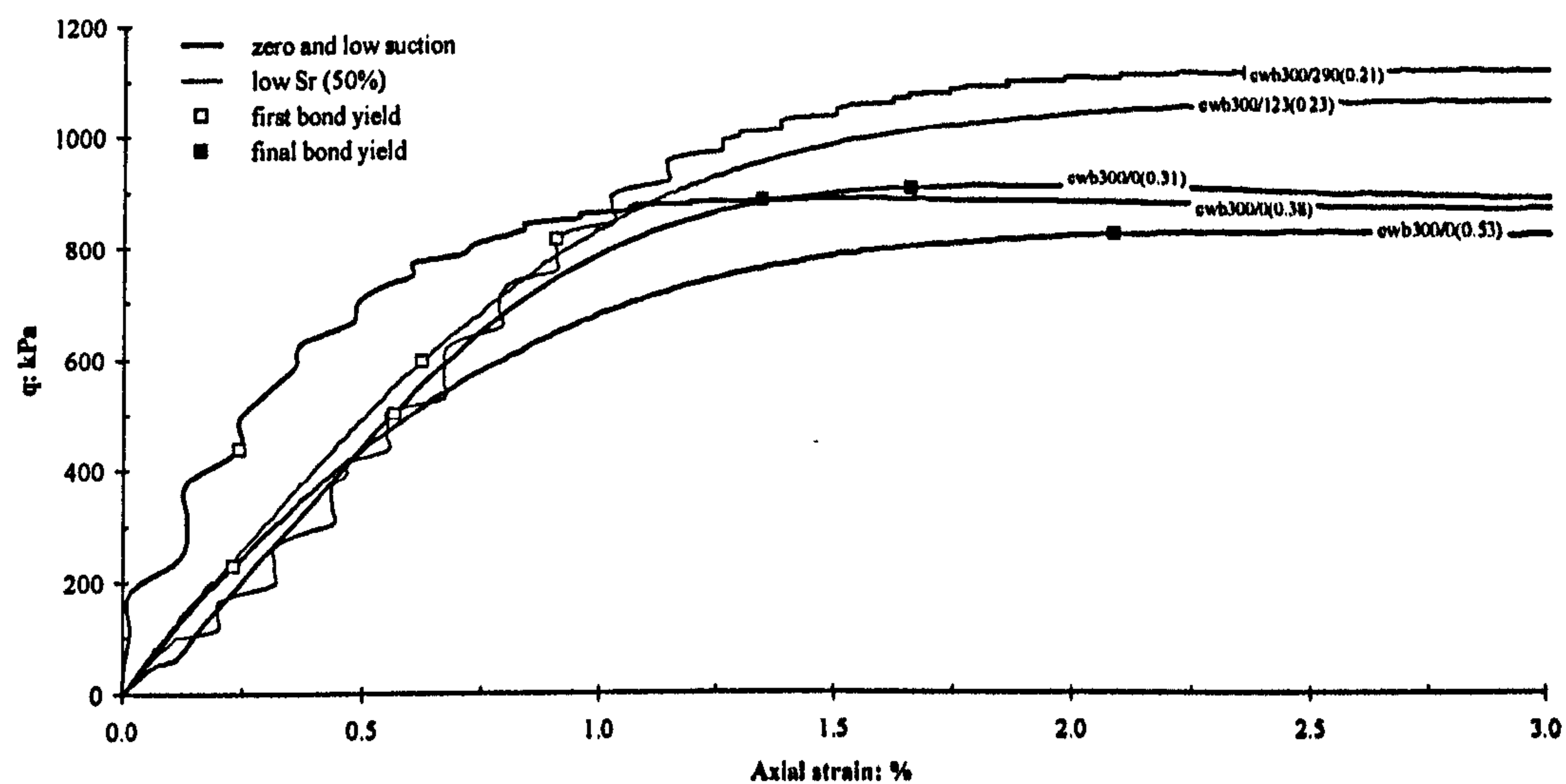


(a)

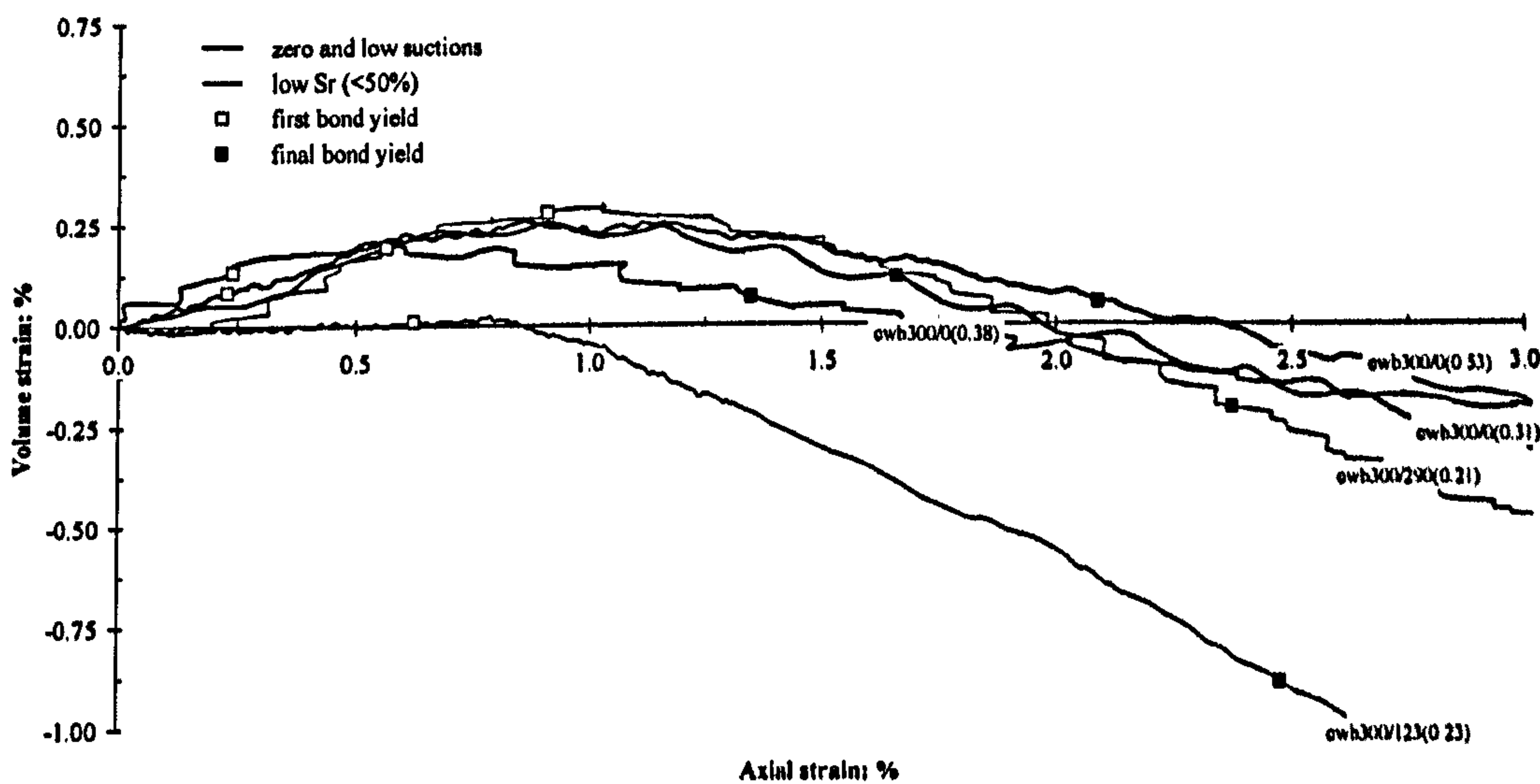


(b)

Figure 7.23: Mean net stress of 100kPa (a) stress-strain curves (b) volume strain-axial strain curves



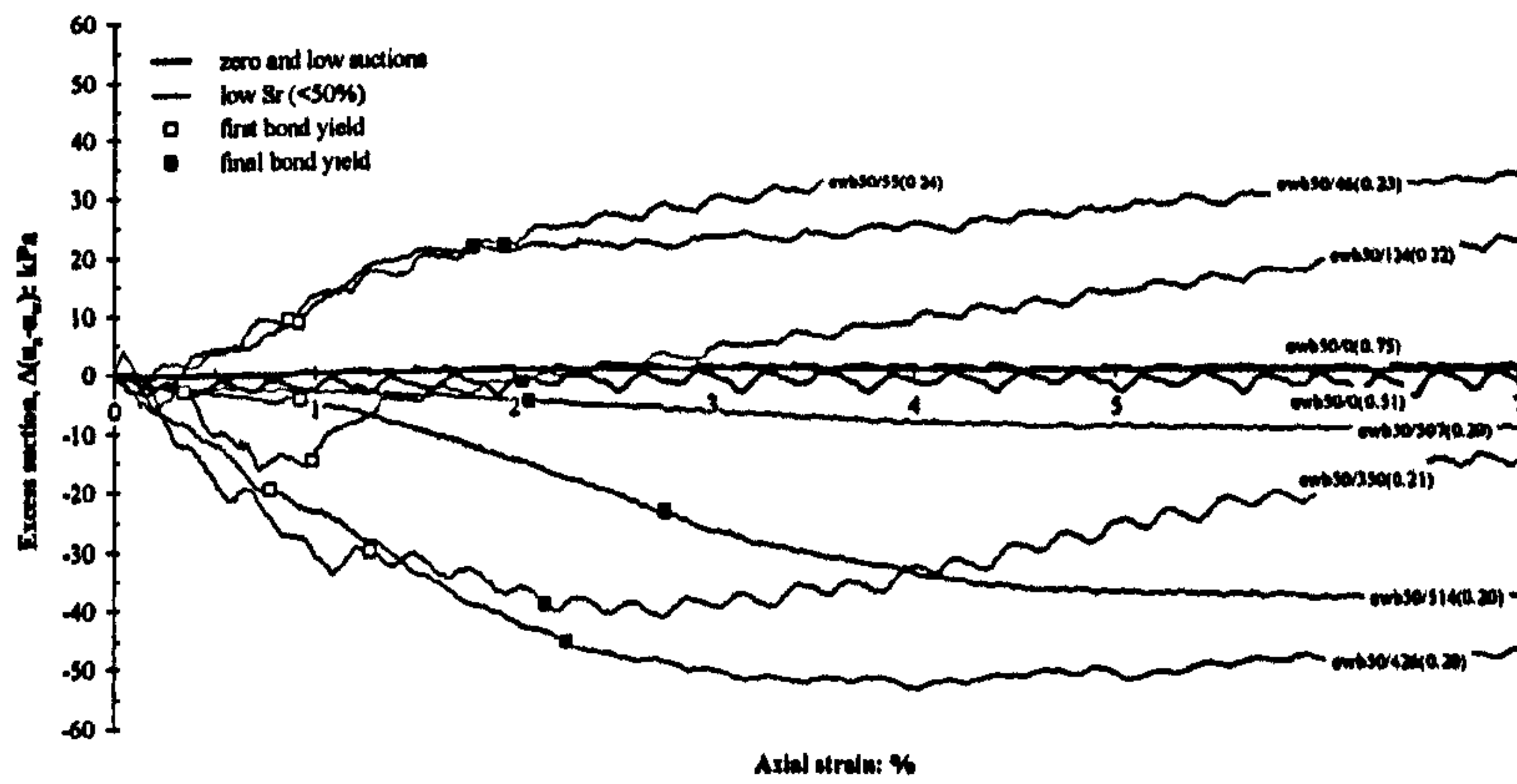
(a)



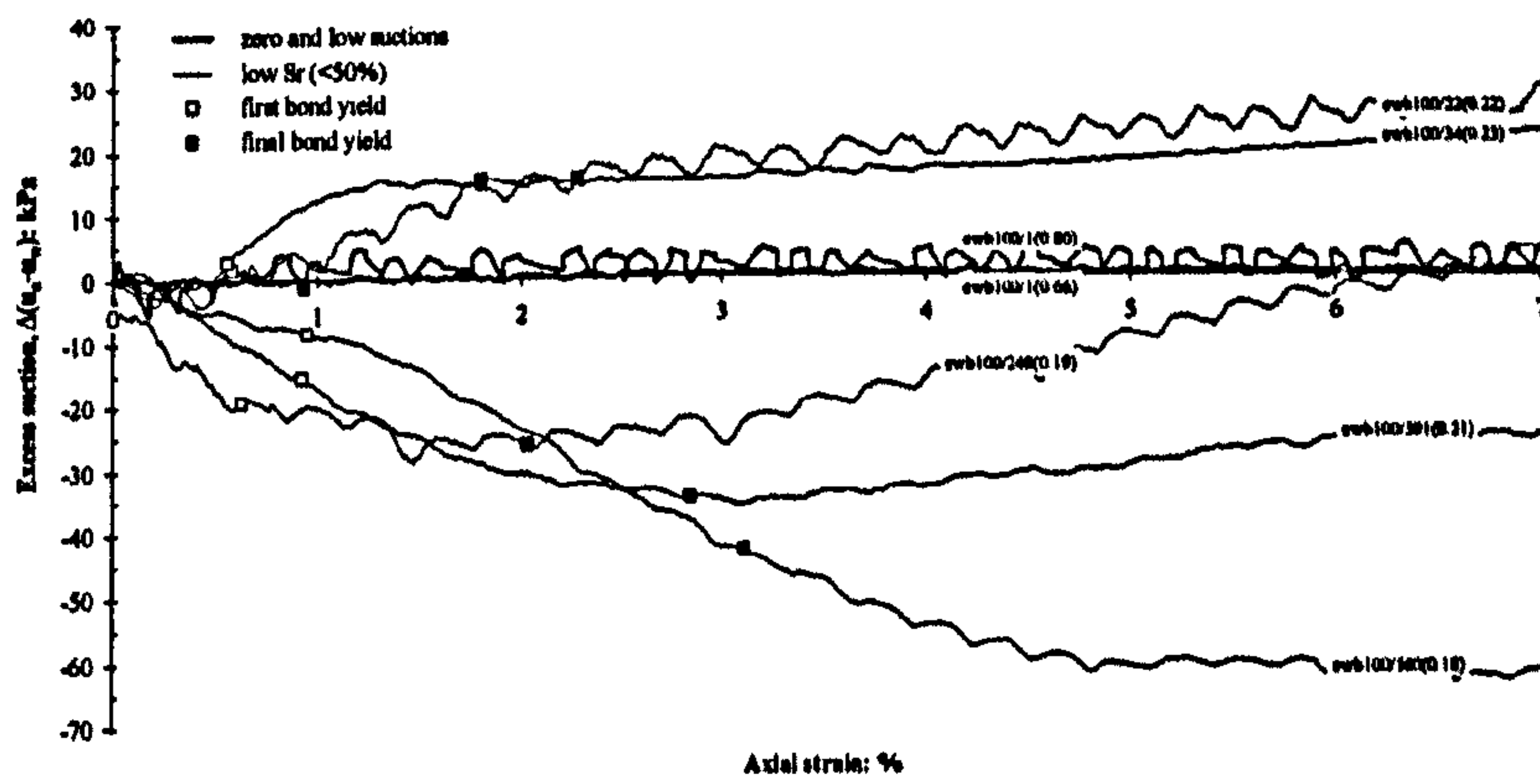
(b)

Figure 7.24: Mean net stress of 300kPa (a) stress-strain curves (b) volume strain-axial strain curves

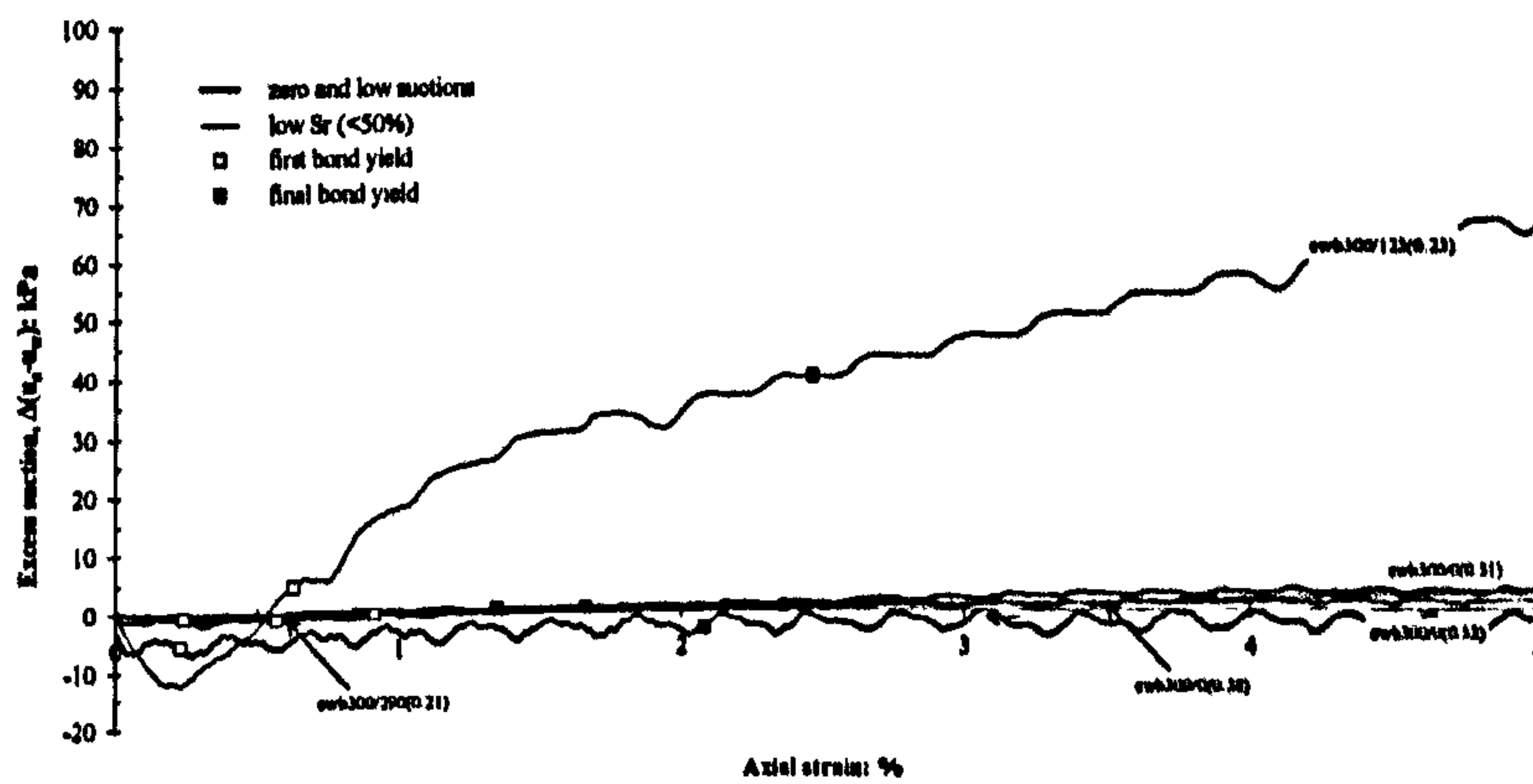




(a)



(b)



(c)

Figure 7.25: Excess suction,  $\Delta(u_a - u_w)$  against axial strain curves for samples at mean net stress,  $p - u_a$  (a) 50kPa (b) 100kPa (c) 300kPa

generally coincides with (or are close to) points of change of slope in the suction response. However for higher suction tests (cwb50/514 in Figure 7.25a and cwb100/560 in Figure 7.25b) the yield point seems to occur just before the major change in slope.

For unsaturated tests, the initial and bond yields in  $q: (p-u_a)$  space as shown in Figure 7.26 and 7.27. Saturated tests plotted as  $q: (p-u_w)$  are also included. Both initial and final bond yield for saturated drained and undrained data are marked for comparison with the unsaturated tests at zero and low suctions. Attempts have been made to draw in bond yield surfaces for different suctions.

It can be seen in Figure 7.26, that the initial bond yield surface seems to increase linearly with the increase in mean net stress over the range of stress under consideration. While there is some scatter in the results, it can be seen that for suctions of 300kPa, the yield surface expands in size, so yield occurs at greater deviator stress. However, at suctions of 450-500kPa, the surface appears to shrink back inside the surface defined for 300kPa.

It can also be seen that the data points from drained and undrained tests seem to show disagreement at higher stress level. It suggests that we should not necessarily expect agreement between saturated and unsaturated tests that follow different stress paths and have different volume change responses. The initial bond yield surface for 500kPa (represented by a dotted line) is close to the initial bond yield surface for  $(u_a-u_w)$  of 100kPa. The position of initial yield surface  $(u_a-u_w)$  of 400kPa is slightly above the yield surface for  $(u_a-u_w)$  of 500kPa.

The final bond yield surfaces for unsaturated samples in shown in Figure 7.27. A similar picture can be seen that the bond yield increases linearly with the increase in mean net stress. The data points represent the unsaturated tests at zero suctions are located slightly above the final yield surface for saturated tests. Therefore, it is better to delineate a separate final yield surface to represent the saturated and unsaturated points (zero suction). The final bond yield surface for  $(u_a-u_w)$  of



100kPa, 200kPa and 300kPa were quite close to each other. These three surfaces also showed a slight deviation upwards with increasing mean net stress. As the matric suction increases up to 400kPa and 500kPa, the yield surface drops back between the yield surfaces for  $(u_a - u_w)$  of 100kPa and 200kPa (Figure 7.27). The position of the final yield surface for  $(u_a - u_w)$  of 400kPa and 500kPa are very close together. Therefore, this picture for final yield shows the same trends as for initial yield.

### 7.3 THE CRITICAL STATE FOR UNSATURATED BONDED SOIL

#### 7.3.1 The Critical State

Frameworks for critical state for unsaturated soil mechanics have been proposed by a number of researchers and comparison with saturated soil mechanics has been a common practice (Alonso et al. 1990; Toll 1990; Wheeler and Sivakumar 1995; Wang et al. 2002; Toll and Ong 2003). The definition of a critical state is a state where further shearing continues without a change in stress or in volume of the soil. It is beyond the scope of this work to consider a full elasto-plastic model for the bonded soil tested. Instead the work considers the stress ratios and volumetric and water content conditions at the ultimate (critical) state.

For an unsaturated soil, the critical state cannot be expressed in terms of effective stress. Therefore, the results will be considered in terms of separate stress state variables, mean net stress  $(p - u_a)$ , suction  $(u_a - u_w)$  and deviator stress,  $q$ .

As described by Toll (1990), an initial simple approach can be adopted in order to verify the saturated critical state and to confirm the variables used. This can be done by examining the samples with zero and low suction values as at this state an approximation to equivalent effective stress can be applied. For low suction tests, the difference between  $(p - u_a)$  and  $(p - u_w)$  is small and comparison can be made

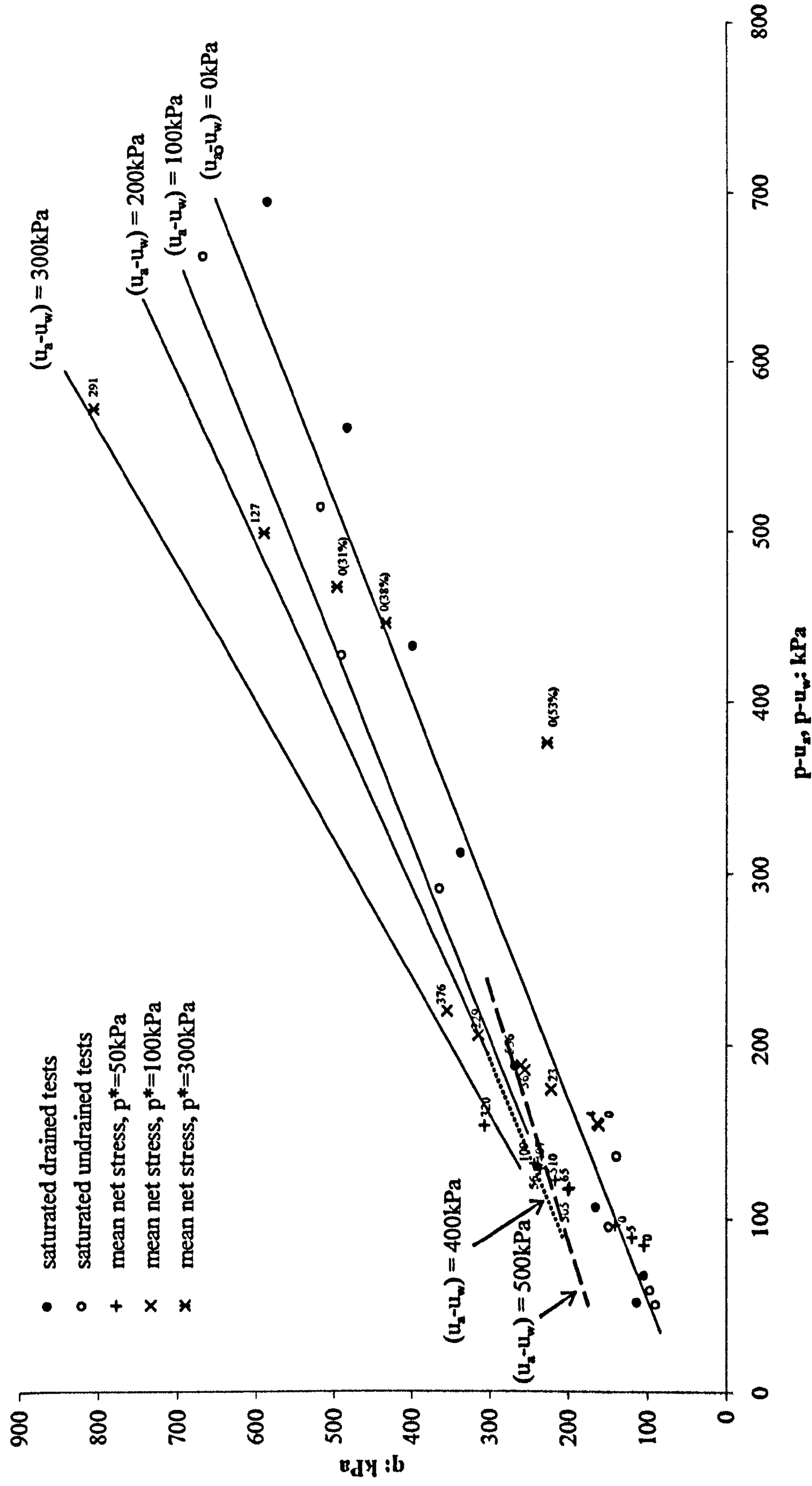


**Figure 7.26: Initial bond yield surface for unsaturated samples**



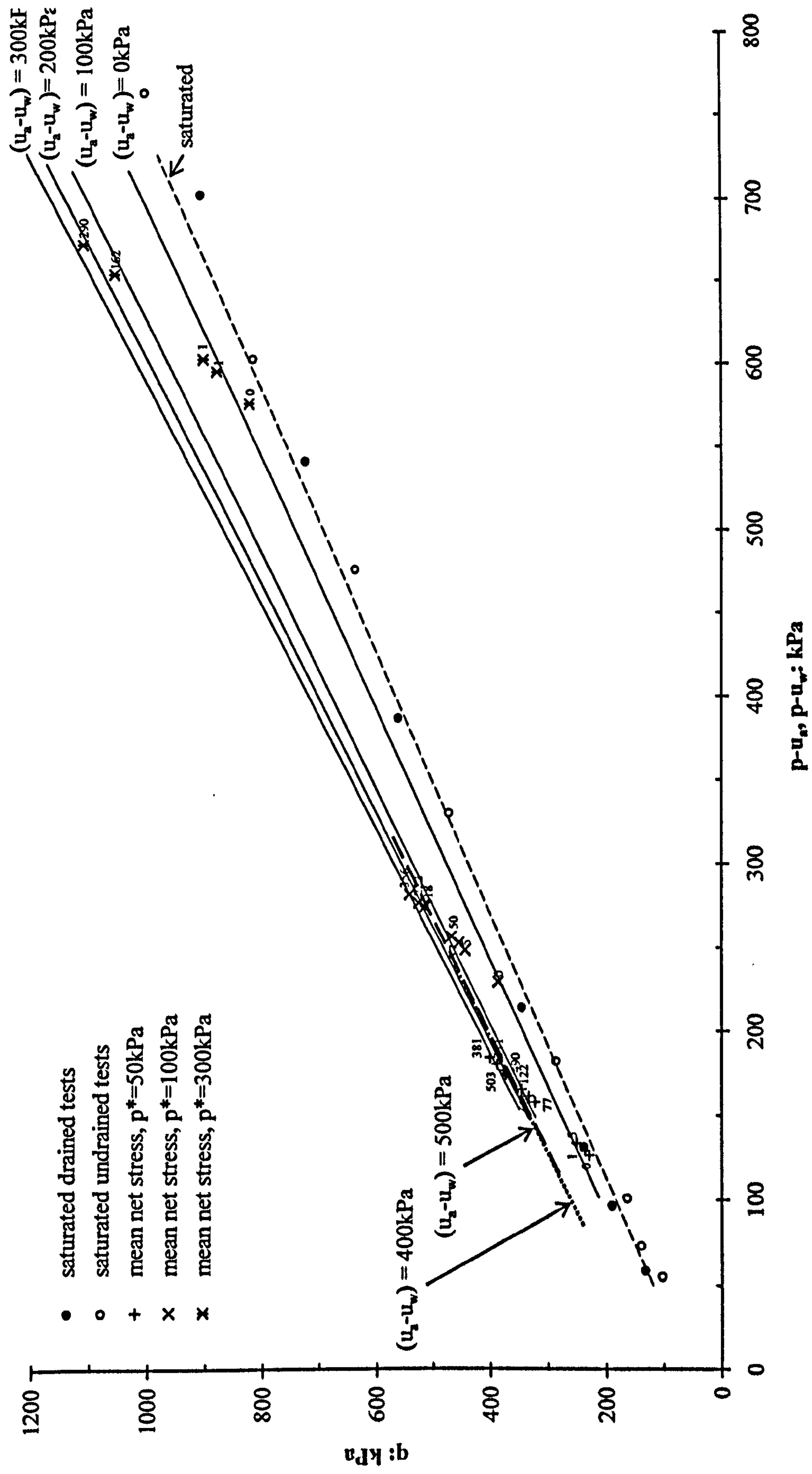


Figure 7.27: Final bond yield surface for the unsaturated samples

between saturated behaviour (expressed in terms of  $p-u_w$ ) and unsaturated behaviour (expressed in  $p-u_a$ ). The plots of  $q$  against  $(p-u_a)$  and  $(p-u_w)$  for cwb50/0(0.75), cwb100/0(0.80) and cwb300/0(0.53) are shown in Figure 7.28. It is seen that the difference between the  $p-u_a$  and  $p-u_w$  is very small.

A true critical state was not achieved in the unsaturated tests as many of the samples had a tendency to continue to dilate up to the end of shearing at large strain. For samples with zero and low suction sheared under mean net stress of 50kPa, the stress-strain and volume strain showed a slight continued drop up to the end of shearing (Figure 7.29a and Figure 7.29b). A similar behaviour can also be seen in samples sheared under mean net stress of 100kPa and 300kPa as shown in Figure 7.30 (a – b) and Figure 7.31 (a – b). In Figure 7.30b, the volume strain curves for samples sheared under mean net stress of 100kPa seem to achieve the critical state although the stress-strain curves shown in Figure 7.30a show that the deviator stress continued to decrease slightly even up to large strain. In all tests, it can be seen that the rate of change of the variables generally decrease towards the end of test. Toll and Ong (2003) noted that it was difficult to define a true critical state for bonded or dense materials as they often fail through the development of distinct shear surfaces which will affect the results. In order to define the critical state more consistently, the same approach used in identifying critical state for saturated samples was also adopted for unsaturated samples.

The critical state for the unsaturated tests was defined based on the assessment on the specific volume paths in  $v - (p-u_w)$  space. The critical state for drained and undrained saturated tests at similar stress levels was also plotted in  $v - p'$  for comparison (Figure 7.32). Assessment of  $v - (p-u_w)$  curves for the unsaturated samples with zero and low suctions, show that all samples showed initial compression behaviour with increasing mean net stress before changing to dilatant behaviour (Figure 7.32). The critical state for unsaturated tests was also located at a point where a “discontinuity” could be seen on the dilatant portion. It was believed that this point of “discontinuity” was the onset of strain localisation. Table



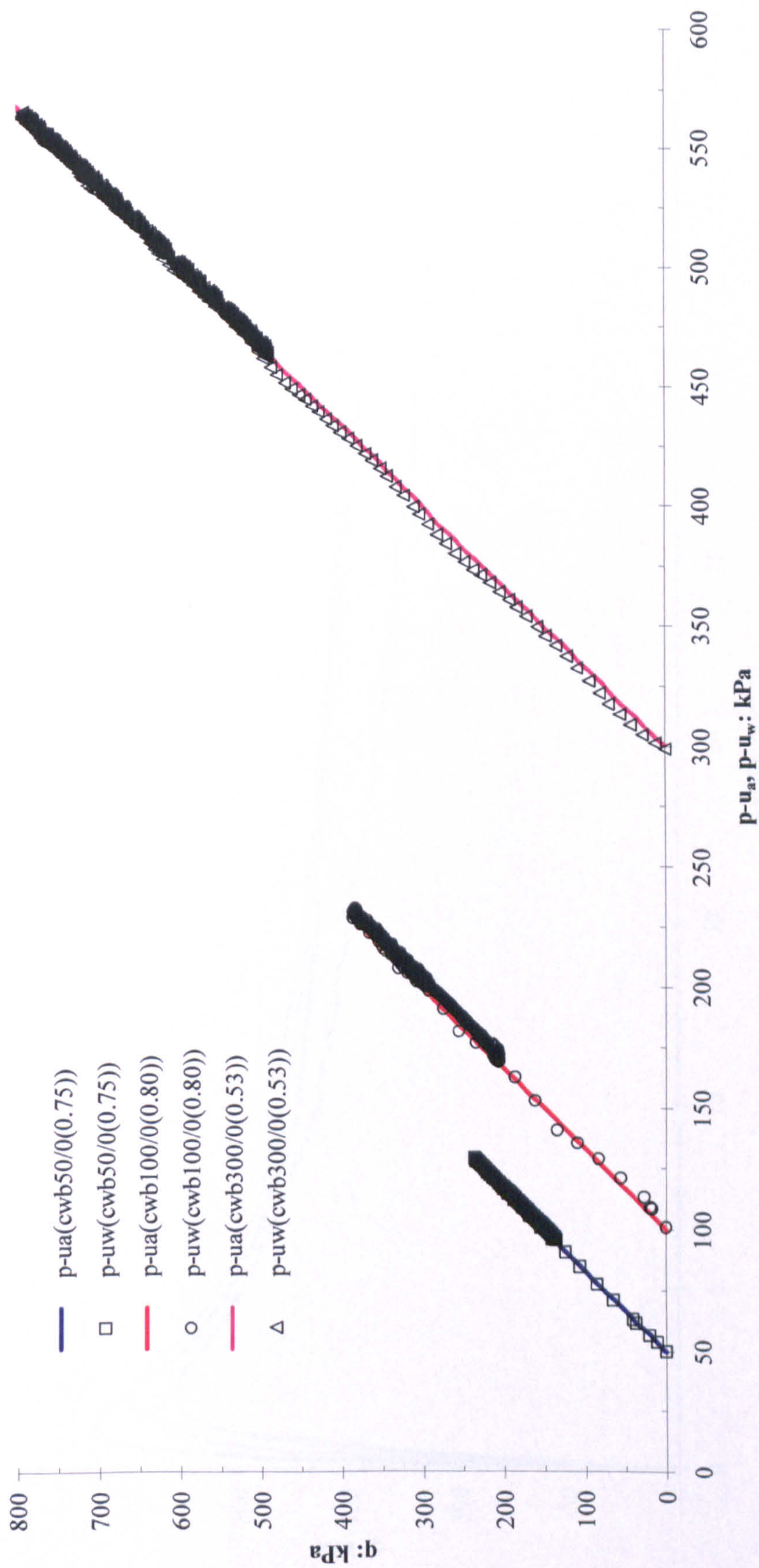


Figure 7.28: Stress paths for unsaturated samples with zero suction values



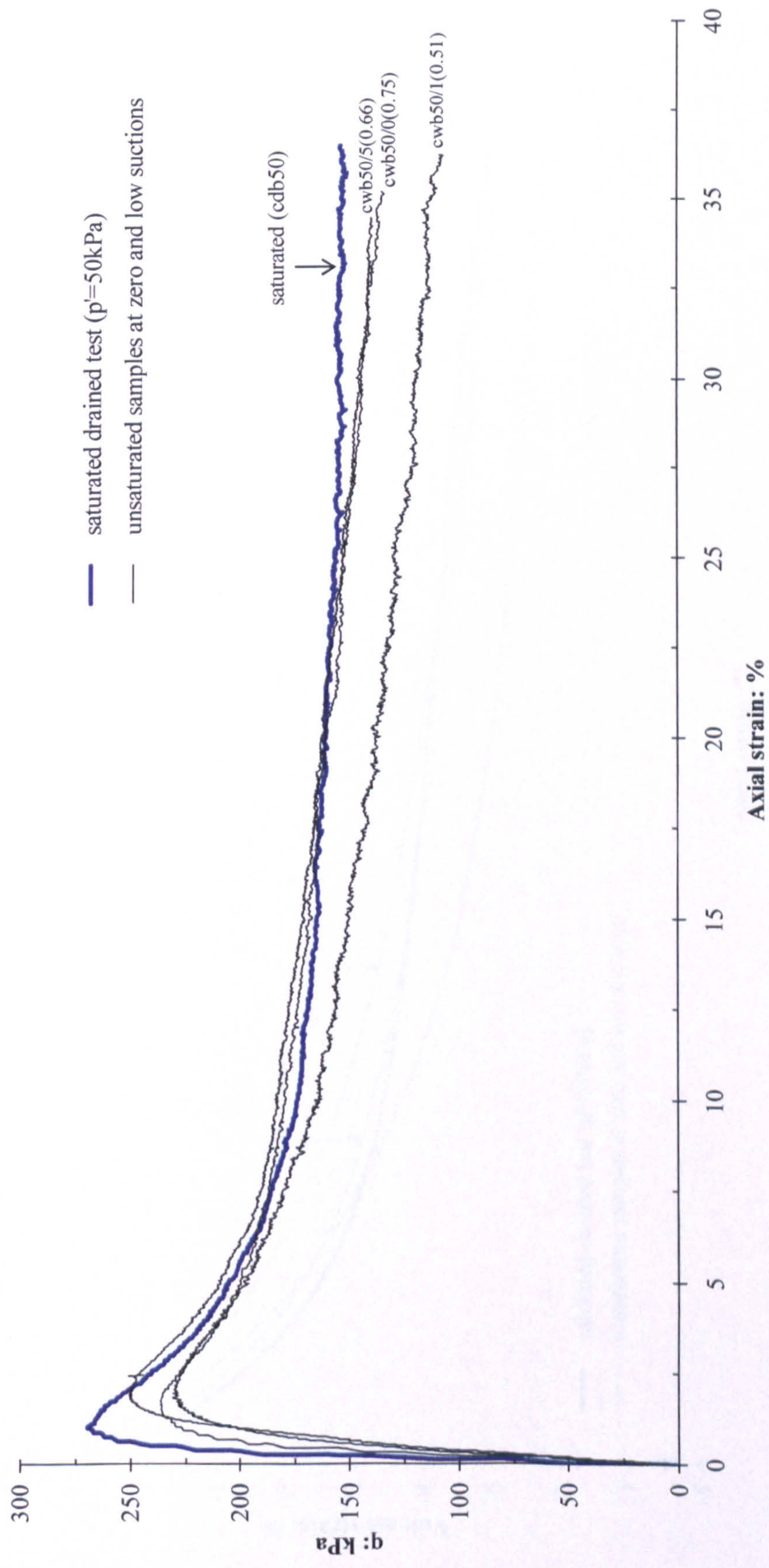


Figure 7.29a: Stress-strain curves for unsaturated samples of cwb50 with zero and low suction values



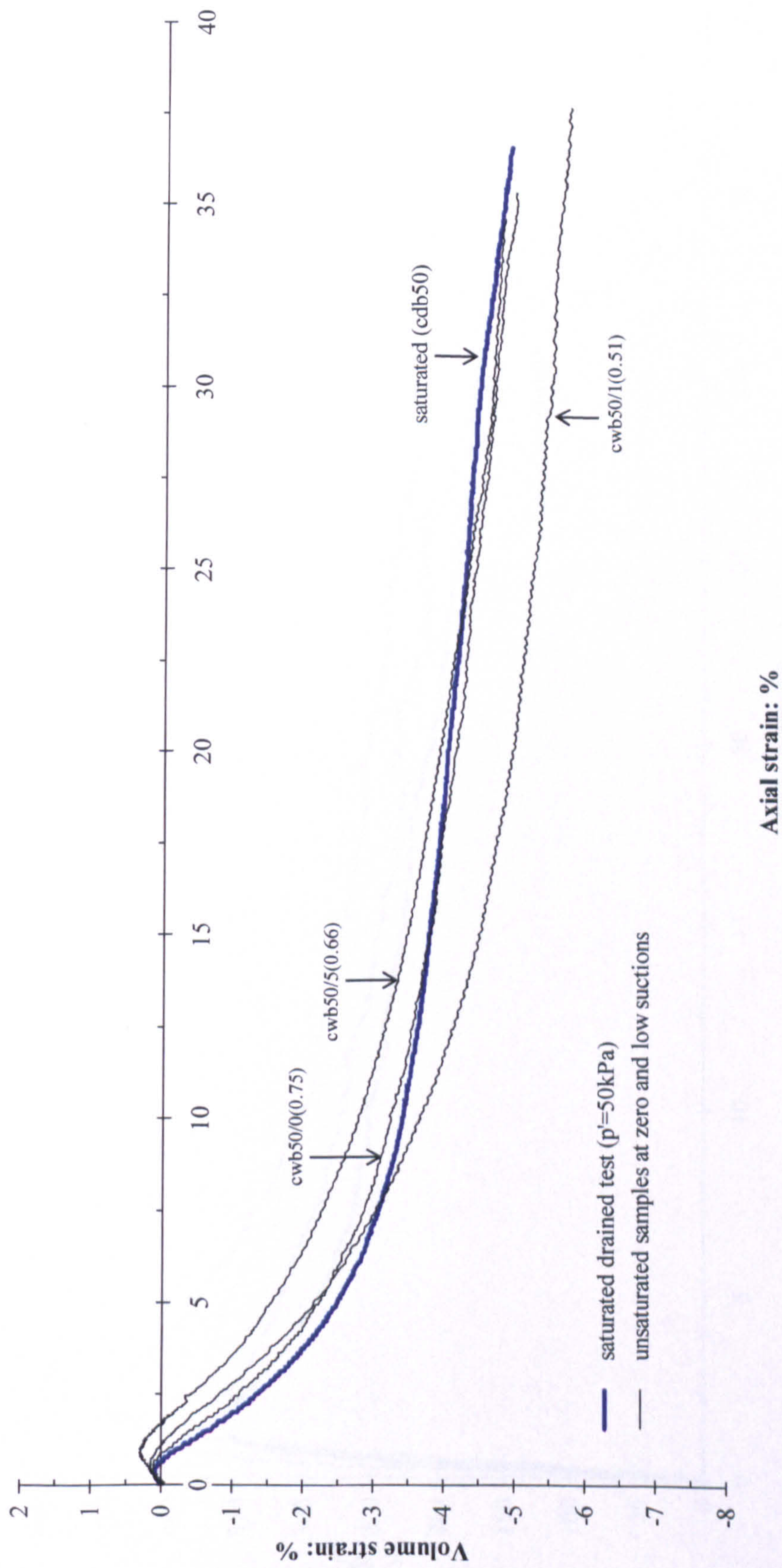


Figure 7.29b: Volume strain curves for unsaturated samples of cwb50 with zero and low suction values



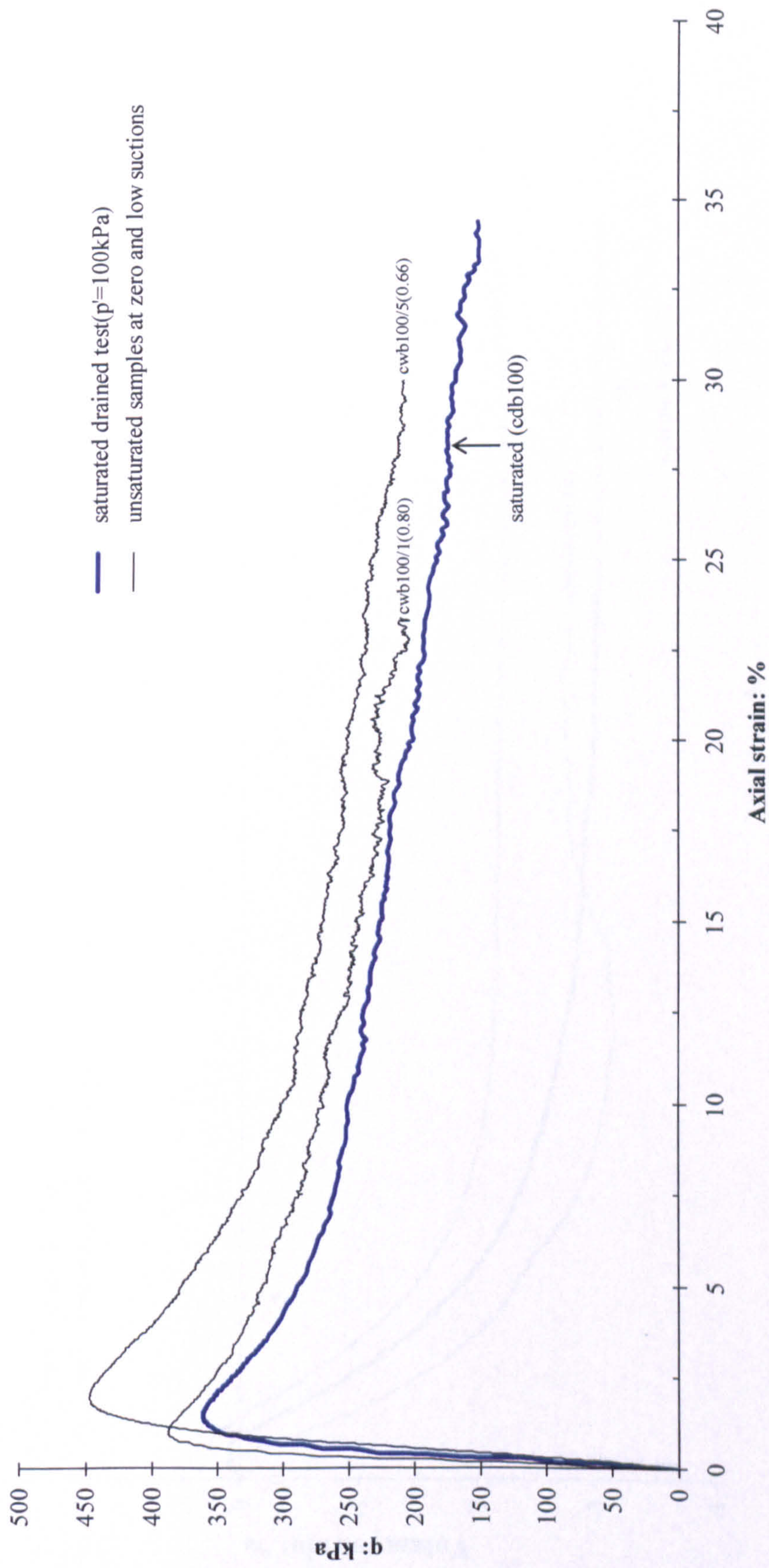


Figure 7.30a: Stress-strain curves for unsaturated samples of cwb100 with zero and low suction values



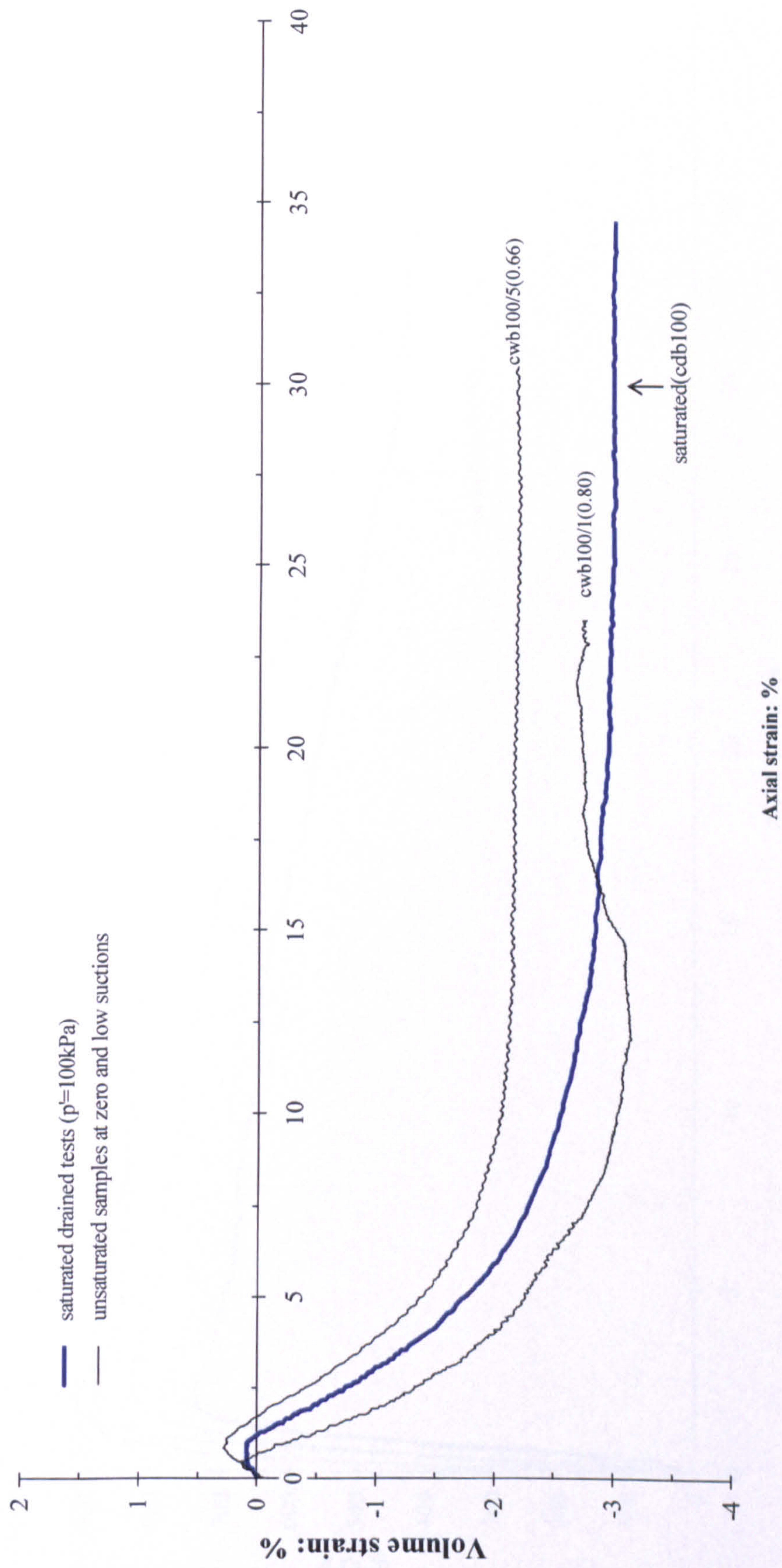


Figure 7.30b: Volume strain curves for unsaturated samples of cwb100 with zero and low suction values



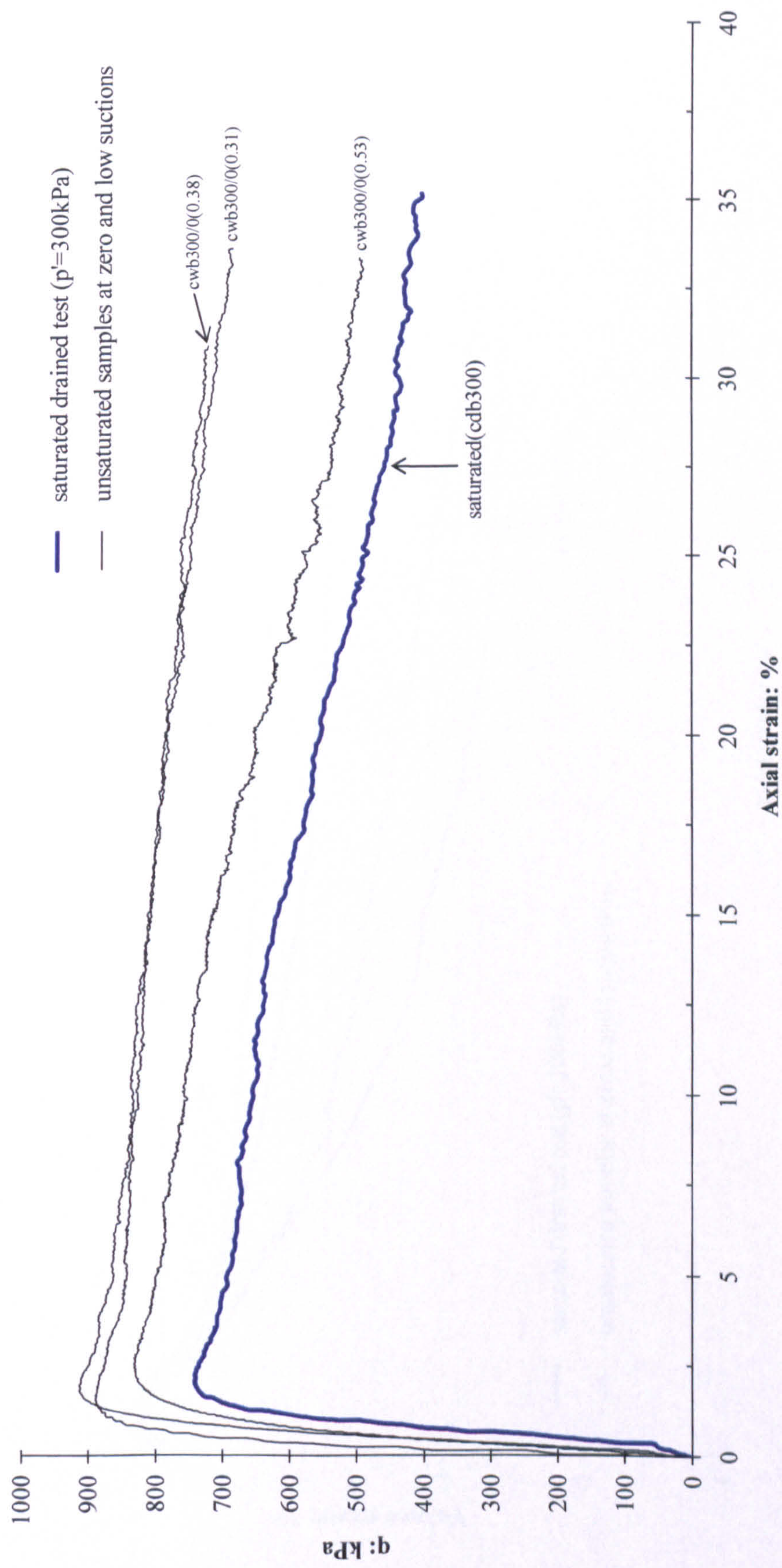


Figure 7.31a: Stress-strain curves for unsaturated samples of cwb300 with zero and low suction values



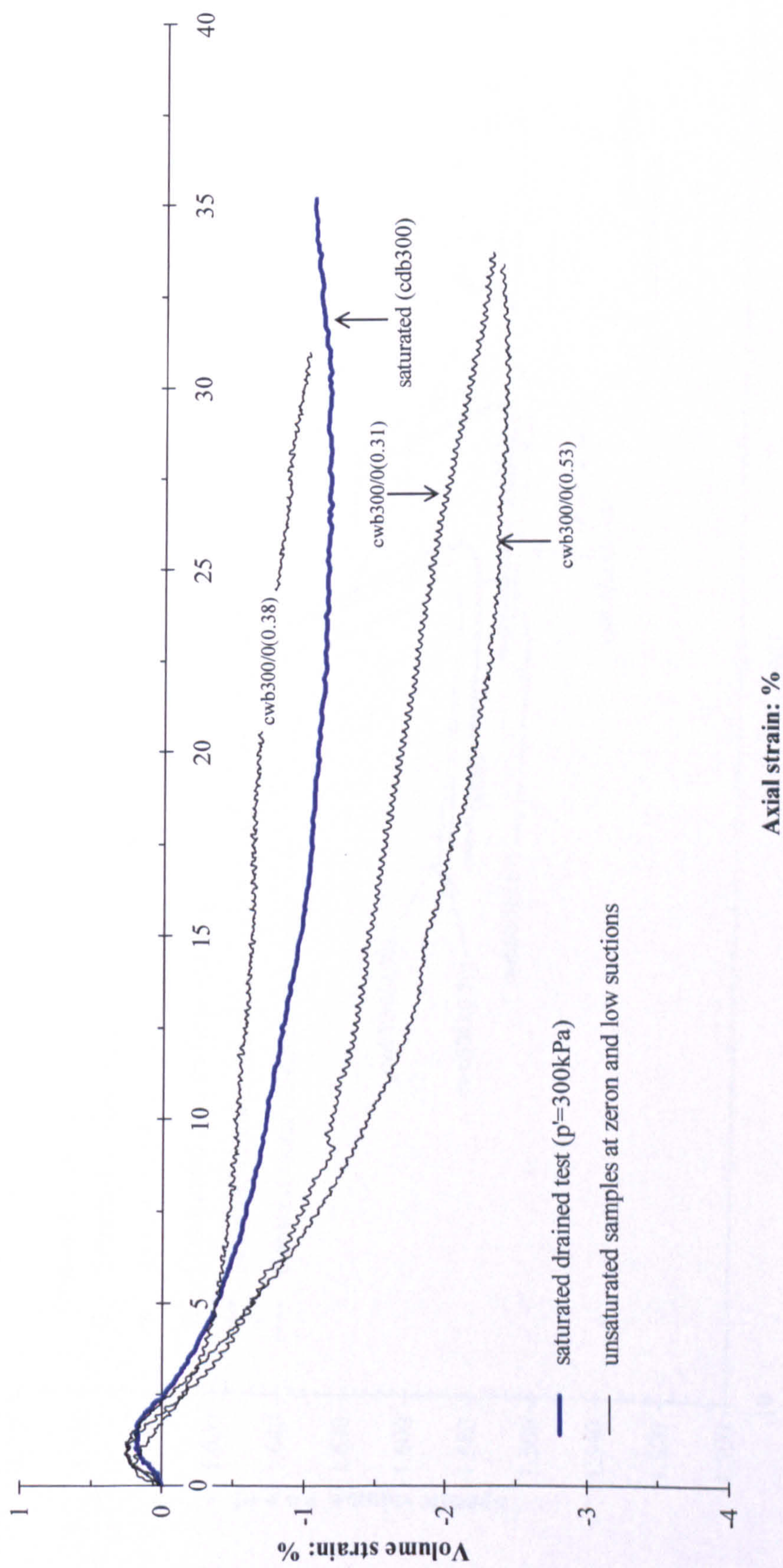


Figure 7.31b: Volume strain curves for unsaturated samples of cwb300 with zero and low suction values



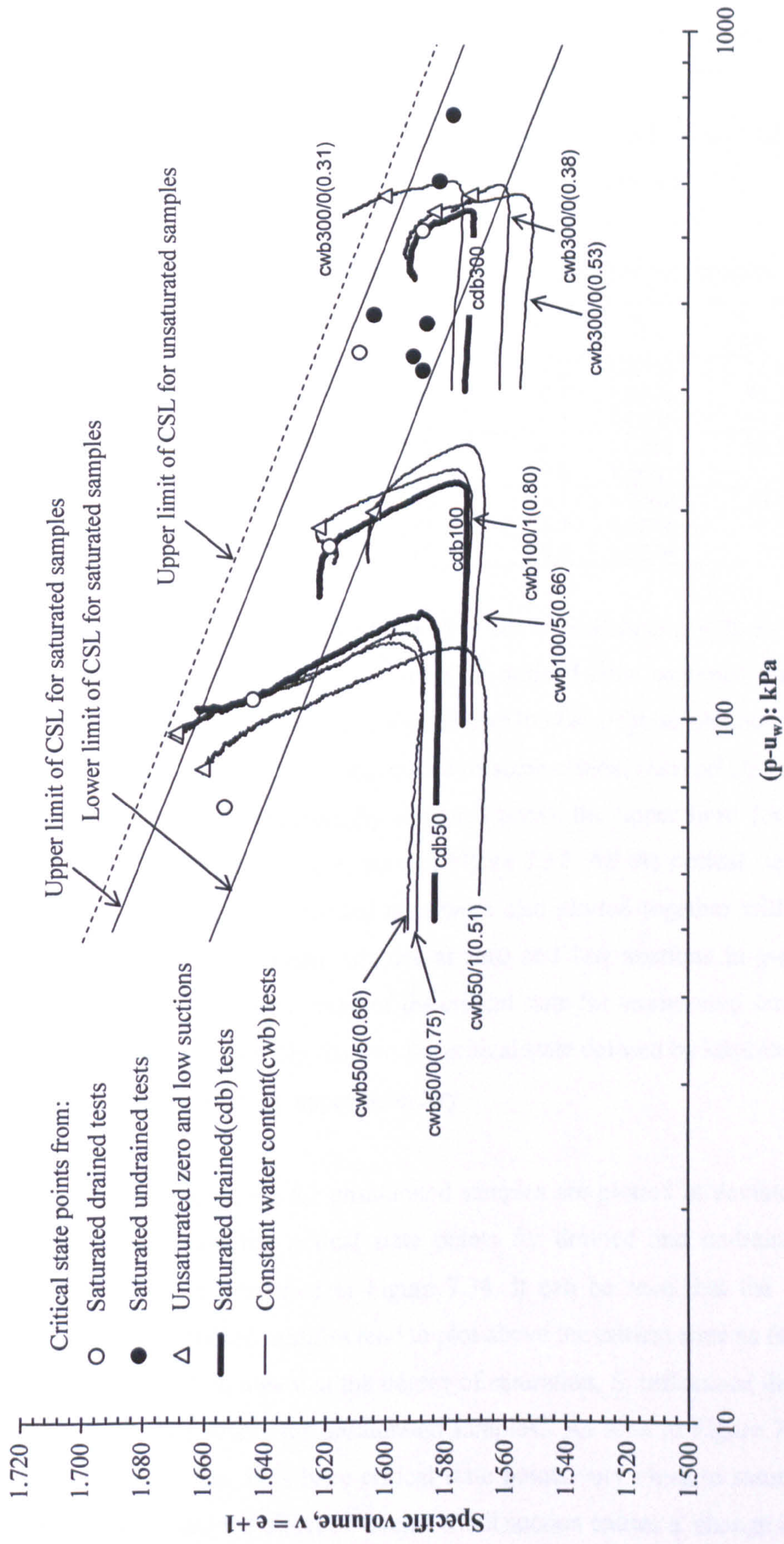


Figure 7.32: Paths followed by saturated and unsaturated samples in  $v$ -( $p-u_w$ ) space



2 shows the values of stress state variables ( $q$ ,  $p-u_w$  and  $u_a-u_w$ ) and phase state variables ( $u$ ,  $w$ ,  $S_r$ ) selected using the “discontinuity” approach.

Table 7.2: The values of stress state variables and phase state variables

Tests	$q$ (kPa)	$p-u_w$ (kPa)	$u_a-u_w$ (kPa)	$v$	$w$ (%)	$S_r$ (%)
cwb50/0(0.75)	137	96	1.2	1.6705	17.8	70.7
cwb50/5(0.66)	141	97	6.1	1.6703	12.1	47.9
cwb50/1(0.51)	108	86	0.1	1.6616	11.6	46.6
cwb100/1(0.80)	269	190	4.1	1.6235	18.1	77.4
cwb100/5(0.66)	298	200	5.5	1.6051	17.2	75.2
cwb300/0(0.53)	735	545	1.1	1.5846	10.6	48.4
cwb300/0(0.38)	825	577	3.3	1.5724	8.7	40.3
cwb300/0(0.31)	821	575	5.4	1.6014	7.0	31.3

In  $v - (p-u_w)$  space (Figure 7.32), most of the critical state points for unsaturated tests fall below the upper limit of the CSL defined from saturated tests but some tests (cwb50/0(0.75), cwb50/5(0.66) and cwb300/0(0.31)) do plot above this limit. In order to accommodate the occurrence of some critical state points located above the upper limit CSL (defined by saturated tests), the upper limit for unsaturated tests was moved slightly up as seen in Figure 7.32. All the critical state points for drained and undrained saturated tests were also plotted together with the critical state points for unsaturated samples at zero and low suctions in  $v-(p-u_w)$  space (Figure 7.33). The overall trend of the critical state for unsaturated samples at zero and low suctions generally fits into the critical state defined by saturated tests, with a small movement of the upper boundary.

The critical state points for unsaturated samples are plotted in deviatoric stress,  $q$  against  $(p-u_w)$  and the critical state points for drained and undrained saturated samples are also presented in Figure 7.34. It can be seen that the critical state points for unsaturated samples tend to plot above the critical state as defined by the saturated tests. It is seen that the degree of saturation,  $S_r$  influenced the distance of the critical state points for unsaturated samples. As seen in Figure 7.34, samples with  $S_r$  higher than 50% have critical state points very close to saturated CSL. It also suggests that the effect of even a small suction causes a change in the critical

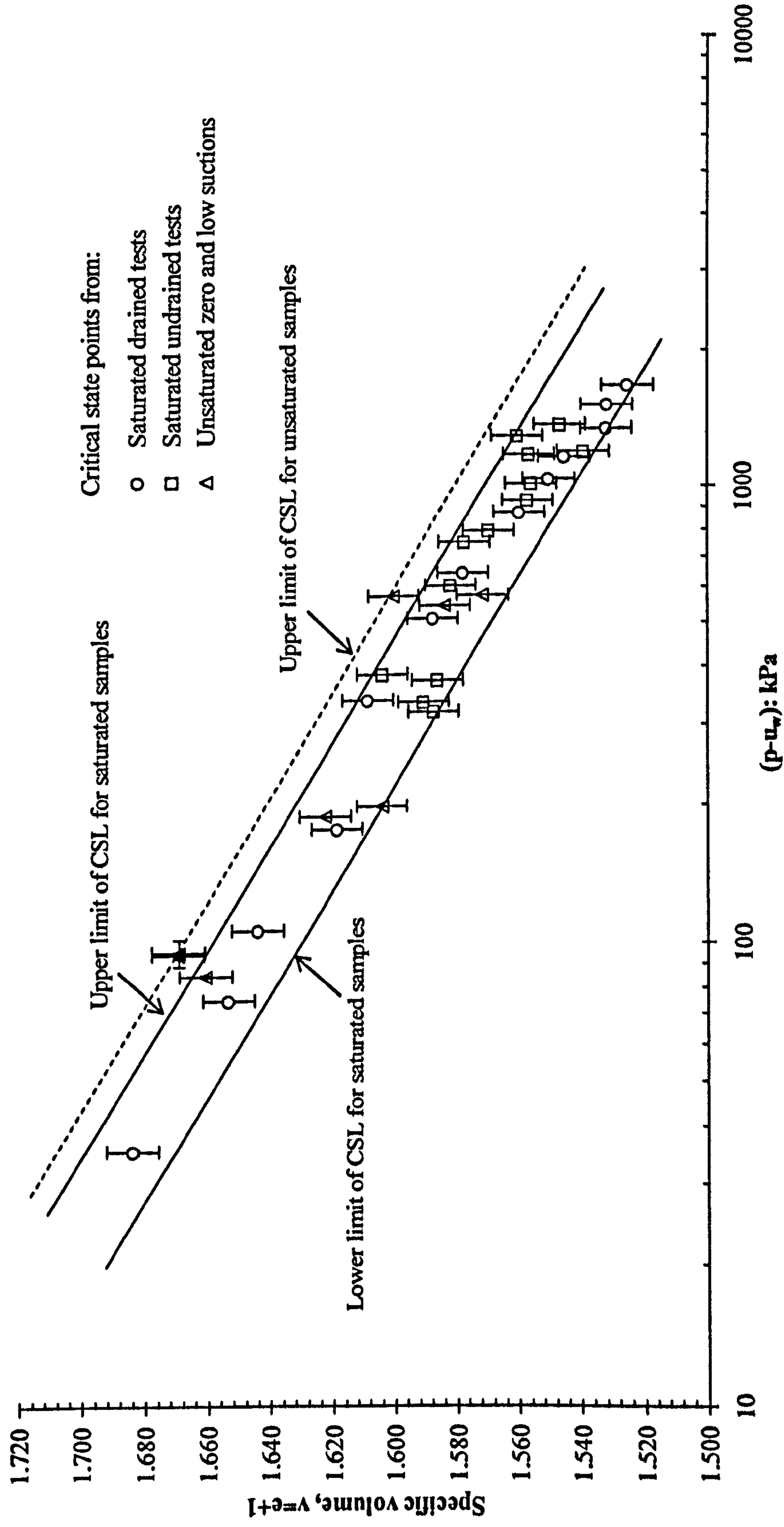


Figure 7.33: The critical state points for saturated and unsaturated samples with zero and low suctions (error bars included)



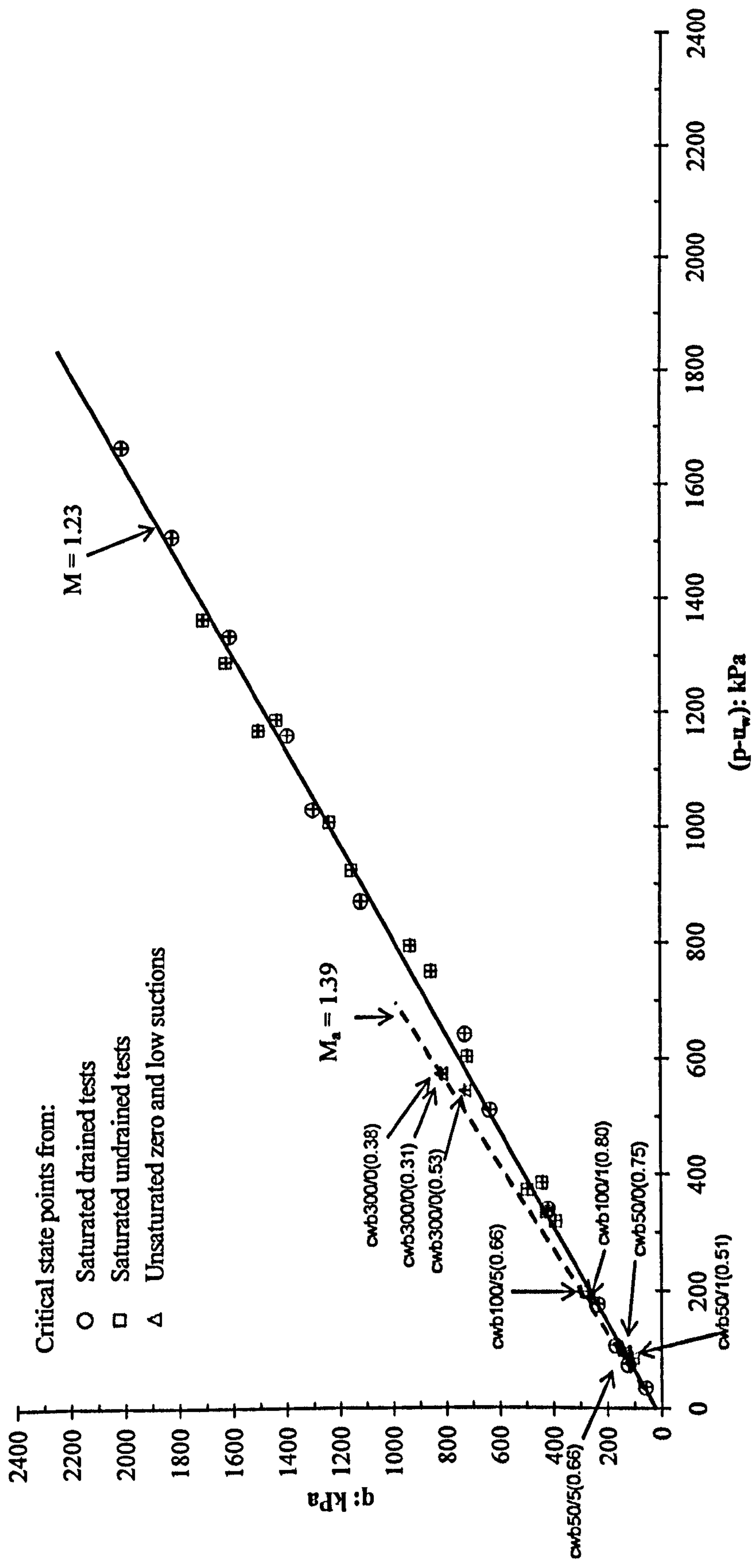


Figure 7.34: Critical state lines for bonded saturated and unsaturated samples (error bars included)

state line probably by the suction contributing to supporting aggregations or grouping of particles.

### 7.3.2 Critical State Stress Ratios

As mentioned in Chapter 2, Fredlund et al. (1978) proposed the shear strength equation for unsaturated soils (Equation 7.1). They suggested that the friction angle with respect to mean net stress,  $\phi^a$  is the same as the friction angle with respect to effective stress,  $\phi'$ . In addition, Fredlund and Rahardjo (1993) also mentioned that the friction angle  $\phi^a$  appears to be essentially equal to the effective angle of internal friction obtained from shear strength tests on saturated specimens. This has been argued by Toll (2000) emphasising that  $\phi^a$  is not always the same as  $\phi'$ . He recommended the use of a general form of the equation represented by shear strength equation proposed by Fredlund et al. (1978).

$$\tau = c' + (\sigma - u_a) \tan \phi^a + (u_a - u_w) \tan \phi^b \quad \dots (7.1)$$

where,

- $\tau$  = shear strength
- $c'$  = effective cohesion of the soil
- $\sigma$  = total stress
- $u_a$  = pore air pressure
- $u_w$  = pore water pressure
- $\phi^a$  = angle of internal friction associated the net normal stress state variable,  $(\sigma - u_a)$
- $\phi^b$  = angle of internal friction associated with matric suction  $(u_a - u_w)$

Toll (1990) examined the concept of critical state for unsaturated compacted lateritic gravel from Kenya. The results of the triaxial tests were analysed in terms of the critical state stress ratios of  $M_a$  (critical state with respect to mean net stress,  $p - u_a$ ) and  $M_b$  (critical state with respect to matric suction,  $u_a - u_w$ ).



For the particular states of the Critical State and taking the cohesion intercept,  $c'$  to be zero for critical state conditions (Atkinson 1993), Equation 7.1 can be rewritten as:

$$\tau_c = (\sigma - u_a) \tan(\varphi^a)_c + (u_a - u_w) \tan(\varphi^b)_c \quad \dots (7.2)$$

where,

$(\varphi^a)_c$  = critical state angle of friction with respect to mean net stress,

$(\sigma - u_a)$

$(\varphi^b)_c$  = critical state angle of friction with respect to matric suction,

$(u_a - u_w)$

Toll (1990) and Toll and Ong (2003) have expressed the equation in more general stress variables as:

$$q = M_a(p - u_a) + M_b(u_a - u_w) \quad \dots (7.3)$$

where,

$q$  = deviator stress,  $(\sigma_1 - \sigma_3)$

$p$  = mean total stress,  $(\sigma_1 + \sigma_2 + \sigma_3)/3$

$M_a$  = critical state stress ratio with respect to mean net stress  $(p - u_a)$

$M_b$  = critical state stress ratio with respect to matric suction  $(u_a - u_w)$

In this study, a similar approach was applied to the results of the unsaturated tests. The data was analysed separately in order to examine the stress ratio due to net stress,  $M_a$  and due to matric suction,  $M_b$ .

### 7.3.2.1 Mean net stress component, $M_a$

In order to estimate the stress ratio due to mean net stress,  $M_a$  the cwb tests at low suctions have been considered. The critical state values were defined earlier as shown in Table 7.2. Eight tests were carried out where the suction at the critical state was 6kPa or less. In the calculation of the  $M_a$ , three assumptions were made relating to the Equation 7.3.

For the cwb tests at low suctions, the  $M_b(u_a - u_w)$  term in Equation 7.3 becomes small and the  $M_a(p - u_a)$  term will be the controlling component. Therefore, if the suction is zero then:

$$M_a = \frac{q}{(p - u_a)} \quad \dots 7.4$$

However, from the cwb data the suction values are non-zero, (Table 7.2) the values could have a small effect particularly at lower values of mean net stress.

At higher degrees of saturation, the value of  $M_a$  would be equivalent to  $M_b$  (Toll 1990). This second assumption would lead to the following equation:

$$M_a = M_b = \frac{q}{(p - u_a) + (u_a - u_w)} = \frac{q}{(p - u_w)} \quad \dots 7.5$$

However, some of the values of degree of saturation are less than 50% even for the tests at low suction (Table 7.2). This assumption therefore may not be valid.

A third possible assumption is to assume that the values of  $M_b$  would be equal to  $M_s$  (the saturated critical state ratio). This assumption would lead to:

$$M_a = \frac{q - M_s(u_a - u_w)}{(p - u_a)} \quad \dots 7.6$$



Table 7.3 shows the values of  $M_a$  calculated based on these three assumptions. The range of average values for  $M_a$  is 1.38 to 1.41. These values equate to an equivalent angle of friction of  $(\varphi^a)_c$  of  $34^\circ - 35^\circ$ .

Table 7.3: The critical state values of the state variables for low suction tests

$q$ (kPa)	$p-u_w$ (kPa)	$u_a-u_w$ (kPa)	$S_r$ (%)	$M_a$ (Eq. 7.4)	$M_a$ (Eq. 7.5)	$M_a$ (Eq. 7.6)
137	96	1.2	70.7	1.42	1.39	1.39
141	97	6.1	47.9	1.50	1.45	1.46
108	86	0.1	46.6	1.44	1.42	1.42
269	190	4.1	77.4	1.35	1.34	1.34
298	200	5.5	75.2	1.46	1.37	1.38
735	545	1.1	48.4	1.25	1.25	1.25
825	577	3.3	40.3	1.43	1.42	1.42
821	575	5.4	31.3	1.43	1.41	1.42
Average				1.41	1.38	1.39

In Figure 7.34, the deviator stress,  $q$ , at critical state against mean effective stress,  $p'$  were plotted. The values for the unsaturated tests at low suction were also superimposed on the plot. It is clearly seen that the value of  $M_a$  is higher than the saturated value of  $M_s = 1.23$ , which is equivalent to  $\varphi' = 31^\circ$ . The results for the bonded soil indicate a significant different between two values. This supports the observation by Toll (2000) that we should not always assume that  $\varphi^a = \varphi'$ .

### 7.3.2.2 Suction component, $M_b$

The values of  $M_b$  were calculated by rearranging Equation 7.3. The  $M_b$  value is given by:

$$M_b = \frac{q - M_a (p - u_a)}{(u_a - u_w)} \qquad \dots 7.7$$

Based on the previous discussion about  $M_a$  values, it was sensible to use an average value of  $M_a = 1.39$  (calculated based on Equation 7.6). Then, for the cwb tests performed at higher suctions, the  $M_b$  values were calculated from Equation 7.7 by assuming a constant value of  $M_a = 1.39$ . There was a test where the value of

$M_a$  gave an apparent negative value of  $M_b$ , therefore the value of  $M_a$  had to be slightly adjusted to from 1.39 to 1.36. For the cwb tests performed at lower suctions, the individual values of  $M_a$  calculated from Equation 7.6 have been used to calculate the  $M_b$  values. Table 7.4 shows the values of  $M_a$  and  $M_b$  calculated for cwb tests at lower and higher suctions.

Table 7.4: The critical state values of the state variables for all tests

$q$ (kPa)	$p-u_w$ (kPa)	$u_a-u_w$ (kPa)	$S_r$ (%)	$M_a$	$M_b$
285	196	492.0	16.9	1.39	0.02
213	121	403.6	18.1	1.39	0.11
210	121	385.9	18.2	1.39	0.11
217	122	479.7	18.9	1.39	0.10
205	118	119.0	19.6	1.39	0.34
348	216	260.5	19.6	1.39	0.18
355	219	392.1	19.9	1.39	0.13
211	121	498.7	19.9	1.39	0.08
230	127	168.8	20.7	1.39	0.32
282	194	100.7	21.8	1.39	0.12
328	209	104.0	21.8	1.39	0.35
753	552	245.4	21.9	1.36	0.00
991	631	300.4	22.6	1.39	0.38
313	155	87.7	24.2	1.39	1.12
821	575	5.4	31.3	1.43	1.41
825	577	3.3	40.3	1.43	1.42
108	86	0.1	46.6	1.44	1.42
141	97	6.1	47.9	1.50	1.45
735	545	1.1	48.4	1.25	1.25
137	96	1.2	70.7	1.42	1.39
298	200	5.5	75.2	1.46	1.37
269	190	4.1	77.4	1.35	1.34

The values presented in Table 7.4 were plotted against degree of saturation,  $S_r$  as shown in Figure 7.35a and Figure 7.35b. It can be seen that in Figure 7.35a,  $M_b$  drops sharply at degree of saturation,  $S_r$  below 30%. The sharp drop in  $M_b$  coincides with a sharp increase in suction (Figure 7.34.b) at degree of saturation,  $S_r$  below 30%, showing a mirror image. This coincides with the sharp change in the water retention behaviour (the end of the desaturation zone).



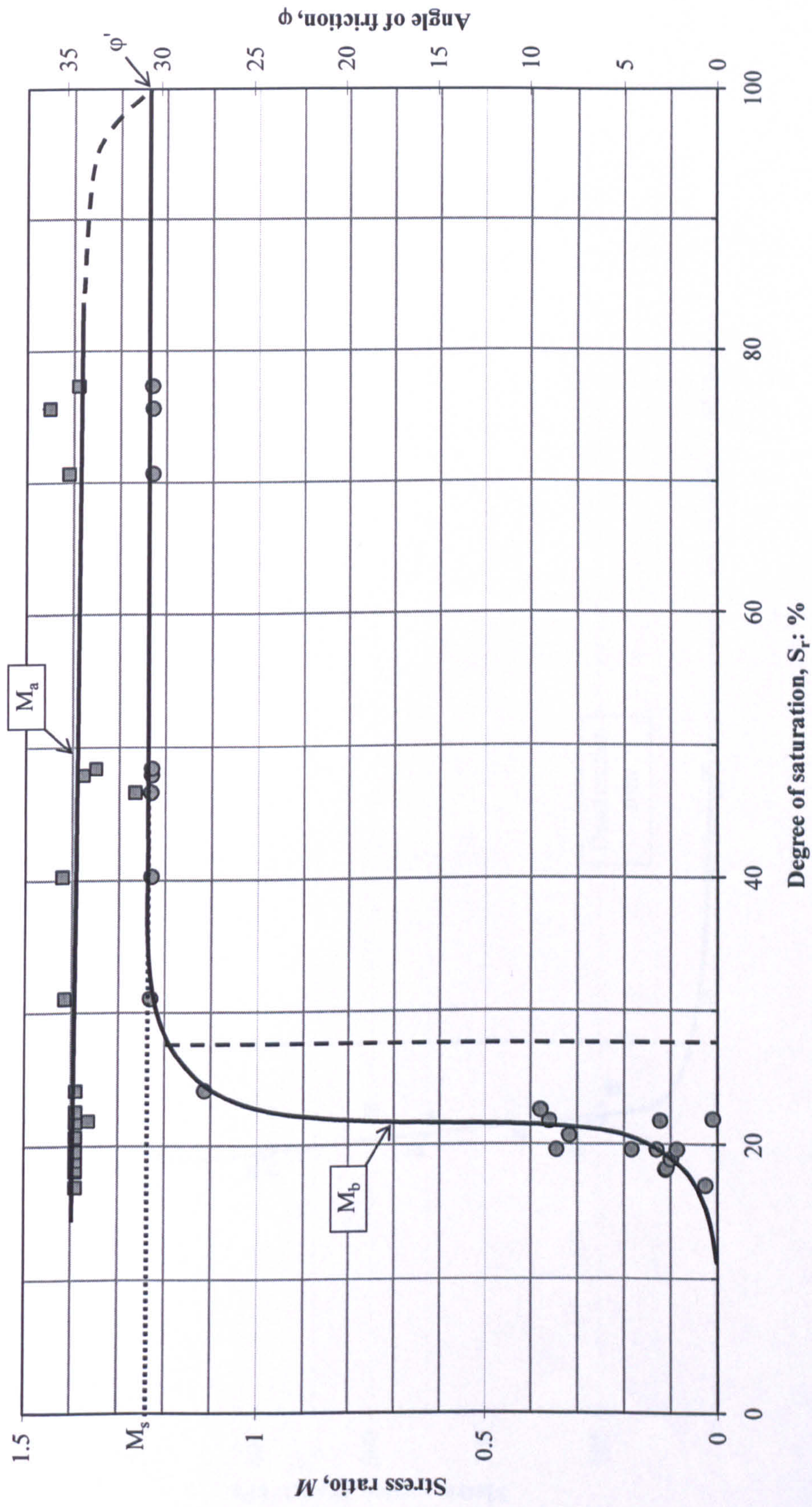


Figure 7.35a: Variation in critical state stress ratios with degree of saturation



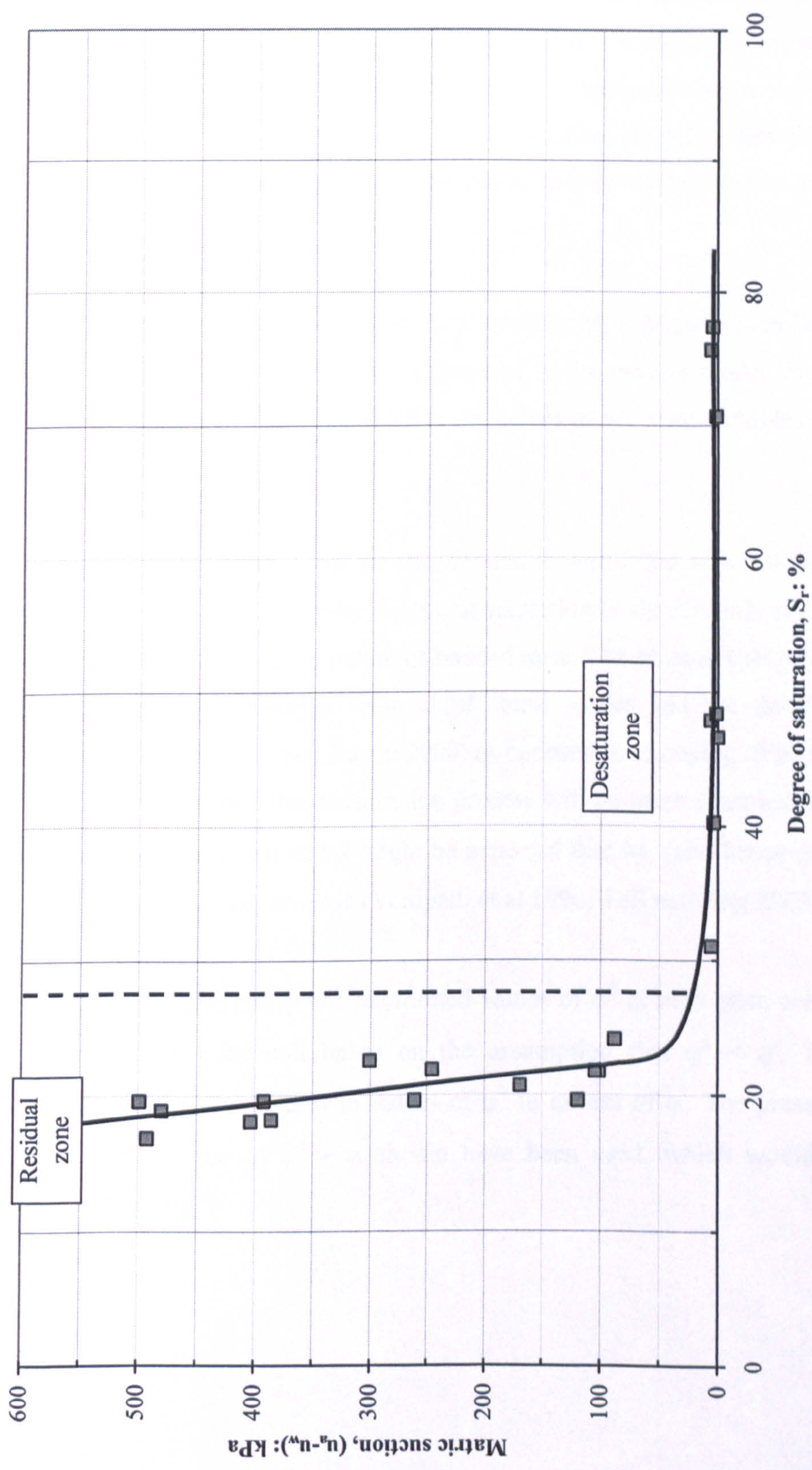


Figure 7.35b: Suction against degree of saturation at critical state



The same data were also plotted in term of variation with suction as shown in Figure 7.36a. The changes in  $M_a$  and  $M_b$  can be related to the different phases of water retention behaviour in Figure 7.36b. The regions of behaviour seem to be (a) before the air entry value  $M_a = M_b = M_s$  (b) in the desaturation stage  $M_a$  rises above  $M_s$  but  $M_b = M_s$  and (c) in the residual stage  $M_a$  remains constant and equal to 1.39 while  $M_b$  starts to reduce.

It does of course have to be noted that the conditions  $M_b = M_s$  in region (b) and  $M_a = 1.39$  in region (c) have been implicitly imposed in the present model. Nevertheless, the possible range of values that satisfies the values of the state variables  $q$ ,  $p-u_a$  and  $u_a-u_w$  is not large.

It is particularly interesting that for this bonded material, the value of  $M_b$  seems to remain close to  $M_s$  even when the degree of saturation is significantly reducing. This is probably due to the uniform nature of bonded sand. The desaturation process in this material probably represent a removal of 'bulk' water and the development of 'meniscus' water (Karube and Kawai 2000) as opposed to emptying of pores. In more widely graded materials, the desaturation process will be more complex (involving a wider range of pore sizes) and it might be expected that  $M_b$  (and hence  $(\phi^b)_c$ ) would drop within the desaturation zone (Vanipalli et al 1996; Toll and Ong 2003).

Toll et al (2006) previously has interpreted values of  $\phi^b$  at peak state conditions for this artificially bonded soil based on the assumption that  $\phi^a = \phi'$ . This led to apparently enormous results with values of  $\phi^b$  in excess of  $\phi'$ . The present analysis suggests that a value of  $\phi^a > \phi'$  should have been used, which would then give sensible value for  $\phi^b$ .



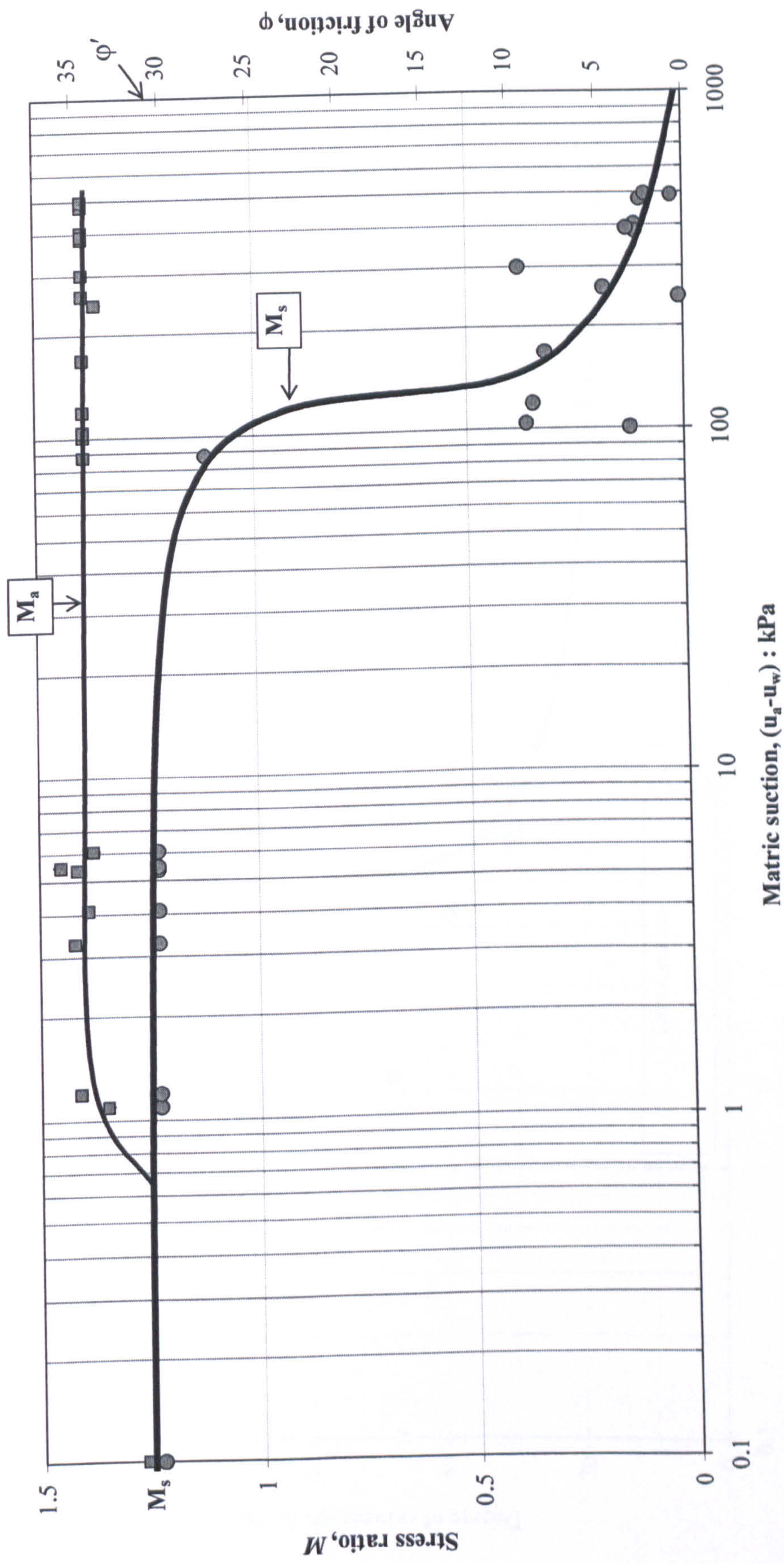


Figure 7.36a: Variation in critical state stress ratios with suction



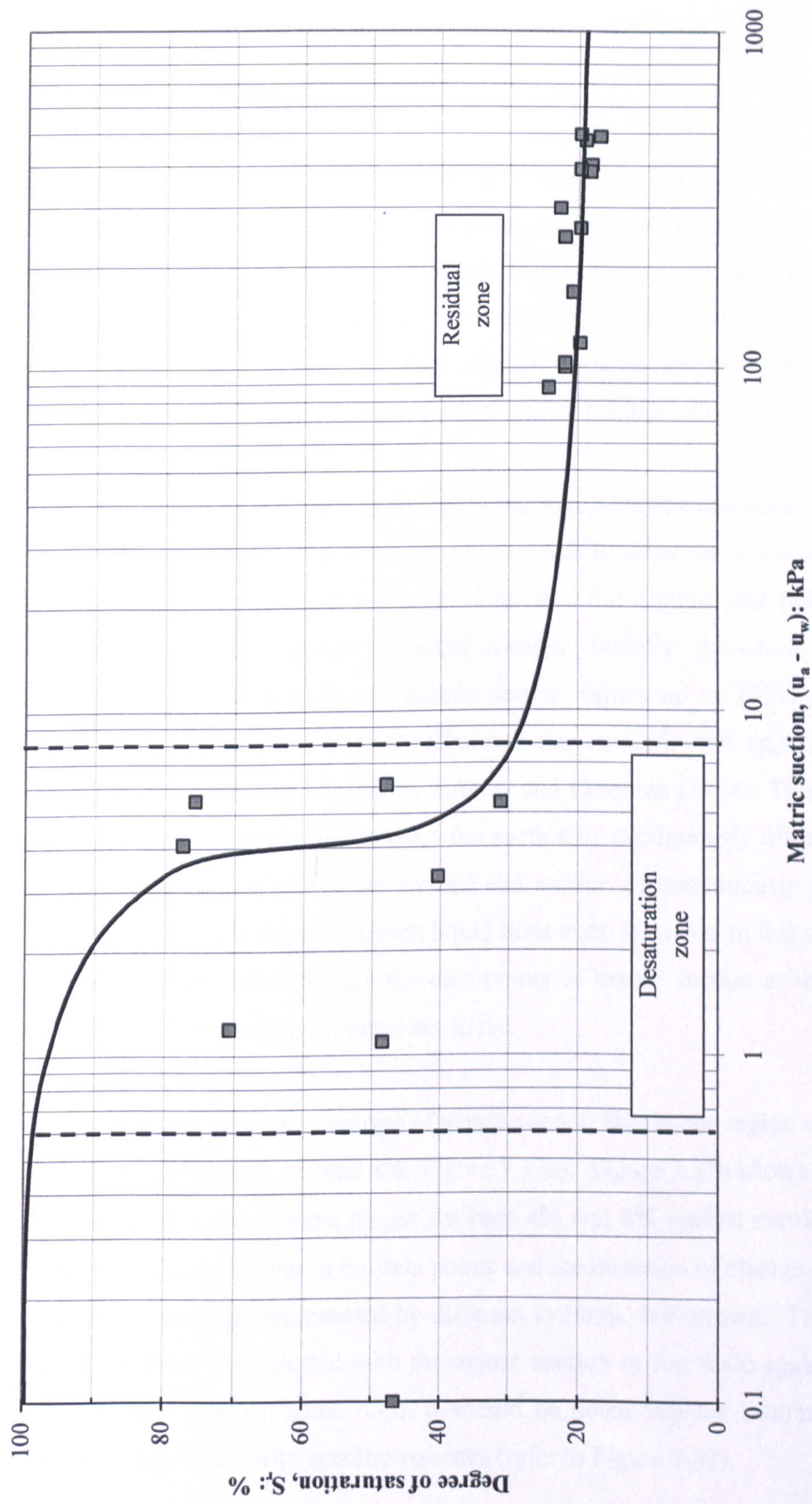


Figure 7.36b: Degree of saturation against suction at critical state



### 7.3.3 Water Content at Critical State

The relationship between water content and matric suction was examined by looking at water retention curves (WRC) at the end of suction equalisation (initial state), after consolidation and after shearing. It was clearly seen that all the tests showed initial compression, followed by dilation in order to achieve the critical state. The compression of samples under constant water content shearing would be expected to cause an increase in pore water pressures (suctions decrease).

In order to observe a clear trend of change in suction, plots of water content against matric suction were prepared. It was found difficult to show the trend of suction when the data were plotted in log scale. Therefore the suction data points were plotted on natural scale against the water content. Initially, the whole range of water content was studied for the matric suction values up to 150kPa (Figure 7.37a). The concept of continuously disturbed line or CDL was applied in this stage which was mentioned earlier by Croney and Coleman (1954). This concept describes a unique relationship between the suction of continuously disturbed soil with the water content. The water content and suction of continuously disturbed soils were measured at the end of each liquid limit tests. However in this study, the CDL line was delineated through the data points of matric suction at the end of shearing (best-fit line) for each mean net stress.

It can be seen that the major changes of matric suction falls in the region where the water content is between 4% and 8% (Figure 7.37a). Figure 7.37b shows a similar plot focusing on water content ranges between 4% and 8% against matric suction up to 600kPa. This plot shows the data points and the direction of change of matric suction for each stage, represented by different symbols and arrows. The WRCs for each stage are then plotted with the matric suction in log scale against water content (natural scale) (Figure 7.38). It should be noted that the saturated water contents are consistent with specific volumes (refer to Figure 7.32).



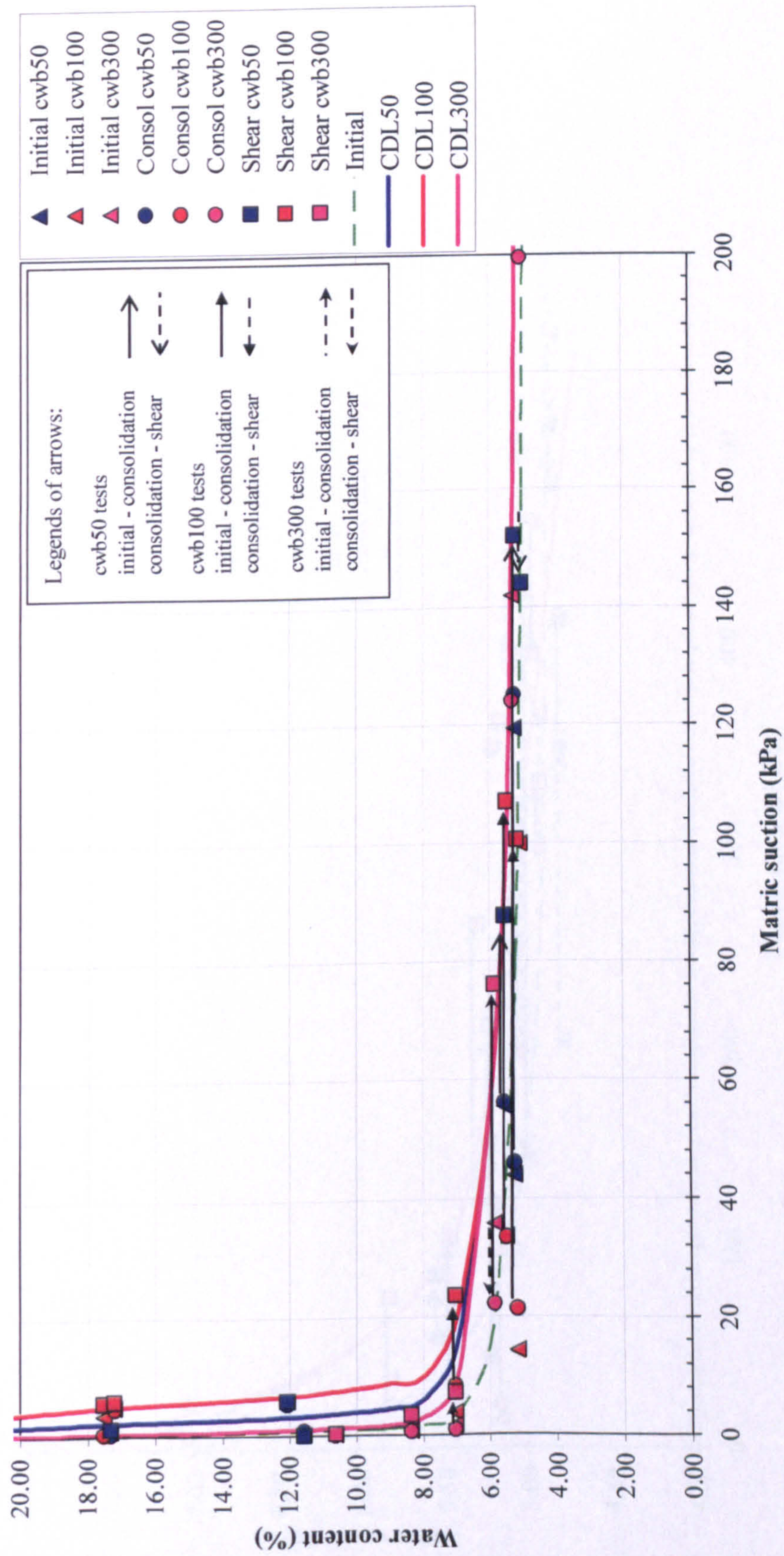


Figure 7.37a: Plot of water content against suction in natural scale (suction values below 200kPa)



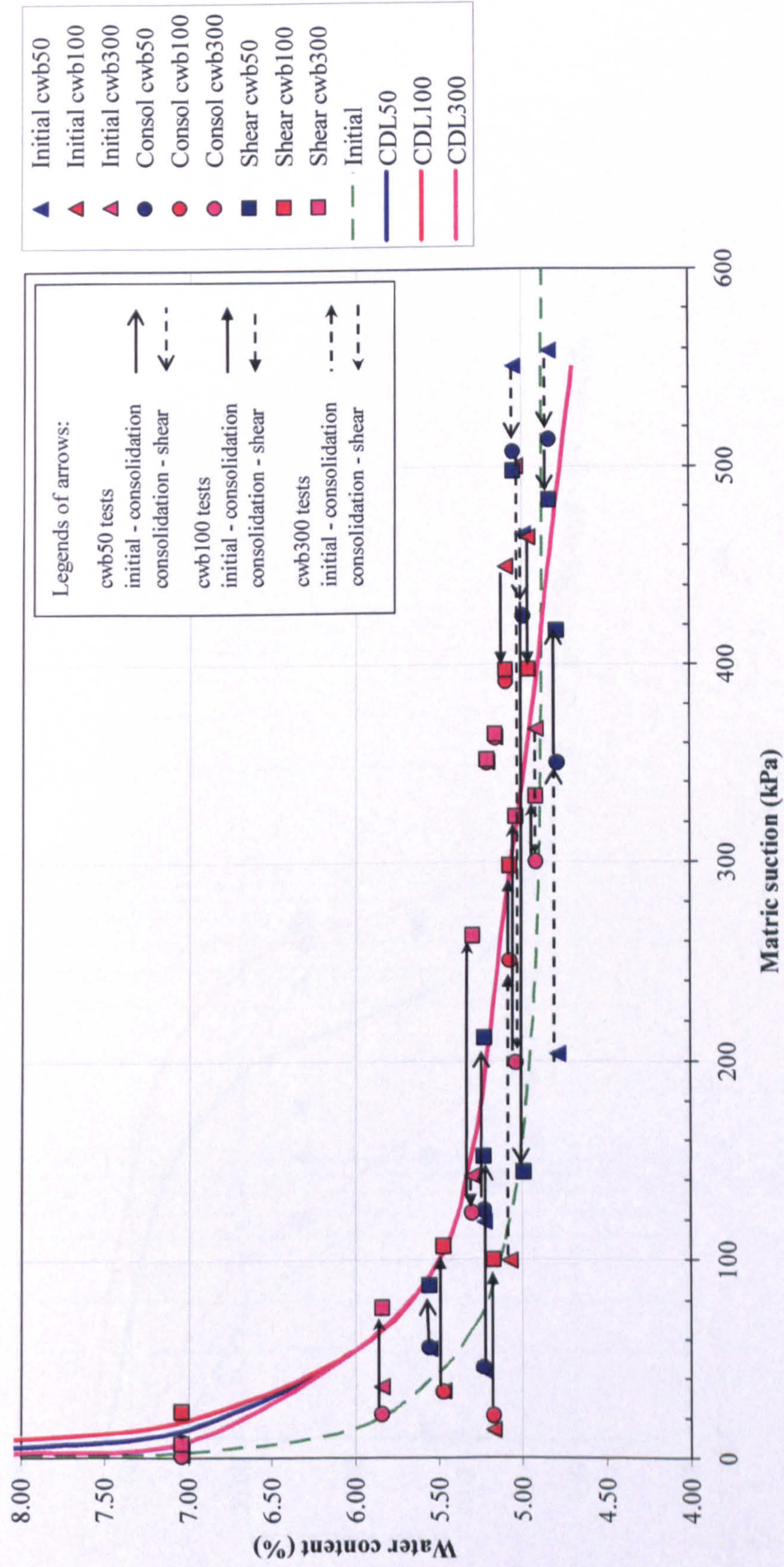


Figure 7.37b: Plot of water content against suction in natural scale (for all range of suction values)



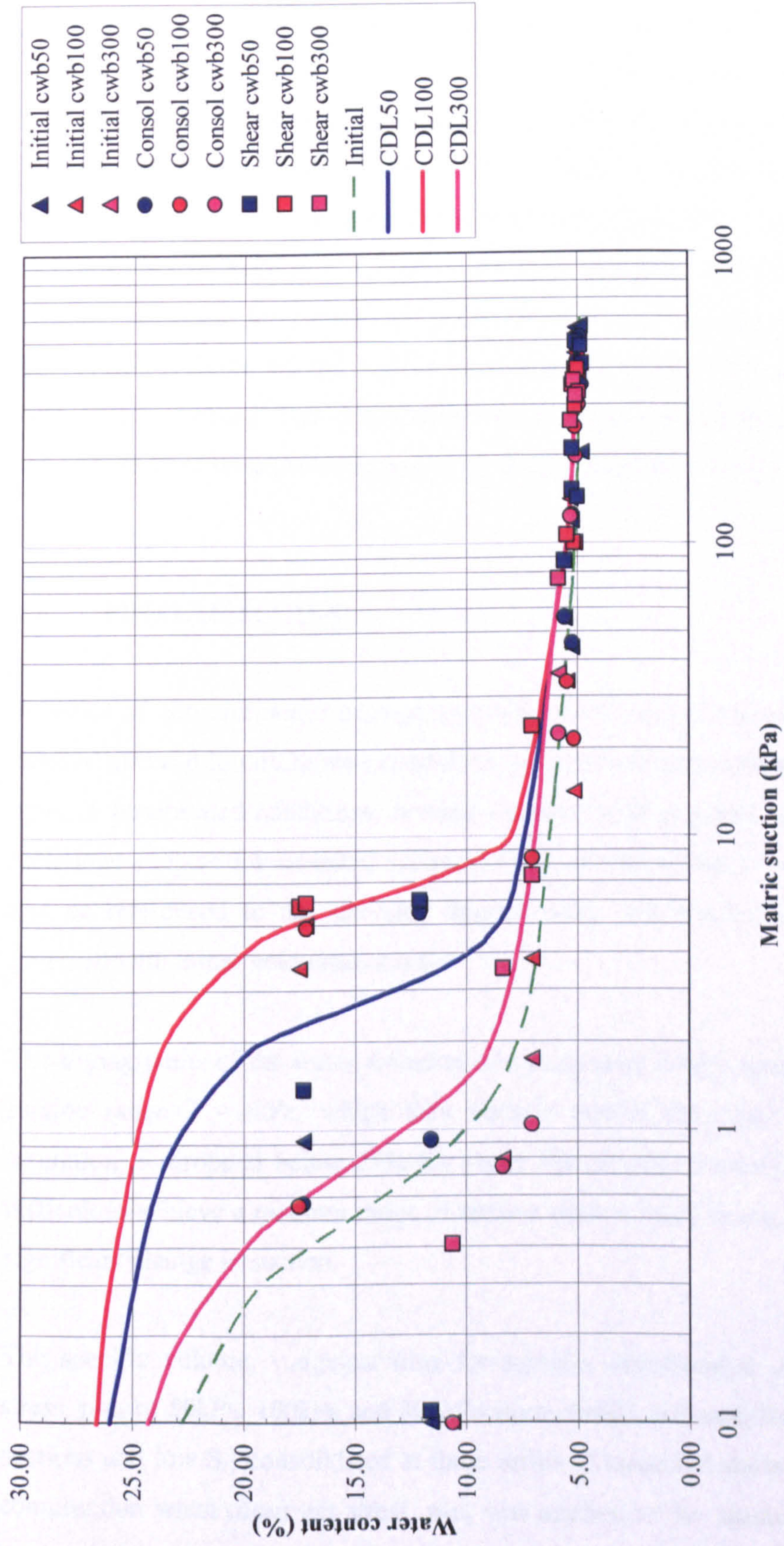


Figure 7.38: The final water retention curve plots for each stage



saturated samples, if the initial effective stress was increased by an amount equal to the suction, the dilatancy of saturated samples would decrease, as saturated samples which were initially consolidated at higher stress would be associated with compression behaviour under shearing. Toll (1990) reported similar behaviour of the lateritic Kiuyu gravel. The behaviour shown by unsaturated samples under shearing has to take into account the role of unsaturated fabric. Group of particles held together by suction can behave like larger particles and hence dilate when sheared. However, the particle group can be compressed during shear, even when the overall volume of the soil is increasing, producing the increase in pwp (decrease in suction). This demonstrates the important role of fabric in controlling the behaviour of unsaturated compared to the saturated soils (Toll 1990).

#### **7.4 FINAL REMARKS**

A series of constant water content (cw) tests were carried out on the artificially bonded material in unsaturated conditions. In order to understand the behaviour of soils in unsaturated conditions, bonded samples were prepared according to the technique adopted for saturated samples. Therefore the results of unsaturated tests can be referenced to the saturated bonded tests. The bonded specimens were prepared with initial void ratio of 0.6.

The drying paths of the water retention curves showed a very steep change in the suction range 2 - 4kPa, which then became almost flat when the degree of saturation,  $S_r$  dropped below 25% (or about 5% of water content). This made it difficult to achieve a medium range of suction since a small change in  $S_r$  lead to a significant change in suction.

The specific volume,  $v$  against time for samples consolidated under mean net stress,  $p-u_a$  of 50kPa, 100kPa and 300kPa were plotted. All samples (zero and low suctions and low  $S_r$ ) consolidated at three series of mean net stress showed initial compression when mean net stress,  $p-u_a$  was applied to the unsaturated samples.



After the initial compression, samples gradually increased before levelling off with time. However, there were a few tests that showed a constant increase in volume change but consolidation was assumed to complete once the gradient of pwp change became smaller (mentioned in Chapter 4). For samples consolidated under  $p-u_a = 300\text{kPa}$ , the amount of compression is clearly influenced by the degree of saturation,  $S_r$ . Samples with a higher suction showed less compression compared to samples with lower suction. However, the effect of suction on amount of compression was not clearly seen in samples consolidated under  $p-u_a$  of 50kPa and 100kPa.

The matric suction of the samples during the consolidation process were plotted against time for all series of  $p-u_a$  of 50kPa, 100kPa and 300kPa. All samples with zero and low suctions showed very small change in matric suction throughout the consolidation process. Suction readings fluctuated due to temperature variation which affected the volume change even though the temperature controlled room attempted to maintain the temperature within  $\pm 1^\circ\text{C}$ . Meanwhile samples with low  $S_r$  presented an initial drop in matric suction when mean net stress,  $p-u_a$  was applied to the samples. The matric suction in the samples gradually increased again followed by almost levelling off with time except cwb50/350(0.21).

The stress-strain curves for the unsaturated samples were presented in three different groups of mean net stress (50, 100 and 300kPa). The stress-strain curve for samples with zero and low suction sheared at lower stress showed a clear peak compared to samples sheared at higher stress. This indicated that samples sheared at low mean net stress behave like an overconsolidated soil. Meanwhile samples sheared at higher mean net stress showed more ductile behaviour.

The unsaturated tests were re-plotted in  $q$  – suction space to show the clear influence of suction on strength. In samples with higher initial matric suction, the suction tended to decrease up to the peak state. Post-peak, the suction continued to decrease before levelled off to the end of shearing. The paths for all unsaturated samples plotted in  $q$  – suction space showed that the peak strength for each group

of mean net stress showed very similar behaviour. The peak strength surfaces looked parallel and indicated some curvature. The curvature of the peak strength in shear strength - suction space occurred mainly at low suction suggesting that the value of  $\phi^b$  was not constant.

All unsaturated samples showed an initial compression followed by dilation. For samples with high suction, there was very small compression followed by dilation up to the end of shearing. For samples with zero and low suctions, volume change tended to level off (or the rate of dilation gets smaller) at larger strain. The volume change showed the effect of mean net stress. Samples sheared at higher stress showed substantial dilation. The effect of suction was clearly seen in each of the test group. Samples with higher suction indicated a greater dilatancy in comparison to samples with zero and low suctions. This behaviour was acknowledged by Toll (1990) as a result of fabric effects.

The excess pwp,  $\Delta u$  against axial strain,  $\epsilon_a$  were plotted for the cwb tests with zero and low suction and samples with low  $S_r$ . For the samples with zero and low suctions, the excess pwp tends to level off up to the end of shearing. It was observed in tests at mean net stress of 50kPa that the increase in initial suction of the samples up to 430kPa resulted in a clear peak of excess pwp. For samples sheared with initial suction above 430kPa, the peak of excess pwp curve became unnoticed or flat. A similar trend can be seen for cwb samples sheared under higher  $p-u_a$  (100kPa). The pwp for samples with zero initial matric suction (cwb100 tests) showed almost no change up to the end of shearing. While samples with higher initial suctions (up to 391kPa), the peak of excess pwp becomes significantly clear, suggesting that the peak of excess pwp is suction dependant. Samples with a higher suction above 391kPa only exhibited positive excess pwp followed by an almost flat response to end of shearing. Samples sheared at higher mean net stress,  $p-u_a$  with high initial suction present small peak in excess pwp and the peak became unnoticeable when suction got higher. However, this could not be confirmed since there were limited data available for samples with higher suction sheared at  $p-u_a=300\text{kPa}$ .



The stress ratio plots suggested the effect of mean net stress and suction. A significant peak of  $q/p^*$  ratio was observed for samples sheared at lower  $p-u_a$  and close to equivalent saturated tests. The peak became unnoticeable when samples were sheared at higher  $p-u_a$ .

A similar approach was adopted in defining the bond yield for unsaturated samples as was used for saturated tests. In order to define more accurate positions of bond yield, assessments were carried out on different type of plots including stress-strain, secant stiffness, volume strain, excess suction and  $v - (p-u_a)$  spaces. In defining final bond yield, personal judgement was involved in trying to take account of all variables used in that process.

The initial bond yield surfaces were represented a linear increase with the increase in mean net stress and matric suction. At lower stress, the initial surface is closely defined by data points up to stress level of 200kPa and then showed some scatter at higher stress. The initial bond yield surface for matric suction of 0kPa and 100kPa were defined by a linear increase of parallel surfaces. However, the initial bond yield surfaces for matric suction 100kPa and 300kPa showed some diversion at stress level of 200kPa. As matric suctions increased higher, the yield surfaces dropped back close to the bond yield surface for matric suction of 100kPa.

A similar trend was also established for final bond yield surface. The final bond yield increased linearly with increased in stress level and matric suction. The final yield surfaces for suction of 100kPa, 200kPa and 300kPa were close at lower stress level but deviated away when increased to higher stress. A similar picture happened for bond yield surface as matric suctions increased higher.

The different between the  $p-u_a$  and  $p-u_w$  is very small for tests at low suction and this meant that an equivalent effective stress could be closely defined for these unsaturated samples. In unsaturated tests, a true critical state was not simply achieved. The unsaturated samples tend to dilate or deviator stress continues to decrease up to the end of shearing. However the rates of change of the variables

generally decrease toward the end of tests. The difficulty in defining the true critical state for the bonded and dense materials was thought to be due to the development of distinct shear surfaces.

A discontinuity (sudden change in path direction) was used to define critical state point. The critical state for unsaturated samples showed a good agreement with data point defined by saturated tests. It was seen that the degree of saturation,  $S_r$ , influenced the distance of the critical state points for unsaturated samples. Samples with  $S_r$  higher than 50% have critical state points very close to saturated CSL. This suggested the effect of even a small suction causes a change in the critical state line probably by the suction contributing in supporting the aggregation or grouping of particles. Observation on  $v - (p - u_a)$  space showed the critical state points for unsaturated samples plot above the upper limit of CSL defined by saturated tests. The overall trend of the critical state for unsaturated samples with zero and low suctions, generally fit into the critical state defined by saturated tests, with a small movement of the upper boundary.

A critical state stress ratio for unsaturated soils was examined based on equation more general stress variables proposed by Toll (1990) and Toll and Ong (2003). The critical state stress ratio variable of  $M_a$  (mean net stress component) and  $M_b$  (matric suction component) were used. These were also presented as critical state angle of friction,  $(\phi^a)_c$  and  $(\phi^b)_c$ . It was found that  $M_a$  is higher than the saturated critical state stress ratio,  $M_s$  (i.e.  $\phi^a > \phi'$ ), suggesting that we should not always make assumption that  $\phi^a = \phi'$ . The changes in  $M_a$  and  $M_b$  can be related to the different phase of water retention behaviour. The region of behaviour indicate that (a) before the air entry value  $M_a = M_b = M_s$  (b) in the desaturation stage  $M_a$  rises above  $M_s$  but  $M_b = M_s$  (c) in the residual stage  $M_a$  remains constant and  $M_b$  starts to reduce. This pattern of behaviour is probably explained by the narrow range of pore size in the uniform bonded sand.



The relationship between water content and matric suction was studied based on the WRC at each stage of suction equalisation, consolidation and shearing. The CDLs or Continuously Disturbed Lines (representing the water content – suction relationship at ultimate state) were plotted using the data points of matric suction at the end of shearing defined by best-fit approach. It was interesting that samples with initial low suction showed an increase in suction to reach the CDL while samples with initial high suction show a decrease to approach the CDL. The decrease in suction during shearing for samples with high initial suction was accompanied by dilation behaviour in terms of volumetric strain. This behaviour is the opposite of what might be expected. In saturated soils, dilative behaviour would produce a drop in pore water pressure (increase in suction). This opposite behaviour expressed by unsaturated samples under shear was explained by Toll (1990), emphasising the role of fabric in controlling the engineering behaviour of unsaturated soils.

**CHAPTER 8****CONCLUSIONS****AND RECOMMENDATIONS****8.1 INTRODUCTION**

In this chapter, the main conclusions highlighted from the result of this study and recommendations for future research are presented. The conclusions are presented in the order of the chapters as follows: technique in sample preparation and testing, behaviour of destructured material in a saturated state, behaviour of bonded material in a saturated state and behaviour of bonded soil in an unsaturated state.

**8.2 CONCLUSIONS****8.2.1 Techniques in Sample Preparation and Testing**

The technique adopted in the sample preparation of a weakly bonded material in a denser state ( $e=0.6$ ) by firing a sand/kaolin mixture has an advantage in producing reproducible samples with properties that are not age-dependent. A new technique for producing looser samples, using coriander seeds has been developed and was used for producing samples with void ratio,  $e = 0.9$ . Microscopic observations of thin sections of the samples showed that the fired kaolin forms bridges between the sand grains, as well as coating the grains. Meanwhile the loose samples produced using coriander seed technique showed very small amount of ash residue left after firing at high temperature. The use of poppy seeds was found to be difficult to handle due to the oily nature of the seeds. However firing the coriander seeds was associated with the presence of smoke and nuisance smell. Therefore it should be carried out in a properly ventilated area. Triaxial testing was carried out on specimens prepared with a void ratio of 0.6



Triaxial equipment was used for carrying out conventional drained and undrained tests on saturated bonded and destructured materials. Samples were initially consolidated under effective stresses up to 1000kPa. In order to achieve higher stress, an air piston was devised capable of applying a cell pressure of up to 2MPa. Constant water content tests were carried out on unsaturated samples. The perspex cell experienced creep due to applied stress. Corrections for creep and penetration of loading ram on volume change were carried out successfully. In order to minimise the creep of the perspex cell due to temperature variation, a bubble wrap was used to cover the cell.

### 8.2.2 Behaviour of Destructured Material in Saturated State

Destructured samples were sheared in drained and undrained tests. Samples sheared at low confining stresses indicated initial compression which was then followed by dilation. It suggests that the behaviour of the destructured material under shearing is similar to the behaviour of dense sand. The destructured samples showed no significant peak in  $q/p'$  ratio. Samples sheared at lower confining pressures sustain a higher value of  $q/p'$  ratio than those at higher confining pressure.

A “discontinuity” approach was used in identifying a sudden change that might be associated with shear surface formation, and the critical (ultimate) state was taken to occur before such strain localisation.

The critical state line for destructured material was found not to be unique in  $v - p'$  space. Therefore, the critical state is represented by a zone with upper and lower limits. The difference between the upper ( $\Gamma=1.7991$ ) and lower limit ( $\Gamma=1.7581$ ) is  $\pm 0.041$ . This variation might be due to errors in void ratio or is more likely caused by the initial fabric and structure, which formed during the remoulding of the samples. On the other hand, critical state defined in  $q - p'$  space for both sets of

tests could be represented by a fairly straight line passing through the origin with minimum scatter of data points giving a slope of  $M = 1.24$ . Therefore, the critical state for destructured material is seen to be a realistically unique line in the  $q - p'$  space but less so in  $v - p'$  space. The critical state parameters for saturated destructured material are defined by  $\lambda = 0.034$ ,  $\Gamma = 1.7581$  and  $1.7991$  and  $M = 1.24$ .

Normalisation of stress paths in  $q/p'_c - p'/p'_c$  showed scattered values in  $q/p'_c$ , corresponding to variation in stress ratio for each test. A further refinement was carried out by re-normalised with the end values of  $q/p'_c$  (equal to  $M$ ). These normalised stress paths in  $q/p'_c/M - p'/p'_c$  space showed clear limiting surfaces. Samples on dense side of the critical state exhibit dilative behaviour (bounded by the Hvorslev surface) and those on the loose side of the critical state show contractive behaviour (bounded by the Roscoe surface).

### 8.2.3 Behaviour of Bonded Material in Saturated State

Bonded samples showed an initial tendency to contract under shear that was then followed by dilation behaviour. Tests sheared at low confining stresses showed a clear peak of  $q/p'$  ratio and this peak became less significant with increasing confining stress. The bonded samples exhibited higher maximum  $q/p'$  ratio values than those of the destructured samples. At high stress levels ( $p'$  above 1500kPa) the maximum stress ratio dropped close to that of the destructured material. This suggested that bonding was gradually destroyed by consolidating to a higher stress level causing the behaviour to become similar to the destructured material.

The bounding surfaces and phase transformation lines for the bonded samples indicated some curvature at low stresses and again at high stress levels. At higher stresses the bounding surfaces and phase transformation line for bonded samples almost coincide with the destructured material, suggesting the contribution of bonding in bonded samples in achieving higher stress ratios than the destructured samples.



Tests on the bonded material were interpreted to identify “initial bond yield” when the bonding start to break down and “final bond yield” when a gross yield is observed. The initial yield surface defined from undrained tests was slightly above that from the drained test. The final bond yield surface defined from both drained and undrained tests showed good agreement.

The critical state for bonded material defined in  $q - p'$  space showed some scattering of data for bonded material and corresponded to the scatter in  $M$  value of 1.23. The critical state in  $v - p'$  space was also represented by a zone with upper and lower limits. The difference between the upper and lower limit was  $\pm 0.0274$  which slightly lower than the range for the destructured material ( $\pm 0.041$ ). The critical state parameters for saturated bonded material are defined by  $\lambda = 0.039$ ,  $\Gamma = 1.8125$  and  $1.8399$  and  $M = 1.23$ .

Comparison between the normalised drained and undrained stress paths of bonded samples and the destructured material clearly exhibited the effect of bonding. The normalised stress paths for the undrained bonded samples even samples which start at lower  $p'/p'_c$  reached states outside the state boundary surface defined by the destructured material. Meanwhile the normalised stress paths for the drained bonded tests show little difference with the destructured surface when approaching the Hvorslev surface. However, the drained bonded material go well beyond the Roscoe surface defined from the destructured material.

#### 8.2.4 Behaviour of Bonded Soil in Unsaturated State

The water retention curves (following a drying path) for the unsaturated samples showed a very steep change at a suction of 2 – 4kPa, which then became almost flat when the degree of saturation,  $S_r$  drops below 25% (or about 5% of water content). This made control of suction difficult since a small change in  $S_r$  could lead to a significant change in suction.

During the consolidation stage, samples experienced initial compression before levelling off with time. Samples with higher suction showed less compression in comparison to samples with lower suction. The matric suction for all samples, generally showed an initial decrease after applying a mean net stress,  $p^*$ , but then levelled off with time. There were a few tests that showed a continuous increase in volume change but consolidation was assumed to be complete once the gradient of pore water pressure change became smaller.

A peak was clearly seen in stress strain curves for samples with zero and low suction which were sheared at lower stress. This suggests that samples sheared at low mean net stress behave like an overconsolidated soil. Meanwhile more ductile behaviour characterised the samples sheared at higher mean net stress.

An influence of suction on strength was clearly seen in deviator stress – suction space. The peak strength surfaces were almost parallel and indicated some curvature mainly at low suction. However at higher suction ( $>400\text{kPa}$ ) the strength dropped to back to the strength close to lower suctions. This suggests that a further increase in suction may contribute to the breaking down of the bond structures.

The initial and final bond yield surfaces were represented by a linear increase with the increase in mean net stress. Sequences of yield surfaces were defined for different suction values. Initially the effect of suction was to expand the yield surface. However, as matric suctions increased higher, the yield surfaces dropped back inside the bond yield surface for lower suctions.

The critical state stress ratio variable of  $M_a$  (mean net stress component) and  $M_b$  (matric suction component) were used to examine the critical state of the bonded material in unsaturated conditions. It was found that  $M_a$  is higher than the saturated critical state stress ratio,  $M_s$  (i.e.  $\phi^a > \phi'$ ), therefore, assumption that  $\phi^a = \phi'$  is not always valid. The changes in  $M_a$  and  $M_b$  can be related to the different phase of water retention behaviour of (a) before the air entry value  $M_a = M_b = M_s$  (b) in the



desaturation stage  $M_a$  rises above  $M_s$  but  $M_b = M_s$  (c) in the residual stage  $M_a$  remains constant and  $M_b$  starts to reduce. This pattern of behaviour is probably explained by the narrow range of pore size in the uniform bonded sand.

The concept of continuously disturbed line (or CDL) or a unique relationship between suction and water content for a continuously disturbed soil was applied to the results of the tests. It is interestingly, samples with initially low suctions showed an increase in suction under shear, while samples with high initial suctions showed a decrease in order to reach the CDL. This behaviour suggests that even though the samples are dilating in volume, the suction is decreasing (pore water pressure increasing) which is not what would be expected based on saturated soil behaviour. The behaviour shown by unsaturated samples under shearing has to take into account the role of fabric. Group of particles held together by suction can behave like larger particles and hence dilation can occur when sheared. However, the particles group can be compressed during shear, even when the overall volume of the soil is increasing, producing an increase in pore water pressure (decrease in suction).

### 8.3 Recommendations

1. The use of artificially bonded and destructured samples using sand and kaolin mixture has minimised the problem in handling, and storage and provides properties that can be reproduced and are age independant. In this study, bonded samples with  $e=0.6$  and  $0.9$  were examined under convention optical microscope with a limited magnification capacity. Scanning electron microscopy (SEM) can be used to observe a further detail of the particle interaction between the sand particles and cementing agent (kaolin) under higher magnification. The natures of sand and fired kaolin can also be studied clearly under SEM. It was observed that a number of cracks present in between bonding and sand particles. The pore distribution can be studied to understand how the distribution of pores will influence the suction across the samples.

2. A technique for developing a loose material with a bonded structure ( $e=0.9$ ) has been successfully achieved by using coriander seeds. Therefore it will be useful to study this loose material in order to understand the engineering behaviour which can simulate the behaviour of equivalent natural soils. These studies should be performed in both states, saturated and unsaturated conditions in order to establish a framework model for the loose soil. However, even the loose samples has been successfully produced, there is a need to find out the technique to handle this state of sample especially during setting up procedures in triaxial tests due to its nature (very brittle), otherwise there will be error resulting from the loss of its material (initial weight).
3. A further study on the influence of the bonded structures in relation to the development of pore water pressure during shearing in undrained conditions as seen in bonded samples. It was found that the change from the contraction to dilation took place at higher stress ratio than that of the destructured samples which author believed it is due to the presence of bonds separating the sand particles.
4. A series of triaxial tests (constant water content tests) on unsaturated samples in destructured state should be performed in order to establish comparative behaviour between the unsaturated bonded soils. This would help to establish a more complete framework for the study of unsaturated bonded soils by providing the equivalent reference state for unsaturated soils. A proper approach should be designed in order to set up samples in destructured state on pedestal since the samples are too soft and weak.
5. In order to minimise error in volume change measurement, it is strongly recommended to use a double wall triaxial cell. This type of triaxial consists of two layers of cells made from perspex. The inner cell is pressurised by the pressure controlled between the inner and outer cells.



Therefore the problem of expansion of inner cell due to imposing of cell pressure can be solved and contraction or dilation of sample can be measured accurately rather than the triaxial with single wall cell. Other related problem is due to the fluctuation of the room temperature which can affect the cell. Ideally, the room temperature should be constant and the less the fluctuation in temperature is better since correction can be carried out with more confident. However, the use of double wall should be able to minimise this problem related to the temperature effect on volume change.

## REFERENCES

- Adam, J. (2000). An assessment of the effects of pozzolanic activity on the behaviour of fly ash. PhD thesis, University of Durham
- Airey, B. D. (1993). Triaxial testing of natural cemented carbonate soil. *Journal of Geotechnical Engineering*, 119(9): 1379-1399.
- Alarcon-Guzman, A., Leonards, G. A. and Chameau, J. L. (1988). Undrained monotonic and cyclic strength of sands. *Geotechnical Engineering ASCE*, 114: 1089-1109.
- Alonso, E. E., Gens, A. and Josa, A. (1990). A constitutive model for partially saturated soils. *Geotechnique*, 40: 405-430.
- Anon. (1979). Classification of rocks and soils for engineering geological mapping. Part I: Rock and soil materials. (IEAG Commission of engineering geological mapping). *Bulletin IEAG*, 19: 364-371.
- Asghari, E., Toll, D. G. and Haeri, S. M. (2003). Triaxial behaviour of a cemented gravely sand Tehran alluvium. *Geotechnical and Geological Engineering* 21: 1-28.
- Atkinson, J. (1993). An introduction to the mechanics of soils and foundations. McGraw-Hill, London.
- Atkinson, J. H. and Bransby, P. L. (1978 ). The mechanics of soils. McGraw-Hill, London.
- Aung, K., Rahardjo, H., Toll, D.G. and Leong, E.C. (2000). Mineralogy and microfabric of unsaturated residual soil. *Proceed. of the Asian Conference on Unsaturated Soils*, Singapore: 317-321.
- Been, K., Jefferies, M. G. and Hachey, J. (1991). The critical state of sands. *Geotechnique*, 41: 365-381.
- Bishop, A. W. (1959). The principle of effective stress. *Tecknisk Ukeblad*, 106: 859-863.
- Bishop, A. W., Alpan, I., Blight, G. E. and Donald, I. B. (1960). Factor controlling the shear strength of partly saturated cohesive soils. *ASCE Res. Conf. Shear Strength of Cohesive Soils*, University Colorado: 503-532.
- Bishop, A. W. and Blight, G. E. (1963). Some aspects of effective stress in saturated and unsaturated soils. *Geotechnique*, 13: 177-197.



- Bishop, A. W. and Donald, I. B. (1961). The experimental study of partly saturated soil in the triaxial apparatus. *Proceed. 5th Int. Conf. Soil Mechanics Foundation Engineering*, Paris: 13-21.
- Blight, G. E. (1967). Effective stress evaluation for unsaturated soils. *J. Soil Mech. Found. Engng. Div., ASCE*(93): 125-148.
- Bressani, L. A. (1990). Experimental properties of bonded soils. Phd thesis, University of London
- Bressani, L. A. (1993). The stiffness behaviour of Corinth marl. *Geotechnical Engineering of Hard Soils-Soft Rocks*, Rotterdam, Balkema: 391-396.
- BS1377 (1990). Standard method of for soils for civil engineering purposes. Part 3: Chemical and electro-chemical tests, British Standard Institution, London.
- BS1377 (1990). Standard methods for civil engineering purposes. Part 1: General requirements and sample preparation, British Standard Institution, London.
- Burland, J. B. (1990). On the compressibility and shear strength of natural clay. *Geotechnique*, 40: 329-378.
- Cassagrande, A. (1936). Characteristics of cohesionless soils affecting the stability of earth fills. *J. Boston Soc. Civil Engineers*, 23(1): 13-32.
- Castro, G. (1969). Liquefaction of sands. Phd thesis, Harvard University
- Chu, J. (1994). An experimental examination of the critical state and other similar concepts for granular soils. *Canadian Geotechnic Journal*, (32): 1065-1075.
- Clayton, C. R. I., Hight, D. W. and Hopper, R. J. (1992). Progressive destructuring of Bothkennar clay: Implication for sampling and reconsolidation procedures. *Geotechnique*, 42: 219-239.
- Clough, G. W., Sitar, N., Bachus, R. C. and Rad, N. S. (1981). Cemented sands under static loading. *Journal of the Geotechnical Engineering Division, ASCE*: 799-817.
- Coleman, J. D. (1962). Stress/strain relationship for partly saturated soils. *Geotechnique*, 12: 348-350.
- Coop, M. R. (1990). The mechanics of uncemented carbonate sands. *Geotechnique*, 40: 607-626.
- Coop, M. R. and Atkinson, J. H. (1993). The mechanics of cemented carbonate sands. *Geotechnique*, 43: 53-67.

- Coop, M. R. and Lee, I. K. (1993). The behaviour of granular soils at elevated stresses. *Predictive soil mechanics*.(eds.) London, Thomas Telford: 186-198.
- Coop, M. R., Sorensen, K. K., Freitas, B. T. and Georgoutsos, G. (2004). Particle breakage during shearing of a carbonate sand. *Geotechnique*, 54: 157-163.
- Croney, D. and Coleman, D., J. (1954). Soil structure in relation to soil suction (pF). *Soil Sciences*, 5(1): 75-84.
- Croney, D., Coleman, J. D. and Black, W. P. M., Eds. (1958). Movement and distribution of water in soil in relation to highway design and performance. *Highway Research Board Special Report*, No. 40. Washington.
- Cuccovillo, T. and Coop, M. R. (1993). The influence of bond strength on the mechanics of carbonate soft rock. *Geotechnical Engineering of Hard Soils-Soft Rocks*, Athen, Balkema: 447-455.
- Cuccovillo, T. and Coop, M. R. (1999). On the mechanics of structured sands. *Geotechnique*, 49: 741-760.
- Escario, V. (1980). Suction controlled penetration and shear tests. *Proceed. 4th Intl. Conf. Expansive Soils*, Denver, ASCE: 781-797.
- Escario, V. and Saez, J. (1986). The shear strength of partly saturated soils. *Geotechnique*, 36: 453-456.
- Espinet, J. and Pelaez, L. (1983). Study on the artificial cementation of sands carbonate calcium. *Report of Civil Engineering Dept.* University of Barcelona, Spain.
- Evans, K. M. (1987). A model study of the end bearing capacity of piles in layered carbonate soils. DPhil thesis, Oxford University
- Faisal, H. A. (2000). Unsaturated tropical residual soils and rainfall induced slope failure in Malaysia. *Proceed. of the Asian Conference on Unsaturated Soils*, Singapore: 41-52.
- Fookes, P. G. (1997). *Tropical Residual Soils*. The Geological Society, London.
- Fourie, A. B. and Papageorgiou, G. (2001). Defining an appropriate steady state line for Merriespruit gold tailings. *Canadian Geotechnic Journal*, 38: 695-706.



- Fredlund, D. G. (1998). Bringing unsaturated soil mechanics into engineering practise. *Proceed. of 2nd International Conference on Unsaturated Soils, UNSAT' 98*, Beijing: 1-36.
- Fredlund, D. G. and Morgenstern, N. R. (1977). Stress state variables for unsaturated soils. *J. Geotech. Eng. Div., ASCE*, 103(5): 447-466.
- Fredlund, D. G., Morgenstern, N. R. and Widger, R. A. (1978). The shear strength of unsaturated soils. *Can. Geotech. J.*, 15: 313-321.
- Fredlund, D. G. and Rahardjo, H. (1993). An overview of unsaturated soil behaviour. In Sandra, L. H. and Warren, K. W.(eds.). *Unsaturated Soils*. New York, *Geotechnical Special Publication*, ASCE: 1-31.
- Fredlund, D. G. and Rahardjo, H. (1993). *Soil Mechanics for Unsaturated Soils*. John Wiley & Sons, New York.
- Gallipoli, D., Gens, A. and Vaunat, J. (2003). An elasto-plastic model for unsaturated soil incorporating the effects of suction and degree of saturation on mechanical behaviour. *Geotechnique*, 53: 123-135.
- Geiser, F., Laloui, L. and Vulliet, L. (1998). Yielding of a remoulding sandy silt in saturated and unsaturated states. *Proceed. of 2nd International Conference on Unsaturated Soils, UNSAT' 98*, Beijing: 54-59.
- Georgiannou, V. N. (1988). The behaviour of clayey sands under monotonic and cyclic loading. PhD thesis, University of London
- Grim, E. R. (1953). *Clay Mineralogy*. McGraw-Hill Book Comp. Inc.
- Haeri, M. S., Hosseini, S. M., Toll, D. G. and Yasrebi, S. H. (2005). The behaviour of an artificially cemented sandy gravel. *Geotechnical and Geological Engineering*, 23: 537-560.
- Hardin, B. O. (1987). 1-D strain in normally consolidated cohesionless soils. *J. Geotechnical Engng Am. Soc. Civ. Engrs*, 113: 1449-1467.
- Hilf, W. (1956). An investigation of pore-water pressure in compacted cohesive soils. Phd dissertation, U.S. Dept. of Interior, Bureau of Reclamation, Design and Construction Div. Denver
- Ho, D. Y. F. and Fredlund, D. G. (1982). Increase in shear strength due to soil suction for two Hong Kong soils. *Proceed. ASCE Geotech. Conf. Engineering and Construction in Tropical and Residual Soils*, Hawaii: 263-295.
- Hosseini, S. M., Haeri, M. S. and Toll, D. G. (2005). Behaviour of gravely sand using critical state concepts. *Scientia Iranica*, 12: 167-177.

- Huang, T. J. and Airey, W. D. (1991). The manufacture of cemented carbonate soils. Research Report R631, School of Civil and Mining Engineering University of Sydney
- Ishihara, K. (1993). Liquefaction and flow failure during earthquakes. *Geotechnique*, 43: 351-415.
- Ishihara, K., Tatsuoka, F. and Yasuda, S. (1975). Undrained deformation and liquefaction of sand under cyclic stresses. *Soils and Foundations*, 15: 29-44.
- Jennings, J. E. and Burland, J. B. (1962). Limitation to the use of effective stress in partly saturated soils. *Geotechnique*, 12: 125-144.
- Karube, D and Kawai, K. (2000). The role of pore water in the mechanical behaviour of unsaturated soils. *Geotechnical and Geological Engineering*, 19: 211-241
- Konrad, J. M. (1990). Minimum undrained strength versus steady-state strength of sands. *Journal of Geotechnical Engineering ASCE*, 116: 948-963.
- Lade, P. V. and Yamamuro, J. A. (1997). Effects of non-plastic fines on static liquefaction of sands. *Canadian Geotechnic Journal*, 34: 905-917.
- Lee, I. K. and Coop, M. R. (1995). The intrinsic behaviour of a decomposed granite soil. *Geotechnique*, 45: 117-130.
- Leroueil, S. and Vaughan, P. R. (1990). The general and congruent effects of structure in natural soils and weak rocks. *Geotechnique*, 40: 467-488.
- Luzzani, L. and Coop, M. R. (2002). On the relationship between particle breakage and the critical state of sands. *Soils and Foundations*, 42: 71-82.
- Maccarini, M. (1987). Laboratory studies of a weakly bonded artificial soil. PhD thesis, University of London
- Maccarini, M. (1993). A comparison of direct shear box tests with triaxial compression tests for a residual soil. *Geotechnical and Geological Engineering*: 69-80.
- Malandraki, V. (1994). The engineering behaviour of a weakly bonded artificial soil. PhD thesis, University of Durham
- Malandraki, V. and Toll, D. G. (1996). The definition of yield for bonded materials. *Geotechnical and Geological Engineering*, 14: 67-82.



- Mancuso, C., Vassallo, R. and Vinale, F. (2000). Effects of moulding water content on the behaviour of an unsaturated silty sand. *Unsaturated Soil for Asia*, Singapore: 545-550.
- Matyas, E. L. and Radhakrishna, H. S. (1968). Volume change characteristics of partially saturated soils. *Geotechnique*, 18: 432-448.
- Medero, M. G. (2001). Analise do comportamento mecanico de um material colapsivel. MSc. thesis, Universidade Federal do Rio Grande do Sul
- Mooney, M. A., Finno, R. J. and Viggiani, M. G. (1998). A unique critical state for sands? *Journal of Geotechnical Engineering ASCE*, 124: 1100-1108.
- Ng, C. W. W., Chiu, C. F. and Rahardjo, H. (2000). Laboratory study of loosely compacted unsaturated volcanic fill in Hong Kong. *Unsaturated Soils for Asia*, Singapore, Balkema: 551-556.
- Poorooshasb, H. B. (1989). Description of flow of sand using state parameters. *Computers and Geotechnics*, 8: 195-218.
- Rahardjo, H., Lim, T. T., Chang, M. F. and Fredlund, D. G. (1995). Shear strength characteristics of a residual soil. *Canadian Geotechnical Journal*, 32: 60-77.
- Ridley, A. M. (1993). The measurement of soil moisture suction. PhD thesis, Imperial College, University of London
- Roscoe, K. H., Schofield, A. N. and Wroth, C. P. (1958). On the yielding of soils. *Geotechnique*, 8: 22-53.
- Sandroni, S. S. (1981). Gneissic residual soils - research carried out at PUC/RJ. *Proceed. Simp. Brasileiro Solo Tropicais em Engenharias*, Rio de Janeiro: 30-65.
- Sangrey, D. A. (1972). Naturally cemented sensitive soils. *Geotechnique*, 22: 139-152.
- Schofield, A. N. and Wroth, C. P. (1968). Critical State Soil Mechanics. McGraw-Hill, London.
- Seed, H. B. and Lee, K. L. (1967). Undrained strength characteristics of cohesionless soils. *J. Soil Mech. and Foundation Div., ASCE*, 93: 333-360.
- Sitar, N. (1981). Behaviour of slopes in weakly cemented soil under static and dynamic loading. PhD thesis, University of California Berkley
- Taha, M. R., Hossain, M. K. and Mofiz, S. A. (2000). Shear strength behaviour of unsaturated granite residual soil. *Unsaturated Soils for Asia*, Singapore, Balkema: 575-580.

- Taylor, W. D. (1948). *Fundamentals of Soil Mechanics*. Wiley, New York.
- Terzaghi, K. (1936). The shear resistance of saturated soils. *Proceed. 1st Intl. Conf. Soil Mechanics Foundation Engineering*, Cambridge: 54-56.
- Toll, D. G. (1988). The behaviour of unsaturated compacted naturally occurring gravel. PhD thesis, University of London
- Toll, D. G. (1990). A framework for unsaturated soil behaviour. *Geotechnique*, 40: 31-44.
- Toll, D. G. (1999). A data acquisition and control system for geotechnical testing. In Kumar, B. and Topping, B. H. V. (eds.), *Computing Development in Civil and Structure Engineering Computing*. Edinburgh, Civil Com Press: 237-242.
- Toll, D. G. (2000). The influence of fabric on the shear behaviour of unsaturated compacted soils. In Shackelford, C., Houston, S. L. and Chang, N. Y. (eds.), *Advances in Unsaturated Soils*, Geotechnical Special Publ. No. 99, American Society of Civil Engineers, Reston: 222-234
- Toll, D. G. (2001). Rainfall-induced landslide in Singapore. *Geotechnical Engineering, ASCE*, 149: 211-216.
- Toll, D. G., Hight, D. W. and Shaw, H. F. (1987). The role of soil fabric in determining the engineering behaviour of compacted lateritic and quartzitic gravels. *Zeitschrift fur Geomorphologie, Suppl. Bd.*, 64: 133-144.
- Toll, D. G. and Malandraki, V. (1993). Triaxial testing on a weakly bonded soils. *Proceed. Intl. Symp. on Geotech. Engineering of Hard Soils-Soft Rocks*, Rotterdam, Balkema: 817-824.
- Toll, D. G. and Ong, B. H. (2003). Critical-state parameters for an unsaturated residual sandy clay. *Geotechnique*, 53: 93-103.
- Toll, D. G., Ong, B. H. and Rahardjo, H. (2000). Triaxial testing of unsaturated samples of undisturbed residual soil from Singapore. *Proceed. of the Unsaturated Soils for Asia*, Singapore, Balkema: 581-586.
- Toll, D. G., Malandraki, V., Ali Rahman, Z. and Gallipoli, D. (2006). Bonded soils: Problematic or Predictable? *Proc. 2<sup>nd</sup> International Conference on Problematic Soils*, Malaysia, Singapore, CI-Premier: 55-62
- Uriel, R. S. and Serrano, A. A. (1973). Geotechnical properties of two collapsible soils of low bulk densities at the site of two dam in Canary Island, Spain. *Proceed. 8th Intl. Conf. Soil Mechanics Foundation and Engineering*, Moscow: 257-264.



- Vanapalli, S. K., Fredlund, D. G., Pufahl, D. E. and Clifton, A. W. (1996). Model for the prediction of shear strength with respect to soil suction. *Canadian Geotechnical Journal*, **33**: 379-392.
- Vargas, H. (1953). Some engineering properties of residual clay soils occurring in southern Brazil. *Proceed. of the 3rd Intl. Conference in Soil Mechanics and Foundation Engineering*, Switzerland: 84-90.
- Vassallo, R. and Mancuso, C. (2000). Soil behaviour in the small and large strain range under controlled suction conditions. *Experimental Evidence and Theoretical Approaches in Unsaturated Soils*, Rotterdam, Balkema: 75-89.
- Vaughan, P. R. (1985). Mechanical and hydraulic properties of in-situ residual soils. *General Report, Session 2, 5th Intl. Conf. on Geomechanics in Tropical Lateritic and Saprolitic Soil*, Brasilia: 231-263.
- Vaughan, P. R. (1988). Characterising the mechanical properties of in-situ residual soil. *Proceed. 2nd Intl. Conf. Geomechanics in Tropical Soils*, Singapore, Balkema: 469-487.
- Vaughan, P. R., Maccarini, M. and Mokhtar, S. M. (1988). Indexing the engineering properties of residual soil. *Quarterly Journal of Engineering Geology*, **21**: 61-84.
- Walker, S. C., Gallipoli, D. and Toll, D. G. (2005). The effect of structure on the water retention of soil tested using different methods of suction measurement. *Advanced Experimental Unsaturated Soil Mechanics Experus 2005*, Trento, Balkema: 33-39.
- Wang, Q., Pufahl, D. E. and Fredlund, D. G. (2002). A study of critical state on an unsaturated silty soil. *Canadian Geotechnic. Journal*, **39**: 213-218.
- Wesley, L. D. (1974). Discussion: Structural behaviour of residual soils of continually wet Highland of Papua New Guinea. *Geotechnique*, **24**: 101-105.
- Wheeler, S. J. and Karube, D. (1996). Constitutive modelling. In Alonso, E. E. and Delage, P. (eds.). *Unsaturated soils/Sols non satur'es*. Balkema: 1323-1356.
- Wheeler, S. J. and Sivakumar, V. (1995). An elasto-plastic critical state framework for unsaturated soil. *Geotechnique*, **45**: 35-53.
- Wong, J. C., Rahardjo, H., Toll, D. G. and Leong, E. C. (2000). Shear strength of undisturbed Bukit Timah granitic soil under infiltration conditions. *Unsaturated Soils for Asia*, Singapore, Balkema: 587-592.

- Yamamuro, J. A. and Lade, P. V. (1998). Steady-state concepts and static liquefaction of silty sands. *Geotechnical and Geoenvironmental Engineering*, 124: 868-877.
- Zakaria, I., Wheeler, S. J. and Anderson, W. F. (1995). Yielding of unsaturated compacted kaolin. In Alonso, E. E. and Delage, P. (eds.). *Unsaturated Soils/Sols Non Satures*, 1: 223-228.
- Zlatovic, S. and Ishihara, K. (1997). Normalized behaviour of very loose non-plastic soils: Effect of fabric. *Soils and Foundations*, 37: 47-56.



## APPENDIX I

From observation of the scatter in results of measurements when the variable is not changing, we can see an error  $E(x)$  compared to the mean value. The implications of these errors can be seen by propagating them through the calculations of other variables.

The “observed” errors will be those variables that are directly measure such as force (N), pressure (kPa), displacement (mm), volume change (cc), dimensions (mm) and weight (g).

### Calculation of Errors, $E$

---

For initial volume,  $V_o = \pi \frac{d_o^2}{4} h_o$

Taking account of errors:  $V_o \pm E(V_o) = \pi \frac{(d_o \pm E(d_o))^2}{4} (h_o \pm E(h_o))$

Therefore, the errors in measuring dimensions are  $\pm 0.01\text{mm}$  and  $d_o=38\text{mm}$  and  $h_o=76\text{mm}$ , so  $V_o=86192.7 \text{ mm}^3$ :

$$E(V_o) = \pi \frac{(d_o \pm E(d_o))^2}{4} (h_o \pm E(h_o)) - V_o$$

$$E(V_o) = \pi \frac{(38 \pm 0.01)^2}{4} (76 \pm 0.01) - 86192.7$$

$$E(V_o) = \pm 57 \text{ mm}^3 \quad [\text{For positive errors } E(V_o) = +57\text{mm}^3. \text{ For negative values } = -57\text{mm}^3]$$


---

For Volume,  $V = V_o - \delta V$

where  $\delta V$  is measured volume change in  $\text{mm}^3$

$$E(V) = (V_o \pm E(V_o)) - (\delta V \pm E(\delta V)) - V = (V_o \pm E(V_o)) - (\delta V \pm E(\delta V)) - (V_o - \delta V)$$

$$E(V) = \pm E(V_o) - \pm E(\delta V)$$

Taking the error in volume change is  $0.002 \text{ cc}$  ( $2 \text{ mm}^3$ ).

$$E(V) = \pm 57 - \pm 2$$

$$E(V) = \pm 59 \text{ mm}^3 \quad [\text{Note that worst case is when } E(V_o) \text{ is positive and } E(\delta V) \text{ is negative}]$$

---

For Height,  $H = H_o - \delta H$

where  $H_o$  is initial height and  $\delta H$  is measured height recorded by axial displacement (error in displacement is 0.005 mm)

$$E(H) = \pm E(H_o) - \pm E(\delta H)$$

Therefore;

$$E(H) = \pm 0.01 - \pm 0.005$$

$$E(H) = \pm 0.015 \text{ mm}$$

---

For void ratio,  $e$

$$e = \frac{V\rho_s}{m_d} - 1$$

where  $\rho_s$  is particle density and  $m_d$  is dry weight.

$$E(e) = \frac{(V \pm E(V))(\rho_s \pm E(\rho_s))}{(m_d \pm E(m_d))} - 1 - e$$

A typical dry weight is 145g and error in weighing is 0.1g, particle density is 2.66 g/cc (0.00266 g/mm<sup>3</sup>) and error is 0.01 g/cc (10<sup>-5</sup> g/mm<sup>3</sup>), for  $V=86193 \pm 59 \text{ mm}^3$  then:

$$E(e) = \frac{(86193 \pm 59)(0.0027 \pm 0.00001)}{(145 \pm 0.1)} - 1 - 0.605$$

$E(e) = \pm 0.008$  [Note that worst case is when  $E(V)$  and  $E(\rho_s)$  are positive and  $E(m_d)$  is negative]

---

For Area,  $A = \frac{V}{H}$

$$E(A) = \frac{V \pm E(V)}{H \pm E(H)} - A$$

For  $V=86193 \pm 59 \text{ mm}^3$  and  $H=76 \pm 0.015 \text{ mm}$ ,  $A=1134.1 \text{ mm}^2$

$$E(A) = \frac{86193 \pm 59}{76 \pm 0.015} - 1134.1$$

$$E(A) = \pm 1 \text{ mm}^2$$



---

For Deviator stress,  $q = \frac{F}{A}$

where  $F$  is force (N) and  $A$  is area ( $\text{mm}^2$ )

$$E(q) = \frac{F \pm E(F)}{A \pm E(A)} - q$$

The scatter for the load cell from the observation of reading before and after shearing stage is about 1.5N with  $\pm 0.8\text{N}$ .

If  $F=0 \pm 0.8 \text{ N}$  and  $A=1134 \pm 1 \text{ mm}^2$ , then  $q=0$  so  $E(q)=\pm 0.0071 \text{ N/mm}^2 = \pm 0.7 \text{ kPa}$

If  $F=2000 \pm 0.8 \text{ N}$  and  $A=1134 \pm 1 \text{ mm}^2$ , then  $q=1764 \text{ kPa}$  so  $E(q)= \pm 2.3 \text{ kPa}$

---

$$p' = \left[ \frac{q + 2\sigma_3}{3} \right] - u$$

Where  $\sigma_3$  is applied cell pressure

If  $q=1764 \pm 4 \text{ kPa}$  and  $\sigma_3=500 \pm 0.1 \text{ kPa}$  and  $u= 400 \pm 0.1 \text{ kPa}$

$p'=521$  so  $E(p')=\pm 1.8 \text{ kPa}$

Therefore, other typical values of  $q$  and  $p'$  need to be calculated using the same procedure

## APPENDIX II

A. Summary of the results of errors analysis for deviator stress  $E(q)$  and effective stress  $E(p')$  for the maximum  $q/p'$  ratio (Destructured samples in saturated tests)

### Drained tests

Applied $p_o'$	$q$ , kPa	$p'$ , kPa	$E(q)$ , kPa	$E(p')$ , kPa
15	49	33	0.72	0.44
20	78	49	0.73	0.44
50	149	101	0.80	0.47
100	269	191	0.90	0.50
200	397	332	0.98	0.53
300	777	557	1.36	0.65
400	941	715	1.49	0.70
500	1187	899	1.72	0.77
600	1342	1049	1.93	0.84
700	1597	1229	2.10	0.90
800	1746	1381	2.17	0.92
900	1955	1556	2.43	1.01
1000	2148	1719	2.62	1.07

### Undrained tests

Applied $p_o'$	$q$ , kPa	$p'$ , kPa	$E(q)$ , kPa	$E(p')$ , kPa
25	79	47	0.78	0.46
60	131	88	0.80	0.47
100	187	136	0.86	0.49
200	338	240	0.98	0.53
300	429	335	1.06	0.53
400	490	394	1.10	0.57
500	487	377	1.10	0.57
600	583	460	1.16	0.59
700	856	667	1.43	0.68
800	942	754	1.48	0.69
900	1096	831	1.63	0.74
1000	1327	1071	1.83	0.81



B. Summary of the results of errors analysis for deviator stress  $E(q)$  and effective stress  $E(p')$  for the maximum  $q/p'$  ratio (Bonded samples in saturated tests)

Drained tests

Applied $p_o'$	$q$ , kPa	$p'$ , kPa	$E(q)$ , kPa	$E(p')$ , kPa
15	132	59	0.83	0.48
30	202	101	0.89	0.50
50	266	140	0.95	0.52
100	361	219	1.02	0.54
200	575	392	1.21	0.60
300	745	547	1.33	0.64
400	936	710	1.49	0.70
500	1284	925	1.84	0.81
600	1483	1094	2.01	0.90
700	1594	1227	2.11	0.90
800	1721	1372	2.22	0.94
900	1857	1521	2.34	0.98
1000	2061	1683	2.52	1.04

Undrained tests

Applied $p_o'$	$q$ , kPa	$p'$ , kPa	$E(q)$ , kPa	$E(p')$ , kPa
25	143	73	0.83	0.48
30	199	98	0.89	0.50
50	249	142	0.93	0.51
100	385	232	1.05	0.55
200	599	398	1.23	0.61
300	764	542	1.38	0.66
400	979	685	1.60	0.73
500	1218	871	1.75	0.78
600	1304	949	1.86	0.82
700	1451	1095	1.99	0.86
800	1583	1185	2.10	0.90
900	1751	1360	2.25	0.95
1000	1848	1462	2.33	0.98

## APPENDIX III

A. Summary of the results of errors analysis for deviator stress  $E(q)$ , effective stress  $E(p')$  and void ratio  $E(e)$  for the Critical State (Destructured samples in saturated tests)

### Drained tests

Applied $p_o'$	$q$ , kPa	$p'$ , kPa	$e$	$E(q)$ , kPa	$E(p')$ , kPa	$E(e)$
15	42	31	0.6083	0.63	0.41	0.0081
20	72	48	0.6116	0.59	0.40	0.0082
50	135	97	0.6097	0.66	0.42	0.0082
100	250	185	0.6045	0.81	0.47	0.0081
200	361	321	0.6068	0.84	0.48	0.0081
300	741	545	0.6073	1.21	0.60	0.0081
400	852	686	0.6042	1.26	0.62	0.0081
500	1064	857	0.6071	1.41	0.67	0.0081
600	1341	1049	0.6032	1.72	0.77	0.0081
700	1599	1231	0.6044	1.84	0.81	0.0080
800	1746	1381	0.6099	1.84	0.81	0.0080
900	1955	1556	0.6024	2.06	0.89	0.0080
1000	2150	1720	0.6017	2.17	0.92	0.0080

### Undrained tests

Applied $p_o'$	$q$ , kPa	$p'$ , kPa	$e$	$E(q)$ , kPa	$E(p')$ , kPa	$E(e)$
25	247	195	0.6048	0.75	0.45	0.0083
60	311	260	0.6103	0.78	0.46	0.0083
100	356	294	0.6018	0.90	0.50	0.0083
200	496	387	0.6093	1.06	0.55	0.0083
300	611	510	0.6103	1.18	0.59	0.0084
400	873	769	0.6097	1.38	0.66	0.0083
500	756	652	0.6022	1.27	0.62	0.0083
600	911	784	0.6152	1.36	0.65	0.0083
700	1136	922	0.6092	1.65	0.75	0.0083
800	1151	980	0.6047	1.63	0.74	0.0082
900	1341	1083	0.6070	1.82	0.81	0.0083
1000	1561	1321	0.6113	2.02	0.87	0.0083



B. Summary of the results of errors analysis for deviator stress  $E(q)$ , effective stress  $E(p')$  and void ratio  $E(e)$  for the Critical State (Bonded samples in saturated tests)

Drained tests

Applied $p_o'$	$q$ , kPa	$p'$ , kPa	$e$	$E(q)$ , kPa	$E(p')$ , kPa	$E(e)$
15	58	36	0.6062	0.69	0.43	0.0082
30	123	76	0.6048	0.73	0.44	0.0082
50	166	108	0.6063	0.76	0.45	0.0083
100	235	179	0.5995	0.82	0.47	0.0082
200	419	341	0.6092	1.00	0.53	0.0083
300	638	512	0.6061	1.17	0.59	0.0082
400	734	644	0.6060	1.25	0.62	0.0082
500	1131	876	0.6031	1.65	0.75	0.0083
600	1313	1037	0.6087	1.81	0.80	0.0083
700	1411	1167	0.6097	0.18	0.14	0.0083
800	1628	1341	0.6092	2.11	0.90	0.0083
900	1844	1515	0.6026	2.32	0.97	0.0083
1000	2030	1673	0.6063	2.49	1.03	0.0083

Undrained tests

Applied $p_o'$	$q$ , kPa	$p'$ , kPa	$e$	$E(q)$ , kPa	$E(p')$ , kPa	$E(e)$
25	425	336	0.6100	0.99	0.53	0.0083
30	392	320	0.6015	0.97	0.52	0.0082
50	441	386	0.6102	1.01	0.54	0.0083
100	497	375	0.6135	1.07	0.56	0.0084
200	724	605	0.6083	1.27	0.62	0.0083
300	863	754	0.6044	1.40	0.67	0.0083
400	944	799	0.6012	1.50	0.70	0.0083
500	1166	931	0.5998	1.64	0.75	0.0082
600	1253	1014	0.6035	1.75	0.78	0.0083
700	1452	1195	0.6017	1.95	0.85	0.0083
800	1519	1176	0.6081	2.01	0.87	0.0083
900	1640	1296	0.6085	2.11	0.90	0.0083
1000	1727	1371	0.6035	2.19	0.93	0.0083